



**HAL**  
open science

# Muon production from heavy-flavour hadron decays in p-Pb and pp collisions with ALICE at the CERN-LHC

Shuang Li

► **To cite this version:**

Shuang Li. Muon production from heavy-flavour hadron decays in p-Pb and pp collisions with ALICE at the CERN-LHC. Other [cond-mat.other]. Université Blaise Pascal - Clermont-Ferrand II, 2015. English. NNT : 2015CLF22602 . tel-01294986

**HAL Id: tel-01294986**

**<https://theses.hal.science/tel-01294986>**

Submitted on 30 Mar 2016

**HAL** is a multi-disciplinary open access archive for the deposit and dissemination of scientific research documents, whether they are published or not. The documents may come from teaching and research institutions in France or abroad, or from public or private research centers.

L'archive ouverte pluridisciplinaire **HAL**, est destinée au dépôt et à la diffusion de documents scientifiques de niveau recherche, publiés ou non, émanant des établissements d'enseignement et de recherche français ou étrangers, des laboratoires publics ou privés.

Numéro d'ordre : DU 2602  
EDSF : 833

PCCF T 1510

CENTRAL CHINA NORMAL UNIVERSITY  
UNIVERSITÉ BLAISE PASCAL

# PHD THESIS

présentée pour obtenir le grade de

DOCTOR OF UNIVERSITY

Spécialité : PHYSIQUE CORPUSCULAIRE

Par

Shuang LI

## Muon production from heavy-flavour hadron decays in p–Pb and pp collisions with ALICE at the CERN-LHC

defended on October 6, 2015

**Jury :**

<i>Examineurs:</i>	R. AVERBECK	–	GSI, Darmstadt
	Y. MA	–	SINAP, Shanghai
	F. PRINO	–	INFN, Torino
	Z. YIN	–	CCNU, Wuhan
	P. ZHUANG	–	THU, Beijing
<i>Directeurs de thèse:</i>	N. BASTID	–	LPC, Clermont–Ferrand
	P. CROCHET	–	LPC, Clermont–Ferrand
	D. ZHOU	–	CCNU, Wuhan
<i>Invited:</i>	X. ZHANG	–	LBNL, CERN



分类号\_\_\_\_\_

密级\_\_\_\_\_

UDC \_\_\_\_\_

编号\_\_\_\_\_

华中师范大学

博士学位论文

题目：LHC/ALICE 实验向前区

重夸克冷核效应的研究

学位申请人姓名：李双

申请学位学生类别：全日制博士

申请学位学科专业：粒子物理与原子核物理

指导教师姓名：周代翠 教授

菲利普·胡克 资深研究员

妮可·巴斯蒂 教授





博士学位论文  
DOCTORAL DISSERTATION



# 博士学位论文

## LHC/ALICE 实验向前区重夸克 冷核效应的研究

论文作者：李双

指导教师：周代翠          教授

菲利普·胡克    资深研究员

妮可·巴斯蒂    教授

学科专业：粒子物理与原子核物理

研究方向：高能重离子碰撞实验

华中师范大学物理科学与技术学院

2015年10月



博士学位论文  
DOCTORAL DISSERTATION



# Dissertation

## **Muon production from heavy-flavour hadron decays in p-Pb and pp collisions with ALICE at the CERN-LHC**

By

**Shuang Li**

**Supervisors: Pr. Daicui Zhou**

**Dr. Philippe Crochet**

**Pr. Nicole Bastid**

**Specialty: Particle Physics and Nuclear Physics**

**Research Area: Heavy-Ion Collision Experiment**

**College of Physical Science and Technology**

**Central China Normal University**

**October 2015**



## 华中师范大学学位论文原创性声明和使用授权说明

### 原创性声明

本人郑重声明：所呈交的学位论文，是本人在导师指导下，独立进行研究工作所取得的研究成果。除文中已经标明引用的内容外，本论文不包含任何其他个人或集体已经发表或撰写过的研究成果。对本文的研究做出贡献的个人和集体，均已在文中以明确方式标明。本声明的法律结果由本人承担。

作者签名：

日期： 年 月 日

### 学位论文版权使用授权书

学位论文作者完全了解华中师范大学有关保留、使用学位论文的规定，即：研究生在校攻读学位期间论文工作的知识产权单位属华中师范大学。学校有权保留并向国家有关部门或机构送交论文的复印件和电子版，允许学位论文被查阅和借阅；学校可以公布学位论文的全部或部分内容，可以允许采用影印、缩印或其它复制手段保存、汇编学位论文。（保密的学位论文在解密后遵守此规定）

保密论文注释：本学位论文属于保密，在 \_\_\_\_ 年解密后适用本授权书。

非保密论文注释：本学位论文不属于保密范围，适用本授权书。

作者签名：

导师签名：

日期： 年 月 日

日期： 年 月 日

本人已经认真阅读“CALIS 高校学位论文全文数据库发布章程”，同意将本人的学位论文提交“CALIS 高校学位论文全文数据库”中全文发布，并可按“章程”中的规定享受相关权益。同意论文提交后滞后： 半年； 一年； 二年发布。

作者签名：

导师签名：

日期： 年 月 日

日期： 年 月 日





## 摘要

自上世纪中期以来,随着高能加速器和探测器的快速发展,大量的新粒子被发现。按照其相互作用特性,它们可以分为:强子,轻子和传递相互作用的媒介子。强子直接参与强相互作用,如:质子,中子和 $\pi$ 介子。轻子直接参与电磁和弱相互作用,如:电子和 $\mu$ 子。随着碰撞能量的升高,我们发现,强子是具有内部结构的。根据标准模型,强子由夸克组成,它们携带色荷,夸克间的强相互作用是通过传递色荷完成的,其对应的传播子称为胶子。夸克和胶子又被统称为部分子。部分子之间的强相互作用由量子色动力学(QCD)来描述。与电磁相互作用(阿贝尔色相互作用)不同,强相互作用(非阿贝尔色相互作用)具有渐近自由的性质,也就是说,量子色动力学耦合常数依赖于相互作用的能量交换:相互作用部分子处于低能或者远距离时表现出强耦合;高能或者近距离时则表现出弱耦合特性。强耦合状态下,部分子被“囚禁”在强子内部而不呈现出自由的状态,即:色禁闭。此时,相关计算只能采用非微扰理论来进行,例如格点QCD(LQCD)。弱耦合状态下,部分子的热动能可能超过将其囚禁在强子中所需的束缚能,从而导致强子“融化”,退禁闭的自由部分子可能形成一种新的物质形态——夸克胶子等离子体(Quark-Gluon Plasma, QGP, 亦为夸克物质)。夸克物质态可以使用微扰QCD理论进行表征。根据LQCD的计算,在低重子数密度的条件下,原本破缺的手征对称性得到恢复,而且随着物理(非微扰)真空的消失,夸克的组分质量将回归到流质量。此外,LQCD还预言,QGP形成时的临界温度和能量密度分别为 $T_c = 154 \pm 9 \text{ MeV}$ 和 $\epsilon_c = 0.34 \pm 0.16 \text{ GeV/fm}^3$ 。宇宙大爆炸理论认为,QGP物质可能存在于大爆炸后数 $\mu\text{s}$ 的早期宇宙(极端高温),以及正在塌陷的中子星内部(高重子数密度)。最近的研究结果还表明,当重子数密度足够高时,费米面附近带不同色荷的夸克由于吸引相互作用可以形成库帕对,产生色超导,使得零温零密时的色对称性在高物质密度时会自发破缺。因此,对QGP物质信号和其性质的研究,能使我们理解多粒子体系的强相互



作用性质，了解早期宇宙的演化，认识质量的起源。因此，夸克退禁闭相变和 QGP 物质特性的研究成为当今物理学特别是高能核物理领域前沿重大课题。

在实验室条件下，高能重离子碰撞是产生极端高温高密环境的唯一途径，它为 QGP 物质的形成提供了必要条件。被剥离带电的两入射原子核被加速到接近于光速实现猛烈对撞，深度非弹性过程导致两核的巨大动能转化为热能沉积在碰撞中心区，在一个有限空间范围内形成极端高温或高重子密度环境，诱导强子物质解除夸克禁闭，形成夸克胶子等离子体这种新物质形态。由于夸克物质体系的膨胀和冷却，QGP 物质相又冻结为强子相，发射出末态可观测的粒子。截止目前，国际上已经先后建造了若干个高能重离子加速器，例如，欧洲核子研究中心 (CERN) 的超级质子同步加速器 (SPS) 和大型强子对撞机 (LHC)，美国布鲁克海文国家实验室 (BNL) 的交变梯度同步加速器 (AGS) 和相对论重离子对撞机 (RHIC)，以及正在建造的德国 GSI 实验中心的 FAIR 固定靶实验加速器。自上世纪七十年代以来，理论和实验工作者已经对 QGP 物质的性质进行了卓有成效的研究。在这些实验中发现的典型的 QGP 信号有：

### 1. SPS 能区

(1) 奇异粒子产额明显增强，被解释为手征对称性在退禁闭物质相中得到恢复，而使得奇异夸克在 QGP 物质中产生阈值的降低（流质量）；

(2)  $J/\psi$  粒子产额压低，被认为是粲夸克偶素 ( $c\bar{c}$ ) 在 QGP 物质中 Debye 屏蔽势作用下熔解而致；

### 2. RHIC 能区

(1) 不同种类带电强子椭圆流的组分夸克数目的标度特性，揭示了部分子在 QGP 内的热化自由度；

(2) 高横动量区域强子谱压低以及喷注强子背向关联的减弱，反映了高能部分子在穿越 QGP 热密介质时发生强相互作用，诱导部分子辐射能量损失所致。

上述实验观测结果与相应理论描述一致，证明了 QGP 物质的存在。



为了系统的深入地研究 QGP 物质性质, 欧洲核子研究中心 (CERN) 建造了目前世界上最高能量的大型强子对撞机 (LHC), 其中有 ALICE, ATLAS, CMS 和 LHCb 四大实验探测装置, 于 2009 年 11 月正式投入运行。其中, ALICE 探测装置专门致力于夸克物质信号及其性质的探测, 并于 2010 和 2011 两个年度采集了质心能量  $\sqrt{s_{NN}} = 2.76$  TeV 铅-铅碰撞数据。相对于 RHIC 能区 ( $\sqrt{s_{NN}} = 200$  GeV 金-金碰撞), LHC 能区实现更重的铅核-铅核碰撞, 其核子-核子质心系能量增大 13-27 倍, 形成的 QGP 系统较前者具有更高温度、更大能量密度、更大的体积和更长的寿命。这为系统地研究 QGP 物质的性质提供了独特的有利条件。

重夸克 (粲夸克和底夸克) 是探测 QGP 信号的黄金探针之一。由于大质量特性, 重夸克主要产生于碰撞初期的硬散射过程, 且重夸克具有更短的形成时间和更硬的碎裂函数。因此, (1) 重夸克早于 QGP 物质形成, 并能穿越随后形成的热密 QGP 介质, 它携带额初始碰撞和 QGP 系统演化阶段的信息; (2) 重夸克的运动学特性可以很好的被其碎裂末态强子所继承。而 LHC 又是当前国际高能实验的能量前沿, 能诱导产生丰富的重夸克产额。因此, 重夸克成为揭示 QGP 物质特性的独特探针。

高能重夸克在穿越热密 QGP 介质时, 将与其组成部分子发生强相互作用而发生胶子辐射, 从而导致重夸克辐射能量损失。根据微扰 QCD (pQCD) 理论预言, 在穿越 QGP 媒质过程中, 相对于夸克, 胶子有更大的辐射能量损失, 而较之轻夸克, 重夸克辐射胶子的几率在一定锥角范围内 (与夸克质量有关) 会被压低, 称之为死角效应, 从而导致重夸克的能量损失比轻夸克小。部分子的能量损失效应可以体现在由其碎裂强子的分布函数上。在实验上, 通过观测末态强子的核修正因子  $R_{AA}$  的大小来表征该效应。 $R_{AA}$  定义为核-核 (如金-金和铅-铅) 碰撞中单位碰撞数诱导产生的粒子产额与核子-核子 (如质子-质子) 碰撞中的粒子产额之比。基于重夸克辐射能量损失的死角效应, 重味强子的  $R_{AA}$  应大于轻强子。但这一现象并未在 RHIC 能区上观测到。已有的 LHC 能区实验结果表明, 在误差范围内, 重味强子的  $R_{AA}$  与轻强子的  $R_{AA}$  一致。随后, 理论研究显示, 这主要是由于轻夸克和胶子的碎裂函数破坏了原有部分子层次上的压低行为。LHC 能区丰富的重夸克产额, 为新的实



验观测量，即：重轻比（开粲或开美强子的  $R_{AA}$  与轻强子的  $R_{AA}$  比值）测量提供了机遇。带粲强子与轻强子之间的重轻比可以反映部分子能量损失对色荷的依赖性，而带底强子与轻强子间的重轻比则可以描述部分子能量损失对其质量的依赖关系。

在质心系能量  $\sqrt{s_{NN}} = 2.76$  TeV 铅-铅对心碰撞中，我们的研究发现，向前区重夸克衰变  $\mu$  子产额的  $R_{AA}$  在高横动量区间呈现出较强的压低特性，它被解释为与 QGP 媒质形成有关的热核效应导致。同时，基于热核效应的理论预言也能够很好的反映实验观测结果。但是，碰撞过程中的冷核效应，即：与 QGP 媒质形成无关的核效应（如：核遮蔽，内禀横动量增宽以及胶子饱和等）对该压低行为的贡献如何，此前人们并不清楚。深入理解冷核效应可以通过研究核子-核（如质子-铅或氩-金）碰撞来实现。在向前区，对冷核效应的相关测量更具优势。相对于中心区，它对应着更大 Bjorken 变量范围。在 2014 年，RHIC 报道了质心系能量  $\sqrt{s_{NN}} = 200$  MeV 氩-金碰撞中重夸克衰变  $\mu^-$  的核修正因子在快度（横动量）范围  $1.4 < |y_{CMS}| < 2.0$  ( $1 < p_T < 6$  GeV/c) 内的测量结果。在低横动量区间，向前区（向后区）存在压低（增强）行为。相应的 Bjorken 变量可以达到  $10^{-3}$  ( $10^{-2}$ )。2013 年，ALICE 对质子-铅（p-Pb）在质心系能量  $\sqrt{s_{NN}} = 5.02$  TeV 碰撞的向前区和向后区分别进行了实验取数。位于向前快度区间的  $\mu$  子谱仪使得相关测量达到极小的 Bjorken 变量：向前区  $\sim 10^{-6}$ ；向后区  $\sim 10^{-3}$ 。显然，相对于 RHIC，ALICE 为研究冷核效应提供了更加有利的条件。此外，ALICE 实验的大统计量数据还允许我们达到更高横动量区域。

本工作基于 ALICE 探测装置和其向前  $\mu$  子谱仪采集的质心系能量 5.02 TeV 质子-铅核碰撞实验数据，重建粒子径迹和质子-铅反应事件，测量最小无偏碰撞和不同碰撞中心度下单举  $\mu$  子横动量谱，扣除各类轻强子  $\pi^\pm$ 、 $K^\pm$  等衰变背景贡献，计算  $\mu$  子重建效率，研究系统误差，得到扣除本地后的重味（粲和底）夸克半轻衰变道  $\mu$  子的产物，计算 p-Pb 碰撞中重夸克衰变  $\mu$  子的产额的核修正因子  $R_{pPb}$  和  $R_{Pbp}$ ，以及向前区一向后区核修正因子  $R_{pPb}$  和  $R_{Pbp}$  的对称性  $R_{FB}$  的实验观测结果，比较模型预言，研究质子-铅核碰撞中的重夸克产生是否存在压低行为，检验冷核效应。



在本工作第一章，我们对 QGP 特性和高能重离子碰撞做简要的介绍，综述了在 SPS, RHIC 和 LHC 能区实验中对 QGP 物质信号的观测结果，以及重夸克穿越 QGP 物质的能量损失效应。第二章介绍 ALICE 探测装置，并重点介绍向前区  $\mu$  子谱仪的各个组成部分以及性能。考虑到已经开始的实验装置升级计划，在本章最后部分，对 ALICE 目前的升级现状进行了简要介绍和讨论。第三章至第五章，主要讨论实验数据分析的具体过程和相应的误差估算。包括初始数据的筛选，效率修正，用做参照的 pp 碰撞结果估算以及背景减除。第六章讨论了系统误差来源，介绍了各种误差计算步骤，进一步系统地计算了各类系统误差及其影响。给出了质心系能量  $\sqrt{s_{NN}} = 5.02$  TeV 质子-核碰撞中向前区和向后区重夸克衰变  $\mu$  子的产生截面。在本论文的最后，我们对以上工作进行了总结和展望。

本研究表明，在最小无偏碰撞中向前区冷核效应导致的压低行为并不明显；而在向后区，明显地增强特性出现在低横动量区间。该结论同 RHIC 测量结果一致。在实验和理论误差范围内，实验结果可以被相关的理论预言所描述。在对不同中心度下的核修正因子的实验观测中发现，在向前区的  $R_{pPb}$  变化并不显著，然而发现在向后区的核修正因子  $R_{pPb}$  对碰撞中心度有明显的依赖特性。综上所述，本工作结果表明，冷核效应对核修正因子的影响较小，这个实验结果证实，在核-核碰撞中观测到的重夸克衰变  $\mu$  子谱在高横动量区间的明显压低现象，主要由热核效应导致。我们比较了与理论的预言，结果显示，理论描述与实验结果一致。为深入揭示部分子在 QGP 介质内的能量损失机制给出了新的线索。

**关键词：**大型强子对撞机 (LHC)；大型重离子碰撞实验 (ALICE)；质子-核碰撞；重夸克产生；重夸克半轻衰变产物  $\mu$  子；核修正因子 ( $R_{pPb}$  和  $R_{pPb}$ )；向前区-向后区对称性 ( $R_{FB}$ )；检测冷核效应



## Résumé

### Introduction

Les collisions d'ions lourds à haute énergie représentent un champ de recherche qui fait l'objet d'une activité intense depuis la fin des années 80. Le but est d'étudier les propriétés d'un nouvel état de la matière, le plasma de quarks et de gluons (QGP), qui se forme dans des conditions extrêmes de température et de pression. La théorie de l'interaction forte, la Chromodynamique Quantique, prédit que la température critique et la densité d'énergie critique correspondant à la transition de phase vers le QGP sont respectivement  $T_c = 154 \pm 9$  MeV et  $\varepsilon_c = 0.34 \pm 0.16$  GeV/fm<sup>3</sup>. De telles conditions sont souvent qualifiées d'extrêmes. En unités courantes, elles correspondent à une densité de  $10^{15}$ g/cm<sup>3</sup> et une température de  $10^{12}$ K. Ces conditions sont celles dans lesquelles baignait l'univers quelques microsecondes après le big bang. Le QGP peut être créé en laboratoire en faisant entrer en collision des noyaux lourds, tels que l'or ou le plomb, préalablement accélérés à des vitesses proches de celle de la lumière. De telles collisions entre ions lourds, dites ultra-relativistes, permettent d'étudier les propriétés d'un système de matière partonique dense et chaud.

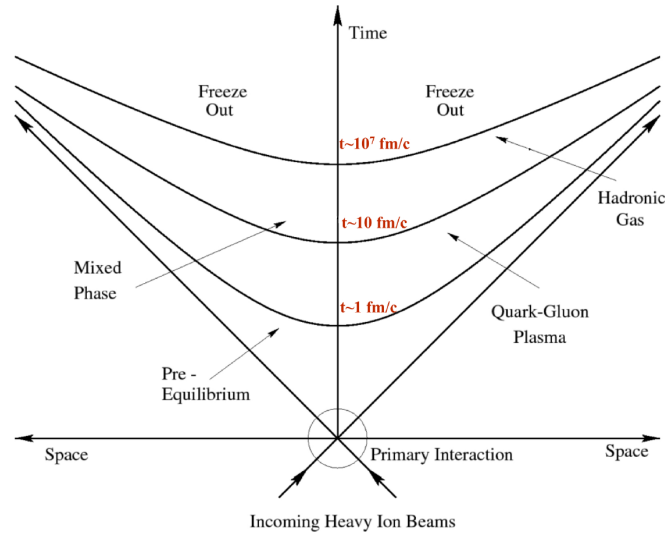


Figure 1: Représentation schématique de l'évolution spatio-temporelle d'une collision d'ions lourds ultra-relativistes.

La figure 1 présente l'évolution spatio-temporelle d'une collision d'ions lourds ultra-relativistes qui peut être résumée comme suit :

- **Etat initial** : Les noyaux sont accélérés à des vitesses proche de la vitesse de la lumière. Dans le référentiel du laboratoire, ils sont aplatis dans la direction du faisceau en raison de la contraction de Lorentz. Aux énergies du LHC, le facteur de contraction de Lorentz est  $\gamma \sim 1500$ . Les noyaux sont alors comprimés dans  $\sim 0.01$  fm, d'ou leur aspect en forme de crêpe. Les nucleons des

deux noyaux entrant en collision sont appelés les participants. Leur nombre total est noté  $N_{\text{part}}$ . Les autres nucléons sont appelés les spectateurs. Le nombre total d'interactions binaires est noté  $N_{\text{coll}}$ . La distance entre le centre des noyaux en collision dans la direction perpendiculaire aux faisceaux est appelée le paramètre d'impact et noté  $b$ . Le degré de centralité de la collision peut être estimé de façon purement géométrique au moyen du modèle de Glauber optique.

- **Pré-équilibre** : La collision se produit dans la région de recouvrement des noyaux en collision et une grande quantité d'énergie est déposée au voisinage du point d'impact. Des partons sont produits dans cet environnement de haute densité d'énergie au moyen de processus durs ( $\tau \sim 0$ ). L'état de pré-équilibre dure pendant un temps typique de  $\tau \sim 1 \text{ fm}/c$ . Les particules de grand moment transverse (jets, quarks lourds et photons) sont principalement produites pendant cette phase. En particulier, les quarks charmés sont produits sur une échelle de temps de  $1/2m_Q \sim 0.1 \text{ fm}/c$ .
- **QGP** : Si la densité d'énergie est suffisamment élevée, le système atteint le QGP, phase de déconfinement caractérisée par des degrés de liberté quarkoniques et gluoniques. Cette phase dure pendant un temps typique de l'ordre de  $10 \text{ fm}/c$  aux énergies du LHC.
- **Hadronisation et freeze-out** : Le système se détend et se refroidit. La température décroît en deçà de la température critique  $T_c$ . Il en résulte une transition de phase entre le QGP et un gaz hadronique. Durant cette étape, des sous-systèmes QGP et gaz hadronique peuvent co-exister. Les interactions inélastiques entre hadrons continuent jusqu'au freeze-out chimique après lequel les interactions élastiques entre hadrons continuent jusqu'au freeze-out cinétique (indiqué "freeze-out" sur la figure 1). Finalement, les particules produites (hadrons et leptons principalement) sont identifiées par les détecteurs.

Jusqu'à maintenant plusieurs expériences de collisions d'ions lourds ultra-relativistes ont été menées auprès du SPS (Super Proton Synchrotron) et du LHC (Large Hadron Collider) au CERN (Centre Européen pour la Recherche Nucléaire) et auprès du RHIC (Relativistic Heavy Ion Collider) au BNL (Brookhaven National Laboratory) aux Etats Unis. De nombreuses signatures de la formation du QGP en laboratoire ont été obtenues. Quelques-unes d'entre elles sont brièvement résumées ci-après.

A cause de leur masse élevée, les hadrons composés de deux ou trois quarks étranges, comme le  $\Xi(\text{uss})$  ou  $\Omega(\text{sss})$ , ont des taux de production faibles. Cependant, dans un QGP, la production d'étrangeté est supposée être augmentée en raison de la restauration de la Symétrie Chirale qui implique une diminution de la masse des quarks. Il a donc été avancé qu'une augmentation de la production d'hadrons étranges pouvait être considérée comme une signature de la formation d'un QGP. Le facteur d'augmentation  $E$ , montré sur la figure 2, est défini comme le rapport du taux de particules étranges (i.e. hadrons composés de quark(s) étrange(s)) dans les

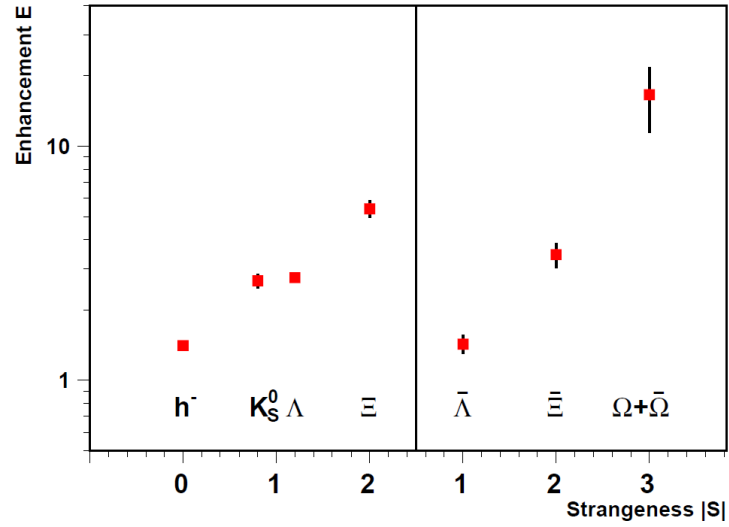


Figure 2: Facteur d'augmentation de particules produites à mi-rapacité par nucléons participants dans les collisions Pb–Pb et p–Pb à 158  $A$  GeV/c.

collisions Pb–Pb relativement à celui mesuré dans les collisions p–Pb. Ce facteur augmente considérablement en fonction du nombre de nucléons participants et il augmente d'autant plus que les particules contiennent plus de quarks étranges e.g. une augmentation de 17 pour les  $\Omega$  and les  $\bar{\Omega}$ .

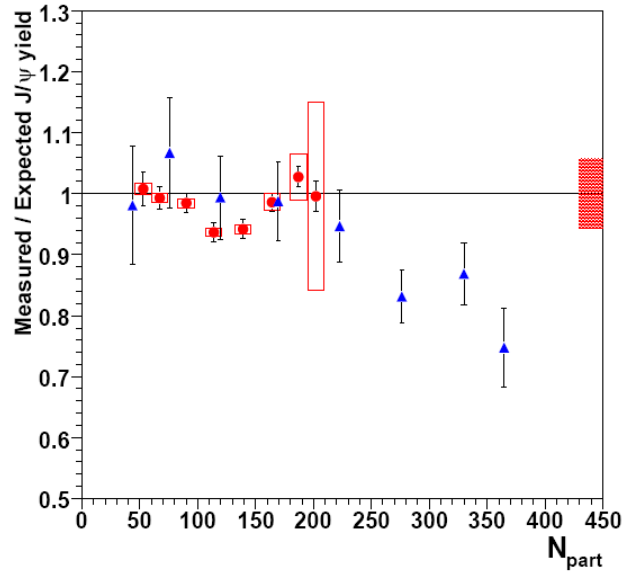


Figure 3: Rapport du taux de production mesuré des  $J/\psi$  sur le taux attendu en absence de suppression anormale, en fonction de  $N_{part}$  dans les collisions In–In (rouge) et Pb–Pb (bleu) aux énergies du SPS.

Les quarkonia se déclinent en charmonia pour les états de type  $c\bar{c}$  et bottomonia pour les états de type  $b\bar{b}$ . Les principaux états charmonia sont  $J/\Psi$  ( $m = 3.1$  GeV/ $c$ , 1S),  $\chi_{c1}$  et  $\Psi'$  (respectivement  $m = 3.5$  et  $3.7$  GeV/ $c$ , 1P et 2S). Les principaux états bottomonia sont  $\Upsilon$  ( $m = 9.5$  GeV/ $c$ , 1S),  $\Upsilon'$  et  $\Upsilon''$  (respectivement  $m = 10.0$  et  $10.4$  GeV/ $c$ , 2S et 3S). Dans les collisions d'ions lourds, la production de quarkonia est affectée par les effets suivants :

- Ecrantage nucléaire : dans un noyau, la fonction de distribution partonique (PDF) dans le nucléon n'est pas une simple superposition de celle d'un nucléon libre. On parle alors de fonction de distribution partonique nucléaire (nPDF). Les PDF modifiées par l'effet d'écrantage à petit  $x$  (variable de Bjorken définie comme la fraction d'impulsion portée par un parton dans le nucléon) jouent un rôle important dans la production de quarks lourds.
- Absorption nucléaire et hadronique : la paire de quarks lourds  $Q\bar{Q}$  peut être détruite par des processus de diffusion inélastique avec les nucléons des noyaux en collision quand elle se propage dans le milieu. Cette suppression est appelée suppression normale.
- Ecrantage de couleur de Debye : la production de quarkonia est supposée être supprimée en présence d'un QGP en raison de l'écrantage de couleur de Debye du potentiel quark-antiquark dans un milieu partonique déconfiné. La longueur d'écrantage de couleur de Debye dépend de la température du QGP. Les différents états quarkonia ayant différentes énergies de liaison, ils ont différentes tailles et sont donc supposés être dissociés à différentes températures.

La figure 3 montre les mesures rapportées aux résultats attendus en présence de suppression normale, dans les collisions d'ions lourds aux énergies du SPS. On constate que le rapport est consistant avec l'unité dans les collisions périphériques (i.e. petits  $N_{\text{part}}$ ) Pb–Pb, ce qui met en évidence le scénario de suppression normale. En revanche, une suppression anormale apparaît dans les collisions centrales (i.e. grands  $N_{\text{part}}$ ). Ce résultat a été interprété comme la manifestation de l'écrantage de couleur de Debye et peut être considéré comme étant une signature de la présence du QGP.

Les dileptons n'étant pas sensibles à l'interaction forte, ils fournissent de précieuses informations sur les propriétés du système dense et chaud produit dans les collisions d'ions lourds. Dans la région de faible masse invariante,  $M_{l+l-} < 1$  GeV/ $c^2$ , la production de dileptons est gouvernée par le couplage des mésons vecteur légers, comme le  $\rho$ , l' $\omega$  et le  $\phi$ , avec le milieu. Dans la région de masse intermédiaire,  $M_{l+l-} > 1$  GeV/ $c^2$ , la radiation thermique du QGP (appelé dileptons thermiques), devient importante. La région des grandes masses est associée aux premiers instants de la collision. La production de dileptons thermique est une sonde propre et pénétrante pour l'étude des propriétés du QGP. La figure 4 montre le spectre de masse invariante  $e^+e^-$  mesuré par la collaboration STAR dans les collisions Au–Au à  $\sqrt{s_{\text{NN}}} = 200$  GeV. On constate que le rapport des mesures avec le cocktail est consistant avec l'unité, en considérant les incertitudes, dans la région  $M_{l+l-} > 1$

$\text{GeV}/c^2$ , tandis qu'un écart important (augmentation) est observé dans la région de masse invariante  $M_{l+l-} < 1 \text{ GeV}/c^2$ . Cette tendance est bien reproduite par des prédictions théoriques reposant sur la brisure spontanée de la Symétrie Chirale. Dans la région  $M_{l+l-} > 1 \text{ GeV}/c^2$ , les prédictions théoriques suggèrent que la fonction spectrale des mésons vecteurs peut être modifiée dans le milieu dense et chaud, ce qui aurait pour origine la restauration de la Symétrie Chirale.

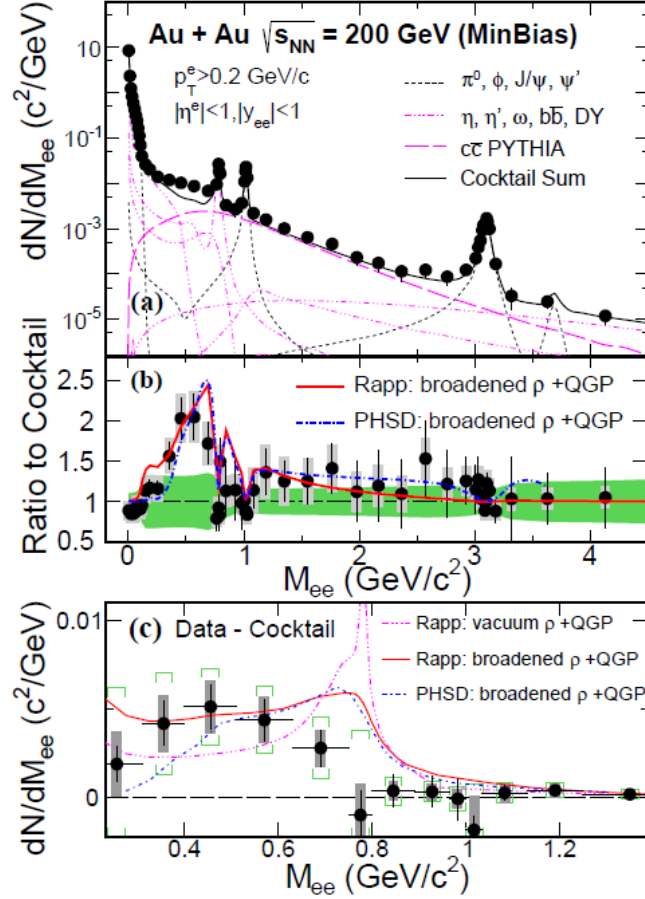


Figure 4: (a) spectre de masse invariante  $e^+e^-$  mesuré dans les collisions Au–Au de biais minimum (centralité 0 – 80%) à  $\sqrt{s_{\text{NN}}} = 200 \text{ GeV}$  comparé à une simulation basée sur un cocktail hadronique. Les barres verticales correspondent aux fluctuations statistiques. Les cadres gris (plus petits que les symboles) correspondent aux incertitudes systématiques. (b) rapport des mesures sur la simulation (points noirs) et rapport des prédictions théoriques sur la simulation (courbes rouge et bleue). Les bandes vertes correspondent aux incertitudes systématiques sur le cocktail. (c) spectre de masse de l'excès (cocktail soustrait aux mesures) dans la région des faibles masses comparé aux prédictions théoriques. Les crochets verts représentent l'incertitude systématique totale et incluent celle inhérente au cocktail.

Les partons durs peuvent se propager dans le milieu dense et chaud produit

dans les collisions et interagir avec ses constituants. Ces interactions résultent en une perte d'énergie via des radiations de gluons et/ou des diffusions élastiques. Des prédictions théoriques indiquent que cette perte d'énergie dépend de la densité du milieu, de la distance parcourue par le parton dans le milieu et de la saveur du parton. La perte d'énergie est souvent appelée atténuation des jets ou "jet quenching". Expérimentalement, elle peut être mise en évidence au moyen du facteur de modification nucléaire  $R_{AA}$ . Ce dernier est défini comme le rapport du taux de production d'une certaine particule mesuré dans les collisions noyau-noyau sur celui mesuré dans les collisions proton-proton puis multiplié par le nombre de collisions nucléon-nucléon dans la classe de collisions noyau-noyau considérée. En l'absence de perte d'énergie résultant du QGP,  $R_{AA} = 1$  à grand  $p_T$  tandis qu'un  $R_{AA} < 1$  reflète la perte d'énergie décrite ci-dessus.

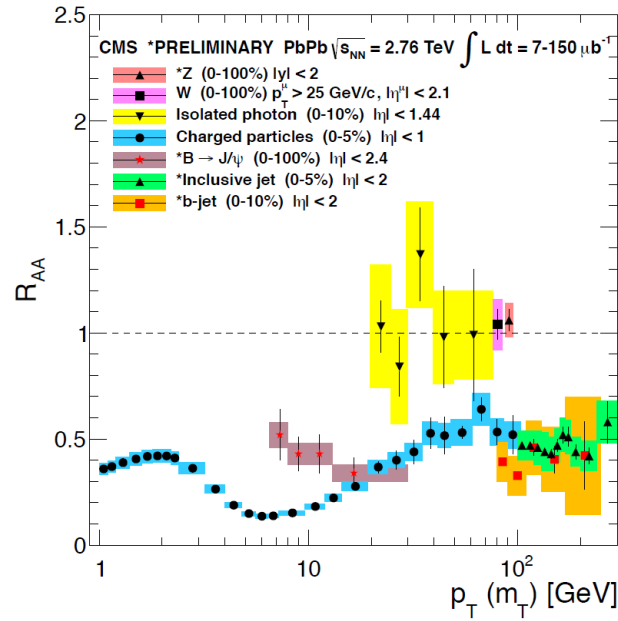


Figure 5: Facteur de modification nucléaire  $R_{AA}$  en fonction de  $p_T$  mesuré par la collaboration CMS dans les collisions Pb-Pb à  $\sqrt{s_{NN}} = 2.76$  TeV pour différentes particules : boson Z, bosons W, photons isolés, particules chargées,  $J/\psi$  indirects, jets inclusifs et b-jets.

Un résumé des mesures de  $R_{AA}$  pour différentes particules est présenté sur la figure 5 pour des collisions Pb-Pb à  $\sqrt{s_{NN}} = 2.76$  TeV. Le  $R_{AA}$  des particules chargées est maximum pour des moments transverses de l'ordre de 2 GeV/c. Le  $R_{AA}$  décroît ensuite avec  $p_T$  dans le domaine  $2 \lesssim p_T \lesssim 7$  GeV/c. Une forte suppression ( $R_{AA} \sim 0.15$ ) est observée dans cette région. Finalement le  $R_{AA}$  atteint 0.6 pour  $p_T \approx 100$  GeV/c. La suppression est également observée pour les  $J/\psi$  indirects et les b-jets à grand  $p_T$ . En revanche, les bosons électrofaibles et les photons isolés ne sont pas supprimés.

Les quarks lourds (charme et beauté) figurent parmi les sondes les plus perti-

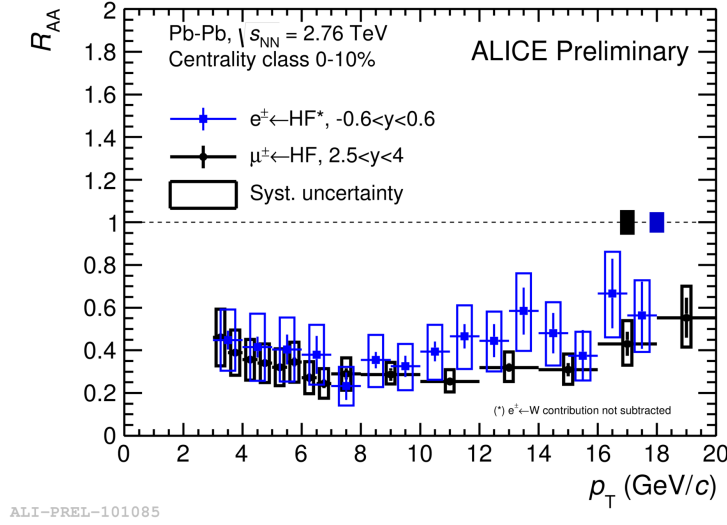


Figure 6: Facteur de modification nucléaire des muons (électrons) provenant de la désintégration des hadrons de saveurs lourdes pour les domaines  $2.5 < y^{\mu} < 4$  ( $|y^e| < 0.6$ ) et  $3 < p_T^{\mu} < 20$  GeV/c ( $3 < p_T^e < 18$  GeV/c) dans les collisions centrales Pb-Pb à  $\sqrt{s_{NN}} = 2.76$  TeV.

mentés du QGP. Ils sont produits dans les processus durs aux tous premiers instants de la collision et se propagent ensuite dans le milieu en interagissant avec ses constituants. Les hadrons de saveurs lourdes (quarkonia et saveurs lourdes ouvertes) fournissent donc des informations essentielles quant aux propriétés du système produit lors de la collision. Les quarkonia sont supposés être sensibles à la température initiale du système via la dissociation des paires quark-antiquark résultant de l'écrantage de couleur de Debye. Les saveurs lourdes ouvertes sont supposées être sensibles à la densité d'énergie du système au travers de la perte d'énergie des quarks lourds. Ces effets, appelés effets nucléaires chauds, peuvent être quantifiés au moyen du facteur de modification nucléaire  $R_{AA}$  défini précédemment. La figure 6 présente le  $R_{AA}$  des électrons (en bleu) et muons (en noir) provenant de la désintégration des hadrons de saveurs lourdes dans les régions de rapidité centrale et avant, respectivement, dans les collisions centrales (0 – 10%) Pb-Pb à  $\sqrt{s_{NN}} = 2.76$  TeV. Une forte suppression, atteignant un facteur 3-4, est observée pour des moments transverses de l'ordre de 8 GeV/c. Notons que pour une compréhension satisfaisante des mécanismes sous-jacents, il est essentiel de pouvoir quantifier les effets nucléaires dits froids et qui ne sont pas directement engendrés par la présence du QGP. Ces effets nucléaires froids peuvent être évalués au moyen des collisions nucléon-noyau en supposant qu'un système dense et chaud n'est pas produit dans ces collisions.

## L'expérience ALICE

Le détecteur ALICE (A Large Ion Collider Experiment) a été conçu pour étudier le QGP produit dans les collisions d'ions lourds aux énergies du LHC. ALICE est constitué d'une partie centrale et d'un spectromètre pour la mesure des muons dans la région avant. Le spectromètre à muons permet la mesure des quarkonia et des hadrons de saveurs lourdes dans leur canal de désintégration muonique dans le domaine en pseudo-rapacité  $-4 < \eta < -2.5$ . Cette thèse présente les résultats concernant la production de muons issus de la désintégration des hadrons de saveurs lourdes dans les collisions p-Pb et Pb-p à  $\sqrt{s_{NN}} = 5.02$  TeV collectées en 2013.

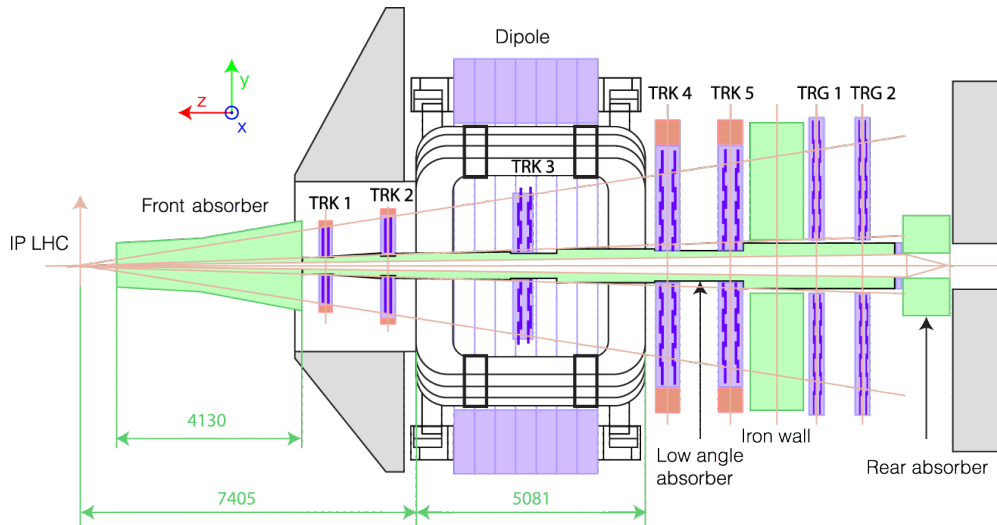


Figure 7: Vue schématique du spectromètre à muons d'ALICE.

Le spectromètre à muons d'ALICE (figure 7) est composé d'un absorbeur frontal (pour réduire le bruit de fond), d'un blindage des faisceaux (pour protéger les détecteurs des particules provenant des faisceaux), d'un aimant dipolaire (qui permet de courber les trajectoires des particules chargées), de 5 stations de tracking (pour la reconstruction des traces) et de 2 stations de trigger (pour l'identification des muons et le déclenchement). Un mur de fer de 1.2 m est placé devant les stations de trigger pour protéger le système de trigger des hadrons "punch-through". De plus, un absorbeur arrière est placé derrière les stations de trigger pour protéger le système des particules dans les faisceaux et arrivant dans la direction opposée au point d'interaction.

L'environnement d'analyse hors ligne d'ALICE, AliRoot, exploite les fonctionnalités fournies par l'environnement ROOT. Il permet de simuler la réponse du détecteur de façon très détaillée et est interfacé avec plusieurs générateurs d'événements. Il permet également de reconstruire et d'analyser les données réelles ou issues de simulations Monte-Carlo. AliRoot a été utilisé afin d'optimiser les performances de chaque sous-détecteur (Technical Design Reports) et pour évaluer les performances de physique de l'ensemble des sous-détecteurs (Physics Performance



Reports). Il permet d'effectuer toutes les tâches, telles que simulation, reconstruction, calibration, alignement, visualisation et analyse, visant à extraire les informations de physique des mesures expérimentales.

## Conditions de prises de données, critères de sélection des événements et corrections d'acceptance et d'efficacité

Les conditions de prises de données, les critères de sélection des traces et les corrections d'acceptance et d'efficacité sont décrites dans le chapitre 3 de la thèse. L'accent est mis sur la détermination de la "centralité" dans les collisions p–Pb. Notons que pour ce système asymétrique, l'énergie des faisceaux est respectivement de 4 TeV et 1.58 TeV pour le proton et le plomb, ce qui engendre un décalage en rapidité du référentiel du centre de masse (CMS) par rapport à celui du laboratoire. Ce décalage est de  $\Delta y = \frac{1}{2} \ln\left(\frac{Z_p A_{Pb}}{Z_{Pb} A_p}\right) \approx 0.465$  dans la direction du proton.

L'échantillon de données utilisé pour l'analyse consiste d'événements sélectionnés en ligne au moyen du système de déclenchement du spectromètre à muons. Ces événements correspondent à des événements de biais minimum auxquels doit être associé au moins une trace avec un  $p_T$  supérieur à un seuil donné dans le système de déclenchement du spectromètre (des événements de biais minimum, MB, sont utilisés pour la normalisation). Deux échantillons d'événements ont été collectés, le premier avec un seuil en  $p_T$  de 0.5 GeV/ $c$  et le second avec un seuil en  $p_T$  de 4.2 GeV/ $c$ . Ils sont respectivement appelés événements déclenchés muon simple bas  $p_T$  (MSL) et muon simple haut  $p_T$  (MSH). Les événements d'empilement (événements avec plus d'une interaction par croisement de faisceaux) représentent environ 2% du lot d'événements de biais minimum. Les critères de sélection des traces associées aux muons se déclinent comme suit. Les traces candidates doivent être reconstruites dans le domaine en rapidité  $-4 < \eta_{LAB} < -2.5$  et avoir un angle polaire à la sortie de l'absorbeur dans le domaine  $170^\circ < \theta_{abs} < 178^\circ$ . Les traces reconstruites dans le système de tracking doivent coïncider avec les traces correspondantes dans le système de trigger. Une coupure sur le produit de l'impulsion de la trace par sa distance d'approche minimale au vertex primaire ( $p \times DCA$ ) est appliquée afin de réduire la contribution des traces fausses et du bruit de fond généré par les faisceaux. Ainsi les traces avec  $p \times DCA > 6\sigma_{p \times DCA}$  sont rejetées. Enfin, la mesure des muons issus de la désintégration des hadrons de saveurs lourdes est effectuée dans le domaine en moment transverse  $2 < p_T < 16$  GeV/ $c$  en combinant les événements MSL jusqu'à  $p_T = 7$  GeV/ $c$  et les événements MSH dans l'intervalle  $7 < p_T < 16$  GeV/ $c$ .

En ce qui concerne la procédure de normalisation, le nombre équivalent d'événements MB est évalué au moyen du facteur d'échelle qui peut être déterminé selon deux approches. Dans l'approche basée sur la sélection hors ligne des événements muon MSH dans le lot d'événements MB, le facteur d'échelle est défini comme le produit entre l'inverse de la probabilité d'obtenir la condition de trigger MSH vérifiée dans un événement MSL et celle d'obtenir la condition de trigger MSL vérifiée dans un événement MB. La seconde méthode est basée sur le rapport des événements déclenchés MB sur ceux déclenchés muon (MSL ou MSH) au

niveau 0, corrigé des effets d'empilement et en considérant la différence de fraction d'événements satisfaisant les critères de qualité pour des lots de type MB, MSL et MSH. Enfin, la moyenne entre les deux approches est utilisée en considérant le nombre d'événements de type MSL (MSH) comme poids. Les résultats sont résumés dans le tableau 1.

$\bar{F}_{\text{norm}}$ (0 – 100%)	p–Pb (rapidité avant) ( <i>moyenne</i> $\pm$ <i>stat.</i> % $\pm$ <i>syst.</i> %)	Pb–p (rapidité arrière) ( <i>moyenne</i> $\pm$ <i>stat.</i> % $\pm$ <i>syst.</i> %)
MSL	$28.20 \pm 0.32\% \pm 0.52\%$	$20.49 \pm 0.24\% \pm 0.33\%$
MSH	$1032.77 \pm 0.67\% \pm 1.09\%$	$798.33 \pm 0.55\% \pm 0.35\%$

Table 1: Facteur de normalisation et incertitude relative dans les collisions p–Pb et Pb–p pour les événements MSL et MSH. Voir le texte pour plus de détails.

La correction d'acceptance  $\times$  efficacité est obtenue en utilisant une stratégie similaire à celle utilisée pour l'analyse des collisions pp et Pb–Pb. Une simulation réaliste du détecteur est implémentée avec AliRoot. Elle utilise en entrée les distributions cinématiques de quarks lourds générés avec PYTHIA et ajustées pour reproduire les calculs de type perturbative QCD au niveau Next Leading Order. La correction d'efficacité est obtenue avec l'environnement des corrections dans AliRoot (CORRFW). Elle est définie comme le rapport entre la distribution des muons reconstruits après la procédure de sélection hors ligne des traces et celle utilisée en entrée. Comme la correction est observée être indépendante de la saveur des quarks utilisée pour  $p_T > 2$  GeV/c, des distributions de quark beaux sont utilisées (comme c'est aussi le cas pour l'analyse des collisions pp et Pb–Pb). La dépendance de la correction à l'activité des événements n'est pas significative. Notons finalement que l'efficacité est identique pour des muons provenant de la désintégration des hadrons lourds et pour des muons inclusifs pour  $p_T > 2$  GeV/c.

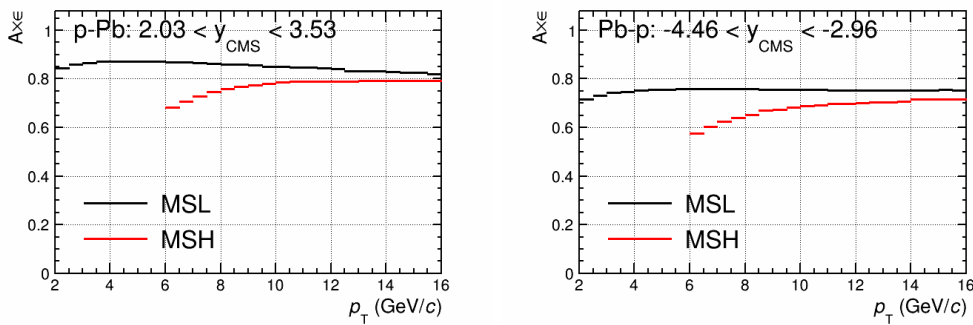


Figure 8: Acceptance  $\times$  efficacité pour des muons issus de la désintégration d'hadrons lourds à rapidité avant ( $2.03 < y_{\text{CMS}} < 3.53$ , gauche) et arrière ( $-4.46 < y_{\text{CMS}} < -2.96$ , droite). Les résultats obtenus en imposant la correspondance avec les événements de type MSL et MSH sont respectivement représentés par les histogrammes noirs et rouges. Voir le texte pour plus de détails.



La figure 8 montre les résultats obtenus dans la configuration p–Pb (rapidité avant,  $2.03 < y_{\text{CMS}} < 3.53$ , gauche) et dans la configuration Pb–p (rapidité arrière,  $-4.46 < y_{\text{CMS}} < -2.96$ , droite). Dans les deux cas, l’efficacité pour les événements MSL et MSH est respectivement représentée par les histogrammes noirs et rouges. Il peut être observé que, pour les événements MSL, l’efficacité dans la configuration p–Pb atteint  $\sim 0.85$  pour  $p_{\text{T}} > 2 \text{ GeV}/c$ , tandis que pour les événements MSH le plateau est difficilement atteint pour  $p_{\text{T}} > 8 \text{ GeV}/c$ . De plus, l’efficacité obtenue dans la configuration Pb–p est inférieure à celle obtenue à rapidité avant. Ceci résulte d’un plus grand nombre de canaux d’électronique endommagés lors de la configuration Pb–p par rapport à la configuration p–Pb.

## Soustraction du bruit de fond

La soustraction du bruit de fond dans les deux régions en rapidité est effectuée à partir des taux de production différentiels en moment transverse des muons corrigés de l’acceptance et des efficacités de tracking et de trigger. Cette soustraction est basée sur un cocktail Monte-Carlo ajusté sur les mesures. Le bruit de fond est principalement composé de muons issus de la désintégration des  $K^{\pm}$  et  $\pi^{\pm}$  primaires. L’analyse est effectuée pour  $p_{\text{T}} > 2 \text{ GeV}/c$  parce qu’à plus bas  $p_{\text{T}}$ , le bruit de fond est trop important pour permettre une extraction fiable du signal. La soustraction du signal dans la région de rapidité avant s’effectue en trois étapes :

- Les spectres des hadrons chargés ( $K^{\pm}$  et  $\pi^{\pm}$ ) mesurés dans la partie centrale d’ALICE sont utilisés en entrée.
  - Lorsque la cinématique de désintégration est considérée, une extrapolation en  $p_{\text{T}}$  des spectres est nécessaire car la région d’intérêt des muons de désintégration est  $2 < p_{\text{T}}^{\mu} < 16 \text{ GeV}/c$ . Cette région correspond respectivement à  $2 < p_{\text{T}}^{K^{\pm}} < 40 \text{ GeV}/c$  et  $2 < p_{\text{T}}^{\pi^{\pm}} < 24 \text{ GeV}/c$  pour les  $K^{\pm}$  et les  $\pi^{\pm}$  alors que les mesures correspondantes ont été effectuées dans la région  $2 < p_{\text{T}}^{K^{\pm}/\pi^{\pm}} < 15 \text{ GeV}/c$ .
- Extrapolation des spectres  $K^{\pm}/\pi^{\pm}$  à la rapidité avant au moyen de simulations Monte-Carlo via

$$\frac{dN^{K^{\pm},\pi^{\pm}}}{dp_{\text{T}}dy}(p_{\text{T}}, y) = \frac{dN_{\text{Donnees}}^{K^{\pm},\pi^{\pm}}}{dp_{\text{T}}dy}(p_{\text{T}}, y_{\text{CB}}) \times F_{\text{extra.}}(p_{\text{T}}, y) \quad (1)$$

$$F_{\text{extra.}}(p_{\text{T}}, y) = \frac{dN_{\text{MC}}^{K^{\pm},\pi^{\pm}}}{dp_{\text{T}}dy}(p_{\text{T}}, \text{forward}) \Big/ \frac{dN_{\text{MC}}^{K^{\pm},\pi^{\pm}}}{dp_{\text{T}}dy}(p_{\text{T}}, y_{\text{CB}}) \quad (2)$$

Notons que :

- $dN_{\text{Donnees}}^{K^\pm, \pi^\pm}/dp_T dy(p_T, y_{CB})$  correspond à la mesure réalisée dans la partie centrale d'ALICE.  $F_{\text{extra.}}(p_T, y)$  est le facteur d'extrapolation en rapidité, défini comme le rapport des taux de production aux rapidités avant et centrale obtenu avec le modèle DPMJET. Le générateur HIJING est utilisé pour estimer les incertitudes systématiques.
  - Afin d'obtenir les muons de désintégration dans les régions de rapidité  $2.03 < y_{\text{CMS}} < 3.53$  (avant, p-Pb) et  $-4.46 < y_{\text{CMS}} < -2.96$  (arrière, Pb-p), les spectres des hadrons chargés sont respectivement nécessaires dans les régions  $0 < y_{\text{CMS}}^{K^\pm, \pi^\pm} < 6$  (avant) et  $-6 < y_{\text{CMS}}^{K^\pm, \pi^\pm} < 0$  (arrière).
  - Le rapport  $F_{\text{extra.}}(p_T, y)$ , et non le taux de production  $dN_{\text{MC}}^{K^\pm, \pi^\pm}/dp_T dy(p_T, \text{avant/arriere})$  est utilisé pour les modèles. Ceci a pour avantage qu'un possible désaccord entre données et simulation s'annule dans une certaine mesure.
- Les muons de désintégration des  $K^\pm/\pi^\pm$  sont finalement obtenus au moyen d'une simulation rapide faisant intervenir la cinématique de désintégration et l'effet de l'absorbeur.

Notons que l'extrapolation en rapidité pourrait dépendre fortement des modèles utilisés. Cependant, il a été vérifié que les deux modèles considérés (DPMJET et HIJING) reproduisent correctement le taux de production de particules chargées en fonction de la rapidité dans la région de rapidité centrale. Les modèles ont également été confrontés aux données de CMS en utilisant les distributions en  $p_T$  dans différents intervalles en rapidité et le facteur d'asymétrie  $Y_{\text{asym}}$  défini comme le rapport des distributions en  $p_T$  dans les régions rapidité arrière et rapidité avant dans le référentiel du centre de masse :

$$Y_{\text{asym}}^{\text{Donnees}} = \frac{\text{arriere}}{\text{avant}} = \left. \frac{\frac{dN^{\text{chg}}}{dp_T}(p_T, \text{arriere})}{\frac{dN^{\text{chg}}}{dp_T}(p_T, \text{avant})} \right|_{\text{Donnees}} \quad (3)$$

Le modèle DPMJET offre une description satisfaisante du rapport avant-centrale mesuré par la collaboration CMS et défini comme :

$$\text{rapport} = \frac{\text{avant}}{\text{centrale}} = \left. \frac{\frac{dN^{\text{chg}}}{dp_T}(p_T, \text{avant})}{\frac{dN^{\text{chg}}}{dp_T}(p_T, \text{centrale})} \right|_{\text{Donnees}} \quad (4)$$

alors qu'il ne parvient pas à décrire les mesures dans la région de rapidité arrière même en considérant les incertitudes systématiques fournies par HIJING. Ceci implique que si la stratégie précédemment exposée peut être utilisée pour l'extrapolation dans la région avant, elle ne peut pas l'être dans la région arrière.

Comme annoncé ci-dessus, la collaboration CMS a mesuré le facteur d'asymétrie  $Y_{\text{asym}}^{\text{Donnees}}$  des particules chargées dans l'intervalle en rapidité  $1.3 < |\eta_{\text{CMS}}^{\text{chg}}| < 1.8$ . En utilisant  $Y_{\text{asym}}^{\text{Donnees}}$  comme facteur d'échelle, il est possible d'extrapoler les spectres  $K^\pm/\pi^\pm$  simulés de la rapidité avant à la rapidité arrière. Les spectres correspondant sont obtenus dans l'intervalle  $-1.8 < y_{\text{CMS}}^{K^\pm, \pi^\pm} < -1.3$ .

$$\begin{aligned} & \frac{dN_{\text{Donnees-ajuste-MC}}^{K^\pm, \pi^\pm}}{dp_T}(p_T, -1.8 < y_{\text{CMS}}^{K^\pm, \pi^\pm} < -1.3) \\ &= \frac{dN_{\text{MC}}^{K^\pm, \pi^\pm}}{dp_T}(p_T, 1.3 < y_{\text{CMS}}^{K^\pm, \pi^\pm} < 1.8) \cdot Y_{\text{asym}}^{\text{Donnees}}(p_T, 1.3 < |\eta_{\text{CMS}}^{\text{chg}}| < 1.8) \end{aligned} \quad (5)$$

Notons cependant que l'intervalle en rapidité d'intérêt pour la présente étude est  $-6 < y_{\text{CMS}}^{K^\pm/\pi^\pm} < 0$ . Une approche conservatrice a donc été développée. La borne inférieure du bruit de fond est estimée en utilisant  $Y_{\text{asym}}^{\text{Donnees}} = 1$  comme indiqué dans l'équation 4.9, ce qui implique une symétrie entre les régions avant et arrière. La borne supérieure du bruit de fond est estimée en utilisant  $2 \times Y_{\text{asym}}^{\text{Donnees}}$  comme indiqué dans l'équation 4.10.

$$\begin{aligned} & \frac{dN_{\text{Donnees-ajuste-MC(Basse)}}^{K^\pm, \pi^\pm}}{dp_T}(p_T, -6 < y_{\text{CMS}}^{K^\pm, \pi^\pm} < 0) \\ &= \frac{dN_{\text{MC}}^{K^\pm, \pi^\pm}}{dp_T}(p_T, 0 < y_{\text{CMS}}^{K^\pm, \pi^\pm} < 6) \cdot Y_{\text{asym(Basse)}}(p_T, 0 < |\eta_{\text{CMS}}^{\text{chg}}| < 6) \end{aligned} \quad (6)$$

$$\begin{aligned} & \frac{dN_{\text{Donnees-ajuste-MC(Haute)}}^{K^\pm, \pi^\pm}}{dp_T}(p_T, -6 < y_{\text{CMS}}^{K^\pm, \pi^\pm} < 0) \\ &= \frac{dN_{\text{MC}}^{K^\pm, \pi^\pm}}{dp_T}(p_T, 0 < y_{\text{CMS}}^{K^\pm, \pi^\pm} < 6) \cdot Y_{\text{asym(Haute)}}(p_T, 0 < |\eta_{\text{CMS}}^{\text{chg}}| < 6) \end{aligned} \quad (7)$$

$Y_{\text{asym(Basse)}}$  and  $Y_{\text{asym(Haute)}}$  correspondent aux facteurs d'échelle utilisés pour obtenir les bornes inférieure et supérieure du bruit de fond comme défini respectivement dans les équations 4.11 and 4.12. Ce dernier est obtenu à partir de mesures effectuées par la collaboration CMS dans l'intervalle  $1.3 < |\eta_{\text{CMS}}^{\text{chg}}| < 1.8$ .

$$Y_{\text{asym(Basse)}}(p_T, 0 < |\eta_{\text{CMS}}^{\text{chg}}| < 6) = 1 \quad (8)$$

$$Y_{\text{asym(Haute)}}(p_T, 0 < |\eta_{\text{CMS}}^{\text{chg}}| < 6) = 2 \times Y_{\text{asym}}^{\text{Donnees}}(p_T, 1.3 < |\eta_{\text{CMS}}^{\text{chg}}| < 1.8) \quad (9)$$

En ce qui concerne la limite supérieure du bruit de fond (Eq. 4.12), des simulations basées sur HIJING et DPMJET ont permis de montrer qu'il est possible d'augmenter  $Y_{\text{asym}}$  mesuré dans l'intervalle  $1.3 < |\eta_{\text{CMS}}^{\text{chg}}| < 1.8$  d'un facteur 2 pour couvrir les mesures dans l'intervalle  $|y_{\text{CMS}}^{K^\pm/\pi^\pm}| < 6$ . Enfin, la moyenne entre les limites inférieure et supérieure est utilisée comme valeur centrale pour l'estimation du bruit de fond dans la région de rapidité arrière en considérant une incertitude systématique supposée uniforme comme présenté dans les équations suivantes.

$$\text{moyenne} = \frac{a + b}{2} \quad (10)$$

$$\sigma_{\text{moyenne}}^2 = \frac{(a - b)^2}{12} \quad (11)$$

$a$  et  $b$  correspondent au bruit de fond estimé (i.e. muons de désintégration primaire) basé respectivement sur l'équation 4.9 pour la limite inférieure et sur l'équation 4.10 pour la limite supérieure.

## La référence pp

La référence pour le calcul du  $R_{AA}$ , i.e. section efficace différentielle de production des muons issus de la désintégration des hadrons lourds dans les collisions pp à  $\sqrt{s} = 5.02$  TeV, est obtenue à partir de l'extrapolation en énergie et en rapidité, basée sur des calculs de type pQCD Next-to-Leading Log (FONLL), des mesures effectuées à  $\sqrt{s} = 7$  TeV. Cette procédure peut être décrite par l'équation suivante.

$$\begin{aligned} & \frac{d\sigma_{pp}^{\text{Cal.}}}{dp_T}(\sqrt{s_{5.02}}, p_T, \Delta y_x) \\ & \simeq F_{\text{scal}}^{\text{FONLL}}(\sqrt{s_{5.02}}|\sqrt{s_7}, \Delta y_x|\Delta y_{ref}; p_T) \cdot \frac{d\sigma_{pp}^{\text{Donnees}}}{dp_T}(\sqrt{s_7}, p_T, \Delta y_{ref}) \\ & = \frac{\frac{d\sigma_{pp}^{\text{FONLL}}}{dp_T}(\sqrt{s_{5.02}}, p_T, \Delta y_x)}{\frac{d\sigma_{pp}^{\text{FONLL}}}{dp_T}(\sqrt{s_7}, p_T, \Delta y_{ref})} \cdot \frac{d\sigma_{pp}^{\text{Donnees}}}{dp_T}(\sqrt{s_7}, p_T, \Delta y_{ref}) \end{aligned} \quad (12)$$

$\Delta y_x$  est l'acceptance pour les collisions pp à  $\sqrt{s} = 5.02$  TeV i.e.  $2.03 < y_{\text{CMS}} < 3.53$  ( $-4.46 < y_{\text{CMS}} < -2.96$ ) dans la région de rapidité avant (arrière). La région correspondante est  $2.5 < |y_{\text{CMS}}| < 4$  pour les collisions pp à  $\sqrt{s} = 7$  TeV. Les spectres de référence pp dans les régions de rapidité avant et arrière sont respectivement présentés dans les parties haute et basse de la figure 9. On peut observer qu'elles sont en bon accord avec les prédictions de FONLL.

Comme la mesure dans les collisions pp à  $\sqrt{s} = 7$  TeV est limitée à  $p_T < 12$  GeV/c, les distributions dans l'intervalle  $12 < p_T < 16$  GeV/c à  $\sqrt{s} = 5.02$  TeV sont obtenues à l'aide d'une extrapolation utilisant FONLL comme suit :

$$\begin{aligned} & \frac{d\sigma_{pp}^{\text{Cal.}}}{dp_T}(\sqrt{s} = 5.02 \text{ TeV}) \\ & = \begin{cases} F_{\text{scal}}^{\text{FONLL}} \cdot \frac{d\sigma_{pp}^{\text{Donnees}}}{dp_T}(\sqrt{s} = 7 \text{ TeV}) & (2 < p_T < 12 \text{ GeV}/c) \\ K(\sqrt{s} = 5.02 \text{ TeV}) \cdot \frac{d\sigma_{pp}^{\text{FONLL}}}{dp_T}(\sqrt{s} = 5.02 \text{ TeV}) & (12 < p_T < 16 \text{ GeV}/c) \end{cases} \end{aligned} \quad (13)$$

$K(\sqrt{s} = 5.02 \text{ TeV})$  correspond à l'écart entre les mesures et FONLL dans un certain intervalle en  $p_T$  et à une certaine énergie et permet d'ajuster les prédictions de FONLL aux mesures dans ce domaine en  $p_T$  et pour cette énergie.

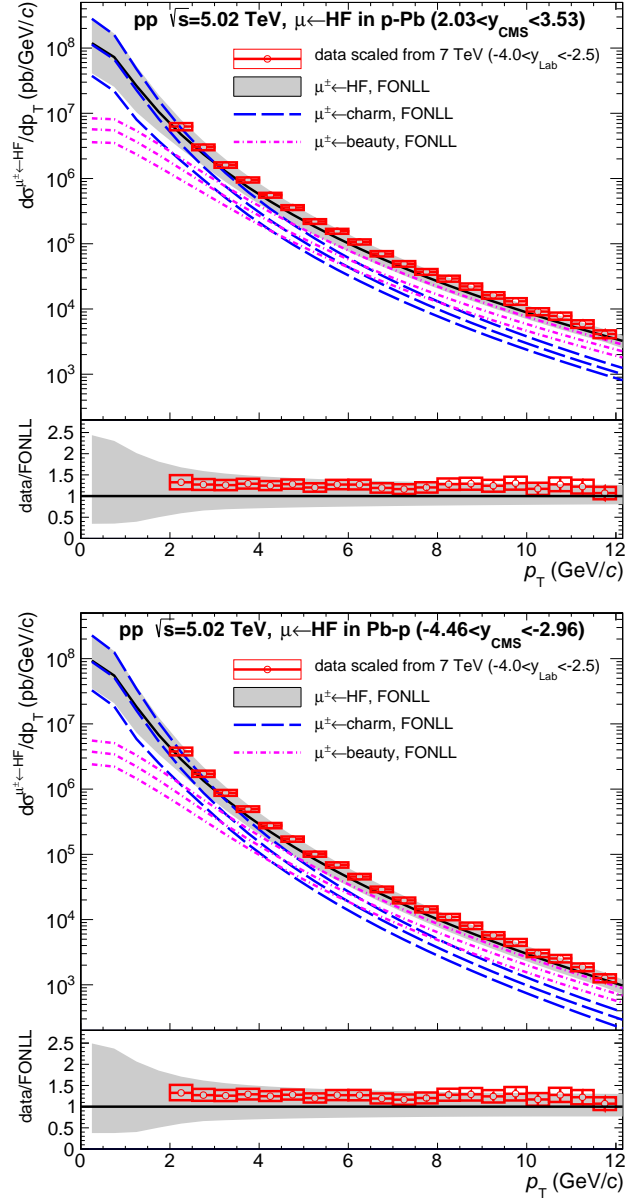


Figure 9: Spectres de référence dans les collisions pp à  $\sqrt{s} = 5.02$  TeV obtenus de l'extrapolation en énergie et en rapidité des données mesurées dans les collisions pp à  $\sqrt{s} = 7$  TeV dans l'intervalle en rapidité  $2.5 < y_{\text{CMS}} < 4$ . Les courbes en traits pleins correspondent aux prédictions théoriques obtenues avec FONLL et la bande correspond aux incertitudes systématiques théoriques. Les résultats des calculs FONLL pour les muons issus de la désintégration des hadrons charmés et beaux sont aussi représentés. La comparaison des résultats extrapolés avec les prédictions de FONLL est présentée en bas des figures.

$$K(\sqrt{s} = 5.02 \text{ TeV}) = \frac{\int_{\min}^{\max} dp_T' \frac{d\sigma_{pp}^{\text{Cal.}}}{dp_T'}(\sqrt{s} = 5.02 \text{ TeV})}{\int_{\min}^{\max} dp_T' \frac{d\sigma_{pp}^{\text{FONLL}}}{dp_T'}(\sqrt{s} = 5.02 \text{ TeV})} \quad (14)$$

Dans l'intervalle en  $p_T$  choisi est  $6 < p_T < 12 \text{ GeV}/c$ , les écarts entre les mesures et les prédictions de FONLL sont les plus petites.

En utilisant les équations 5.12 et 5.13, la référence pp est obtenue jusqu'à  $p_T = 16 \text{ GeV}/c$ . Elle est présentée sur la figure 10. Les résultats obtenus dans l'intervalle  $2 < p_T < 12 \text{ GeV}/c$  sont ceux présentés sur la figure 9. Le facteur d'échelle  $K(\sqrt{s} = 5.02 \text{ TeV})$  vaut  $\sim 1.23$  dans les deux régions de rapidité. Modifier la limite inférieure de l'intervalle en  $p_T$  utilisé pour l'extrapolation de 6 à 4  $\text{GeV}/c$  résulte en un écart de 2 – 3%. Cet effet peut être raisonnablement ignoré puisque les incertitudes associées aux prédictions FONLL sont respectivement  $\sim 25\%$  et  $\sim 30\%$  dans l'intervalle  $12 < p_T < 16 \text{ GeV}/c$ , dans les régions de rapidité avant et arrière.

## Résultats et discussion

La figure 11 montre le facteur de modification nucléaire  $R_{pPb}$  des muons issus de la désintégration des hadrons lourds en fonction de  $p_T$  dans les collisions p–Pb à  $\sqrt{s} = 5.02 \text{ TeV}$  dans les régions de rapidité avant (haut) et arrière (bas) qui permettent de sonder respectivement les régions d'écrantage et d'anti-écrantage. Les incertitudes statistiques, systématiques et de normalisation sont respectivement représentées par les barres verticales, les cadres et le cadre noir à  $R_{pPb} = 1$ . En considérant les incertitudes, le  $R_{pPb}$  est compatible avec l'unité sur l'ensemble de l'intervalle en  $p_T$  exploré. Ceci démontre que les effets CNM sont faibles et que la forte suppression du taux de production des muons observée dans les collisions centrales Pb–Pb résulte d'effets dans l'état final (Fig. 6). Dans la région de rapidité arrière, le  $R_{pPb}$  est légèrement supérieur à l'unité ( $\sim 2\sigma$ ) dans la région des  $p_T$  intermédiaires ( $2 < p_T < 4 \text{ GeV}/c$ ). Il est cependant compatible avec l'unité sur l'ensemble du domaine en  $p_T$  exploré quand les incertitudes systématiques sont considérées.

La figure 11 montre également la comparaison avec des prédictions théoriques. Les résultats dans la région de rapidité avant sont correctement décrits par un calcul de type pQCD utilisant la paramétrisation EPS09 NLO des PDF nucléaires (courbe rouge). Ils sont également bien reproduits par des calculs incluant l'écrantage nucléaire, l'élargissement du  $k_T$  et la perte d'énergie dans un milieu froid (courbe verte). Ceci tend à confirmer que les effets nucléaires froids sont faibles dans la région en  $p_T$  explorée. Dans la région de rapidité arrière, les prédictions basées sur la paramétrisation EPS09 (courbe rouge) reproduisent également les mesures, tout comme un calcul incluant des effets de diffusion multiple des partons durs dans le noyau de plomb lors des interactions dans les états initial et final (courbe bleue).

Le  $R_{pPb}$  a également été étudié en fonction de  $p_T$  dans deux intervalles de rapidité. Les résultats sont présentés sur la figure 12 dans la région de rapidité avant

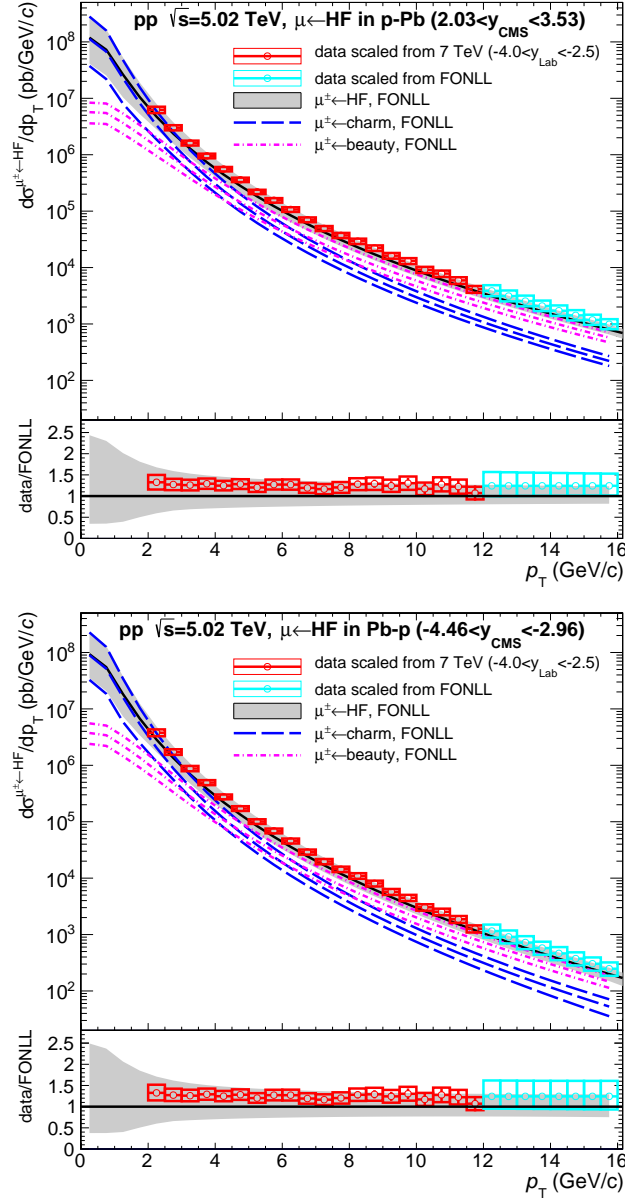


Figure 10: Spectres de référence dans les collisions pp à  $\sqrt{s} = 5.02$  TeV obtenus de l'extrapolation en énergie et en rapidité dans l'intervalle  $2 < p_T < 12$  GeV/c (rouge), des données mesurées dans les collisions pp à  $\sqrt{s} = 7$  TeV dans l'intervalle en rapidité  $2.5 < y_{\text{CMS}} < 4$ , Les résultats pour  $p_T > 12$  GeV/c (bleu) proviennent de l'extrapolation décrite dans le texte. La comparaison des résultats extrapolés avec les prédictions de FONLL est présentée en bas des figures.

(haut) et arrière (bas) Aucune dépendance significative du  $R_{\text{pPb}}$  n'est observé en fonction de la rapidité.

Les effets nucléaires froids peuvent aussi être étudiés au moyen du rapport avant-

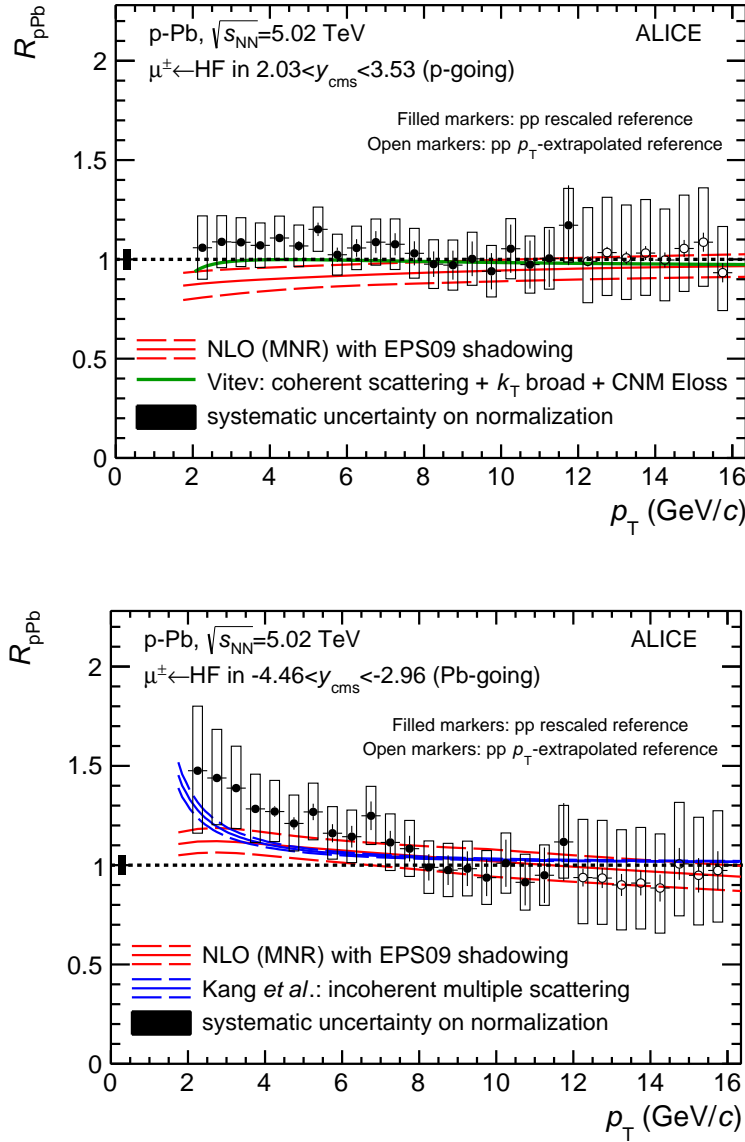


Figure 11: Facteur de modification nucléaire des muons issus de la désintégration des hadrons lourds en fonction de  $p_T$  dans les collisions p–Pb à  $\sqrt{s} = 5.02$  TeV dans la région de rapidité avant (haut) et arrière (bas). Voir le texte pour plus de détails.

arrière  $R_{FB}$  défini comme :

$$R_{FB}(2.96 < |y_{cms}| < 3.53) = \frac{dN^{\text{forward}}/dp_T(2.96 < y_{cms} < 3.53)}{dN^{\text{backward}}/dp_T(-3.53 < y_{cms} < -2.96)}. \quad (15)$$

L'avantage principal de ce rapport est que les incertitudes associées à la référence pp et à la fonction de recouvrement s'annulent. L'inconvénient est la statistique limitée puisque l'intervalle en rapidité commun  $y_{cms}$  couvert dans les régions de rapidités avant et arrière est petit ( $\Delta y = 0.57$ ).

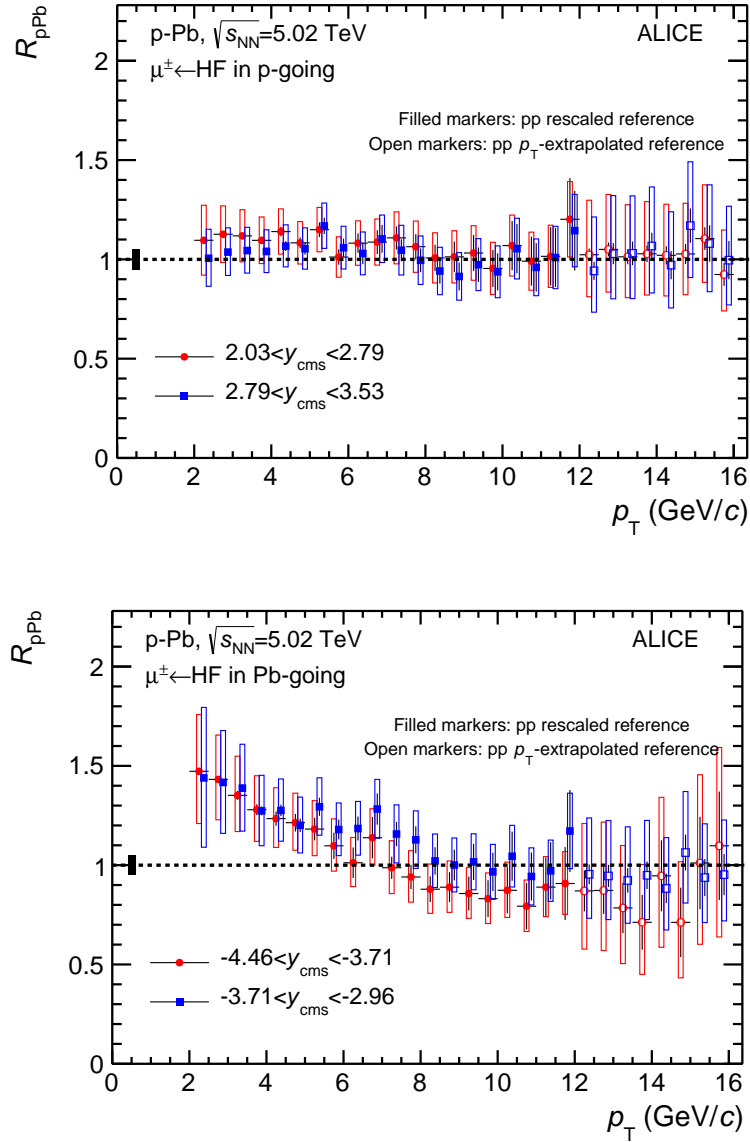


Figure 12: Similaire à la figure 11 mais pour 2 intervalles de rapidité reportés sur la figure. Pour plus de visibilité, les points des intervalles de rapidité  $2.79 < y_{\text{CMS}} < 3.53$  et  $-3.71 < y_{\text{CMS}} < -2.96$  sont déplacés horizontalement.

La figure 13 montre le  $R_{\text{FB}}$  mesuré dans l'intervalle  $2 < p_{\text{T}} < 16 \text{ GeV}/c$ . Le  $R_{\text{FB}}$  est plus petit que l'unité dans l'intervalle  $2 < p_{\text{T}} < 4 \text{ GeV}/c$  et devient proche de l'unité à plus grand  $p_{\text{T}}$ . Il est bien reproduit par les calculs pQCD utilisant la paramétrisation EPS09 NLO des PDF nucléaires sur l'ensemble du domaine en  $p_{\text{T}}$  exploré. Ces deux observations confirment les conclusions obtenues plus haut sur la base du  $R_{\text{pPb}}$ .

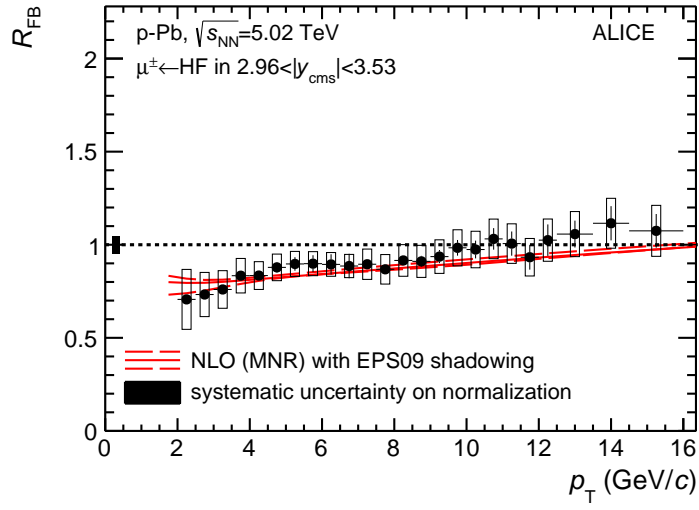


Figure 13: Rapport avant-arrière comme décrit dans le texte. Les résultats des calculs pQCD utilisant la paramétrisation EPS09 NLO des PDF nucléaires sont représentés par les courbes rouges. Les incertitudes statistiques, systématiques et de normalisation sont respectivement représentées par les barres, les cadres et le cadre noir à  $R_{FB} = 1$ .



## Abstract

Heavy ions such as gold (Au) or lead (Pb), colliding at extremely high energies, allow to create a femptoscopic system ( $10^{-14}$  m diameter) with a temperature of several trillions of degrees. In such a high temperature environment, quarks and gluons are no longer bound into nucleons but form a new state of matter known as the Quark-Gluon Plasma (QGP) in which they roam freely.

Heavy quarks (charm and beauty) are among the most relevant probes of the QGP as they are produced in initial hard scatterings in the early stage of the collision and subsequently propagate through the medium interacting with its constituents. The heavy-flavour hadrons (quarkonia and open heavy-flavours) can therefore provide essential information on the properties of the system formed in the collision. Quarkonia are expected to be sensitive to the initial temperature of the system through quark-anti quark pair dissociation due to color screening. Open heavy-flavours are expected to be sensitive to the energy density of the system through in-medium energy loss of heavy quarks. These so-called hot nuclear matter effects can be quantified with the nuclear modification factor  $R_{AA}$  which is defined as the ratio of the particle yields in nucleus–nucleus and in pp collisions. At high transverse momentum,  $R_{AA}$  is found to be lower than unity, indicating a suppression of the yields in AA collision i.e. the presence of hot nuclear effects. However, for a meaningful understanding of the underlying mechanisms, it is essential to quantify the cold nuclear matter effects which are not directly resulting from the QGP. These cold nuclear matter effects can be accessed by studying nucleon–nucleus collisions assuming that a hot and dense system is not formed in such collisions.

ALICE (A Large Ion Collider Experiment) detector is designed to address the physics of the QGP in nucleus–nucleus collisions at the LHC. ALICE mainly consists of a central barrel and a muon spectrometer. The muon spectrometer allows one to measure quarkonia and open heavy-flavour hadrons in their muon decay channels at forward rapidity ( $-4 < \eta < -2.5$ ).

The thesis presents results about the production yield of muons from heavy-flavour hadron decays in p–Pb and Pb–p collisions at  $\sqrt{s_{NN}} = 5.02$  TeV recorded during the 2013 LHC run. The first chapter of the thesis is dedicated to a general overview of the QGP signatures and properties. Chapter 2 presents the apparatus with special emphasis on the muon spectrometer and the ALICE offline framework. Chapter 3 addresses the data taking conditions, muon selection criteria and the acceptance  $\times$  efficiency correction. A particular emphasis is placed on the centrality determination in p–Pb collisions. Chapter 4 presents the subtraction of background muons from primary pion and kaon decays. Chapter 5 presents the estimation of pp reference by means of a pQCD-based energy scaling procedure. Chapter 6 shows the transverse momentum and centrality dependence of the experimental results of muons from heavy-flavour hadron decays, including the production cross sections, nuclear modification factor and forward-to-backward ratio. The results are discussed and compared to model predictions and other measurements.

**Keywords:** LHC, ALICE experiment; p–Pb collisions; muons; cold nuclear matter effects; nuclear modification factor; forward-to-backward ratio; pQCD



# Contents

<b>1</b>	<b>Introduction</b>	<b>1</b>
1.1	Quantum ChromoDynamics and Quark Gluon Plasma . . . . .	1
1.1.1	The Standard Model and QCD . . . . .	1
1.1.2	Lattice QCD calculations . . . . .	4
1.2	Studying the QGP with heavy-ion collisions . . . . .	6
1.2.1	Space-time evolution of heavy-ion colliding system . . . . .	6
1.2.2	Signatures of the QGP from SPS to LHC . . . . .	8
1.2.3	Cold and Hot Nuclear Matter Effects . . . . .	17
1.3	Heavy-Flavours as probes of the QGP . . . . .	22
1.3.1	Heavy-Flavour production in heavy-ion collisions . . . . .	23
1.3.2	Studying heavy-flavours from their decay muons . . . . .	36
<b>2</b>	<b>The ALICE Experiment</b>	<b>41</b>
2.1	ALICE Setup . . . . .	41
2.2	Global Detectors . . . . .	43
2.3	Central Barrel Detectors . . . . .	44
2.4	The Forward muon spectrometer . . . . .	47
2.4.1	The absorbers . . . . .	51
2.4.2	Dipole Magnet . . . . .	51
2.4.3	Tracking Stations . . . . .	52
2.4.4	Trigger Stations . . . . .	56
2.5	Future Upgrade of the Muon Spectrometer . . . . .	58
2.5.1	Muon Tracking Upgrade . . . . .	59
2.5.2	Muon Trigger Upgrade . . . . .	59
2.5.3	Muon Forward Tracker (MFT) . . . . .	60
2.6	ALICE Offline Framework . . . . .	61
<b>3</b>	<b>Data samples, Muon Selection Criteria and Acceptance <math>\times</math> Efficiency Correction</b>	<b>65</b>
3.1	Data Samples . . . . .	66
3.1.1	Event Selection . . . . .	66
3.1.2	Pile-up Effect . . . . .	68
3.1.3	Normalization of Muon Triggers to Minimum Bias . . . . .	71
3.2	Muon Track Selection . . . . .	83
3.2.1	Track Selection . . . . .	85
3.2.2	Detailed study of the $p \times$ DCA cut . . . . .	89
3.3	Event Activity Classification . . . . .	92
3.3.1	The Strategies . . . . .	92
3.3.2	Multiplicity in p-Pb collisions . . . . .	94
3.3.3	Event Activity Dependence in p-Pb Muon Triggered Events . . . . .	96



3.4	Acceptance $\times$ Efficiency Correction . . . . .	100
3.4.1	Aspects of correction efficiency . . . . .	100
3.4.2	Strategy and Results . . . . .	101
3.4.3	Systematic Uncertainty on the Efficiency . . . . .	105
<b>4</b>	<b>Subtraction of the background contribution of muons from charged pion and kaon decays</b>	<b>111</b>
4.1	Experience Gained from Previous Analyses . . . . .	111
4.1.1	Muon Sources . . . . .	111
4.1.2	Background Estimation Strategies . . . . .	114
4.2	Background Estimation in multiplicity integrated p–Pb Collisions Based on a Data-Driven Method . . . . .	116
4.2.1	Summary of the Strategy . . . . .	116
4.2.2	Input Charged Hadron Distributions . . . . .	120
4.2.3	Rapidity Extrapolation . . . . .	125
4.2.4	Conversion at Muon Level and Systematic Uncertainty . . . . .	135
4.2.5	Cross-Checks and Discussion . . . . .	142
4.3	Background within Individual Event Activity Classes in p–Pb Collisions . . . . .	147
4.3.1	Challenges and Solutions . . . . .	147
4.3.2	Charged Hadron Spectra with Different Estimators . . . . .	148
4.3.3	Event Activity Determination . . . . .	151
4.3.4	Deviation between Data and Monte-Carlo . . . . .	158
4.3.5	Rapidity Extrapolation . . . . .	163
4.3.6	Estimated Background and Systematic Uncertainty . . . . .	167
4.3.7	Discussion . . . . .	168
<b>5</b>	<b>The pp Reference</b>	<b>175</b>
5.1	pQCD-based Energy Scaling Procedure . . . . .	175
5.1.1	The Strategy . . . . .	176
5.1.2	Uncertainty Determination in Model . . . . .	177
5.1.3	Strategy Validation for the Rapidity Shift . . . . .	182
5.1.4	Energy Scaling Factor . . . . .	186
5.2	The pp Reference Estimated at $\sqrt{s} = 5.02$ TeV . . . . .	190
5.2.1	Results Based on the Measurement at $\sqrt{s} = 7$ TeV . . . . .	191
5.2.2	Extrapolation to Higher Transverse Momentum . . . . .	192
5.3	Discussion . . . . .	194
5.3.1	Combination of the Results From Different Energies . . . . .	194
5.3.2	Alternative Strategy for the Reference at High $p_T$ . . . . .	197
<b>6</b>	<b>Muons from Heavy-Flavour Hadron Decays in p–Pb Collisions at <math>\sqrt{s_{NN}} = 5.02</math> TeV</b>	<b>201</b>
6.1	Summary of the Analysis Strategy . . . . .	201
6.2	Summary of the Systematic Uncertainty . . . . .	203
6.2.1	Sources of Systematic Uncertainty . . . . .	203



---

6.2.2	Error Propagation . . . . .	206
6.3	Production Cross Section . . . . .	215
6.4	Nuclear Modification Factor . . . . .	217
6.4.1	Measurements in Multiplicity Integrated Collisions . . . . .	217
6.4.2	Event Activity Dependence . . . . .	217
6.4.3	Discussion . . . . .	223
6.5	Forward-To-Backward Ratio . . . . .	226
6.5.1	Measurements in Multiplicity Integrated Collisions . . . . .	226
6.5.2	Event Activity Dependence . . . . .	228
<b>Conclusions</b>		<b>231</b>
<b>Bibliography</b>		<b>233</b>
<b>Appendix</b>		<b>259</b>
<b>Publication List</b>		<b>271</b>
<b>Presentation List</b>		<b>273</b>
<b>Acknowledgments</b>		<b>275</b>



# List of Figures

1	Représentation schématique de l'évolution spatio-temporelle d'une collision d'ions lourds ultra-relativistes. . . . .	vii
2	Facteur d'augmentation de particules produites à mi-rapacité par nucléons participants dans les collisions Pb–Pb et p–Pb à 158 $A$ GeV/ $c$ . . . . .	ix
3	Rapport du taux de production mesuré des $J/\psi$ sur le taux attendu en absence de suppression anormale, en fonction de $N_{\text{part}}$ dans les collisions In–In (rouge) et Pb–Pb (bleu) aux énergies du SPS. . . . .	ix
4	(a) spectre de masse invariante $e^+e^-$ mesuré dans les collisions Au–Au de biais minimum (centralité 0–80%) à $\sqrt{s_{\text{NN}}} = 200$ GeV comparé à une simulation basée sur un cocktail hadronique. Les barres verticales correspondent aux fluctuations statistiques. Les cadres gris (plus petits que les symboles) correspondent aux incertitudes systématiques. (b) rapport des mesures sur la simulation (points noirs) et rapport des prédictions théoriques sur la simulation (courbes rouge et bleue). Les bandes vertes correspondent aux incertitudes systématiques sur le cocktail. (c) spectre de masse de l'excès (cocktail soustrait aux mesures) dans la région des faibles masses comparé aux prédictions théoriques. Les crochets verts représentent l'incertitude systématique totale et incluent celle inhérente au cocktail. . . . .	xi
5	Facteur de modification nucléaire $R_{\text{AA}}$ en fonction de $p_{\text{T}}$ mesuré par la collaboration CMS dans les collisions Pb–Pb à $\sqrt{s_{\text{NN}}} = 2.76$ TeV pour différentes particules : boson Z, bosons W, photons isolés, particules chargées, $J/\psi$ indirects, jets inclusifs et b-jets. . . . .	xii
6	Facteur de modification nucléaire des muons (électrons) provenant de la désintégration des hadrons de saveurs lourdes pour les domaines $2.5 < y^{\mu} < 4$ ( $ y^e  < 0.6$ ) et $3 < p_{\text{T}}^{\mu} < 20$ GeV/ $c$ ( $3 < p_{\text{T}}^e < 18$ GeV/ $c$ ) dans les collisions centrales Pb–Pb à $\sqrt{s_{\text{NN}}} = 2.76$ TeV. . . . .	xiii
7	Vue schématique du spectromètre à muons d'ALICE. . . . .	xiv
8	Acceptance $\times$ efficacité pour des muons issus de la désintégration d'hadrons lourds à rapidité avant ( $2.03 < y_{\text{CMS}} < 3.53$ , gauche) et arrière ( $-4.46 < y_{\text{CMS}} < -2.96$ , droite). Les résultats obtenus en imposant la correspondance avec les événements de type MSL et MSH sont respectivement représentés par les histogrammes noirs et rouges. Voir le texte pour plus de détails. . . . .	xvi



9	Spectres de référence dans les collisions pp à $\sqrt{s} = 5.02$ TeV obtenus de l'extrapolation en énergie et en rapidité des données mesurées dans les collisions pp à $\sqrt{s} = 7$ TeV dans l'intervalle en rapidité $2.5 < y_{\text{CMS}} < 4$ . Les courbes en traits pleins correspondent aux prédictions théoriques obtenues avec FONLL et la bande correspond aux incertitudes systématiques théoriques. Les résultats des calculs FONLL pour les muons issus de la désintégration des hadrons charmés et beaux sont aussi représentés. La comparaison des résultats extrapolés avec les prédictions de FONLL est présentée en bas des figures. . . . .	xxi
10	Spectres de référence dans les collisions pp à $\sqrt{s} = 5.02$ TeV obtenus de l'extrapolation en énergie et en rapidité dans l'intervalle $2 < p_{\text{T}} < 12$ GeV/c (rouge), des données mesurées dans les collisions pp à $\sqrt{s} = 7$ TeV dans l'intervalle en rapidité $2.5 < y_{\text{CMS}} < 4$ , Les résultats pour $p_{\text{T}} > 12$ GeV/c (bleu) proviennent de l'extrapolation décrite dans le texte. La comparaison des résultats extrapolés avec les prédictions de FONLL est présentée en bas des figures. . . . .	xxiii
11	Facteur de modification nucléaire des muons issus de la désintégration des hadrons lourds en fonction de $p_{\text{T}}$ dans les collisions p-Pb à $\sqrt{s} = 5.02$ TeV dans la région de rapidité avant (haut) et arrière (bas). Voir le texte pour plus de détails. . . . .	xxiv
12	Similaire à la figure 11 mais pour 2 intervalles de rapidité reportés sur la figure. Pour plus de visibilité, les points des intervalles de rapidité $2.79 < y_{\text{CMS}} < 3.53$ et $-3.71 < y_{\text{CMS}} < -2.96$ sont déplacés horizontalement. . . . .	xxv
13	Rapport avant-arrière comme décrit dans le texte. Les résultats des calculs pQCD utilisant la paramétrisation EPS09 NLO des PDF nucléaires sont représentés par les courbes rouges. Les incertitudes statistiques, systématiques et de normalisation sont respectivement représentées par les barres, les cadres et le cadre noir à $R_{\text{FB}} = 1$ . . .	xxvi
1.1	Summary of Higgs boson mass measurements from the individual analyses of ATLAS and CMS and from the combined analyses. The systematic (narrower, magenta-shaded bands), statistical (wider, yellow-shaded bands), and total (black error bars) uncertainties are indicated. The (red) vertical line and corresponding (gray) shaded column indicate the central value and the total uncertainty of the combined measurement, respectively. Figure taken from Ref. [3]. . .	2
1.2	Elementary particles (left) and fundamental interactions (right) in the Standard Model. Figures taken from Ref. [4]. . . . .	2



1.3	Summary of running coupling constant, $\alpha_s$ , measured as a function of the energy scale, $Q$ . The respective degree of perturbative QCD theory used in the extraction of $\alpha_s$ is indicated in brackets (NLO: next-to-leading order; NNLO: next-to-next-to leading order; NNLO: NNLO matched with resummed next-to-leading logs; N <sup>3</sup> LO (NNNLO): next-to-NNLO). Figure taken from Ref. [2]. . . . .	3
1.4	Left: scaled energy density as a function of $T/T_c$ from Lattice QCD [7, 8]; Right: $(\varepsilon - 3p)/T^4$ at $\mu_B=0, 210, 410$ and $530$ MeV as a function of $T/T_c$ (from bottom to top, [9]). Figures taken from Ref. [7] and [9], respectively. . . . .	4
1.5	Deconfinement and Chiral Symmetry restoration in 2-flavour QCD. Left: $\langle L \rangle$ (left) the order parameter for deconfinement in the pure gauge limit ( $m_q \rightarrow \infty$ ). Right: $\langle \bar{\psi}\psi \rangle$ the order parameter for Chiral symmetry broken in the chiral limit ( $m_q \rightarrow 0$ ). Also shown are the corresponding susceptibilities as a function of the gauge coupling $\beta = 6/g^2$ . Figures taken from Ref. [7]. . . . .	5
1.6	Schematic phase diagram of QCD matter in the $(T, \mu_B)$ plane. Figure taken from Ref. [22]. . . . .	6
1.7	Sketch of the heavy-ion collision space-time evolution. Figure taken from Ref. [34]. . . . .	7
1.8	Critical temperature (left) at chemical freeze-out and baryonic chemical potential (middle) as a function of energy from the fitting of data with thermal model. The resulting temperature as a function of baryonic chemical potential (right). Figures taken from Ref. [44]. . . . .	9
1.9	Left: Scheme showing the strangeness production in the QGP. Right: Enhancement factor for the mid-rapidity yields per participating nucleon at $158 A$ GeV/c Pb–Pb collisions relative to p–Pb collisions for various strange and non-strange hadron species; Figures taken from Ref. [39] and [38], respectively. . . . .	10
1.10	Left: Measured $J/\Psi$ production yields normalised to the yields expected assuming that the only source of suppression is the ordinary absorption by the nuclear medium as a function of $N_{\text{part}}$ , in In–In (red) and Pb–Pb (blue) collisions at SPS energies. Right: Inclusive $J/\Psi R_{AA}$ as a function of the number of participating nucleons measured in Pb–Pb collisions at $\sqrt{s_{NN}} = 2.76$ TeV compared to PHENIX results in Au–Au collisions at $\sqrt{s_{NN}} = 200$ GeV at mid-rapidity and forward rapidity. See Ref. [59] for details. Figures taken from Ref. [60] and [59], respectively. . . . .	11
1.11	Left: Schematic initial anisotropic geometry of the collision fireball; Right: Elliptic Flow ( $v_2$ ) of identified hadrons measured in 20 – 40% in Pb–Pb collisions at $\sqrt{s_{NN}} = 2.76$ TeV with ALICE, together with model comparison. See Ref. [81] for details; Figure taken from Ref. [81].	13



1.12 (a) $e^+e^-$ invariant mass spectrum measured in $\sqrt{s_{NN}} = 200$ GeV Au–Au minimum bias (0 – 80%) collisions compared to a hadronic cocktail simulation. The vertical bars on data points depict the statistical uncertainties, while the systematic uncertainties are shown as grey boxes (smaller than the marker). (b) Ratio of data over cocktail (black points) and ratio of model calculations over cocktail (red and blue curves). Green bands depict systematic uncertainties on the cocktail. (c) Mass spectrum of the excess (data minus cocktail) in the low-mass region compared to model calculations. Green brackets depict the total systematic uncertainties including those from cocktails. See Ref. [82] for details. Figure taken from Ref. [82]. . . . .	14
1.13 Left: sketch of di-jet production and pQCD collinear factorisation in hadronic collisions (see text for details). Right: jet quenching in nucleus-nucleus collision which can be characterised by a transport coefficient $\hat{q}$ , gluon density $dN_g/dy$ and temperature $T$ ). Figures taken from Ref. [91]. . . . .	16
1.14 Nuclear modification factor $R_{AA}$ as a function of $p_T$ ( $m_T$ ) measured by the CMS Collaboration in Pb–Pb collisions at $\sqrt{s_{NN}} = 2.76$ TeV for different particle species: Z bosons [97], W bosons [98], isolated photons [99], charged particles [100], non-prompt J/Ψ [101], inclusive jets [102] and b-jets [103]. See each reference for the detail. Figure taken from Ref. [104]. . . . .	17
1.15 Left: comparison of gluon modifications at $Q^2 = 1.69\text{GeV}^2$ for Pb nucleus ( $R_G^{\text{Pb}}$ ) obtained from different models, see Ref. [105] for detail. Middle: parton distributions in a proton. Right: $x$ and $A$ dependence of the saturation scale $Q_s$ . Figures taken from Ref. [105], [109] and [110], respectively. . . . .	18
1.16 Power $\alpha$ of the $A$ dependence of the invariant cross section extrapolated as $A^\alpha$ , as a function of $p_T$ . Data are collected for different hadron species in p–A collisions at Fermilab [119]. Figure taken from Ref. [119]. . . . .	20
1.17 Left: typical gluon radiation diagram in BDMPS approach [127]. Right: generalized suppression factor, $\mathcal{D}$ , as a function of $\theta$ and $M/\sqrt{s}$ , see Ref. [128] for detail. Figures taken from Ref. [38] and [129], respectively. . . . .	21
1.18 Predictions of the $R_{AA}$ of non-photonic electrons from the decay of quenched heavy quark (c+b) jets compared to RHIC measurements in central Au+Au reactions at 200 AGeV (see Ref. [131] for details). Figure taken from Ref. [136]. . . . .	22
1.19 Quark masses in the QCD vacuum and the Higgs vacuum. A large fraction of the light quark masses is due to the chiral symmetry breaking in the QCD vacuum. Figure taken from Ref. [137]. . . . .	23



1.20	Left: energy dependence of the total nucleon-nucleon charm production cross section. In case of proton-nucleus (p-A) or deuteron-nucleus (d-A) collisions, the measured cross sections have been scaled down by the number of binary nucleon-nucleon collisions calculated using the Glauber model. Right: inclusive beauty production cross section per rapidity unit measured at mid-rapidity as a function of the center of mass energy in pp collisions (PHENIX and ALICE) and p $\bar{p}$ collisions (UA1 and CDF). The NLO MNR calculations [140] (and its uncertainties) are represented by solid (dashed) lines. Figures taken from Ref. [138] and [139], respectively. . . . .	24
1.21	$R_{AA}$ as a function of $p_T$ at mid-rapidity for different energy loss mechanisms, for D mesons (left) and B mesons (right). See the text for detail. Figures taken from Ref. [141]. . . . .	25
1.22	Left: suppression of charm quarks (the full curve), light quarks (the dashed curve) and gluons (the dot-dashed curve) as a function of momentum. Middle: Comparison of charm quark (the full curve) and D-meson suppression predictions (the dashed curve). Right: comparison of light hadron suppression predictions (the full curve) with light quark (the dashed curve) and gluon (the dot-dashed curve) suppression predictions. Figures taken from Ref. [143]. . . . .	26
1.23	Nuclear modification factor predicted by the employed transport model for D-meson produced in central Pb-Pb collisions at $\sqrt{s_{NN}} = 2.76$ TeV. Data from ALICE are shown for comparison. Figures taken from Ref. [153]. . . . .	27
1.24	Top: $p_T$ -differential cross section for prompt $D^0$ , $D^+$ and $D^{*+}$ mesons in pp collisions at $\sqrt{s} = 2.76$ TeV compared with FONLL and GM-VFNS theoretical predictions. Bottom: the ratio of the measured cross section and the central values from FONLL and GM-VFNS calculations. Figure taken from Ref. [138]. . . . .	27
1.25	Invariant differential production cross sections of electrons from heavy-flavour hadron decays measured by ALICE and ATLAS in pp collisions at $\sqrt{s} = 7$ TeV in different rapidity intervals (see text). FONLL pQCD calculations [140, 154, 155] with the same rapidity selections are shown for comparison. Figure taken from Ref. [156]. . . . .	28
1.26	Average $R_{AA}$ of prompt $D^0$ , $D^+$ and $D^{*+}$ mesons as a function of $N_{part}$ compared with non-prompt $J/\Psi$ measured by CMS in the central rapidity region in $6.5 < p_T < 30$ GeV/c. Vertical bars are the statistical uncertainties, empty boxes are the total uncorrelated systematic uncertainties, filled boxes are the correlated systematic uncertainties. Figure taken from Ref. [161]. . . . .	30
1.27	$R_{AA}$ of $D^0$ mesons ( $ y^D  < 0.5$ ) and charged pions ( $ y^{\pi^\pm}  < 0.8$ ) as a function of $p_T$ , for semi-central (30 – 50%) Pb-Pb collisions at $\sqrt{s_{NN}} = 2.76$ TeV. Figure taken from Ref. [162]. . . . .	31



1.28	Nuclear modification factor of muons (electrons) from heavy-flavour hadron decays in $2.5 < y^\mu < 4$ ( $ y^e  < 0.6$ ) and $3 < p_T^\mu < 20$ GeV/ $c$ ( $3 < p_T^e < 18$ GeV/ $c$ ) in central Pb–Pb collisions at $\sqrt{s_{NN}} = 2.76$ TeV. Figure taken from Ref. [164]. . . . .	31
1.29	Comparison of prompt $D^0$ meson and charged-particle $v_2$ in three centrality classes as a function of $p_T$ . Both measurements are done with the event plane method. Figure taken from Ref. [165]. . . . .	32
1.30	Elliptic flow of electrons and muons from heavy-flavour hadron decays as a function of $p_T$ , for Pb–Pb collisions at $\sqrt{s_{NN}} = 2.76$ TeV in the centrality range 20 – 40%. Figure taken from Ref. [166]. . . . .	32
1.31	Nuclear modification factor as a function of $p_T$ for prompt $D^0$ , $D^+$ , $D^{*+}$ and $D_s^+$ mesons in p–Pb collisions at $\sqrt{s_{NN}} = 5.02$ TeV. Statistical (bars), systematic (empty boxes), and normalization (full box) uncertainties are shown. Figure taken from Ref. [170]. . . . .	34
1.32	Nuclear modification factor $R_{pA}^{FONLL}$ of $B^+$ (left panel), $B^0$ (middle panel), and $B_s^0$ (right panel) mesons measured in p–Pb collisions at $\sqrt{s_{NN}} = 5.02$ . The vertical bars represent the statistical uncertainty while the total systematic uncertainties are plotted as boxes around the data points. Figure taken from Ref. [172]. . . . .	34
1.33	Nuclear modification factor of beauty-hadron decay electrons and inclusive heavy-flavour hadron electrons. The error bars (boxes) represent the statistical (systematic) uncertainties. Figure taken from Ref. [173]. . . . .	35
1.34	The fully-corrected like-sign-subtracted heavy-flavour $e - \mu$ pair yield in (red circles) $\langle N_{coll} \rangle$ -scaled pp collisions (blue boxes) and d–Au collisions, shifted in $\Delta\phi$ for clarity. The bars are statistical uncertainties. The boxes are the systematic uncertainties from the decay and punch-through background subtraction. The overall normalization uncertainties of 16.1% and 13.4% in pp and d–Au collisions, respectively, and 5.7% uncertainty from $\langle N_{coll} \rangle$ are not included. Figure taken from Ref. [176]. . . . .	35
1.35	The average electro-magnetic energy loss, $dE/dx$ , of a muon in hydrogen, iron and uranium as a function of muon energy (see text for details). Figure taken from Ref. [2]. . . . .	36
1.36	Quantities used to describe multiple scatterings: the lateral displacement of the muon trajectory on a projected plane of material, together with the scattering angle. Figures taken from Ref. [2]. . . . .	37
1.37	$p_T$ correlations between the "mother" HF hadron and the "daughter" lepton for muons at forward (left) and electrons at mid-rapidity (right). See the text for details. . . . .	38
2.1	Schematic layout of ALICE with various detector systems, indicated in the figure with their acronyms. Figure taken from [195]. . . . .	42



2.2	Conceptual view of particle identification with the ALICE detector. The solid and dashed band both represent the identification capabilities, while the later one correspond to the relativistic rise of Bethe Bloch in the TPC. Figure taken from Ref. [214]. . . . .	48
2.3	Sketch of the ALICE muon spectrometer. Figure taken from Ref. [215].	48
2.4	Invariant mass distribution of $\mu^+\mu^-$ pairs measured by ALICE for pp collisions at $\sqrt{s} = 7$ TeV ( $\mathcal{L} = 1.35$ pb $^{-1}$ , corresponding to the full 2011 dimuon-triggered data sample). Figure taken from Ref. [194].	50
2.5	Layout of the front absorber (left) and small angle beam shielding (right). Figures taken from Ref. [220]. . . . .	51
2.6	Conceptual view of the dipole magnet. Figure taken from Ref. [220].	52
2.7	Layout of the tracking station 2 (left) and 4, 5 (right). see text for details. Figures taken from Ref. [216]. . . . .	53
2.8	Principle of muon track reconstruction with the 5 tracking stations in the bending plane (i.e. the plane perpendicular to the magnetic field). Adapted from Ref. [42]. . . . .	54
2.9	Relative transverse momentum ( $\sigma_{p_T}/p_T$ ) resolution of the tracks reconstructed with the ALICE muon spectrometer. Black points are the results based on raw OCDB, while the red and blue ones are based on different mis-alignments for testing. The data period is LHC11h.	56
2.10	Principle of the $p_T$ cut performed by the trigger in the bending plane. Adapted from Ref. [42, 227]. . . . .	57
2.11	Layout of the MFT detector in ALICE. Figure from Ref. [234]. . . . .	60
2.12	Schematic view of the AliRoot framework. Figure taken from Ref. [245].	62
2.13	Data processing framework. Figure taken from Ref. [245]. . . . .	64
3.1	Schematic plot for $Q^2$ as a function of $x$ within various acceptances from different experiments. See text for details. Figure taken from [255].	65
3.2	Pile-up rate for different triggers at both forward (upper plots) and backward rapidity (bottom plots). The results are calculated at hardware (red) and software (black) level, respectively. . . . .	70
3.3	Purity (top-left), $L0bRate_{MB}$ (top-right) of minimum bias events, $N_{colliding}$ (bottom-left) and pile-up correction factor (bottom-right) as a function of run number in <b>LHC13d</b> period. . . . .	73
3.4	Similar with Fig. 3.3 but for <b>LHC13e</b> period. . . . .	74
3.5	Similar with Fig. 3.3 but for <b>LHC13f</b> period. . . . .	74
3.6	$L0b$ counters information for MB (top-left), MSL (top-middle), and MSH (top-right) trigger events; the fraction of MSL (bottom-left) and MSH (bottom-right) trigger events with Physics Selection in <b>LHC13d</b> period. . . . .	75
3.7	Similar to Fig. 3.6 but for <b>LHC13e</b> period. . . . .	76
3.8	Similar to Fig. 3.6 but for <b>LHC13f</b> period. . . . .	77
3.9	Normalization factor from the scaler method for different runs and triggers in <b>LHC13d</b> period: MSL (left) and MSH (right). . . . .	77



3.10	Similar to Fig. 3.9 but for <b>LHC13e</b> period. . . . .	78
3.11	Similar to Fig. 3.9 but for <b>LHC13f</b> period. . . . .	78
3.12	Number of MB (upper-left), MSL (upper-right), MB&&0MSL (bottom-left) and MSL&&0MSH (bottom-right) for different runs in <b>LHC13d</b> period. . . . .	79
3.13	Similar to Fig. 3.12 but for <b>LHC13e</b> period. . . . .	79
3.14	Similar to Fig. 3.12 but for <b>LHC13f</b> period. . . . .	80
3.15	Normalization factor from the offline method for different runs and triggers in <b>LHC13d</b> period: MSL (left) and MSH (right.) . . . . .	80
3.16	Similar to Fig. 3.15 but for <b>LHC13e</b> period. . . . .	81
3.17	Similar to Fig. 3.15 but for <b>LHC13f</b> period. . . . .	81
3.18	Weighted mean of the normalization factor with the statistical uncertainty and systematic uncertainty for different runs and triggers in <b>LHC13d</b> and <b>LHC13e</b> periods: mean value for MSL trigger events with statistical uncertainty (top-left) and corresponding systematic uncertainty (top-right); mean value for MSH trigger events with statistical uncertainty (bottom-left) and corresponding systematic uncertainty (bottom-right). . . . .	82
3.19	Similar to Fig. 3.18 but for <b>LHC13f</b> period. . . . .	83
3.20	Trigger matching and $p \times$ DCA cut effect on different muon sources with Monte Carlo simulations ("LHC13b2_efix" that is the full simulation with DPMJET model). Upper: $p_T$ spectra of various muon sources after the muon event selection (Sec. 3.1.1) and the tracks within the acceptance of the muon spectrometer. Middle: similar as upper one, but with adding trigger matching cut. Bottom: in analogy to the middle one, but with adding $p \times$ DCA cut. . . . .	84
3.21	Transverse momentum distributions of inclusive muons with different selection cuts at event and track level in p–Pb (left) and Pb–p (right) collisions. . . . .	86
3.22	Muon <i>Charge Asymmetry</i> obtained with different triggers and data samples after the standard procedure of selection is applied: LHC13d (upper), LHC13e (middle) and LHC13f periods (lower). Results from different triggers are shown as the curves with different color in each plot: MB (black), MSL (green) and MSH (red). . . . .	88
3.23	Left: $p_T$ spectra for different triggers with <b>LHC13d</b> and <b>LHC13e</b> periods normalized to the number of (equivalent) MB events in the range $2.03 < y_{\text{CMS}} < 3.53$ , and the used normalization factor is from Tab. 3.3. The results for different triggers are shown as the curves with different colors: MB (black), MSL (red) and MSH (green). Right: ratio of the normalized spectra for different triggers within the overlap $p_T$ regions: MB/MSL (black) and MSL/MSH (red). Note that only statistical uncertainties are shown. . . . .	89
3.24	Similar with Fig. 3.23 but for <b>LHC13f</b> period in the range $-4.46 < y_{\text{CMS}} < -2.96$ . . . . .	89



3.25	Quantities used to describe the multiple scattering with the front absorber. See text for details. Figure taken from Ref. [281]. . . . .	90
3.26	Left: the corrected $p \times$ DCA distribution as a function of $p_T$ with MSH in LHC13f period (Pb–p, not full statistics). Right: similar results but applying an additional cut on $6 \cdot \sigma_{p \times \text{DCA}}$ . . . . .	91
3.27	Ratio of the $p_T$ spectra with different scenarios of the $p \times$ DCA cut with respect to the ones without $p \times$ DCA cut: MSL results for LHC13d (left) and LHC13f (right). The standard muon selection cuts are implemented. Figures provided by Z. M. Zhang. . . . .	92
3.28	A cartoon example of the correlation of the final state observable $N_{\text{ch}}$ with Glauber calculated quantities ( $b$ , $N_{\text{part}}$ ). The plotted distribution and various values are illustrative and not actual measurements. Figure taken from Ref. [35]. . . . .	94
3.29	Distribution of the sum of amplitudes in the V0A hodoscopes (backward, Pb-going), as well as the NBD-Glauber fit; centrality classes are indicated by vertical lines. The inset shows a zoom-in on the most peripheral events. Figure taken from Ref. [283]. . . . .	95
3.30	Multiplicity fluctuation bias calculated from the NBD-Glauber MC as the ratio between mean multiplicity per ancestor and the mean NBD multiplicity in p–Pb and Pb–Pb calculations. Note that, CL1 ( $ \eta  < 1.4$ ) denotes the clusters measured in the 2 <sup>nd</sup> layer of Silicon Pixel detector, V0A ( $2.8 < \eta < 5.1$ ) is the amplitude measured by the V0 hodoscopes on the A-side (the Pb-remnant side), V0M is the sum of V0A ( $2.8 < \eta < 5.1$ ) + V0C ( $-3.7 < \eta < -1.7$ ) and ZNA is the energy deposited in Zero-Degree Neutron calorimeter on the A-side. Figure taken from Ref. [283]. . . . .	95
3.31	Top: number of participating nucleons versus impact parameter. Bottom: multiplicity versus the number of participating nucleons from the Glauber fit to V0A amplitude. The quantities are calculated with a Glauber Monte Carlo of p–Pb (left) and Pb–Pb (right) collisions. Figures taken from Ref. [283]. . . . .	96
3.32	Number of MB events scaled with the bin width versus event activity: OADB (Offline Analysis Data Base) based on LHC13bc (left) and LHC13de (right). See text for details. . . . .	97
3.33	Ratio (=scenario2/scenario1) of the normalization factors from different scenarios versus event activity and estimator. The left three plots are the results including pile-up events, while the right three are the ones excluding pile-up events. The upper, middle and bottom two plots are the results based on V0A, CL1 and ZNA, respectively. Concerning the results with ZNA, various scenarios are implemented. See the text for detail. . . . .	98



3.34	Fraction of pile-up event tagged using various values of the parameters at software level as a function of event activity. Results for MSL data based on V0A for the event activity determination with LHC13de (left) and LHC13f (right). See text for details. Figures taken from Ref. [263]. . . . .	100
3.35	Performance study of muons from heavy-flavour hadron decays corrected with the efficiency obtained with charm (namely, eff1) and beauty (namely, eff2), respectively. Results are shown versus $p_T$ (left) and $y$ (right). Figures taken from Ref. [287]. . . . .	102
3.36	Muon detection efficiency dependence with centrality for 4 different values of the minimum transverse momentum of muons; it was obtained by embedding pure $J/\Psi$ signal in the LHC10h data (Pb–Pb collisions at $\sqrt{s_{NN}} = 2.76$ TeV). Figure taken from Ref. [288]. . . . .	103
3.37	Acceptance $\times$ efficiency for muons from heavy-flavour hadron decays at forward ( $2.03 < y_{CMS} < 3.53$ , left panel) and backward rapidity ( $-4.46 < y_{CMS} < -2.96$ ). Results by asking matching with MSL and MSH rigged events are shown as black and red curves, respectively. See text for detail. . . . .	104
3.38	Acceptance $\times$ efficiency for muons from heavy-flavour hadron decays by asking the matching with MSL (left panel) and MSH (right panel) in the considered $p_T$ ranges. In each panel, the results are obtained both at forward (p–Pb) and backward rapidity (Pb–p) rapidity. . . . .	104
3.39	Trigger response function from pure $J/\Psi$ simulation in Pb–Pb collisions at $\sqrt{s_{NN}} = 2.76$ TeV. Figure taken from Ref. [290]. . . . .	105
3.40	Ratio of the MSH distribution over MSL distribution after acceptance $\times$ efficiency correction. The upper two panels are the results in p–Pb configuration (forward rapidity) within various rapidity intervals, while the bottom ones corresponds to the Pb–p configuration (backward rapidity). See text for details. . . . .	106
3.41	The tracking efficiency of $J/\Psi \rightarrow \mu^+\mu^-$ measured in data and (data-tuned) MC simulations for LHC13d period. Figure taken from Ref. [289]. . . . .	107
3.42	Comparison of acceptance $\times$ efficiency of muons from heavy-flavour hadron decays, for MSH triggered events in p–Pb configuration (LHC13e), obtained by using different mis-alignments with respect to the default ones (i.e. realistic). The acceptance $\times$ efficiency versus $p_T$ are shown on the left side, while the further comparison together with the quoted systematic uncertainty ( $0.5\% \times p_T$ in GeV/c, red bands) is presented on the right side. Results displayed in the upper, middle and bottom panel are corresponding to $\mu^\pm$ , $\mu^+$ and $\mu^-$ , respectively. . . . .	109



4.1	Transverse momentum distribution of reconstructed tracks in the muon spectrometer after all selection cuts are applied. The distributions are obtained from a PYTHIA (tune Perugia-0) simulation of pp collisions at $\sqrt{s} = 7$ TeV, together with the main sources of muons. Taken from Ref. [160]. . . . .	111
4.2	Left: transverse momentum distributions of reconstructed tracks in the muon spectrometer after all selection cuts are applied, according to DPMJET (LHC13b2_efix) simulations of p-Pb collisions at $\sqrt{s} = 5.02$ in $-4 < \eta_{LAB} < -2.5$ . Right: different sources of primary muons. See text for details. . . . .	112
4.3	The fraction of signal (heavy-flavour hadron decay muons) and background (primary decay muons) obtained with DPMJET simulations performed at forward (left) and backward (right) rapidity, respectively.	113
4.4	Left: distributions of muons from pion decays in different mother pion $p_T^{\pi^\pm}$ regions with a flat transverse momentum distribution of charged pions as input and a cut on the muon production distance at $\rho < 130$ cm. Right: ratio of the number of muons for $p_T^\mu < 16$ GeV/c over the ones for $p_T^\mu < p_T^{\max}$ , where $p_T^{\max}$ is the maximum transverse momentum of its mother pions $p_T^{\max} = p_T^{\text{Pion}}$ , shown as a function of $p_T^{\text{Pion}}$ . See text for details. . . . .	121
4.5	Same as the right panel of Fig. 4.4, but for $p_T^\mu < 20$ GeV/c. See text for details. . . . .	121
4.6	Same as Fig. 4.4, but for charged kaons. . . . .	121
4.7	Same as Fig. 4.5, but for charged kaons. . . . .	122
4.8	Distribution of muons from charged pion (left) and kaon (right) decays in $5.5 <  y_{LAB}  < 6.5$ . . . . .	122
4.9	$p_T$ spectra of charged pions (left) and kaons (right) measured in p-Pb collisions at $\sqrt{s_{NN}} = 5.02$ TeV for different V0A multiplicity event classes. The systematic and statistical uncertainty are plotted as color boxes and vertical error bars, respectively. Figures taken from Ref. [307]. . . . .	123
4.10	Statistical uncertainty (upper left), correlated (middle left) and uncorrelated (bottom left) systematic uncertainties for charged pions combined in 0 – 100%. Plots in right panels are for kaons. . . . .	124
4.11	Transverse momentum distribution of charged pions (left) and kaons (right) measured by ALICE at mid-rapidity in $2 < p_T < 15$ GeV/c and extrapolated up to 24 and 40 GeV/c, respectively. See text for details. . . . .	125
4.12	Upper: transverse momentum distribution of charged pions (upper left), as well as the quoted systematic uncertainty (upper right) in the range $2 < p_T < 24$ GeV/c. Bottom: similar results for kaons in the interval $2 < p_T < 40$ GeV/c. See text for details. . . . .	126



4.13	Pseudorapidity density of charged particles measured in NSD p–Pb collisions at $\sqrt{s_{NN}} = 5.02$ TeV compared to theoretical predictions. Figure taken from Ref. [308]. . . . .	127
4.14	Transverse momentum distributions of charged particles in NSD p–Pb collisions for different pseudo-rapidity ranges (upper panel). The spectra are scaled by the factors indicated on the figure. The histogram represents the reference spectrum in pp collisions (see text). The lower panel shows the ratio of the spectra at backward pseudo-rapidities to that at $ \eta_{CMS}  < 0.3$ . The vertical bars (boxes) represent the statistical (systematic) uncertainties. Figure taken from Ref. [314].	128
4.15	Ratio of the spectra for backward pseudo-rapidities to that at $ \eta_{CMS}  < 0.3$ obtained with DPMJET (upper left), HIJING (upper right) and PYTHIA+EPS09 (bottom). The vertical bars denote the statistical uncertainties. . . . .	129
4.16	Left: charged particle transverse momentum spectra in p–Pb collisions at $\sqrt{s_{NN}} = 5.02$ TeV for various pseudo-rapidity ranges (see legend for details). The spectra have been scaled by the quoted factors to provide better visibility. Right: the related asymmetry between backward and forward as a function of $p_T$ for $0.3 <  \eta_{CMS}  < 0.8$ , $0.8 <  \eta_{CMS}  < 1.3$ and $1.3 <  \eta_{CMS}  < 1.8$ . The vertical bars denotes the systematic uncertainty. Extracted from Ref. [309]. . . . .	130
4.17	$Y_{asym}$ obtained with DPMJET, HIJING and PYTHIA+EPS09 for various pseudo-rapidity ranges (see legend for details). . . . .	131
4.18	Left: ratio of the distribution at forward ( $0.8 < \eta_{CMS} < 1.3$ ) to that at mid-rapidity ( $0.3 < \eta_{CMS} < 0.8$ ), calculated with DPMJET, HIJING and PYTHIA+EPS09. Derived results from CMS are also shown. The vertical bars of data indicate the systematic uncertainties. Right: same as the left panel, taking the deviation of HIJING with respect to DPMJET as the systematic uncertainty. . . . .	132
4.19	Rapidity extrapolation factor $F_{extra.}$ versus $p_T$ and $y_{CMS}$ for pions (upper left) and kaons (upper right), and versus $y_{cms}$ for pions (bottom left) and kaons (bottom right) in the range $2 < p_T < 20$ GeV/c. These results are obtained with DPMJET simulations. Note that forward rapidity represents negative side in Monte-Carlo productions which is contrary to our definition. . . . .	133
4.20	Same as Fig. 4.19, but based on HIJING simulations. . . . .	133
4.21	$p_T$ and $y_{cms}$ -differential distributions for pions (upper left) and kaons (upper right), and $p_T$ -differential distributions for pions (bottom left) and kaons (bottom right) obtained by taking as input the central barrel measurements together with the rapidity extrapolation factor calculated with DPMJET. . . . .	134
4.22	Same as Fig. 4.21, but calculated with HIJING. . . . .	134



4.23	Left: $Y_{\text{asym}}$ defined within different rapidity intervals with HIJING simulation. Right: ratio with taking as the reference $Y_{\text{asym}}$ in $1.3 <  \eta_{\text{CMS}}  < 1.8$ . See text for details. . . . .	135
4.24	Ratio of the yields of muons from charged pion and kaon decays when applying a cut on $\rho$ varied within $110 < \rho < 150$ cm over $\rho < 130$ cm, as shown in the left and right panels, respectively. . . . .	137
4.25	Muons from pions decays in the range $2.03 < y_{\text{CMS}} < 3.53$ : results from different models (upper left). Different sources of systematic uncertainties (middle left). Results with total systematic uncertainties (bottom left). The right three plots are similar to the left ones, but for muons from kaon decays. See text for details. . . . .	138
4.26	Left: $p_{\text{T}}$ distributions of muons from pion decays (red), kaon decays (blue) and combined pion and kaon decays (black) at forward rapidity $2.03 < y_{\text{CMS}} < 3.53$ . Right: different sources of systematics. . . . .	138
4.27	Muons from pions decays in the range $2.96 < y_{\text{CMS}} < 3.53$ : results from different models (upper left). Different sources of systematic uncertainties (middle left). Results with total systematic uncertainties (bottom left). The right three plots are similar to the left ones, but for muons from kaon decays. See text for details. . . . .	139
4.28	Left: $p_{\text{T}}$ distributions of muons from pion decays (red), kaon decays (blue) and combined pion and kaon decays (black) at forward rapidity $2.96 < y_{\text{CMS}} < 3.53$ . Right: different sources of systematics. . . . .	139
4.29	Muons from pions decays in the range $-4.46 < y_{\text{CMS}} < -2.96$ : different sources of systematic uncertainties (upper left). Results with total systematic uncertainties (bottom left). The right three plots are similar to the left ones, but for muons from kaon decays. See text for details. . . . .	140
4.30	Left: $p_{\text{T}}$ distributions of muons from pion decays (red), kaon decays (blue) and combined pion and kaon decays (black) at forward rapidity $-4.46 < y_{\text{CMS}} < -2.96$ . Right: different sources of systematics. . . . .	140
4.31	Muons from pion decays in the range $-3.53 < y_{\text{CMS}} < -2.96$ : different sources of systematic uncertainties (upper left). Results with total systematic uncertainties (bottom left). The right three plots are similar to the left ones, but for muons from kaon decays. See text for details. . . . .	141
4.32	Left: $p_{\text{T}}$ distributions of muons from pion decays (red), kaon decays (blue) and combined pion and kaon decays (black) at forward rapidity $-3.53 < y_{\text{CMS}} < -2.96$ . Right: different sources of systematics. . . . .	141
4.33	Fraction of the estimated background with respect to inclusive muons in the rapidity range $2.03 < y_{\text{CMS}} < 3.53$ (left) and $-4.46 < y_{\text{CMS}} < -2.96$ (right). The boxes denote the total systematic uncertainty on the background. . . . .	142



4.34	Fraction of the estimated background with respect to inclusive muons in the rapidity range $2.96 < y_{\text{CMS}} < 3.53$ (black) and $-3.54 < y_{\text{CMS}} < -2.96$ (red). The boxes denote the total systematic uncertainty on the background. . . . .	143
4.35	Decay probability of charged pions as a function of $p_z$ estimated at $\rho < 130$ cm, by means of the fast simulation . See the text for details.	143
4.36	Left: $p_T$ distributions from the fast and the full simulations in the rapidity range $-4 < y_{\text{LAB}} < -2.5$ . Right: ratio of the distribution from the full distribution to that from the fast simulation. The boxes correspond to the combined statistical and systematic uncertainties.	144
4.37	Upper left: backward-to-forward ratio of charged pions which decay into muons in $2.5 <  y_{\text{LAB}}  < 4$ (i.e. corresponding to $2.03 <  y_{\text{CMS}}  < 3.53$ at forward and $-4.46 <  y_{\text{CMS}}  < -2.96$ at backward rapidity in the CMS frame) without taking into account the absorber effect (i.e. no cut on decay length $\rho$ ). The lower, upper and mean value are obtained via Eq. 4.9, 4.10 and 4.13, respectively. The shadowed region denotes the corresponding systematic uncertainty. Upper right: similar to the upper left one, but including the absorber effect ( $\rho < 130$ cm). Bottom: similar to the upper two plots, but for the muons from pion decays. . . . .	145
4.38	Similar to Fig. 4.37, but in the rapidity range $2.96 <  y_{\text{CMS}}  < 3.53$ .	146
4.39	Relative statistical and (total) systematic uncertainty of charged pions measured at central rapidity $0 < y_{\text{CMS}} < 0.5$ with V0A (upper), CL1 (middle) and ZNA (bottom). . . . .	149
4.40	Same as Fig. 4.39, but for charged kaons. . . . .	150
4.41	$p_T$ distributions of charged kaons in 10–20% with taking ZNA as the event activity estimator, after the $p_T$ interpolation down to $p_T = 2$ GeV/c and the $p_T$ extrapolation up to $p_T = 40$ GeV/c. See text for details. . . . .	151
4.42	$p_T$ distributions of charged pions within different event activity bins with taking V0A (upper), CL1 (middle) and ZNA (bottom) as the event activity estimators. The distribution and the related total systematic uncertainty are shown in the left and right panel, respectively.	152
4.43	Same as Fig. 4.42, but for kaons with both the $p_T$ interpolation/extrapolation, shown in the range $2 < p_T^{K^\pm} < 40$ GeV/c. . . . .	153
4.44	Distribution of the sum of amplitudes in the V0A hodoscopes (Pb-going), reproduced by the NBD-Glauber fit ( $N_{\text{part}} \times \text{NBD}$ , $\mu = 11.0$ and $k = 0.44$ ). Event activity classes are indicated by vertical bands. See Ref. [283] for details. . . . .	154
4.45	Event entries versus impact parameter with the event activity class defined by the MC Glauber model. See text for details. . . . .	154
4.46	Schematic representation of the colliding geometry via Optical Glauber Model, with transverse (a) and longitudinal (b) views. Figure taken from Ref. [35]. . . . .	156



4.47	Geometrical variables in p–Pb collisions at $\sqrt{s_{NN}} = 5.02$ TeV, based on the Optical Glauber Model: nuclear charge density (upper left), thickness function (upper right), total number of participants (bottom left) and total number of binary collisions (bottom right). . . . .	156
4.48	Left: total inelastic cross section estimated via Optical Glauber Model in p–Pb collisions at $\sqrt{s_{NN}} = 5.02$ TeV. Right: event activity versus the impact parameter, which is obtained by slicing the $b$ -differential cross section to obtain the desired fraction of the total integral. . . . .	157
4.49	Event entries versus impact parameter with the event activity class defined by the Optical Glauber. See text for details. . . . .	158
4.50	Comparison of impact parameter ranges obtained by means of MC Glauber ( $x$ -axis, geometrical slicing) and Optical Glauber ( $y$ -axis, multiplicity slicing) within a given event activity interval. The results are derived from Fig. 4.45 and 4.49, respectively. See text for details. . . . .	159
4.51	Left: total number of events within a given event activity bin; the results based on the related impact parameter range defined by MC (multiplicity slicing) and Optical (geometry slicing) Glauber model as shown as black and red points, respectively. Right: deviation with respect to the one based on Optical Glauber. . . . .	159
4.52	Left: $\eta$ spectra of charged particles within different event activity bins measured by the ATLAS Collaboration. Right: distributions measured in central and semi-central collisions to that in peripheral collisions together with the fitted results which are obtained from [319]. Extracted from Ref. [319] . . . . .	160
4.53	$\eta$ extrapolation with Gaussian function in the range 5 – 10%. Similar to the procedure for $p_T$ extrapolation, as shown in Sec. 4.2.2. . . . .	161
4.54	Left: same as the left panel of Fig. 4.52 but with $\eta$ extrapolation to have the results in the range $-7 < \eta_{LAB} < 6$ . Right: the related systematic uncertainty. . . . .	161
4.55	Up: $\eta$ distributions of charged particles measured by ALICE (0 – 100%) and ATLAS (0 – 90%), as well as $K^\pm/\pi^\pm$ $\eta$ distributions from DPMJET (0 – 90%) and HIJING (0 – 90%). Bottom: ratio of the distributions in data and MC. See text for details. . . . .	162
4.56	$\eta$ distribution of charged particles measured by ALICE at mid-rapidity (squares) and forward rapidity (triangles), and ATLAS with the extrapolation (dashed area). $K^\pm/\pi^\pm$ $\eta$ distributions from DPMJET (circles) and HIJING (inverse triangles) shown for comparison (see the text). . . . .	162
4.57	$\eta$ distributions of charged particles measured by ATLAS with the extrapolation (band) up to $\eta_{CMS} = \pm 6$ within different event activity bins. The two vertical dashed lines indicate the acceptance of ATLAS. The results of $K^\pm/\pi^\pm$ predicted by DPMJET (red) and HIJING (blue) are shown for comparison. . . . .	163



4.58	Comparison of the $\eta$ distributions of charged particles measured by ATLAS with respect to the ones of $K^\pm/\pi^\pm$ predicted by DPMJET and HIJING. The two vertical dashed lines indicate the acceptance of ATLAS. . . . .	164
4.59	$Y_{\text{asym}}(1.3 <  \eta_{\text{CMS}}  < 1.8)$ of charged particles measured by CMS for multiplicity integrated collisions (black), $E_T > 40$ GeV (red) and $E_T < 20$ GeV (blue). The vertical bars indicate the systematic uncertainty. Adapted from Ref. [309]. . . . .	165
4.60	Left: $Y_{\text{asym}}(1.3 <  \eta_{\text{CMS}}  < 1.8)$ of charged particles within different event activity classes. They are obtained by using a parameterization procedure, which takes as input the CMS measurements in multiplicity integrated collisions (0 – 100%) and the one with $E_T > 40$ GeV (0 – 3%). Middle: ratio of $Y_{\text{asym}}(1.3 <  \eta_{\text{CMS}}  < 1.8)$ estimated in 73 – 100% to the available data. Right: further comparison between the estimated results and data. The vertical bars indicate the systematic uncertainty. See text for details. . . . .	166
4.61	Same as Fig. 4.60, but taking as input the CMS measurements in 0 – 100% and in 73 – 100%. . . . .	166
4.62	Same as Fig. 4.60, but taking as input the CMS measurements in 0 – 3% and in 73 – 100%. . . . .	167
4.63	Left: average results of $Y_{\text{asym}}(1.3 <  \eta_{\text{CMS}}  < 1.8)$ based on different scenarios for the parameterization procedure. Right: the corresponding systematic uncertainty within different event activity classes. See text for details. . . . .	168
4.64	Upper left: $p_T$ distributions of muons from $\pi^\pm$ (red), $K^\pm$ (blue) and $K^\pm/\pi^\pm$ (black) decays at forward rapidity $2.03 < y_{\text{CMS}} < 3.53$ in the event activity 5 – 10%. The used estimator is V0A. Upper right: the different sources of systematic uncertainty. Lower two: same as the upper plots but at backward rapidity $-4.46 < y_{\text{CMS}} < -2.96$ . . . . .	169
4.65	Upper left: $p_T$ distributions of muons from $K^\pm/\pi^\pm$ decays within different event activity bins at forward rapidity $2.03 < y_{\text{CMS}} < 3.53$ . The results are based on V0A. Upper right: background to inclusive muon ratio. Middle: same as upper plots but for CL1 estimator. Bottom: same as upper plots but for ZNA estimator. . . . .	170
4.66	Same as Fig. 4.65 but for $-4.46 < y_{\text{CMS}} < -2.96$ . . . . .	171
4.67	Left: ratios of particle yields measured in pp, p–Pb, and Pb–Pb collisions with ALICE at mid-rapidity; Right: ratios of particle yields in the range $ y  < 1$ as a function of the track multiplicity for $ \eta  < 2.4$ . Model predictions are shown for comparison. Figures taken from Ref. [321] (left) and [322] (right), respectively. . . . .	172
4.68	Kaon to pion ratio predicted by DPMJET within various event activity classes. . . . .	172



4.69	Ratio of the asymmetry factor in $2 <  \eta_{\text{CMS}}  < 6$ in with respect to the one in $1 <  \eta_{\text{CMS}}  < 2$ . Results are obtained with HIJING for different event activity classes. See the text for details. . . . .	173
4.70	Asymmetry factor in data $Y_{\text{asym}}^{(\text{inclusive muon})}$ : results are obtained within $2.96 < y_{\text{CMS}} < 3.22$ (black) and $3.22 < y_{\text{CMS}} < 3.53$ (blue). The results based on the estimated decay muons (red) are shown for comparison. The related upper and low band are defined in the same way as in the multiplicity integrated collisions (Eq. 4.11 and 4.12). . . . .	173
5.1	Left: production cross sections (up) of heavy quark pairs in $2.03 < y_{\text{CMS}} < 3.53$ in pp collisions at $\sqrt{s} = 5.02$ TeV, as well as the relative uncertainty for charm (middle) and bottom (bottom), respectively. Right: same as in the left panel but in the rapidity range $-4.46 < y_{\text{CMS}} < -2.96$ . . . . .	178
5.2	Ratio of the production cross sections of heavy-quark pairs generated within $2.03 < y_{\text{CMS}} < 3.53$ and $-4.46 < y_{\text{CMS}} < -2.96$ as a function of $p_{\text{T}}$ . Results for charm and bottom are shown as the red and blue curves, respectively. . . . .	179
5.3	Production cross section of muons from heavy-flavour hadron decays within different channels and different rapidity regions: $2.03 < y_{\text{CMS}} < 3.53$ (left) and $-4.46 < y_{\text{CMS}} < -2.96$ (right), as a function of (muon) $p_{\text{T}}$ . . . . .	179
5.4	Ratio of the production cross sections of muons from different sources (shown in the text) within $2.03 < y_{\text{CMS}} < 3.53$ and $-4.46 < y_{\text{CMS}} < -2.96$ . Results for different sources are shown by the curves with different colors. . . . .	180
5.5	Production cross section of muons from charm and bottom, including direct decay and feed down component, in the rapidity regions: $2.03 < y_{\text{CMS}} < 3.53$ (left) and $-4.46 < y_{\text{CMS}} < -2.96$ (right), as a function of (muon) $p_{\text{T}}$ . . . . .	181
5.6	Left: $p_{\text{T}}$ -differential cross section of muons from heavy-flavour hadron decays at forward rapidity ( $2.5 < y_{\text{CMS}} < 4$ ) in pp collisions at $\sqrt{s} = 7$ TeV. Right: same as left in the five rapidity ranges reported in the figure. The grey bands represent FONLL predictions. Figures taken from Ref. [160] . . . . .	183
5.7	$p_{\text{T}}$ -differential cross section of muons from heavy-flavour hadron decays at forward rapidity ( $2.5 < y_{\text{CMS}} < 4$ ) in pp collisions at $\sqrt{s} = 2.76$ TeV. The grey bands represent the FONLL predictions. Figures taken from Ref. [159]. . . . .	183
5.8	Scheme of the combination among rapidity bins; $C_1$ , $C_2$ and $C_3$ denote the combined rapidity regions of $2.8 < y_{\text{CMS}} < 4$ , $2.5 < y_{\text{CMS}} < 3.7$ and $2.8 < y_{\text{CMS}} < 3.7$ , respectively, together with $C_0$ indicating the results in the full acceptance $2.5 < y_{\text{CMS}} < 4$ . . . . .	184



5.9	$p_T$ -differential cross section of muons from heavy-flavour hadron decays, obtained after scaling the measurements within different rapidity intervals in pp collisions at 7 TeV (red) compared to the one obtained in the full acceptance in pp collisions at 2.76 TeV (blue). . .	184
5.10	Relative deviation of the scaled results with respect to the one based on full acceptance (left) and the measurement at 2.76 TeV (right). .	185
5.11	$p_T$ -differential cross section of muons from heavy-flavour hadron decays, obtained by extrapolating the measurements within different rapidity intervals to the full acceptance in pp collisions at $\sqrt{s} = 7$ TeV. Results obtained after scaling (blue) are compared to the measurements made in the full acceptance (red). . . . .	186
5.12	Relative deviation of the cross sections in the full acceptance extrapolated from the ones within different rapidity intervals with respect to the available measurement the same region. . . . .	187
5.13	Left: $p_T$ -differential cross section of muons from heavy-flavour hadron decays in pp collisions at $\sqrt{s} = 7$ TeV. The distributions are presented in the four rapidity intervals reported in the figure. In the high $p_T$ region, the distributions are fitted with power-law functions. Right: same as Fig. 5.12 but obtained with the results of the fits shown in the left panel. . . . .	187
5.14	Upper: FONLL scaling factor from $\sqrt{s} = 7$ TeV ( $2.5 < y_{\text{CMS}} < 4$ ) to 5.02 TeV ( $2.03 < y_{\text{CMS}} < 3.53$ ) for the measurement of the $p_T$ -differential cross section of muons from heavy-flavour hadron decays with different combinations of <b>quark masses</b> as indicated on the figure (left), as well as the related relative systematic uncertainty (right). Middle: FONLL scaling factor with different combinations of <b>QCD scales</b> indicated on the figure (left); related relative systematic uncertainty (right). Bottom: FONLL scaling factor with different <b>QCD scales (red boxes) and quark masses (blue boxes)</b> , as well as the total systematic uncertainty marked as yellow bands (left), and the corresponding relative systematic uncertainty (right). . . . .	188
5.15	Same as Fig. 5.14 but for the rapidity interval $-4.46 < y_{\text{CMS}} < -2.96$ .	189
5.16	The reference for pp collisions at $\sqrt{s} = 5.02$ TeV obtained by means of the energy scaling procedure, which takes as input the $p_T$ -differential cross section of muons from heavy-flavour hadron decays measured within the full acceptance ( $2.5 < y_{\text{CMS}} < 4$ ) for pp collisions at 7 TeV, and the results are extrapolated to forward ( $2.03 < y_{\text{CMS}} < 3.53$ , left) and backward ( $-4.46 < y_{\text{CMS}} < -2.96$ , right) rapidity, respectively. In both panels, the solid curves are FONLL calculations and the bands display the theoretical systematic uncertainties. Also shown, are the FONLL calculations and systematic theoretical uncertainties for muons from charm (long dashed curves) and beauty (dashed curves) decays. Results obtained after scaling (red boxes) are compared to FONLL predictions (grey bands) in the bottom panels. . . .	190



5.17	Relative <b>statistical uncertainty</b> of the estimated pp reference at forward ( $2.03 < y_{\text{CMS}} < 3.53$ , left) and backward ( $-4.46 < y_{\text{CMS}} < -2.96$ , right) rapidity. . . . .	191
5.18	Relative <b>systematic uncertainty</b> of the estimated pp reference at forward ( $2.03 < y_{\text{CMS}} < 3.53$ , left) and backward ( $-4.46 < y_{\text{CMS}} < -2.96$ , right) rapidity. . . . .	191
5.19	The reference for pp collisions at $\sqrt{s} = 5.02$ TeV obtained by means of the energy scaling procedure in the range $2 < p_{\text{T}} < 12$ GeV/ $c$ (i.e. red boxes), taking as input the $p_{\text{T}}$ -differential cross section of muons from heavy-flavour hadron decays measured within the full acceptance ( $2.5 < y_{\text{CMS}} < 4$ ) for pp collisions at 7 TeV, and the results are extrapolated to forward ( $2.03 < y_{\text{CMS}} < 3.53$ , left) and backward ( $-4.46 < y_{\text{CMS}} < -2.96$ , right), respectively. Results above 12 GeV/ $c$ (i.e. light blue boxes) are obtained by tuning the $p_{\text{T}}$ -differential cross section in pp collisions at $\sqrt{s} = 5.02$ TeV, predicted by FONLL, to match the obtained pp reference in the range $6 < p_{\text{T}} < 12$ GeV/ $c$ . FONLL predictions are similar with the ones presented in Fig. 5.16. Results obtained after scaling (red and light blue boxes) are compared to FONLL predictions (grey bands) in the bottom panels. . . . .	193
5.20	Left: ratio of the pp reference obtained with the mentioned two scenarios, Eq. 5.12 (red+light blue) and 5.16 (black), to the FONLL predictions at forward rapidity ( $2.03 < y_{\text{CMS}} < 3.53$ ). The shadowing region indicates the relative systematic uncertainty predicted by FONLL. Right: same as left panel but at backward rapidity ( $-4.46 < y_{\text{CMS}} < -2.96$ ). See text for details. . . . .	194
5.21	FONLL scaling factor from $\sqrt{s} = 2.76$ TeV ( $2.5 < y_{\text{CMS}} < 4$ ) to 5.02 TeV ( $2.03 < y_{\text{CMS}} < 3.53$ ) for the measurement of the $p_{\text{T}}$ -differential cross section of muons from heavy-flavour hadron decays with different QCD scales (red boxes) and quark masses (blue boxes), as well as the total systematic uncertainty marked as yellow bands (left), and the corresponding relative systematic uncertainty (right). . . . .	195
5.22	Same as Fig. 5.21 but scaling to 5.02 TeV in the range $-4.46 < y_{\text{CMS}} < -2.96$ . . . . .	195
5.23	$p_{\text{T}}$ -differential cross section of muons from heavy-flavour hadron decays for $2.03 < y_{\text{CMS}} < 3.53$ (left) and $-4.46 < y_{\text{CMS}} < -2.96$ (right) in pp collisions at $\sqrt{s} = 5.02$ TeV. The results are obtained by taking the pp data from 2.76 TeV (green) and 7 TeV (light blue). Red markers correspond to the weighted averaged between them (see the text for details). FONLL predictions are represented by the grey band (muons from heavy-flavour hadron decays) and, by the blue (muons from charm decays) and magenta (muons from bottom decays) curves. The bottom panels show the comparison with FONLL predictions. . . . .	196



5.24	Left: $p_T$ -differential cross section of muons from heavy-flavour hadron decays in $2.03 < y_{\text{CMS}} < 3.53$ (forward) with the weighted mean (red) and results based on 7 TeV (blue). Right: the relative deviation between the results shown in the left panel. . . . .	197
6.1	Left: relative statistical uncertainty on the nuclear modification factor of muons from heavy-flavour hadron decays, as a function of $p_T$ , in multiplicity integrated p-Pb collisions at $\sqrt{s_{\text{NN}}} = 5.02$ TeV at forward rapidity ( $2.03 < y_{\text{CMS}} < 3.53$ ). Right: same as the left panel but at backward rapidity ( $-4.46 < y_{\text{CMS}} < -2.96$ ). . . . .	209
6.2	Same as Fig. 6.1 but within different event classes using V0A as the event estimator. . . . .	209
6.3	Left: relative systematic uncertainty on the nuclear modification factor of muons from heavy-flavour hadron decays, as a function of $p_T$ , in multiplicity integrated p-Pb collisions at $\sqrt{s_{\text{NN}}} = 5.02$ TeV at forward rapidity ( $2.03 < y_{\text{CMS}} < 3.53$ ); Right: same as the left panel but at backward rapidity ( $-4.46 < y_{\text{CMS}} < -2.96$ ). . . . .	210
6.4	Same as the left panel of Fig. 6.3 but within different event activity classes using "mult." as the event activity estimator. . . . .	210
6.5	Same as the right panel of Fig. 6.3 but within different event activity classes using "mult." as the event activity estimator. . . . .	211
6.6	Relative systematic uncertainty on the nuclear modification factor of muons from heavy-flavour hadron decays at forward rapidity in $2 < p_T < 6$ GeV/ $c$ as a function of event activity using "mult." as the event estimator, in p-Pb collisions at $\sqrt{s_{\text{NN}}} = 5.02$ TeV. The left (right) panel shows the various components of the uncertainties that are correlated (un-correlated) among event activity classes. . . . .	212
6.7	Same as Fig. 6.6 but at backward rapidity. . . . .	212
6.8	Left: relative statistical uncertainty on the forward-to-backward ratio of muons from heavy-flavour hadron decays, as a function of $p_T$ , in multiplicity integrated p-Pb collisions at $\sqrt{s_{\text{NN}}} = 5.02$ TeV. Right: same as left within different event activity classes using V0A as the event estimator. . . . .	214
6.9	Relative systematic uncertainty on the forward-to-backward ratio of muons from heavy-flavour hadron decays, as a function of $p_T$ , in multiplicity integrated p-Pb collisions at $\sqrt{s_{\text{NN}}} = 5.02$ TeV. . . . .	214
6.10	Same as Fig. 6.9 but within different event activity classes using "mult." as the event activity estimator. . . . .	215
6.11	Relative systematic uncertainty on the forward-to-backward ratio of muons from heavy-flavour hadron decays, as a function of event activity using "mult." as the event estimator, in p-Pb collisions at $\sqrt{s_{\text{NN}}} = 5.02$ TeV. The $p_T$ range considered is $2 < p_T < 6$ GeV/ $c$ . The left (right) panel shows the various components of the uncertainties that are correlated (un-correlated) among event activity classes. . . . .	216



6.12	$p_T$ -differential cross section of muons from heavy-flavour hadron decays in multiplicity integrated p–Pb collisions at $\sqrt{s_{NN}} = 5.02$ TeV at forward ( $2.03 < y_{CMS} < 3.53$ , p-going, blue) and backward rapidity ( $-4.46 < y_{CMS} < -2.96$ , Pb-going, green). Statistical uncertainties (bars) and systematic uncertainties (boxes) are shown. . . . .	216
6.13	$p_T$ -differential nuclear modification factor of muons from heavy-flavour hadron decays in p–Pb collisions at $\sqrt{s_{NN}} = 5.02$ TeV at forward (upper) and backward rapidity (bottom). pQCD calculations with the EPS09 [105] NLO parameterization of nuclear PDFs [286], are shown as the red bands both at forward and backward rapidity. In addition, model calculations including nuclear shadowing, $k_T$ broadening and CNM energy loss [328] are presented as green curves at forward rapidity. Another model calculation, considering the incoherent multiple scattering effects is displayed as blue bands at backward rapidity. Statistical uncertainties (bars), systematic uncertainties (open boxes) and normalization uncertainties (black box at $R_{pPb} = 1$ ) are shown. . . . .	218
6.14	$p_T$ -differential nuclear modification factor of muons from heavy-flavour hadron decays in p–Pb collisions at $\sqrt{s_{NN}} = 5.02$ TeV in two sub-rapidity bins at forward (upper) and backward rapidity (bottom). Statistical uncertainties (bars), systematic uncertainties (open boxes) and normalization uncertainties same comment as in Fig. 6.13 are shown. For visibility, the points for the rapidity intervals $2.79 < y_{CMS} < 3.53$ and $-3.71 < y_{CMS} < -2.96$ are shifted horizontally. . . . .	219
6.15	$p_T$ -differential nuclear modification factor of muons from heavy-flavour hadron decays at forward rapidity within different event activity classes using "mult." as the event estimator, in p–Pb collisions at $\sqrt{s_{NN}} = 5.02$ TeV. Statistical uncertainties (bars) and systematic uncertainties (open boxes) are shown. . . . .	220
6.16	Same as Fig. 6.15 but at backward rapidity. . . . .	221
6.17	Nuclear modification factor of muons from heavy-flavour hadron decays at forward rapidity in $2 < p_T < 6$ GeV/c (upper) and $6 < p_T < 12$ GeV/c (bottom) as a function of event activity, in p–Pb collisions at $\sqrt{s_{NN}} = 5.02$ TeV. The results are obtained with taking "mult." as the event activity estimator. In each panel, the open (full) boxes denote the uncertainties that are un-correlated (correlated) among event activity classes; the related statistical uncertainties shown as vertical bars are small and not visible. . . . .	222
6.18	Same as Fig. 6.17 but at backward rapidity. . . . .	223



6.19	The nuclear modification factor $R_{dAu}$ , for negatively charged heavy-flavor muons in d–Au collisions for the (a) 60–88%, (b) 0–20%, and (c) 0–100% most central collisions. The black boxes on the right side indicate the global scaling uncertainty. Vertical bars represent the statistical uncertainties, while the boxes denote the systematic uncertainties. The red dashed (blue solid) lines in each panel are calculations at forward (backward) rapidity based on the EPS09s nPDF set [331]. The theoretical calculation shown in (c) is for forward rapidity [328]. Figure taken from Ref. [182]. . . . .	224
6.20	Nuclear modification factor of muons from heavy-flavour hadron decays in centrality classes 0–10% (red) measured at forward rapidity ( $2.5 < y < 4$ ) in Pb–Pb collisions at $\sqrt{s_{NN}} = 2.76$ TeV, as well as the results in multiplicity integrated p–Pb collisions at forward (black, $2.03 < y_{CMS} < 3.53$ ) and backward rapidity (green, $-4.46 < y_{CMS} < -2.96$ ), at $\sqrt{s_{NN}} = 5.02$ TeV. . . . .	226
6.21	$p_T$ -differential production cross sections of muons from heavy-flavour hadron decays measured at forward ( $2.96 < y_{CMS} < 3.53$ , red) and backward rapidity ( $-3.53 < y_{CMS} < -2.96$ , blue) as a function of $p_T$ , in p–Pb collisions at $\sqrt{s_{NN}} = 5.02$ TeV. The normalization procedure is the same as Fig. 6.12. . . . .	227
6.22	Forward-to-backward ratio of muons from heavy-flavour hadron decays. pQCD calculations with the EPS09 [105] NLO parameterization of nuclear PDFs [286], are shown as the red curves. Statistical uncertainties (bars), systematic uncertainties (open boxes) and normalization uncertainties (black box at $R_{FB} = 1$ ) are shown. . . . .	227
6.23	Same as Fig. 6.22 but within different event activity classes using "mult." as the event estimator. . . . .	228
6.24	Forward-to-backward ratio of muons from heavy-flavour hadron decays in $2 < p_T < 6$ GeV/ $c$ (upper) and $6 < p_T < 12$ GeV/ $c$ (bottom) as a function of the collision event activity, in p–Pb collisions at $\sqrt{s_{NN}} = 5.02$ TeV. The results are obtained with taking "mult." as the event activity estimator. The open (full) boxes denote the uncertainties that are un-correlated (correlated) among event activity classes; the related statistical uncertainties shown as vertical bars are small and not visible. . . . .	229
6.25	$p_T$ -differential nuclear modification factor of muons from heavy-flavour hadron decays at forward rapidity within different event activity classes using V0A as the event estimator, in p–Pb collisions at $\sqrt{s_{NN}} = 5.02$ TeV. Statistical uncertainties (bars) and systematic uncertainties (open boxes) are shown. . . . .	263
6.26	Same as Fig. 6.25 but using CL1 as the event estimator. . . . .	263
6.27	Same as Fig. 6.26 but using ZNA as the event estimator. . . . .	264
6.28	Same as Fig. 6.25 but at backward rapidity. . . . .	264



6.29	Same as Fig. 6.26 but at backward rapidity. . . . .	265
6.30	Same as Fig. 6.27 but at backward rapidity. . . . .	265
6.31	Nuclear modification factor of muons from heavy-flavour hadron decays at forward rapidity in $2 < p_T < 6$ GeV/ $c$ (upper) and $6 < p_T < 12$ GeV/ $c$ (bottom) as a function of event activity, in p-Pb collisions at $\sqrt{s_{NN}} = 5.02$ TeV. The results obtained with different estimators are shown. In each panel, the open (full) boxes denote the uncertainties that are un-correlated (correlated) among event activity classes; the related statistical uncertainties shown as vertical bars are small and not visible. . . . .	266
6.32	Same as Fig. 6.31 but at backward rapidity. . . . .	267
6.33	Forward-to-backward ratio of muons from heavy-flavour hadron decays in different event activity classes using CL1 as the event estimator. Statistical uncertainties (bars) and systematic uncertainties (open boxes) are shown. . . . .	268
6.34	Same as Fig. 6.33 but with taking ZN as the event activity estimator. . . . .	268
6.35	Forward-to-backward ratio of muons from heavy-flavour hadron decays in $2 < p_T < 6$ GeV/ $c$ (upper) and $6 < p_T < 12$ GeV/ $c$ (bottom) as a function of collision event activity, in p-Pb collisions at $\sqrt{s_{NN}} = 5.02$ TeV. The results are obtained with various event activity estimators. The open (full) boxes denote the uncertainties that are un-correlated (correlated) among event activity classes; the related statistical uncertainties shown as vertical bars are small and not visible. . . . .	269



# List of Tables

1	Facteur de normalisation et incertitude relative dans les collisions p–Pb et Pb–p pour les événements MSL et MSH. Voir le texte pour plus de détails. . . . .	xvi
1.1	Main characteristics of central heavy-ion collisions at SPS, RHIC and LHC. From top to bottom are shown the maximum available energy per nucleon pair in the center-of-mass for Pb–Pb or Au–Au collisions ( $\sqrt{s_{NN}}$ ), the charged particle multiplicity at mid-rapidity ( $dN_{ch}/dy _{y=0}$ ), the equilibration time of the QGP ( $\tau_{QGP}^0$ ), the ratio of the QGP temperature to the critical temperature ( $T_{QGP}/T_c$ ), the energy density ( $\varepsilon$ ), the lifetime of the QGP ( $\tau_{QGP}$ ), the lifetime of the fireball at freeze-out ( $\tau_f$ ), the volume of the fireball at freeze-out ( $V_f$ ), the baryonic chemical potential ( $\mu_B$ ). Adapted from Ref. [41, 42].	8
1.2	Overview of the measurements related to selected channel conducted at RHIC ( $\sqrt{s_{NN}} \leq 0.2$ TeV and at the LHC ( $\sqrt{s_{NN}} \leq 7$ TeV) until 2014. For each collision system, center-of-mass energy $\sqrt{s_{NN}}$ , and channel investigated, the phase space coverage is given as well. . . . .	39
2.1	Summary of the LHC nominal run conditions for different collision system, center-of-mass energy, integrated luminosity (defined as the ratio of the number of events detected in a certain time to the interaction cross-section), running time and the geometrical cross sections [35]. Adapted from Ref. [190, 191]. . . . .	41
2.2	Names, acceptances, positions and dimensions of the ALICE detector sub-systems. Adapted from Ref. [42, 194, 202]. . . . .	45
2.3	Summary of the main characteristics of the muon spectrometer. Adapted from Ref. [202]. . . . .	49
2.4	Summary of the main data sets collected with the ALICE detector during Run 1: the year, the colliding system, the energy of center-of-mass and the integrated luminosity. See the text for details. Adapted from Ref. [228, 205]. . . . .	58
3.1	Summary of the single muon triggers for the data in p–Pb (LHC13d, LHC13e periods) and Pb–p (LHC13f period) collisions. The names (MB: minimum bias, MSL: muon trigger with low $p_T$ cut and MSH: muon trigger with high $p_T$ cut), the related $p_T$ threshold (at 50% efficiency), the trigger input together with the identification (ID) are listed. See text for details. Extracted from the ALICE Electronic Logbook. . . . .	66
3.2	Summary of the extracted statistics after applying various selection cuts at event level: physics selection, centrality QA and primary vertex reconstruction. See text for details. . . . .	68



3.3	Normalization factor and the related uncertainties obtained in p–Pb and Pb–p collisions with MSL and MSH. See text for details. . . . .	82
3.4	Integrated luminosity in p–Pb and Pb–p collisions with MSL and MSH. See text for details. . . . .	83
3.5	Summary of the extracted statistics after applying various selection cuts at track level: physics selection, centrality QA, primary vertex reconstruction, acceptance cut ( $\eta_{\text{LAB}}$ ), polar angle limitation ( $\theta_{\text{abs}}$ ), trigger matching and the correlation between momentum and DCA ( $p \times \text{DCA}$ ). See text for details. . . . .	86
3.6	Different components of the systematic uncertainty on detector response. . . . .	108
4.1	Multiplicity range for different event activity class. See text for details.	153
4.2	Mean values of geometrical variables ( $\langle b \rangle$ , $\langle N_{\text{part}} \rangle$ and $\langle N_{\text{coll}} \rangle$ ) calculated within the event activity classes. They are obtained with a Glauber Monte Carlo calculation, coupled to a NBD to fit the V0A distribution (see Tab. 4.1). . . . .	155
4.3	Impact parameter ranges within a given event activity classes. See text for details. . . . .	157
5.1	Different sources of systematic uncertainty on the estimated reference both at forward and backward rapidity for pp collisions at $\sqrt{s} = 5.02$ TeV: combined systematic uncertainty on energy scaling and data input, the one on rapidity extrapolation/shift and normalization. . .	194
6.1	$\langle T_{\text{pPb}} \rangle$ (in $\text{mb}^{-1}$ ) values and its systematic uncertainties from various event activity estimators V0A, CL1 and ZNA, as well as from an hybrid model. The latter indicated as "mult." is obtained assuming the charged-particle multiplicity at mid-rapidity is proportional to the number of participants ( $\langle N_{\text{part}} \rangle$ ) [283]. . . . .	204
6.2	Summary of the sources of the systematic uncertainty for $Q_{\text{pPb}}$ and $Q_{\text{FB}}$ . Type I indicates the uncertainties correlated between event activity bins. Type II denotes the uncertainties correlated between colliding systems (pp and p–Pb/Pb–p). Type III stands for the uncertainties correlated between $p_{\text{T}}$ bins. Type IV denotes the uncertainties correlated between p–Pb and Pb–p configurations. . . . .	207

# Introduction

---

High energy heavy-ion collisions are a research field which has been actively investigated since the seventies of the last century. The aim is to study the properties of a new state of matter, the Quark-Gluon Plasma (QGP), which forms under extreme conditions of temperature and energy density. In this chapter, I briefly summarize the properties of the QGP as predicted by theory and derived from experimental measurements.

## 1.1 Quantum ChromoDynamics and Quark Gluon Plasma

### 1.1.1 The Standard Model and QCD

According to modern physics, nature can be quantitatively understood with four fundamental forces: gravity, strong, weak and electromagnetic. It is realized that the gravity is governed by Einstein's general relativity [1], while the other three forces can be described by a Quantum Field Theory (QFT) of particle physics, Standard Model (SM [2]). In the SM, the internal symmetry is  $SU(3) \times SU(2) \times SU(1)$ , which roughly corresponds to strong, weak and electromagnetic forces, together with the elementary particles such as Higgs boson, gauge bosons, leptons and quarks.

The Higgs boson is a particle whose existence has been postulated in order to explain the origin of mass of subatomic particles that are inherently massless in the SM. The Higgs boson has a positive parity and no spin in SM. Its existence has recently been confirmed by the ATLAS and CMS experiments at the CERN Large Hadron Collider (LHC), see Fig. 1.1. The **Nobel Prize in Physics 2013** was awarded jointly to F. Englert and P. W. Higgs for the prediction of this fundamental particle. The gauge boson species, including graviton (not discovered yet), gluons, W and Z, and photons, are the propagators of strong, weak and electromagnetic interaction, respectively. The leptons are either charged (e.g. electrons, muons) or neutral (neutrinos). The quarks are the basic constituents of hadronic matter. They are sensitive to the strong interaction, which is described by Quantum ChromoDynamics (QCD). Quarks have six flavors: up (u), down (d), charm (c), strange (s), top (t) and beauty (b), which are organized into three families.

The present knowledge of the properties of elementary particles, such as their mass, electric charge and spin, are shown in the left panel of Fig. 1.2. A summary of fundamental interactions is presented in the right panel.

QCD, as mentioned above, the non-Abelian gauge theory that describes the strong interaction of colored quarks and gluons, is the  $SU(3)$  component of the Stan-

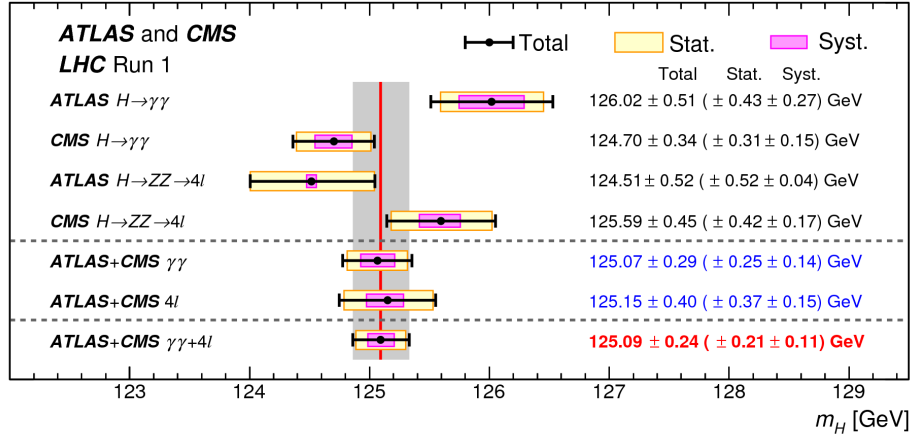


Figure 1.1: Summary of Higgs boson mass measurements from the individual analyses of ATLAS and CMS and from the combined analyses. The systematic (narrower, magenta-shaded bands), statistical (wider, yellow-shaded bands), and total (black error bars) uncertainties are indicated. The (red) vertical line and corresponding (gray) shaded column indicate the central value and the total uncertainty of the combined measurement, respectively. Figure taken from Ref. [3].

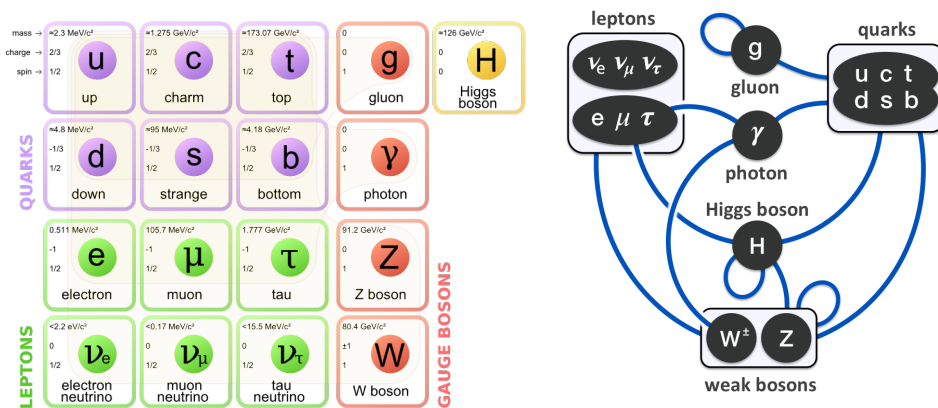


Figure 1.2: Elementary particles (left) and fundamental interactions (right) in the Standard Model. Figures taken from Ref. [4].

standard Model. One of the fundamental parameters of QCD is the coupling constant. It states the interaction strength and can be quantified by the running coupling constant,  $\alpha_s$ . The physics of QCD reveals two peculiar properties concerning the relation between  $\alpha_s$  and  $Q$  (momentum transfer, i.e. the amount of momentum that one particle gives to another one).

The first one, called confinement, reflects that the strong force is inversely proportional to the distance between two quarks. Because of this, when you separate a quark from other quarks (or increase the distance between them), the energy in the gluon field is large enough to create another quark pair when pulled beyond a certain distance. Quarks are thus forever bound into hadrons. In this case,  $\alpha_s$  is large: (1) the Chiral Symmetry is broken<sup>§</sup> (caused by the non-zero quark masses) [5]; (2)  $Q$  is small (see Fig. 1.3), and the distance between the incident quarks is larger than  $1/\Lambda_{\text{QCD}}$  (i.e.  $Q$  and  $\Lambda_{\text{QCD}}$  are of similar magnitude), where  $\Lambda_{\text{QCD}} \sim 200$  MeV is a constant QCD scale. It indicates that the perturbatively-defined coupling will diverge [2]; (3) (non-perturbative) QCD in the strong coupling region can be computed via statistical realisations on the lattice [6], in short Lattice QCD [7, 8, 9, 10, 11, 12, 13]. More details will be given in the following.

The second remarkable feature of QCD is the domain of asymptotic freedom, deconfinement, for which quarks and gluons interact weakly in a Quark-Gluon Plasma. In this case,  $\alpha_s$  is small: (1) the Chiral Symmetry is restored; (2)  $Q$  is large (see Fig. 1.3), and the distance between the incident quarks is smaller than  $1/\Lambda_{\text{QCD}}$  (or  $Q \gg \Lambda_{\text{QCD}}$ ); (3) perturbative QCD (pQCD [14, 15]) is validated to describe the QGP; (4) alternatively, the statistical thermodynamics [16, 17, 18] would be a sufficient approximation to address the thermal properties of the hot and dense QGP.

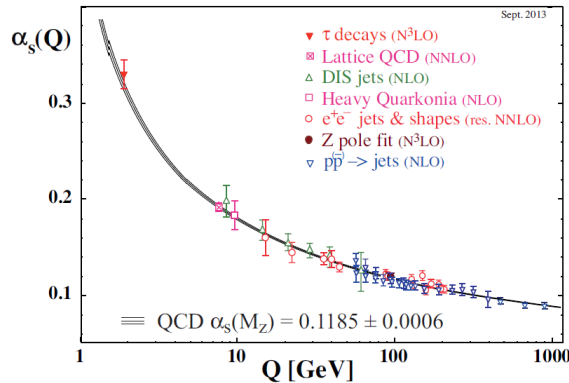


Figure 1.3: Summary of running coupling constant,  $\alpha_s$ , measured as a function of the energy scale,  $Q$ . The respective degree of perturbative QCD theory used in the extraction of  $\alpha_s$  is indicated in brackets (NLO: next-to-leading order; NNLO: next-to-next-to leading order; NNLO: NNLO matched with resummed next-to-leading logs; N<sup>3</sup>LO (NNNLO): next-to-NNLO). Figure taken from Ref. [2].

These two amazing features were predicted by D. J. Gross, H. D. Politzer and

<sup>§</sup>this will be discussed in more detail later in this chapter.

F. Wilczek, who awarded the **Nobel Prize in Physics 2004**. Figure 1.3 shows a compilation of various experimental measurements of  $\alpha_s$  together with theoretical predictions.

### 1.1.2 Lattice QCD calculations

As discussed above, QCD predicts a new form of strong interaction matter under extreme conditions of temperature and energy density, the QGP, in which quarks and gluons normally confined within hadrons can roam freely [19, 20]. The transition occurs when the energy density of the matter is similar to that inside a hadron, for example, proton [21].

According to the predictions from Lattice QCD, the energy density of the system undergoes a rapid rise (that indicates the liberation of degrees of freedom) around the critical temperature  $T_c \sim 175$  MeV in 2-flavor QCD [7], as displayed in the left panel of Fig. 1.4. The density is enhanced by almost an order of magnitude near  $T_c$ , and is fairly flat beyond  $T_c$ . The horizontal arrows show the results based on non-interacting and massless partons (i.e. an ideal gas characterized by  $p = \varepsilon/3$ ). Note that, (1) the particle number density is proportional to  $T^3$  for both boson and fermion particles as obtained via thermodynamics in the very high temperature region, while the energy density is proportional to  $T^4$  by means of the Stefan Boltzmann limit (i.e. non-interacting gas of massless quarks and gluons) that is not reached at high  $T$  [20]; (2) the flat behavior observed at high temperature indicates a dependence on the effective number of degrees of freedom; It is argued that [22] the phase transition can change from second order to first order when decreasing the strange quark mass, hence, the order of the phase transition is notoriously difficult to describe due to the unknown value of strange quark mass. In the right panel of Fig. 1.4, the deviation of energy density with respect to the one of an ideal gas displayed as a function of temperature indicates the presence of strong interaction near the critical temperature  $T_c$  [21].

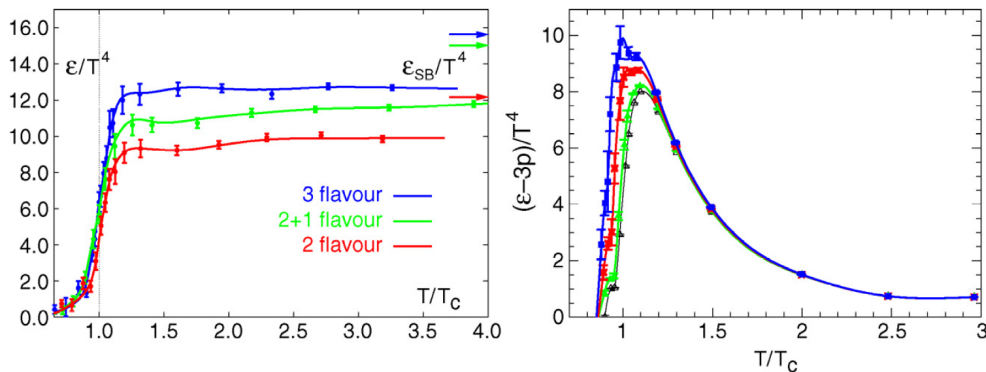


Figure 1.4: Left: scaled energy density as a function of  $T/T_c$  from Lattice QCD [7, 8]; Right:  $(\varepsilon - 3p)/T^4$  at  $\mu_B=0, 210, 410$  and  $530$  MeV as a function of  $T/T_c$  (from bottom to top, [9]). Figures taken from Ref. [7] and [9], respectively.

Within Lattice QCD, the deconfinement transition can be quantified by means

of  $\langle L \rangle$ , which is the order parameter for deconfinement:  $\langle L \rangle \sim 0$  with  $T < T_c$  indicates the confined phase, whereas  $\langle L \rangle \gg 0$  with  $T > T_c$  indicates the deconfinement phase [7]. The Polyakov loop susceptibility ( $\chi_L$ ) is the related observable, which indicates a sudden change. The results are shown in the left panel of Fig. 1.5. On the other hand, the Chiral symmetry restoration (see 1.1.1) can be quantified in terms of  $\langle \bar{\psi}\psi \rangle$ , the chiral condensate [7, 23],  $\langle \bar{\psi}\psi \rangle > 0$  for  $T < T_c$  denotes the chirally broken system with large effective quark mass, while  $\langle \bar{\psi}\psi \rangle \sim 0$  for  $T > T_c$  corresponds to the chirally restored system with small effective quark mass. The corresponding chiral susceptibility ( $\chi_m$ ) is shown in the chiral limit in the right panel of Fig. 1.5. The behavior of the observable, which is presented in the case of 2-flavour QCD with light quarks, clearly shows that: (1) the regions of most rapid change in  $\langle L \rangle$  and  $\langle \bar{\psi}\psi \rangle$  coincide; (2) deconfinement and chiral transitions coincide in the chiral transition region [24]. The corresponding critical temperature has recently been studied versus the baryonic chemical potential ( $\mu_B$  [25]). It is found to be  $T_c = 154 \pm 9$  MeV when the baryonic chemical potential vanishes [26]. More details can be found in Ref. [27, 28].

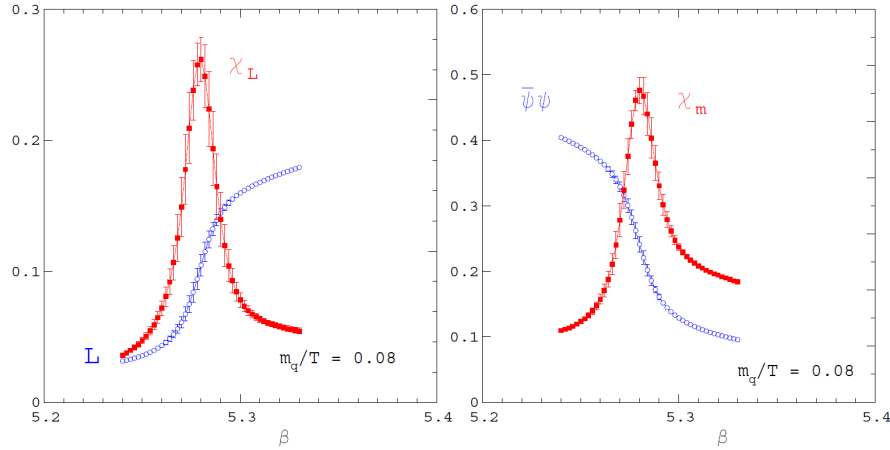


Figure 1.5: Deconfinement and Chiral Symmetry restoration in 2-flavour QCD. Left:  $\langle L \rangle$  (left) the order parameter for deconfinement in the pure gauge limit ( $m_q \rightarrow \infty$ ). Right:  $\langle \bar{\psi}\psi \rangle$  the order parameter for Chiral symmetry broken in the chiral limit ( $m_q \rightarrow 0$ ). Also shown are the corresponding susceptibilities as a function of the gauge coupling  $\beta = 6/g^2$ . Figures taken from Ref. [7].

Figure 1.6 shows the QCD phase diagram in the plane temperature-baryon chemical potential. The two phases of hadronic matter and QGP are shown in the temperature and baryonic chemical potential ( $T, \mu_B$ ) plane. The regions probed by experiments at SPS, RHIC, LHC (ALICE) and SIS (CBM) are also marked in red in Fig. 1.6. An other transition is predicted in the low temperature and high density region, which corresponds to the color-flavor locked (CFL) phase predicted to exist in the cores of neutron stars [29]. In the low energy region, a triple point (or tri-critical point) where hadronic matter, QGP and quarkyonic matter all coexist, is predicted (see Ref. [30] for details).

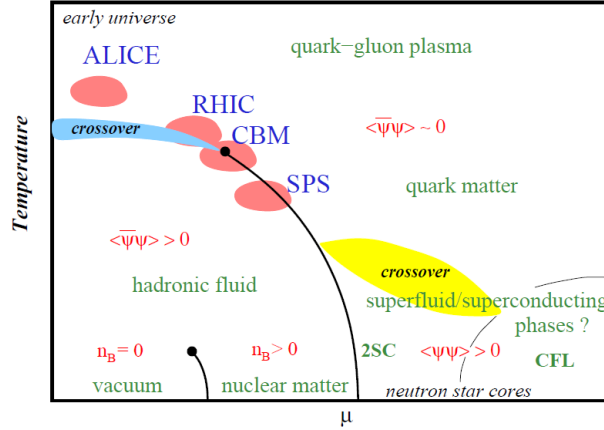


Figure 1.6: Schematic phase diagram of QCD matter in the  $(T, \mu_B)$  plane. Figure taken from Ref. [22].

## 1.2 Studying the QGP with heavy-ion collisions

As mentioned, Lattice QCD predicts a phase transition from normal nuclear matter to the state of deconfined quarks and gluons, the so-called Quark-Gluon Plasma (QGP). It can be created when the temperature raises above a critical temperature  $T_c = 154 \pm 9$  MeV at zero baryon chemical potential, or when the energy density of the produced system is larger than  $\varepsilon_c = 0.34 \pm 0.16$  GeV/fm<sup>3</sup> [31]. Such conditions are often referred to as extreme: in units commonly used in daily life we would have to deal with densities larger than about 10<sup>15</sup>g/cm<sup>3</sup> and temperatures beyond 10<sup>12</sup>K [32]. The considerations of the evolution of our Universe point out that such a QGP state could have existed few microseconds after the Big Bang [33]. The matter within such extreme conditions can be created in the laboratory by colliding heavy-nuclei at ultra-relativistic energies. Such collisions allow to study the properties of the produced hot and dense partonic matter.

### 1.2.1 Space-time evolution of heavy-ion colliding system

As presented in Fig. 1.7, the space-time evolution of a heavy-ion colliding system can be summarized as follows:

- **Initial stage:** the injected nuclei travel almost at the speed of light in high-energy collision, and they are squeezed in the direction of the beam axis due to Lorentz contraction in the laboratory frame. At LHC energy, the Lorentz contraction factor is  $\gamma \sim 1500$  and the nucleus is squeezed to  $\sim 0.01$  fm, resulting in the two pancake-like colliding nuclei. The nucleons suffering primary interactions are called participants with its total number indicated as  $N_{\text{part}}$ , and others are called spectators. The total number of binary nucleon-nucleon interactions is normally denoted as  $N_{\text{coll}}$ . The distance between the central points of the colliding nucleus is defined as the impact parameter  $b$ . The centrality percentile can be quantified by the pure geometry of the impact

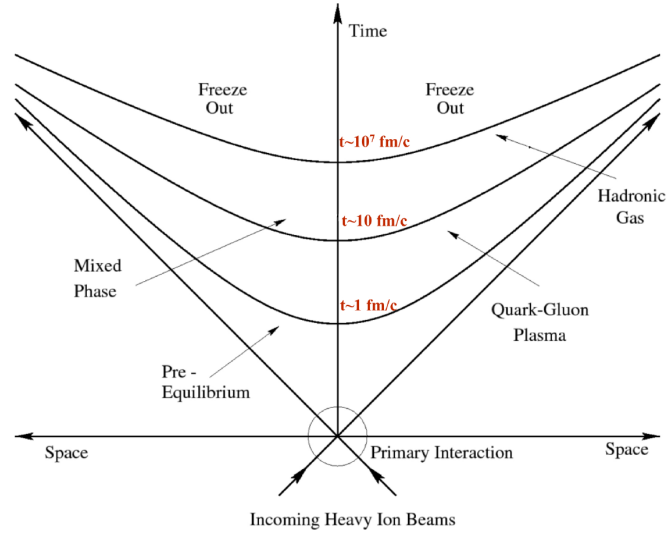


Figure 1.7: Sketch of the heavy-ion collision space-time evolution. Figure taken from Ref. [34].

parameter via Optical Glauber model [35].

- **Pre-equilibrium:** the collision occurs in the overlap region of two colliding nuclei, and a large amount of energy is deposited near the collision point. Partons are produced within this high-energy density environment via hard ( $\tau \sim 0$ ) processes. The pre-equilibrium state lasts for a typical time scale  $\tau \sim 1$  fm/c. High transverse momentum particles (jets, heavy quarks, photons) are mainly produced in this stage. For instance, charm quarks are produced on time scale of about  $1/2m_Q \sim 0.1$  fm/c.
- **QGP phase:** If the energy density is sufficient high, the system reaches the deconfinement phase with partonic and gluonic degrees of freedom. The deconfinement state typically lasts for a time scale  $\sim 10$  fm/c at LHC energy.
- **Hadronization and Freeze-out:** The system expands and cools down, and the temperature drops below the critical one  $T_c$ , resulting in the transition from QGP phase to hadrons gas (hadronization). After the transition, the hadron gas can in principle continue to interact inelastically until the chemical freeze-out<sup>§</sup>. During this procedure, a "mixed phase" is expected to exist between the QGP phase and the hadronic phase. Subsequently, the hadronic system continues to expand and interact elastically until the kinetic freeze-out<sup>¶</sup> (or freeze-out as indicated in Fig. 1.7). The final escaped particles (hadrons and leptons, mainly) are recorded and identified by the detectors.

Various heavy-ion experiments have been operated at the SPS (Super Proton Synchrotron) and LHC (Large Hadron Collider) at CERN (European Center for

<sup>§</sup>the stage when the population of all hadron states is fixed or inelastic scatterings cease [36, 37].

<sup>¶</sup>the moment when the particle momentum distributions do not change or the elastic scatterings stop [38, 39, 40].



Nuclear Research), as well as at the RHIC (Relativistic Heavy Ion Collider) at BNL (Brookhaven National Laboratory) in U.S.A. Table 1.1 summarizes the mentioned heavy-ion facilities together with the typical parameters related to the particle production in nucleus-nucleus collisions and global features of the produced systems.

Parameters	SPS	RHIC	LHC
system	Pb–Pb	Au–Au	Pb–Pb
$\sqrt{s_{NN}}/A$ (GeV)	17	200	2760
$dN_{ch}/dy _{y=0}$	500	850	1600
$\tau_{QGP}^0$ (fm/c)	$\sim 1$	$\sim 0.2$	$\sim 0.1$
$T_{QGP}/T_c$	1.1	1.9	3-4.2
$\varepsilon$ (at 1fm/c) (GeV/fm <sup>3</sup> )	$\sim 3$	$\sim 5$	15
$\tau_{QGP}$ (fm/c)	$\leq 2$	2-4	$\geq 10$
$\tau_f$ (fm/c)	$\sim 4$	$\sim 7$	$\sim 10$
$V_f$ (fm <sup>3</sup> )	$\sim 10^3$	$2 - 3 \times 10^3$	$\sim 5 \times 10^3$
$\mu_B$ (MeV)	250	20	$\sim 0$
Process	soft $\rightarrow$ semi-hard $\rightarrow$ hard		

Table 1.1: Main characteristics of central heavy-ion collisions at SPS, RHIC and LHC. From top to bottom are shown the maximum available energy per nucleon pair in the center-of-mass for Pb–Pb or Au–Au collisions ( $\sqrt{s_{NN}}$ ), the charged particle multiplicity at mid-rapidity ( $dN_{ch}/dy|_{y=0}$ ), the equilibration time of the QGP ( $\tau_{QGP}^0$ ), the ratio of the QGP temperature to the critical temperature ( $T_{QGP}/T_c$ ), the energy density ( $\varepsilon$ ), the lifetime of the QGP ( $\tau_{QGP}$ ), the lifetime of the fireball at freeze-out ( $\tau_f$ ), the volume of the fireball at freeze-out ( $V_f$ ), the baryonic chemical potential ( $\mu_B$ ). Adapted from Ref. [41, 42].

The initial scattering processes among partons (quarks and gluons) can be divided into two parts [38]: hard processes which have large transverse momentum transfer  $Q$  ( $Q \gg \Lambda_{QCD}$ ), short timescale and a production cross section that is proportional to the number of binary collisions ( $\sigma_{hard} \propto N_{coll}$ ); soft processes which have small  $Q$ , e.g.  $Q < 2$  GeV/c, long timescale and a production cross section proportional to the number of participants ( $\sigma_{soft} \propto N_{part}$ ). (Note that the vast majority of particles comes from soft processes). Hence, the measured yields of particles enable to identify the underlying production mechanism. On the other hand, the interactions of partons with the surrounding medium allow one to pin down relevant properties of this medium.

## 1.2.2 Signatures of the QGP from SPS to LHC

### 1.2.2.1 Thermodynamic properties of the QGP

In the framework of thermal models such as the Hadron Resonance Gas model (HRG [16, 17, 18, 43, 36]), thermodynamic properties of the hot and dense medium at the phase boundary (chemical freeze-out) can be characterized by a set of param-

eters [39], such as temperature  $T$  and baryon chemical potential  $\mu_B$ , together with a certain number of conservation laws involving e.g. baryon number and strangeness. Technically, temperature and baryon chemical potential are obtained by adjusting the model parameters in order to describe the measured particle yields in the final state. The corresponding  $(T_c, \mu_B)$  obtained at different energies corresponding to the range  $25 < \mu_B < 800$  GeV/ $c$  are reported in Fig. 1.8.

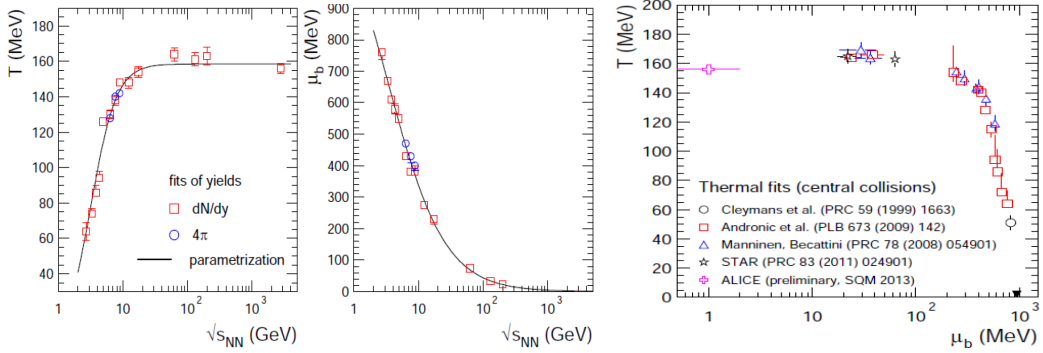


Figure 1.8: Critical temperature (left) at chemical freeze-out and baryonic chemical potential (middle) as a function of energy from the fitting of data with thermal model. The resulting temperature as a function of baryonic chemical potential (right). Figures taken from Ref. [44].

The temperature seems to saturate at  $T_c \sim 160$  MeV for  $\sqrt{s} > 10$  GeV, as shown in the left panel of Fig. 1.8. The analysis based on the present and future measurements performed at mid-rapidity at the LHC can test thoroughly this behavior. The calculated  $\mu_B$  as a function of  $\sqrt{s}$  is presented in the middle panel of Fig. 1.8. It is found that  $\mu_B$  decreases with increasing  $\sqrt{s}$  (since the amount of generated entropy increases with  $\sqrt{s}$  while the net baryon number is limited by the value inside the initial nuclei [45]:  $\mu_B \sim 1$  MeV at the LHC).  $\mu_B$  decreases smoothly at high  $\sqrt{s}$ . This is known as the  $T_c$  saturation phenomenon [45]. The resulting  $T_c$  as a function of  $\mu_B$  is displayed in the right panel of Fig. 1.8. It shows that, within significant uncertainties, the results are consistent with the phase transition case from Lattice QCD. Note that, for the used thermal model, i.e. HRG, the only parameters are  $T_c$ ,  $\mu_B$  and  $V$  (fireball volume), taking as inputs the yields rather than the ratio of the yields, while other approaches considering an additional parameter such as  $\gamma_s$  (strangeness suppression factor [36]) are proposed to describe the data. The fit of experimental data (i.e. transverse mass or momentum spectra) with a hydro-inspired models, such as the blast-wave approach, can also provide the transverse flow velocity and the temperature, at kinetic freeze-out [46].

### 1.2.2.2 Strangeness enhancement

Due to their large masses, hadrons carrying more than two or three strange quarks such as  $\Xi$ (uss) and  $\Omega$ (sss) have very small production rate. However, in the QGP, strangeness production is expected to be enhanced as a result of Chiral Symmetry restoration which implies smaller quark masses. Strange quarks are produced

by (mainly) gluon fusion, as sketched in the left panel of Fig. 1.9. Hence, it has been argued that strangeness enhancement could be considered as a signature for the formation of the QGP [47, 48, 49, 50, 51]. The observable  $E$ , the enhancement factor shown in the right panel of Fig. 1.9, is defined as the ratios of the yields of strange particles (i.e. including strange quark) per participating nucleon in Pb–Pb collisions relative to p–Pb collisions. It strongly increases for particles with higher strangeness, e.g. about 17 for  $\Omega$  and  $\bar{\Omega}$  at SPS energies. Recent reviews concerning strangeness production in heavy-ion collisions can be found in Ref. [52, 53], together with the measurements in Ref. [54, 55].

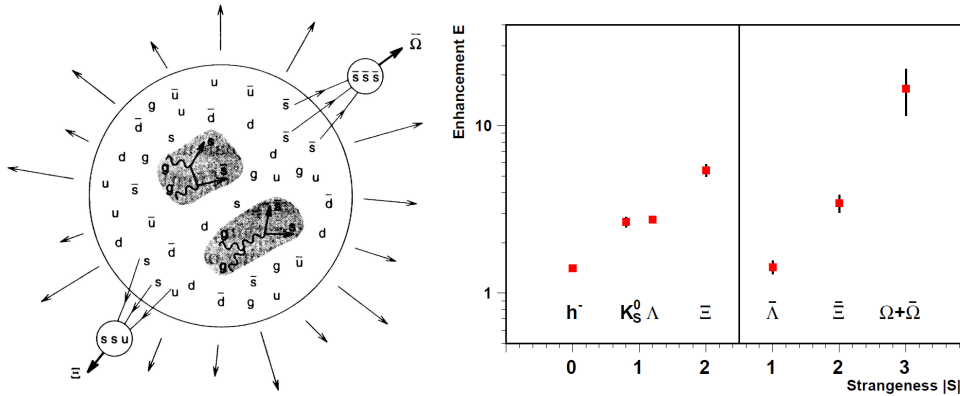


Figure 1.9: Left: Scheme showing the strangeness production in the QGP. Right: Enhancement factor for the mid-rapidity yields per participating nucleon at 158 A GeV/c Pb–Pb collisions relative to p–Pb collisions for various strange and non-strange hadron species; Figures taken from Ref. [39] and [38], respectively.

Nevertheless, it is argued [56, 57] that the strangeness enhancement can also be interpreted by means of a canonical suppression in the pp reference system, indicating possible issues when considering the enhancement of strange and multi-strange baryons as a signature of QGP formation.

### 1.2.2.3 Quarkonium production

Quarkonium states are usually referred to as charmonia for  $\bar{c}c$  pairs and bottomonia for  $\bar{b}b$  pairs. The main charmonium states are [2]  $J/\Psi$  ( $m = 3.1$  GeV/c, 1S),  $\chi_{c1}$  and  $\Psi'$  ( $m = 3.5$  and 3.7 GeV/c, respectively, 1P and 2S). The main bottomonium states are [2]  $\Upsilon$  ( $m = 9.5$  GeV/c, 1S),  $\Upsilon'$ ,  $\Upsilon''$  and  $\Upsilon(10580)$  ( $m = 10.0$ , 10.4 and 10.6 GeV/c, respectively, 2S and 3S). In heavy-ion collisions, quarkonium production yields are affected by the following effects:

- nuclear shadowing: in a nucleus the parton distribution function (PDF) in a nucleus is different from a simple superposition of the PDF in a free nucleon, these are the nuclear parton distribution functions (nPDFs). The modified PDF induced by the shadowing effect at small  $x$  (i.e. Bjorken-variable, fractional momentum carried by a parton in a nucleus) plays an important role in heavy-quark production;

- nuclear/hadronic absorption: the produced  $Q\bar{Q}$  pairs can be broken up by means of inelastic scattering with the nucleons of the colliding nucleus when propagating through the medium. This is referred as to quarkonium normal suppression;
- Debye screening: quarkonia production is anticipated to be suppressed in the presence of a QGP due to the Debye screening of the quark-antiquark potential in the deconfined partonic medium. The Debye screening length depends on the temperature of the QGP. Different quarkonia states have different binding energies and thus different radii. Therefore, they are expected to disassociate at different temperatures [58].

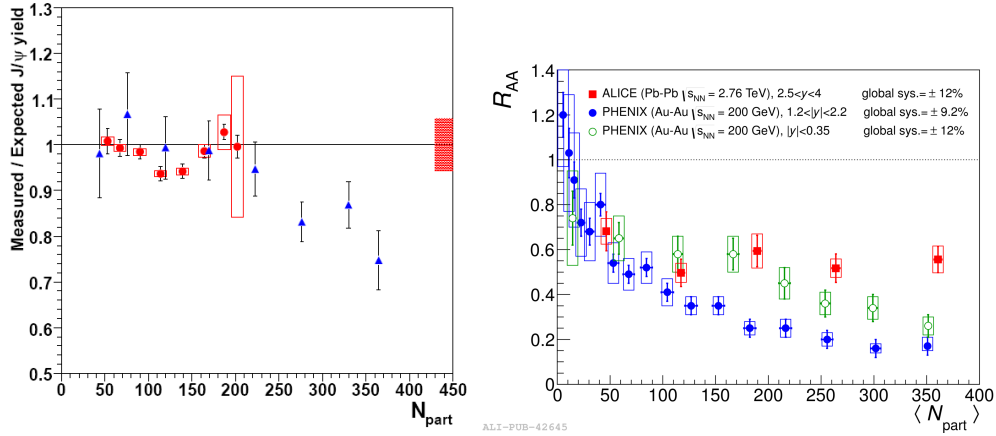


Figure 1.10: Left: Measured  $J/\psi$  production yields normalised to the yields expected assuming that the only source of suppression is the ordinary absorption by the nuclear medium as a function of  $N_{part}$ , in In–In (red) and Pb–Pb (blue) collisions at SPS energies. Right: Inclusive  $J/\psi$   $R_{AA}$  as a function of the number of participating nucleons measured in Pb–Pb collisions at  $\sqrt{s_{NN}} = 2.76$  TeV compared to PHENIX results in Au–Au collisions at  $\sqrt{s_{NN}} = 200$  GeV at mid-rapidity and forward rapidity. See Ref. [59] for details. Figures taken from Ref. [60] and [59], respectively.

The left panel of Fig. 1.10 shows the measurements [60] that are normalized to the results based on the normal suppression behavior (i.e. nuclear absorption), in nucleus-nucleus at SPS energies. One can see that the data are consistent with unity in peripheral Pb–Pb collisions (small  $N_{part}$  value), evidencing the normal suppression scenario, while a visible anomalous suppression pattern appears in central collisions (large  $N_{part}$  value). This result was interpreted by means of the Debye screening, which can be taken as a signal of the QGP creation [61]. The inclusive  $J/\psi$   $R_{AA}$ <sup>§</sup> measured by ALICE at  $\sqrt{s_{NN}} = 2.76$  TeV in the range  $2.5 < y < 4$  and  $p_T \geq 0$  is presented as a function of  $N_{part}$  in the right panel of Fig. 1.10. It shows a clear  $J/\psi$  suppression for number of participants larger than about 50 (0 – 80%, i.e. 80% at maximum of the total inelastic cross section) centrality region. In addition, the

<sup>§</sup>the corresponding definition will be shown later in this chapter.



results do not exhibit a significant centrality dependence. The comparison with the PHENIX measurements at  $\sqrt{s_{NN}} = 200$  GeV at forward rapidity  $1.2 < |y| < 2.2$  which shows that the ALICE  $R_{AA}$  measurement is larger by about a factor three for  $N_{part} \geq 180$ . This deviation can be interpreted by considering the heavy-quark regeneration [62, 63, 64, 65] occurring in the hadronization procedure, e.g.  $c + \bar{c} \rightarrow J/\Psi + X$  in QGP and  $D + \bar{D} \rightarrow J/\Psi + X$  in hadron gas environment. The regeneration effect was predicted to be small at RHIC energies while it is more important at LHC energies due to the large number of  $c\bar{c}$  pairs that are produced. A different observable was also studied, i.e. the normalized averaged transverse momentum square [66],  $r_{AA} = \langle p_T^2 \rangle_{AA} / \langle p_T^2 \rangle_{pp}$ , show that  $r_{AA}$  is expected to be sensitive to the charm quark thermalization, therefore, it can be used to quantify the initial production and regeneration. It was found that  $r_{AA} > 1$  at SPS energies (Cronin effect known as the multi-scattering in the initial stage),  $r_{AA} \sim 1$  at RHIC due to the compatible contribution between initial production and regeneration and  $r_{AA} < 1$  at LHC since the regeneration is important. See Ref. [66] for the detail.

#### 1.2.2.4 Collective Flow

Collective flow [67, 68, 69] is an observable sensitive to the EoS (equation of state) and transport properties [19, 21, 69, 70], of the system formed in heavy-ion collisions, the so-called fireball. The energy density of the fireball is not identical from its central (core) to boundary (corona), resulting in a pressure gradient towards this direction. For central collisions, the produced pressure gradient is radially symmetric, and it can not only generate the radial flow (or isotropic flow [21, 71, 72, 73]), but also boost particles towards radial direction, which is more significant for particles with larger mass (i.e. mass ordering behavior).

In case of non-central collisions, the geometrical anisotropy of the overlap region of the colliding nuclei (or non-zero spatial eccentricity) is transferred into an anisotropic behavior of the momentum space. This behavior can be quantified by the anisotropic flow, and the Relativistic Hydrodynamics theory is normally employed to describe this collectivity when the (local) thermal equilibrium is achieved. Experimentally, the anisotropic flow can be studied by measuring the azimuthal distributions of the final emitted particles with respect to the reaction plane, which is defined as the plane including impact parameter and beam axis, as shown in the left panel of Fig. 1.11. The related azimuthal distributions can be characterised by a Fourier expansion via

$$\frac{dN}{d\varphi} \propto 1 + 2 \sum_{n=1}^{\infty} v_n \cos[n(\varphi - \Psi_{RP})] \quad (1.1)$$

$$v_n = \langle \cos[2(\phi - \Psi_{RP})] \rangle \quad (1.2)$$

where,  $\varphi$  denotes the azimuthal angle in the transverse plane;  $\Psi_{RP}$  indicates the azimuthal angle of the reaction plane;  $v_n$  are the Fourier coefficients. The first harmonic Fourier coefficient,  $v_1$ , the so-called directed flow, represents an overall shift of the distribution in the transverse plane [72]. The second harmonic,  $v_2$ ,

indicating the elliptic flow, is a measure of how efficiently hydrodynamics translates the spatial anisotropy to the momentum anisotropy. Triangular flow,  $v_3$ , depends more on the spatial distribution of the initial energy density fluctuations. Higher harmonic coefficients,  $v_n$  ( $n > 3$ ), encode more detailed information on the initial fluctuations and their propagation through the QGP evolution [72, 74].

The  $p_T$  dependence of  $v_2$  of the various parton species, as presented in the right panel Fig. 1.11, can be discussed in three different  $p_T$  regions.

- low  $p_T$ : it is dominated by the soft particles, which follow the hydrodynamic evolution, resulting in a significant sensitivity to the EoS and also initial conditions. The mass ordering is also described by the hydrodynamics;
- high  $p_T$ : it is dominated by the hard particles, which are not likely to thermalize and undergo the collective hydrodynamical-like expansion. Depending on their orientation relative to the reaction plane, particles have to travel a different path length inside the fireball, suffering the energy loss via (in)elastic processes (to be discussed later). This path-length dependence of energy loss can therefore introduce an azimuthal anisotropy;
- intermediate  $p_T$ : this is the region of the interplay between soft and hard processes. At intermediate  $p_T$ , hadrons could be mainly produced via coalescence [75, 76] or recombination [77, 78].

Note that a scaling behavior of  $v_2$  with the number of constituent quarks (NCQ), is predicted to exist for different particle species. This behavior was confirmed well by the RHIC measurements, while some deviations are observed of about 10-20% for  $p_T > 1.2$  GeV/c at the LHC (ALICE results). See Ref. [79, 80] for a recent review.

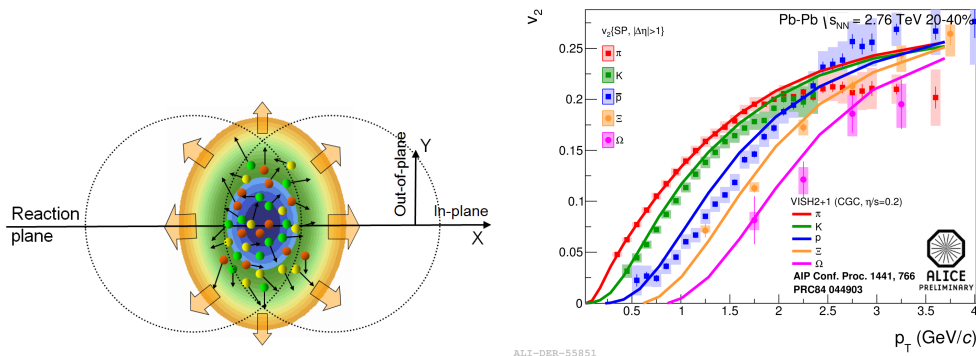


Figure 1.11: Left: Schematic initial anisotropic geometry of the collision fireball; Right: Elliptic Flow ( $v_2$ ) of identified hadrons measured in 20 – 40% in Pb–Pb collisions at  $\sqrt{s_{NN}} = 2.76$  TeV with ALICE, together with model comparison. See Ref. [81] for details; Figure taken from Ref. [81].

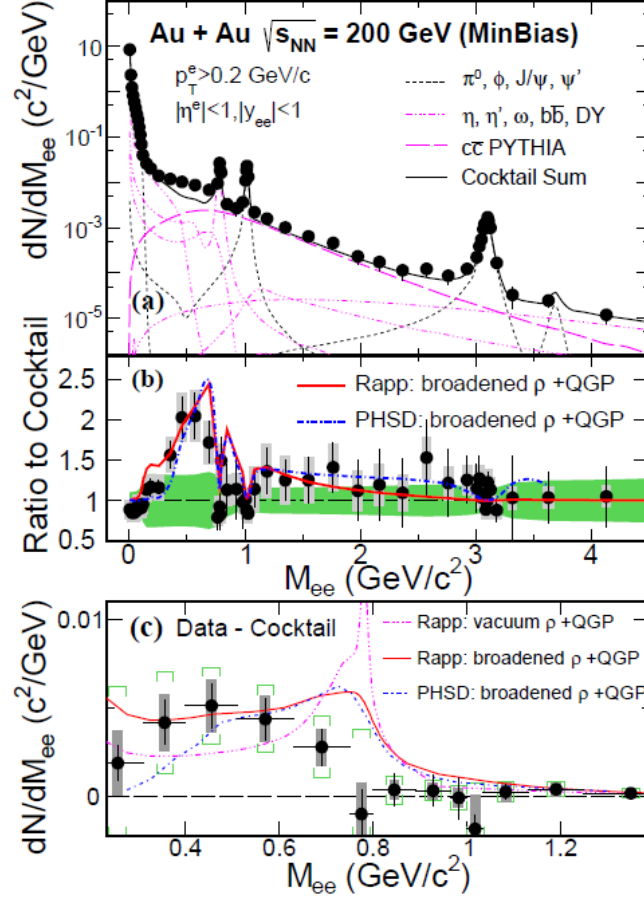


Figure 1.12: (a)  $e^+e^-$  invariant mass spectrum measured in  $\sqrt{s_{NN}} = 200$  GeV Au–Au minimum bias (0 – 80%) collisions compared to a hadronic cocktail simulation. The vertical bars on data points depict the statistical uncertainties, while the systematic uncertainties are shown as grey boxes (smaller than the marker). (b) Ratio of data over cocktail (black points) and ratio of model calculations over cocktail (red and blue curves). Green bands depict systematic uncertainties on the cocktail. (c) Mass spectrum of the excess (data minus cocktail) in the low-mass region compared to model calculations. Green brackets depict the total systematic uncertainties including those from cocktails. See Ref. [82] for details. Figure taken from Ref. [82].



### 1.2.2.5 Dilepton spectrum

Dileptons provide unique insights into the properties of the hot and dense medium created in heavy-ion collisions, because leptons do not suffer strong interactions [83, 84, 85]. In the low invariant-mass region,  $M_{l+l-} < 1 \text{ GeV}/c^2$ , the dileptons emitted from the hadronic medium are governed by the coupling of light vector mesons such as  $\rho$ ,  $\omega$  and  $\phi$ , with the medium and are expected to be the dominant contribution [86]. In the intermediate-mass region,  $M_{l+l-} > 1 \text{ GeV}/c^2$ , thermal radiation from the Quark-Gluon Plasma, the so-called thermal dileptons, becomes significant. Higher masses correspond to earlier stages of the production [87]. Therefore, the thermal dilepton production is a clean and penetrating probe for studying properties of QCD medium.

Figure 1.12 shows the  $e^+e^-$  invariant mass spectrum measured with STAR in Au–Au collisions at  $\sqrt{s_{\text{NN}}} = 200 \text{ GeV}$  [82]. One can see that the ratio with respect to cocktail is consistent within uncertainties with unity in the range  $M_{l+l-} > 1 \text{ GeV}/c^2$ , while a significant deviation (enhancement) is observed in the invariant mass range  $M_{l+l-} < 1 \text{ GeV}/c^2$ . This trend can be well described by the model predictions based on the spontaneously broken chiral symmetry in this range. Concerning the results in the range  $M_{l+l-} > 1 \text{ GeV}/c^2$ , model predictions suggest that vector meson spectra can be modified in a hot and dense medium, reflecting the restoration of the broken chiral symmetry [88, 89].

### 1.2.2.6 Hard processes at high $p_T$ and high mass

As shown in the left panel of Fig. 1.13, the production cross section of high- $p_T$  hadrons in hadronic (A–B) collisions, can be calculated from the underlying parton-parton processes by using the QCD "factorisation theorem" [15],

$$\sigma_{\text{AB} \rightarrow \text{h}}^{\text{hard}} = f_{a/A}(x_1, Q^2) \otimes f_{b/B}(x_2, Q^2) \otimes \sigma_{ab \rightarrow c}^{\text{hard}}(x_1, x_2, Q^2) \otimes D_{c \rightarrow \text{h}}(z, Q^2) \quad (1.3)$$

where,  $f_{a/A}(x_1, Q^2)$ ,  $\sigma_{ab \rightarrow c}^{\text{hard}}(x_1, x_2, Q^2)$  and  $D_{c \rightarrow \text{h}}(z, Q^2)$  are the PDFs, partonic cross section and fragmentation function (FF), respectively. One can see that, after the hadronization [90], the partons become observable as jets; two symmetric jets (or back-to-back jets) formed in the opposite directions are predicted to exist at leading order.

Hard partons can propagate through a certain distance inside the hot and dense medium formed in the collisions, as shown in the right panel of Fig. 1.13, and interact with medium constituents. This induces energy loss via gluon radiation and/or elastic scattering. According to the model calculations, the energy loss depends on the density of the medium, the distance travelled inside the medium and the flavour of a given parton (more detailed discussion will be shown in Sec. 1.2.3). The energy loss effect becomes evident in a phenomenon known as "jet quenching" [92]. That means that one allows to select hard processes occurring in the "corona" of the fireball by triggering on a high-energy jet (or hadron), for which one of the two partons can exit from the medium crossing only a small amount of matter and therefore losing a small amount of energy, while the other one has a long path

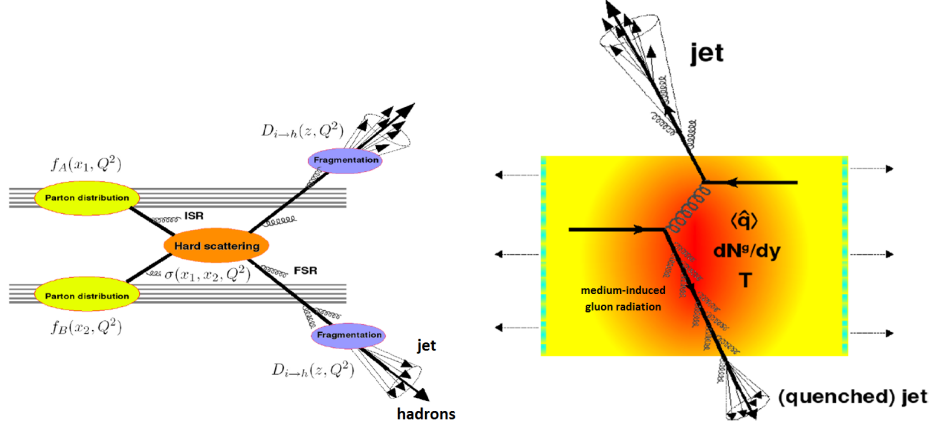


Figure 1.13: Left: sketch of di-jet production and pQCD collinear factorisation in hadronic collisions (see text for details). Right: jet quenching in nucleus-nucleus collision which can be characterised by a transport coefficient  $\hat{q}$ , gluon density  $dN_g/dy$  and temperature  $T$ ). Figures taken from Ref. [91].

in the medium and it is strongly quenched [93]. This is the so-called "surface-bias". Experimentally, the nuclear modification factor,  $R_{AA}$ , see Eq. 1.4, can be employed to quantify this medium-induced energy loss effect. It is defined as the ratio of particle yields measured in nucleus-nucleus collisions to that in binary-scaled nucleon-nucleon collisions at the same energy.

$$R_{AA}(p_T, y) = \frac{1}{N_{\text{coll}}} \times \frac{dN_{AA}^2/dp_T dy}{dN_{pp}^2/dp_T dy} \quad (1.4)$$

where,  $dN_{AA}^2/dp_T dy$  and  $dN_{pp}^2/dp_T dy$  are the  $p_T$ - and  $y$ -differential yield in nucleus-nucleus (A–A) and nucleon-nucleon (pp) collisions, respectively.  $R_{AA}=1$  when the  $N_{\text{coll}}$  scaling behavior is achieved at high  $p_T$ , while  $R_{AA}<1$  for  $N_{\text{part}}$  scaling at low  $p_T$ . This native expectation can be modified by including the nuclear matter effects, such as hot nuclear matter (HNM) effects which are related to the creation of the hot and dense medium in nucleus-nucleus collisions, and cold nuclear matter (CNM) effects for the remaining components. A more detailed discussion of HNM and CNM is shown in the next sub-section.

Due to large mass, the electroweak bosons ( $W$  and  $Z$ ) are produced in initial hard scattering processes, and they are expected not to be modified by the medium. Their leptonic decay products can therefore go through the created QCD medium freely. Measurements of dileptons from electroweak bosons can thus serve as reference to the processes expected to be modified in the hot and dense medium, often referred to as the QGP.

Photons are electromagnetic probes that can be produced during all stages of a heavy-ion collision. Direct photons are the components that are not originating from hadronic decays such as  $\pi^0$ ,  $\eta \rightarrow \gamma\gamma$ , these are the so-called decay photons. They are usually further classified into [94, 95] prompt photons (created in collisions of incoming partons and in parton fragmentation) and thermal photons (emitted from

a thermally equilibrated hot matter). Since photons carry no color charge they do not interact strongly with the hadronic medium, and they are not influenced by the hadronization processes. Consequently, the photons carry purely the information about their production environment, practically unmodified to a detector [96].

A summary of  $R_{AA}$  measurements for different particle species is shown in Fig. 1.14 for Pb–Pb collisions at  $\sqrt{s_{NN}} = 2.76$  TeV. The inclusive charged-particle  $R_{AA}$  shows a pronounced maximum ( $\sim 0.5$ ) at  $p_T \approx 2$  GeV/ $c$ . Then,  $R_{AA}$  decreases with increasing  $p_T$  in the range  $2 \lesssim p_T \lesssim 7$  GeV/ $c$ . A strong suppression ( $\sim 0.15$ ) is observed in this region. Finally,  $R_{AA}$  increases up to about 0.6 at  $p_T \approx 100$  GeV/ $c$ . The rise can be understood as a decrease of the parton fractional energy loss with increasing  $p_T$ , reflecting the weak energy dependence of pQCD radiative energy loss on parton energy, as well as the influence induced by the  $p_T$  shape of the parent parton and the related fragmentation function [41]. The suppression is also observed for the measurements of non-prompt  $J/\Psi$ , inclusive and b-jets at high  $p_T$ . Electroweak bosons (W and Z) and isolated photons are not suppressed, within the currently still large statistical uncertainties.

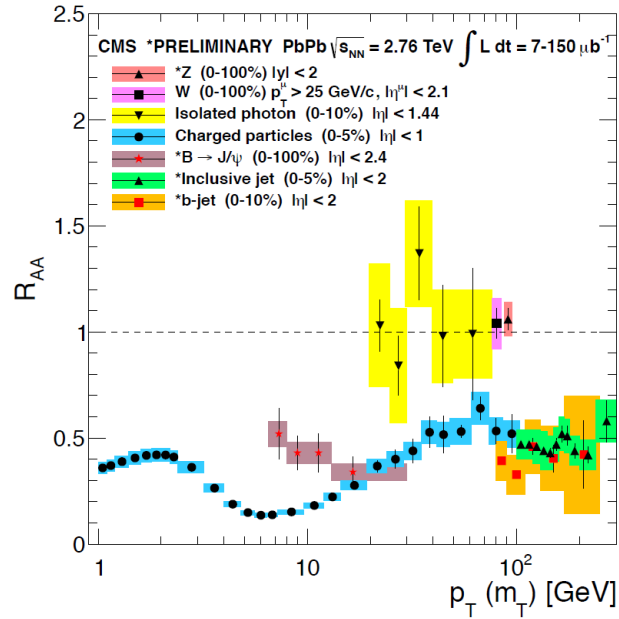


Figure 1.14: Nuclear modification factor  $R_{AA}$  as a function of  $p_T$  ( $m_T$ ) measured by the CMS Collaboration in Pb–Pb collisions at  $\sqrt{s_{NN}} = 2.76$  TeV for different particle species: Z bosons [97], W bosons [98], isolated photons [99], charged particles [100], non-prompt  $J/\Psi$  [101], inclusive jets [102] and b-jets [103]. See each reference for the detail. Figure taken from Ref. [104].

### 1.2.3 Cold and Hot Nuclear Matter Effects

#### 1.2.3.1 Nuclear modification of the parton distribution functions (PDFs)

According to the studies of deep-inelastic scattering on nuclei, it was discovered that the parton distribution functions of nucleons bound in nuclei differ from those of the free nucleons. This effect is the CNM effect and it can be quantified by a ratio,  $R_i^{\text{nucleus}}$  where  $i$  denotes a selected parton.  $R_i^{\text{nucleus}}$  is defined as the ratio of the nuclear parton distribution functions (nPDFs) with respect to the parton distribution functions (PDFs) of free nucleons. In the left panel of Fig. 1.15 the results of gluon PDF modification for a Pb nucleus, based on different models, are presented as a function of  $x$ . According to the different behaviors displayed in different  $x$  regions, the nuclear effects on the PDFs can be divided into four parts [105, 106]: shadowing effect in  $x \lesssim 0.1$ , anti-shadowing effect in  $0.1 \lesssim x \lesssim 0.3$ , EMC effect [107] in  $0.3 \lesssim x \lesssim 0.7$  and Fermi motion [108] term for  $x \rightarrow 1$ . The shadowing (or anti-shadowing) behavior can make a universal contribution to the particle production in heavy-ion collisions [106].  $R_{AA}$  can be suppressed due to the shadowing (small  $x$ ) contribution, while it can be enhanced for anti-shadowing (intermediate  $x$ ). In the case of heavy quark production, low  $x$  means low  $p_T$ , therefore, one expects  $R_{AA} < 1$  at low  $p_T$  due to shadowing.

Note that heavy quark production at low  $x$  means low  $p_T$ , so shadowing implies  $R_{AA} < 1$  at low  $p_T$ .

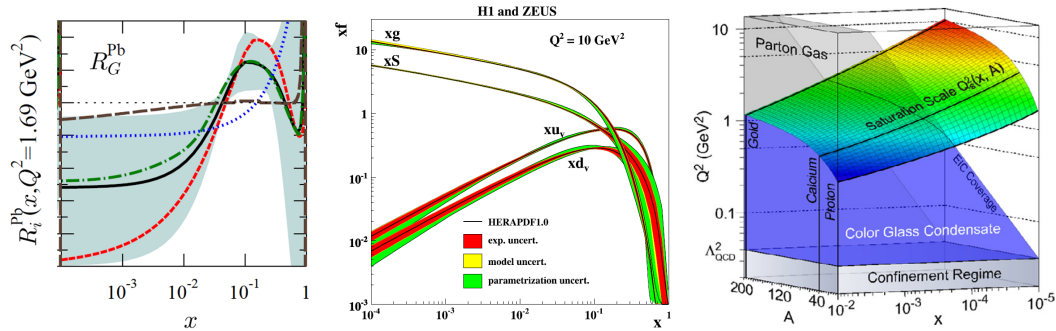


Figure 1.15: Left: comparison of gluon modifications at  $Q^2 = 1.69\text{GeV}^2$  for Pb nucleus ( $R_G^{\text{Pb}}$ ) obtained from different models, see Ref. [105] for detail. Middle: parton distributions in a proton. Right:  $x$  and  $A$  dependence of the saturation scale  $Q_s$ . Figures taken from Ref. [105], [109] and [110], respectively.

The middle panel of Fig. 1.15 presents the distributions of valence partons (u and d quarks), sea quarks and gluons as a function of  $x$ , together with the related uncertainties shown as bands. The deviation of the density between gluons and valence quarks increases with decreasing  $x$ . This behavior can be interpreted by the Color Glass Condensate (CGC) theory [111, 112].

In the framework of CGC, the valence parton sources (with large  $x$ ) are treated as static sources with color charge, and they are able to radiate soft gluons (with small  $x$ ) via a classical gauge field quantified by means of Stochastic Yang-Mills



equation [113, 114, 115]. Hence, partons in a small  $x$  region are mainly gluons. The size of the gluon,  $r \sim 1/Q$ , generated from valence parton radiation, decreases with increasing  $Q$ , which is limited by the size resolution of the adopted probe,  $r_s$ . That means that the probe cannot "see" gluons with a size  $r < r_s$ , corresponding to  $Q > Q_s$ , namely saturation.  $Q_s = Q_s(x, A)$  is the saturation scale, as shown in the right panel of Fig. 1.15, and it is the most important parameter in the CGC theory. It is used to control the occupation number of gluons in a small  $x$  region. The empirical evidence for the CGC is reviewed in Ref. [19], as well as the further investigation shown in Ref. [116]. Now, the CGC theory is widely used to describe the measurements in heavy-ion collisions, and it can also be employed to model the initial-state evolution of the hydrodynamic matter [117]. It is interesting to see that the CGC can be tested rigorously by studying the average number of charged particles in proton-lead (p-Pb) collisions at LHC energies. As discussed in Ref. [118], the average number of charged particles predicted by the CGC depends logarithmically on the number of participants in terms of CGC, while it depends linearly based on the other typical models. Finally, the corresponding yields of considered particles can also be suppressed, when considering purely the saturation effect from the initial condition. Note that the CGC effect is not significant at high  $p_T$ .

### 1.2.3.2 Cronin effect (or $k_T$ broadening)

The Cronin effect plays a role at intermediate  $p_T$  (e.g.  $p_T \sim 2-4$  GeV/c), and it is one of the CNM effects. As displayed in Fig. 1.16, the invariant cross section of the particle production presents a power law dependence in  $A$ , the mass number, for the invariant cross sections, extrapolated as  $A^\alpha$ , in p-A collisions at Fermilab [119]. In this case, the power  $\alpha$  gives similar information as the  $R_{AA}$ . For the measured hadron species, the  $\alpha$  values are larger than unity in  $p_T \gtrsim 2$  GeV/c, which can be interpreted as the partons in the projectile nucleon suffer multiple scatterings with the ones in the target nucleon, before fragmenting into hadrons [120]. Note that,

- the parton in the projectile nucleon gains additional transverse momentum,  $k_T$ , during the multiple parton scattering;
- the gained component can be transformed to hadron spectra, resulting in a shift towards high  $p_T$ ;
- the shift is more significant for hadrons with larger masses, corresponding to harder fragmentation functions.

One can see that the "Cronin effect" allows to shift the hadron spectra towards high  $p_T$ , consequently, it depletes at a certain extend the hadrons spectra in the low  $p_T$  region. The effect is stronger for the hadrons with larger masses. A peak phenomenon is therefore expected for the resulting  $R_{AA}$  at intermediate  $p_T$ , which has been shown already in the earlier Fermilab measurements. The peak value is larger for the hadron species with larger masses (see Fig. 1.16). Additionally, the "Cronin effect" decreases with increasing  $p_T$  or the collision energy. More related

theoretical and experimental results can be found in Ref. [121, 122, 123]. There are still other cold nuclear matter effects, such as the energy loss in the cold nuclear matter and the possible final-state effect.

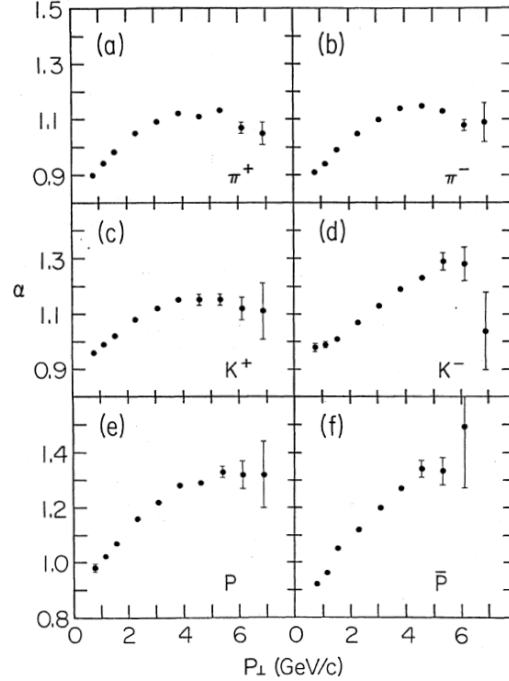


Figure 1.16: Power  $\alpha$  of the  $A$  dependence of the invariant cross section extrapolated as  $A^\alpha$ , as a function of  $p_T$ . Data are collected for different hadron species in p-A collisions at Fermilab [119]. Figure taken from Ref. [119].

### 1.2.3.3 Energy loss of fast partons

As mentioned in the previous section, partons with large transverse momentum ( $k_T$ ) can lose the energy when propagating through the hot and dense medium created in heavy-ion collisions. The in-medium energy loss is a hot nuclear matter effect, and the related mechanism was motivated by Bjorken in 1982 [124]. When including some further investigations, it can be summarized into two dominant processes.

**Energy loss via inelastic interactions** ( $2 \rightarrow 2 + X$ ) with the medium [125], for example the gluon bremsstrahlung [126]. The typical diagram for the strong interaction is shown in left panel of Fig. 1.17. After entering into the medium, the projectile partons interact with the medium constituents via the exchange of color charge, and then, they undergo the radiative procedure by emitting gluons. The emitted (softer) gluons can also couple with the medium constituents, having the transverse momentum,  $q_T$ . The reinteractions are characterized by a mean free path [38],  $\lambda$ , which is shown in the left panel of Fig. 1.17. Finally, the resulting contributions of reinteractions are added together coherently.

In contrast to fast partons, whose trajectory can be treated as a straight line,

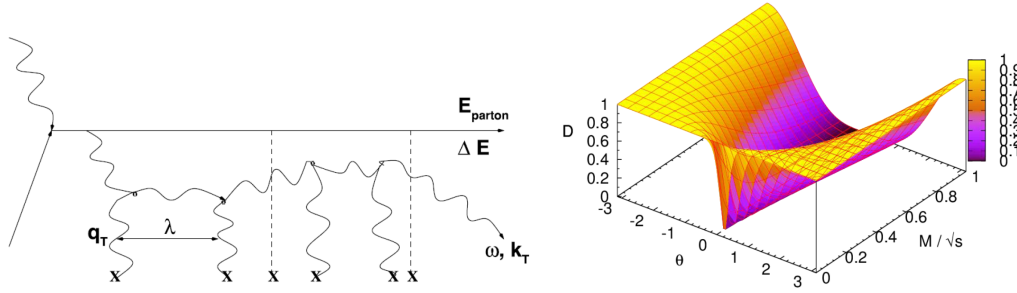


Figure 1.17: Left: typical gluon radiation diagram in BDMPS approach [127]. Right: generalized suppression factor,  $\mathcal{D}$ , as a function of  $\theta$  and  $M/\sqrt{s}$ , see Ref. [128] for detail. Figures taken from Ref. [38] and [129], respectively.

the multiple interactions between the emitted softer gluons and the medium induce a random walk in its transverse momentum,  $k_T$ , together with the energy density,  $\omega$ . The derived models, e.g. BDMPS [127], can predict the average energy loss of fast partons as,

$$\Delta E \propto \alpha_s C_R \hat{q} L^2 \quad (1.5)$$

where,  $\alpha_s$  denotes the running coupling;  $C_R$  indicates the Casimir factor, which is  $4/3$  ( $3$ ) for quark-gluon (gluon-gluon) coupling,  $\hat{q} = \langle q_T^2 \rangle_{\text{medium}} / \lambda$  is the transport coefficient which characterizes the "scattering power" of the created medium, and it is defined as the average transverse momentum squared,  $\langle q_T^2 \rangle$ , transferred to the projectile per unit of mean free path,  $L$  is the path length of the parton traveled inside the medium. For parton with large masses such as charm and beauty quarks, the gluon radiation probability is suppressed at small angles relative to the quark direction, the so-called dead-cone effect [130]. The corresponding suppression factor is obtained as [130]

$$\left(1 + \frac{\theta_0^2}{\theta^2}\right)^{-2} \quad (1.6)$$

where,  $\theta$  is the angle between the parton and the emitted gluon;  $\theta_0 = M/E \ll 1$ ;  $M$  and  $E$  are the mass and energy of the parton. However, it can also be expressed as [128]:

$$\left(1 + \frac{\theta_0^2}{\sin^2 \theta}\right)^{-2}. \quad (1.7)$$

One can see that Eq. 1.6 and Eq. 1.7 are consistent at small angles. When drawing the dead-cone picture in the full range of  $\theta$  ( $-\pi < \theta < +\pi$ ) and  $M/\sqrt{s}$  ( $0 < M/\sqrt{s} < 1$ ), the generalized suppression factor,  $\mathcal{D}$ , can be written as [128]

$$\mathcal{D} = \left(1 + \frac{M^2}{s \cdot \tan^2(\frac{\theta}{2})}\right)^{-2} \quad (1.8)$$

where  $s$  is the squared center-of-mass energy, i.e.  $s = 2E^2 + 2E\sqrt{E^2 - M^2} - M^2$ . As shown in the right panel of Fig. 1.17, the suppression factor saturates to unity in the backward region (i.e.  $\mathcal{D} \sim 1$  at  $\theta \sim \pm\pi$ ). It is argued [128] that the quark

mass plays only a role in the forward region when the energy of the quark becomes of the order of its mass.

Based on the gluon radiation model, the averaged energy loss of different particles can be written as

$$\Delta E_g^{(M=0, C_R=3)} > \Delta E_q^{(M\sim 0, C_R=4/3)} \sim \Delta E_c^{(M\sim 1.5\text{GeV}, C_R=4/3)} > \Delta E_b^{(M\sim 5\text{GeV}, C_R=4/3)} \quad (1.9)$$

where g, q, c and b denote gluon, light quark, charm and beauty quark, respectively. Eq. 1.9 shows a color charge and mass dependence of the radiative energy loss.

**Energy loss via elastic interactions** ( $2 \rightarrow 2$ ) or collisional energy loss. It is found [131] that the partons experience multiple elastic scatterings with the constituents of the medium, the resulting energy loss plays an important role when describing the measurement of non-photonic electrons from heavy-flavour hadron decays at RHIC, as presented in Fig. 1.18. The predictions considering only the energy loss via inelastic interactions, are shown as the yellow bands at about 0.6-0.8. A very large deviation with respect to data is found within the whole  $p_T$  range. However, the predictions including the elastic component allow to describe the STAR measurements within uncertainties. The theory concerning the collisional energy loss, together with further investigations is shown in Ref. [132, 133, 134, 135].

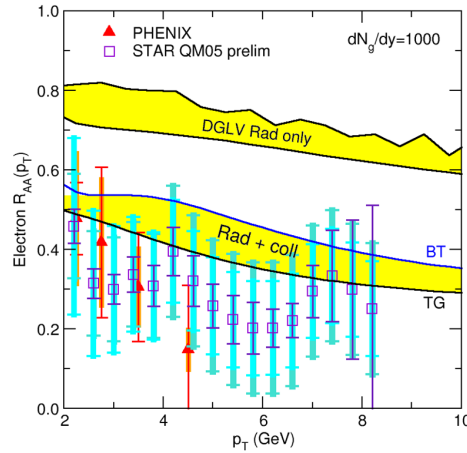


Figure 1.18: Predictions of the  $R_{AA}$  of non-photonic electrons from the decay of quenched heavy quark (c+b) jets compared to RHIC measurements in central Au+Au reactions at 200 AGeV (see Ref. [131] for details). Figure taken from Ref. [136].

One can see that the yields are suppressed at high  $p_T$  when considering only the energy loss effect. In other words, the particle yields are shifted towards low  $p_T$ .

In short summary, in the absence of nuclear effects, the nuclear modification factor,  $R_{AA}$  is smaller than unity in the low  $p_T$  region and then increase monotonously with increasing  $p_T$ , resulting in a  $R_{AA}$  to be close to unity when the  $N_{coll}$  scaling (or binary scaling) behavior is dominant at high  $p_T$ . These trends can be modified when considering the cold and hot nuclear matter effects, e.g. Cronin effect, shadowing



(or gluon saturation) effects and energy loss effects. One can see that the study of the  $R_{AA}$  behavior enables to provide information on the energy loss mechanisms and on the properties of the QGP.

## 1.3 Heavy-Flavours as probes of the QGP

In this section, we discuss in detail the relevance of heavy flavours as probes of the QGP.

### 1.3.1 Heavy-Flavour production in heavy-ion collisions

#### 1.3.1.1 Heavy flavours as hard probes

As presented in the left panel of Fig. 1.2, the quarks can be classified into two groups: light quarks (LQ) with mass  $m \leq \Lambda_{\text{QCD}}$ , i.e. u, d and s quarks, and heavy quarks (HQ) with  $m \gg \Lambda_{\text{QCD}}$ , i.e. c and b quarks (the t quark which has a mean lifetime  $c\tau < 5 \times 10^{-25}\text{s}$  [2] decays before it can hadronize). In the early stage of heavy-ion collisions, HQ pairs are produced via hard scatterings with large momentum transfer, at time scales of the order of  $1/2m_Q \sim 0.1$  (0.02) fm/c  $< \tau_{\text{QGP}}$  for c (b) quark. The subsequent strong interaction with QGP constituents does not affect the HQ masses. The thermal production is therefore expected to be negligible inside the QGP, as well as the conservation of the flavour when interaction with its constituents. That means that there is almost no additional influence concerning the original production yields of HQ, which enables to experience the full evolution of the fireball. HQ allow one to probe the mechanisms of multiple interactions with the medium, as well as the strength of the collective expansion of the created system. They are studied by measuring the heavy-flavour (HF) hadrons (including charm and beauty quarks) such as D mesons ( $D^0$ ,  $D^+$ ,  $D^{*+}$  and  $D_s^+$  originated from charm quark), B mesons ( $B^0$ ,  $B^+$  and  $B_s$  originated from beauty quark) and their decay particles ( $e^\pm$  and  $\mu^\pm$  from heavy-flavour hadron decays and  $J/\Psi$  from B).

Theoretically, as shown in Fig. 1.19, the strong interaction does not affect HQ masses: "HQ masses are almost exclusively generated through their coupling to the Higgs field in the electro-weak sector, while masses of LQ are dominated by spontaneous breaking of chiral symmetry in QCD. This means that in a QGP, where chiral symmetry might be restored, LQ are left with their bare current masses while HQ remain heavy" [137]. Experimentally, as displayed in Fig. 1.20, the HQ are copiously produced at the LHC. The latest measurements show a significant increase of the production cross-sections with respect to RHIC by a factor of 5 and 50 for charm and bottom, respectively (see Ref. [138, 139] for details). The HF production with ALICE at the LHC can be measured within two channels: hidden heavy-flavour particles (i.e. zero charm/beauty quantum number), namely quarkonia (e.g.  $J/\Psi$  and  $\Upsilon$  families), as well as open heavy-flavour ones (i.e. non-zero charm/beauty quantum number). In the following, we focus on open heavy-flavour physics. Open heavy-flavour hadrons can be measured in ALICE via their hadronic decay channels

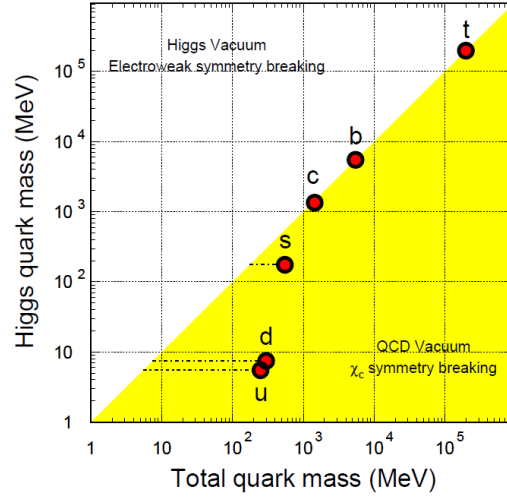


Figure 1.19: Quark masses in the QCD vacuum and the Higgs vacuum. A large fraction of the light quark masses is due to the chiral symmetry breaking in the QCD vacuum. Figure taken from Ref. [137].

and semi-electronic decay channel at mid-rapidity, as well as via their semi-muonic decay channel at forward rapidity.

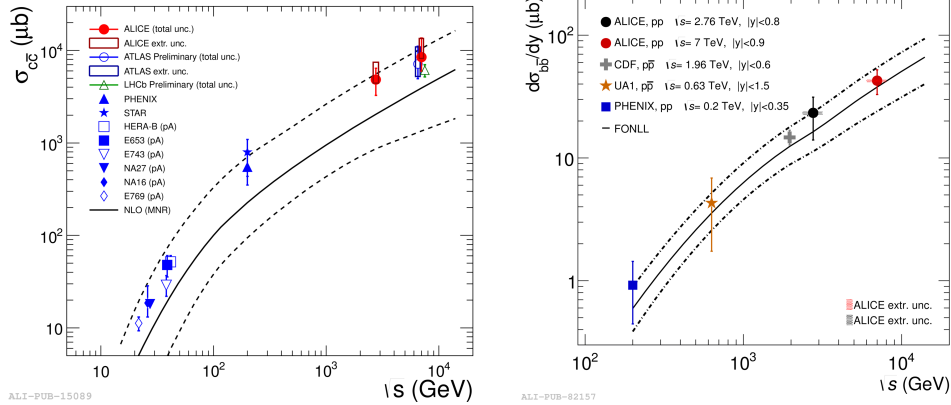


Figure 1.20: Left: energy dependence of the total nucleon-nucleon charm production cross section. In case of proton-nucleus (p-A) or deuteron-nucleus (d-A) collisions, the measured cross sections have been scaled down by the number of binary nucleon-nucleon collisions calculated using the Glauber model. Right: inclusive beauty production cross section per rapidity unit measured at mid-rapidity as a function of the center of mass energy in pp collisions (PHENIX and ALICE) and p $\bar{p}$  collisions (UA1 and CDF). The NLO MNR calculations [140] (and its uncertainties) are represented by solid (dashed) lines. Figures taken from Ref. [138] and [139], respectively.

### 1.3.1.2 Energy loss and transport approach from models

As introduced in the previous section, heavy quarks lose energy via (in)elastic interaction processes when propagating through the hot and dense medium. The resulting effect can be studied by means of the nuclear modification factor,  $R_{AA}$ . In order to perform the comparison with the experiments,  $R_{AA}$  predictions at hadron level are shown in Fig. 1.21. The curves in different styles are the model calculations including different energy loss mechanisms for charm (left) and beauty quarks (right). According to the predictions obtained at mid-rapidity in central nucleus-nucleus collisions, we can see that the predictions at the LHC without and with including the inelastic component, act differently at high  $p_T$ . If one considers only the elastic interactions, the related  $R_{AA}$  increases with increasing  $p_T$ . It tends to flatten with considering the radiative contribution. The predictions for RHIC are shown as well for comparison, and they can match well the experimental results [141]. According to the theoretical calculations, it is realized that:

- the collisional energy loss (elastic interactions) dominates in the low  $p_T$  region, while the radiative component (inelastic interactions) dominates at high  $p_T$ ;
- the radiative component "eats" a certain amount of the increasing behavior predicted by the collisional component in  $R_{AA}$  at high  $p_T$ ;
- the lighter charm quark suffers larger energy loss (i.e. mass dependence/ordering, see Eq. 1.9) than the bottom quark, resulting in the smaller  $R_{AA}$  of D mesons at high  $p_T$  when comparing with the one of B mesons. This mass ordering has been evidenced at LHC energies by comparing the  $R_{AA}$  of D mesons to that of non-prompt  $J/\Psi$  [142].

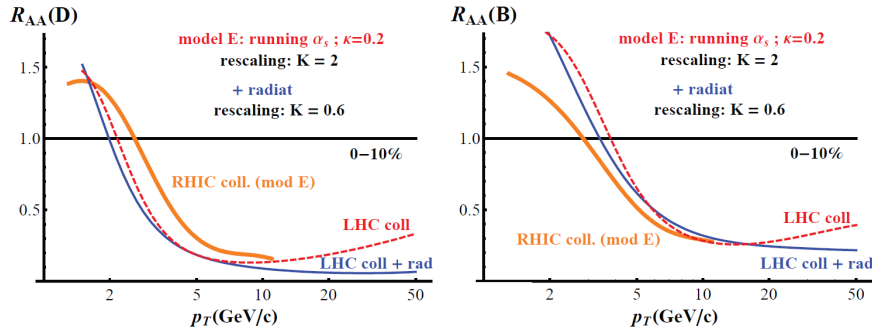


Figure 1.21:  $R_{AA}$  as a function of  $p_T$  at mid-rapidity for different energy loss mechanisms, for D mesons (left) and B mesons (right). See the text for detail. Figures taken from Ref. [141].

Due to the color charge dependence of the radiative energy loss (Eq. 1.9), gluons lose more energy than quarks in the QGP. This ordering is preserved after considering the collisional component, as shown in the left panel of Fig. 1.22. Note that both gluons and light quarks can contribute to the fragmentation into charged hadrons, while the gluons have a significant contribution in the low momentum region in

particular [143]. Naively, one would expect the  $R_{AA}$  of light hadrons to be smaller than that of heavy-flavour hadrons. However, experimental results show that the  $R_{AA}$  of D mesons and light hadrons  $R_{AA}$  are similar [144]. This is the so-called "heavy flavour puzzle at LHC".

The fact is that the fragmentation function distorts the bare light quark and gluon suppression behavior [143], which is different with respect to the one of heavy quarks  $R_{AA}^{D\text{-meson}} \sim R_{AA}^{\text{bare } c \text{ quark}}$  (see the middle panel of Fig. 1.22). The right panel of Fig. 1.22 shows the comparison of  $R_{AA}$  of charged hadrons, bare light quarks and gluons, indicating that the suppression of charged hadrons is similar to the one of bare light quarks ( $R_{AA}^{h^\pm} \sim R_{AA}^{\text{light quark}}$ ). Note that the derived mode [143] can describe the present  $R_{AA}$  measured in different centrality classes at LHC and RHIC in the region  $p_T \gtrsim 5 \text{ GeV}/c$  [145, 146].

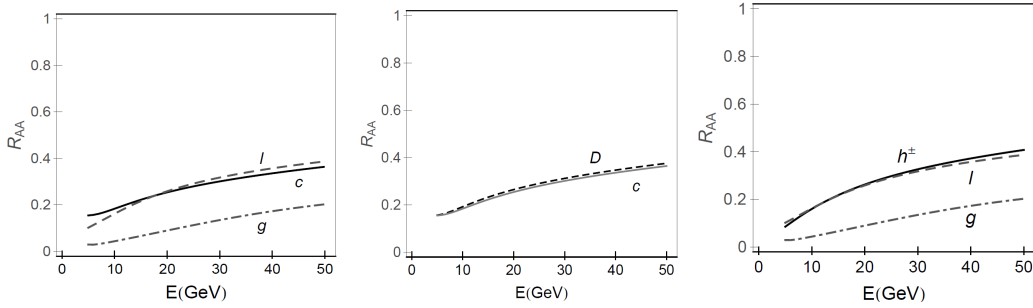


Figure 1.22: Left: suppression of charm quarks (the full curve), light quarks (the dashed curve) and gluons (the dot-dashed curve) as a function of momentum. Middle: Comparison of charm quark (the full curve) and D-meson suppression predictions (the dashed curve). Right: comparison of light hadron suppression predictions (the full curve) with light quark (the dashed curve) and gluon (the dot-dashed curve) suppression predictions. Figures taken from Ref. [143].

In the underlying thermal medium formed by the heat-bath particles, the HQ propagate as Brownian particles, which can be quantified by a Boltzmann equation [147] as follows:

$$\frac{d}{dt} f_Q(t, \vec{x}, \vec{p}) = \left[ \frac{\partial}{\partial t} + \frac{\vec{p}}{E} \frac{\partial}{\partial \vec{x}} + \vec{F} \frac{\partial}{\partial \vec{p}} \right] f_Q(t, \vec{x}, \vec{p}) = \left[ \frac{\partial f_Q}{\partial t} \right]_{\text{collisions}} \quad (1.10)$$

where,  $\vec{p}$ ,  $E = \sqrt{m_0^2 + \vec{p}^2}$  and  $\vec{x}$  are the three-momentum, energy and three-dimensional space of HQ at time  $t$  inside the thermal medium, respectively;  $\vec{F}$  is the external mean-field force;  $\left[ \frac{\partial f_Q}{\partial t} \right]_{\text{collisions}}$  denotes the collision integral.  $\vec{F}$  would vanish in case of a homogeneous medium. In the limit of small momentum transfers, the Boltzmann equation is reduced to the Fokker-Plank Equation (FPE, [147]).

$$\frac{\partial}{\partial t} f_Q(t, \vec{p}) = \frac{\partial}{\partial p_i} \{ A_i(\vec{p}) f_Q(\vec{p}) + \frac{\partial}{\partial p_j} [ B_{ij}(\vec{p}) f_Q(\vec{p}) ] \} \quad (1.11)$$

where,  $A_i(\vec{p})$  and  $B_{ij}(\vec{p})$  are the drag and the diffusion coefficients of HQ, respectively. In the framework of FPE, HQ interactions are conveniently encoded in the drag and

diffusion coefficients. Note that the FPE is equivalent to an ordinary stochastic differential equation, Langevin equation (LVE) [147]. See Ref. [147] for details.

The derived models [148] including hard interaction via the heavy-quark recombination during the hadronization procedure of the fireball, can provide powerful constraints on heavy-flavor diffusion and hadronization. As shown in Fig. 1.23, within uncertainties, the theoretical calculations can reproduce well the  $R_{AA}$  measurement of D-meson and  $D_s$ -meson production in central Pb–Pb collisions at  $\sqrt{s_{NN}} = 2.76$  TeV. One can see that both the predictions for average D-meson and  $D_s$   $R_{AA}$  show a maximum around  $p_T = 1 - 2$  GeV/c, induced by the transverse flow [149]. The maximum  $R_{AA}$  is about 0.8 for D mesons, while it can be larger than 1.5 for  $D_s$  due to the c-quark recombination/coalescence and the enhanced strangeness in Pb–Pb collisions. The corresponding measurement of  $D_s$  does not allow to conclude about an enhancement due to the present statistics. Note that the considered model calculations has only elastic scatterings of the charm quarks with the medium constituents.

Concerning the heavy-flavour flow based on the transport models, there are many remarkable predictions, e.g. at intermediate  $p_T$ , the collisional energy loss gives larger elliptic flow than the radiative one [141, 150], and the recombination process allows to increase the radial and elliptic flow when comparing with the fragmentation [148, 151]. They are useful to further understand the current and/or future measurements of heavy-flavour production. More general discussion with the explored model for the heavy-flavour transport in medium is shown in Ref. [152].

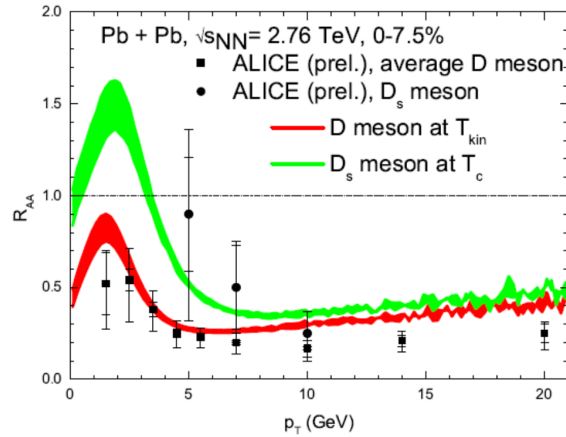


Figure 1.23: Nuclear modification factor predicted by the employed transport model for D-meson produced in central Pb–Pb collisions at  $\sqrt{s_{NN}} = 2.76$  TeV. Data from ALICE are shown for comparison. Figures taken from Ref. [153].

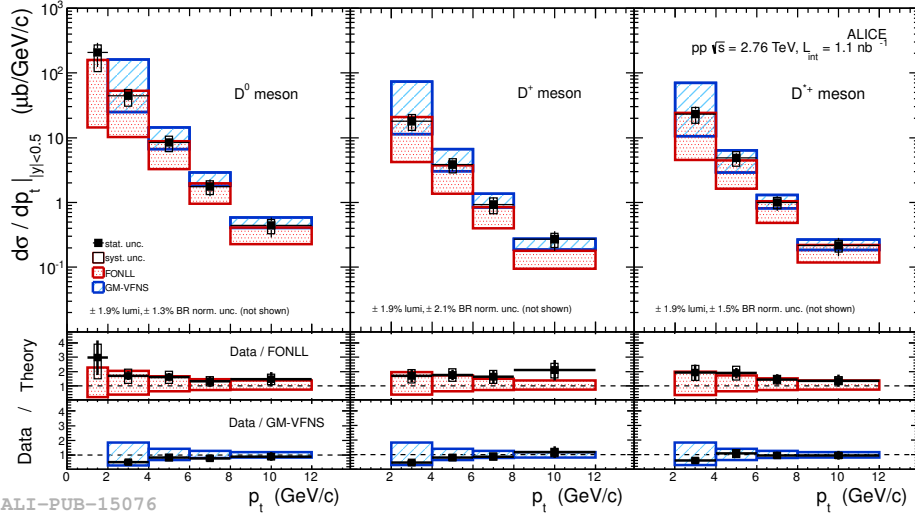


Figure 1.24: Top:  $p_T$ -differential cross section for prompt  $D^0$ ,  $D^+$  and  $D^{*+}$  mesons in pp collisions at  $\sqrt{s} = 2.76$  TeV compared with FONLL and GM-VFNS theoretical predictions. Bottom: the ratio of the measured cross section and the central values from FONLL and GM-VFNS calculations. Figure taken from Ref. [138].

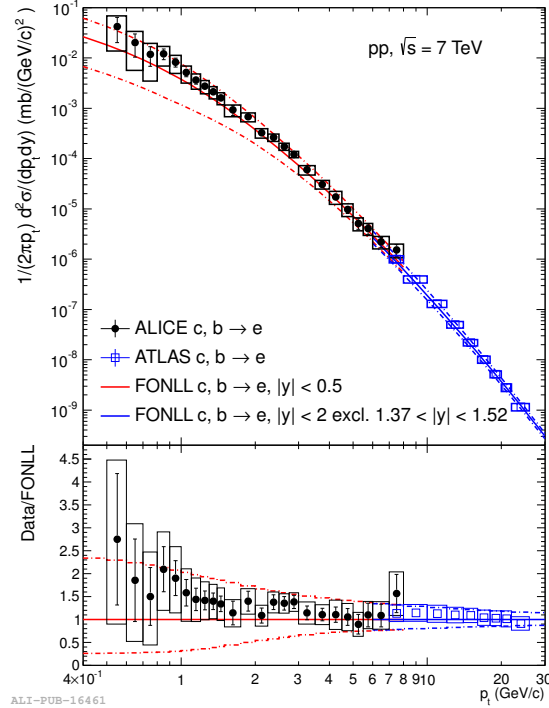


Figure 1.25: Invariant differential production cross sections of electrons from heavy-flavour hadron decays measured by ALICE and ATLAS in pp collisions at  $\sqrt{s} = 7$  TeV in different rapidity intervals (see text). FONLL pQCD calculations [140, 154, 155] with the same rapidity selections are shown for comparison. Figure taken from Ref. [156].



### 1.3.1.3 Selected measurements of open heavy-flavour production at the RHIC and the LHC

#### $p_T$ -differential production cross sections in pp collisions at $\sqrt{s} = 2.76/7$ TeV

With ALICE, charmed mesons can be reconstructed at mid-rapidity from their hadronic decay channels [2]:  $D^0 \rightarrow K^- \pi^+$  (BR = 3.88%),  $D^+ \rightarrow K^- \pi^+ \pi^+$  (BR = 9.13%),  $D^{*+} \rightarrow D^0 \pi^+$  (BR = 67.7%) and  $D_s^+ \rightarrow \phi \pi^+ \rightarrow K^+ K^- \pi^+$  (BR = 2.28%). The top panels of Fig. 1.24 present the measurement of the  $p_T$ -differential production cross sections of prompt  $D^0$ ,  $D^+$  and  $D^{*+}$  mesons (i.e. decay from charm quarks, directly) in pp collisions at  $\sqrt{s} = 2.76$  TeV, together with the FONLL [140, 154, 155] and the GM-VFNS [157] theoretical predictions, while the bottom panels represent the ratio of the measured cross sections and the calculations. It is found that, (1) FONLL and GM-VFNS theoretical predictions are compatible with the measurements within the experimental and theoretical uncertainties; (2) the central prediction of FONLL tends to underestimate the charm production whereas the central GM-VFNS calculation seems to overestimate it. This behaviour is in accordance with our results on the prompt  $D^0$ ,  $D^+$  and  $D^{*+}$ -meson  $p_T$ -differential cross sections at  $\sqrt{s} = 7$  TeV [158].

The  $p_T$ -differential production cross section of electrons from heavy-flavour hadron decays at mid-rapidity in pp collisions at  $\sqrt{s} = 7$  TeV, is shown in Fig. 1.25. It combines the measurement from ALICE up to 8 GeV/ $c$  and the data from ATLAS at higher  $p_T$  [156]. The predictions based on FONLL pQCD calculations [140, 154, 155] are obtained in the rapidity intervals covered by ALICE and ATLAS, respectively. One can see that FONLL is in agreement with both data sets when considering the experimental and theoretical uncertainties.

Concerning the production cross section of muons from heavy-flavour hadron decays measured in pp collisions at 2.76 [159] and 7 TeV [160], they are summarized and discussed in detail in Chap. 5.

#### Nuclear modification factor measured in Pb–Pb collisions at $\sqrt{s_{NN}} = 2.76$ TeV

The mass ordering of heavy-quark energy loss at parton level,  $\Delta E_c > \Delta E_b$ , see Eq. 1.9, can be inherited by the fragmented hadrons, therefore  $R_{AA}(D) < R_{AA}(B)$  is expected. The corresponding measurements performed by ALICE and CMS in Pb–Pb collisions at  $\sqrt{s_{NN}} = 2.76$  TeV [161], are presented in Fig. 1.26. It shows the average  $R_{AA}$  of prompt  $D^0$ ,  $D^+$  and  $D^{*+}$  mesons in the range  $|y| < 0.5$  and  $8 < p_T < 16$  GeV/ $c$ , together with the  $R_{AA}$  of non-prompt  $J/\Psi$  ( $B \rightarrow J/\Psi + X$ ) performed in  $|y| < 1.2$  and  $6.5 < p_T < 30$  GeV/ $c$ , both as a function of  $N_{part}$ .  $R_{AA}$  of non-prompt  $J/\Psi$  (i.e. beauty) is larger than that of D mesons (i.e. charm), and this behavior can be well described by the model including in-medium energy loss, different  $p_T$  shape of the parent parton spectra and the different fragmentation functions. See Ref. [161] for details. Hence, the two measurements provide the hints

for the mass ordering of the energy loss induced by the hot medium.

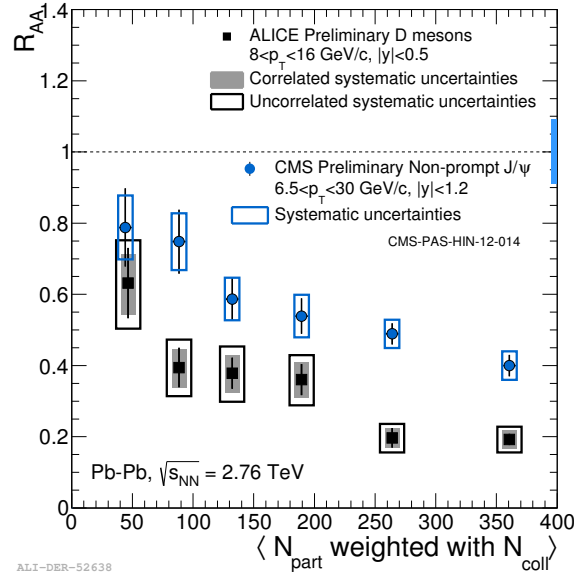


Figure 1.26: Average  $R_{AA}$  of prompt  $D^0$ ,  $D^+$  and  $D^{*+}$  mesons as a function of  $N_{part}$  compared with non-prompt  $J/\Psi$  measured by CMS in the central rapidity region in  $6.5 < p_T < 30$  GeV/c. Vertical bars are the statistical uncertainties, empty boxes are the total uncorrelated systematic uncertainties, filled boxes are the correlated systematic uncertainties. Figure taken from Ref. [161].

Figure 1.27 shows the  $R_{AA}$  of D mesons ( $|y^D| < 0.5$ , black) and the charged-pion  $R_{AA}$  ( $|y^{\pi^\pm}| < 0.8$ , green) as a function of  $p_T$  in semi-central (30 – 50%) Pb–Pb collisions at  $\sqrt{s_{NN}} = 2.76$  TeV. The vertical bars and open boxes indicate the statistical and systematic uncertainties, respectively. Within the significant uncertainties, one can see that  $R_{AA}$  of D mesons and charged pions are compatible but there is a region at low/intermediate  $p_T$  where the central values of D-meson  $R_{AA}$  are all above those of charged pions. Note that this effect is small, but also models predict a small difference as a consequence of the interplay of different energy loss (charm quark loses less energy), different  $p_T$  shapes of parent partons (charm quark spectrum is harder) and different fragmentation functions (charm-quark fragmentation function is harder).

Figure 1.28 presents the  $R_{AA}$  of electrons ( $|y^e| < 0.6$ , blue) and muons ( $2.5 < y^\mu < 4$ , black) from heavy-flavour hadron decays at central and forward rapidity, respectively, in the 10% most central Pb–Pb collisions at  $\sqrt{s_{NN}} = 2.76$  TeV. One can see a strong suppression reaching a factor of about 3-4 both for electrons and muons at  $p_T \sim 8$  GeV/c. While the two measurements are well in agreement in the overlapping  $p_T$  range, both muon and electron<sup>§</sup> measurements show a hint for an increasing  $R_{AA}$  toward larger  $p_T$ . Note that the agreement behavior between them is validated in semi-central Pb–Pb collisions at  $\sqrt{s_{NN}} = 2.76$  TeV [163].

<sup>§</sup>further update needed in order to subtract the component  $e \leftarrow W$ , in particular at high  $p_T$ .

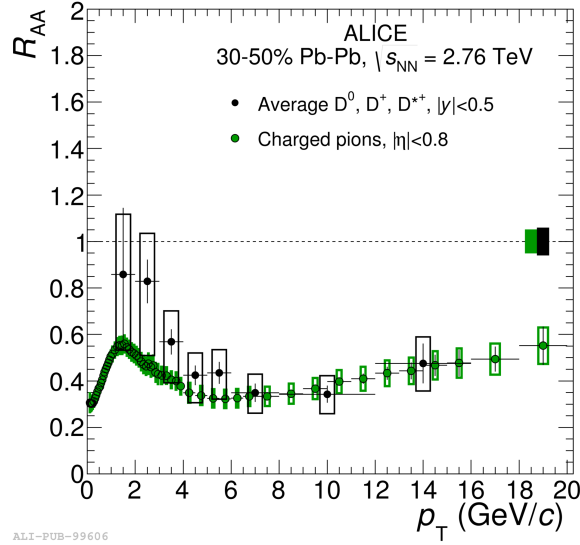


Figure 1.27:  $R_{AA}$  of  $D^0$  mesons ( $|y^D| < 0.5$ ) and charged pions ( $|y^{\pi^\pm}| < 0.8$ ) as a function of  $p_T$ , for semi-central (30 – 50%) Pb–Pb collisions at  $\sqrt{s_{NN}} = 2.76$  TeV. Figure taken from Ref. [162].

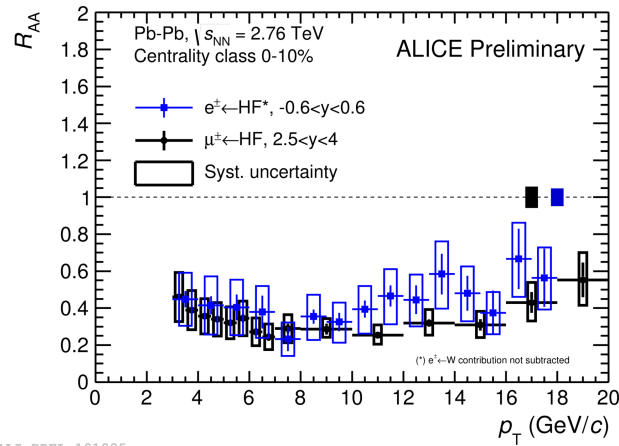
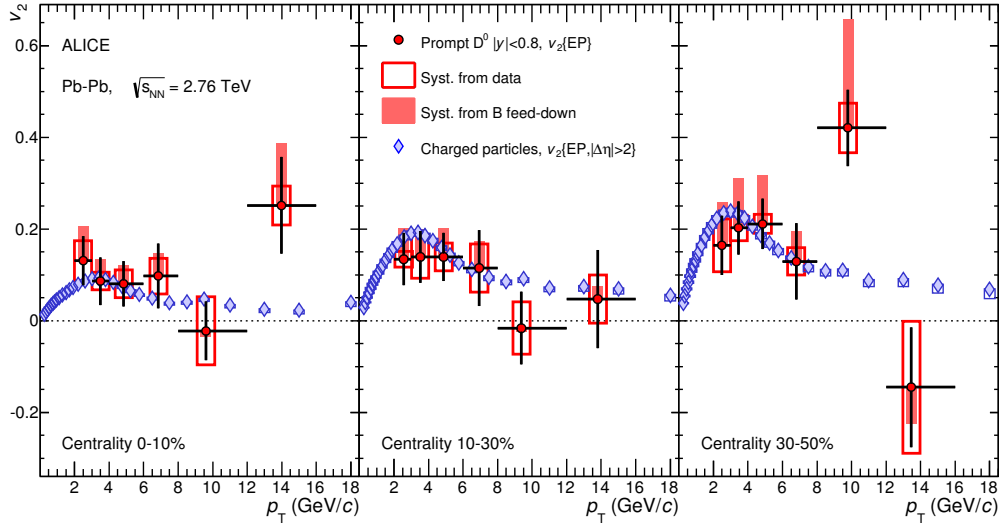
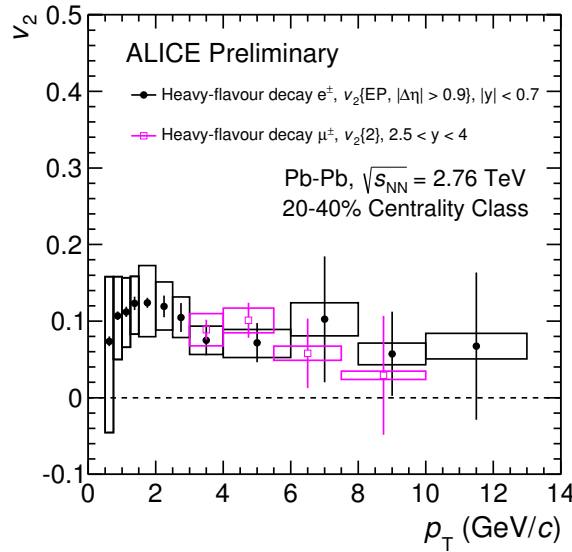


Figure 1.28: Nuclear modification factor of muons (electrons) from heavy-flavour hadron decays in  $2.5 < y^\mu < 4$  ( $|y^e| < 0.6$ ) and  $3 < p_T^\mu < 20$  GeV/c ( $3 < p_T^e < 18$  GeV/c) in central Pb–Pb collisions at  $\sqrt{s_{NN}} = 2.76$  TeV. Figure taken from Ref. [164].



ALI-PUB-70100

Figure 1.29: Comparison of prompt  $D^0$  meson and charged-particle  $v_2$  in three centrality classes as a function of  $p_T$ . Both measurements are done with the event plane method. Figure taken from Ref. [165].



ALI-PREL-77628

Figure 1.30: Elliptic flow of electrons and muons from heavy-flavour hadron decays as a function of  $p_T$ , for Pb–Pb collisions at  $\sqrt{s_{NN}} = 2.76$  TeV in the centrality range 20 – 40%. Figure taken from Ref. [166].



## Open heavy-flavour elliptic flow in Pb–Pb collisions at $\sqrt{s_{\text{NN}}} = 2.76$ TeV

It is expected that the interactions between medium constituents and charm quarks allow to transfer to the latter information on the azimuthal anisotropy of the medium during the collective expansion of the system. Figure 1.29 shows the  $D^0$  meson  $v_2$  in the three centrality classes 0–10%, 10–30% and 30–50% as a function of  $p_{\text{T}}$ . The  $D^0$  meson  $v_2$  is compared with that of charged particles [167], for the same centrality classes, and both of them are obtained with the event plane method. One can see that the magnitude of  $v_2$  is similar for charmed hadrons and light-flavour hadrons. A positive  $v_2$  is measured in semi-central collisions and intermediate  $p_{\text{T}}$  ( $2 < p_{\text{T}} < 6$  GeV/ $c$ ) with a  $5.7\sigma$  significance. Moreover, there is an indication for a decrease of  $D^0$  meson  $v_2$  towards more central collisions. These results suggest that charm quarks participate in the collective expansion of the system.

The elliptic flow of muons from heavy-flavour hadron decays has been measured at forward rapidity ( $2.5 < y^{\mu} < 4$ ) and  $3 < p_{\text{T}}^{\mu} < 10$  GeV/ $c$  in semi-central (20–40%) Pb–Pb collisions at  $\sqrt{s_{\text{NN}}} = 2.76$  TeV. The analysis is performed via two-particle correlation method (2-particle Q-cumulant [42]). The observation of a positive  $v_2$  in 20–40% at intermediate  $p_{\text{T}}$  with a significance larger than  $3\sigma$  when combining statistical and systematic uncertainties [168], suggests that heavy quarks suffer significant re-scatterings in the medium and inherit the azimuthal anisotropy produced by the collective expansion of the fireball [168]. The  $v_2$  of electrons from heavy-flavour hadron decays is measured at mid-rapidity ( $|y^e| < 0.7$ ) and  $0.5 < p_{\text{T}}^e < 13$  GeV/ $c$  in the same centrality class. It is based on the Event Plane method (EP [42]). One can see that the  $v_2$  of heavy-flavour hadron decay electrons at mid-rapidity is compatible with that of heavy-flavour hadron decay muons at forward rapidity [169].

## Nuclear modification factor and electron-muon correlations measured in nucleon-nucleus collisions (e.g. p–Pb and d–Au collisions)

Figure 1.31 shows the nuclear modification factor  $R_{\text{pPb}}$  of the four D-meson species ( $D^0$ ,  $D^+$ ,  $D^{*+}$  and  $D_s^+$ ) measured at mid-rapidity ( $-0.96 < y_{\text{CMS}} < 0.04$ ) with ALICE, in p–Pb collisions at  $\sqrt{s_{\text{NN}}} = 5.02$  TeV. The results are consistent among the meson species, and they are compatible with unity in the measured  $p_{\text{T}}$  range within the uncertainties. Therefore the D-meson production in p–Pb collisions is consistent within statistical and systematic uncertainties with the binary collision scaling of the production in pp collisions. Moreover, within the uncertainties, the  $D_s^+$  nuclear modification factor is compatible with that of non-strange D mesons [170]. Note that the average  $R_{\text{pPb}}$  of prompt  $D^0$ ,  $D^+$  and  $D^{*+}$  is still consistent with unity within uncertainties in the range  $1 < p_{\text{T}} < 24$  GeV/ $c$  [170, 171].

Figure 1.32 shows the nuclear modification factor of B mesons measured at mid-rapidity ( $|y_{\text{CMS}}| < 1.93$ ) with CMS, in p–Pb collisions at  $\sqrt{s_{\text{NN}}} = 5.02$  TeV. Results of  $B^+$ ,  $B^0$  and  $B_s^0$  are presented in the left, middle and right panel, respectively. The vertical bars (open boxes) represent the statistical (systematic) uncertainty around the data points. Note that the used pp reference is taken from the FONLL

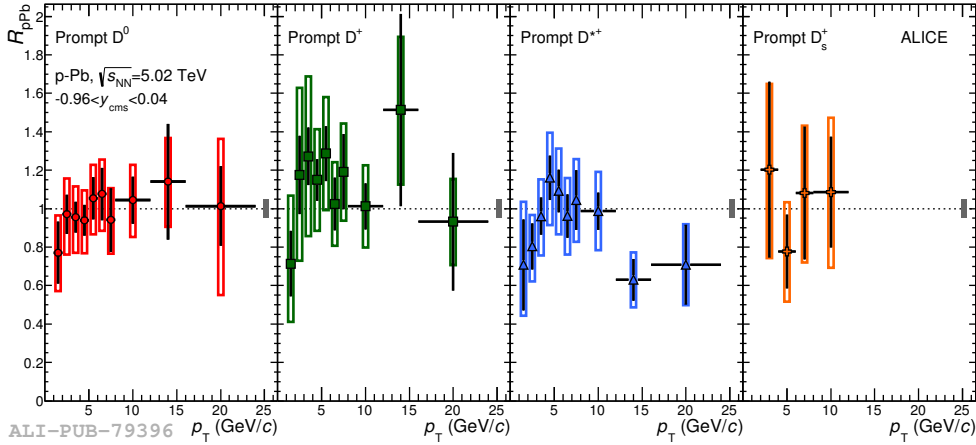


Figure 1.31: Nuclear modification factor as a function of  $p_T$  for prompt  $D^0$ ,  $D^+$ ,  $D^{*+}$  and  $D_s^+$  mesons in p-Pb collisions at  $\sqrt{s_{NN}} = 5.02$  TeV. Statistical (bars), systematic (empty boxes), and normalization (full box) uncertainties are shown. Figure taken from Ref. [170].

predictions, and the induced systematic is displayed as full yellow boxes. One can see that the measured nuclear modification factor  $R_{pA}^{\text{FONLL}}$  as a function of  $p_T^{\text{B-Meson}}$  is compatible with unity within the statistical and systematic uncertainties.

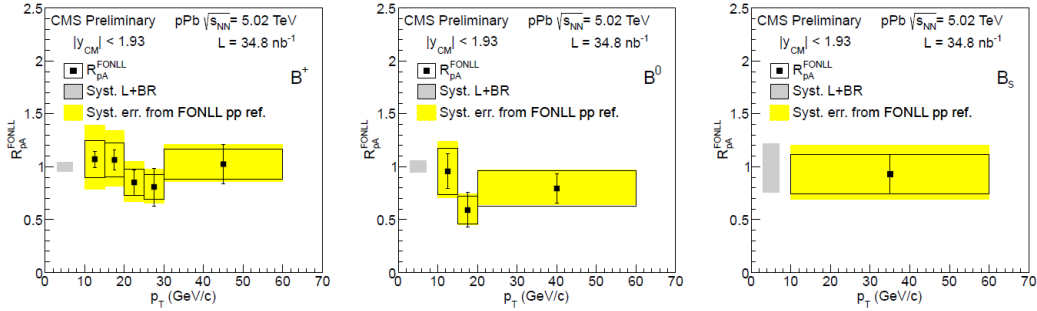


Figure 1.32: Nuclear modification factor  $R_{pA}^{\text{FONLL}}$  of  $B^+$  (left panel),  $B^0$  (middle panel), and  $B_s^0$  (right panel) mesons measured in p-Pb collisions at  $\sqrt{s_{NN}} = 5.02$ . The vertical bars represent the statistical uncertainty while the total systematic uncertainties are plotted as boxes around the data points. Figure taken from Ref. [172].

The  $R_{pPb}$  of electrons from inclusive heavy-flavour hadron decays, is measured via the semi-leptonic channel at mid-rapidity, as shown in Fig. 1.33. Within uncertainties, it is compatible with unity. Thanks to the high resolution of the track impact parameter achieved with ALICE, one can isolate the beauty-decay contribution exploiting the larger lifetime of beauty hadrons ( $c\tau \approx 500\mu\text{m}$  [2]) compared to that of charm hadrons. The electrons from their semileptonic decays have, consequently, a larger average impact parameter with respect to other electron contributions [171]. Figure 1.33 shows the obtained  $R_{pPb}$  of electrons from beauty-hadron decays as well. It is consistent with unity within uncertainties, and it is also compatible with that of electrons from heavy-flavour hadron decays.

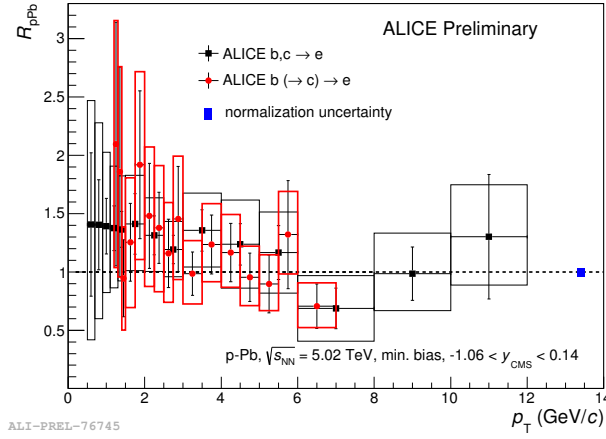


Figure 1.33: Nuclear modification factor of beauty-hadron decay electrons and inclusive heavy-flavour hadron electrons. The error bars (boxes) represent the statistical (systematic) uncertainties. Figure taken from Ref. [173].

These results show that cold nuclear matter effects are small, indicating that the suppression observed in the most central Pb–Pb collisions at  $\sqrt{s_{NN}}=2.76$  TeV [174, 175] results from an effect due to the presence of the hot and dense medium.

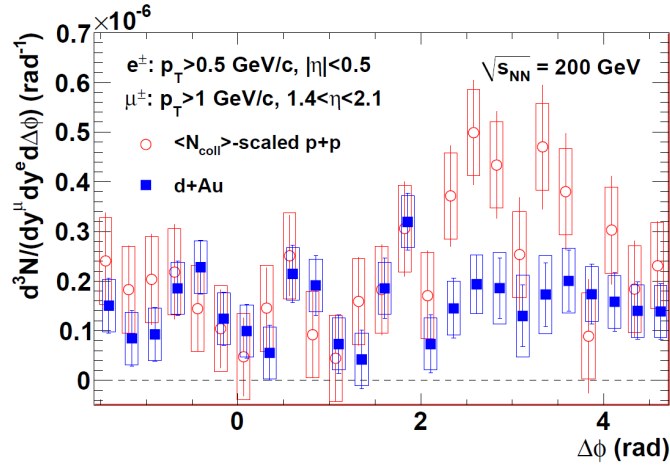


Figure 1.34: The fully-corrected like-sign-subtracted heavy-flavour  $e - \mu$  pair yield in (red circles)  $\langle N_{\text{coll}} \rangle$ -scaled pp collisions (blue boxes) and d–Au collisions, shifted in  $\Delta\phi$  for clarity. The bars are statistical uncertainties. The boxes are the systematic uncertainties from the decay and punch-through background subtraction. The overall normalization uncertainties of 16.1% and 13.4% in pp and d–Au collisions, respectively, and 5.7% uncertainty from  $\langle N_{\text{coll}} \rangle$  are not included. Figure taken from Ref. [176].

The like-sign subtracted  $e^\pm - \mu^\mp$  pair yield is predominantly from  $c\bar{c}$  decays, and it is sensitive to initial- and final-state energy loss. Figure 1.34 shows the fully-corrected measurements of electron-muon pair yields as a function of  $\Delta\phi$  (azimuthal angle) for electrons with  $p_T^e > 0.5$  GeV/c and  $|\eta^e| < 0.5$  and muons with  $p_T^\mu > 1.0$

GeV/c and  $1.4 < \eta^\mu < 2.1$  in d–Au collisions at  $\sqrt{s_{NN}} = 200$  GeV (blue). It is found that there is a much less distinct back-to-back peak in d–Au collisions nearby  $\Delta\phi = \pi$  with respect to the one in pp collisions (red). Note that the pp-pair correlations are scaled by the d–Au  $\langle N_{\text{coll}} \rangle = 7.59 \pm 0.43$  [176]. The peak in d–Au collisions is suppressed compared to pp collisions, indicating a medium modification to the yield per collision in d–Au [176].

### 1.3.2 Studying heavy-flavours from their decay muons

Muons were discovered by S. H. Neddermeyer and C. D. Anderson in 1936 when studying the cosmic radiation [177]. As shown in Fig. 1.2, a muon is a elementary particle with mass  $m=105.7$  MeV/c<sup>2</sup>, as well as the spontaneous decay (BR~100%) into an electron and neutrino-anti-neutrino pair via

$$\mu^- \rightarrow e^- + \bar{\nu}_e + \nu_\tau \quad (1.12)$$

$$\mu^+ \rightarrow e^+ + \nu_e + \bar{\nu}_\tau \quad (1.13)$$

The probability of the muon spontaneous decay behaves like the general radioactive decay:

$$P(t) = 1 - e^{-t/\tau} \quad (1.14)$$

where,  $\tau \sim 2.2 \mu\text{s}$  [2] is the mean lifetime. A muon can thus be considered as a "stable" particle for most of high-energy physics applications.

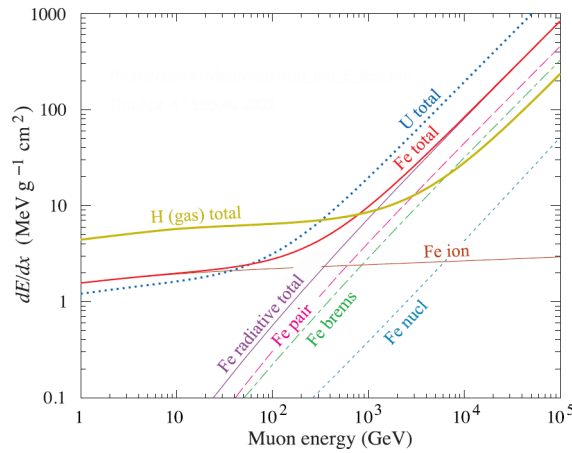


Figure 1.35: The average electro-magnetic energy loss,  $dE/dx$ , of a muon in hydrogen, iron and uranium as a function of muon energy (see text for details). Figure taken from Ref. [2].

Since a muon has a very long lifetime and the related (semi-)leptonic decay channels are clean for many heavy particles such as  $\tau$ ,  $W$  and  $Z$ , many of new particle/physics searches contain muons as final detectable particles. By exploiting the fact that muons can penetrate more deeply in matter when comparing with electrons and charged hadrons, this behavior allows to identify muons via the interaction with

the considered material. The muon energy loss induced by the electro-magnetic interaction can be classified into four processes: ionization,  $e^+e^-$  pair production, bremsstrahlung and photo-nuclear reactions [178]. Figure 1.35 shows the average electro-magnetic energy loss of muons when in hydrogen, iron and uranium as a function of muon energy. One can see that it is dominated by ionization in the energy range below 100 GeV, which corresponds to  $dE/dx \sim 1.4$  GeV/m in Fe ion [178]

After entering the material, the muons can be deflected by the material constituents via multiple scattering (MS), as shown in Fig. 1.36. For the outgoing muons, the Root Mean Square (RMS) of the related scattering angle,  $\theta^{\text{RMS}}$ , is quantified by the Gaussian distribution in case of small angle scatterings. The obtained  $\theta^{\text{RMS}}$  is expressed as [2]

$$\theta^{\text{RMS}} = \frac{0.0136\text{GeV}}{\beta c \cdot p} z \sqrt{x/X_0} [1 + 0.038 \cdot \ln(x/X_0)] \quad (1.15)$$

where,  $\beta c$  and  $p$  denote the velocity and momentum of injected muon, respectively;  $z$  indicates the charge number of constituent particle in the material;  $x/X_0$  is the thickness of the scattering material (in radiation lengths). It is worth noting that the results concerning large angle scatterings (i.e. few  $\theta^{\text{RMS}}$ ) can be quantified by the Rutherford scattering.

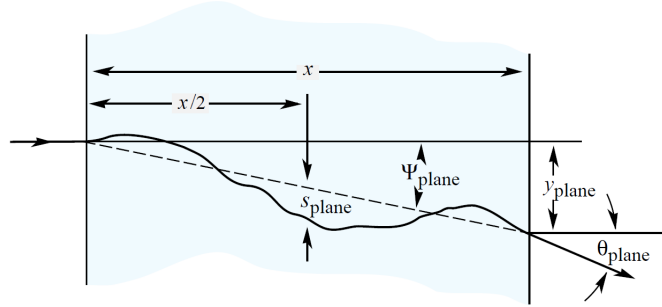


Figure 1.36: Quantities used to describe multiple scatterings: the lateral displacement of the muon trajectory on a projected plane of material, together with the scattering angle. Figures taken from Ref. [2].

Due to the decay kinematics, the correlation between the transverse momentum of HF hadrons ( $p_{\text{T}}^{\text{HF}}$ ) and the transverse momentum of their decay muons ( $p_{\text{T}}^{\mu \leftarrow \text{HF}}$ ) in the muon spectrometer ( $-4 < \eta_{\text{LAB}}^{\mu} < -2.5$ ), behaves roughly,

$$p_{\text{T}}^{\text{D}} \sim 2p_{\text{T}}^{\mu \leftarrow \text{D}} \quad (1.16)$$

$$p_{\text{T}}^{\text{B}} \sim 2p_{\text{T}}^{\mu \leftarrow (\text{D} \leftarrow \text{B})} \quad (1.17)$$

at high  $p_{\text{T}}^{\mu}$ , as shown in the right panel of Fig. 1.37. Note that the branching ratio (BR) for different decay channels is  $\text{BR}(\mu \leftarrow \text{D}) \sim 10\%$ ,  $\text{BR}(\mu \leftarrow \text{B}) \sim 11\%$  and  $\text{BR}(\mu \leftarrow \text{D} \leftarrow \text{B}) \sim 10\%$  [154]. One can see that, (1) the results for D and B mesons are close to each other in the range  $p_{\text{T}}^{\mu} > 2$  GeV/c; (2) muons from heavy-flavour hadron decays can easily access the physics at high transverse momentum;

(3) at low  $p_T$ , the correlation between the lepton momentum and the mother B momentum, is basically lost.

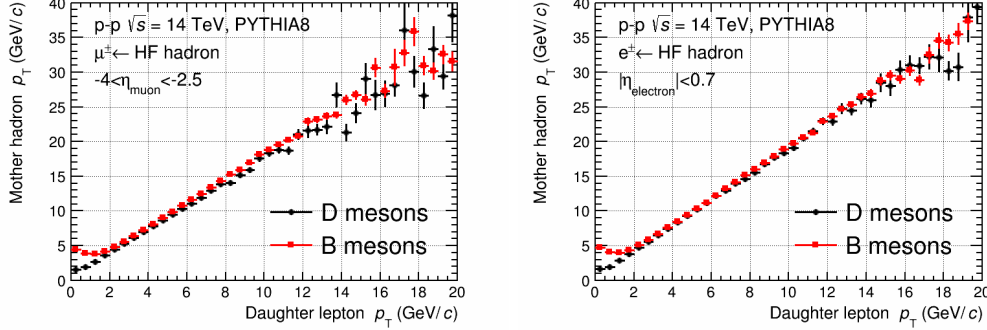


Figure 1.37:  $p_T$  correlations between the "mother" HF hadron and the "daughter" lepton for muons at forward (left) and electrons at mid-rapidity (right). See the text for details.

The right panel of Fig. 1.37 presents the correlation between the transverse momentum of HF hadrons ( $p_T^{\text{HF}}$ ) and the transverse momentum of their decay electrons ( $p_T^{e \leftarrow \text{HF}}$ ) at mid-rapidity ( $|\eta_{\text{LAB}}^e| < 0.7$ ). A similar behavior is found with respect to the muon decay channel. This behavior could be one of the candidates to explain an interesting phenomenon: the measurement of heavy-flavour production via semi-lepton decay channels that are performed at mid- and forward rapidity with ALICE, shows consistent results for the nuclear modification factor (Fig. 1.28) and elliptic flow (Fig. 1.30) in Pb–Pb collisions at  $\sqrt{s_{\text{NN}}} = 2.76$  TeV. Note that a similar behavior was observed of the (semi-)leptonic measurements performed at mid- and forward rapidity with PHENIX [179, 180].

As final, the measurements of muons and electrons from heavy-flavour hadron decays from different heavy-ion facilities, are summarized in Tab. 1.2 for RHIC and LHC programs.

Exp.	System	$\sqrt{s_{NN}}$ (TeV)	Channel	Phase space		Ref.
				$\Delta p_T$ (GeV/c)	$\Delta y$	
RHIC	pp	0.2	$c, b \rightarrow \mu^-$	$1 < p_T < 7$	$1.4 <  y  < 1.9$	[181]
	d-Au	0.2	$c, b \rightarrow \mu^-$	$1 < p_T < 6$	$1.4 <  y  < 2.0$	[182]
	Cu-Cu	0.2	$c, b \rightarrow e^-$	$1 < p_T < 4$	$1.4 <  y  < 1.9$	[181]
	Au-Au	0.13	$c, b \rightarrow e^\pm$	$0.5 < p_T < 3.0$	$ y  < 0.35$	[183]
0.2		$c, b \rightarrow e^\pm$	$1.2 < p_T < 10$	$ y  < 1$	[184, 185]	
LHC	pp	2.76	$c, b \rightarrow \mu^\pm$	$2 < p_T < 10$	$2.5 < y < 4$	[159]
			$c, b \rightarrow e^\pm$	$0.5 < p_T < 12$	$ y  < 0.8$	[186]
			$b \rightarrow e^\pm$	$1 < p_T < 10$	$ y  < 0.8$	[139]
	pp	7	$c, b \rightarrow \mu^\pm$	$2 < p_T < 12$	$2.5 < y < 4$	[160]
			$c, b \rightarrow e^\pm$	$0.5 < p_T < 8$	$ y  < 0.5$	[156]
			$b \rightarrow e^\pm$	$1 < p_T < 8$	$ y  < 0.8$	[187]
	Pb-Pb	2.76	$c, b \rightarrow \mu^\pm$	$2 < p_T < 12$	$2.5 < y < 4$	[159]
p-Pb	5.02	$c, b \rightarrow \mu^\pm$	$2 < p_T < 16$	$-4 < y < -2.96$ $2.5 < y < 3.53$	[171]	
		$c, b \rightarrow e^\pm$	$0.5 < p_T < 12$	$-1.06 < y < 0.14$	[188]	
		$b \rightarrow e^\pm$	$1.5 < p_T < 7$		[171]	

Table 1.2: Overview of the measurements related to selected channel conducted at RHIC ( $\sqrt{s_{NN}} \leq 0.2$  TeV and at the LHC ( $\sqrt{s_{NN}} \leq 7$  TeV) until 2014. For each collision system, center-of-mass energy  $\sqrt{s_{NN}}$ , and channel investigated, the phase space coverage is given as well.



# The ALICE Experiment

The LHC is so far the world's largest and most powerful particle accelerator. It is designed to allow physicists to test the predictions of different theories of particle physics like the Standard Model and, in particular, search for the Higgs boson and of the large family of new particles predicted by supersymmetric theories [189]. The LHC is expected to address some of the unsolved questions of physics, advancing human understanding of physical laws, e.g. the origin of mass, extra dimensions, the Higgs boson, dark energy and matter as well as the properties of antimatter and the Quark-Gluon Plasma (QGP). The LHC nominal running conditions are shown in Tab. 2.1 for different collision systems.

Collision System	$\sqrt{s_{\text{NN}}}$ (TeV)	$\mathcal{L}$ ( $\text{cm}^{-2}\text{s}^{-1}$ )	Running time (s)	$\sigma_{\text{geom}}$ (b)
pp	14.0	$10^{34}$	$10^7$	0.07
Pb–Pb	5.5	$10^{27}$	$10^6$	7.7
p–Pb	8.8	$10^{29}$	$10^6$	1.9
Ar–Ar	6.3	$10^{29}$	$10^6$	2.7

Table 2.1: Summary of the LHC nominal run conditions for different collision system, center-of-mass energy, integrated luminosity (defined as the ratio of the number of events detected in a certain time to the interaction cross-section), running time and the geometrical cross sections [35]. Adapted from Ref. [190, 191].

There are four main particle detectors installed around the collision points: **ATLAS** (A Toroidal LHC ApparatuS), **CMS** (Compact Muon Solenoid), **LHCb** (Large Hadron Collider beauty) and **ALICE** (A Large Ion Collider Experiment). The ALICE detector is designed to address the physics of the Quark-Gluon Plasma in nucleus-nucleus collisions. Physics with ALICE and the corresponding detector performance are described in detail in the Physics Performance Report [192, 193, 194]. The ALICE collaboration is composed of 1550 members from 151 institutes in 37 countries [195]. In the following section, I briefly describe the ALICE experiment.

## 2.1 ALICE Setup

In contrary to previous experiments dedicated to heavy-ion collisions at AGS, SPS and RHIC, ALICE is able to address a broad range of observables. The detector has been optimized to cope with the very high multiplicity environment (up to 4000 particles per unity of rapidity at mid-rapidity) which can be accessed in central

nucleus-nucleus collisions at the LHC. It provides tracking and particle identification over a large range of transverse momentum ( $p_T$ ), from very low ( $\sim 100$  MeV/ $c$ ) up to fairly high values ( $\geq 100$  GeV/ $c$ ). The detector layout is displayed in Fig. 2.1. The sub-system names, acceptances, positions and dimensions are summarized in Tab. 2.2. Note that the ALICE reference frame is defined with x-axis pointing towards the center of the detector, y-axis pointing toward the sky and z-axis going opposite to the muon spectrometer. The ALICE detector consists of three parts:

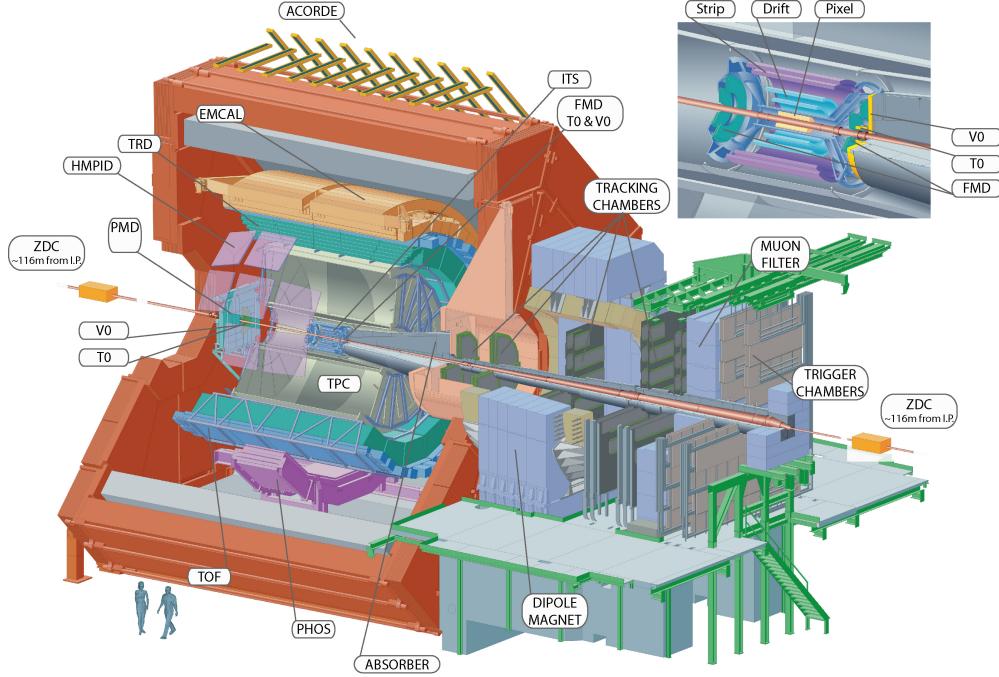


Figure 2.1: Schematic layout of ALICE with various detector systems, indicated in the figure with their acronyms. Figure taken from [195].

- **Global Detectors:** Zero Degree Calorimeter (ZDC), Photon Multiplicity Detector (PMD), Forward Multiplicity Detector (FMD), T0 and V0 detectors, which are located in the forward and backward pseudo-rapidity regions. They are mainly used for global event characterization (e.g. centrality determination, multiplicity measurement, and event plane reconstruction in heavy-ion collisions), background rejection and triggering-related purposes.
- **Central Barrel Detectors:** the central barrel system covers a pseudo-rapidity range  $-0.9 < \eta < 0.9$  ( $45^\circ < \theta < 135^\circ$ ), and it is embedded in the large L3 solenoid magnet ( $0.2 \text{ T} < B < 0.5 \text{ T}$  [196]). The central detectors are the Inner Tracking System (ITS) made of six cylindrical layers of high resolution silicon pixel (SPD), drift (SDD) and strip (SSD) detectors, the cylindrical Time-Projection Chamber (TPC), the Transition Radiation Detector (TRD), the Time-Of-Flight (TOF), the High Momentum Particle Identification Detector (HMPID) and two electromagnetic calorimeters: the

PHoton Spectrometer (PHOS) and the ElectroMagnetic CALorimeter (EMCal<sup>§</sup>). All central barrel detectors cover the full azimuth, except HMPID, PHOS, and EMCal [194].

- **Forward muon spectrometer:** the muon spectrometer is primarily designed for quarkonium physics via measurement of the production of charmonia and bottomonia ( $J/\Psi$  and  $\Upsilon$  families), low-mass resonance and open heavy-flavour physics in the semi-muonic decay channel. It is located at small angles ( $2^\circ < \theta < 10^\circ$ ,  $-4 < \eta < -2.5$ ) in order to provide, firstly, a good acceptance down to zero transverse momentum since the low  $p_T$  measurements can only be accessed at small angles where the muons are Lorentz boosted. Secondly, it can also provide a manageable background from hadron decays [42]. The ALICE muon spectrometer is composed of a front absorber (to reduce the background), a beam shield (to protect the detectors from particles emerging from the beam pipe), a dipole magnet with a 3 Tm field integral placed outside the L3 magnet (which enables momentum measurement), five tracking stations (made of Cathode Pad Chambers, CPC) for muon reconstruction and two trigger stations (made of Resistive Plate Chambers, RPC) for muon identification and triggering. A 1.2 m thick iron wall is located in front of the two trigger stations. It protects the trigger system from punch-through hadrons. In addition, a rear absorber is placed at the end of the muon spectrometer. It can protect the trigger chambers from particles generated in the opposite side with respect to the interaction point. The analyses presented in this thesis use data collected with this muon spectrometer. A more detailed description of the detector layout and of its tracking and trigger algorithms is given in Sec. 2.4.

Finally, the apparatus is completed by an array of scintillators, ALICE COsmic Ray DETector (ACORDE). ACORDE is designed to detect high-energy atmospheric muons coming from cosmic ray showers, by triggering the arrival of muons on the top of the ALICE L3 magnet. With long time of data taking, it allows recording cosmic events with very high multiplicity of parallel muon tracks as well, the so-called muon bundles [198].

## 2.2 Global Detectors

Several small detectors (ZDC, PMD, FMD, V0, T0), as shown in Tab. 2.2, used for global event characterization and triggering are located at small angles. In the following, they are described in detail.

**ZDC: Zero Degree Calorimeter [199]** The ZDC is dedicated to the measurement of the energy carried by the spectator nucleons (i.e. the ones not involved in

---

<sup>§</sup>extension of EMCal by adding calorimeter modules on the opposite side (Di-Jet Calorimeter, DCal) are other important ingredients of the ALICE detector. See Ref. [197] for details.



the interaction) at zero degree with respect to the beam direction. Hence, the ZDC allows one to quantify the number of participants, as well as to determine the centrality of the nucleus-nucleus collisions [192]. The ZDC detector is composed by two hadronic calorimeters: the neutron calorimeter (ZN, measuring the spectator neutrons) and the proton calorimeter (ZP, measuring the spectator protons) which are placed on both sides of the interaction point (IP), at a distance of about 110 m from it. The system is completed by two electromagnetic calorimeters (ZEM, measuring the participating nucleons) located at about 7 m from the IP (on the other side of the muon spectrometer), which allows to resolve ambiguities in the determination of the centrality.

**PMD: Photon Multiplicity Detector [200]** The PMD is a pre-shower detector that allows to measure event-by-event photon multiplicity and spatial  $(\eta - \varphi)$  distribution of photons. It is located at  $z = 360$  cm in the forward region  $2.3 < \eta < 3.7$ , and has a full azimuthal coverage. The detector is composed of a gas proportional counter that is used to detect charged particles when they enter the detector and veto them as well, a layer of iron and lead that is able to absorb charged particles. The resulting photon showers of electrons are detected by the gas proportional counter. The counters are highly granulated to allow the PMD to resolve showers from different photons.

**FMD: Forward Multiplicity Detector [201]** The FMD consists of five circular silicon rings which are equipped with 51200 readout channels. It allows to measure multiplicity, correlations, event plane and collective flow. As shown in Tab. 2.2, its acceptance covers the pseudo-rapidity range  $-3.4 < \eta < -1.7$  and  $1.7 < \eta < 5.1$ . When combined with the ITS, the acceptance extends to  $-3.4 < \eta < 5.1$ .

**V0 [201]** The V0 detector is made of two arrays of scintillator counters (V0A and V0C) connected to photomultipliers, located at 340 cm (PMD side, V0A) and 90 cm (muon spectrometer side, V0C) from the IP, with a pseudo-rapidity coverage of  $2.8 < \eta < 5.1$  (V0A) and  $-3.7 < \eta < -1.7$  (V0C). As shown in Tab. 2.2, both sub-systems have full azimuthal coverage. The V0 is used for trigger-related purposes, centrality selection and luminosity measurement.

**T0 [201]** The T0 detector is made of two arrays of Cherenkov counters (T0A and T0C) with 12 individual counters per array, located 375 cm (PMD side, T0A) and 72.7 cm (muon spectrometer side, T0C) from the IP, with a pseudo-rapidity coverage of  $4.61 < \eta < 4.92$  (T0A) and  $-3.28 < \eta < -2.97$  (T0C). It provides a start time for the TOF system (since the time resolution of T0 is better than 50 ps), and measures the vertex position (with a precision of  $\pm 1.5$  cm). Meanwhile, it can be used for the luminosity measurement.

Detector	Acceptance ( $\eta, \varphi$ )	Position (m)	Dimension (m <sup>2</sup> )
ZDC: ZN	$ \eta  > 8.8$	$\pm 113$	$2 \times 0.0049$
ZDC: ZP	$6.5 <  \eta  < 7.5$ $-10^\circ < \varphi < 10^\circ$	$\pm 113$	$2 \times 0.027$
ZDC: ZEM	$4.8 <  \eta  < 5.7$ $-16^\circ < \varphi < 16^\circ$ and $-164^\circ < \varphi < 169^\circ$	7.3	$2 \times 0.0049$
PMD	$2.3 < \eta < 3.7$	3.64	2.59
FMD Disk 1	$3.62 < \eta < 5.03$	inner: 3.2	0.266
FMD Disk 2	$1.7 < \eta < 3.68$	inner: 0.834 outer: 0.752	
FMD Disk 3	$-3.4 < \eta < -1.7$	inner: -0.628 outer: -0.752	
V0A	$2.8 < \eta < 5.1$	3.4	0.548
V0C	$-3.7 < \eta < -1.7$	-0.897	0.315
T0A	$4.61 < \eta < 4.92$	3.75	0.0038
T0C	$-3.28 < \eta < -2.97$	-0.727	0.0038
SPD (ITS layer 1, 2)	$ \eta  < 2,  \eta  < 1.4$	0.039, 0.076	0.21
SDD (ITS layer 3, 4)	$ \eta  < 0.9,  \eta  < 0.9$	0.150, 0.239	1.31
SSD (ITS layer 5, 6)	$ \eta  < 0.97,  \eta  < 0.97$	0.380, 0.430	5.0
TPC	$ \eta  < 0.9$ ( $r = 2.8\text{m}$ ) $ \eta  < 1.5$ ( $r = 1.4\text{m}$ )	0.848, 2.466	readout 32.5 m <sup>2</sup> Vol. 90 m <sup>3</sup>
TRD	$ \eta  < 0.84$	2.90, 3.68	716
TOF	$ \eta  < 0.9$	3.87	141
HMPID	$ \eta  < 0.6$ $1.2^\circ < \varphi < 58.8^\circ$	5.0	11
PHOS	$ \eta  < 0.12$ $220^\circ < \varphi < 320^\circ$	4.6	8.6
EMCAL	$ \eta  < 0.7$ $80^\circ < \varphi < 187^\circ$	4.36	44
ACORDE	$ \eta  < 1.3$ $-60^\circ < \varphi < 60^\circ$	48.5	43
Muon Tracking: 1	$-4 < \eta < -2.5$	-5.36	4.7
Muon Tracking: 2		-6.86	7.9
Muon Tracking: 3		-9.83	14.4
Muon Tracking: 4		-12.92	26.5
Muon Tracking: 5		-14.22	41.8
Muon Trigger: 1		-16.12	64.6
Muon Trigger: 2		-17.12	73.1

Table 2.2: Names, acceptances, positions and dimensions of the ALICE detector sub-systems. Adapted from Ref. [42, 194, 202].



## 2.3 Central Barrel Detectors

The central part of ALICE contains several sub-systems. They are used for measurements of hadrons, electrons, and photons within  $|\eta| < 0.9$ , as shown in Fig. 2.1. It consists of the ITS, TPC, TRD, and TOF. Additionally, there are two electromagnetic calorimeters, EMCAL and PHOS (and since Run-2 also DCAL), and a ring imaging Čerenkov detector for High-Momentum Particle IDentification (HMPID). The above three detectors have limited pseudo-rapidity and azimuthal coverage. The central barrel detectors are placed in the L3 magnet inherited from the LEP experiment L3. It is a non-superconducting magnet with an inner length of 12.1 m and a radius of 5.75 m.

**ITS: Inner Tracking System [203, 204]** The main purpose of the ITS is to provide precise track and vertex reconstruction close to the interaction point. It consists of three different silicon detector-technologies, including 2 layers of Silicon Pixel Detectors (SPD), 2 layers of Silicon Drift Detectors (SDD), and 2 layers of Silicon Strip Detector (SSD). This arrangement of the detector is arranged to provide excellent resolution on the track impact parameter (distance of closest approach of the track to the primary interaction vertex), to improve the momentum resolution obtained with the TPC (to-be discussed later), reaching a  $p_T$  resolution better than 4% at  $p_T = 20$  GeV/ $c$  [202, 205], and to extend the tracking capabilities to low momentum tracks that are not reconstructed with the TPC, e.g. allowing the tracking of charged pions down to  $p_T \sim 80$  MeV/ $c$ . In addition, the SDD and SSD layers provide PID via the measurement of the specific energy loss  $dE/dx$ .

**TPC: Time Projection Chamber [206]** The large TPC is the main tracking detector of ALICE central barrel, with the cylindrical drift volume of 95 m<sup>3</sup> encompassing the ITS. There is an electric field which allows to "push" the electrons drift towards the MWPC (multi-wire proportional chambers) located at the two sides of the cylindrical volume. Therefore, the charged particles, when traversing the gas-filled drift volume, ionise the gas, resulting in the electrons to drift away from along its track. The related z-coordinate (along the cylinder axis) is determined by measuring the drift time from the ionization event. Hence, it is in charge of tracking and determining charged particle momenta with a good two-track separation, to enable particle identification via  $dE/dx$ . It allows to reconstruct charged-particle  $p_T$  from 100 MeV/ $c$  (with  $\sim 1\%$  resolution) up to 100 GeV/ $c$  (with  $\sim 5\%$  resolution if ITS is included as well). The drawback of using the TPC is its drift time, which limits the luminosity that the ALICE experiment can afford [191].

**TRD: Transition Radiation Detector [207, 208]** The TRD is located radially right outside the TPC, with full azimuthal coverage in the range of  $|\eta| < 0.84$ <sup>§</sup>. It relies on the phenomenon of transition radiation identification of electrons with momentum above 1 GeV/ $c$ . Transition radiation occurs when a particle crosses

<sup>§</sup>the full azimuthal coverage will be insured from Run 2 on.



the boundary between two materials with different dielectric constants. Due to the different threshold of the transition radiation, electrons and charged pions can be distinguished by the TRD.

**TOF: Time Of Flight [209, 210]** The TOF detector is placed outside the TRD. It is in charge of particle identification in the intermediate momentum range ( $0.2 < p < 2.5$  GeV/ $c$ ), in the pseudo-rapidity range  $|\eta| < 0.9$  with full azimuthal coverage. When combining the ITS and the TPC (for vertex reconstruction and  $dE/dx$  measurement at low momentum), one can perform event-by-event identification of pions, kaons and protons. The particle travel length ( $l$ ) and momentum ( $p$ ) reconstructed in the ITS and the TPC, and the mass can be obtained by means of the time-of-flight ( $t$ ) provided by the TOF:  $m = p\sqrt{t^2/(l^2 - 1)}$ .

**HMPID: High Momentum Particle Identification Detector [211]**

The HMPID is located at a radius of 5 m. It has a pseudo-rapidity coverage of  $|\eta| < 0.6$  and an azimuthal acceptance of  $\sim 58^\circ$ . The detector consists of 7 modules of  $1.5 \times 1.5$  m<sup>2</sup> focusing Ring Imaging Cherenkov (RICH) counters. The HMPID extends ALICE's capability for  $\pi/K$  and  $K/p$  separation up to 3 and 5 GeV/ $c$ , respectively. It enables the inclusive measurement of identified hadrons in the range  $1 < p_T < 5$  GeV/ $c$ .

**PHOS: PHOton Spectrometer [212]** The PHOS is a high-granularity calorimeter measuring photons and neutral mesons (through the two photon decay channel). It is located in the bottom part of the central barrel, at 460 cm from the interaction point. It covers the pseudo-rapidity acceptance of  $|\eta| < 0.12$  and the azimuthal range  $220^\circ < \varphi < 320^\circ$ . The detector consists of an electromagnetic calorimeter of dense scintillating crystals ( $\sim 20X_0$ ) and detection cells made of lead-tungstate crystal (PbWO<sub>4</sub>). A set of multi-wire proportional chambers, Charged-Particle Veto (CPV), in front of PHOS is used to reject charged particles.

**EMCal: ElectroMagnetic Calorimeter [213]** The EMCal detector is placed around the TOF. It covers  $|\eta| < 0.7$  and  $80^\circ < \varphi < 187^\circ$ , as shown in Tab. 2.2. The EMCal is a Pb-scintillator sampling calorimeter measuring photons,  $\pi^0$  and  $\eta$  via their decay photons like the PHOS detector. It has a larger acceptance than the PHOS but has a lower granularity and resolution. When used together with the TPC and ITS, the EMCAL allows jets to be reconstructed completely in pp and in Pb-Pb collisions.

A brief summary of the particle identification for different species with the ALICE detector sub-systems is displayed in Fig. 2.2.

## 2.4 The Forward muon spectrometer

The ALICE forward muon spectrometer is capable of detecting muons in the pseudo-rapidity range  $-4 < \eta < -2.5$  corresponding to the polar angle range

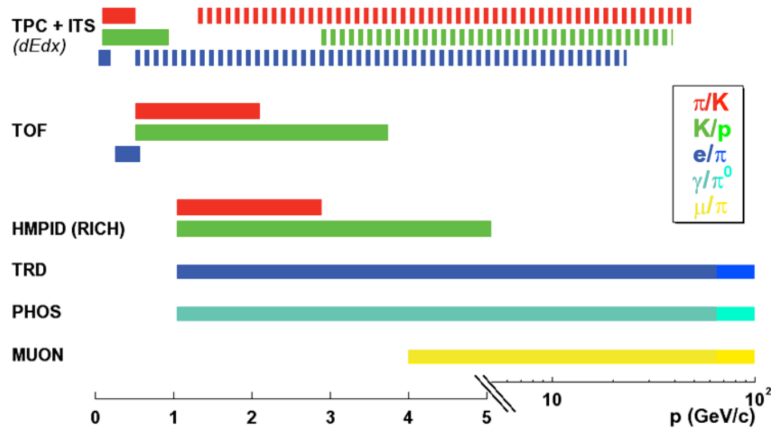


Figure 2.2: Conceptual view of particle identification with the ALICE detector. The solid and dashed band both represent the identification capabilities, while the later one correspond to the relativistic rise of Bethe Bloch in the TPC. Figure taken from Ref. [214].

$2^\circ < \theta < 10^\circ$ . As shown in Fig. 2.3, it includes a front absorber with the role to stop hadrons and photons before entering the spectrometer. The inner beam shield protects the detectors from background particles produced at small angles. The penetrating tracks are reconstructed by means of five tracking stations made of ten planes of Cathode Pad Chambers (CPC), located between 5 and 14 m from the interaction point, with a precision better than  $100 \mu\text{m}$ . The third tracking station is placed inside a dipole magnet, which produces a maximum field of 0.7 T. The field integral from the IP to the muon filter is 3 Tm. Two trigger stations made of four planes of Resistive Plate Chambers (RPC) are located at the end of the spectrometer, behind a muon filter made of a 1.2 m thick iron wall. It allows one to select and trigger on not only pairs of muons, including the ones from the quarkonium decays (the  $J/\Psi$  and  $\Upsilon$  families), but also on single muons from open heavy-flavour hadron decays (mainly, D and B mesons), see Sec. 2.4.4 for details. The rear absorber is located at the end of the muon spectrometer to protect trigger stations from the background generated by the LHC accelerator. It can filter the particles produced in the LHC tunnel in the direction opposite to the primary interaction point. A set of main parameters of the detector are summarized in Tab. 2.3.

As shown in Fig. 2.4 the invariant mass distributions of  $\mu^+\mu^-$  pairs, the main purpose of the ALICE muon spectrometer is to measure quarkonia ( $J/\Psi$ ,  $\Psi'$ ,  $\Upsilon$ ,  $\Upsilon'$  and  $\Upsilon''$ ) via their decay in the  $\mu^+\mu^-$  channel. In addition, the low-mass resonances such as  $\rho$ ,  $\omega$  and  $\phi$  can also be studied. The muon spectrometer provides accurate measurements down to zero transverse momentum and momentum above  $\sim 4 \text{ GeV}/c$ , due to the large amount of material (e.g. front absorber and muon filter) used to reduce the flux of hadrons. A mass resolution of  $\sim 1\%$  in the dimuon mass region around  $10 \text{ GeV}/c^2$  is needed (and achieved) in order to separate  $\Upsilon$ ,  $\Upsilon'$  and  $\Upsilon''$  from each other.

It is known [216] that the quarkonium signals are sitting on top of a continuum

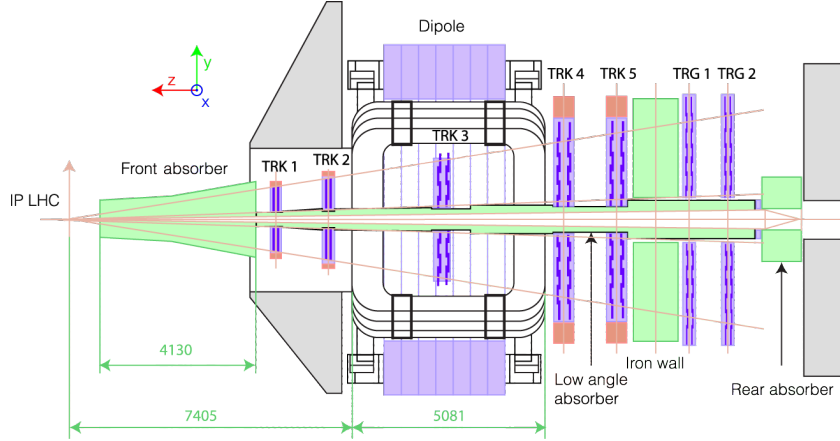


Figure 2.3: Sketch of the ALICE muon spectrometer. Figure taken from Ref. [215].

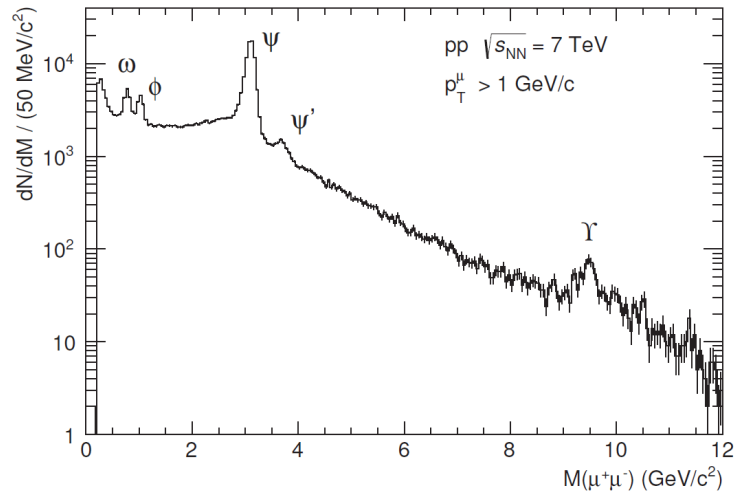


Figure 2.4: Invariant mass distribution of  $\mu^+\mu^-$  pairs measured by ALICE for pp collisions at  $\sqrt{s} = 7$  TeV ( $\mathcal{L} = 1.35$  pb $^{-1}$ , corresponding to the full 2011 dimuon-triggered data sample). Figure taken from Ref. [194].

Muon Detection	
polar and azimuthal angle coverage	$2^\circ < \theta < 10^\circ, 2\pi$
minimum muon momentum	4 GeV/c
pseudo-rapidity coverage	$-4 < \eta < -2.5$
Front Absorber	
longitudinal position from IP	$-5030 < z < -900$ mm
total thickness of materials	$\sim 10\lambda_{int}, \sim 60X_0$ (carbon-concrete-steel)
Dipole Magnet	
nominal magnetic field, the integral	$\sim 0.7$ T, 3 Tm
free gap between poles	2.972—3.956 m
overall magnet length	4.97 m
longitudinal position from IP	$-z = 9.94$ m (centre of the dipole coils)
Tracking Chambers	
num. of st., num. of planes of each st.	5, 2
longitudinal position of stations	$-z = 5357, 6860, 9830,$ 12920, 14221 mm
anode-cathode gap	2.1 (2.5) mm for st. 1 (2-5)
gas mixture	80%Ar/20% CO <sub>2</sub>
pad size st. 1 (bending plane)	$4.2 \times 6.3, 4.2 \times 12.6, 4.2 \times 25.2$ mm <sup>2</sup>
pad size st. 2 (bending plane)	$5 \times 7.5, 5 \times 15, 5 \times 30$ mm <sup>2</sup>
pad size st. 3-5 (bending plane)	$5 \times 25, 5 \times 50, 5 \times 100$ mm <sup>2</sup>
max. hit dens. st. 1-5	5.0, 2.1, 0.7, 0.5, $0.6 \times 10^{-2}$ hits/cm <sup>2</sup>
spatial resolution (bending plane)	$\sim 70$ $\mu$ m
Trigger Chambers	
num. of st., num. of planes of each st.	2, 2
longitudinal position of stations	$-z = 16120, 17120$ mm
total num. of RPCs, total active surface	72, $\sim 140$ m <sup>2</sup>
gas gap	single, 2 mm
electrode material and resistivity	Bakelite <sup>TM</sup> , $\rho = 2 - 8 \times 10^9$ $\Omega$ cm
gas mixture	Ar/C <sub>2</sub> H <sub>2</sub> F <sub>4</sub> /i-buthane/SF <sub>6</sub> (50.5/41.3/7.2/1)
pitch of readout strips (bending plane)	10.6, 21.2, 42.5 mm (for trigger st. 1)
max. strip occupancy (non-)bend. plane	3% (10%) in central Pb–Pb
max. hit rate on RPCs	3 (40) Hz/cm <sup>2</sup> in Pb–Pb (Ar–Ar)

Table 2.3: Summary of the main characteristics of the muon spectrometer. Adapted from Ref. [202].

mainly coming from open heavy-flavour hadron decays. This opens the possibility to study the heavy-flavour production via their semi-muonic channel, the so-called single muon decay channel in the following. The heavy-flavour hadron decay muons have been measured with the muon spectrometer in pp [160, 159] and Pb–Pb [159] collisions at  $\sqrt{s} = 7/2.76$  and  $\sqrt{s_{NN}} = 2.76$  TeV, respectively. Many other topics concerning the measurement of single muons have been developed. For example, one can cite the performance study of the B-hadron cross-section [217] by means of the single muon decay channel, that can be reconstructed from low  $p_T$  up to about  $p_T = 20$  GeV/ $c$  in pp collisions at  $\sqrt{s} = 14$  TeV and the  $e - \mu$  coincidences [218] with muon detected in the spectrometer and the electron in the central barrel.

The ongoing analyses about the electroweak boson production (i.e.  $W$  and  $Z$ ) via their single muon decay channel, are performed in pp collisions at  $\sqrt{s} = 7, 8$  TeV and p–Pb collisions at  $\sqrt{s_{NN}} = 5.02$  TeV [219].

### 2.4.1 The absorbers

In the ALICE muon spectrometer, several passive absorber systems, including a front hadron absorber close to the IP, a lead-steel-tungsten shield at small angles around the beam pipe and a muon filter, shield the spectrometer from most of the reaction products.

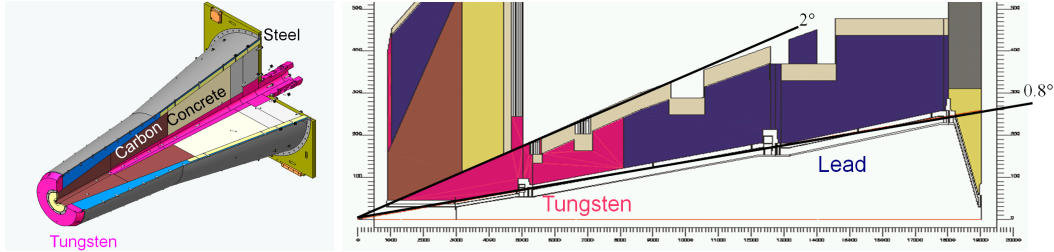


Figure 2.5: Layout of the front absorber (left) and small angle beam shielding (right). Figures taken from Ref. [220].

The front absorber has 4 m of length ( $\sim 10 \lambda_{\text{int}}$ ) and 37 tons of weight. Its front face is placed at 90 cm from the IP. The main parameters concerning its position and the thickness are summarized in Tab. 2.3. It is mainly made of carbon, concrete and steel, as shown in the left panel of Fig. 2.5, in order to limit small-angle multiple-scattering and energy loss of the punch-through muons [221]. Consequently, the background, mainly, due to primary  $\pi^\pm$  and  $K^\pm$  decays, can be largely suppressed before entering the tracking stations. The inner beam shield, throughout the length of the front absorber and the remaining parts of the spectrometer, is made of tungsten, lead and stainless steel, as displayed in the right panel of Fig. 2.5. It allows to minimize the background arising from primary particles emitted in the collision and from their showers produced in the beam pipe and in the shield itself, so as to protect the tracking and trigger chambers. An additional protection consisting of an iron wall (muon filter) with 1.2 m of thickness and 300 tons of weight is placed after the last tracking chamber, in front of the first trigger chamber, as well as a

rear absorber placed at the end of the muon spectrometer for further protection of the trigger stations from the background generated by the LHC accelerator. The front absorber and the muon filter are able to stop muons with momentum less than  $4 \text{ GeV}/c$ .

### 2.4.2 Dipole Magnet

The dipole magnet, as shown in Fig. 2.6, is located at 7 m from the IP, outside the L3 magnet. It has  $\sim 5 \text{ m}$  of length and 900 tons of weight. The magnetic strength, 0.7 T maximum in the horizontal plane in the direction perpendicular to the beam axis, has been defined by the requirements on mass resolution [221], and the field integral between the IP and the muon filter is 3 Tm. The dipole magnet enables momentum measurement of the muon tracks. This means that the trajectory of injected charged particles is deflected, hence, the related particle momenta and charge can be obtained by means of the Sagitta method [222].

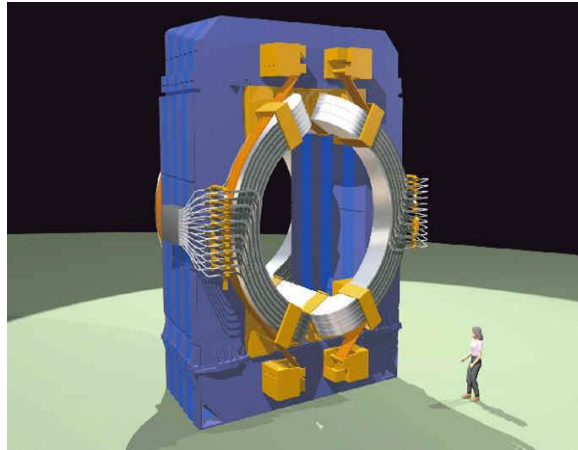


Figure 2.6: Conceptual view of the dipole magnet. Figure taken from Ref. [220].

### 2.4.3 Tracking Stations

The tracking system of the ALICE muon spectrometer covers a total area of  $\sim 100 \text{ m}^2$ , with the design driven by two main requirements [221, 214]: the spatial position resolution of  $\sim 100 \mu\text{m}$  (which is necessary for an invariant mass resolution of  $100 \text{ MeV}/c^2$  at the  $\Upsilon$  mass) and the capability to operate in a high particle multiplicity environment (a maximum hit density of about  $5 \times 10^{-2} \text{ cm}^{-2}$  was expected in central Pb–Pb collisions). These requirements are fulfilled by employing Cathode Pad Chambers (CPC). They are arranged in five stations: two stations are placed before, one station inside and two stations after the dipole magnet. Each station is made of two chamber planes. Each chamber has two cathode planes which are both readout to provide two-dimensional hit information. In order to keep the occupancy at a 5% level, a large segmentation of the readout pads is needed. Since the hit density decreases with the distance from the beam, larger pads are used at

larger transverse radii. The muon tracking system is equipped with a total of  $10^6$  electronics channels.

The first two stations are based on a quadrant structure with the readout electronics distributed on their surface, as shown in the left panel of Fig. 2.7. For the other stations, as displayed in the right panel of Fig. 2.7, a slat architecture has been chosen. The maximum size of a slat is  $40 \times 280 \text{ cm}^2$  and the electronics is implemented on the side of the slats. Multiple scattering of muons in the chambers is minimised by using composite materials (e.g. carbon fibre). The chamber thickness corresponds to about  $0.03 X_0$ . The position of the tracking stations is monitored by a rather sophisticated system of about 100 optical lines with an accuracy better than  $20 \mu\text{m}$ , while 160 lines are used to monitor their planarity, the so-called Geometry Monitoring System (GMS).

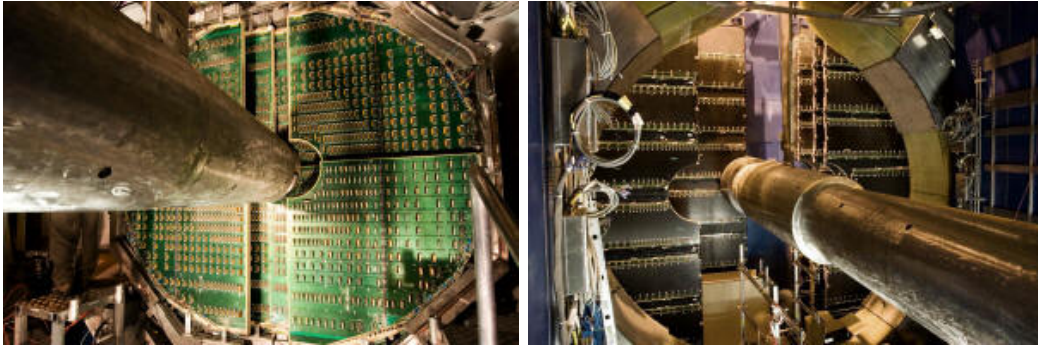


Figure 2.7: Layout of the tracking station 2 (left) and 4, 5 (right). see text for details. Figures taken from Ref. [216].

The front-end board (MANU, MANas NUMérique, 64-channel) consists of 4 Multiplexed ANALogic Signal processor chips (MANAS, 16-channel, acts a role of charge amplifier, filter and shaper chip), several ADC's and the controller chip (MARC, Muon Arm Readout Chip). The MARC is in charge of the zero suppression and the communication at the Data Signal Processor (DSP) level. Up to 26 MANUs are connected (via PATCH bus) to the translator board which allows the data transfer to the Concentrator ReadOut Cluster Unit System (CROCUS, for a total number of 20 CROCUS). The main tasks of the CROCUS are to concentrate data from the chambers, to ship them to the DAQ, to perform the calibration of the front-end electronics and to dispatch the signals from the central trigger processor.

Concerning the muon track reconstruction, the cluster-finder algorithm allows to associate clusters to the detector digits by taking the raw data as inputs. Then the charge signal (induced on the CPC pads from the passage of the charged particles) is fitted with a Mathieson-function-based expression [42, 223]. The cluster coordinates are obtained from this fitting procedure, and are used as inputs for the subsequent muon track reconstruction procedure. Two independent tracking algorithms have been developed. The first one is based on the traditional procedure (i.e. fit the position of the track associated clusters to reconstruct the track), while the other is based on the Kalman filter [224]. The latter is the default option. Concerning the two mentioned tracking algorithms, the same procedure of the restrictions are

applied [42]:

- first estimation of track momenta should be  $3 < p < 3000 \text{ GeV}/c$
- a cut on  $\chi^2$  is applied at both the cluster and track levels
- the reconstructable track should include 1/2 clusters on stations 1, 2 and 3, while 3/4 clusters on stations 4 and 5 [214].

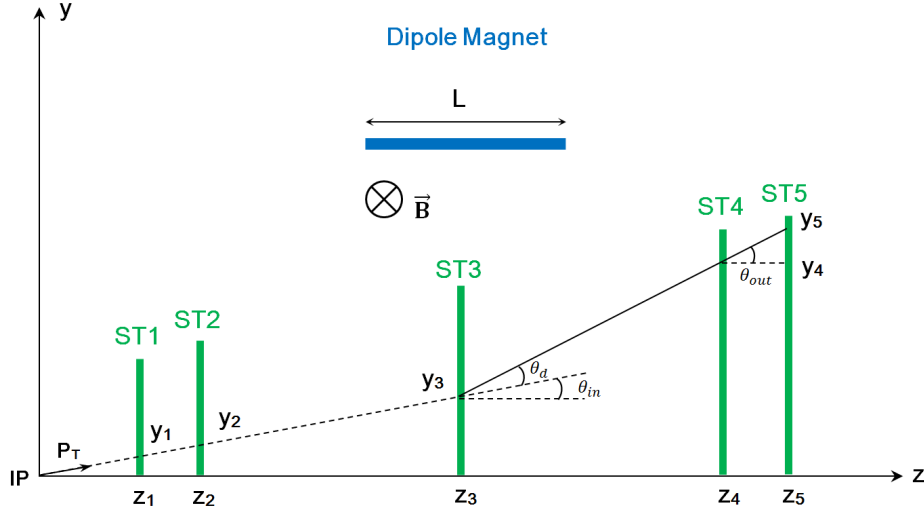


Figure 2.8: Principle of muon track reconstruction with the 5 tracking stations in the bending plane (i.e. the plane perpendicular to the magnetic field). Adapted from Ref. [42].

The muon track reconstruction starts from stations 4 and 5 since they are less subject to background induced by the soft particles escaping the front absorber. At the beginning, the algorithm allows one to link cluster pairs on stations 4 and 5, independently, and to create segments by joining the two clusters position with a straight line. Then, the obtained segments are extrapolated through the magnetic field to the primary vertex (IP), as shown in Fig. 2.8, in order to have a first estimation of the corresponding track parameters, such as the position, slope, inverse bending momentum and the related errors as well. The momentum  $p$  of the track candidates can be obtained by analysing the deflection of the charged particle travels in the magnetic field which is ordered by Lorentz force, and the resulting circular orbit of curvature radius  $R$  (in homogeneous magnetic field) is calculated as,

$$p[\text{GeV}/c] = 0.3[\text{T}] \times R[\text{cm}] = 0.3[\text{T}] \times \frac{L[\text{cm}]}{\theta_d} \quad (2.1)$$

$$\theta_d \equiv \theta_{\text{out}} - \theta_{\text{in}} \approx \frac{y_5 - y_4}{z_5 - z_4} - \frac{y_2 - y_1}{z_2 - z_1} \quad (2.2)$$

where,  $L$  is the length of the magnet and  $\theta_d$  is the deflection angle, with the geometry described in Fig. 2.8. Consequently, with Eq. 2.1, the first restriction for the two tracking algorithms is applied as  $3 < p < 3000 \text{ GeV}/c$ .



The second step of the tracking algorithms is to consider as departure the guessed track from station 5 (station 4) clusters and extrapolate it to the station 4 (station 5). The algorithm can search for at least one cluster on that station that could be associated to the track (i.e. the restriction of 3/4 clusters on stations 4 and 5). Another restriction, a cut on  $\chi^2$ , is applied to associate clusters to track candidates. The Kalman based reconstruction algorithm considers all clusters that pass the criteria, while the traditional one usually considers the best associated cluster, the one with the lowest  $\chi^2$ . Once a cluster is associated, the track parameters have to be re-calculated. Note that the employed Kalman algorithm uses the Kalman filter procedure, while the traditional algorithm needs to fit again the associated clusters to evaluate the new parameters. The next step is the track extrapolation back to station 3. As before, a  $\chi^2$  cut is imposed as a cluster selection criteria as well as a  $\chi^2$  cut on the track. A minimum requirement of one cluster associated to the track candidates has to be considered: including at least 1/2 clusters on station 3. After that, the remaining tracks with the re-evaluated parameters are extrapolated down to station 2, and later to station 1. It is necessary to mention that the selection criteria are the same as the one implemented at station 3: the  $\chi^2$  cut on the clusters and the track and a minimum of 1 associated cluster.

When finishing the full reconstruction of the tracks in the tracking stations, the so-called tracker track, one can get the first reconstructed track parameters: the uncorrected track parameters. Then their parameters can be extrapolated in two ways of operations by [42]:

- taking into account both the energy loss induced by the absorbers and the small-angle multiple-scatterings by means of the Badier-Branson plane [225], which allows to correct the parameters of the first reconstructed track points to the primary vertex position (measured with the SPD). The correction method consists of calculating the deviation angle from the most probable position of the muon to the end of the absorber, the radiation length of the material and the vertex position. After correction, the track parameters are related to the primary vertex. Note that, the distribution of the energy loss is very wide ( $\sim 4$  GeV) and very asymmetric, hence, even if the energy loss is corrected on average, the fluctuations are still important. The operations described in this item are of particular interest for the study of muons from heavy-flavour hadron decays near the vertex position;
- taking into account only the energy loss effect. It allows the DCA analysis (Distance of Closest Approach, defined as the distance between the extrapolated muon track and the interaction vertex in the plane perpendicular to the beam direction and containing the vertex) and the study of background noise when muons are produced far from the vertex; the track parameters determined in this case are named as the parameters related to DCA.

Figure 2.9 shows the relative transverse momentum resolution of tracks reconstructed in the muon spectrometer. The results are based on the LHC11h data (Pb-Pb at  $\sqrt{s_{NN}} = 2.76$  TeV) with all the standard selection procedure (see Chap. 3), as

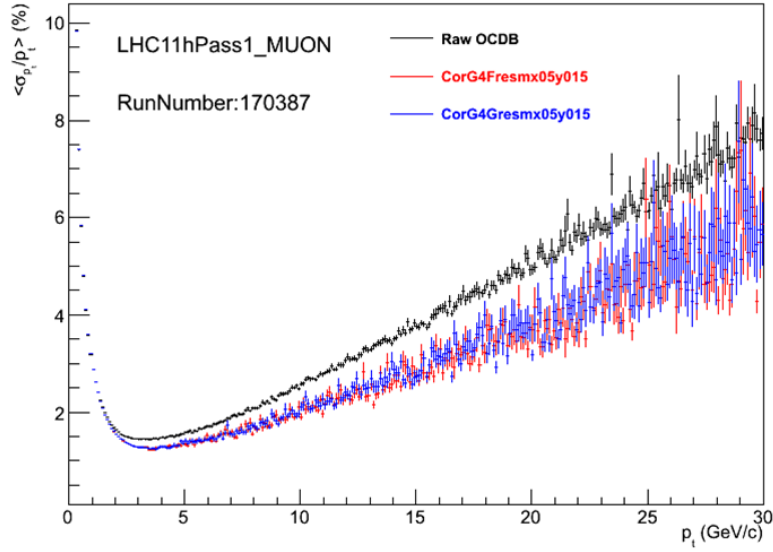


Figure 2.9: Relative transverse momentum ( $\sigma_{p_T}/p_T$ ) resolution of the tracks reconstructed with the ALICE muon spectrometer. Black points are the results based on raw OCDB, while the red and blue ones are based on different mis-alignments for testing. The data period is LHC11h.

well as the different mis-alignments. One can see that, first,  $\sigma_{p_T}/p_T$  decreases with increasing the  $p_T$  at low transverse momentum, then, it increases with increasing  $p_T$  at high transverse momentum. The observed trends can be well understood with considering the multiple-scattering and mis-alignment effects. In the low momentum region, the trend of  $\sigma_{p_T}/p_T$  is induced by the multiple-scattering of low energy tracks when crossing the tracking chambers. This effect is less pronounced with increasing  $p_T$ , resulting in the decreasing behavior of  $\sigma_{p_T}/p_T$ . Due to fact that tracks with large  $p_T$  can be little deflected in a given magnetic field, a smaller cell size is therefore required to ensure the resolution of track position, and this can be limited by the spatial resolution which is predicted to worsen linearly with increasing  $p_T$ . Meanwhile, the mis-alignment effect increases with increasing  $p_T$ . Note that similar behavior is observed for the momentum resolution.

#### 2.4.4 Trigger Stations

About 80% low  $p_T$  muons from charged hadron ( $\pi^\pm$  and  $K^\pm$ ) decays are expected [226] to reach the trigger stations in central Pb–Pb collisions with the nominal LHC run conditions shown in Tab. 2.1. It is therefore mandatory to apply a  $p_T$  cut at the trigger level, in order to reduce the probability of recording events where these low  $p_T$  muons are not accompanied by the high  $p_T$  ones emitted in the decay of heavy quarkonia, as well as in the semi-muonic decay of open heavy-flavour hadrons.

The  $p_T$  selection procedure is totally dependent on the position of muons (to be shown later, Eq. 2.5), and requires a spatial resolution better than 1 cm. It can be

achieved by employing the Resistive Plate Chambers (RPCs) operated in streamer mode. The trigger stations consist of 4 RPC planes arranged in 2 stations, 1 m apart from each other, placed behind the iron muon filter. The total active area is  $\sim 140 \text{ m}^2$ . The RPC is made up of "low-resistivity" ( $\rho \sim 2 \times 10^9 \Omega \cdot \text{cm}$ ) bakelite electrodes separated by 2 mm wide gas gap. The results from extensive testing show that RPCs are able to tolerate several ALICE-years of data taking with heavy-ion beams [221]. The segmented strips allow to read the x-y coordinates of the RPC hits, and they are typically a few tens of cm long and 1-4 cm wide. The strip size increases with the corresponding distance from the beam axis. The RPC strips are equipped with dual-threshold front-end discriminators, which basically reach a time resolution better than 2 ns.

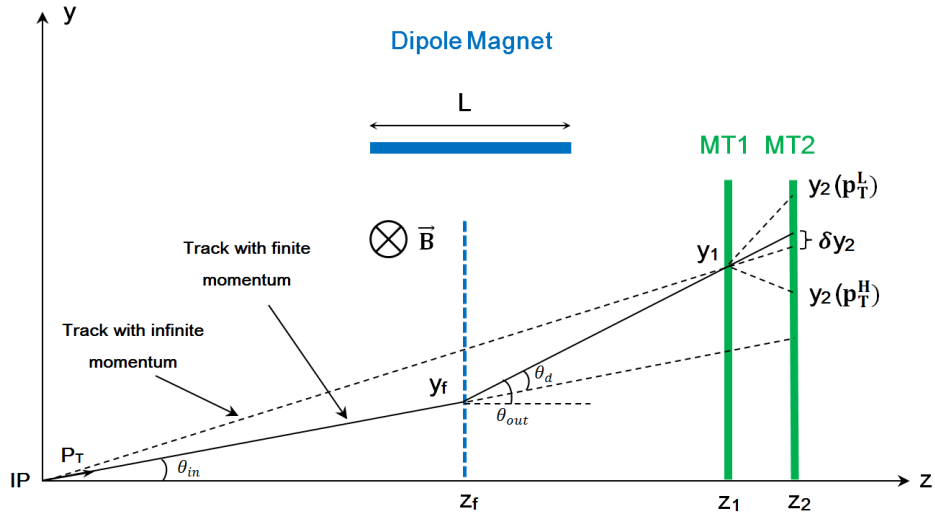


Figure 2.10: Principle of the  $p_T$  cut performed by the trigger in the bending plane. Adapted from Ref. [42, 227].

The selection of candidate muon tracks, namely, trigger tracks, is implemented via an algorithm at the electronics level. The algorithm takes as input the measured position of the clusters on the first trigger station,  $(y_1, z_1)$ , as displayed in the  $Y$  plane (bending plane) in Fig. 2.10. Then, the two points,  $(y_1, z_1)$  and the primary vertex, can form a trajectory, the dashed line, corresponding to the muon with infinite momentum  $p$ . It enables to be extrapolated to the second trigger station at point  $(y_2^{\text{inf}}, z_2)$ . However, the trajectory of entering muon with finite momentum is deflected when going through the magnetic field, as showed by the solid line in Fig. 2.10. It can reach the point  $(y_1, z_1)$  at the station 1, then be extrapolated to point  $(y_2, z_2)$  at station 2. Hence, one can measure the deviation of the track relative to a particle with infinite momentum on the station 2, labeled as  $\delta y_2 = y_2 - y_2^{\text{inf}}$  in Fig. 2.10. In general  $\delta y_2$  is of the order of few cm. In addition, the measured deviation should be smaller than a certain value, for instance,  $\delta y_2 \leq \delta Y_2 = y_2(p_T^L) - y_2(p_T^H)$ , which corresponds to the desired  $p_T$  coverage  $p_T^L < p_T < p_T^H$  [226]. According to the geometry and small angle approximation, the deviation and the deflection

angle are calculated by means of

$$\delta y_2 \approx \frac{z_f}{z_1} \cdot (z_2 - z_1) \cdot \theta_d \quad (2.3)$$

$$\theta_d \equiv \theta_{\text{out}} - \theta_{\text{in}} \approx \frac{1}{z_f} \cdot \frac{z_1 y_2 - z_2 y_1}{z_2 - z_1} \quad (2.4)$$

where  $z_f$  is the  $z$  coordinate of the magnetic field, as shown in Fig. 2.10. By considering the relation shown in Eq. 2.1, one can see that  $\theta_d \propto \frac{1}{p} \propto \frac{1}{p_T}$ , hence, Eq. 2.3 can be re-written as,

$$\delta y_2 \approx \frac{z_f}{z_1} \cdot (z_2 - z_1) \cdot \frac{1}{p_T} \quad (2.5)$$

Finally, the subsequent cuts on this deviation, performed by means of the LUT (Look-Up-Tables), allow one to reject the low  $p_T$  particles which have obviously large deviation. The developed two sets of cuts, named low  $p_T$  and high  $p_T$  cuts, are loaded in the LUT in the local board. The so-called "all  $p_T$ " corresponds to the case for which no cut on the deviation is applied at the LUT level. Six following trigger signals are delivered to the ALICE Central Trigger Processor (CTP), less than 800 ns after the interaction, at a 40 MHz frequency [226]:

- at least one single muon above low (high)  $p_T$  cut, called "single muon low (high)  $p_T$ ";
- at least two muons with opposite deviation sign, each of them above low (high)  $p_T$  cut, called "unlike-sign dimuon low (high)  $p_T$ ";
- at least two muons with same deviation sign, each of them above low (high)  $p_T$  cut, called "like-sign dimuon low (high)  $p_T$ ".

Note that, (1) low  $p_T$  and high  $p_T$  cuts represent usually a compromise between background rejection and signal detection efficiency in the mass region of the  $J/\Psi$  ( $p_T$  cut  $\sim 1$  GeV/ $c$ ) and  $\Upsilon$  ( $p_T$  cut  $\sim 2$  GeV/ $c$ ) resonances, respectively, and a  $p_T$  threshold of 4.2 GeV/ $c$  has been recently implemented for the  $W$  production study [219]; (2) "all  $p_T$ " indicates no  $p_T$  cut on the single muon.

## 2.5 Future Upgrade of the Muon Spectrometer

During the Run 1 period (2010-2013), ALICE has recorded the data sets summarized in Table 2.4. Run 1 has been followed by a Long Shutdown from March 2013 until the beginning of 2015. This has been used to upgrade the accelerator in order to deliver higher beam energy and luminosity and to complete the installation of missing parts of the detectors. Run 2 (2015-2018) will be followed by another Long Shutdown in 2019 and by a Run 3 which is expected to start in 2022.

During the Long Shutdown in 2019-2020, the ALICE collaboration is going to significantly upgrade both the hardware (detectors) and software (online data acquisition) in order to record an integrated luminosity of about  $\sim 10$  nb $^{-1}$  in central Pb–Pb collisions (a factor 100 more than the statistics collected during Run 1). The new



year	2010		2011		2012	2013	
system	pp	pp	Pb–Pb	pp	pp	p–Pb/Pb–p	pp
$\sqrt{s_{NN}}$ (TeV)	7	7	2.76	2.76	8	5.02	2.76
$\mathcal{L}$ (nb <sup>-1</sup> )	$1.7 \times 10^{-2}$	5000	$8 \times 10^{-2}$	20	$10^4$	14/17	130

Table 2.4: Summary of the main data sets collected with the ALICE detector during Run 1: the year, the colliding system, the energy of center-of-mass and the integrated luminosity. See the text for details. Adapted from Ref. [228, 205].

ITS with improved pointing resolution [229, 230], a continuous-readout TPC [231] based on GEM technology, the muon spectrometer upgrade [232, 233, 234] and the new online data processing system [232, 235] are key elements of the ALICE upgrade. Because the expected instantaneous luminosity in Run 2 is expected to be above  $10^{33} \text{ cm}^{-2}\text{s}^{-1}$  ( $10^{27} \text{ cm}^{-2}\text{s}^{-1}$ ) for pp (Pb–Pb) collisions, due to the very high interaction rate, there is no trigger but data recorded in continuously. In this case, the Muon Trigger acts as the Muon Identifier (MID, [236]). The upgrade of the muon spectrometer includes the following three parts.

### 2.5.1 Muon Tracking Upgrade

For the Muon Tracking Stations, two upgrades are considered [232].

- **Front-End Electronics (FEE) Upgrade:**

The upgrade of FEE consists in increasing the readout rate to a minimum of 5 kHz while keeping the dead-time below 10%, requiring the total readout time below 20  $\mu\text{s}$ . This is achieved by means of a new MANU card with an architecture similar to the current one. The ADCs, working at 1 MHz with a digitisation time of 32  $\mu\text{s}$  in the present design, is replaced by 10 MHz ADCs with a digitisation time of 3.2  $\mu\text{s}$ .

- **Readout Electronics Upgrade:**

One also needs to update the CROCUS readout system in order to access the goal of a maximum readout time below 20  $\mu\text{s}$ , which can be fulfilled by a new one based on state-of-the-art Field-Programmable Gate Arrays (FPGAs). The general idea is to keep the same readout scheme and cabling infrastructure between the detectors and the CROCUS. In order to de-randomize the data transferred to the DAQ, this system implements a multi-event buffering able to store data from several central Pb–Pb collisions. The trigger signals are still managed by the Trigger Crocus Interface (TCI). The new CROCUS system combined to the new MANU allows readout times below 20  $\mu\text{s}$ .

### 2.5.2 Muon Trigger Upgrade

In view of the upcoming high collision rate in Run 2 (2015–2018) [232], the current trigger chambers cannot longer be operated in streamer (maxi avalanche)

mode because of ageing issues. A genuine avalanche mode is going to be used. This needs amplification of the signal i.e. new FEE and readout electronics.

- **Front-End Electronics Upgrade:**

The RPC detectors were operated in maxi avalanche mode in Run 1, with a FE electronics (ADULT ASIC) that does not include any amplification stage. The resulting limit on the instantaneous counting rate cannot satisfy well the expected one after Long Shutdown 2. Moreover, due to the limits on ageing [232], the RPC cannot afford a safe operation in the future running conditions. It requires the genuine avalanche mode for RPCs in the FE electronics. As a first step one has to build a FE card prototype, based on commercial fast amplifiers, to perform measurements of signal to noise level, fast and total charge, spatial and timing resolution and detection efficiency. In parallel the development of an ASIC (called FEERIC, Front-End Electronics Rapid Integrated Circuit) based on existing circuits [232] is required. Some prototypes are tested with cosmic rays and proton beams.

- **Readout Electronics Upgrade:**

An additional limitation of the present Muon Trigger system is the readout speed. It is 110  $\mu\text{s}$  in Run 1 [232], causing an unacceptable dead-time of more than 30% for the increased trigger rates after the 2019-2020 shutdown. With the new design for the 234 Local cards receiving the LVDS signals from the FE electronics and the 16 Regional concentrator cards [237], the transfer time can be reduced to few  $\mu\text{s}$  together with the dead-time brought down to  $\sim < 10\%$ .

### 2.5.3 Muon Forward Tracker (MFT)

The ALICE Muon Forward Tracker, MFT [234], has been envisaged to overcome the limitations of the muon spectrometer due to the absence of track points close the primary vertex before the muon suffers the multiple scattering induced by the front absorber.

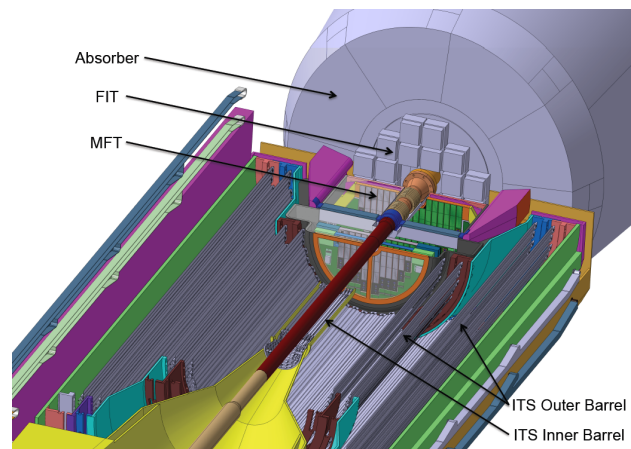


Figure 2.11: Layout of the MFT detector in ALICE. Figure from Ref. [234].



The MFT consists of two half cones, as shown in Fig. 2.11. Each half-MFT cone consists of 5 half-disks positioned along the beam axis, in the direction of the muon spectrometer (same side as V0C) at  $z = -460, -493, -531, -687, -768$  mm from the nominal interaction point. The first two half-disks are identical (called Half-Disk-0 and 1), while the remaining three half-disks are all different and are called Half-Disk-2, Half-Disk-3 and Half-Disk-4 respectively. The MFT covers the pseudo-rapidity acceptance  $-3.6 < \eta_{\text{LAB}} < -2.5$  [234]. The presence of the MFT in the forward rapidity region can offer new opportunities, by accessing new measurements out of reach with the current muon spectrometer such as the separation of prompt and non-prompt  $J/\Psi$  (i.e.  $J/\Psi$  from B decays), and  $\Psi'$ , as well as the production of muons from charm decays and beauty decays [238], separately. The precision of several other measurements can be also increased [239].

The MFT enables the possibility to match the extrapolated muon tracks, coming from the tracking chambers after the absorber, with the clusters measured in the MFT planes before the absorber. The matching procedure between the muon tracks and the MFT clusters being correct, muon tracks should gain enough pointing accuracy to permit a reliable measurement of their offset [240], which is defined as the transverse distance between the primary vertex and the muon track.

The expected performance of the ALICE MUON spectrometer upgraded with the addition of the MFT, can be summarized as follows [233, 239]:

- **charmonium measurements**

- measurement of prompt  $J/\Psi$  production down to  $p_T = 0$ ; note that the prompt  $J/\Psi$  production is expected to be sensitive to charm quark recombination mechanisms in the low  $p_T$  region;
- measurement of non-prompt  $J/\Psi$  down to  $p_T = 1$  GeV/ $c$ . This allows to access the b-hadron cross section down to  $p_T = 0$  without any extrapolation;
- for the separation of prompt and non-prompt  $J/\Psi$ , it is found that the uncertainty on the measurement of the ratio between prompt and non-prompt  $J/\Psi$  can stay below  $\sim 20\%$  down to  $p_T = 1$  GeV/ $c$ ;
- $\Psi'$  measurement with an uncertainty as low as  $\sim 10\%$  down to zero  $p_T$ .

- **open heavy-flavour measurements**

- unravel muons from open heavy-flavour hadron decays down to  $p_T$  of about 1 and 2 GeV/ $c$ , for charm and beauty, respectively. The corresponding uncertainty is about 10% in the low  $p_T$  region in central Pb–Pb collisions. This gives access to new observable such as the double ratio of the nuclear modification factor of beauty to that of charm and investigate in detail the features of the in-medium parton energy loss.

- **low-mass dimuon measurements**



- measurement of prompt dimuon sources in the low-mass region, below  $\sim 1.2 \text{ GeV}/c^2$ . This will be improved dramatically with the MFT. A mass resolution of about  $15 \text{ MeV}/c^2$  is expected for the  $\omega$  and  $\phi$  resonances. This represents a factor 4 improvement with respect to the present situation without MFT. It should therefore be possible to reliably measure the thermal dimuon continuum as well as the in-medium modified line shape of the  $\rho$  resonance. A precision of  $\sim 20\%$  is expected for the measurement of these sources.

## 2.6 ALICE Offline Framework

This section is devoted to the ALICE Offline Framework, AliRoot [195], which heavily uses the facilities provided by the ROOT framework [241]. It allows to simulate the detector in a detailed way and it is interfaced to various event generations, meanwhile, it enables to reconstruct and analyse the data coming from real interactions or the Monte-Carlo simulations. For this purpose, AliRoot has already been used during the production of the Technical Design Report [242] of each detector system to optimise their design, as well as to evaluate the physics performance of the full ALICE detector [243, 244]. The framework is written in C++. It enables the user tasks such as simulation, reconstruction, calibration, alignment, visualization and analysis, aiming at the extraction of physics information based on the collected experimental data.

The online/offline analysis framework in HEP is a set of software tools that enables data processing [245], for example, the previous CERN Program Library [246] was a toolkit to build a framework. The structure of the framework is shown in Fig. 2.12: the core of the program is the STEER module, which provides steering, run management, interface classes and base classes. The simulation and reconstruction codes designed for the different detectors are independent so that different detector groups can work simultaneously on the program while minimizing the interference [214]. The use of an Object Oriented programming language (i.e. C++), allowing a defined class hierarchy, realizes the modularity structure in a natural way.

### Simulation

Due to the large number of particles produced in heavy-ion collisions, it is a challenge to develop a reasonable algorithm to reconstruct each particle trajectory. The framework of the simulation with the ALICE detector consists of event generators [247], transport of particles traversing the detectors, energy deposition (i.e. hits), detector response (i.e. summable digits), generation of digits from summable digits, optional event merging of underlying events and the creation of raw data [245]. For each step, one can find the detailed description in Ref. [195].

The framework has a high degree of flexibility for the selection of desired event generators (e.g. PYTHIA, DPMJET, HIJING ...) in order to provide different predictions for the observables, such as multiplicities,  $p_T$ - and rapidity-distributions. The detector response is simulated via the most common transport codes, for ex-

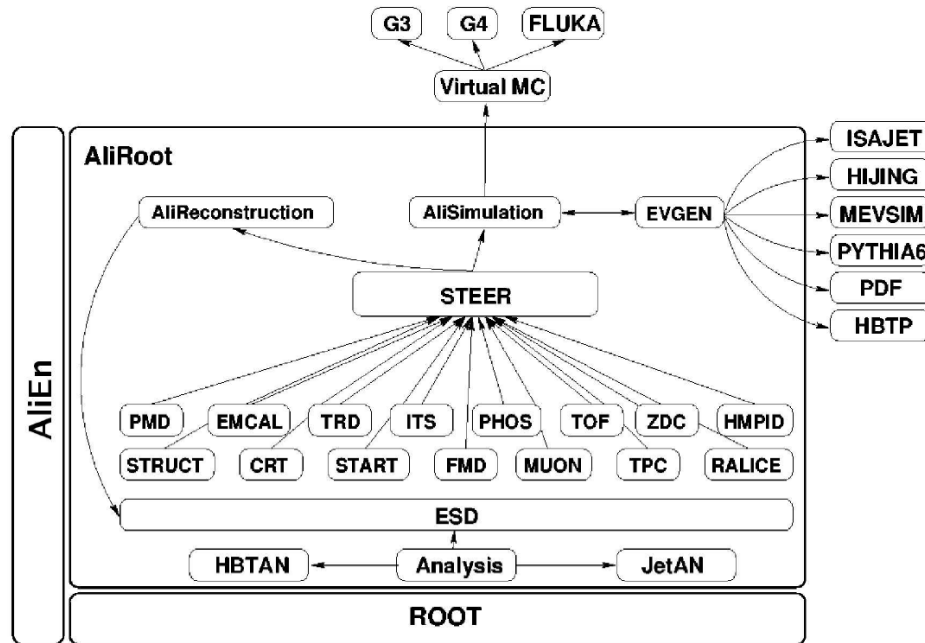


Figure 2.12: Schematic view of the AliRoot framework. Figure taken from Ref. [245].

ample, GEANT3, GEANT4 and FLUKA, which are connected to the simulation framework by employing the Virtual Monte-Carlo (VMC) Interface of AliRoot. As displayed in Fig. 2.12, the VMC is able to provide a single interface for various detector simulators, as well as an interface to construct the geometry of detectors.

During the simulation procedure, the kinematics tree including, for example, the information of particles created by the employed event generators, can be produced. The data produced by the event generators contain full information about the generated particles [42] such as the decay history (i.e. mother-daughter relationship). Then, the generated particles are transported through the detectors. When propagating through the detectors, the related response caused by each crossing particle is simulated and the resulting hits are stored. As shown in Fig. 2.13, the hits are converted into digits by taking into account the detector and associated electronics response function, for example, the noise-related ones. The digits are eventually converted into raw-data, which are stored in binary format.

## Reconstruction

The reconstruction framework of AliRoot uses as input the digits data in root trees or raw data, as shown in Fig. 2.13, which are the output from the real detector or the simulation framework. It starts with a local reconstruction of clusters in each sub-detector, then, the track (candidates) and vertex are reconstructed and particle types are identified as well. The output of the reconstruction procedure is the Event Summary Data (ESD) which contains the list of reconstructed tracks (particles with physical information) and its global properties, such as the information of the charged particle tracks, decays with V0, kink and cascade topologies. A further

selection performed through user defined tasks, enables the creation of Analysis Object Data (AOD) files, which contains a more compact information used for a specific analysis.

The framework provides a simple user interface allowing to configure the reconstruction procedure, to include or exclude detectors, and to ensure the correct sequence of the reconstruction steps.

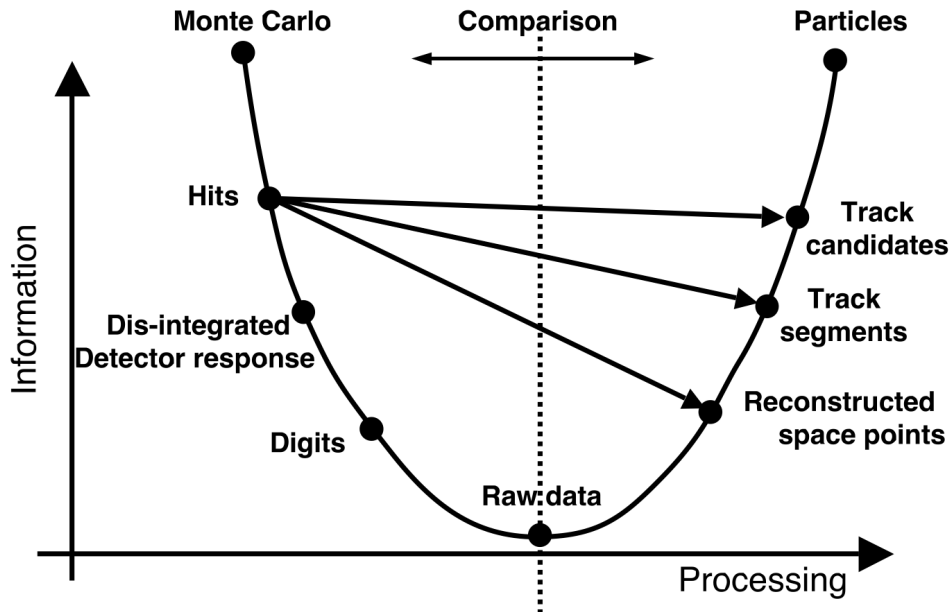


Figure 2.13: Data processing framework. Figure taken from Ref. [245].

### Worldwide LHC Computing Grid

The Worldwide LHC Computing Grid (WLCG, [248, 249]) project is a global collaboration of more than 170 computer centers in 42 countries, linking up national and international grid infrastructures. WLCG is the largest computing grid in the world. It is designed to provide an effective solution to the data-analysis challenge of the LHC (which is about 15 million gigabytes every year).

Users are able to submit jobs from one of the many entry points into this system. For each job, the related request can be almost anything such as the storage, the processing capacity, and the availability of analysis software [249]. Meanwhile, the peak data-transfer rates of WLCG is about 10 gigabytes per second [249].

### Analysis framework for single muons

The analysis framework of data taken with the ALICE muon spectrometer is detailed in Ref. [42]. The same framework is used to study muons from heavy-flavour hadron decays in p-Pb collisions at  $\sqrt{s_{NN}} = 5.02$  TeV.

### AliRoot splitting and O<sup>2</sup> project

The Physics Working Groups (PWGs) involved in the analysis part are not shown



in Fig. 2.12. It is realized that there is an increase frequency of the PWGs related code deployment to the Grid. In addition, it is better to simplify the committing procedure for the code users. Hence, an AliRoot split program (or factorizing PWGs out of AliRoot [250, 251, 252]) has been implemented in order to increase "the time between code ready and data processed". The splitting occurred at the beginning of 2015. Now, we have the "small" AliPhysics package under active development by the users, while the "big" AliRoot core package becomes more stable than before.

The current ALICE organization of the online and offline computing is composed of the three groups: the DAQ, HLT and Offline [253]. The upcoming Run 2 data are treated following the same organization as in Run 1, whereas Run 3 (after Long Shutdown 2) requires a more integrated structure with a single common system. The O<sup>2</sup> (Online and Offline) project has been launched to design and build the system for Run 3 with the new common computing structure. The goal is to build a unified computing system after Long Shutdown 2 as shown in the TDR preparation [254]. Hence, AliRoot splitting and O<sup>2</sup> project allow to make the computing in a better shape in the upcoming data taking periods.



# Data samples, Muon Selection Criteria and Acceptance $\times$ Efficiency Correction

I move to my PhD topics related to heavy-flavour hadron decay muon measurements in p–Pb collisions at forward and backward rapidity and I start with a discussion related to data collected with the ALICE muon spectrometer in p–Pb collisions at  $\sqrt{s_{NN}} = 5.02$  TeV. In this Chapter, I would like to show the statistics of the data at both event and track level, as well as the study of several points that are relevant for the analysis, such as the standard selection criteria of muons, pile-up effects and the normalization procedure of muon triggered samples. The last section is dedicated to discuss the acceptance  $\times$  efficiency determination.

For the p–Pb asymmetric collision system, the energy of the colliding beams are 4 TeV and 1.58 TeV for p and Pb per nucleon, respectively, and the center-of-mass (CMS) frame does not coincide with the laboratory one. Hence, there is a rapidity shift effect of the CMS frame in the longitudinal direction of  $\Delta y = \frac{1}{2} \ln\left(\frac{Z_p A_{Pb}}{Z_{Pb} A_p}\right) \approx 0.465$  units in the proton direction.

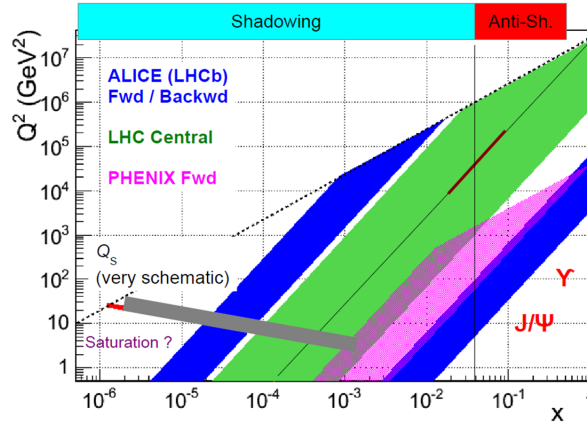


Figure 3.1: Schematic plot for  $Q^2$  as a function of  $x$  within various acceptances from different experiments. See text for details. Figure taken from [255].

The used data are collected with two different beam configurations, by inverting the sense of the orbits of the two particle species. For the first case, the proton is moving towards the Muon spectrometer. The corresponding measurement of muons covers the forward rapidity interval  $2.03 < y_{CMS} < 3.53$ , the so-called p–Pb collisions. That means that muons are measured in the proton fragmentation region.

For the second case of beam configuration, the Pb nucleus is moving towards the Muon Spectrometer, the resulting measurement is performed at backward rapidity  $-4.46 < y_{\text{CMS}} < -2.96$ , the so-called Pb-p collisions. This means that muons are measured in the Pb fragmentation region. Figure 3.1 shows the correlation between four-momentum transfer squared ( $Q^2$ ) and the Bjorken- $x$ , obtained within different acceptances of the corresponding detectors. The Bjorken- $x$  range can be roughly separated into two regions: shadowing and anti-shadowing (see also the left panel of Fig. 1.15). Consequently, the shadowing (anti-shadowing) region can be accessed by performing the measurement at forward (backward) rapidity.

### 3.1 Data Samples

As summarized in Tab. 3.1, data samples for p-Pb (muons measured at forward rapidity, LHC13d and LHC13e periods) and Pb-p (muons measured at backward rapidity, LHC13f period) collisions have been collected at  $\sqrt{s_{\text{NN}}} = 5.02$  TeV with a minimum bias trigger (MB, i.e. CINT7) and muon triggers (CMSL7, CMSH7). The single muon sample was collected with a trigger  $p_{\text{T}}$  thresholds of about 0.5 GeV/ $c$  and 4.2 GeV/ $c$  (50% of the trigger efficiency). They are referred as muon single low (MSL) and muon single high (MSH), respectively. Note that the MSH triggered data are not downscaled.

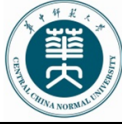
The desired triggers with their identification name (trigger string), as well as the trigger input and ID at hardware level are listed in in Tab. 3.1. More detailed information concerning the naming scheme for ALICE trigger classes, can be found in Ref. [256].

Triggers	$p_{\text{T}}$ threshold (GeV/ $c$ )	trigger string	trigger input name (ID)
MB	-	CINT7-B-NOPF-ALLNOTRD CMSL7-B-NOPF-ALLNOTRD CMSH7-B-NOPF-ALLNOTRD	-
MSL	0.5	CMSL7-B-NOPF-MUON	0MSL (13)
MSH	4.2	CMSH7-B-NOPF-MUON	0MSH (14)

Table 3.1: Summary of the single muon triggers for the data in p-Pb (LHC13d, LHC13e periods) and Pb-p (LHC13f period) collisions. The names (MB: minimum bias, MSL: muon trigger with low  $p_{\text{T}}$  cut and MSH: muon trigger with high  $p_{\text{T}}$  cut), the related  $p_{\text{T}}$  threshold (at 50% efficiency), the trigger input together with the identification (ID) are listed. See text for details. Extracted from the ALICE Electronic Logbook.

#### 3.1.1 Event Selection

For the event selection, the standard cuts are applied to reject the remaining background events after the online event selection at hardware level. The criteria



contains the following selection cuts.

First one is the offline physics event selection (or physics selection [257]) procedure including the rejection of background induced by the machine such as beam-gas interactions [258]. It is implemented by cutting on the time information from both V0A and V0C. Moreover, the background can be further identified according to the correlation between the number of tracklets and SPD clusters (see Ref. [257] for detail). The Zero Degree Calorimeters (ZDC) located at 112.m on both sides of the interaction point are also used in the offline event selection.

The second one is the primary vertex selection, including the vertex finding procedure with SPD [259, 260]. The number of vertex contributors is defined as the number of SPD tracklets that are used in the determination of the vertex position. It is known that [261] the value of the contributors is negative when the vertex reconstruction fails: "-2" indicating the absence of reconstructed points in SPD and "-1" indicating that it is not possible to build suitable tracklets. Events with at least 1 contributor are selected for the following analysis.

Apart from these two selection cuts, the global QA (Quality Assurance, for example, the centrality-related QA) and Muon QA are considered for each run, together with the pile-up rate (Sec. 3.1.2). Note that this QA selection procedure is implemented both for MSL and MSH triggered events. Finally, the following runs for a given period are considered as "good" runs, and are used in this thesis. The related reconstruction pass number, AOD version and total number of runs are listed as well.

- LHC13d (forward rapidity), muon\_pass2, AOD134, 20 runs in total:  
195682 195724 195725 195726 195727 195760 195765 195767 195783 195787  
195826 195827 195829 195830 195831 195867 195869 195871 195872 195873
- LHC13e (forward rapidity), muon\_pass2, AOD134, 25 runs in total:  
195949 195950 195954 195955 195958 195989 195994 196000 196006 196085  
196089 196090 196091 196105 196107 196185 196187 196194 196199 196200  
196201 196214 196308 196309 196310
- LHC13f (backward rapidity), muon\_pass2, AOD, 63 runs in total:  
196474 196475 196477 196528 196535 196563 196564 196566 196568 196601  
196605 196608 196646 196648 196701 196702 196720 196721 196722 196772  
196773 196774 196869 196876 196965 196972 196973 196974 197003 197011  
197089 197091 197092 197098 197099 197138 197139 197142 197143 197144  
197145 197147 197148 197150 197152 197153 197184 197189 197247 197254  
197255 197256 197258 197298 197299 197302 197341 197342 197348 197349  
197386 197387 197388

Note that, (1) run 196433 in LHC13f (pure MB run, muon triggers not activated) and run 196311 in LHC13e (pure muon trigger run, MB trigger not activated) have been rejected from the analysis; (2) both LHC13d and LHC13e periods correspond to p-Pb collisions (forward rapidity). The difference between them is the magnetic field polarity (L3/Dipole), which is "L3-/Dipole-" for LHC13d and "L3+/Dipole+"



for LHC13e (and LHC13f). Hence, data from these two periods can be combined together (LHC13de) in the following analysis. Finally, the same alignment configuration is used for all the periods.

Table 3.2 summarizes the statistics after the application of the event selections, as well as the rejection percentage for each trigger within different periods in multiplicity integrated collisions. It is necessary to mention that the primary vertex selection cut reject almost no events and the pile-up events are kept.

	LHC13d and LHC13e (Rej.%)		LHC13f (Rej.%)	
	MSL	MSH	MSL	MSH
+ Phys. Sel.	14.6M	10.0M	26.4M	15.7M
+ Cent. QA	14.6M (0.3%)	10.0M (0.4%)	26.3M (0.3%)	15.4M (2.1%)
+ Vtx. Sel	14.6M (0.1%)	10.0M (0.1%)	26.3M (0.1%)	15.3M (0.2%)

Table 3.2: Summary of the extracted statistics after applying various selection cuts at event level: physics selection, centrality QA and primary vertex reconstruction. See text for details.

### 3.1.2 Pile-up Effect

The pile-up is defined as a event with superposition of collisions. There are two species: the collisions are from the same or different bunching crossing. It is known that the probability to have a given number of collisions during one bunch crossing can be expressed by a Poisson distribution. The corresponding mean value of the distribution can be calculated for each run using the number of bunch crossing without a collision. The related typical parameter, pile-up rate, is defined as the ratio of probability to have more than one collision to the probability to have at least one collision.

The pile-up effect can be studied at both hardware and software level, and further corrected through the factor  $F_{\text{pileup}}$  (see below).

#### 3.1.2.1 Pile-up factor obtained at hardware level

The pile-up correction factor obtained at hardware level,  $F_{\text{pileup}}^{\text{HW}}$ , is defined as the mean number of interactions per MB trigger.

$$F_{\text{pileup}}^{\text{HW}} = \frac{\mu}{1 - e^{-\mu}} \quad (3.1)$$

$$\mu = -\ln(1 - \text{purity}_{\text{MB}} \cdot \frac{L0bRate_{\text{MB}}}{N_{\text{colliding}} \cdot f_{\text{LHC}}}) \quad (3.2)$$

where,  $\mu$  is the mean number of collisions in all bunches, and it is also the mean value of the Poisson distribution [262]

$$p(n, \mu) = \frac{\mu^n}{n!} \cdot e^{-\mu} \quad (3.3)$$



which gives the probability to have  $n$  collisions per bunch crossing;  $1 - e^{-\mu}$  gives the probability to have at least one collision in the non-empty bunches;  $purity_{MB}$  is the fraction of minimum bias (MB) events which satisfies the V0 timing cut;  $L0bRate_{MB}$  and  $N_{colliding}$  are the number of MB events recorded by the  $L0b$  (level-0 trigger before the veto) counters and the number of interacting bunches, respectively;  $f_{LHC} = 11245$  Hz is the collision frequency of the LHC.

For low values of  $\mu$ , Eq. 3.1 can be re-written as

$$F_{pileup}^{HW} \approx 1 + \frac{\mu}{2} \quad (3.4)$$

$\mu \ll 1$  indicates that most of the bunch crossing are empty. The rate of pile-up is obtained as

$$\frac{p(n \geq 2, \mu)}{p(n \geq 1, \mu)} \approx \frac{\mu}{2} \quad (3.5)$$

### 3.1.2.2 Pile-up factor obtained at software level

$$F_{pileup}^{SW} = \frac{(n_{total} - n_{pileup}) + \alpha \cdot n_{pileup}}{n_{total}} = 1 + \beta \cdot \frac{n_{pileup}}{n_{total}} \quad (3.6)$$

$$\beta = \alpha - 1 \geq 1 \quad (3.7)$$

where,  $n_{total}$  is the number of events after the offline selection, and  $n_{pileup}$  is the number of events tagged as pile-up events at software level;  $\alpha \geq 2$  is the mean number of collisions in the tagged pile-up events.

Note that, the pile-up event selection is implemented according to the SPD pile-up identification procedure, which is based on multiple reconstructed interaction vertices in the same event. Candidate pile-up vertices are then selected based on their number of contributors and their distance to the main vertex. In this case, the employed parameters for the tagging are the default ones proposed for p-Pb collisions. Also, one can tune the parameters in order to give consistent results with respect to the ones from hardware [263].

### 3.1.2.3 Comparison

The pile-up rate obtained at hardware and software level can be compared with different triggers for both p-Pb and Pb-p configurations. The corresponding results are summarized in Fig. 3.2. In each plot, the black curve is the pile-up rate at software level,  $n_{pileup}/n_{total}$ , as a function of run number, while the red curve,  $\mu/2$ , presents the pile-up rate at hardware level. The upper two plots are the results for p-Pb configuration (LHC13de, forward rapidity) for MSL (left) and MSH (right). One can see the results shown in the last bin (196311) is zero since 196311 is a pure muon trigger run (without MB trigger). The bottom two plots are the ones obtained for Pb-p configuration (LHC13f, backward rapidity) with also the MSL and MSH results shown on the left and right side, respectively. It is obvious to see

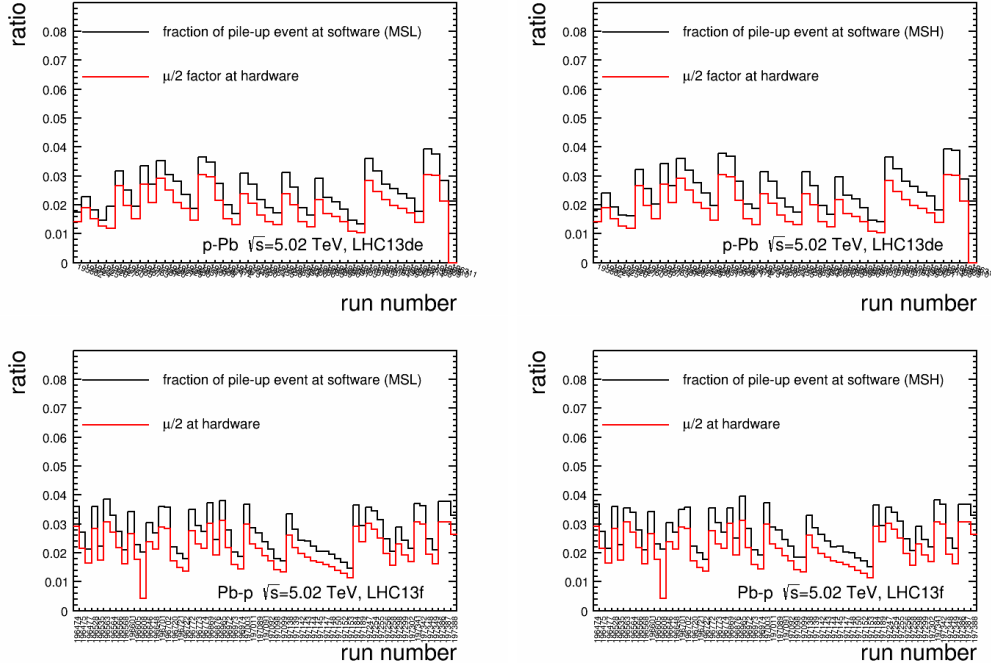


Figure 3.2: Pile-up rate for different triggers at both forward (upper plots) and backward rapidity (bottom plots). The results are calculated at hardware (red) and software (black) level, respectively.

that this run 196608 behaves differently. That is because the associated number of MB events per bunch crossing at hardware level is larger than that for other runs.

One can notice the difference of pile-up rate between hardware and software,  $\mu/2 < n_{\text{pileup}}/n_{\text{total}}$ . It can be understood because the efficiency of pile-up tagging at software level is not 100% with the default parameters for tagging. Hence, it was found that  $\mu/2 \propto n_{\text{pileup}}/n_{\text{total}}$  since  $F_{\text{pileup}}^{\text{HW}} \propto F_{\text{pileup}}^{\text{SW}}$ . The pile-up rate calculated with different methods and different triggers is  $\sim 2 - 3\%$  both at forward and backward rapidity for the muon triggered data. It means that the pile-up effect is negligible in multiplicity integrated collisions [264]. Similar conclusion was found for the effect on the  $p_T$  spectra obtained with different triggers and periods.

The pile-up effect within different event activity classes (to be discussed in Sec. 3.3) has been also investigated. For different trigger samples (MB, MSL and MSH), it was found [263] a visible event activity estimator dependence, and strong pile-up contribution in the most central collisions such as  $0 - 5\%$  (see Sec. 3.3 for the centrality determination in p-Pb collisions). Moreover, the pile-up is more important in Pb-p than in p-Pb collisions. More information is given in Sec. 3.3.

The pile-up from different bunch crossings in p-Pb collisions, was investigated in Ref. [265].



### 3.1.3 Normalization of Muon Triggers to Minimum Bias

In experimental physics, a trigger means a system that uses simple criteria to rapidly decide which events to keep when only a small fraction of the total can be recorded [266]. The trigger systems are totally necessary when considering limitations in the real-world: data storage capacity and rates. Since experiments are typically searching for "interesting" events, for example, the particles generated with very large (transverse) momentum, that occur at a relatively low rate, trigger systems are used to identify the events that should be recorded for later analysis. It is easy to see that the desired event samples to study rare signals, such as muons from heavy-flavour hadron decays, are not the minimum bias (MB) events. As discussed in Sec. 3.1.1, since we employ the muon triggered events to measure muons from heavy-flavour hadron decays up to high transverse momentum ( $p_T$ ), a procedure to normalize to the equivalent number of MB events is needed.

The cross section of muons from heavy-flavour hadron decays in pp collisions at  $\sqrt{s} = 7$  TeV, was published in 2011 [160], and no  $p_T$  threshold was set for the used muon trigger data. It was found [160] that the ratios, defined as the distributions in MB events to that in muon trigger events, were **independent** on  $p_T$  or  $\eta$  when applying all the analysis cuts, indicating that the numbers of the different event triggers can be treated as the scalers for the muon track multiplicity. Consequently, the multiplicity scaling method was proposed to normalize the muon triggered events. In the present analysis, as shown in Tab. 3.1, the  $p_T$  threshold for the used data is 0.5 GeV/c, and the **independent behavior** observed in pp collisions at  $\sqrt{s} = 7$  TeV could be biased in this case.

In the following, first, I briefly introduce the employed methods for normalization, and then, discuss the obtained results concerning the normalization factor and associated uncertainties. They are shown for both MSL and MSH triggered events in different periods.

#### 3.1.3.1 Normalization strategy

It is known that the muon triggered events (MSL and MSH) are just a sub-sample of MB events, the corresponding fraction being defined as the probability of having one low(high)- $p_T$  triggered muon in events for which the MB condition is satisfied. This is the inverse of the normalization factor,  $F_{\text{norm}}$ .  $F_{\text{norm}}$  is calculated with two different scenarios: scaler and offline methods. It enables the determination of the number of equivalent MB events.

The scaler method [267, 268] takes as input the information of  $L0b$  counters to avoid statistical fluctuations. The corresponding normalization factor is

$$F_{\text{norm}}^{\text{MSL(MSH)}} = \frac{L0b_{\text{MB}} \times \text{purity}_{\text{MB}} \times F_{\text{pile-up}}}{L0b_{\text{MSL(MSH)}} \times PS_{\text{MSL(MSH)}}} \quad (3.8)$$

where,  $L0b_{\text{MB}}$ ,  $L0b_{\text{MSL}}$  and  $L0b_{\text{MSH}}$  are the scaler values recorded for MB events, muon single low  $p_T$  and muon single high  $p_T$  triggered events, respectively and  $\text{purity}_{\text{MB}}$  is the fraction of events which satisfy the V0 timing cut, as shown in

Eq. 3.2. The purity is better than 99% for most of the runs (see upper-left panel in Fig. 3.3, 3.4 and 3.5 for LHC13d, LHC13e and LHC13f periods, respectively).  $PS_{\text{MSL(MSH)}}$  is the fraction of accepted MSL (MSH) triggered events that pass the Physics Selection.  $F_{\text{pileup}}$  is the pile-up correction factor for MB events (see Sec. 3.1.2 and, Eq. 3.1 and 3.2).

The offline method [269] is implemented by means of the trigger outputs and the Central Trigger Processor (CTP) trigger inputs. The corresponding normalization factor for MSL and MSH triggers is defined as:

$$F_{\text{norm}}^{\text{MSL}} = \frac{N_{\text{MB}} \times F_{\text{pile-up}}}{N_{(\text{MB}\&\&0\text{MSL})}} \quad (3.9)$$

$$F_{\text{norm}}^{\text{MSH}} = \frac{N_{\text{MB}} \times F_{\text{pile-up}}}{N_{(\text{MB}\&\&0\text{MSL})}} \times \frac{N_{\text{MSL}}}{N_{(\text{MSL}\&\&0\text{MSH})}} \quad (3.10)$$

where,  $N_{\text{MB}}$ ,  $N_{\text{MSL}}$  are the number of MB and MSL triggers in the muon trigger sample, 0MSL (= 13) and 0MSH (= 14), as shown in Tab. 3.1, are the ID of the CTP trigger inputs for muon single low (MSL) and muon single high (MSH) triggers. Note that MSL triggered events are used to derive the normalization factor of MSH triggered events since the number of MSH triggered events in the MB sample (CMSH7-B-NOPF-ALLNOTRD, see Tab. 3.1) is too small for a precise determination of the fraction.

It is also necessary to mention that the normalization strategy with scaler and offline methods was also implemented in pp [270] and Pb-Pb analysis [271]. Recently, it was employed for  $J/\Psi$  and  $\Upsilon$  measurements as well as p-Pb collisions [268, 272].

Moreover, there are still other methods to calculate the normalization factor. For example, one can estimate the  $F_{\text{norm}}$  with the MB sample [273],

$$F_{\text{norm}}^{\text{MSL}} = \left( \frac{N_{\text{MB}} \times F_{\text{pile-up}}}{N_{\text{MBinMSL}}} \right)_{\text{MB sample}} \quad (3.11)$$

$$F_{\text{norm}}^{\text{MSH}} = \left( \frac{N_{\text{MB}} \times F_{\text{pile-up}}}{N_{\text{MBinMSH}}} \right)_{\text{MB sample}} \quad (3.12)$$

where,  $N_{\text{MBinMSL}}$  ( $N_{\text{MBinMSH}}$ ) is the number of triggered events containing the string CMSL7(CMSH7)-B-NOPF-ALLNOTRD, i.e. low(high)- $p_{\text{T}}$  muons in the MB sample. The corresponding results are significantly biased by the limited statistics, in particular for LHC13f (Pb-p) since only one run, 196433, is a pure MB sample (see Sec. 3.1.1). Indeed, there are two other MB data samples collected in p-Pb collisions within different periods, LHC13b and LHC13c. One needs to keep in mind that the normalization factor could be different in different data taking periods due to the pile-up, beam-gas contamination, trigger chamber efficiency *etc.* If beam or trigger conditions changes are observed, one can in principle change these normalization factors [274]. Consequently, one should use the information that is directly taken from the desired period such as trigger inputs, see Eq. 3.9 and 3.10. Considering the fact that the muon trigger efficiency does not change, and the beam-gas contamination is small in LHC13d/LHC13e, the normalization factor obtained via the

MB sample LHC13b/LHC13c should not change too much with respect to the one from rare samples LHC13d/LHC13e.

Moreover, one can estimate  $F_{\text{norm}}$  in rare samples via only the trigger output [275] using:

$$F_{\text{norm}}^{\text{MSL}} = \left( \frac{N_{\text{MB}}/C_{\text{MB}} \times F_{\text{pile-up}}}{N_{\text{MBinMSL}}/C_{\text{MBinMSL}}} / C_{\text{MSL}} \right)_{\text{rare sample}} \quad (3.13)$$

$$F_{\text{norm}}^{\text{MSH}} = \left( \frac{N_{\text{MSL}}/C_{\text{MSL}}}{N_{\text{MSH}}} \times \frac{N_{\text{MB}}/C_{\text{MB}} \times F_{\text{pile-up}}}{N_{\text{MBinMSL}}/C_{\text{MBinMSL}}} \right)_{\text{rare sample}} \quad (3.14)$$

where,  $C_{\text{MB}}$ ,  $C_{\text{MSL}}$  and  $C_{\text{MBinMSL}}$  are the downscale factors related to the fired trigger with string CINT7-B-NOPF-ALLNOTRD, CMSL7-B-NOPF-MUON and CMSL7-B-NOPF-ALLNOTRD (Tab. 3.1), respectively. One can see that this is similar to Eq. 3.9 and 3.10.

### 3.1.3.2 Results based on the scaler method

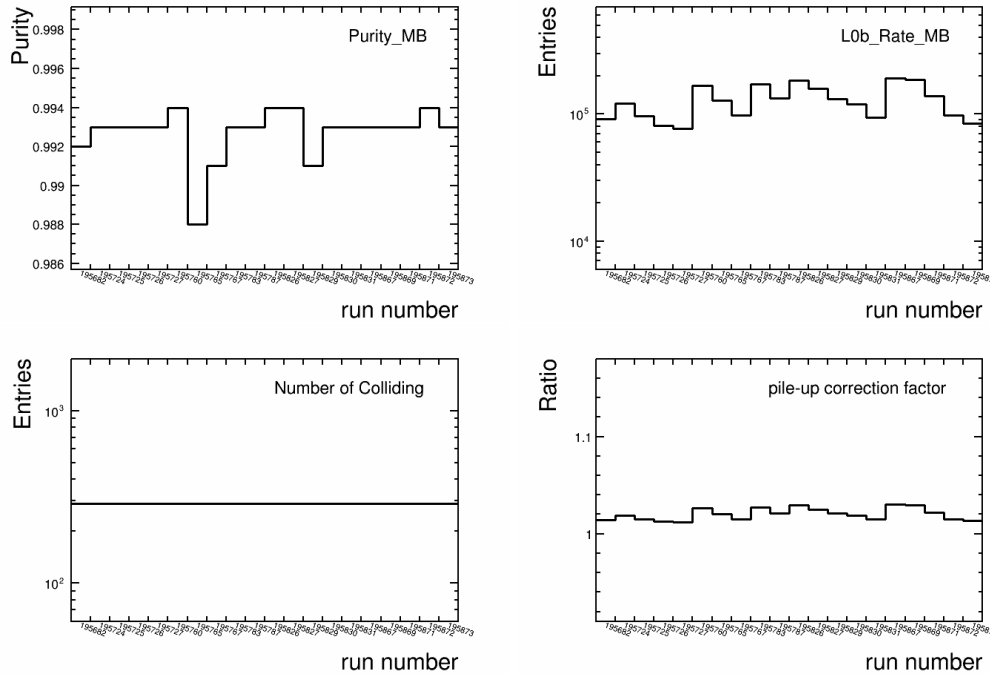


Figure 3.3: Purity (top-left),  $L0bRate_{\text{MB}}$  (top-right) of minimum bias events,  $N_{\text{colliding}}$  (bottom-left) and pile-up correction factor (bottom-right) as a function of run number in **LHC13d** period.

Before discussing the normalization factor results, we need to calculate the pile-up correction factor,  $F_{\text{pile-up}}$ , which is defined in Eq. 3.1 and 3.2. Figure 3.3, 3.4 and 3.5 present  $\text{purity}_{\text{MB}}$  (upper-left),  $L0bRate_{\text{MB}}$  (upper-right),  $N_{\text{colliding}}$  (bottom-left) and pile-up factor (bottom-right) as a function of the run number in LHC13d

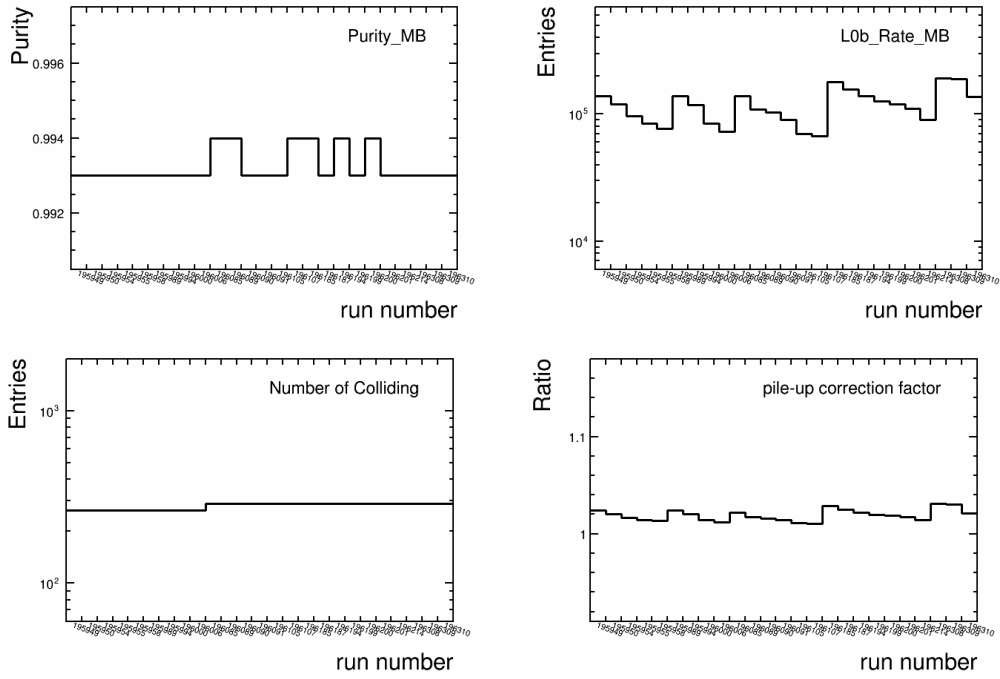


Figure 3.4: Similar with Fig. 3.3 but for **LHC13e** period.

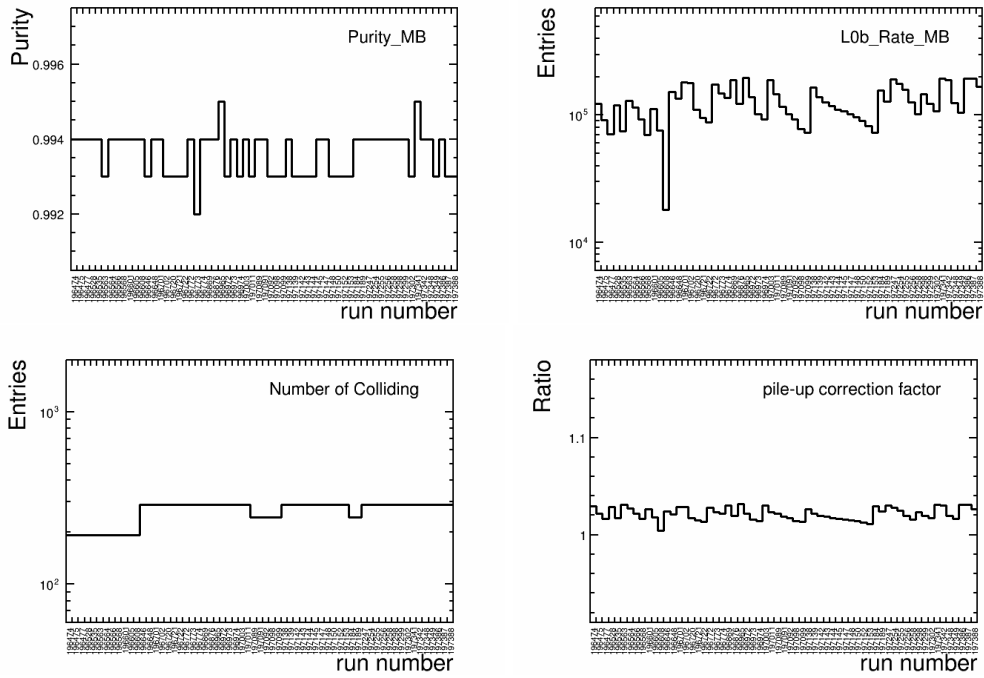


Figure 3.5: Similar with Fig. 3.3 but for **LHC13f** period.

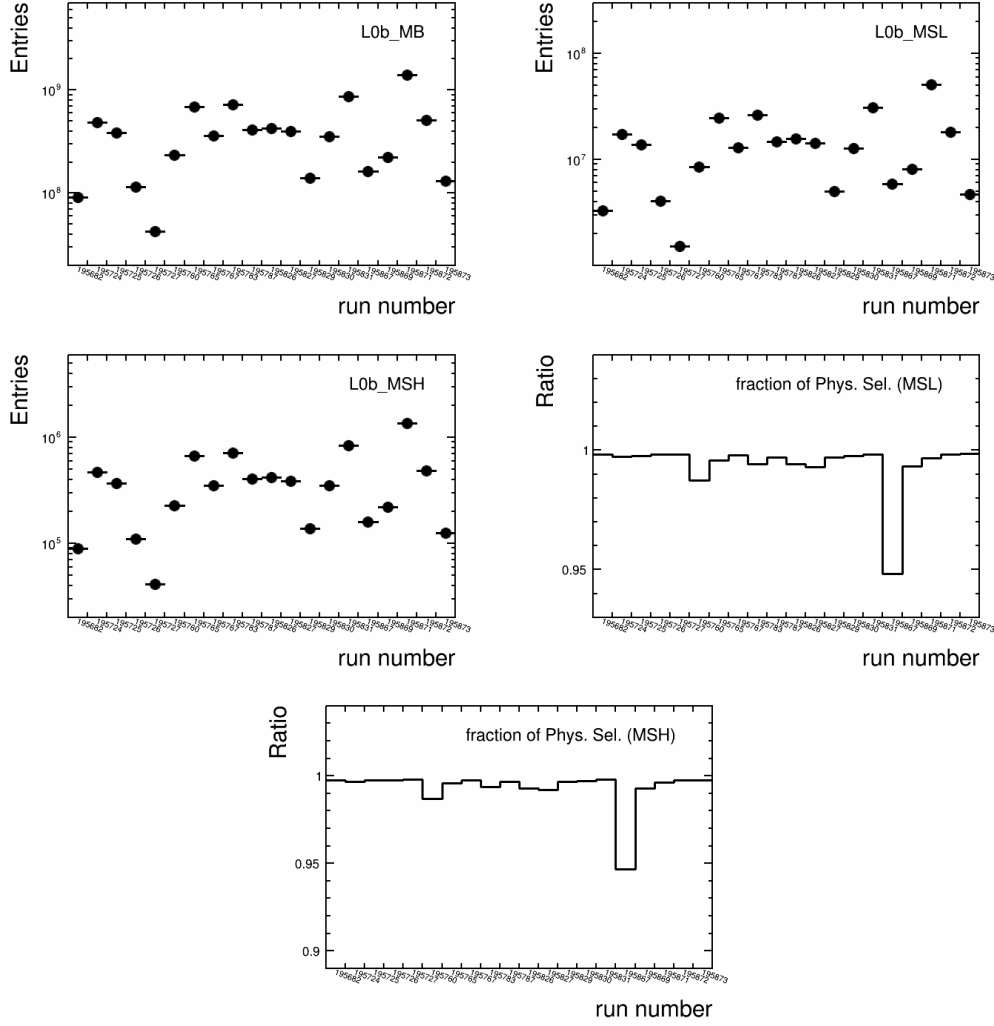


Figure 3.6:  $L0b$  counters information for MB (top-left), MSL (top-middle), and MSH (top-right) trigger events; the fraction of MSL (bottom-left) and MSH (bottom-right) trigger events with Physics Selection in **LHC13d** period.

(p-Pb), LHC13e (p-Pb) and LHC13f (Pb-p), respectively. One can observe that: (1) the *purity* of MB triggered events is better than  $\sim 99\%$  for each run in all periods; (2) the mean value of the pile-up correction factor is  $\sim 1.02 - 1.03$  for all the periods, indicating that the pile-up probability is  $\sim < 3\%$  in multiplicity integrated collisions.

Figures 3.6, 3.7 and 3.8 show the values of  $L0b_{MB}$ ,  $L0b_{MSL}$ ,  $L0b_{MSH}$ ,  $PS_{MSL}$  and  $PS_{MSH}$  that are needed to determine the normalization factors with the scaler method (Eq. 3.8), in LHC13d (forward), LHC13e (forward) and LHC13f (backward) periods, respectively. The fraction of events that pass the physics selection is larger than  $\sim 95\%$  both for MSL and MSH triggered events in all used periods with the exception of one run of LHC13f. The derived normalization factors based on the

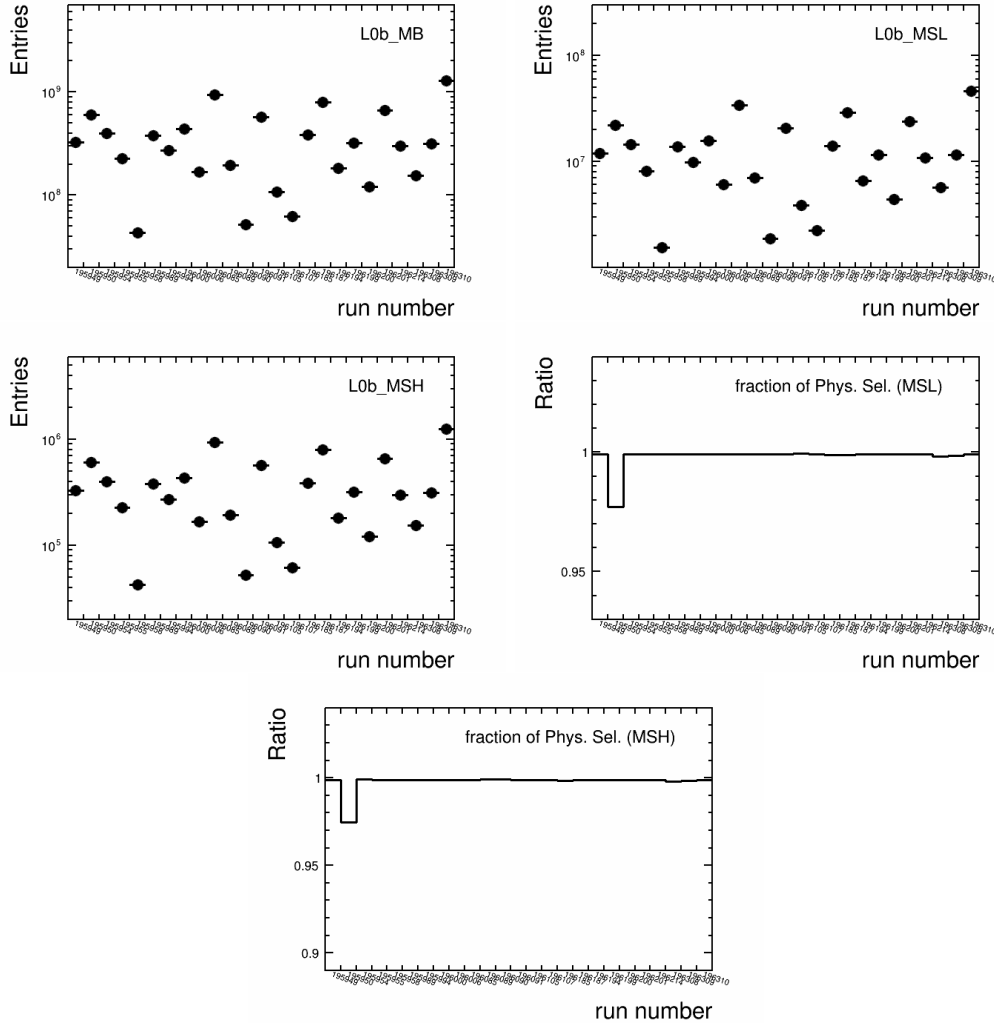


Figure 3.7: Similar to Fig. 3.6 but for **LHC13e** period.

scaler method (Eq. 3.8) are summarized in Fig. 3.9, 3.10 and 3.11 for each run. The vertical bars indicate the statistical uncertainties which take into account the statistical uncertainties on  $L0b_{MB}$ ,  $L0b_{MSL}$  and  $L0b_{MSH}$  scaler inputs. It is found that the obtained  $F_{norm}^{scaler}$  is independent of the run number for a given trigger and period. In addition, the related statistical uncertainties are not significant.

### 3.1.3.3 Results based the offline method

In order to get the normalization factor with the offline method according to Eq. 3.9 and Eq. 3.10, we need to calculate  $N_{MB}$ ,  $N_{MSL}$ ,  $N_{(MB\&\&MSL)}$  and  $N_{(MSL\&\&MSH)}$  as shown in Fig. 3.12, 3.13 and 3.14 for LHC13d (p-Pb), LHC13e (p-Pb) and LHC13f (Pb-p) periods, respectively.

Finally, the normalization factors from the offline method (Eq. 3.9 and Eq. 3.10) are displayed in Fig. 3.15, 3.16 and 3.17 for LHC13d (p-Pb), LHC13e (p-Pb) and

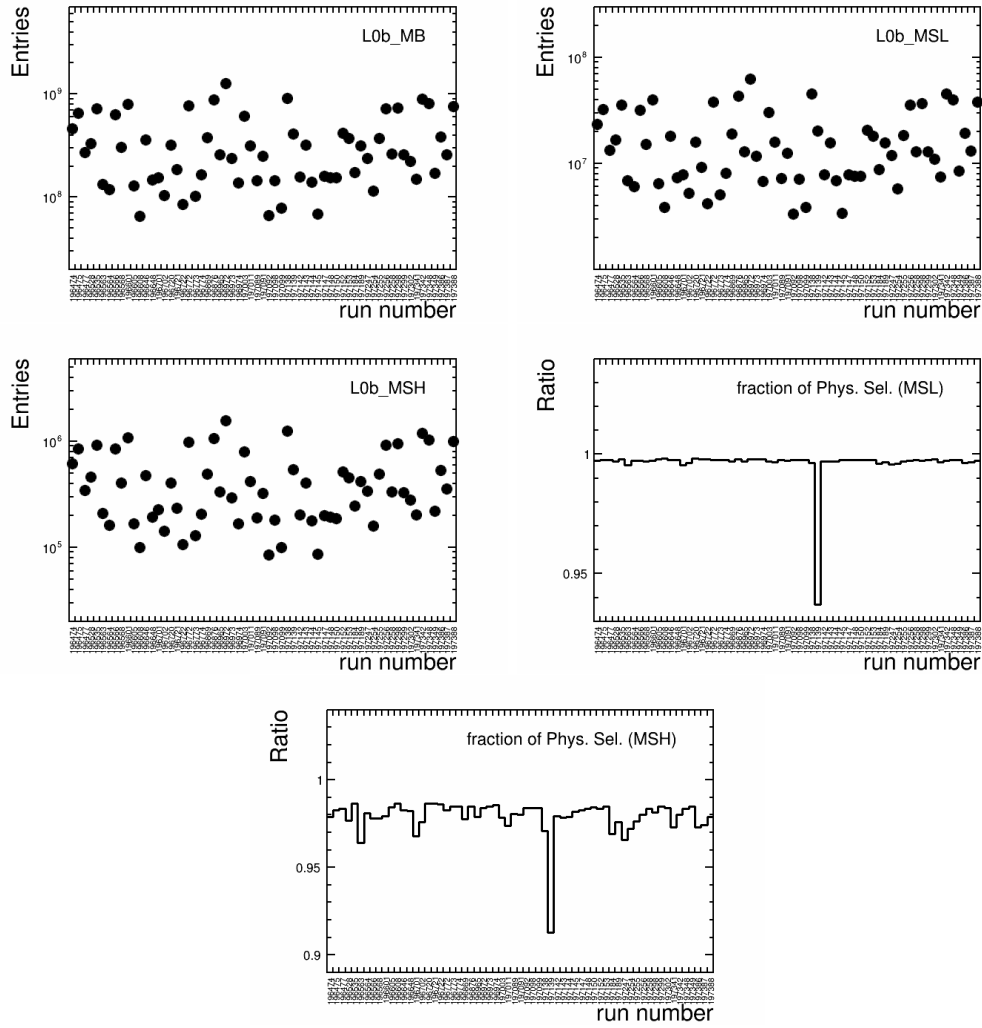


Figure 3.8: Similar to Fig. 3.6 but for LHC13f period.

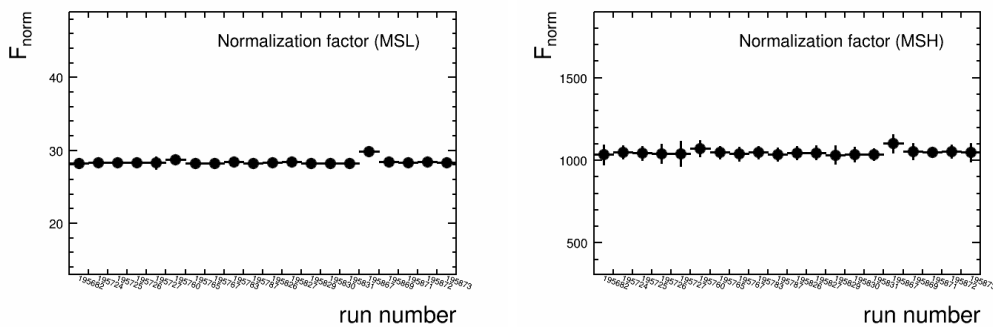


Figure 3.9: Normalization factor from the scaler method for different runs and triggers in LHC13d period: MSL (left) and MSH (right).

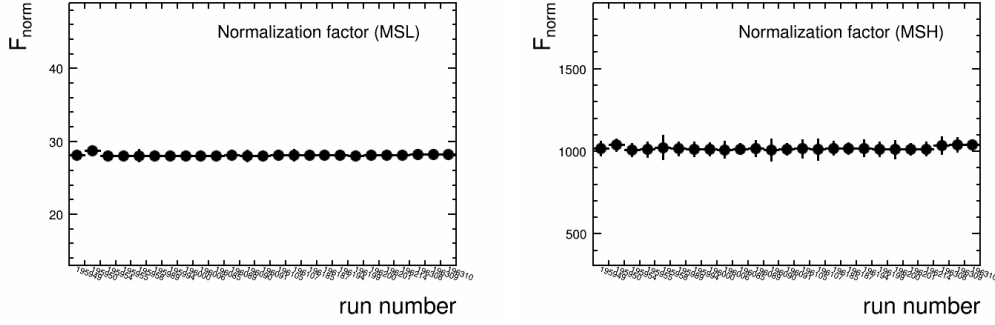


Figure 3.10: Similar to Fig. 3.9 but for LHC13e period.

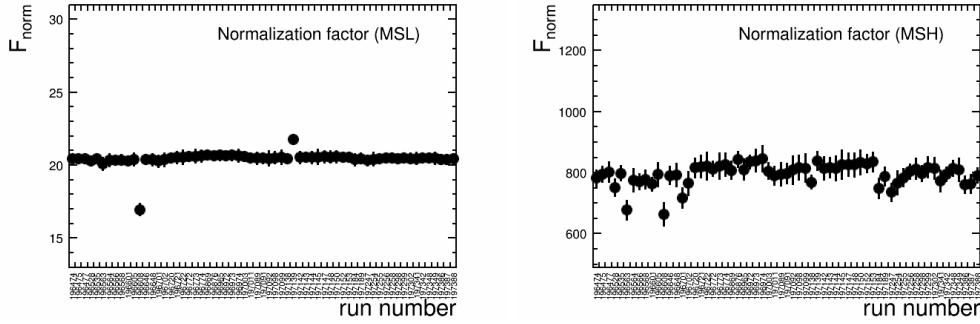


Figure 3.11: Similar to Fig. 3.9 but for LHC13f period.

LHC13f (Pb-p), respectively. The vertical bars are the statistical uncertainties that are obtained from the ones on  $N_{MB}$ ,  $N_{MSL}$ ,  $N_{(MB \& MSL)}$  and  $N_{(MSL \& MSH)}$ . When comparing the statistical uncertainties affecting the results with scaler and offline methods, one can notice that the statistical uncertainties are much larger for the latter method.

### 3.1.3.4 Weighted average of the normalization factor

Once we have calculated the normalization factors with their statistical uncertainty from both scaler and offline methods for different runs and triggers, a weighted average together with the related uncertainties can be determined within two steps. First, we use the statistical uncertainty as a weight [276] to get the average over different methods in the selected run  $i$  as,

$$\bar{F}_{\text{norm}(i)} = \frac{F_{\text{norm}(i)}^{\text{scaler}} \cdot w_{(i)}^{\text{scaler}} + F_{\text{norm}(i)}^{\text{offline}} \cdot w_{(i)}^{\text{offline}}}{w_{(i)}^{\text{scaler}} + w_{(i)}^{\text{offline}}} \quad (3.15)$$

$$\sigma_{\bar{F}_{\text{norm}(i)}}^2 = \frac{1}{\Sigma w} = \frac{1}{w_{(i)}^{\text{scaler}} + w_{(i)}^{\text{offline}}} \quad (3.16)$$

$$w_{(i)} = \frac{1}{\sigma_{(i)}^2} \quad (3.17)$$

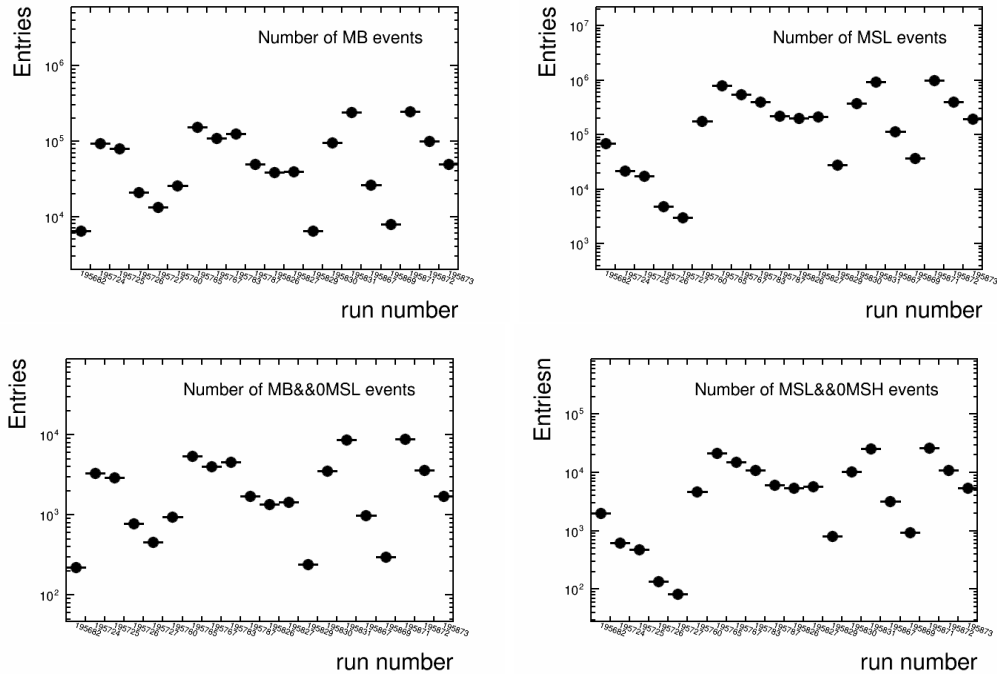


Figure 3.12: Number of MB (upper-left), MSL (upper-right), MB&&MSL (bottom-left) and MSL&&MSH (bottom-right) for different runs in **LHC13d** period.

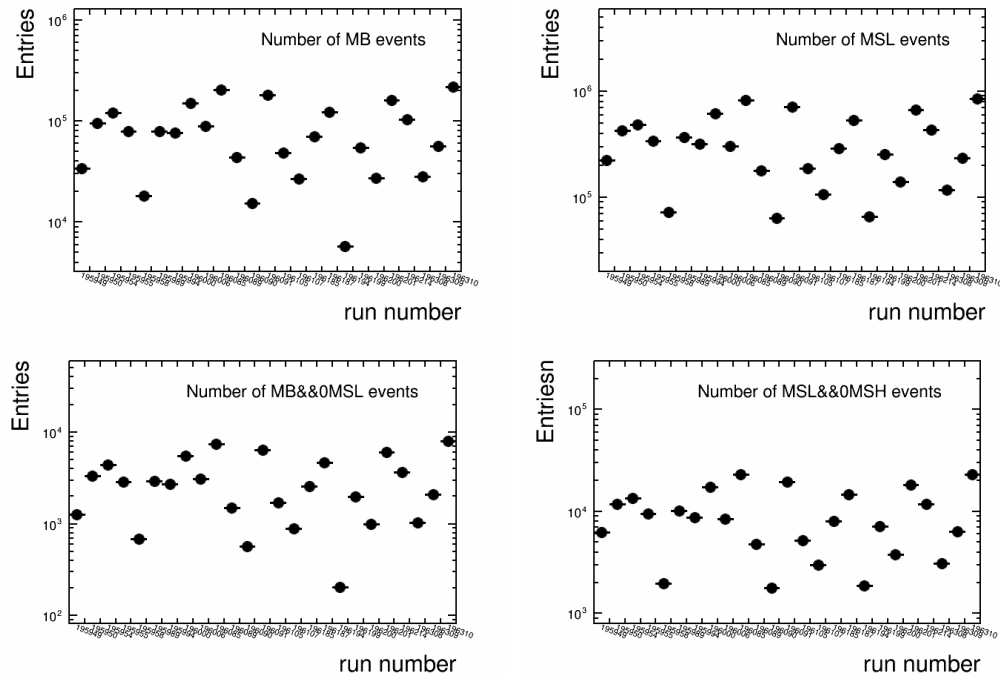


Figure 3.13: Similar to Fig. 3.12 but for **LHC13e** period.

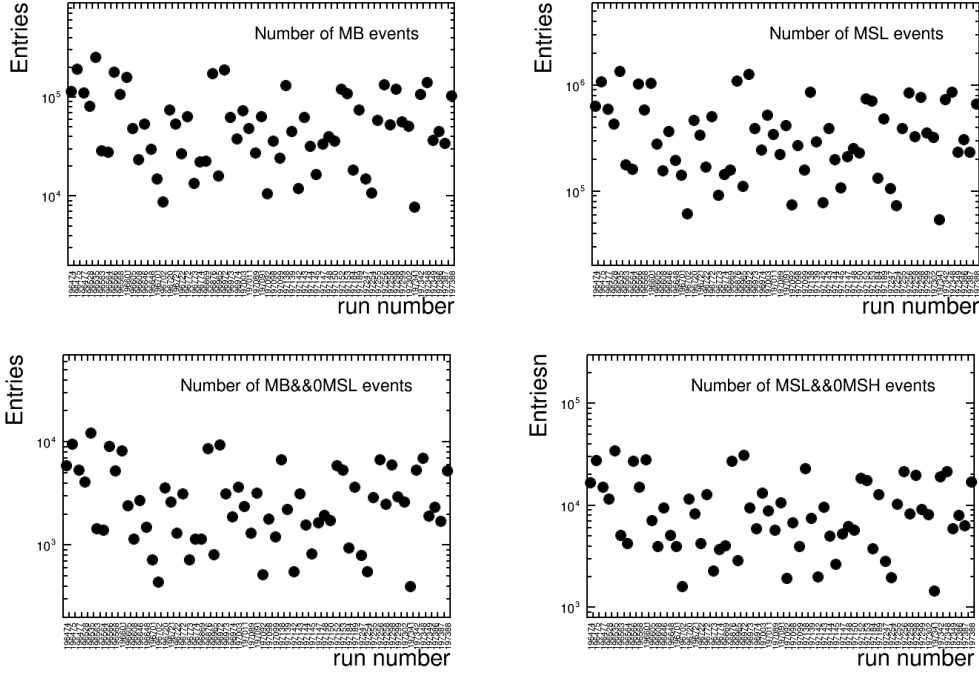


Figure 3.14: Similar to Fig. 3.12 but for **LHC13f** period.

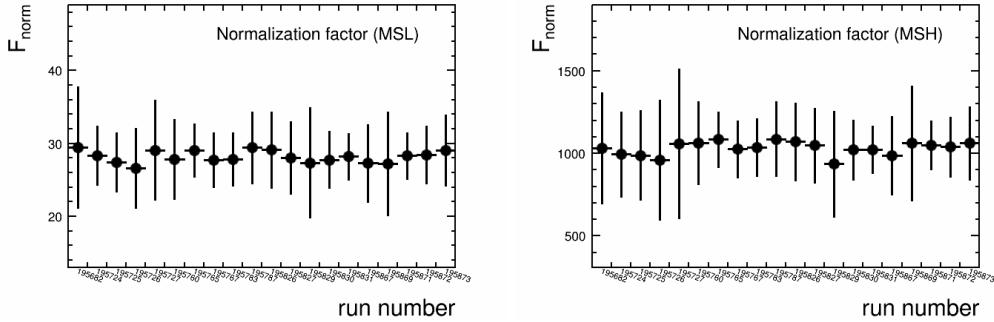


Figure 3.15: Normalization factor from the offline method for different runs and triggers in **LHC13d** period: MSL (left) and MSH (right.)

$$d_{(i)} = \frac{F_{\text{norm}(i)}^{\text{offline}} - F_{\text{norm}(i)}^{\text{scaler}}}{F_{\text{norm}(i)}^{\text{offline}}} \quad (3.18)$$

where,  $F_{\text{norm}(i)}$  and  $\sigma_{(i)}$  are the normalization factor and the related statistical uncertainty for a given run  $i$  with the employed method;  $w_i$  is the related weight;  $d_{(i)}$  is the deviation between the methods. Then, the number of desired trigger events (MSL or MSH) within a run  $i$  is taken as the weight to get the average over runs,

$$\bar{F}_{\text{norm}} = \frac{\sum_i^{\text{Runs}} \bar{F}_{\text{norm}(i)} \cdot W_{(i)}}{\sum_i^{\text{Runs}} W_{(i)}} \quad (3.19)$$

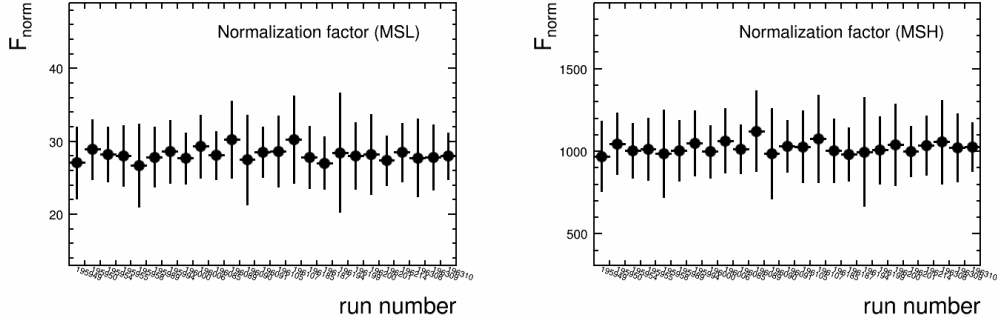


Figure 3.16: Similar to Fig. 3.15 but for **LHC13e** period.

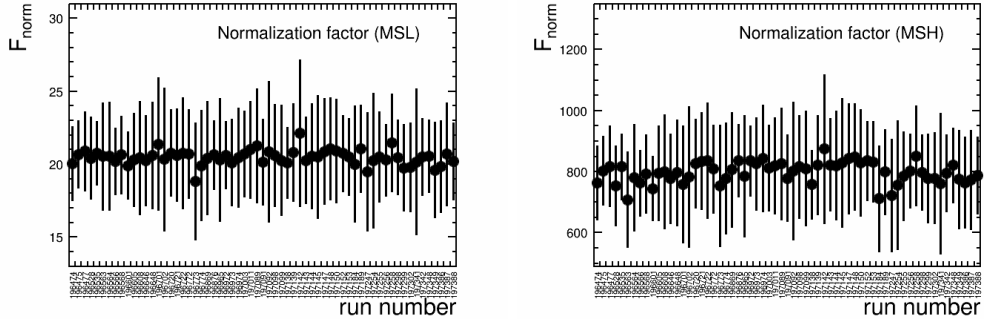


Figure 3.17: Similar to Fig. 3.15 but for **LHC13f** period.

$$\sigma_{\bar{F}_{\text{norm}}} = \frac{\sum_i^{\text{Runs}} \sigma_{\bar{F}_{\text{norm}(i)}} \cdot W_i}{\sum_i^{\text{Runs}} W_i} \quad (3.20)$$

with

$$W_i = N_{\text{MSL/MSH}(i)} \quad (3.21)$$

and

$$d = \frac{\sum_i^{\text{Runs}} d_{(i)} \cdot W_i}{\sum_i^{\text{Runs}} W_i} \quad (3.22)$$

where,  $\bar{F}_{\text{norm}}$  is the final weighted average of the normalization factor;  $\sigma_{\bar{F}_{\text{norm}}}$  and  $d$  are the related statistical and systematic uncertainty, respectively;  $W_i$  is the weight defined as the number of MSL or MSH events within a selected run  $i$ . The values of  $\bar{F}_{\text{norm}(i)}$  and  $d_{(i)}$  are shown in Fig. 3.18 and 3.19 for LHC13d and LHC13e periods (p–Pb collisions) and LHC13f period (Pb–p collisions), as a function of run number. It is worth to mention that the final weighted mean, as well as the systematic uncertainty are displayed in the last bin of each plot. The related results are also summarized in Tab. 3.3, as  $\bar{F}_{\text{norm}} \pm \text{stat.}\% \pm \text{syst.}\%$ , where  $\text{stat.}\% = \sigma_{\bar{F}_{\text{norm}}}/\bar{F}_{\text{norm}}$  and  $\text{syst.}\% = d/\bar{F}_{\text{norm}}$  denote the relative statistical and systematic uncertainty, respectively. We quote 1% as the systematic uncertainty on the normalization procedure for MSL and MSH at both forward and backward rapidity.

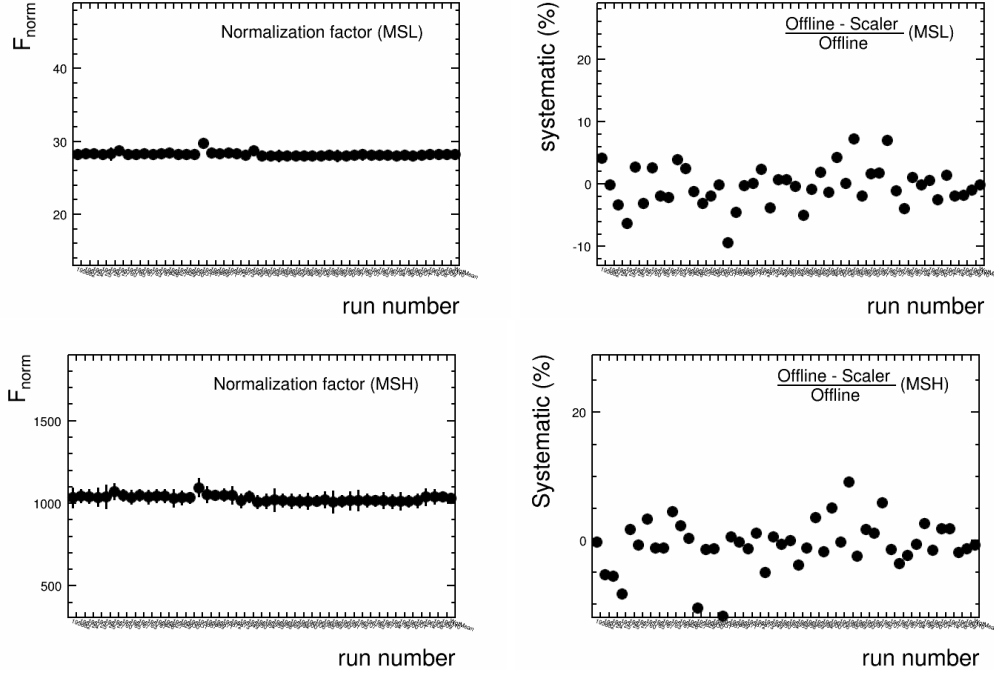


Figure 3.18: Weighted mean of the normalization factor with the statistical uncertainty and systematic uncertainty for different runs and triggers in **LHC13d** and **LHC13e** periods: mean value for MSL trigger events with statistical uncertainty (top-left) and corresponding systematic uncertainty (top-right); mean value for MSH trigger events with statistical uncertainty (bottom-left) and corresponding systematic uncertainty (bottom-right).

$\bar{F}_{\text{norm}}$ (0 – 100%)	p–Pb (forward rapidity) ( <i>mean</i> $\pm$ <i>stat.</i> % $\pm$ <i>syst.</i> %)	Pb–p (backward rapidity) ( <i>mean</i> $\pm$ <i>stat.</i> % $\pm$ <i>syst.</i> %)
MSL	$28.20 \pm 0.32\% \pm 0.52\%$	$20.49 \pm 0.24\% \pm 0.33\%$
MSH	$1032.77 \pm 0.67\% \pm 1.09\%$	$798.33 \pm 0.55\% \pm 0.35\%$

Table 3.3: Normalization factor and the related uncertainties obtained in p–Pb and Pb–p collisions with MSL and MSH. See text for details.

### 3.1.3.5 Integrated luminosity

With the normalization factor  $\bar{F}_{\text{norm}}$ , one can get the integrated luminosity  $\mathcal{L}$  as

$$\mathcal{L} = \frac{\bar{F}_{\text{norm}} \cdot N_{\text{MSL/MSH}}}{\sigma_{\text{MB}}} \quad (3.23)$$

where,  $\sigma_{\text{MB}}$  is the MB trigger cross section in p–Pb collisions at  $\sqrt{s_{\text{NN}}} = 5.02$  TeV. In this analysis, the used results of  $\sigma_{\text{MB}}$  are obtained with the V0-based method, which has  $\sim 1\%$  deviation with respect to the one based on T0 [277].  $\sigma_{\text{MB}}$  is measured with the van der Meer scans [277], and  $\sigma_{\text{MB}} = 2.09 \pm 0.07$  b ( $\sigma_{\text{MB}} = 2.12 \pm 0.07$  b) for p–Pb (Pb–p) collisions. Tab. 3.4 shows the values of integrated luminosity of the

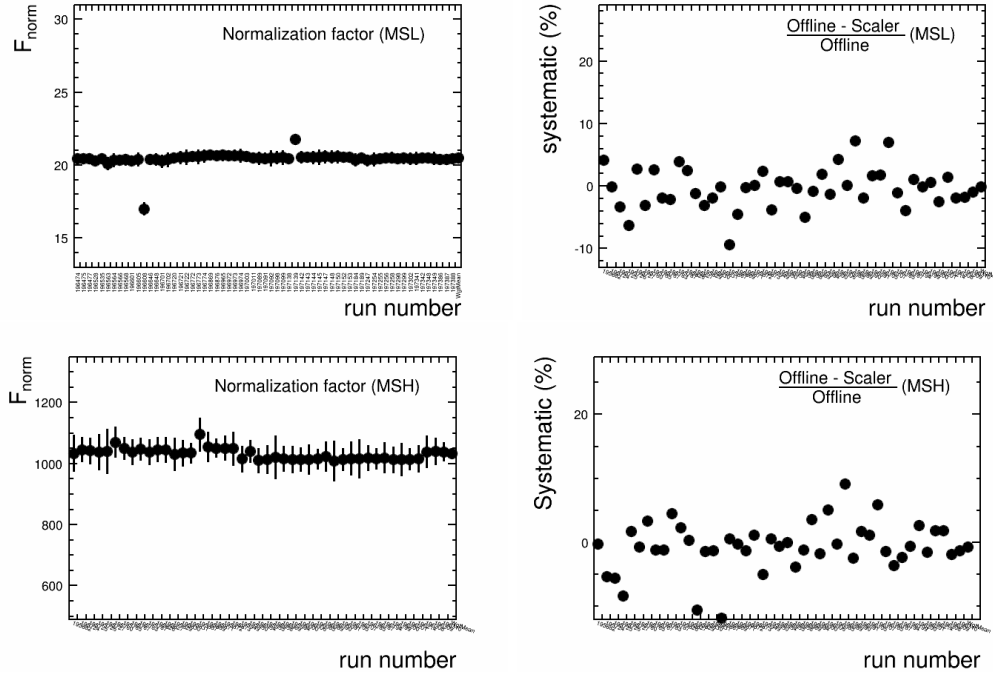


Figure 3.19: Similar to Fig. 3.18 but for LHC13f period.

used data samples. One can find that they are smaller than the results presented in Ref. [278], due to the event selection implemented in the analysis.

Integrated Luminosity ( $\mathcal{L}$ ) $\mu b^{-1}$	p-Pb collisions (forward rapidity)	Pb-p collisions (backward rapidity)
MSL	196	254
MSH	4900	5800

Table 3.4: Integrated luminosity in p-Pb and Pb-p collisions with MSL and MSH. See text for details.

In addition, after the muon selection at track level, one can cross check the  $p_T$  spectra normalized to the number of (equivalent) MB events:  $(\frac{1}{N_{MB}} \cdot \frac{dN}{dp_T})$ ,  $(\frac{1}{F_{norm}^{MSL} \cdot N_{MSL}} \cdot \frac{dN}{dp_T})$  and  $(\frac{1}{F_{norm}^{MSH} \cdot N_{MSH}} \cdot \frac{dN}{dp_T})$ . The above distributions are expected to be consistent within the overlap  $p_T$  regions among them if the efficiency correction is applied. See Sec. 3.2.1 for details.

## 3.2 Muon Track Selection

In this section, I focus on the discussion about the various muon selection cuts applied at track level, in particular the effect of trigger matching and  $p \times DCA$  cuts.

Muon tracks are required, firstly, to be reconstructed within the acceptance of the muon spectrometer ( $-4 < y_{LAB} < -2.5$ ) and to have a polar angle at the

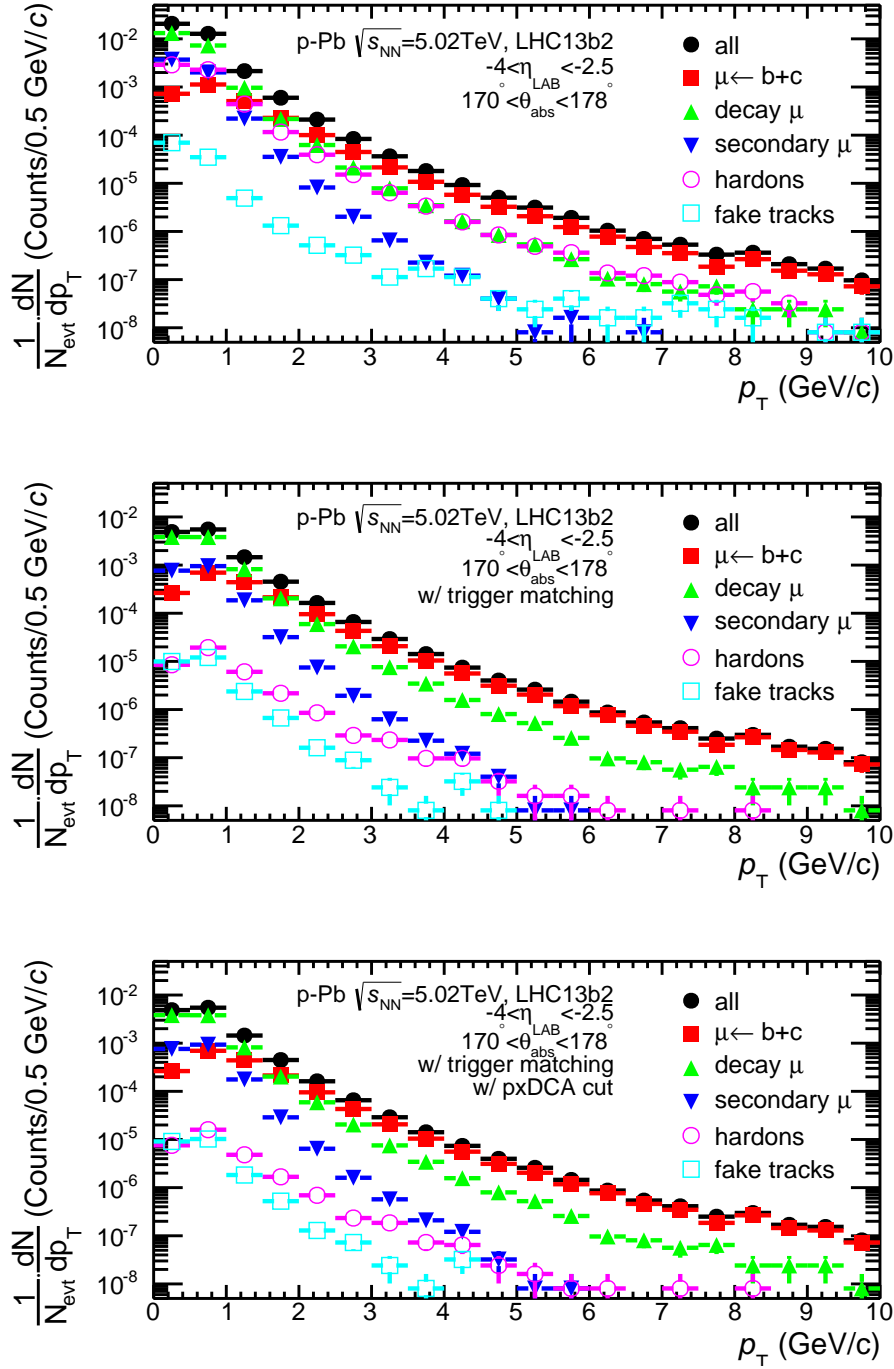


Figure 3.20: Trigger matching and  $p \times \text{DCA}$  cut effect on different muon sources with Monte Carlo simulations ("LHC13b2\_efix" that is the full simulation with DPMJET model). Upper:  $p_T$  spectra of various muon sources after the muon event selection (Sec. 3.1.1) and the tracks within the acceptance of the muon spectrometer. Middle: similar as upper one, but with adding trigger matching cut. Bottom: in analogy to the middle one, but with adding  $p \times \text{DCA}$  cut.



end of the absorber in the interval  $170^\circ < \theta_{\text{abs}} < 178^\circ$ . One also requires that the track candidate in the tracking system (i.e. tracker track) matches the track reconstructed in the trigger system (i.e. trigger track). This selection can reject effectively, not only the hadrons that cross the front absorber, but also the tracks with low energy, mainly corresponding to the particles generated in the absorber (i.e. secondary muons). Finally, the  $p \times \text{DCA}$  cut within  $6 \sigma$  (to be discussed in Sec. 3.2.2) was applied in order to remove further beam-induced background and particles produced in the absorber. The  $p \times \text{DCA}$  is discussed in detail in Sec. 3.2.2.

Figure 3.20 shows the trigger matching and  $p \times \text{DCA}$  cut effects on different muon sources using a MC production (LHC13b2\_efix) with the DPMJET generator for p–Pb collisions at  $\sqrt{s_{\text{NN}}} = 5.02$  TeV. In the upper panel, one can see the normalized  $p_{\text{T}}$  spectra of muons from different sources. The standard event selection cuts have been implemented. Additionally, the geometrical and acceptance cuts are also considered. One can see that punch-through hadron contribution (i.e. the hadrons going through the front absorber) is very large and similar to the one of  $\mu$  from primary  $K^\pm/\pi^\pm$  decays (i.e. primary decay muons). It can be rejected efficiently with the trigger matching cut, as shown in the middle panel of Fig. 3.20. In addition, the low energy particles such as secondary muons generated in interactions with the absorber, as well as fake tracks (i.e. tracks that are not associated to one single particle crossing the whole spectrometer;  $< 1\%$  for  $p_{\text{T}} > 2$  GeV/ $c$ ) are also strongly suppressed by about one order of magnitude in the low  $p_{\text{T}}$  region. In the bottom panel, we apply an additional  $p \times \text{DCA}$  cut in order to remove further fake tracks. Note that the  $p \times \text{DCA}$  cut is powerful to remove beam-gas background (not existing in Monte-Carlo). The related effect is not visible since the fake track contribution is negligible after the matching requirement. These conclusions confirm the results of the previous performance studies [42], together with the ones of pp simulations at  $\sqrt{s} = 7$  TeV [42, 194].

### 3.2.1 Track Selection

#### 3.2.1.1 Statistics after each selection cut

Table 3.5 summarizes the statistics of the used data after each selection cut, as well as the rejection percentage for different triggered events within different periods in the multiplicity-integrated sample. It is realized that the primary vertex reconstruction cut rejects almost no track for both MSL and MSH trigger samples within different periods ( $< 0.2\%$ ); the matching between tracker track and trigger track rejects more statistics in Pb–p (backward) with respect to the one in p–Pb (forward). Similar conclusion is found for the  $p \times \text{DCA}$  cut effect. It indicates that more punch-through hadrons and/or low energy particles are produced in Pb–p than in p–Pb collisions. The effect is more visible with MSH triggered events since a higher  $p_{\text{T}}$  range is accessible.

The effect of the employed cuts on the measured  $p_{\text{T}}$  distributions of inclusive muons is shown in Fig. 3.21 for MSL triggered events. One can observe that the cuts have different effects in p–Pb (forward) and Pb–p (backward) collisions, which

	LHC13d and LHC13e (Rej.%)		LHC13f (Rej.%)	
	MSL	MSH	MSL	MSH
+ Phys. Sel.	10.2M	6.8M	16.4M	8.8M
+ Cent. QA	10.1M (0.2%)	6.8M (0.3%)	16.3M (0.2%)	8.6M (2.6%)
+ Vtx. Sel	10.1M (0.1%)	6.8M (0.1%)	16.3M (0.1%)	8.6M (0.2%)
+ $\eta_{\text{LAB}}$	9.4M (7.0%)	6.3M (7.3%)	15.0M (8.1%)	7.7M (10.6%)
+ $\theta_{\text{abs}}$	9.4M (0.5%)	6.3M (0.5%)	14.9M (0.8%)	7.6M (1.0%)
+ TrM.	8.2M (12.6%)	3.6M (42.3%)	12.1M (18.8%)	3.4M (55.5%)
+ $p \times \text{DCA}$	8.2M (0.1%)	3.6M (0.5%)	12.0M (0.3%)	3.3M (3.6%)

Table 3.5: Summary of the extracted statistics after applying various selection cuts at track level: physics selection, centrality QA, primary vertex reconstruction, acceptance cut ( $\eta_{\text{LAB}}$ ), polar angle limitation ( $\theta_{\text{abs}}$ ), trigger matching and the correlation between momentum and DCA ( $p \times \text{DCA}$ ). See text for details.

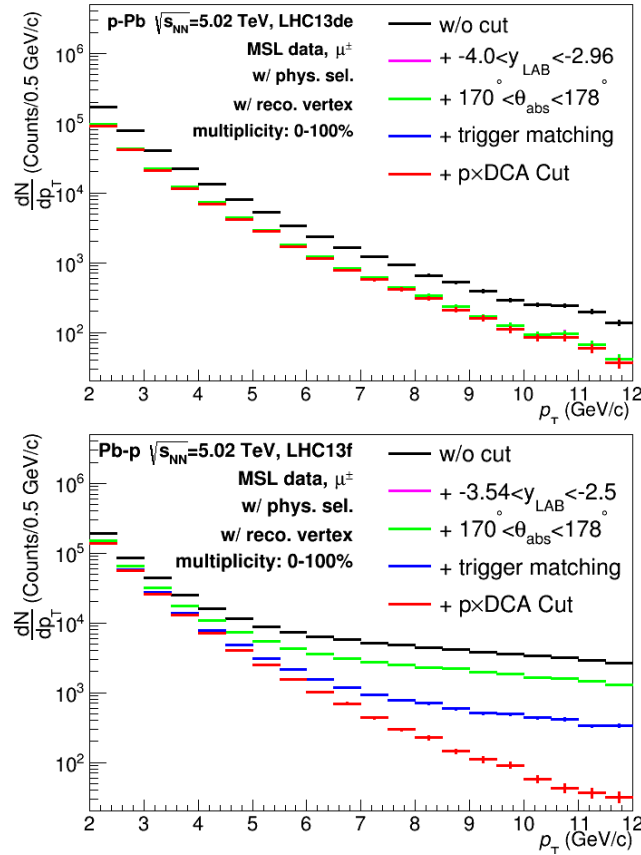


Figure 3.21: Transverse momentum distributions of inclusive muons with different selection cuts at event and track level in p-Pb (left) and Pb-p (right) collisions.



are presented in the left and right panel, respectively. This can be explained by the beam-induced background contamination which is more pronounced in Pb–p than in p–Pb collisions, since the data samples in p–Pb collisions was collected first, then the orbits of the projectile and target beams were inverted without shutdown of the detector. Moreover, the beam-induced background is larger in MSH than that in MSL, see Tab. 3.5, since a higher  $p_T$  can be investigated, where the beam-gas contribution is large.

### 3.2.1.2 Charge Asymmetry

Considering that muons with opposite charge signs behave differently in the magnetic field region, one can think that a ratio defined as the  $p_T$  spectrum of  $\mu^+$  to that of  $\mu^-$ , the so-called *Charge Asymmetry*, is not consistent with unity due to the fact that it changes with opposite trends for the inverting field. It is interesting to check it in the considered data periods. The *Charge Asymmetry* obtained in LHC13d, LHC13e and LHC13f periods is shown in the upper, middle and bottom of Fig. 3.22, respectively. The results of different triggers are shown with different colors: MB (black), MSL (green) and MSH (red). It is found that MSH results are different with respect to the ones of MB and MSL in the three periods. This could be due to the  $p_T$  threshold effect. So, it is better to focus in the high  $p_T$  region, for example, in the range  $10 < p_T < 16$  GeV/ $c$ , where the  $p_T$  threshold effect is expected to be small. In MSH triggered events in LHC13d, the ratio is larger than unity, while it is close to unity in MSL triggered events.

Moreover, the *Charge Asymmetry* with MSH in LHC13d is different compared the ones in LHC13e and LHC13f periods, which are smaller than unity in the  $p_T$  range  $10 < p_T < 15$  GeV/ $c$ . This behavior could be caused by the change in the polarity of magnetic field from LHC13d to LHC13e/LHC13f. Note that the *Charge Asymmetry* can also be affected by the tracking efficiency and the mis-alignment effect.

### 3.2.1.3 Normalized spectra with different triggers

As mentioned in Sec. 3.1.3.5, the normalization procedure can be cross checked with normalized  $p_T$  spectra for muon trigger samples, and then, comparing with the corresponding results for MB-triggered events after efficiency correction (see Sec. 3.4). They are expected to be consistent within the overlap  $p_T$  regions. Fig. 3.23 shows the obtained results for combined periods LHC13d and LHC13e (forward, p–Pb). The normalized  $p_T$  spectrum for MB (black) is displayed up to 4 GeV/ $c$  due to the limited statistics, while the MSL (red) and MSH (green) results are shown up to 13 and 16 GeV/ $c$ , respectively. The number of equivalent MB events,  $N_{\text{equi. MB}}^{\text{MSL/MSH}}$ , is calculated as,

$$N_{\text{equi. MB}}^{\text{MSL/MSH}} = \bar{F}_{\text{norm}}^{\text{MSL/MSH}} \cdot N_{\text{MSL/MSH}} \quad (3.24)$$

where,  $\bar{F}_{\text{norm}}^{\text{MSL/MSH}}$  is the normalization factor for MSL or MSH triggered events (Tab. 3.3).

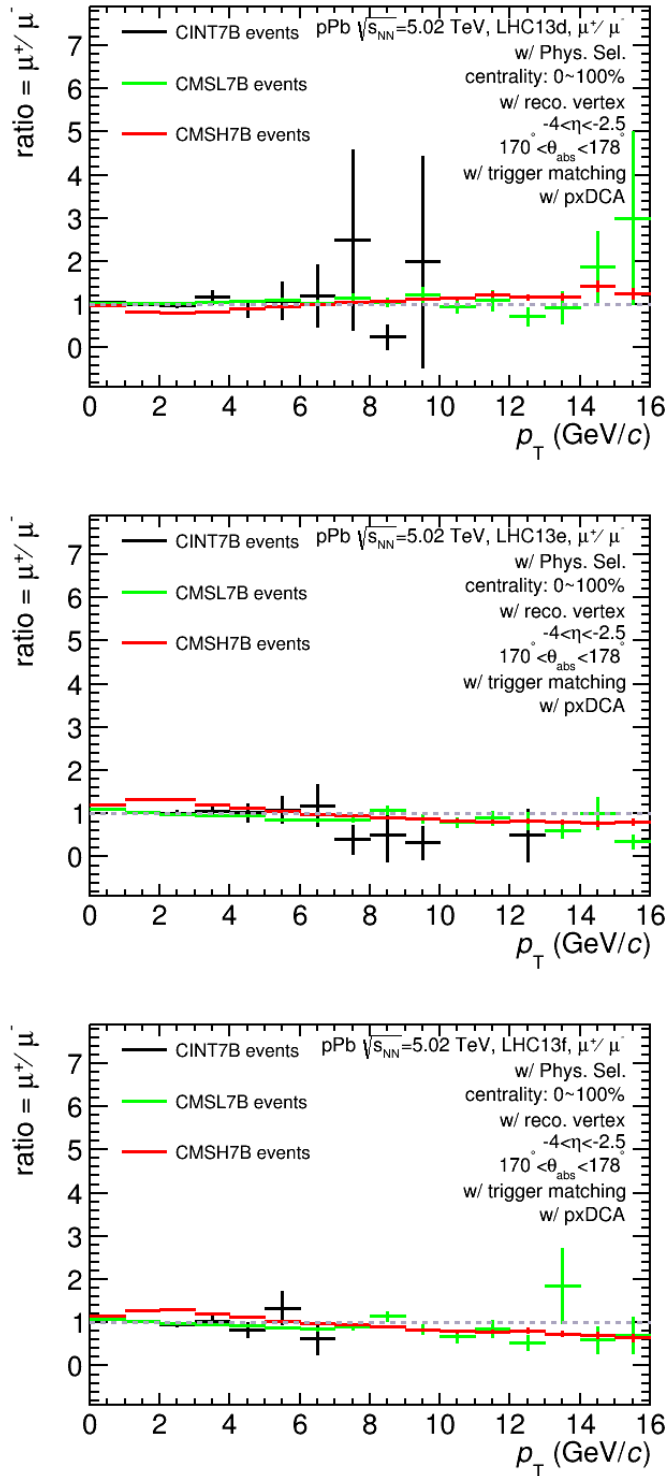


Figure 3.22: Muon *Charge Asymmetry* obtained with different triggers and data samples after the standard procedure of selection is applied: LHC13d (upper), LHC13e (middle) and LHC13f periods (lower). Results from different triggers are shown as the curves with different color in each plot: MB (black), MSL (green) and MSH (red).

In the left panel of Fig. 3.23, one can see the distributions up to  $p_T = 16$  GeV/c. The ratios between them within the overlap  $p_T$  regions are shown in the right panel to make a clear comparison. It is found that the ratios are consistent with unity within uncertainties. Similar behavior can be observed for LHC13f period (backward, Pb-p), see Fig. 3.24 for details.

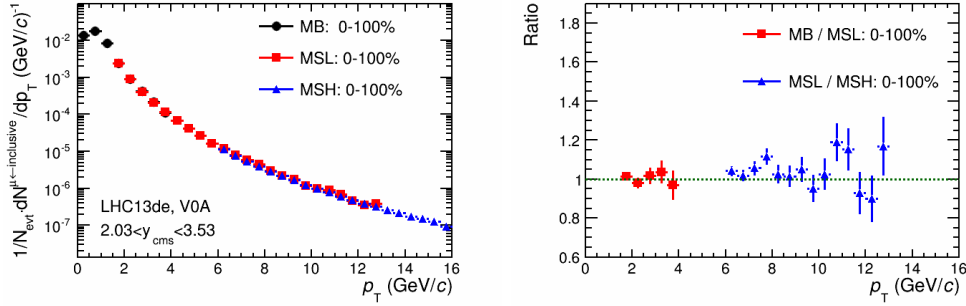


Figure 3.23: Left:  $p_T$  spectra for different triggers with **LHC13d** and **LHC13e** periods normalized to the number of (equivalent) MB events in the range  $2.03 < y_{\text{CMS}} < 3.53$ , and the used normalization factor is from Tab. 3.3. The results for different triggers are shown as the curves with different colors: MB (black), MSL (red) and MSH (green). Right: ratio of the normalized spectra for different triggers within the overlap  $p_T$  regions: MB/MSL (black) and MSL/MSH (red). Note that only statistical uncertainties are shown.

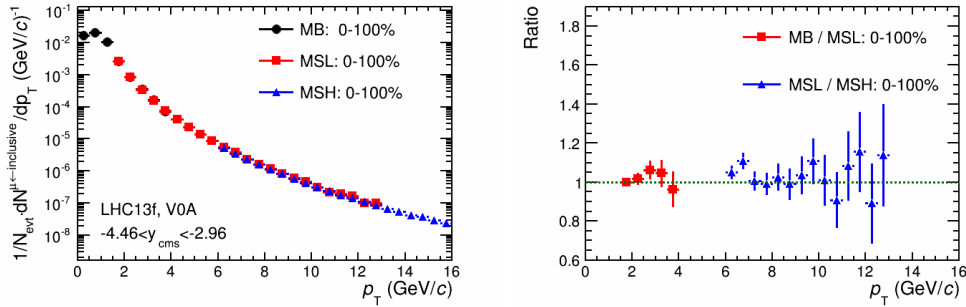


Figure 3.24: Similar with Fig. 3.23 but for **LHC13f** period in the range  $-4.46 < y_{\text{CMS}} < -2.96$ .

## 3.2.2 Detailed study of the $p \times \text{DCA}$ cut

### 3.2.2.1 Short history of the variable $p \times \text{DCA}$

The beam-gas induced background is produced by interaction of the high-energy projectile and target particles with the residual gas in the beam tube. The beam-gas contribution is mainly located in the high  $p_T$  region, as well as for large DCA values. In order to separate this component, the  $\eta - \theta_{\text{abs}}$  correlation cut was first proposed [279] (since a sharp cut on DCA cannot achieve the aim efficiently), and

then the further improvement was done by considering the position of primary vertex [280].

On the other hand, one can separate the punch-through hadrons from muons by studying the multiple Coulomb scattering effect in the front absorber. As introduced in Sec. 1.3.2, the small deflection angle of entering charged particles induced by Coulomb scattering can be roughly described by a Gaussian distribution, and the RMS of the deflection angle is shown as Eq. 1.15.

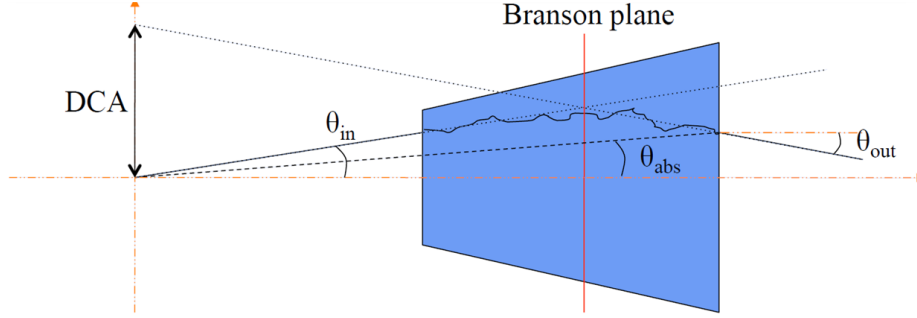


Figure 3.25: Quantities used to describe the multiple scattering with the front absorber. See text for details. Figure taken from Ref. [281].

Figure 3.25 shows the Coulomb scattering of a particle traversing the absorber. The  $\theta_{\text{in}}$  and  $\theta_{\text{out}}$  are the polar angles of the input and output particles, while  $\theta_{\text{abs}}$  is the one related to the absorber. For a given momentum, it is known that  $\sigma_{\text{DCA}} \propto \sigma_{\theta_{\text{deflect}}} \equiv \sigma_{(\theta_{\text{out}} - \theta_{\text{in}})} \propto \sigma_{(\theta_{\text{abs}} - \theta_{\text{in}})} \propto 1/p$  [281]. Based on this relation, the variables  $p \times (\theta_{\text{abs}} - \theta_{\text{in}})$  and  $p \times \text{DCA}$  were proposed and validated to separate fake tracks in MC and remaining punch-through hadrons in data (after the physics selection procedure). Finally, the  $p \times \text{DCA}$  cut with further improvement including momentum resolution and track slope resolution is considered [282], and the related deviation is given as [42],

$$p \times \text{DCA} \equiv p_{\text{CMS}} \times \text{DCA}_{\text{calib}} < N \cdot \sigma_{p \times \text{DCA}} \quad (3.25)$$

$$\sigma_{p \times \text{DCA}} = \sqrt{[(1 + p_{\text{CMS}} \cdot n \cdot \Delta_m) \sigma_{\text{meas}}(p \times \text{DCA})]^2 + (p_{\text{CMS}} \cdot L_{\text{trk}} \cdot \Delta_s)^2} \quad (3.26)$$

where,  $p_{\text{CMS}} = \frac{1}{2}(p_{\text{trk}} + p_{\text{vtx}})$  is the momentum of a incident particle suffering scattering, where  $p_{\text{vtx}}$  is the momentum of the incident particle corrected for the energy loss induced by the absorbers and the multiple-scatterings by means of the Badier-Branson plane (Sec. 2.4.3), and  $p_{\text{trk}}$  is the momentum without any correction;  $\text{DCA}_{\text{calib}}$  is the DCA variable relative to the reconstructed vertex position;  $N$  is the cut on  $p \times \text{DCA}$  set by user (which is 6, as default, in p-Pb collisions);  $n$  is introduced to cut off the momentum resolution in  $n \cdot \Delta_m$ , normally one can set  $n \simeq N$ ;  $\Delta_m$  is the momentum resolution coming from the sagitta for the track momentum determination;  $\sigma_{\text{meas}}(p \times \text{DCA})$  is the measured deviation of the variable  $p \times \text{DCA}$ , which does not change significantly among different periods;  $L_{\text{trk}} = 535$

cm is the distance between the primary vertex and the first tracking chamber;  $\Delta_s$  is the slope resolution of the reconstructed track. One can see that the implementation of the  $p \times \text{DCA}$  cut is not straightforward and it depends on parameters which have to be determined for each reconstructed track. Its resolution can change with time. Moreover, according to a performance study, it has been shown [42] that the  $p \times \text{DCA}$  cut will almost not reject the signals (i.e. muons from heavy-flavour hadron decays).

### 3.2.2.2 Impact on the p–Pb data

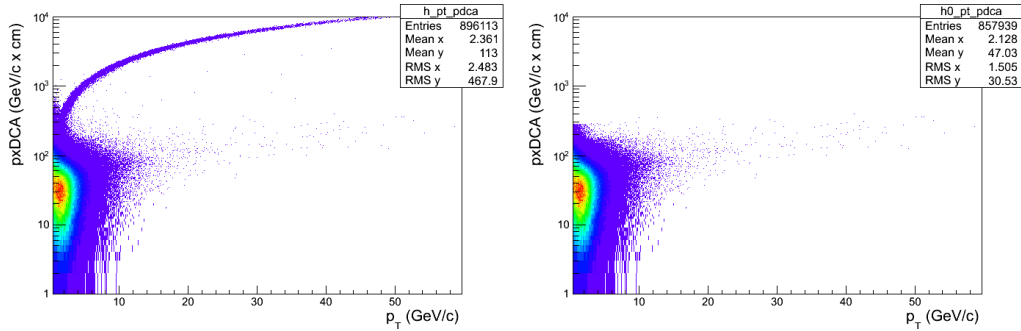


Figure 3.26: Left: the corrected  $p \times \text{DCA}$  distribution as a function of  $p_T$  with MSH in LHC13f period (Pb–p, not full statistics). Right: similar results but applying an additional cut on  $6 \cdot \sigma_{p \times \text{DCA}}$ .

In order to check the  $p \times \text{DCA}$  cut effect in the p–Pb analysis, we have studied the  $p \times \text{DCA}$  distribution as a function of  $p_T$  (Fig. 3.26). In the left panel, one can see the obtained results for MSH triggers in the period LHC13f (Pb–p) without the  $p \times \text{DCA}$  cut. There is a visible tail extending to high  $p_T$  located in the region with large  $p \times \text{DCA}$ . When applying the  $p \times \text{DCA}$  cut at  $6 \cdot \sigma_{p \times \text{DCA}}$ , the distributions shown in the right panel of Fig. 3.26 is obtained, indicating that the tail can be rejected by the adopted  $p \times \text{DCA}$  cut. Based on this performance study, it is known that particles with large  $p \times \text{DCA}$  are mainly formed by the high energetic hadrons, consequently, the tail in data is dominated by the beam-gas component, which can be separated from muons via the correlation between momentum and DCA ( $p \times \text{DCA}$ ).

We can also check the validity of the cut by varying the default  $p \times \text{DCA}$  cut ( $6 \cdot \sigma_{p \times \text{DCA}}$  in p–Pb collisions). In the left panel of Fig. 3.27, we show the comparison of the inclusive muon distributions (for MSL-triggered events in the period LHC13d, i.e. p–Pb collisions) with and without the  $p \times \text{DCA}$  cut. Note that, (1) various scenarios of the  $p \times \text{DCA}$  cut are used ( $N \cdot \sigma_{p \times \text{DCA}}$ ,  $5 < N < 7$ ); (2) the standard selection cuts are applied at both event and track level; (3) the related acceptance  $\times$  efficiency correction is implemented for each  $p \times \text{DCA}$  cut, and there is almost no difference among them. Within the statistical uncertainties, similar results are observed and the different scenarios present consistent results in the range  $p_T > 1$  GeV/c. However, a significant rejection in LHC13f period (Pb–p, right) is observed with increasing  $p_T$ . Finally, the different results in LHC13d (p–Pb) and LHC13f (Pb–p) indicate, as mentioned before, that the beam-gas contribution is much larger

in the Pb–p sample, in particular in the high  $p_T$  region.

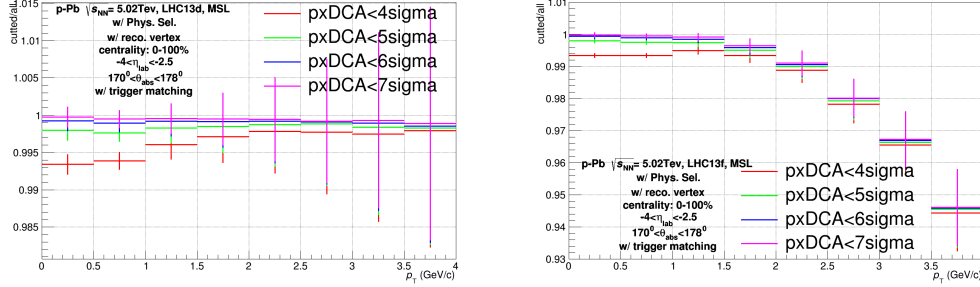


Figure 3.27: Ratio of the  $p_T$  spectra with different scenarios of the  $p \times$  DCA cut with respect to the ones without  $p \times$  DCA cut: MSL results for LHC13d (left) and LHC13f (right). The standard muon selection cuts are implemented. Figures provided by Z. M. Zhang.

### 3.3 Event Activity Classification

#### 3.3.1 The Strategies

Since initial/final-state effects are expected to vary as a function of the impact parameter of the collision ( $\vec{b}$ , 2-dim vector connecting the centers of the two colliding nuclei), it is crucial to measure the centrality-dependence of various observables, and to categorize each event according to its centrality. In order to study the scaling of particle production with the collision geometry, one needs to determine in each centrality class  $N_{\text{coll}}$  and/or  $N_{\text{part}}$ , which are the number of nucleon-nucleon collisions and the number of participant nucleons in the interaction, respectively.

Concerning the definition of centrality, the scenarios are different between model and data. In models, one can obtain the centrality percentile,  $c$ , via Optical Glauber Model [35], which is based on the pure geometry of the impact parameter,

$$c = \frac{\int_0^b db' \cdot d\sigma/db'}{\int_0^\infty db' \cdot d\sigma/db'} = \frac{1}{\sigma_{\text{AA}}} \cdot \int_0^b db' \cdot \frac{d\sigma}{db'} \quad (3.27)$$

where,  $b$  is the impact parameter,  $\sigma_{\text{AA}}$  is the hadronic cross section in A–A collisions;  $\frac{d\sigma}{db}$  is the differential interaction cross section and  $c$  is the centrality class expressed as "X-Y%" ("X" and "Y" denote the corresponding range of the fraction of the interaction cross section). The corresponding geometrical variables ( $N_{\text{coll}}$  and  $N_{\text{part}}$ ) can be obtained as well (see Ref. [35] and Chap. 4 for details).

The centrality classification can also be implemented in data based on observables (such as the multiplicity of the produced particles or energy of spectator nucleons) that are related to the centrality of the collision. For example in ALICE, the centrality can be defined as the percentile of the hadronic cross section exploiting the multiplicity distribution in the V0 [258]. The most central events correspond to

those at high multiplicity, so  $N_{\text{ch}} > N_{\text{ch}}^{\text{THR}}$ . Equivalently,

$$c \approx \left( \frac{1}{\sigma_{\text{AA}}} \cdot \int_{N_{\text{ch}}^{\text{THR}}}^{\infty} \frac{d\sigma}{dN'_{\text{ch}}} dN'_{\text{ch}} \right)_{V0} \approx \left( \frac{1}{\sigma_{\text{AA}}} \cdot \int_0^{E_{\text{T}}^{\text{THR}}} \frac{d\sigma}{dE'_{\text{T}}} dE'_{\text{T}} \right)_{\text{ZDC}} \quad (3.28)$$

Note that the Anchor Point (AP) is a key parameter. It is defined as the amplitude of signal in the V0 detector equivalent to 90% of the hadronic cross section (in Pb–Pb collisions at  $\sqrt{s_{\text{NN}}} = 2.76$  TeV [258]), which determines the absolute scale of the centrality. This means that the percentile of the hadronic cross section can be determined for any value of the V0 amplitude by integrating the measured V0 amplitude distribution normalized at the anchor point  $V0_{\text{AP}}$  such as 90% of the hadronic cross section in the Pb–Pb case. Note that this 90% determines the absolute scale of the centrality, which requires the knowledge of trigger efficiency and the remaining background contamination in nuclear collision events [258]. One can stop the centrality classification task here without requiring the related geometrical variables. **To determine the relationship between charged-particle multiplicity and the collision properties, such as the impact parameter  $b$ , number of participating nucleons  $N_{\text{part}}$ , binary nucleon-nucleon collisions  $N_{\text{coll}}$ , or nuclear overlap function  $T_{\text{AA}} = N_{\text{coll}}/\sigma_{\text{NN}}^{\text{inel}}$ , where  $\sigma_{\text{NN}}^{\text{inel}}$  is the inelastic nucleon-nucleon cross section, it is customary to use the Glauber Monte-Carlo model combined with a simple model for particle production.**

The general idea is shown in Fig. 3.28 where the centrality is defined by binning the charged-particle distribution within a selected range in order to obtain the desired fraction of the total integral. The geometrical variables in a given centrality class are calculated by means of the MC Glauber Model [35]. One can reproduce the measured distribution of charged-particles with the ones of ancestors, which are defined as the objects allowed to emit independently, i.e. sources of particles in MC Glauber. The distributions of ancestors are quantified by the NBD (Negative Binomial Distribution), which was able to describe the charged-particle multiplicity,  $d\sigma/dN_{\text{ch}}$ , measured over a wide range of rapidity in pp and p $\bar{p}$  collisions at high energy [258]. As shown in Ref. [258, 283], the NBD-derived distributions together with a set of parameters are optimized to well describe the data. Therefore, the obtained distributions allow one to obtain the colliding geometry from the Glauber model.

In this case, a given centrality class, defined by sharp cuts in the measured charged-particle multiplicity with V0, corresponds to the same class in the simulated distribution. One can calculate the mean value of impact parameter  $\langle b \rangle$ , the mean number of participants  $\langle N_{\text{part}} \rangle$ , the mean number of binary collisions  $\langle N_{\text{coll}} \rangle$  and the average nuclear overlap function  $\langle T_{\text{AA}} \rangle = \langle N_{\text{coll}} \rangle / \sigma_{\text{NN}}^{\text{inel}}$  for centrality classes defined by sharp cuts in the simulated multiplicity distribution, corresponding to given percentiles of the hadronic cross section. Note that the basic assumption underlying this procedure is that the impact parameter  $b$  is monotonically related to particle multiplicity, both at mid- and forward rapidity.

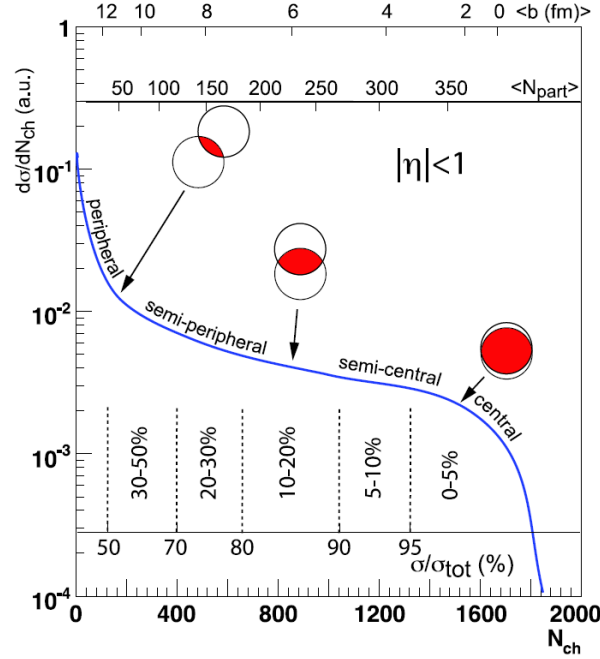


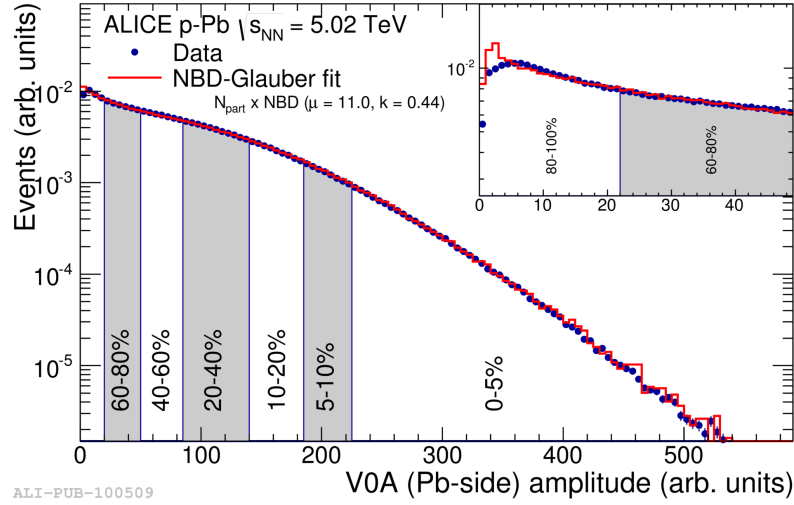
Figure 3.28: A cartoon example of the correlation of the final state observable  $N_{ch}$  with Glauber calculated quantities ( $b$ ,  $N_{part}$ ). The plotted distribution and various values are illustrative and not actual measurements. Figure taken from Ref. [35].

### 3.3.2 Multiplicity in p–Pb collisions

Figure 3.29 shows the measured charged-particle multiplicity with V0A in p–Pb collisions at  $\sqrt{s_{NN}} = 5,02$  TeV, as well as the reproduced distribution modeled by the NBD-Glauber model (explained in the text). Based on these results, one can get the geometrical variables based on the method shown above for Pb–Pb collisions.

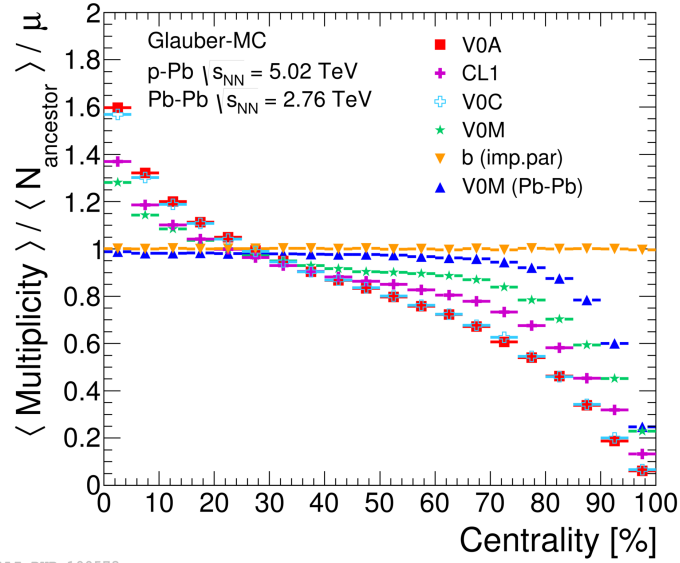
Finally, it is found [283] that the centrality defined in p–Pb collisions is more affected by multiplicity fluctuations than in Pb–Pb collisions. The ratio of the averaged multiplicity per average participant divided by the mean multiplicity of the NBD, is proposed to quantify the fluctuations, as presented in Fig. 3.30. The defined ratio should be consistent with unity in case of unbiased results. However, the result indicates a positive (negative) bias in central (peripheral) events for p–Pb collisions, much larger when comparing with the ones obtained in Pb–Pb collisions, where the correlation between multiplicity and number of participant nucleons is narrow, and multiplicity fluctuations are small, so that only the most peripheral events are biased [283].

As illustrated in Fig. 3.31, the sizeable bias in p–Pb collisions is induced by the loose correlation between the observed charged-particle multiplicity and the desired geometrical variables ( $b$ ,  $N_{part}$  and  $N_{coll}$ ), which is not the case in Pb–Pb collisions. Considering the large fluctuations in p–Pb collisions, a centrality classification of the events based on the multiplicity may select a sample of nucleon-nucleon collisions which is biased compared to a sample defined by cuts on the impact parameter



ALI-PUB-100509

Figure 3.29: Distribution of the sum of amplitudes in the V0A hodoscopes (backward, Pb-going), as well as the NBD-Glauber fit; centrality classes are indicated by vertical lines. The inset shows a zoom-in on the most peripheral events. Figure taken from Ref. [283].



ALI-PUB-100573

Figure 3.30: Multiplicity fluctuation bias calculated from the NBD-Glauber MC as the ratio between mean multiplicity per ancestor and the mean NBD multiplicity in p-Pb and Pb-Pb calculations. Note that, CL1 ( $|\eta| < 1.4$ ) denotes the clusters measured in the 2<sup>nd</sup> layer of Silicon Pixel detector, V0A ( $2.8 < \eta < 5.1$ ) is the amplitude measured by the V0 hodoscopes on the A-side (the Pb-remnant side), V0M is the sum of V0A ( $2.8 < \eta < 5.1$ ) + V0C ( $-3.7 < \eta < -1.7$ ) and ZNA is the energy deposited in Zero-Degree Neutron calorimeter on the A-side. Figure taken from Ref. [283].

$b$  [283]. Since the results depend on the centrality estimator, one defines "event activity" rather than "centrality" in p–Pb collisions [283].

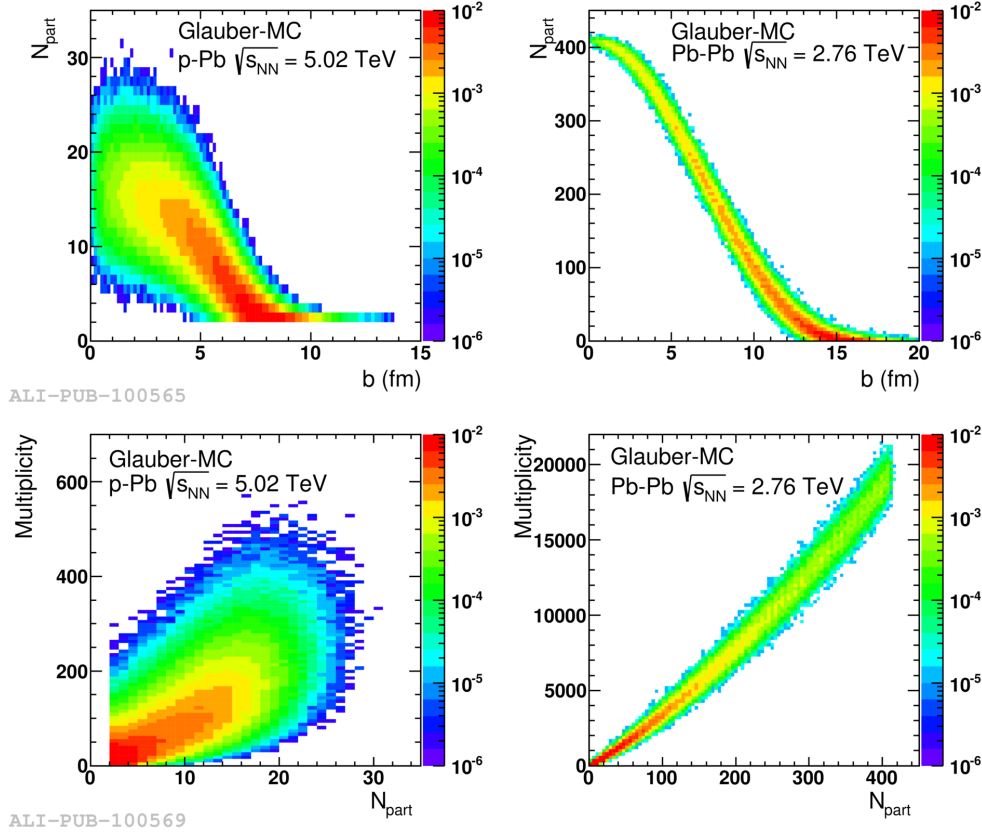


Figure 3.31: Top: number of participating nucleons versus impact parameter. Bottom: multiplicity versus the number of participating nucleons from the Glauber fit to V0A amplitude. The quantities are calculated with a Glauber Monte Carlo for p–Pb (left) and Pb–Pb (right) collisions. Figures taken from Ref. [283].

### 3.3.3 Event Activity Dependence in p–Pb Muon Triggered Events

In this sub-section, I introduce the "event activity" determination, including flatness of MB events, effect of pile-up, and normalization.

#### 3.3.3.1 Number of MB events versus event activity

Figure 3.32 shows the number of MB events in LHC13de (forward, p–Pb collisions) scaled by the event activity interval width as a function of the event class. The results of different estimators are displayed as the curves with different colors: V0A (black), CL1 (red) and ZNA (green). In the left panel, one can see the results based on the OADB (Offline Analysis Data Base) parameters extracted from LHC13b and LHC13c periods: the results observed in the most peripheral bin 60 – 100% drop due to the event activity resolution which is bad in this region; V0A results behave

as expected (i.e. flat in the range 0 – 60%) which is not the case with ZNA/CL1 in the 0 – 5% bin. Further studies with the ZNA using conditions from LHC13d and LHC13e periods, are presented in the right panel of Fig. 3.32, while the results based on V0A and CL1 are not updated. The flatness for ZNA is improved as expected, in particular in the 0 – 5% multiplicity bin. Further discussions can be found in Sec. 3.3.3.2. More detailed information can be found in Ref. [284].

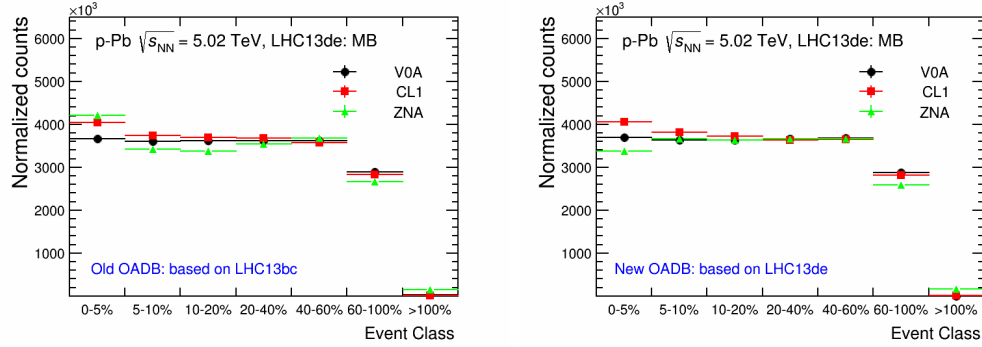


Figure 3.32: Number of MB events scaled with the bin width versus event activity: OADB (Offline Analysis Data Base) based on LHC13bc (left) and LHC13de (right). See text for details.

### 3.3.3.2 Effect on normalization

In Sec. 3.1.3, we discussed in detail the normalization strategy in multiplicity integrated collisions. Based on these results, two scenarios can be used for the normalization procedure within different event activity classes.

Based on the weighted average of the normalization factor (Tab. 3.3), the **first scenario** is proposed by assuming a completely flat behavior of the corresponding number of equivalent MB events when plotted as a function of event activity. In this case, the number of equivalent MB events within a given activity bin,  $x\%$ , is obtained as

$$N_{\text{MB}}^{x\%} = N_{\text{MB}}^{0-100\%} \cdot \frac{x}{100} = \bar{F}_{\text{norm}}^{0-100\%} \cdot N_{\text{MSL/MSH}}^{0-100\%} \cdot \frac{x}{100} \quad (3.29)$$

where,  $\bar{F}_{\text{norm}}^{0-100\%}$  is the normalization factor given in Tab. 3.3;  $N_{\text{MSL/MSH}}^{0-100\%}$  is the number of MSL/MSH events in multiplicity integrated collisions. Subsequently, one can define a "equivalent" normalization factor,  $\bar{F}_{\text{norm}}^{x\%}$ , within a given activity bin,  $x\%$ , as,

$$\bar{F}_{\text{norm}}^{x\%} = \frac{N_{\text{MB}}^{x\%}}{N_{\text{MSL/MSH}}^{x\%}} \quad (3.30)$$

This scenario was the one adopted for the study of the production of  $J/\Psi$  and  $\Upsilon$  in p–Pb collisions [268, 272].

On the other hand, one can determine the normalization factor within a given activity interval using the same procedure described for the 0–100% interval (Eq. 3.9 and 3.10). This is the "scenario 2" in the following.

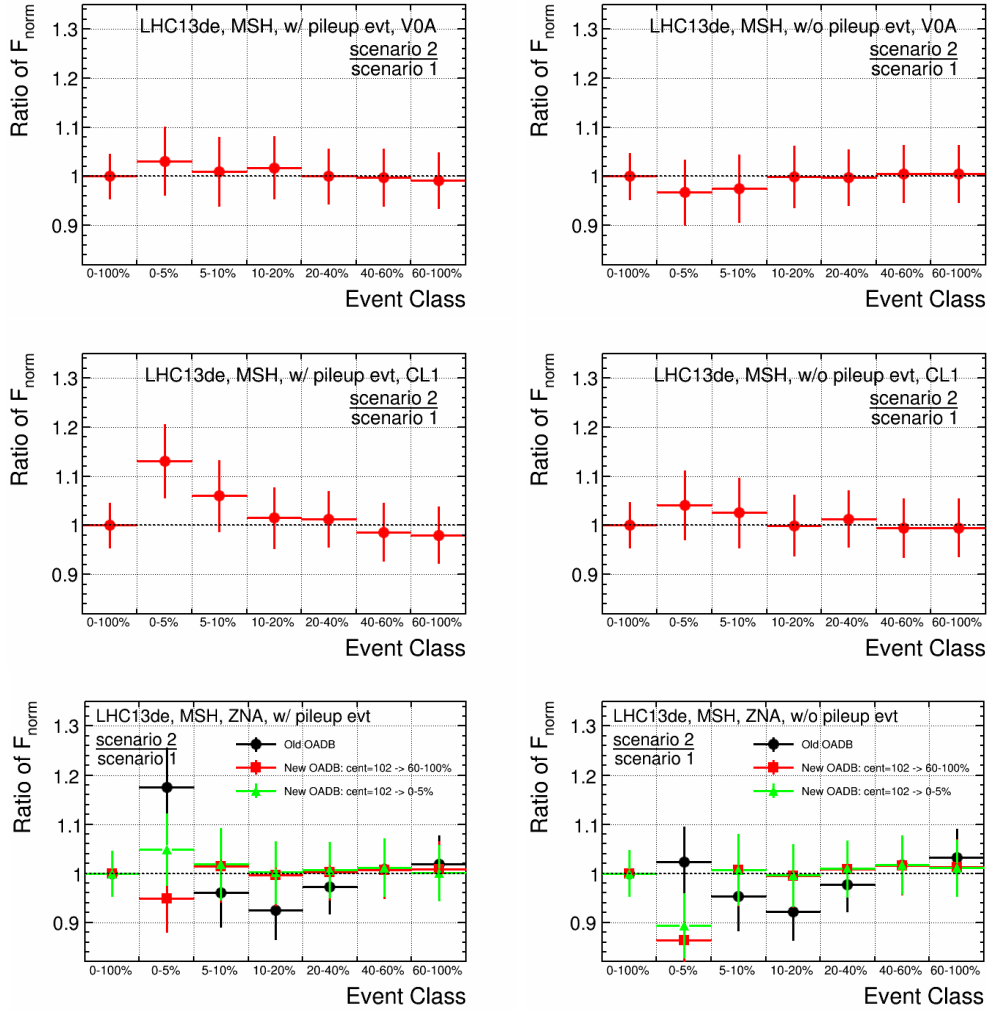


Figure 3.33: Ratio ( $=\text{scenario2}/\text{scenario1}$ ) of the normalization factors from different scenarios versus event activity and estimator. The left three plots are the results including pile-up events, while the right three are the ones excluding pile-up events. The upper, middle and bottom two plots are the results based on V0A, CL1 and ZNA, respectively. Concerning the results with ZNA, various scenarios are implemented. See the text for detail.



A comparison between the two scenarios is shown in Fig. 3.33 for MSH triggered events and, LHC13d and LHC13e periods. In each panel, we present the ratio of the normalization factor obtained from scenario 2 to that from scenario 1. The vertical bars indicate the combined statistical and systematic uncertainty. Note the the results presented in the left side include pile-up events, while in the right side pile-up events are rejected. It is found that:

- the ratios are equal to unity in 0-100% since the two scenarios are identical by definition in this range;
- results based on V0A (upper panels):
  - for both the results with (left) and without (right) pile-up events, the obtained ratios are consistent with unity within uncertainty; this means that V0A is little affected by the pile-up effect;
- results based on CL1 (middle panels):
  - a visible deviation is observed in the most central collisions when including pile-up events (left); the deviation is reduced when excluding them (right);
- results based on ZNA (bottom panels):
  - results based on the old OADB (LHC13bc) are shown as black points; for the ones based on the new OADB (LHC13de): the event activity value with "102" is assigned to the most peripheral (60 – 100%) and the most central collisions (0 – 5%) are displayed as red and green points, respectively;
  - the pile-up rejection decreases the deviation found in the most central collisions;

Similar conclusion is also found for MSL triggered events.

### 3.3.3.3 Effect of pile-up

Figure 3.34 shows the pile-up event contribution with MSL data based on V0A activity estimator in LHC13de (p-Pb, forward) and LHC13f (Pb-p, backward) period. The tagging procedure needs the optimization of some parameters such as the minimum contributors to the pile-up vertices in SPD and the minimum distance for the SPD pile-up vertex. The optimized values of about 4 and 0.6 [263], respectively, to have a compromise between high tagging efficiency and low rate of false positives. It is indicated as "n4d6" in Fig. 3.34. The observed pile-up effect is large ( $\sim 10\%$ ) in the most central collisions (0-5%), in particular for LHC13f (backward). The results tagged with different values of parameters show a visible difference in each activity interval. The effect is less pronounced with decreasing event activity. Similar trends were found for the pile-up fraction with MB and MSH data, based on CL1 and ZNA [263]. It is difficult to correct the pile-up effect in the most central

collisions (i.e. 0-5%) which is very large. This multiplicity bin is excluded in the study of the event activity dependence of muons from heavy-flavour hadron decays.

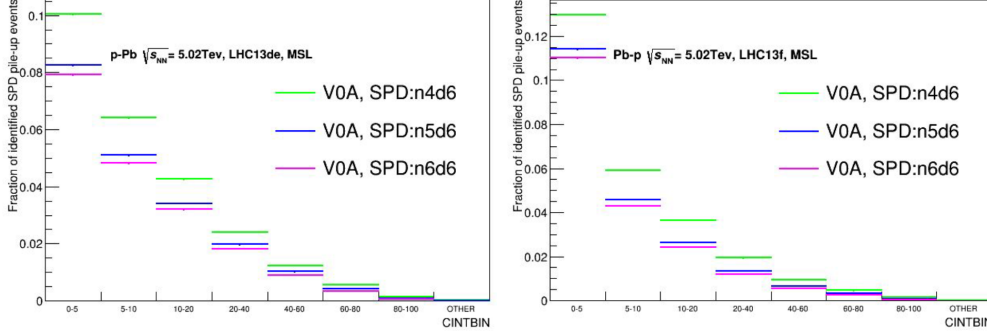


Figure 3.34: Fraction of pile-up event tagged using various values of the parameters at software level as a function of event activity. Results for MSL data based on V0A for the event activity determination with LHC13de (left) and LHC13f (right). See text for details. Figures taken from Ref. [263].

## 3.4 Acceptance $\times$ Efficiency Correction

### 3.4.1 Aspects of correction efficiency

The efficiency of muon reconstruction and selection is one of the the key elements for the data analysis and the physics result extraction. The acceptance  $\times$  efficiency correction includes the following two aspects [42]:

- detection efficiency, the one associated to the muon detection using trigger and tracking stations
  - trigger efficiency: it is obtained by means of the employed trigger algorithm for the track candidates (see Sec. 2.4.4). The effect of the possible dead channels with trigger chambers is also included;
  - tracking efficiency: it is from the track detection (or reconstruction) via the tracking stations, hence, it depends on the chamber occupancy which is related to the input track multiplicity;
  - matching efficiency: indicating the matching quantity between the tracker track and the corresponding trigger track;
- acceptance efficiency, the one related to the detector acceptance, which is introduced by the selection cuts implemented in the analysis
  - the efficiency due to  $\theta_{\text{abs}}$  cut: we apply the geometric cut  $170^\circ < \theta_{\text{abs}} < 178^\circ$  in order to avoid the effects induced by different materials in the front absorber. Note that the  $\theta_{\text{abs}}$  cut can reject some tracks reconstructed within the pseudo-rapidity acceptance ( $-4 < y_{\text{LAB}} < -2.5$ ), which have to be corrected as well.



Note that, (1) some sources listed above may have a correlation (i.e. dependence among them), for instance, the trigger matching efficiency can also be linked to the acceptance component since it is implemented as a  $p_T$  threshold in practice for the reconstructed tracks; (2)  $p \times DCA$  cut has a negligible effect on the efficiency.

Finally, we can use the name "Acceptance  $\times$  Efficiency Correction" to include all the factors mentioned above, and the obtained efficiency is therefore a global one. Alternatively, one can unfold them one by one, as shown in Ref. [191]. I follow the former scenario in this analysis.

### 3.4.2 Strategy and Results

For the efficiency correction, AliRoot provides the Official Correction Framework (CORRFW, [285]). CORRFW has been developed with the purpose of assisting the ALICE users in deriving the corrections for the acceptance and detection efficiency. It can be grouped into two main categories:

- **container classes** enable the storage of both real and simulated data in N-dimensional grids, as well as the correction maps calculation for the considered data period;
- **selection classes** provide the interface for general selections common to several analyses, at different stages of the selection process, for example, generator, acceptance and reconstruction *etc.*

A more detailed description of CORRFW can be found in Ref. [285].

Based on CORRFW, in the following, we show the obtained Acceptance  $\times$  Efficiency correction factors used to determine the yields of muons from heavy-flavour hadron decays in pp, Pb–Pb and p–Pb collisions.

#### 3.4.2.1 Results for muons from heavy-flavour hadron decays in pp and Pb–Pb collisions

For pp collisions at  $\sqrt{s} = 7/2.76$  TeV, the efficiency was obtained according to [42]:

1. **signal inputs for simulation:**  
kinematic distribution of heavy-quarks (i.e. charm and beauty), obtained from PYTHIA predictions tuned to be consistent with NLO pQCD calculations (HVQMNR [286]);
2. **perform simulation:**  
perform the heavy-quark hadronization and semi-muonic decay using PYTHIA, then propagate the muons through the experimental apparatus with GEANT3, considering the realistic detector condition of the desired data period;
3. **reconstruction:**  
reconstruct the simulated muon tracks from heavy-flavour hadrons within the realistic detector configuration;

#### 4. offline efficiency calculation:

the acceptance  $\times$  efficiency correction factor is defined as the distribution of the reconstructed muons (after implementing all the selection cuts as in data, for instance trigger matching and  $p \times$  DCA) with respect to the one at generation level.

Note that the mentioned strategy can be implemented both for charm and beauty. It is found [287] that muons from charm and beauty decays have almost the same efficiencies for  $p_T > 2$  GeV/c, as shown in Fig. 3.35. The deviation between them is  $< 1\%$  and can be neglected.

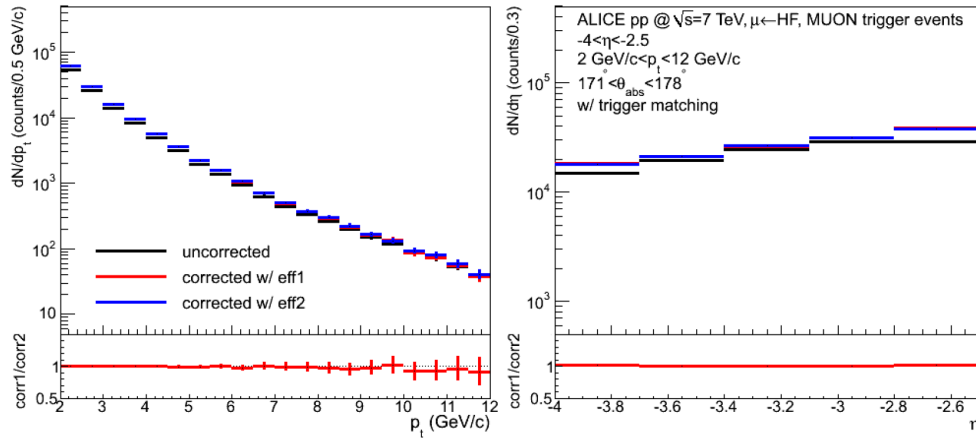


Figure 3.35: Performance study of muons from heavy-flavour hadron decays corrected with the efficiency obtained with charm (namely, eff1) and beauty (namely, eff2), respectively. Results are shown versus  $p_T$  (left) and  $y$  (right). Figures taken from Ref. [287].

For Pb–Pb collisions at  $\sqrt{s_{NN}} = 2.76$  TeV, an additional embedding technique is required in order to obtain the centrality dependence of the acceptance  $\times$  efficiency in realistic conditions of detector occupancy. The related procedure can be summarized as [42]:

1. simulate a sample of events with a given number of selected signal, for example  $J/\Psi$  or heavy-flavour hadron decay muons, in each of them;
2. propagate these signals into the detectors via the transport code (GEANT3);
3. then merge the simulated hits in the detectors, produced by the input signal, with the detected hits in real data event by event to build the so-called embedded event;
4. after the reconstruction of the embedded events as the real data, the reconstruction efficiency for embedded signals is obtained according to the MC information of the input signal in the simulation.

The obtained efficiency of muons from heavy-flavour hadron decays in Pb–Pb collisions at  $\sqrt{s_{NN}} = 2.76$  TeV, is shown in Fig. 3.36. It is realized that the efficiency

drops by  $4 \pm 1\%$  in the 10% most central collisions with respect to peripheral collisions. Note that the efficiency obtained in Pb–Pb collisions is independent of the input muon sources, and same result has been obtained when beauty is embedded in simulations instead of  $J/\Psi$  [42].

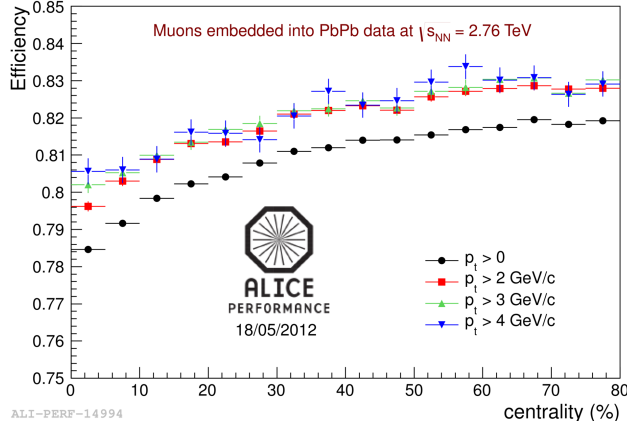


Figure 3.36: Muon detection efficiency dependence with centrality for 4 different values of the minimum transverse momentum of muons; it was obtained by embedding pure  $J/\Psi$  signal in the LHC10h data (Pb–Pb collisions at  $\sqrt{s_{NN}} = 2.76$  TeV). Figure taken from Ref. [288].

### 3.4.2.2 Results for muons from heavy-flavour hadron decays in p–Pb collisions

#### Multiplicity integrated efficiency

In p–Pb collisions at  $\sqrt{s_{NN}} = 5.02$  TeV, we calculate the multiplicity integrated acceptance  $\times$  efficiency correction factor by taking as input the beauty signals. Figure 3.37 shows the results obtained in the p–Pb configuration (forward rapidity  $2.03 < y_{CMS} < 3.53$ , left) and in the Pb–p configuration (backward rapidity  $-4.46 < y_{CMS} < -2.96$ , right). In each panel, the efficiency for low (MSL) and high (MSH)  $p_T$  triggered muon events, are displayed as black and red curves, respectively. One can see that, for MSL triggered events, the efficiency in p–Pb configuration reaches  $\sim 0.85$  for  $p_T > 2$  GeV/ $c$ , while for MSH triggered events the plateau is hardly reached for  $p_T > 8$  GeV/ $c$ . Moreover, the efficiency obtained in Pb–p configuration is smaller than that at forward rapidity. This is due to the fact that a larger number of dead channels was present in the LHC13f with respect to LHC13d and LHC13e periods.

Figure 3.38 shows the acceptance  $\times$  efficiency for muons from heavy-flavour hadron decays as a function of  $y_{LAB}$  in multiplicity integrated p–Pb collisions at  $\sqrt{s_{NN}} = 5.02$  TeV. They are obtained with MSL (left panel) and MSH triggered events (right panel) for  $2 < p_T < 12$  GeV/ $c$  and  $6 < p_T < 12$  GeV/ $c$ , respectively. One can see that the acceptance  $\times$  efficiency with MSL triggered events shows an

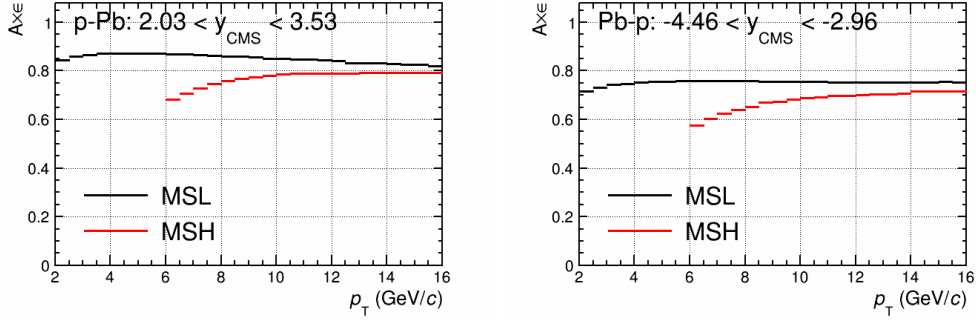


Figure 3.37: Acceptance  $\times$  efficiency for muons from heavy-flavour hadron decays at forward ( $2.03 < y_{\text{CMS}} < 3.53$ , left panel) and backward rapidity ( $-4.46 < y_{\text{CMS}} < -2.96$ ). Results by asking matching with MSL and MSH triggered events are shown as black and red curves, respectively. See text for detail.

increasing trend towards central rapidity, while this trend is less pronounced with MSH triggered events in a higher  $p_{\text{T}}$  interval. The acceptance  $\times$  efficiency in p-Pb collisions (forward rapidity) is larger than that in Pb-p collisions (backward rapidity), as already pointed out above when the  $p_{\text{T}}$  dependence of the efficiency was discussed.

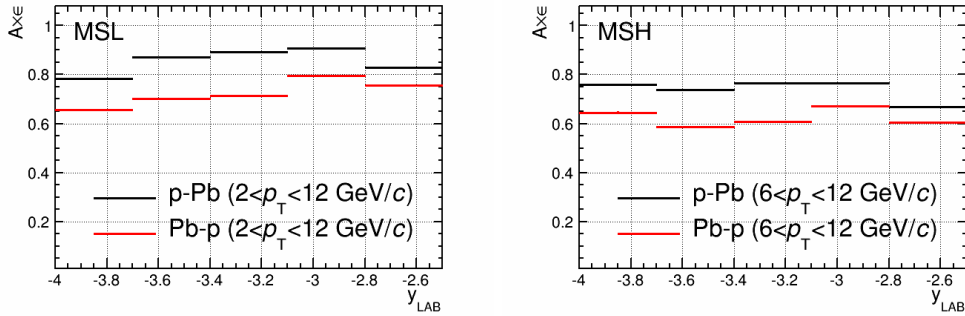


Figure 3.38: Acceptance  $\times$  efficiency for muons from heavy-flavour hadron decays by asking the matching with MSL (left panel) and MSH (right panel) in the considered  $p_{\text{T}}$  ranges. In each panel, the results are obtained both at forward (p-Pb) and backward rapidity (Pb-p) rapidity.

### Event activity dependence of acceptance $\times$ efficiency

As shown in Fig. 3.36, the efficiency for muons from heavy-flavour hadron decays decreases by about 4% in the most central Pb-Pb collisions at  $\sqrt{s_{\text{NN}}} = 2.76$  TeV as compared to peripheral collisions. For p-Pb collisions at  $\sqrt{s_{\text{NN}}} = 5.02$  TeV, the multiplicities are much smaller when compared with Pb-Pb collisions. The multiplicity dependence is expected to be even less pronounced in p-Pb collisions.

This is confirmed by the recent analysis shown in Ref. [289] where it is argued that the tracking efficiency is not sensitive to the event activity both at forward and backward rapidity in p–Pb collisions at  $\sqrt{s_{NN}} = 5.02$  TeV. Consequently, it is not necessary to estimate the efficiency within individual event activity bins, using an embedding procedure.

### 3.4.3 Systematic Uncertainty on the Efficiency

This sub-section is dedicated to the estimate of the systematic uncertainty on the trigger, tracking and matching efficiencies, which is due to possible imperfections in the description of the detector response and alignment in the simulations.

#### 3.4.3.1 Systematic uncertainty on trigger efficiency

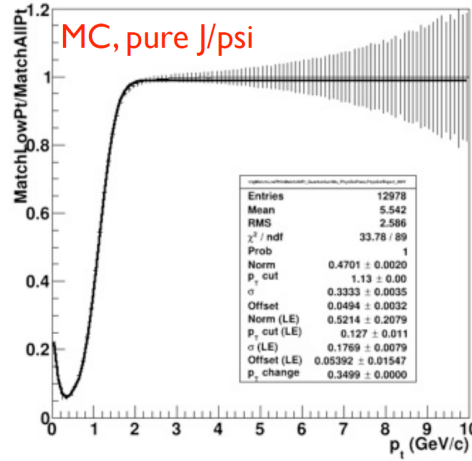


Figure 3.39: Trigger response function from pure  $J/\Psi$  simulation in Pb–Pb collisions at  $\sqrt{s_{NN}} = 2.76$  TeV. Figure taken from Ref. [290].

The trigger response function is defined as the ratio of the distributions matched with a low or high  $p_T$  cut over the ones matched without  $p_T$  selection (all  $p_T$ ). The obtained result from pure  $J/\Psi \rightarrow \mu^+\mu^-$  simulated in Pb–Pb collisions at  $\sqrt{s_{NN}} = 2.76$  TeV, is shown in Fig. 3.39. One can see that it contains two parts [290]: the **plateau** exhibits a constant value around unity at high  $p_T$ , depending on the RPC or intrinsic trigger chambers efficiency; the **shape** versus  $p_T$  is affected by the  $p_T$  threshold or the employed trigger algorithm. Hence, for different triggers, the related systematic uncertainty can be estimated separately, and the obtained uncertainty on the plateau and shape are summed in quadrature to obtain the final results. Concerning the uncertainty on the plateau behavior, it can be obtained with the following procedure [290, 291]:

- calculate the trigger chamber efficiency by means of the standard OCDB (Offline Conditions Data Base);

- modify the obtained efficiency map with a shift representing reasonable variation of this map (i.e. each local board efficiency is reduced by 2%);
- make a simulation with the modified efficiency map;
- the deviation allows to estimate the systematics on the efficiency.

It is found [290, 291] that the systematic uncertainty on the plateau is about 1% for single muon triggers (MSL and MSH).

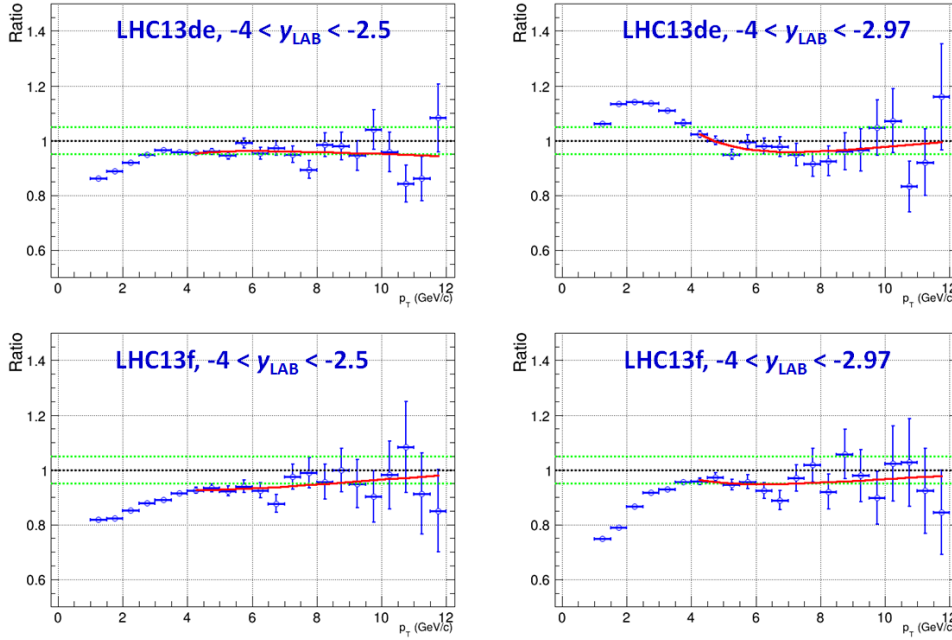


Figure 3.40: Ratio of the MSH distribution over MSL distribution after acceptance  $\times$  efficiency correction. The upper two panels are the results in p–Pb configuration (forward rapidity) within various rapidity intervals, while the bottom ones corresponds to the Pb–p configuration (backward rapidity). See text for details.

The uncertainty on the shape is negligible for MSL in the range  $p_T > 2$  GeV/ $c$ , where the analysis of heavy-flavour hadron decay muons is performed, since the associated  $p_T$  threshold is set at 0.5 GeV/ $c$ , and the resulting effect is expected small at  $p_T = 2$  GeV/ $c$ . However, it is not the same case for MSH, because the related  $p_T$  threshold is set at 4.2 GeV/ $c$ . The procedure of the uncertainty estimation can be summarized as,

- calculate the efficiency for MSL and MSH by means of MC simulations;
- extract the MSL and MSH distributions in data via requiring the trigger matching with low and high  $p_T$ , respectively, and then, correct the distributions with the related efficiency;
- make a ratio of MSH results over MSL ones, as shown in Fig. 3.40 (blue points). The statistical fluctuation is significant at high  $p_T$ . In order to overcome this

issue, first, we fit the MSH and MSL distribution with a power-law function at intermediate  $p_T$ , respectively. Second, one can extrapolate the fitted results at higher  $p_T$ . Third, we calculate the above ratio based on the fitted results at high  $p_T$ , which are also displayed in Fig. 3.40 (red curves).

- the ratio between the results of MSH and MSL ( $p_T$  and  $y$  dependent) gives the systematic uncertainty.

Figure 3.40 summarizes the obtained ratios between the MSH and MSL distributions within different rapidity intervals in p–Pb (forward rapidity) and Pb–p (backward rapidity) configurations. In each panel, the two dashed green lines indicate the values equal to 1.05 and 0.95 (or  $\pm 5\%$  varying range). One can see that there is  $\sim 5\%$  deviation at maximum. Further improvement concerning the fitting procedure, for example, the fitting method and fitting range, gives a similar results ( $\sim 4\%$ , [292]).

### 3.4.3.2 Systematic uncertainty on tracking efficiency

The systematic uncertainty on muon tracking efficiency was studied in  $J/\Psi \rightarrow \mu^+\mu^-$  analysis [268, 289]. The tracking efficiency measured on the data is biased by the related algorithm, and it is about 90%, 85% and 74% [268] for LHC13d (p–Pb), LHC13e (p–Pb) and LHC13f (Pb–p), respectively, which performs a run per run variation [268]. The MC simulation is tuned to reproduce the single muon distribution in data. Finally, the difference of the tracking efficiency observed between data and MC is taken as the systematic uncertainty for  $HF \rightarrow \mu$ , and is about 2% (3%) in p–Pb (Pb–p) configuration, resulting in the 4% (6%) for  $J/\Psi \rightarrow \mu^+\mu^-$ . The corresponding results of LHC13d period (p–Pb) are shown in Fig. 3.41.

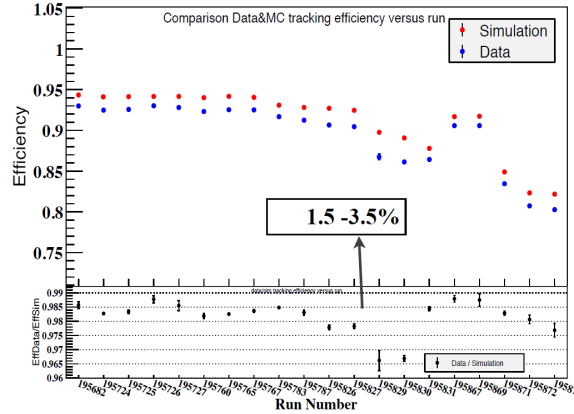


Figure 3.41: The tracking efficiency of  $J/\Psi \rightarrow \mu^+\mu^-$  measured in data and (data-tuned) MC simulations for LHC13d period. Figure taken from Ref. [289].

### 3.4.3.3 Systematic uncertainty on matching efficiency

The systematic uncertainty on the trigger-tracking matching efficiency is estimated by the difference of tracking efficiency observed in MC simulation and data

when applying different  $\chi^2$  cuts on the matching between the tracker track (i.e. reconstructed in the tracking stations) and the trigger track (i.e. reconstructed in the trigger stations). It is  $\sim 0.5\%$  for single muons [293].

### 3.4.3.4 Systematic uncertainty on mis-alignment effect

In previous analyses of pp collisions at  $\sqrt{s} = 7/2.76$  TeV and Pb–Pb collisions at  $\sqrt{s_{\text{NN}}} = 2.76$  TeV collected before 2012, the systematic uncertainty on mis-alignment effect was estimated to be  $1\% \times p_{\text{T}}$  (GeV/ $c$ ). After 2012, the alignment effect of the Muon spectrometer has been further improved for the  $\Upsilon$  analysis, in particular. Hence, it is necessary to cross check this effect with several mis-alignment configuration files obtained in p–Pb collisions at  $\sqrt{s_{\text{NN}}} = 5.02$  TeV.

Figure 3.42 shows the  $p_{\text{T}}$ -dependent efficiency estimated with different mis-alignments (left) for MSH triggered events in p–Pb configuration (LHC13e), as well as the comparison with respect to the (default) one obtained from realistic detector configuration (right). The upper, middle and bottom panels are the results for  $\mu^{\pm}$ ,  $\mu^+$  and  $\mu^-$ , respectively. It is found that  $\mu^{\pm}$  results based on different mis-alignment configuration files, are similar, and the differences when comparing with the realistic case, is inside the red bands formed by  $0.5\% \times p_{\text{T}}$  (GeV/ $c$ ). These deviations are larger for  $\mu^+$  and  $\mu^-$ , however, they can still be covered conservatively in the considered  $p_{\text{T}}$  region. We take therefore  $0.5\% \times p_{\text{T}}$  (in GeV/ $c$ ) as a conservative systematic uncertainty on mis-alignment in p–Pb collisions.

Finally, Tab. 3.6 summarizes the different components of the systematic uncertainty on the efficiency. They can be added together in quadrature to have the total systematic uncertainty. When presenting the measurement as a function of  $p_{\text{T}}$ , all of them are considered as un-correlated among  $p_{\text{T}}$  bins. Meanwhile, all of them are un-correlated between p–Pb and Pb–p configurations (or, un-correlated between forward and backward rapidity).

Detector Response	LHC13de		LHC13f	
	MSL	MSH	MSL	MSH
trigger efficiency	1%	$1\% \oplus 4\%$	1%	$1\% \oplus 4\%$
tracking efficiency	2%		3%	
matching efficiency	1%			
mis-alignment	$0.5\% \times p_{\text{T}}$			

Table 3.6: Different components of the systematic uncertainty on detector response.

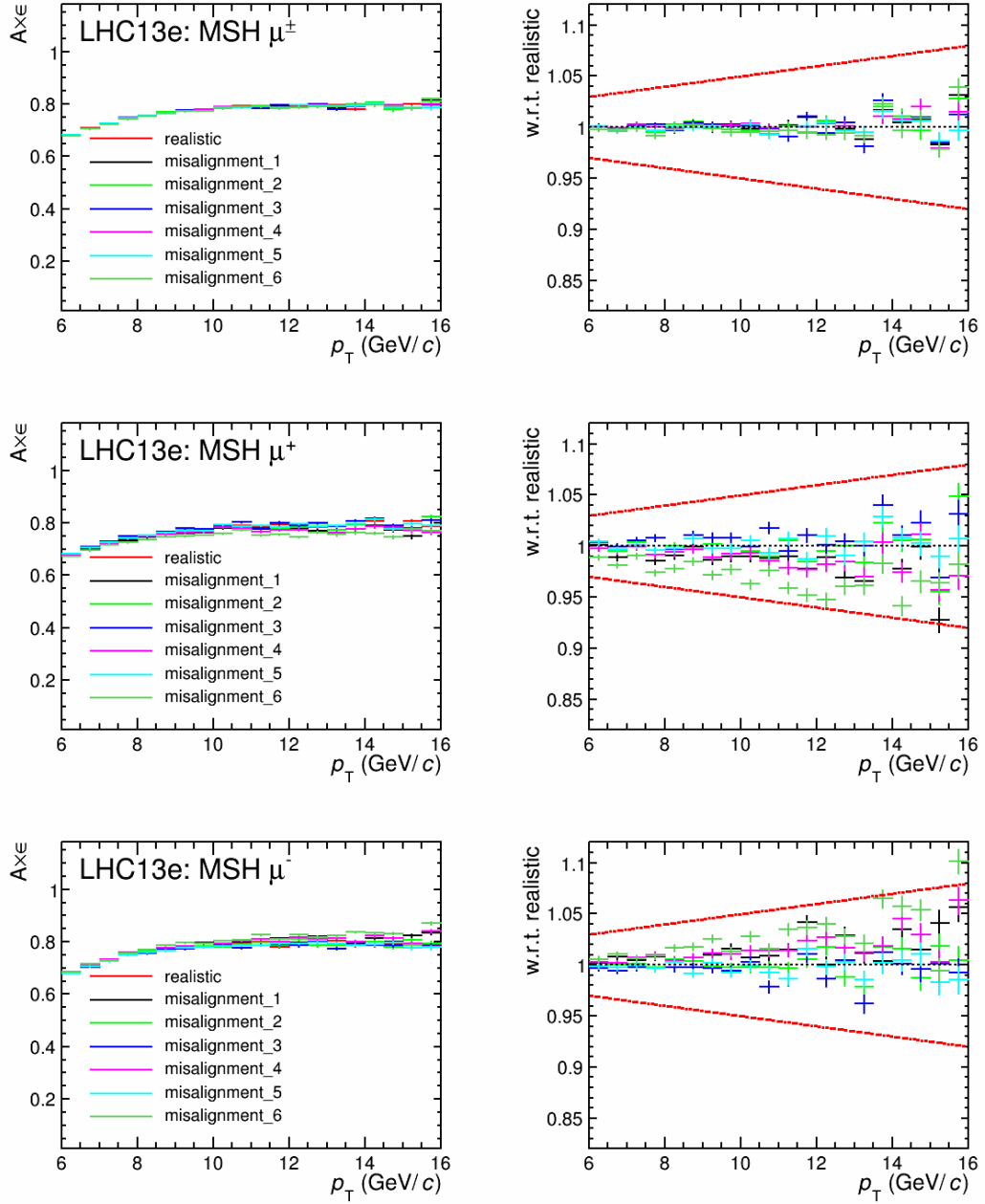


Figure 3.42: Comparison of acceptance  $\times$  efficiency of muons from heavy-flavour hadron decays, for MSH triggered events in p–Pb configuration (LHC13e), obtained by using different mis-alignments with respect to the default ones (i.e. realistic). The acceptance  $\times$  efficiency versus  $p_T$  are shown on the left side, while the further comparison together with the quoted systematic uncertainty ( $0.5\% \times p_T$  in GeV/c, red bands) is presented on the right side. Results displayed in the upper, middle and bottom panel are corresponding to  $\mu^\pm$ ,  $\mu^+$  and  $\mu^-$ , respectively.



# Subtraction of the background contribution of muons from charged pion and kaon decays

In this chapter, I discuss the background subtraction which is one of the most important elements for single muon analyses. The chapter is structured as follows. Section 4.1 summarizes the useful experience gained from previous analysis, for example, the muon sources and the available strategies for background estimation in pp and Pb–Pb collisions. Section 4.2 is dedicated to the estimate of the background in multiplicity integrated (0 – 100%) collisions, as well as within different event activity classes (Sec. 4.3) in p–Pb collisions at  $\sqrt{s_{NN}} = 5.02$  TeV. Further discussions concerning the analysis procedures can be found at the end of the sections.

## 4.1 Experience Gained from Previous Analyses

### 4.1.1 Muon Sources

#### 4.1.1.1 Results in pp Collisions at 7 TeV

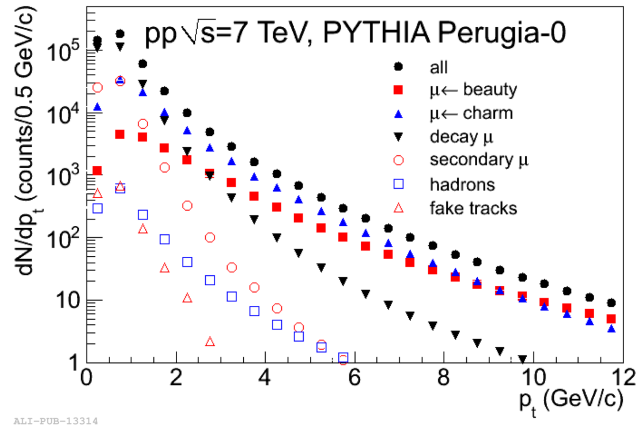


Figure 4.1: Transverse momentum distribution of reconstructed tracks in the muon spectrometer after all selection cuts are applied. The distributions are obtained from a PYTHIA (tune Perugia-0) simulation of pp collisions at  $\sqrt{s} = 7$  TeV, together with the main sources of muons. Taken from Ref. [160].

Figure 4.1 shows the transverse momentum distributions of muons from various

sources, after all the standard selection cuts are applied, simulated with PYTHIA in pp collisions at  $\sqrt{s} = 7$  TeV. One can see that the signal, i.e. the muons from heavy-flavour hadron decays,  $\mu \leftarrow c/b$ , prevails over the other components in the range  $p_T > 5 - 7$  GeV/c, with a crossing point between charm and beauty contributions around  $p_T = 7 - 9$  GeV/c. Note that the crossing point from FONLL predictions is around  $p_T = 4 - 7$  GeV/c (see Fig. 5.5 in Chap. 5 for details). The simulation results at  $\sqrt{s} = 7$  TeV indicate that the punch-through hadrons and the fake track (i.e. the tracks that are not associated to one single particle crossing the whole spectrometer) contributions are largely suppressed and negligible. The muons from electroweak boson ( $W$  and  $Z$ ) decays dominate in the  $p_T$  range 30–40 GeV/c. They are not taken into account in the pp analysis which extends only up to  $p_T = 10 - 12$  GeV/c. The secondary muons that are generated via interactions with the front absorber, are relevant only at low  $p_T$  and can be rejected by applying the cut  $p_T > 2$  GeV/c. Alternatively, one can implement a cut on the distance between the extrapolated muon track to the FMD to the closest fired strip of the FMD [214]. Finally, the main source of background in the  $p_T$ -differential inclusive spectrum consists of muons from primary particle decays, i.e. light hadrons,  $\pi^\pm$  and  $K^\pm$ , mainly [287]. This contribution dominates the muon yield for  $p_T < 2$  GeV/c and prevents a measurement of muons from heavy-flavour decays at low  $p_T$ . At higher  $p_T$ , it will be subtracted from the inclusive muon sample to obtain the heavy-flavour hadron decay muons. Note that the  $J/\Psi$  contribution was found to be about 5% at maximum in pp collisions at  $\sqrt{s} = 7$  TeV [287].

#### 4.1.1.2 Results in p–Pb collisions at 5.02 TeV

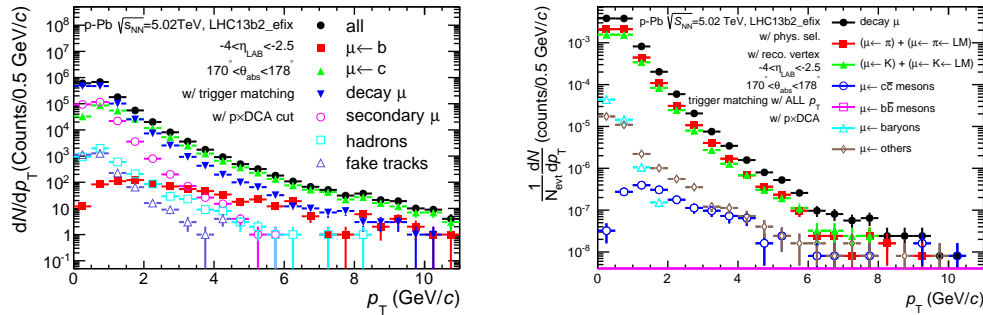


Figure 4.2: Left: transverse momentum distributions of reconstructed tracks in the muon spectrometer after all selection cuts are applied, according to DPMJET (LHC13b2\_eFix) simulations of p–Pb collisions at  $\sqrt{s} = 5.02$  in  $-4 < \eta_{LAB} < -2.5$ . Right: different sources of primary muons. See text for details.

The  $p_T$  distributions of the different muon sources, as shown in the left panel of Fig. 4.2, are obtained according to full AliRoot simulations using GEANT3 transport code and DPMJET event generator. Note that these available productions are anchored to LHC13b and LHC13c periods (i.e. MB samples for p–Pb collisions at  $\sqrt{s_{NN}} = 5.02$  TeV), which are different from the real data that we use in this analysis

(i.e. LHC13d and LHC3e in p–Pb configuration). Similar trends are seen as in pp collisions, see Fig. 4.1 for details. The right panel of Fig. 4.2 presents the different sources of muons from primary particle decays, including  $\pi^\pm$  and  $K^\pm$  which are the dominant components together with some other mesons and baryons, for example,  $J/\Psi$  and low mass resonances  $\eta$ ,  $\rho$ ,  $\omega$  and  $\phi$ . The results are consistent with the ones obtained in pp analysis [287].

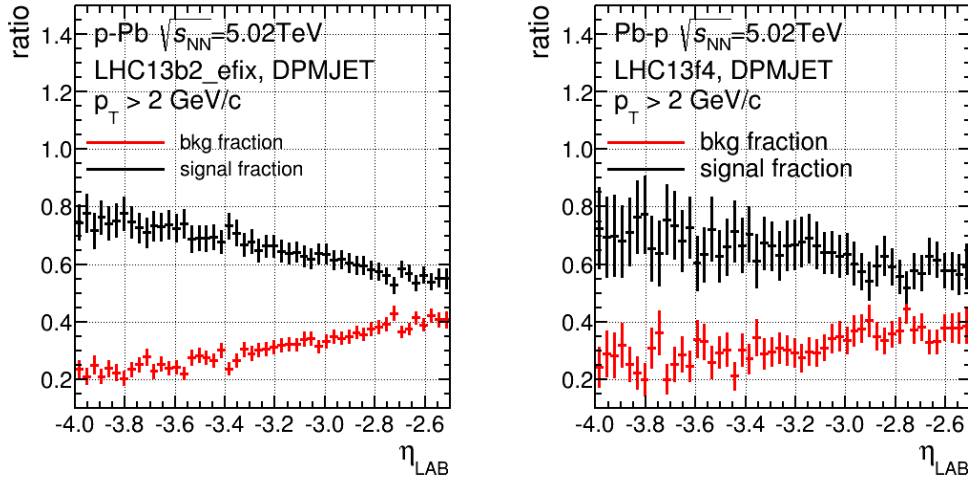


Figure 4.3: The fraction of signal (heavy-flavour hadron decay muons) and background (primary decay muons) obtained with DPMJET simulations performed at forward (left) and backward (right) rapidity, respectively.

Figure 4.3 displays the background and signal fractions versus  $\eta_{\text{LAB}}$ . The results obtained at forward (p–Pb) and backward rapidity (Pb–p) are shown in the left and right panel, respectively. The background fraction increases toward central barrel at forward rapidity, while it decreases for the signal. Concerning the results at backward rapidity, similar trends are observed even if it is limited by the statistics. This behavior is consistent with the measurements of the  $p_T$  ( $\eta$ )-dependence of heavy-flavour hadron decay muons performed by ATLAS in pp collisions at  $\sqrt{s} = 7$  TeV [34, 294].

For the measurements performed at forward ( $2.03 < y_{\text{CMS}} < 3.53$ ) and backward ( $-4.46 < y_{\text{CMS}} < -2.96$ ) rapidity, I focus on the transverse momentum range  $2 < p_T < 16$  GeV/c where the remaining background contribution are muons from primary  $\pi^\pm$  and  $K^\pm$  decays. Note that, (1) the electroweak bosons contribution is  $\sim < 2\%$  up to 16 GeV/c both at forward and backward rapidity in p–Pb collisions at  $\sqrt{s_{\text{NN}}} = 5.02$  TeV [219]; (2) the  $J/\Psi$  contribution is about 3% (4%) at maximum at forward (backward) rapidity [295].

## 4.1.2 Background Estimation Strategies

### 4.1.2.1 DCA-fitting Approach

A combined fit method of DCA (Distance of Closest Approach, defined as the distance between the extrapolated muon track and the interaction vertex in the plane perpendicular to the beam direction and containing the vertex), was proposed to separate the signal and background in 2009 [296, 297], exploiting the fact that signal and background behave differently because of the multiple scattering inside the front absorber, resulting in the different shapes of DCA (see Ref. [296, 297] for details.) When using the combined fit method of DCA to extract the signal and background, the induced systematic uncertainty is the dominant component. Moreover, one should take into account the particle species dependence. Consequently, the proposed strategy suffers from significant uncertainties.

The "combined fit" procedure is however a very useful tool for future analyses. For instance, the analysis of the muons from  $W$  bosons decays is achieved with a "combined fit of transverse momentum distribution" in p-Pb collisions at  $\sqrt{s_{\text{NN}}} = 5.02$  TeV [219], as well as the performance study of charm and bottom separation with MFT which is based on the "combined fit of offset distribution" [233].

### 4.1.2.2 Vertex Unfolding Method

The mean decay length of muons from heavy-flavour hadrons is small ( $c\tau_{D^\pm} = 311.8 \mu\text{m}$  and  $c\tau_{B^\pm} = 492 \mu\text{m}$  [2]), compared to those of charged  $\pi^\pm$  and  $K^\pm$  decays much more larger ( $c\tau_{\pi^\pm} \approx 7.8$  m and  $c\tau_{K^\pm} \approx 3.7$  m [2]), resulting in the  $z$ -position dependence of the latter component. It is argued [214, 298] that the contribution of muons from charged  $\pi^\pm$  and  $K^\pm$  decay in the measured data sample shows a linear dependence on the  $z$ -position of the interaction point increasing with increasing distance between the interaction point and the front absorber. This indicates the possibility to separate the two sources in heavy-ion collisions. This has already been successfully tested in MC productions and used in the performance study [299]. Moreover, the vertex folding strategy was implemented in pp collisions at  $\sqrt{s} = 7$  TeV [300, 301] and p-Pb collisions at  $\sqrt{s_{\text{NN}}} = 5.02$  TeV [302], and the expected behavior was evidenced with data.

One of the advantages of the vertex unfolding method is that it allows to access the measurement down to low  $p_{\text{T}}$ . However, it has strong statistics dependence and it is limited by the narrow range of available vertex position ( $-10 < v_z < 10$  cm at maximum) used in the unfolding procedure.

### 4.1.2.3 MC-based Method Used in pp Analysis

Muons from heavy-flavour hadrons decays were measured by means of a MC-based method in pp collisions at  $\sqrt{s} = 7/2.76$  TeV [160, 159]. The employed strategy for background subtraction can be summarized as:

- extract the  $p_{\text{T}}$ -differential spectra  $dN/dp_{\text{T}}$  of primary  $K^\pm/\pi^\pm$  decay muons from MC simulation (PYTHIA and PHOJET);



- normalize it to the measured muon distribution at low  $p_T$  ( $p_T < 1$  GeV/ $c$ ) where decay muons are the dominant contribution;
- subtract from inclusive muon  $dN/dp_T$  to obtain the heavy-flavour hadron decay muon distribution.

The related systematic uncertainty contains two parts: the one on model ( $\sim 13\%$ ) estimated by using different inputs (PYTHIA and PHOJET), as well as one on transport code (5 – 20%,  $p_T$ -dependent), obtained by varying 100% the yield of muons from secondary  $K^\pm/\pi^\pm$  decays. Finally, the estimated fraction of decay muons is  $\sim 19\%$  of the total muon yield in the range  $p_T > 4$  GeV/ $c$ .

This strategy has strong dependence on the MC since the shape of the background is obtained directly from the predictions. This method was implemented in p-Pb collisions at  $\sqrt{s_{NN}} = 5.02$  TeV, and the associated results were shown in Ref. [303]. The cold nuclear matter effects are not significant at forward rapidity, while a clear enhancement is observed in the low  $p_T$  region at backward rapidity. The deviation between data and the used MC is not taken into account in this strategy. The optimized strategy by means of the data-driven method, is employed finally (see Sec. 4.2).

#### 4.1.2.4 Data-driven Method Implemented in Pb–Pb Analysis

##### Results of $R_{AA}$ analysis in Pb–Pb collisions at $\sqrt{s_{NN}} = 2.76$ TeV

For the background subtraction in Pb–Pb collisions, it is necessary to mentioned that, (1) the strategy used in pp collisions is not validated because  $R_{AA}$  is unknown at forward rapidity; (2) the available  $R_{AA}$  of charged hadrons measured at mid-rapidity ( $\eta < 2.5$ ) by ATLAS, shows that there is almost no rapidity dependence; (3) therefore, one would expect it is still validated within wider range ( $\eta < 4$ ). The strategy used to estimate the background for  $R_{AA}$  and  $v_2$  analysis in Pb–Pb collisions at  $\sqrt{s_{NN}} = 2.76$  TeV, is shown below [159]:

- take as input the measured  $K^\pm/\pi^\pm$  spectra in pp collisions together with the corresponding nuclear modification factor  $R_{AA}$  in Pb–Pb collisions at central rapidity measured with ALICE [304, 305]
- extrapolate  $K^\pm/\pi^\pm$  spectra in pp collisions to forward rapidity by means of Monte-Carlo (MC) simulations according to [306]

$$\frac{d^2 N_{pp}^{K,\pi^\pm}}{dp_T dy} = \left[ \frac{d^2 N_{pp}^{K,\pi^\pm}}{dp_T dy} \right]_{y=0} \cdot \exp\left(\frac{-y^2}{2\sigma_y^2}\right) \quad (4.1)$$

where,  $\left[ \frac{d^2 N_{pp}^{K,\pi^\pm}}{dp_T dy} \right]_{y=0}$  denotes the charged particle spectra measured at central rapidity;  $\sigma_y = 3.3$  describes the rapidity extrapolation, estimated from PYTHIA and PHOJET (systematic uncertainty:  $\sim 15\%$ )

- get the charged hadron spectra in Pb–Pb collisions at forward rapidity by scaling the extrapolated  $K^\pm/\pi^\pm$  spectra in pp collisions with their  $R_{AA}$  at central rapidity

$$\frac{d^2 N_{\text{PbPb}}^{K,\pi^\pm}}{dp_T dy} = \langle T_{AA} \rangle \cdot \frac{d^2 N_{\text{pp}}^{K,\pi^\pm}}{dp_T dy} \cdot \left[ R_{AA}^{K,\pi^\pm}(p_T) \right]_{y=0} \quad (4.2)$$

then, within 100% the  $R_{AA}$  of  $K^\pm/\pi^\pm$  to estimate the systematic uncertainty on unknown quenching effect at forward rapidity

- produce the  $K^\pm/\pi^\pm$  decay muon background in MC with fast detector simulation (7 – 11% of total muon yield in the region  $p_T > 4 \text{ GeV}/c$ )

The rapidity extrapolation method used in pp collisions is based on the one proposed by PHENIX [306]. It is argued [306] that the rapidity extrapolation can be represented as a parameterized function, as shown in Eq. 4.1. However, one can implement the rapidity extrapolation without using a parameterization procedure. In this case, the estimation of parameter  $\sigma_y$  can be avoided. For the rapidity extrapolation in Pb–Pb collisions, as presented in Eq. 4.2, it is based on an assumption:

$$R_{AA}^{K^\pm/\pi^\pm}(p_T, y) = n_y \cdot R_{AA}^{K^\pm/\pi^\pm}(p_T, y = 0) \quad (4.3)$$

where,  $n_y$  indicating the rapidity dependence of quenching effect. Note that the parameter  $n_y$  changes within  $0 < n_y < 3$  according to the BDMPS model [42]. Finally,  $n_y$  is varied by 100% to estimate the related systematic uncertainty. Note that the  $p_T$  distributions of  $\mu \leftarrow \pi^\pm$  and  $\mu \leftarrow K^\pm$  estimated in pp/Pb–Pb collisions, are similar with each other. It could be induced by, (1) the compensation between the larger abundance of  $\pi^\pm$  and their longer lifetime, which makes more  $\pi^\pm$  to decay before the absorber with respect to  $K^\pm$ ; (2) different  $p_T$  spectra of  $\pi^\pm$  and  $K^\pm$ . Finally, they are similar in different collision systems where the relative abundance of pions and kaons can change.

Concerning the nuclear modification factor of muons from heavy-flavour hadron decays in p–Pb collisions at  $\sqrt{s_{NN}} = 5.02 \text{ TeV}$ , it is expected to be close to unity according to model predictions, indicating that cold nuclear matter effects are small. One needs to control the systematic uncertainty in order to have precision measurement. This is the key point to implement a new strategy for background subtraction in p–Pb collisions.

## 4.2 Background Estimation in multiplicity integrated p–Pb Collisions Based on a Data-Driven Method

### 4.2.1 Summary of the Strategy

Based on the experience summarized in the previous section, we developed the strategies for background subtraction both at forward (p–Pb,  $2.03 < y_{\text{CMS}} < 3.53$ ) and backward (Pb–p,  $-4.46 < y_{\text{CMS}} < -2.96$ ) rapidity, which are presented in this

section. I first summarize the general procedures. Then, the detailed explanation and validation concerning each step are introduced one-by-one in the subsequent sub-sections.

The so-called background is composed, mainly of muons from primary  $K^\pm$  and  $\pi^\pm$  decays. The analysis is performed in the range  $p_T > 2$  GeV/ $c$  because at low  $p_T$ , the large background does not allow for a reliable measurement of signal from heavy-flavour hadron decay muons. The strategy at **forward rapidity** includes three steps:

- take as input the charged hadron ( $K^\pm$  and  $\pi^\pm$ ) spectra measured in the Central Barrel (CB) [307] (see Sec. 4.2.2 for details).
  - When considering the decay kinematics, one may need a  $p_T$  extrapolation for the inputs spectra since the desired  $p_T$  range of the decay muons is  $2 < p_T^\mu < 16$  GeV/ $c$ . The resulting needs for input  $p_T$  ranges are  $2 < p_T^{K^\pm} < 40$  GeV/ $c$  and  $2 < p_T^{\pi^\pm} < 24$  GeV/ $c$  for  $K^\pm$  and  $\pi^\pm$ , respectively, while the corresponding measurements are validated in  $2 < p_T^{K^\pm/\pi^\pm} < 15$  GeV/ $c$ .
- extrapolate the  $K^\pm/\pi^\pm$  spectra to forward rapidity by means of MC simulations according to (see Sec. 4.2.3 for details)

$$\frac{dN^{K^\pm, \pi^\pm}}{dp_T dy}(p_T, y) = \frac{dN_{\text{Data}}^{K^\pm, \pi^\pm}}{dp_T dy}(p_T, y_{\text{CB}}) \times F_{\text{extra.}}(p_T, y) \quad (4.4)$$

$$F_{\text{extra.}}(p_T, y) = \frac{dN_{\text{MC}}^{K^\pm, \pi^\pm}}{dp_T dy}(p_T, \text{forward}) \Big/ \frac{dN_{\text{MC}}^{K^\pm, \pi^\pm}}{dp_T dy}(p_T, y_{\text{CB}}) \quad (4.5)$$

Note that,

- $dN_{\text{Data}}^{K^\pm, \pi^\pm}/dp_T dy(p_T, y_{\text{CB}})$  is the Central Barrel inputs measured with ALICE;  $F_{\text{extra.}}(p_T, y)$  is the rapidity extrapolation factor, defined as the ratio of the yields at forward to that at central rapidity in DPMJET; HIJING production are generated locally to estimate the systematic uncertainty on the model;
- in order to have the decay muons in the rapidity ranges  $2.03 < y_{\text{CMS}} < 3.53$  (forward, p-Pb) and  $-4.46 < y_{\text{CMS}} < -2.96$  (backward, Pb-p), the related charged hadrons are needed in the range  $0 < y_{\text{CMS}}^{K^\pm, \pi^\pm} < 6$  (forward) and  $-6 < y_{\text{CMS}}^{K^\pm, \pi^\pm} < 0$  (backward), respectively;
- one can see that we use the ratio  $F_{\text{extra.}}(p_T, y)$ , not the yield  $dN_{\text{MC}}^{K^\pm, \pi^\pm}/dp_T dy(p_T, \text{forward/backward})$  from models. This means that a possible deviation between data and MC can cancel to a certain extent in the defined ratio;
- produce the  $K^\pm/\pi^\pm$  decay muons by means of a fast simulation of decay kinematics and absorber effect (as in Pb-Pb analysis)

- note that the mentioned fast simulation procedure including the absorber effect is discussed in Sec. 4.2.4.

The strategy at forward rapidity has a dependence on the MC generator since the rapidity extrapolation factor is obtained from DPMJET and HIJING. It is found [308] that both models can describe well the rapidity spectra of the charged particles measured in the central barrel (DPMJET does a better job). This indicates that the rapidity dependence of the employed models is reasonable in this region.

With the models (DPMJET and HIJING), we make a cross check with respect to the CMS measurements [309], presented as the  $p_T$  spectra of charged particles within different rapidity intervals, as well as the derived asymmetry factor  $Y_{\text{asym}}$  defined as the ratio of the  $p_T$  spectra at backward rapidity to the one at forward rapidity in the center-of-mass frame.

$$Y_{\text{asym}}^{\text{Data}} = \frac{\text{backward}}{\text{forward}} = \frac{\left. \frac{dN^{\text{chg}}}{dp_T}(p_T, \text{backward}) \right|_{\text{Data}}}{\left. \frac{dN^{\text{chg}}}{dp_T}(p_T, \text{forward}) \right|_{\text{Data}}} \quad (4.6)$$

Note that the asymmetry factor  $Y_{\text{asym}}$  is defined within symmetric (pseudo-)rapidity regions, for example,  $-b < \eta_{\text{CMS}}^{\text{chg}} < -a$  and  $a < \eta_{\text{CMS}}^{\text{chg}} < b$  for the coverage at backward and forward rapidity, respectively, where (positive)  $a$  and  $b$  are the limits of the selected interval.

It is ambitious to expect that the  $p_T$  spectra can be reproduced by the models, and this can be confirmed by the results of charged particles measured with ALICE at central rapidity [310]: there is a difference of about factor 2 in the yields between the data and DPMJET at high  $p_T$ . For our analysis, the model will be tuned to be consistent with data, in order to reduce as more as possible the deviation between them. Note that we do not need the  $p_T$  spectra but the ratio ( $Y_{\text{asym}}^{\text{Data}}$ ), which can be used to scale the simulated  $p_T$  spectra at forward to backward rapidity. It is realized that the DPMJET model can reproduce well the forward-to-central ratio derived from CMS measurements,

$$\text{ratio} = \frac{\text{forward}}{\text{central}} = \frac{\left. \frac{dN^{\text{chg}}}{dp_T}(p_T, \text{forward}) \right|_{\text{Data}}}{\left. \frac{dN^{\text{chg}}}{dp_T}(p_T, \text{central}) \right|_{\text{Data}}} \quad (4.7)$$

while it does not work for backward case, even considering the systematic uncertainty given by HIJING. That means, firstly, that the strategy at forward rapidity is validated by the reasonable MC predictions; secondly, one cannot implement the same strategy at backward as at forward rapidity (see Sec. 4.2.3 for details).

As mentioned, the CMS Collaboration provides the measurement of asymmetry factor  $Y_{\text{asym}}^{\text{Data}}$  of the charged particles within symmetric rapidity intervals. The selected one is  $1.3 < |\eta_{\text{CMS}}^{\text{chg}}| < 1.8$ . By taking the  $Y_{\text{asym}}^{\text{Data}}$  as the scaling factor, one can scale the simulated  $K^\pm/\pi^\pm$  spectra at forward to **backward rapidity**, the resulting spectra is observed in the range  $-1.8 < y_{\text{CMS}}^{K^\pm, \pi^\pm} < -1.3$  (at backward rapidity).



$$\begin{aligned} & \frac{dN_{\text{Data-tuned-MC}}^{K^\pm, \pi^\pm}}{dp_T}(p_T, -1.8 < y_{\text{CMS}}^{K^\pm, \pi^\pm} < -1.3) \\ &= \frac{dN_{\text{MC}}^{K^\pm, \pi^\pm}}{dp_T}(p_T, 1.3 < y_{\text{CMS}}^{K^\pm, \pi^\pm} < 1.8) \cdot Y_{\text{asym}}^{\text{Data}}(p_T, 1.3 < |\eta_{\text{CMS}}^{\text{chg}}| < 1.8) \end{aligned} \quad (4.8)$$

However, it is not the acceptance that we need, which is  $-6 < y_{\text{CMS}}^{K^\pm/\pi^\pm} < 0$  at backward rapidity. A conservative strategy to estimate the background at backward rapidity is proposed: the lower band of the background is based on  $Y_{\text{asym}}^{\text{Data}} = 1$ , as shown in Eq. 4.9, indicating a symmetry particle production between forward and backward rapidity, while the upper band is based on  $2 \times Y_{\text{asym}}^{\text{Data}}$ , as displayed in Eq. 4.10.

$$\begin{aligned} & \frac{dN_{\text{Data-tuned-MC(Lower)}}^{K^\pm, \pi^\pm}}{dp_T}(p_T, -6 < y_{\text{CMS}}^{K^\pm, \pi^\pm} < 0) \\ &= \frac{dN_{\text{MC}}^{K^\pm, \pi^\pm}}{dp_T}(p_T, 0 < y_{\text{CMS}}^{K^\pm, \pi^\pm} < 6) \cdot Y_{\text{asym(Lower)}}(p_T, 0 < |\eta_{\text{CMS}}^{\text{chg}}| < 6) \end{aligned} \quad (4.9)$$

$$\begin{aligned} & \frac{dN_{\text{Data-tuned-MC(Upper)}}^{K^\pm, \pi^\pm}}{dp_T}(p_T, -6 < y_{\text{CMS}}^{K^\pm, \pi^\pm} < 0) \\ &= \frac{dN_{\text{MC}}^{K^\pm, \pi^\pm}}{dp_T}(p_T, 0 < y_{\text{CMS}}^{K^\pm, \pi^\pm} < 6) \cdot Y_{\text{asym(Upper)}}(p_T, 0 < |\eta_{\text{CMS}}^{\text{chg}}| < 6) \end{aligned} \quad (4.10)$$

where,  $Y_{\text{asym(Lower)}}$  and  $Y_{\text{asym(Upper)}}$  indicate the scaling factor used to get the related lower and upper band of the background, as defined in Eq. 4.11 and 4.12, respectively. Note that the latter one is obtained from the CMS measurements in the range  $1.3 < |\eta_{\text{CMS}}^{\text{chg}}| < 1.8$ .

$$Y_{\text{asym(Lower)}}(p_T, 0 < |\eta_{\text{CMS}}^{\text{chg}}| < 6) = 1 \quad (4.11)$$

$$Y_{\text{asym(Upper)}}(p_T, 0 < |\eta_{\text{CMS}}^{\text{chg}}| < 6) = 2 \times Y_{\text{asym}}^{\text{Data}}(p_T, 1.3 < |\eta_{\text{CMS}}^{\text{chg}}| < 1.8) \quad (4.12)$$

Concerning the upper limit (Eq. 4.12), we have implemented a cross check with HIJING simulation. It is safe to increase the  $Y_{\text{asym}}$  measured in  $1.3 < |\eta_{\text{CMS}}^{\text{chg}}| < 1.8$  by a factor of 2, to cover the results in  $|y_{\text{CMS}}^{K^\pm/\pi^\pm}| < 6$ . Similar conclusion is found with DPMJET. Finally, we take the average between the lower and upper limit as the central value for the background calculation at backward rapidity together with the related systematic uncertainty obtained by assuming an uniform distribution, as presented in the following equations,

$$\text{mean} = \frac{a + b}{2} \quad (4.13)$$



$$\sigma_{\text{mean}}^2 = \frac{(a - b)^2}{12} \quad (4.14)$$

where,  $a$  and  $b$  denote the estimated background (i.e. primary decay muons) based on Eq. 4.9 (lower band) and 4.10 (upper band), respectively.

## 4.2.2 Input Charged Hadron Distributions

### 4.2.2.1 Acceptance Determination of Charged Hadrons

One needs to estimate the transverse momentum and rapidity range needed for the mother  $\pi^\pm$  and  $K^\pm$  in order to obtain the decay muons in the interval  $2 < p_T^\mu < 16$  GeV/ $c$  and in the acceptance of the muon spectrometer.

For charged pions, we build a  $p_T$  distribution modeled by a power-law function up to 40 GeV/ $c$ . Then, we use this distribution to scale the muons generated with a flat pion  $p_T^{\pi^\pm}$  distribution after applying a cut on the distance between their production point and the collision decay point at  $\rho = 130$  cm (i.e. pions that decay before reaching a distance corresponding to one unit of the mean interaction length in the absorber, see Sec. 4.2.4 for details). The results in different intervals of  $p_T^\pi$  are shown in the left panel of Fig. 4.4. We can conclude that for pions, one needs to simulate up to a  $p_T^{\pi^\pm}$  value of 28 GeV/ $c$  since pions with  $p_T^{\pi^\pm} > 28$  GeV/ $c$  do not contribute to muons with  $p_T^\mu < 16$  GeV/ $c$ . Indeed, this is conservative for our analysis. We can define the ratio between the number of muons with  $p_T^\mu < 16$  GeV/ $c$  and the one for muons with  $p_T^\mu < p_T^{\text{max},\pi^\pm}$ , where  $p_T^{\text{max},\pi^\pm}$  is the upper limit in the selected charged pion  $p_T^{\pi^\pm}$  range. The obtained results are shown in the right panel of Fig. 4.4. One can see that this ratio seems saturate at  $\sim 97\%$  nearby 24 GeV/ $c$ . Charged pions in  $24 < p_T^{\pi^\pm} < 40$  GeV/ $c$  can give a  $\sim < 1\%$  contribution to muons with  $p_T^\mu > 16$  GeV/ $c$ . Therefore, for charged pions, the upper band of transverse momentum has been fixed to 24 GeV/ $c$ . In addition, we have cross checked that the mentioned ratio saturates at 97.7% around  $p_T^{\pi^\pm} = 32$  GeV/ $c$ , resulting in a  $\sim < 1\%$  deviation with respect to  $\sim 98\%$  observed at  $p_T^{\pi^\pm} = 24$  GeV/ $c$ , as displayed in Fig. 4.5.

When implementing the same procedure for kaons up to  $p_T^{K^\pm} = 60$  GeV/ $c$ , as shown in the left panel of Fig. 4.6, we can find that kaons at high  $p_T^{K^\pm}$  produce decay muons with very low  $p_T^\mu$ . Note that this behavior is different when comparing with pion (left panel of Fig. 4.4). Because the mass of kaons is larger than that of pions, with the momentum conservation, one would expect the momentum fraction of  $\mu \leftarrow K^\pm$  is smaller than that of  $\mu \leftarrow \pi^\pm$ . Similarly, one can define the ratio between the number of muons with  $p_T^\mu < 16$  GeV/ $c$  and the one for muons with  $p_T^\mu < p_T^{\text{max},K^\pm}$ , where  $p_T^{\text{max},K^\pm}$  is the upper limit in the selected charged kaon  $p_T^{K^\pm}$  range. The result is shown in the right panel of Fig. 4.6. We can see that this ratio saturates at  $\sim 98.45\%$  nearby 40 GeV/ $c$ . That means the charged kaons in  $40 < p_T^{K^\pm} < 60$  GeV/ $c$  can give a  $\sim < 1\%$  contribution of muons with  $p_T^\mu > 16$  GeV/ $c$ . Therefore, for charged kaons, the upper band of transverse momentum has been fixed to 40 GeV/ $c$ . Moreover, we cross checked that the ratio enables to

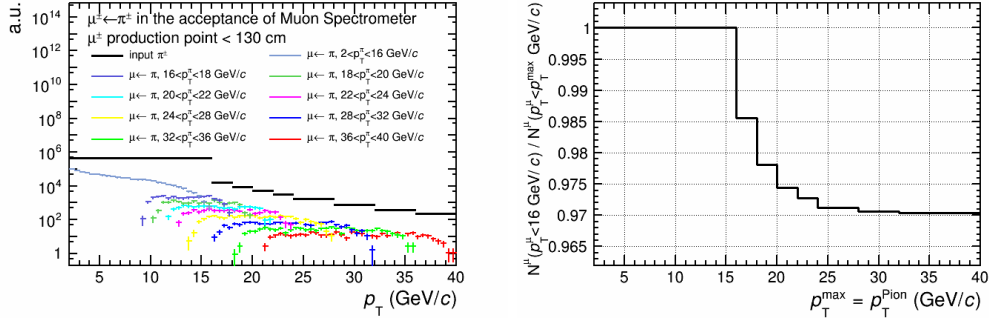


Figure 4.4: Left: distributions of muons from pion decays in different mother pion  $p_T^{\pi^\pm}$  regions with a flat transverse momentum distribution of charged pions as input and a cut on the muon production distance at  $\rho < 130$  cm. Right: ratio of the number of muons for  $p_T^\mu < 16$  GeV/c over the ones for  $p_T^\mu < p_T^{\max}$ , where  $p_T^{\max}$  is the maximum transverse momentum of its mother pions  $p_T^{\max} = p_T^{\text{Pion}}$ , shown as a function of  $p_T^{\text{Pion}}$ . See text for details.

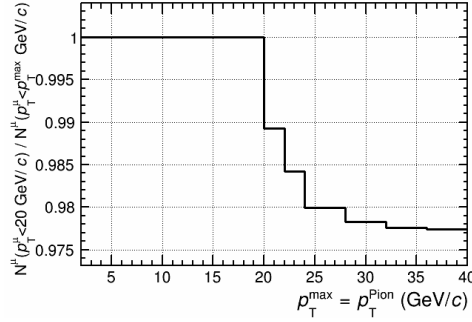


Figure 4.5: Same as the right panel of Fig. 4.4, but for  $p_T^\mu < 20$  GeV/c. See text for details.

saturate at 98.5% around  $p_T^{K^\pm} = 50$  GeV/c, resulting in a negligible deviation with respect to  $\sim 98.55\%$  observed at  $p_T^{K^\pm} = 40$  GeV/c, as presented in Fig. 4.7.

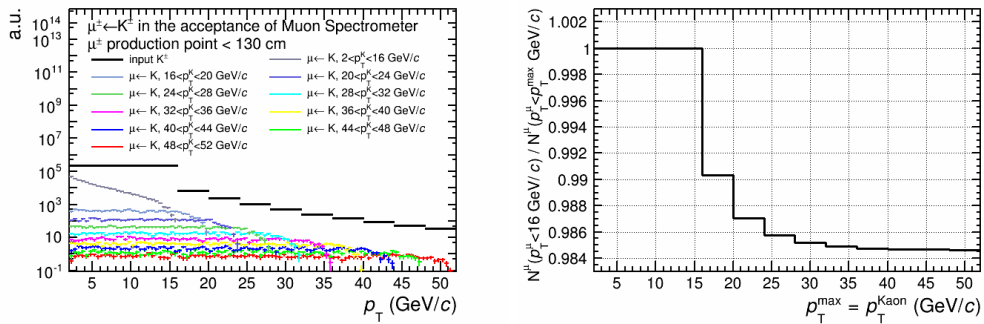


Figure 4.6: Same as Fig. 4.4, but for charged kaons.

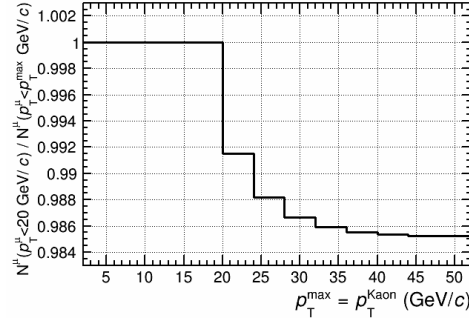


Figure 4.7: Same as Fig. 4.5, but for charged kaons.

One can also use a similar procedure to estimate the rapidity range, and the corresponding results for pions and kaons are displayed in the left and right panels of Fig. 4.8, respectively. The charged pions and kaons with  $|y_{\text{LAB}}^{K^\pm/\pi^\pm}| > 6.5$  do not contribute to the decay muon sample in the range  $|y_{\text{LAB}}^\mu| < 4.5$ . We can conclude that both for pions and kaons, the upper limit of  $|y_{\text{CMS}}^{K/\pi^\pm}|$  is 6.

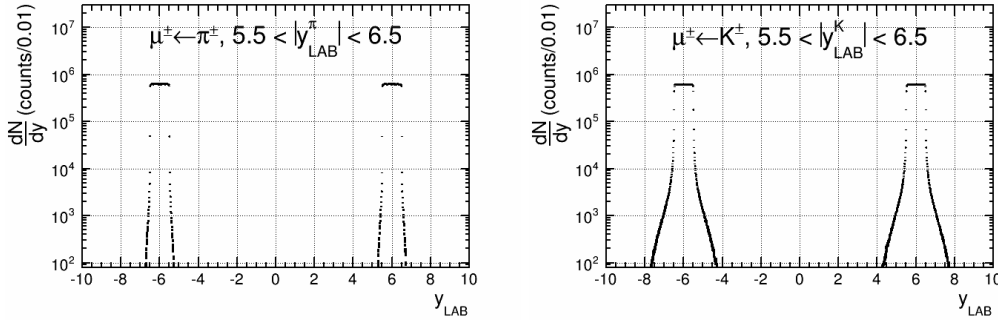


Figure 4.8: Distribution of muons from charged pion (left) and kaon (right) decays in  $5.5 < |y_{\text{LAB}}| < 6.5$ .

#### 4.2.2.2 Transverse Momentum Extrapolation

Figure 4.9 shows the  $p_{\text{T}}$ -differential spectra of charged pions and kaons measured in p-Pb collisions at  $\sqrt{s_{\text{NN}}} = 5.02$  TeV for different V0A multiplicity event classes, which are taken as the inputs for the background estimation (see Sec. 4.2.1). One can combine the results in 0 – 100% from different multiplicity bins. Concerning the error propagation in the combination procedure, it is summarized as:

- statistical uncertainty: the relative error is  $1/\sqrt{N_i}$  in the selected  $p_{\text{T}}$  bin  $i$ , where  $N_i$  is the related statistics; the total statistics  $\Sigma N_i$  is calculated by adding together the results within individual event activity bins; the related statistical uncertainty of the combined result is  $1/\sqrt{\Sigma N_i}$

- systematic uncertainty: the ones correlated among event activity (e.g. PID systematic uncertainties) are added linearly and the ones un-correlated (e.g. track and event selection) are added quadratically at final.

The combined results of charged pions and kaons are shown in Fig. 4.10. The relative statistical uncertainty is  $\sim 3.5\%$  and  $\sim 4.5\%$  up to  $p_T = 15$  GeV/c for pions and kaons, respectively, and the related systematic uncertainty is  $\sim 5.6\%$  (3.55%) and  $\sim 5.6\%$  (6%) for the correlated (un-correlated) components.

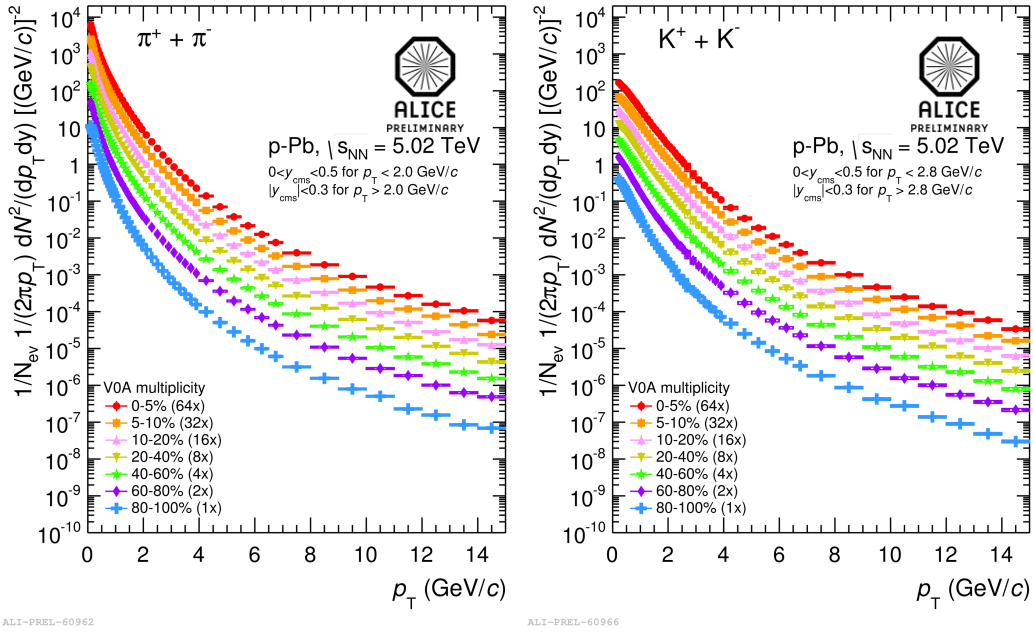


Figure 4.9:  $p_T$  spectra of charged pions (left) and kaons (right) measured in p-Pb collisions at  $\sqrt{s_{NN}} = 5.02$  TeV for different VOA multiplicity event classes. The systematic and statistical uncertainty are plotted as color boxes and vertical error bars, respectively. Figures taken from Ref. [307].

Note that the pion results are obtained in the rapidity range  $|y_{CMS}| < 0.3$  for  $2 < p_T < 15$  GeV/c, while kaons are shown in  $|y_{CMS}| < 0.3$  for  $2.8 < p_T < 15$  GeV/c and  $0 < y_{CMS} < 0.5$  for  $2 < p_T < 2.8$  GeV/c. Note that: (1) the  $p_T$  distribution of kaons in  $2 < p_T < 15$  GeV/c is obtained by combing the available measurements in  $2 < p_T < 2.8$  GeV/c and  $2.8 < p_T < 15$  GeV/c; (2) a 5% systematic uncertainty is proposed considering the different rapidity coverage in the range  $p_T > 2$  GeV/c [311]. (3) the correlated systematic uncertainty of kaons in 0 – 100% is zero for  $2 < p_T < 2.8$  GeV/c (middle right panel of Fig. 4.10) since the un-correlated component is dominant in this range. Hence, one needs to implement the  $p_T$  extrapolation for pions and kaons up to 24 and 40 GeV/c, respectively, in order to obtain the decay muons in the interval  $2 < p_T^\mu < 16$  GeV/c.

Derived from Ref. [312, 313], the proposed strategy for the  $p_T$  extrapolation can be summarized as:

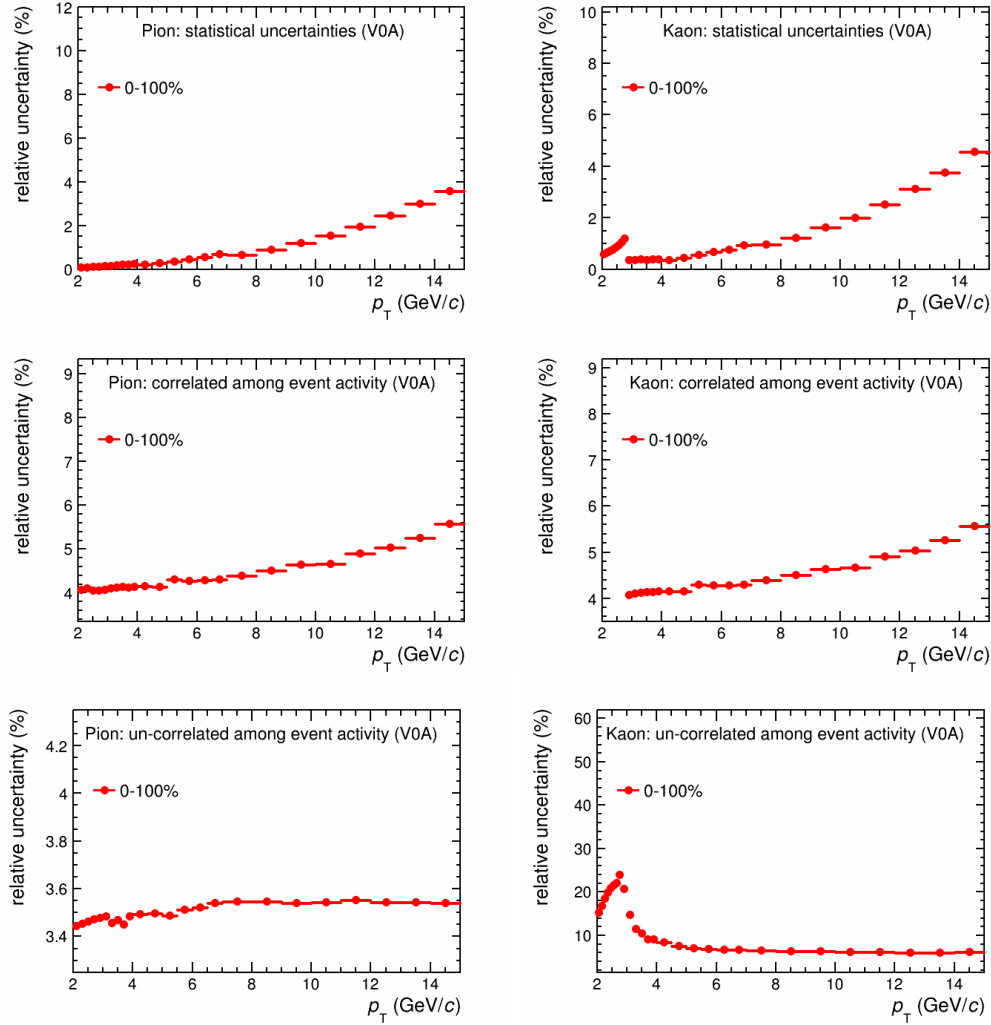


Figure 4.10: Statistical uncertainty (upper left), correlated (middle left) and un-correlated (bottom left) systematic uncertainties for charged pions combined in 0 – 100%. Plots in right panels are for kaons.

- combine statistical and systematic uncertainty via  $\sqrt{\text{stat.}^2 + \text{syst.}^2}$  in each  $p_T$  bin;
- sample with a gaussian probability expressed as  $\text{Gaus}(\text{central value}, \sqrt{\text{stat.}^2 + \text{syst.}^2})$ ;
- fit the obtained trials with power-law function in the range  $2 < p_T < 15$  GeV/c;
- cut on the parameters of the fitting procedure by  $\chi^2/NDF \leq 1$ ;
- extrapolate the fitted results up to higher  $p_T$ ;

- take the envelop formed by the extrapolated results at high  $p_T$  as the systematic uncertainty on the extrapolation procedure.

The extrapolated results for pions and kaons are presented in the left and right panel of Fig. 4.11, respectively. In each plot, the blue lines denote the samples obtained by combining the statistical and systematic uncertainty in the range  $2 < p_T < 15$  GeV/ $c$ , and the black lines indicate the trials fitted with the power-law function, which are extrapolated up to 24 and 40 GeV/ $c$  for pions and kaons, respectively. The red boxes formed by the different trails in the interval  $p_T > 15$  GeV/ $c$ , are the  $p_T$  extrapolated results together with the systematic uncertainty. The green points are the measured data for  $p_T > 15$  GeV/ $c$  that are shown as a cross check of the extrapolation procedure: systematic in the  $p_T$  region  $p_T > 15$  GeV/ $c$  is not underestimated by the extrapolated results.

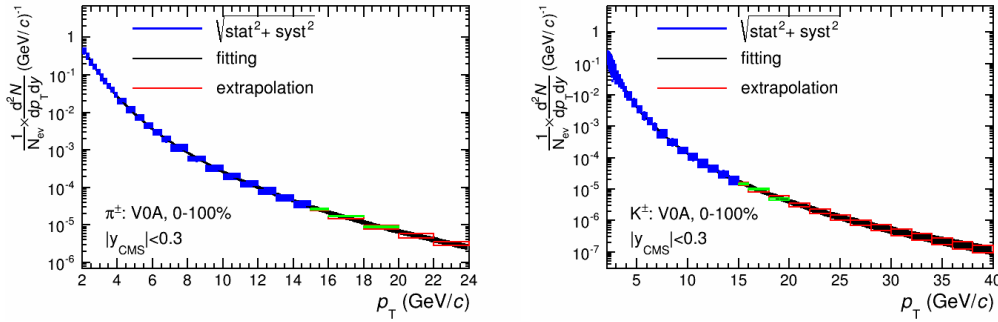


Figure 4.11: Transverse momentum distribution of charged pions (left) and kaons (right) measured by ALICE at mid-rapidity in  $2 < p_T < 15$  GeV/ $c$  and extrapolated up to 24 and 40 GeV/ $c$ , respectively. See text for details.

The transverse momentum distributions of charged pions and kaons after the  $p_T$  extrapolation, are shown in Fig. 4.12 together with the systematic uncertainty. The quoted uncertainties are calculated according to:

- $p_T < 15$  GeV/ $c$ : combine statistical and systematic uncertainty from data via  $\sqrt{stat.^2 + syst.^2}$ , and take the combined results as the final uncertainty;
- $p_T > 15$  GeV/ $c$ : take the systematic uncertainty on  $p_T$  extrapolation as the total one. Note that a 5% additional systematic uncertainty is considered for kaons due to the different rapidity coverage in the range  $2 < p_T < 2.8$  GeV/ $c$  ( $0 < y_{CMS} < 0.5$ ) and  $2.8 < p_T < 15$  GeV/ $c$  ( $|y_{CMS}| < 0.3$ ).

One can see that the total uncertainty is  $\sim 5 - 13\%$  ( $10 - 28\%$ ) for pions (kaons) in the  $p_T$  region  $2 < p_T < 24$  ( $2 < p_T < 40$ ) GeV/ $c$ .

### 4.2.3 Rapidity Extrapolation

After obtaining the transverse momentum distributions of charged pions and kaons in the ranges  $2 < p_T^{\pi^\pm} < 24$  and  $2 < p_T^{K^\pm} < 40$  GeV/ $c$ , respectively, at

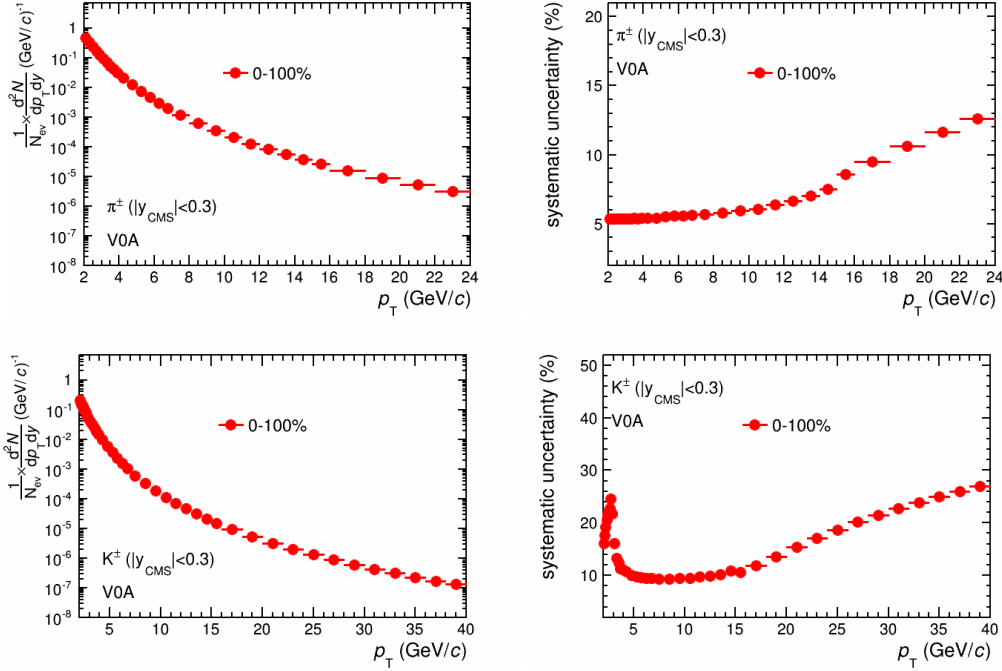


Figure 4.12: Upper: transverse momentum distribution of charged pions (upper left), as well as the quoted systematic uncertainty (upper right) in the range  $2 < p_T < 24$  GeV/c. Bottom: similar results for kaons in the interval  $2 < p_T < 40$  GeV/c. See text for details.

mid-rapidity, a model-based strategy is employed to extrapolate them to forward rapidity. A data-tuned cocktail strategy is implemented to extrapolate to backward rapidity (see Sec. 4.2.1 for the general introduction).

#### 4.2.3.1 Rapidity dependence: data versus MC

Figure 4.13 shows the pseudo-rapidity density of charged particles measured with ALICE in p–Pb collisions at  $\sqrt{s_{NN}} = 5.02$  TeV for  $|\eta_{LAB}| < 2$  in the laboratory system. One can see a visible asymmetry between forward (negative side, p-going) and backward (positive side, Pb-going)  $\eta_{CMS}$ . Note that the sign convention used for  $\eta_{CMS}$  in this figure is opposite to that used for  $y$ . The measurement is compared to various models that allow to describe similar measurements in other collision systems (see Ref. [308] for details). It is found [308] that DPMJET (normalized to NSD, Non-Single Diffractive) and HIJING 2.1, where the gluon shadowing parameter  $s_g = 0.28$  was tuned to describe experimental data on rapidity distributions in d–Au collisions at  $\sqrt{s_{NN}} = 0.2$  TeV (RHIC), give values that are close to the data. Moreover, both of them enable to describe the pseudo-rapidity shape relatively well (DPMJET does a better job as compared to HIJING).

It is worth noting that the DPMJET can also reproduce well the pseudo-rapidity shape of charged particles measured with ATLAS and ALICE within a wider accep-

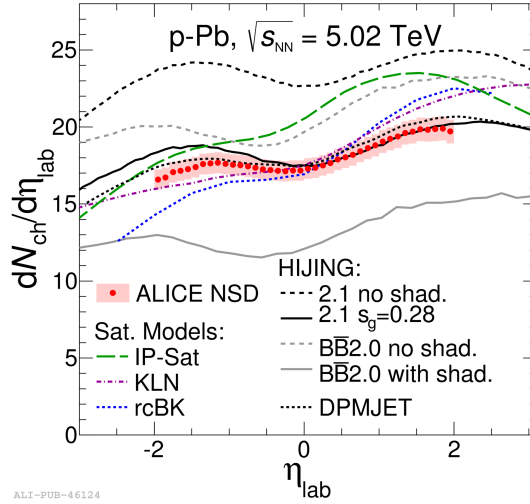


Figure 4.13: Pseudorapidity density of charged particles measured in NSD p-Pb collisions at  $\sqrt{s_{NN}} = 5.02$  TeV compared to theoretical predictions. Figure taken from Ref. [308].

tance, as well as in different event activity intervals. A more detailed discussion is given in Sec. 4.3.

#### 4.2.3.2 Transverse Momentum Dependence: Data versus MC

Figure 4.14 shows the transverse momentum distributions of charged particles in NSD p-Pb collisions for different pseudo-rapidity ranges measured with ALICE. Note that the positive pseudo-rapidity region in Fig. 4.14 indicates the Pb-going direction (backward), while the negative region denotes the p-going direction (forward). One can see that, at high  $p_T$ , the  $p_T$  distributions for  $|\eta_{CMS}| < 0.3$  in p-Pb collisions are similar to that in pp collisions, as expected in absence of nuclear effects. The ratios of the spectra for backward pseudo-rapidities to that at  $|\eta_{CMS}| < 0.3$ , is shown in the bottom panel. In the low  $p_T$  region, the slope of the ratio seems to increase when going from central to forward pseudo-rapidity, indicating a softening effect of the  $p_T$  spectrum [314]. However, this effect is small since the ratios are compatible with each other within uncertainties. It is found [310] that the DPMJET model overpredicts the spectra by about 33% for  $p_T < 0.7$  GeV/c and underpredicts them by up to 50% for  $p_T > 0.7$  GeV/c.

As mentioned in Sec. 4.2.1, the rapidity extrapolation factor, see Eq. 4.5, is defined as the ratio of the  $p_T$  spectra within different (pseudo-)rapidity intervals. The deviation of  $p_T$  distributions between data and MC can cancel out to a certain extent in the ratio. Hence, we cross checked the results shown in the lower panel of Fig. 4.14 with different models. This is summarized in Fig. 4.15. It is found that the results of DPMJET (upper left) are consistent with unity within uncertainties, while HIJING (upper right) gives large deviations near  $p_T = 8 - 9$  GeV/c. The results of PYTHIA+EPS09 (bottom) shows a flat behavior with unity. Finally, we can see

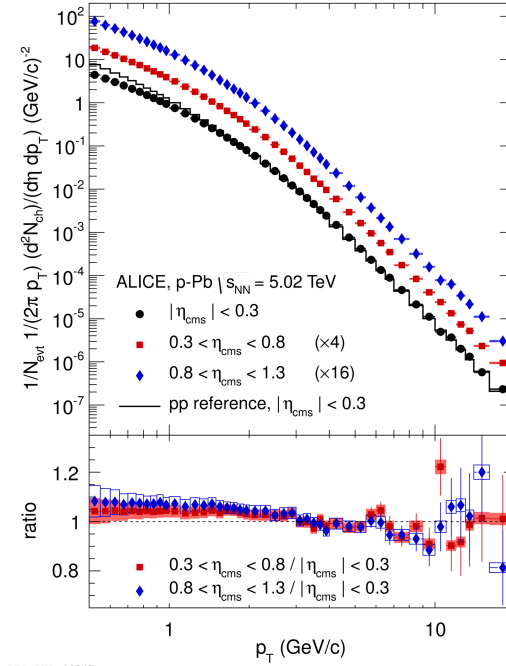


Figure 4.14: Transverse momentum distributions of charged particles in NSD p–Pb collisions for different pseudo-rapidity ranges (upper panel). The spectra are scaled by the factors indicated on the figure. The histogram represents the reference spectrum in pp collisions (see text). The lower panel shows the ratio of the spectra at backward pseudo-rapidity to that at  $|\eta_{\text{CMS}}| < 0.3$ . The vertical bars (boxes) represent the statistical (systematic) uncertainties. Figure taken from Ref. [314].

that DPMJET can describe the data displayed in the lower panel of Fig. 4.14.

CMS provided [309] also the measurement of  $p_T$ -differential spectra of charged particles in p–Pb collisions at  $\sqrt{s_{\text{NN}}} = 5.02$  TeV, as shown in the left panel of Fig. 4.16. The positive pseudo-rapidity values in Fig. 4.16 correspond to the proton beam direction (forward), while the negative values to the Pb beam direction (backward). The asymmetry factor,  $Y_{\text{asym}}$  (see Eq. 4.6), defined as the ratio of the  $p_T$  spectra at backward rapidity to the one within the symmetric rapidity interval at forward rapidity, is displayed in the right panel. One can see that, in all the three pseudo-rapidity intervals, the value of  $Y_{\text{asym}}$  increases with increasing  $p_T$  in the range  $0.4 < p_T < 3$  GeV/c, then decreases down to unity at a  $p_T$  of  $\sim 10$  GeV/c, and remains compatible with unity up to the highest  $p_T$  values. In addition, at the lowest  $p_T$  value,  $Y_{\text{asym}}$  is consistent with unity in the range  $0.3 < |\eta_{\text{CMS}}| < 0.8$ , but is above unity in the more forward (backward) pseudo-rapidity regions. For  $p_T > 10$  GeV/c,  $Y_{\text{asym}}$  is larger than unity as predicted by models including nuclear modification of the PDFs [309].

The asymmetry factor  $Y_{\text{asym}}$  calculated according to DPMJET, HIJING and PYTHIA+EPS09 for different pseudo-rapidity ranges are shown in Fig. 4.17. One can see a deviation with respect to the CMS measurements presented in the right

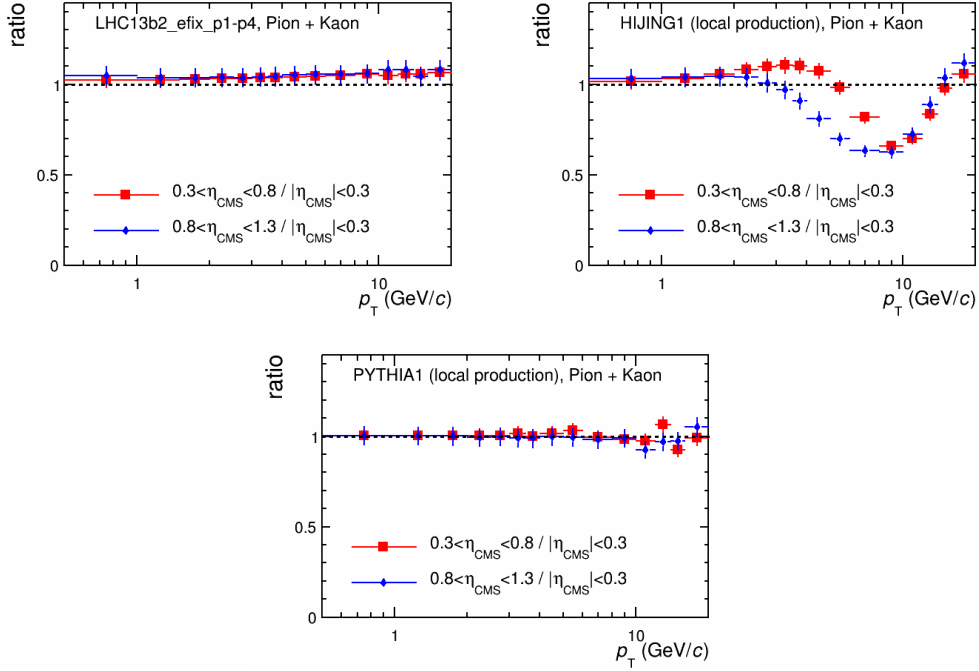


Figure 4.15: Ratio of the spectra for backward pseudo-rapidities to that at  $|\eta_{\text{CMS}}| < 0.3$  obtained with DPMJET (upper left), HIJING (upper right) and PYTHIA+EPS09 (bottom). The vertical bars denote the statistical uncertainties.

panel of Fig. 4.16. Further cross checks suggest that the deviation between data and MC concerning  $Y_{\text{asym}}$ , are not induced by the predictions at forward rapidity. As shown in Fig. 4.18, the measured forward-to-central ratio defined as the distribution at forward ( $0.8 < \eta_{\text{CMS}} < 1.3$ ) to the one obtained at central rapidity ( $0.3 < \eta_{\text{CMS}} < 0.8$ ), is compared with MC (DPMJET, HIJING and PYTHIA+EPS09). In the left panel, one can see that DPMJET and PYTHIA can reproduce the data derived from the left plot of Fig. 4.16, while HIJING gives large deviations. The data can be covered by the DPMJET results with taking the difference between DPMJET and HIJING as the additional systematic uncertainty, as shown in the right panel of Fig. 4.18. This means that the deviation of  $Y_{\text{asym}}$  observed between data and MC is due to the results at backward rapidity. Further cross checks are implemented with the results in the ranges  $1.3 < \eta_{\text{CMS}} < 1.8$  (forward) and  $0.3 < \eta_{\text{CMS}} < 0.8$  (central), and same conclusion can be drawn.

#### 4.2.3.3 Rapidity Extrapolation at Forward Rapidity

As discussed above, the combined results of DPMJET and HIJING enable to describe the CMS measurements at forward rapidity. With these two models, we can get the rapidity extrapolation factor  $F_{\text{extra.}}(p_T, y)$  via Eq. 4.5, which is defined as the distributions at forward with respect to the one obtained at central rapidity ( $|\eta_{\text{CMS}}| < 0.3$ ). The  $F_{\text{extra.}}(p_T, y)$  obtained with DPMJET is shown in Fig. 4.19 for

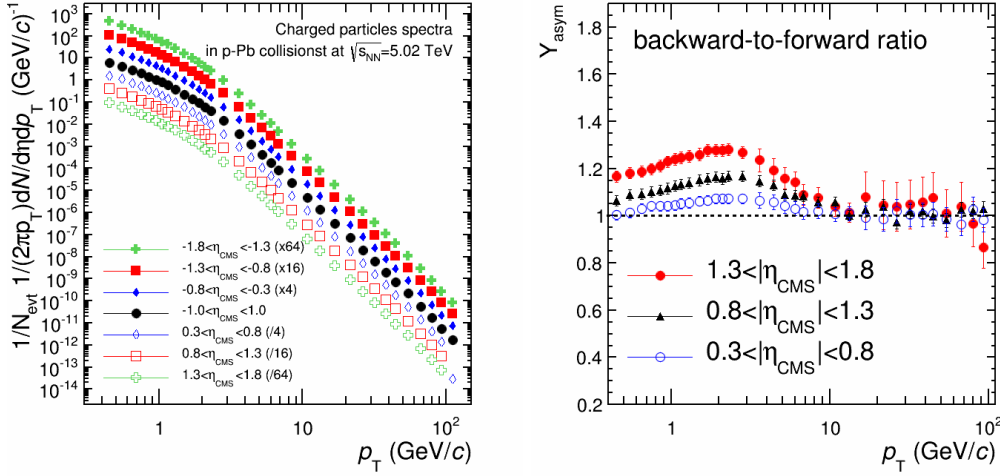


Figure 4.16: Left: charged particle transverse momentum spectra in p-Pb collisions at  $\sqrt{s_{NN}} = 5.02$  TeV for various pseudo-rapidity ranges (see legend for details). The spectra have been scaled by the quoted factors to provide better visibility. Right: the related asymmetry between backward and forward as a function of  $p_T$  for  $0.3 < |\eta_{CMS}| < 0.8$ ,  $0.8 < |\eta_{CMS}| < 1.3$  and  $1.3 < |\eta_{CMS}| < 1.8$ . The vertical bars denotes the systematic uncertainty. Extracted from Ref. [309].

pions and kaons. The upper two plots are the 2-dimensional  $F_{extra.}$  as a function of  $p_T$  and  $y_{cms}$  for charged pions and kaons, respectively. The bottom two plots are the related distributions as a function of  $y_{cms}$  in the  $p_T$  range  $2 < p_T < 20$  GeV/c. Note that:

- the forward rapidity (p-going direction) means the negative side in Monte-Carlo productions which in contrary to the convention used for the data;
- due to the limited statistics, the upper limit in  $p_T$  is 20 GeV/c. A  $p_T$  extrapolation is requested to obtain the results up to 24 and 40 GeV/c for pions and kaons. It is done with a similar procedure as discussed in Sec. 4.2.2;
- the normalization is implemented in the range  $|y_{CMS}| < 0.3$ , resulting in

$$\int_{-0.3}^{0.3} dy \cdot F_{extra.}(p_T, y) = 1 \quad (4.15)$$

Similar results based on HIJING are shown in Fig. 4.20.

With  $F_{extra.}$  shown in Fig. 4.19 and 4.20, one can extrapolate the  $K^\pm/\pi^\pm$  distributions from central to forward rapidity via Eq 4.4. The obtained distributions as a function of  $p_T$  and  $y_{CMS}$  are shown in the upper two panels of Fig. 4.21, and the results as a function of  $p_T$  ( $-6 < y_{CMS} < 0$ ) are presented in the bottom two panels. Note that we use the same (relative) uncertainty on the  $p_T$  extrapolation of pions and kaons as the ones obtained in  $|y_{CMS}| < 0.3$  (see Sec. 4.2.2). Similar results based on HIJING are shown in Fig. 4.22.

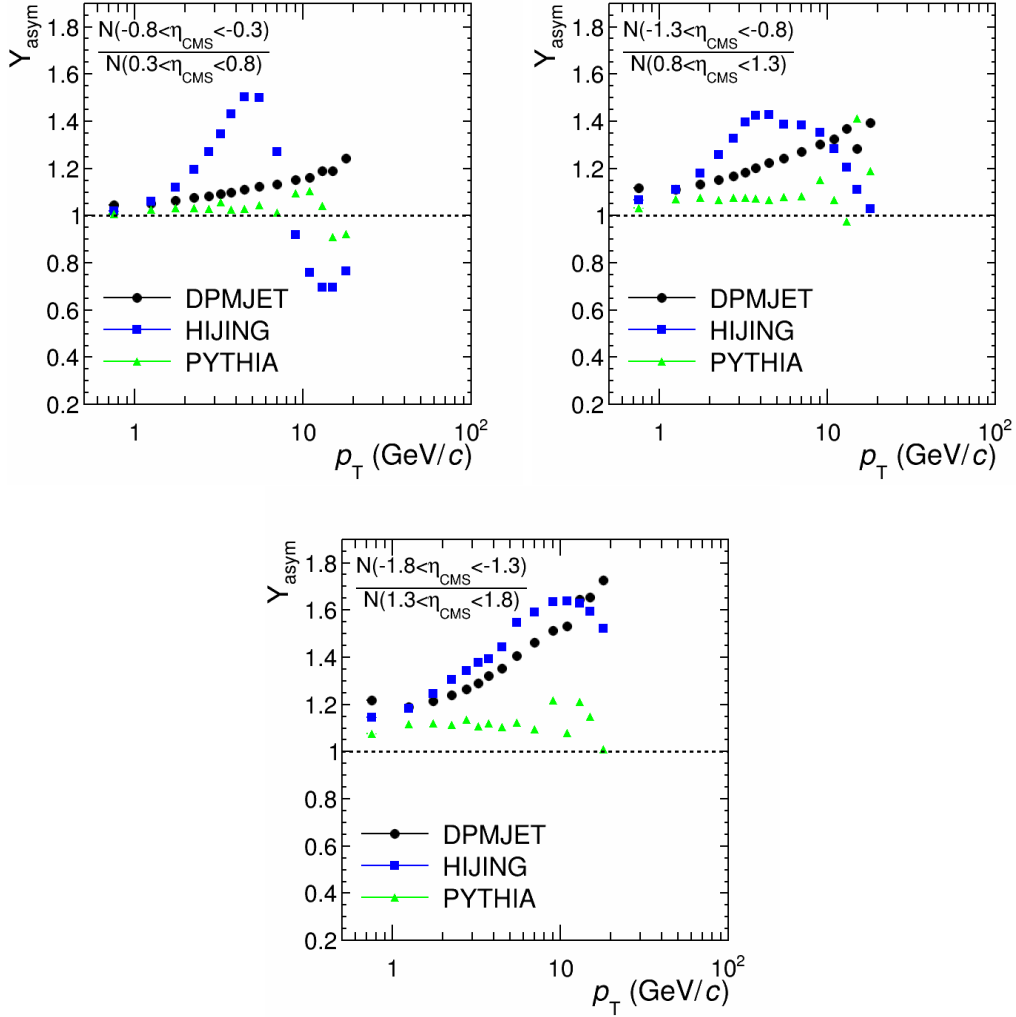


Figure 4.17:  $Y_{\text{asym}}$  obtained with DPMJET, HIJING and PYTHIA+EPS09 for various pseudo-rapidity ranges (see legend for details).

#### 4.2.3.4 Rapidity Extrapolation at Backward Rapidity

As discussed in the previous section, MC predictions (DPMJET and HIJING) cannot reproduce the CMS measurements of the asymmetry factor,  $Y_{\text{asym}}^{\text{Data}}$  (Eq. 4.5). This indicates that a different strategy is needed for the related rapidity extrapolation procedure.

Since  $Y_{\text{asym}}^{\text{Data}}$  is defined as the charged-particle distribution within symmetric pseudo-rapidity intervals between backward and forward rapidity, one can take it as the scaling factor in order to scale charged-particle distributions predicted at forward to backward rapidity. The challenge is that the rapidity coverage of  $Y_{\text{asym}}^{\text{Data}}$  such as  $1.3 < |\eta_{\text{CMS}}| < 1.8$  (Fig. 4.16), does not coincide with the considered one  $|y_{\text{CMS}}| < 6$ . Note that there is a very small difference between  $\eta$  and  $y$  for  $K^\pm/\pi^\pm$

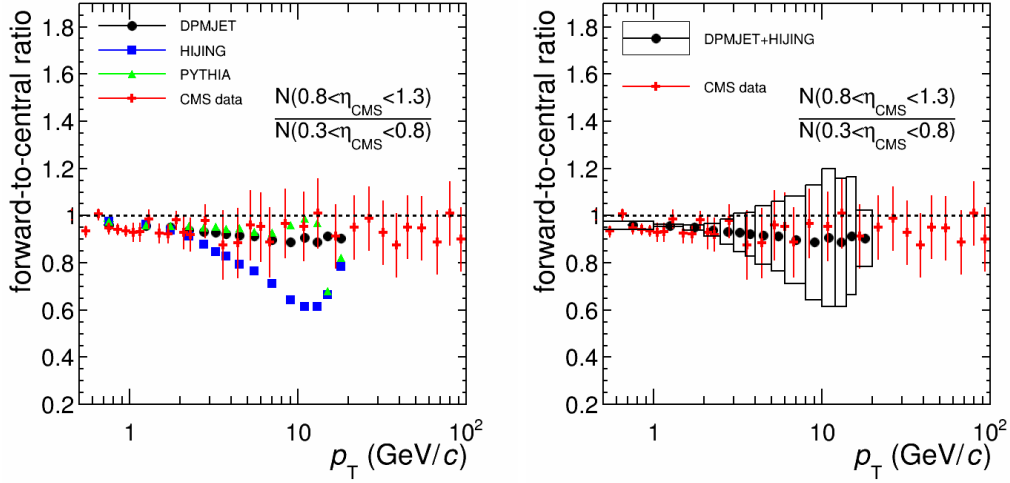


Figure 4.18: Left: ratio of the distribution at forward ( $0.8 < \eta_{\text{CMS}} < 1.3$ ) to that at mid-rapidity ( $0.3 < \eta_{\text{CMS}} < 0.8$ ), calculated with DPMJET, HIJING and PYTHIA+EPS09. Derived results from CMS are also shown. The vertical bars of data indicate the systematic uncertainties. Right: same as the left panel, taking the deviation of HIJING with respect to DPMJET as the systematic uncertainty.

at forward/backward rapidity for  $p_T > 2 \text{ GeV}/c$ . We used a conservative strategy to estimate the background at backward rapidity. The **lower band** of the background is based on  $Y_{\text{asym}}^{\text{Data}} = 1$ , see Eq. 4.9, while the upper band is based on the following assumption. We assume that the  $2 \times Y_{\text{asym}}^{\text{Data}} (1.3 < |\eta_{\text{CMS}}| < 1.8)$ , see Eq. 4.10, allows to cover the different rapidity acceptance between  $-1.8 < y_{\text{CMS}} - 1.3$  and  $-6 < y_{\text{CMS}} < 0$ . This assumption can be checked by means of MC simulations. The  $Y_{\text{asym}}$  defined within various rapidity ranges with HIJING, are shown in the left panel of Fig. 4.23. Two dashed lines indicate the values equal to 1 and  $\sim 2.6$ . Note that the maximum value of  $Y_{\text{asym}}^{\text{Data}} (1.3 < |\eta_{\text{CMS}}| < 1.8)$  is about 1.3 at  $p_T \sim 2 - 3 \text{ GeV}/c$ , see Fig. 4.16. One can see that most of the  $Y_{\text{asym}}$  values are smaller than 2.6 ( $= 2 \times 1.3$ ). Further comparison is done by taking the results in  $1.3 < |\eta_{\text{CMS}}| < 1.8$  as a reference, and the obtained double ratio is presented in the right panel. It is found that almost all of the results are not larger than 2, indicating the  $2 \times Y_{\text{asym}} (1.3 < |\eta_{\text{CMS}}| < 1.8)$  enables to cover the results up to  $\eta_{\text{CMS}} \sim 6$  (backward). This means that the assumption is supported by the HIJING simulation. A similar conclusion is obtained using DPMJET and PHTHIA+EPS09.

Finally, the  $p_T$ -**dependent upper band** is obtained according to Eq. 4.10, resulting in the  $p_T$ -**dependent mean value** and the corresponding **dispersion** described in Eq. 4.13 and 4.14, respectively.

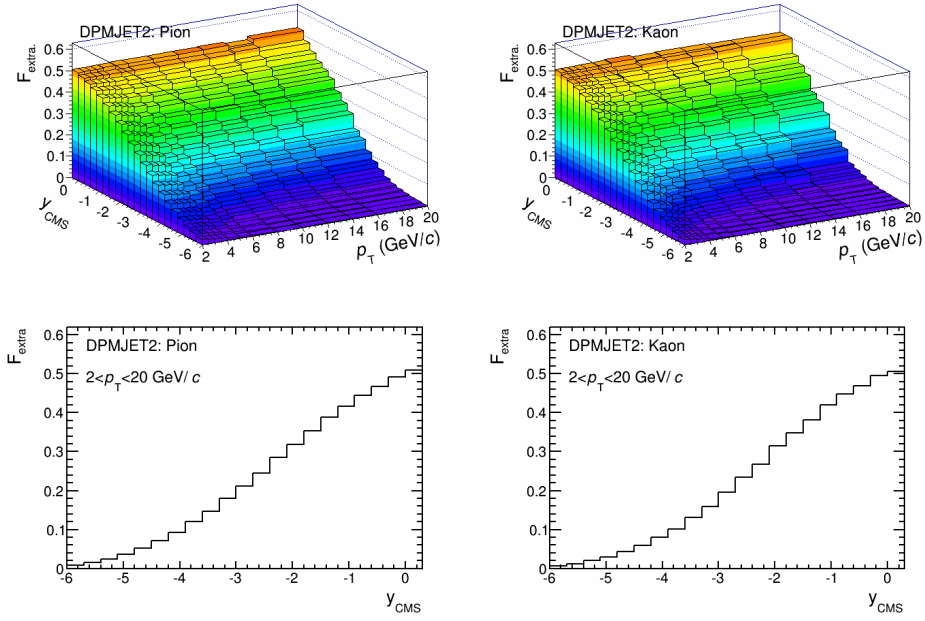


Figure 4.19: Rapidity extrapolation factor  $F_{\text{extra}}$  versus  $p_T$  and  $y_{\text{CMS}}$  for pions (upper left) and kaons (upper right), and versus  $y_{\text{CMS}}$  for pions (bottom left) and kaons (bottom right) in the range  $2 < p_T < 20 \text{ GeV}/c$ . These results are obtained with DPMJET simulations. Note that forward rapidity represents negative side in Monte-Carlo productions which is contrary to our definition.

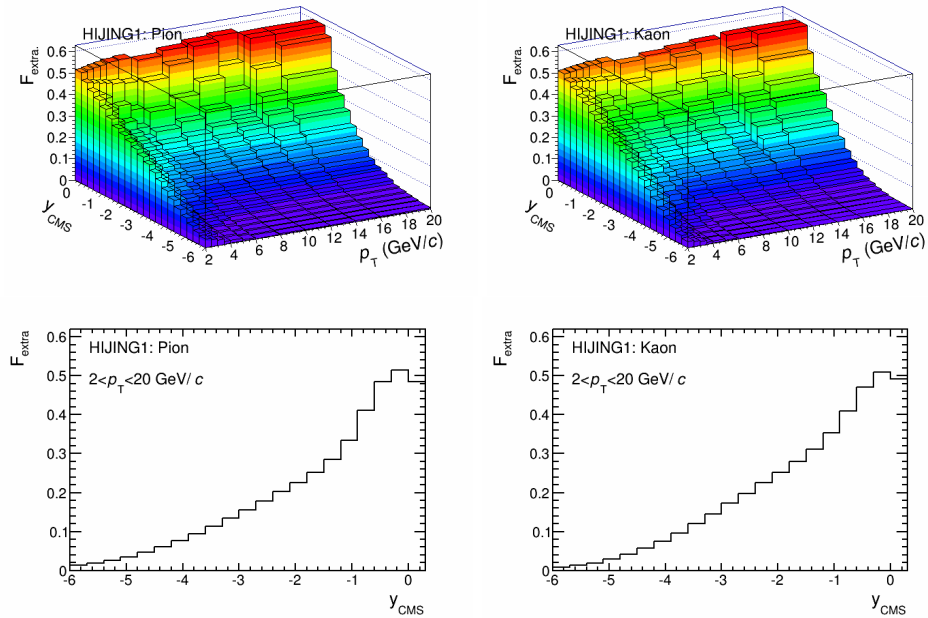


Figure 4.20: Same as Fig. 4.19, but based on HIJING simulations.

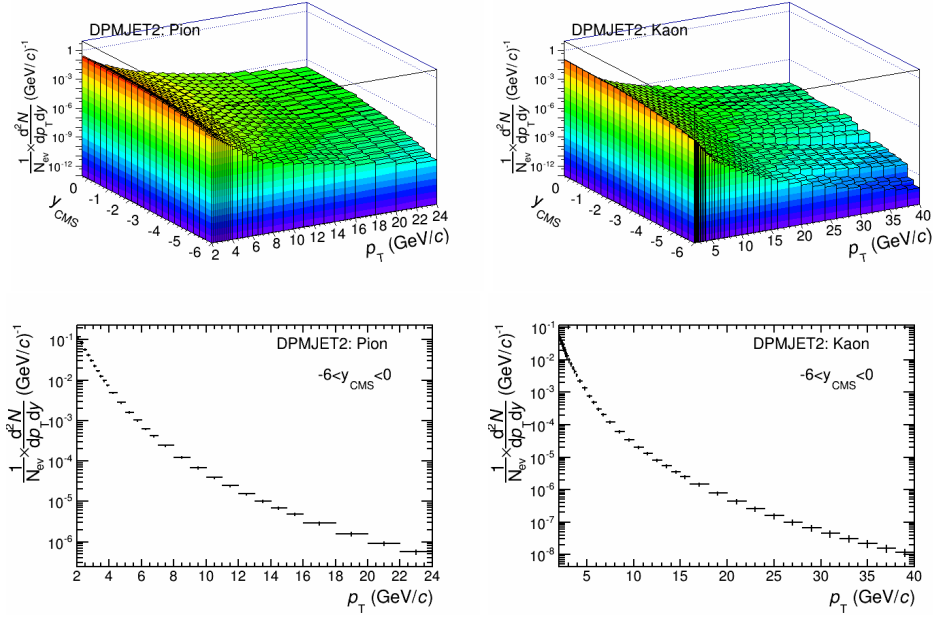


Figure 4.21:  $p_T$  and  $y_{cms}$ -differential distributions for pions (upper left) and kaons (upper right), and  $p_T$ -differential distributions for pions (bottom left) and kaons (bottom right) obtained by taking as input the central barrel measurements together with the rapidity extrapolation factor calculated with DPMJET.

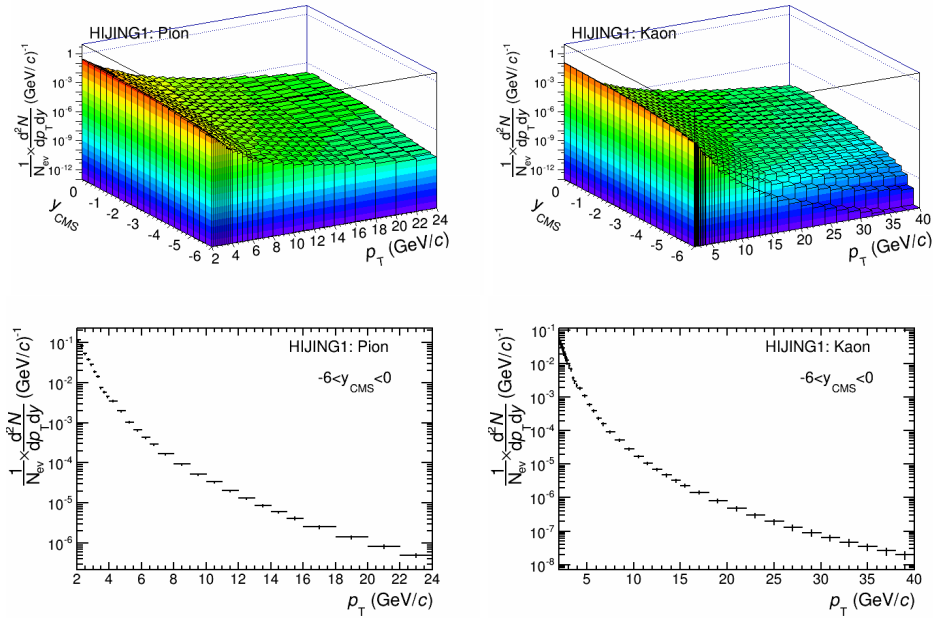


Figure 4.22: Same as Fig. 4.21, but calculated with HIJING.

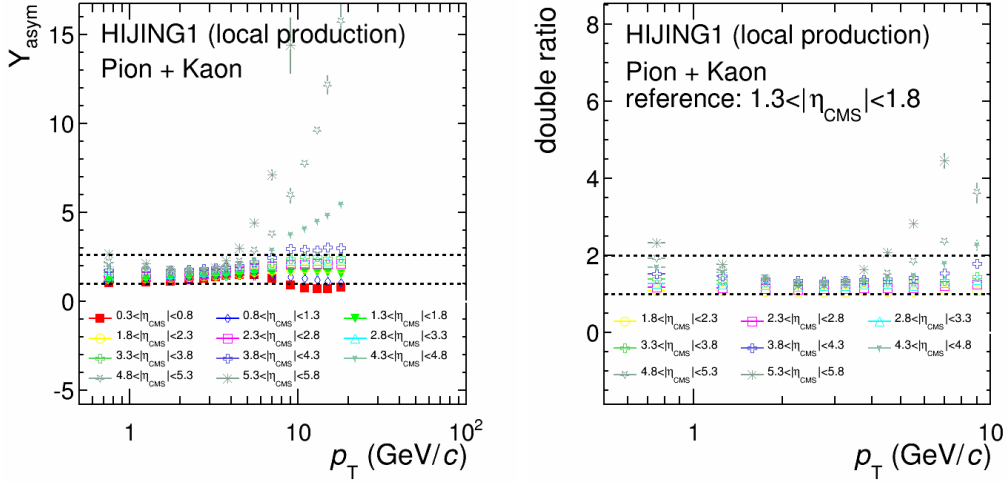


Figure 4.23: Left:  $Y_{\text{asym}}$  defined within different rapidity intervals with HIJING simulation. Right: ratio with taking as the reference  $Y_{\text{asym}}$  in  $1.3 < |\eta_{\text{CMS}}| < 1.8$ . See text for details.

#### 4.2.4 Conversion at Muon Level and Systematic Uncertainty

Up to now, we obtained the  $K^\pm/\pi^\pm$  spectra both at forward ( $0 < y_{\text{CMS}} < 6$ ) and backward rapidity ( $-6 < y_{\text{CMS}} < 0$ ). The next step is to convert the charged hadron spectra to their decay muon spectra. The employed method is a fast simulation procedure which is discussed in Sec. 4.2.4.1. After that, the estimated muons from  $K^\pm$  and  $\pi^\pm$  decays are shown within the desired rapidity windows.

##### 4.2.4.1 Fast Simulation Procedure

The fast simulation procedure allows us to obtain the desired results up to high  $p_T$  and to save CPU time and disk space. For our analysis, it is employed to convert the charged hadron spectra ( $\pi^\pm$  and  $K^\pm$ ) at muon level by including the effect induced by the detector (i.e. multiple-scattering with the front absorber). It is known that the small-angle multiple-scattering in the entering muons can occur in the absorber, which has been represented by applying a sharp cut on  $\rho = 130$  cm:

- $\rho$  is the distance between the interaction vertex and the muon production point related to the first scattering, the so-called decay length;
- sharp cut at  $130 = 90 + 40$  cm, where 90 cm is the distance between the interaction point and the front face of the front absorber and 40 cm is the mean path travelled by  $K^\pm/\pi^\pm$  in the front absorber before the interaction.

The fast simulation procedure can be summarized into the following steps:

- generate the charged  $\pi^\pm$  ( $K^\pm$ ) with uniform  $p_T$  and  $y_{\text{LAB}}$  in the range  $2 < p_T^{\pi^\pm} < 24$  GeV/c ( $2 < p_T^{K^\pm} < 40$  GeV/c) and  $-6.5 < y_{\text{LAB}}^{K^\pm/\pi^\pm} < 6.5$

- one needs to consider the rapidity shift effect  $\Delta y \sim 0.465$  in p–Pb collisions, hence, the rapidity intervals shown in the laboratory frame is  $-6.5 < y_{\text{LAB}}^{K^\pm/\pi^\pm} < 6.5$  in order to cover the corresponding one in the center-of-mass frame  $-6 < y_{\text{CMS}}^{K^\pm/\pi^\pm} < 6$ ;
- it can be noticed that the selected acceptance applied at hadron level is used to enable the decay muon shown in the range  $2 < p_{\text{T}}^\mu < 16 \text{ GeV}/c$ ,  $2.03 < y_{\text{CMS}}^\mu < 3.53$  (forward) and  $-4.46 < y_{\text{CMS}}^\mu < -2.96$  (backward);
- employ the PYTHIA decayer and force the semi-muonic decay of  $p_{\text{T}}^\pm$  and  $K^\pm$ ; the subsequent correction by considering the branching ratio (BR) is implemented
  - $\text{BR}(\mu \leftarrow \pi^\pm) = 1$  and  $\text{BR}(\mu \leftarrow K^\pm) = 0.67$ ;
- weighting procedure:
  1. apply the absorber cut to restrict charged hadrons that decay at distance  $\rho \leq 130 \text{ cm}$ ;
  2. based on the MC information, for each muon, one can extract the transverse momentum of its mother hadron,  $p_{\text{T}}^{\text{flat } K^\pm/\pi^\pm}$ ;
  3. weight the above muon spectra according to a scaling factor, which is defined as the ratio of the provided inputs of charged  $K^\pm/\pi^\pm$  at  $p_{\text{T}}^{\text{inputs}} = p_{\text{T}}^{\text{flat } K^\pm/\pi^\pm}$  to that of simulated flat  $K^\pm/\pi^\pm$  at  $p_{\text{T}}^{\text{flat}} = p_{\text{T}}^{\text{flat } K^\pm/\pi^\pm}$ ;
  4. take into account the systematic uncertainties on the provided  $K^\pm/\pi^\pm$  spectra, as well as the one on rapidity extrapolation factor (for instance, Eq. 4.5);
  5. finally, one can normalize the weighted muon distribution with the total number of generated mother  $K^\pm/\pi^\pm$ .

#### 4.2.4.2 Systematic Uncertainty on Absorber-Related Effects

Based on the fast simulation procedure, one can convert the hadron spectra to muon level. According to performance studies, the parameter  $\rho$  can be varied in the range  $110 < \rho < 150 \text{ cm}$  in order to include the possible systematics due to the path of pions and kaons travelling in the front absorber. The resulting deviation of background with respect to the one obtained using  $\rho = 130 \text{ cm}$ , allows to give the systematic uncertainty on this absorber-related effect. It is the 15% both for  $\pi^\pm$  and  $K^\pm$ , as shown in the left and right panels of Fig. 4.24. The same strategy was implemented in  $R_{\text{AA}}$  and  $v_2$  analyses in Pb–Pb collisions at  $\sqrt{s_{\text{NN}}} = 2.76 \text{ TeV}$  [159, 315].

#### 4.2.4.3 Background Estimated at Forward and Backward Rapidity with the Systematic Uncertainty

Figure 4.25 shows the estimated background due to decay muons in the rapidity range  $2.03 < y_{\text{CMS}} < 3.53$ . The  $p_{\text{T}}$  distributions of muons from pion decays with

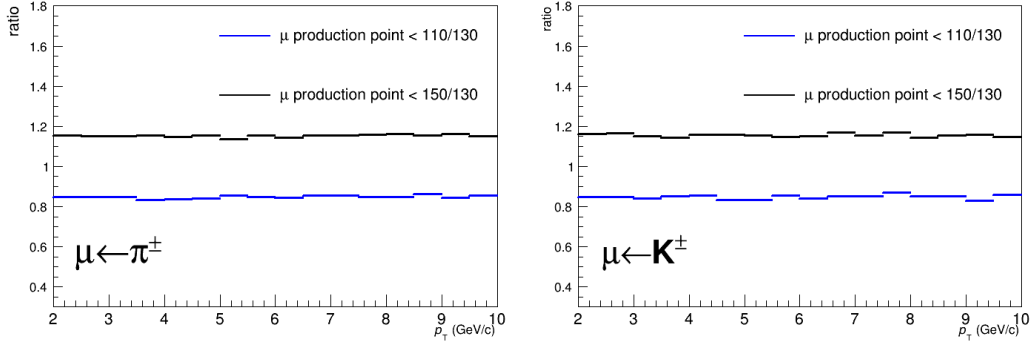


Figure 4.24: Ratio of the yields of muons from charged pion and kaon decays when applying a cut on  $\rho$  varied within  $110 < \rho < 150$  cm over  $\rho < 130$  cm, as shown in the left and right panels, respectively.

DPMJET and HIJING are presented in the upper left panel. We take the results based on DPMJET as the central value, and the deviation with respect to HIJING as the systematic uncertainty due to the modeling of cold nuclear matter effects, which is included in the middle left plot. The contribution from the central barrel input (with the  $p_T$  and  $y$  extrapolation) varies within 5 – 10% in the range  $2 < p_T < 16$  GeV/ $c$ . The systematic uncertainty on the absorber effect is  $\sim 15\%$  as discussed in the previous sub-section. The total systematic uncertainty on muons from pion decays is about 20 – 50% ( $p_T$ -dependent) in the considered  $p_T$  region. The bottom left plot shows the  $p_T$  distributions of muons from pion decays together with the total systematic uncertainty. The right three plots are similar to the left three ones, but for the muons from kaon decays. The total systematic uncertainty varies within 20 – 35%, the one on models being dominant in the intermediate  $p_T$  region. When combining together the contributions from pions and kaons, the results are shown in Fig. 4.26. That concerns the  $p_T$  distributions of muons from pion decays (red), kaon decays (blue) and both pion and kaon decays (black) in the rapidity range  $2.03 < y_{\text{CMS}} < 3.53$  (left) with different sources of systematics (right). One can see that the yields of muons from pion decays are similar to those from kaon decays, and this is consistent with the behavior found in Pb–Pb analysis (see Sec. 4.1.2.4). The total systematic uncertainty is  $\sim 20 - 30\%$  in the  $p_T$  range  $2 < p_T < 16$  GeV/ $c$ , while the uncertainty on models is dominant in the intermediate  $p_T$  region. The systematic uncertainty on the absorber-related effect is correlated between the contributions from pions and kaons, adding linearly during the combination.

Similarly, Fig. 4.27 shows the estimated background in the rapidity range  $2.96 < y_{\text{CMS}} < 3.53$  with which allows one to define the forward-to-backward ratio ( $R_{\text{FB}}$ , see Eq. 6.7). The total systematic uncertainty of muons from pion (kaon) decays is  $\sim 20 - 50\%$  ( $20 - 35\%$ ) in the given  $p_T$  region. Figure 4.28 presents the combined results together with the systematic uncertainty. Similar yields of muons from pion and kaon decays are also observed, and the total systematic uncertainty varies within  $\sim 18 - 30\%$  in the interval  $2 < p_T < 16$  GeV/ $c$ , while the uncertainty on models is dominant in the intermediate  $p_T$  region.

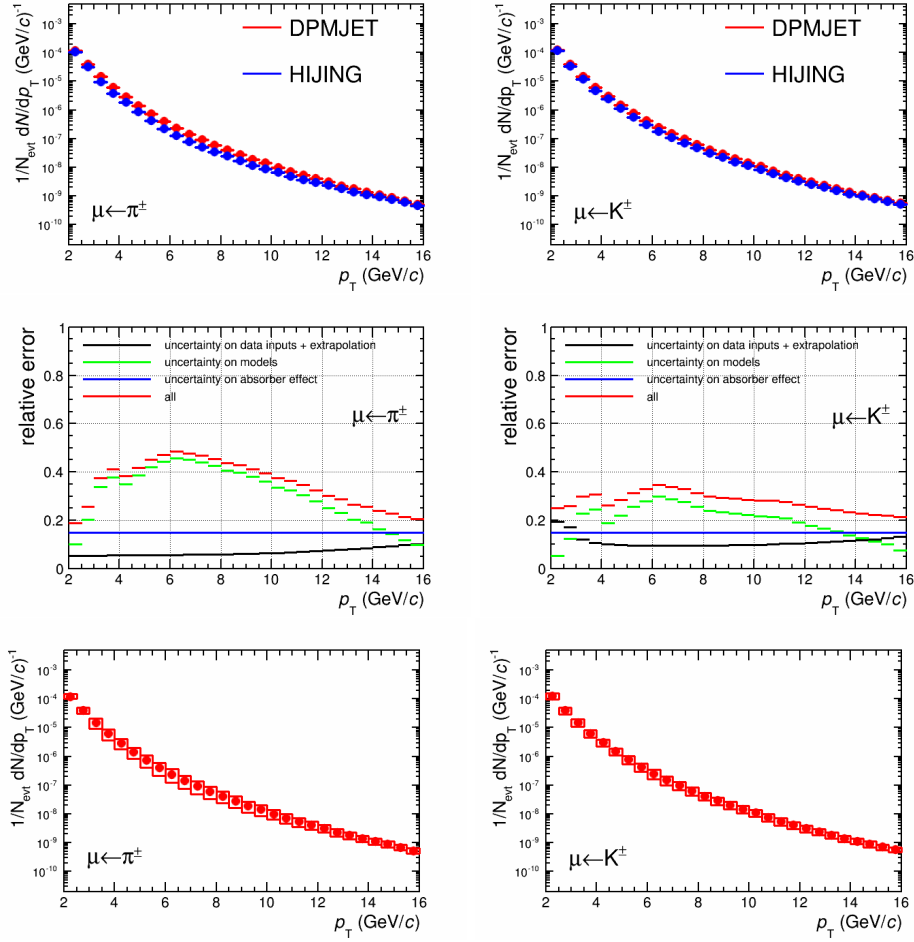


Figure 4.25: Muons from pions decays in the range  $2.03 < y_{\text{CMS}} < 3.53$ : results from different models (upper left). Different sources of systematic uncertainties (middle left). Results with total systematic uncertainties (bottom left). The right three plots are similar to the left ones, but for muons from kaon decays. See text for details.

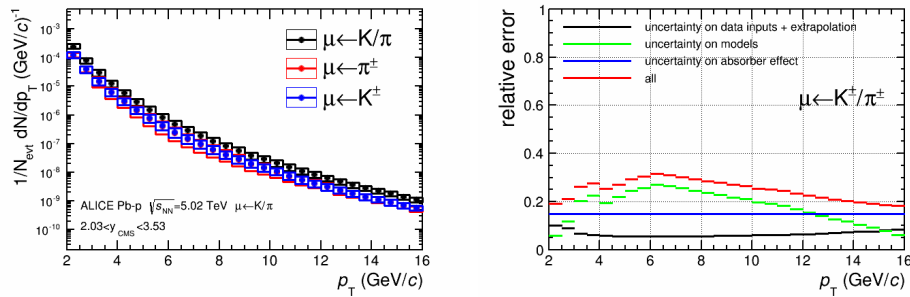


Figure 4.26: Left:  $p_T$  distributions of muons from pion decays (red), kaon decays (blue) and combined pion and kaon decays (black) at forward rapidity  $2.03 < y_{\text{CMS}} < 3.53$ . Right: different sources of systematics.

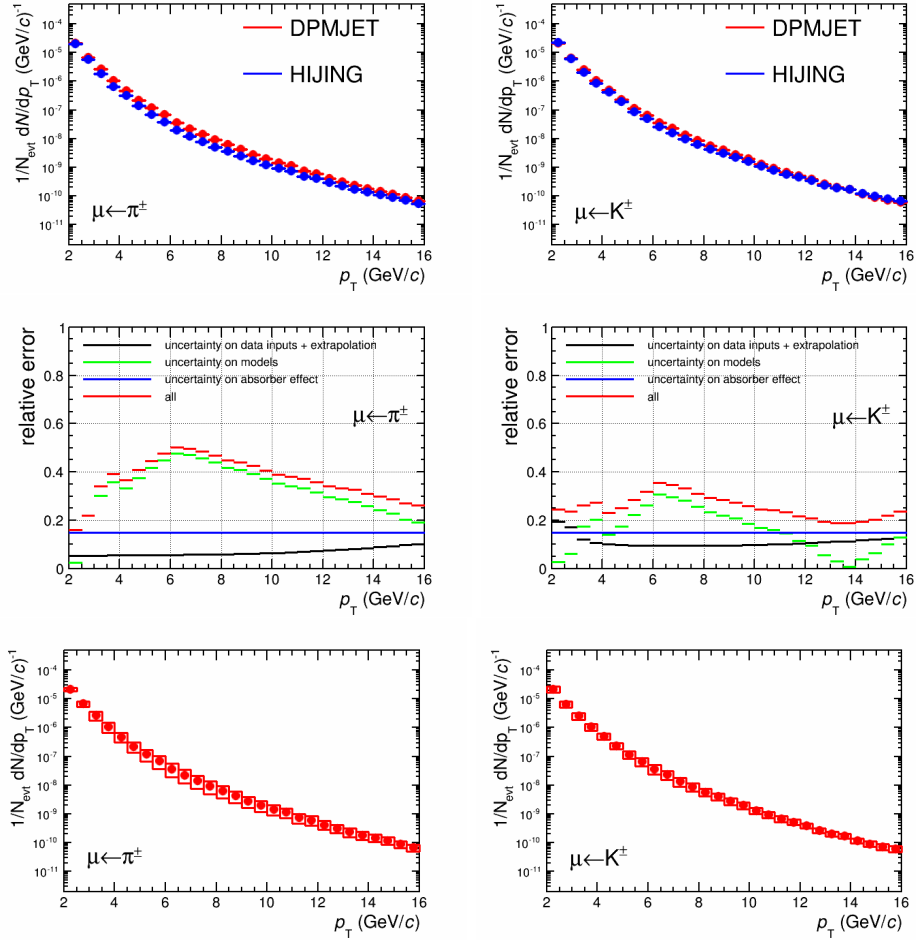


Figure 4.27: Muons from pions decays in the range  $2.96 < y_{\text{CMS}} < 3.53$ : results from different models (upper left). Different sources of systematic uncertainties (middle left). Results with total systematic uncertainties (bottom left). The right three plots are similar to the left ones, but for muons from kaon decays. See text for details.

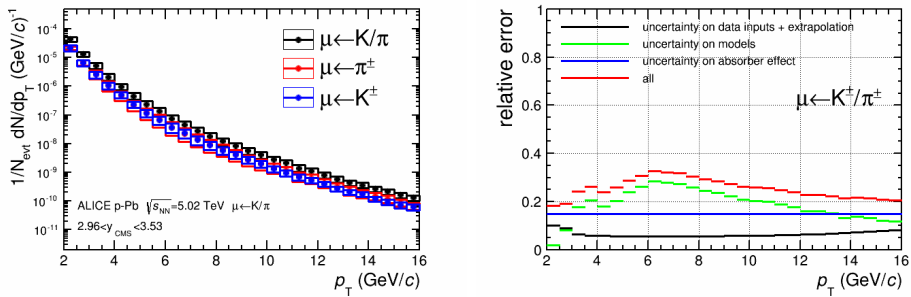


Figure 4.28: Left:  $p_T$  distributions of muons from pion decays (red), kaon decays (blue) and combined pion and kaon decays (black) at forward rapidity  $2.96 < y_{\text{CMS}} < 3.53$ . Right: different sources of systematics.

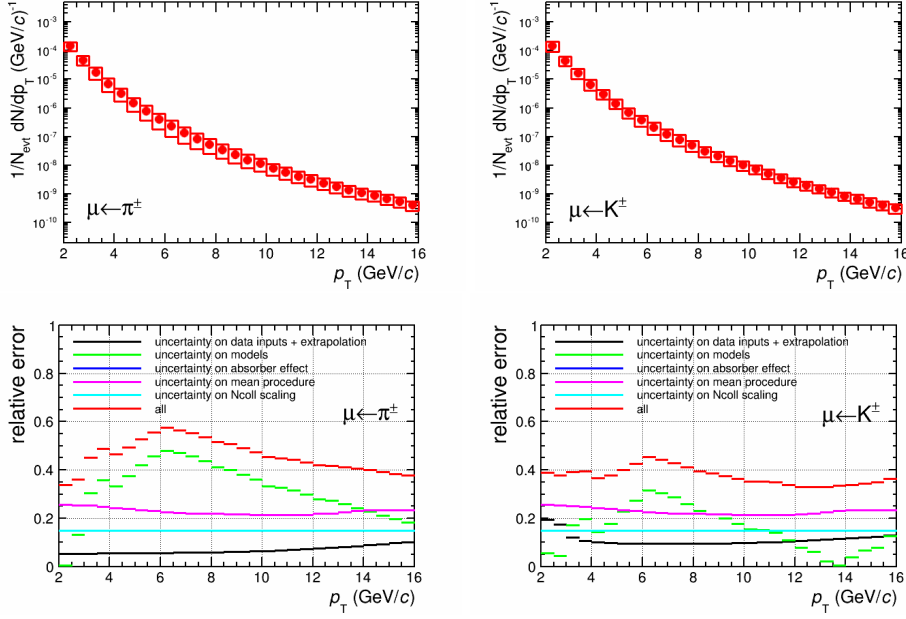


Figure 4.29: Muons from pions decays in the range  $-4.46 < y_{\text{CMS}} < -2.96$ : different sources of systematic uncertainties (upper left). Results with total systematic uncertainties (bottom left). The right three plots are similar to the left ones, but for muons from kaon decays. See text for details.

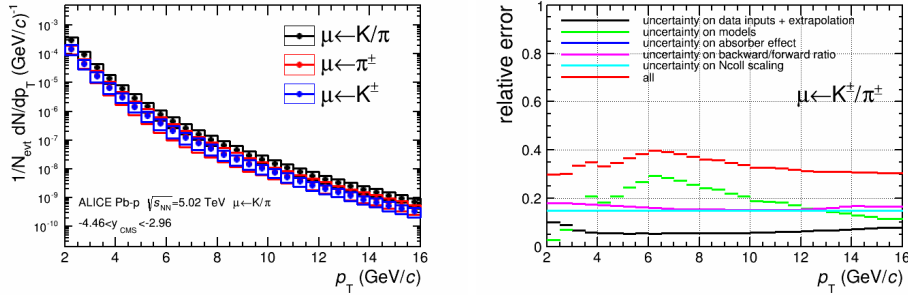


Figure 4.30: Left:  $p_T$  distributions of muons from pion decays (red), kaon decays (blue) and combined pion and kaon decays (black) at forward rapidity  $-4.46 < y_{\text{CMS}} < -2.96$ . Right: different sources of systematics.

Figure 4.29 shows the estimated background at backward rapidity  $-4.46 < y_{\text{CMS}} < -2.96$ . The  $p_T$  distribution of muons from pion (kaon) decays is shown in the upper left (upper right) panel together with the total systematic uncertainty (red boxes). The different sources of systematic uncertainty are displayed in the bottom left (bottom right) panel. The uncertainty on the mean procedure is obtained via Eq. 4.14. The uncertainty on  $N_{\text{coll}}$  is induced by the deviation of  $Y_{\text{asym}}^{\text{Data}}$  with unity at high  $p_T$  ( $\sim 15\%$ ). It is correlated between the pion and kaon components. The total systematic uncertainty is  $\sim 30 - 60\%$  ( $35 - 45\%$ ) for pion (kaon)

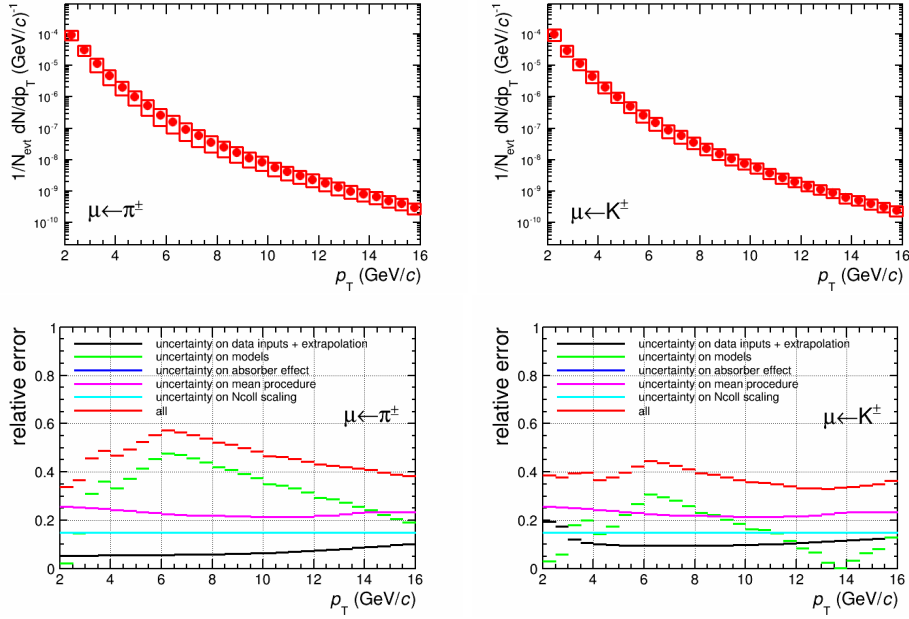


Figure 4.31: Muons from pion decays in the range  $-3.53 < y_{\text{CMS}} < -2.96$ : different sources of systematic uncertainties (upper left). Results with total systematic uncertainties (bottom left). The right three plots are similar to the left ones, but for muons from kaon decays. See text for details.

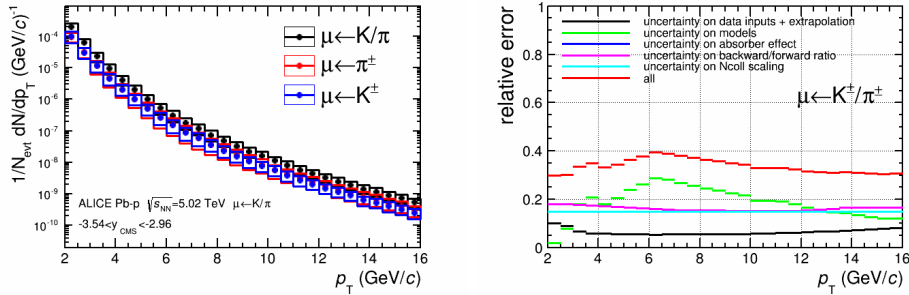


Figure 4.32: Left:  $p_T$  distributions of muons from pion decays (red), kaon decays (blue) and combined pion and kaon decays (black) at forward rapidity  $-3.53 < y_{\text{CMS}} < -2.96$ . Right: different sources of systematics.

components in the considered  $p_T$  region. Figure 4.30 shows the combined results and also the systematic uncertainty sources. The  $p_T$  distributions of muons from pion decays, kaon decays and combined pion and kaon decays are displayed in the left panel and the different sources of systematic uncertainty are shown in the right panel. It is found that the total systematic uncertainty varies within 30 – 40%. The uncertainty on models is still dominant at intermediate  $p_T$ .

Figures 4.31 and 4.31 show similar results as Fig. 4.29 and 4.30, but for  $-3.53 < y_{\text{CMS}} < -2.96$ . Finally, the total systematic uncertainty is 30 – 40% in the  $p_T$  range  $2 < p_T < 16$  GeV/c.

#### 4.2.4.4 Fraction of Background with respect to Inclusive Muons

In order to quantify the background contribution with respect to the inclusive muons, the ratio background/inclusive is calculated both at forward and backward rapidity.

Figure 4.33 shows the background fraction as a function of  $p_T$ , obtained at forward ( $2.03 < y_{\text{CMS}} < 3.53$ , left) and backward ( $-4.46 < y_{\text{CMS}} < -2.96$ , right) rapidity, respectively. The boxes indicate the total systematic uncertainty on the estimated background. One can see that the fraction decreases with increasing  $p_T$  and varies from  $\sim 27\%$  (35%) at  $p_T = 2 \text{ GeV}/c$  to 2% (2%) at high  $p_T$ , at forward (backward) rapidity.

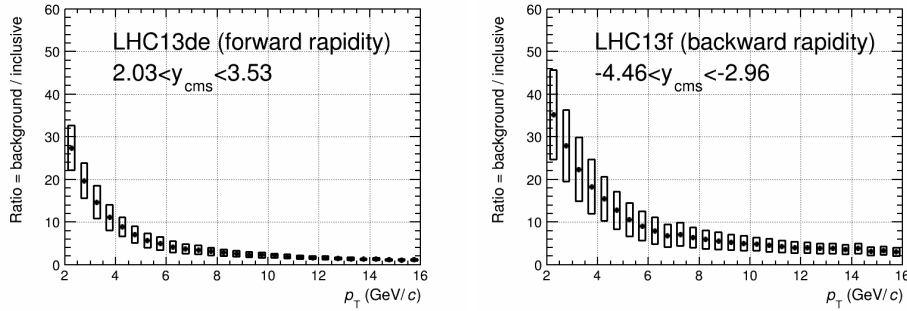


Figure 4.33: Fraction of the estimated background with respect to inclusive muons in the rapidity range  $2.03 < y_{\text{CMS}} < 3.53$  (left) and  $-4.46 < y_{\text{CMS}} < -2.96$  (right). The boxes denote the total systematic uncertainty on the background.

The background fractions are compared in the restricted acceptance  $2.96 < |y_{\text{CMS}}| < 3.53$ , see Fig. 4.34. The background fraction decreases from about 19% to 1% with increasing  $p_T$  at forward rapidity ( $2.96 < y_{\text{CMS}} < 3.53$ , black), and from about 42% to 3% at backward rapidity ( $-3.54 < y_{\text{CMS}} < -2.96$ , red), indicating larger background contribution in the later region.

### 4.2.5 Cross-Checks and Discussion

In this sub-section, some cross-checks concerning the strategy for background estimation are reported for discussion.

#### 4.2.5.1 Decay probability versus longitudinal momentum

The first comment is about the decay probability from the fast simulation procedure. It is known that  $K^\pm/\pi^\pm$  with large longitudinal momentum ( $p_z$ ) have a small probability to decay into muons at a distance  $\rho < 130 \text{ cm}$ . The decay probability is defined as

$$\text{probability} = \frac{Y^{K^\pm/\pi^\pm \rightarrow \mu}}{Y^{K^\pm/\pi^\pm}} \quad (4.16)$$

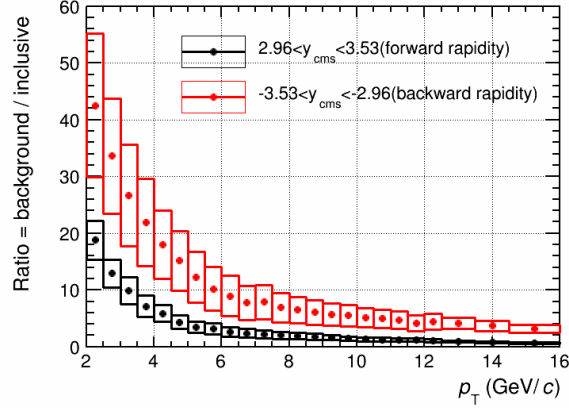


Figure 4.34: Fraction of the estimated background with respect to inclusive muons in the rapidity range  $2.96 < y_{\text{CMS}} < 3.53$  (black) and  $-3.54 < y_{\text{CMS}} < -2.96$  (red). The boxes denote the total systematic uncertainty on the background.

where,  $Y^{K^\pm/\pi^\pm \rightarrow \mu}$  indicates the distributions of muons from  $K^\pm/\pi^\pm$  decays,  $Y^{K^\pm/\pi^\pm}$  denotes the total distribution of  $K^\pm/\pi^\pm$ .

The probability can be obtained via the fast simulation procedure as:

- extract the  $p_z$  distribution of  $K^\pm/\pi^\pm$  with DPMJET simulation (LHC13b2\_efix);
- take the extracted distribution as input to the fast simulation procedure, and then convert to muons;
- absorber effect implemented by cutting on the decay length ( $\rho < 130$  cm).

The obtained result is shown in Fig. 4.35. One can see that the probability decreases with increasing  $p_z$ , as expected.

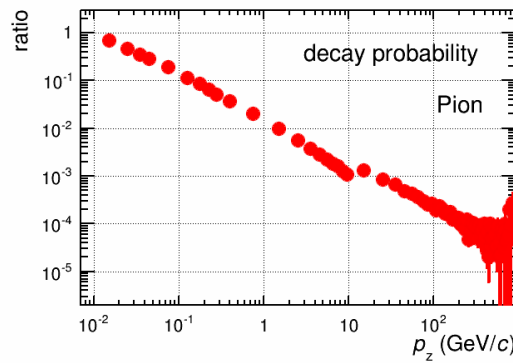


Figure 4.35: Decay probability of charged pions as a function of  $p_z$  estimated at  $\rho < 130$  cm, by means of the fast simulation. See the text for details.

#### 4.2.5.2 Fast Simulation versus Full Simulation

The second comment concerns the comparison of the absorber effect between the fast and the full simulation. The comparison is implemented according to the following procedure:

- obtain the  $p_T$  distributions of  $K^\pm/\pi^\pm$  at pure kinematics level by means of full MC simulation;
- perform the fast simulation by taking as input the above distribution: use the input to scale muons generated with a flat  $K^\pm$  or  $\pi^\pm$  distribution after cutting on the decay length ( $\rho < 130$  cm);
- compare the scaled  $p_T$  distribution of muons with the ones obtained at reconstruction level of full simulation.

The  $p_T$  distributions of muons from charged pion and kaon decays obtained from the fast and the full simulation in the rapidity range  $-4 < y_{\text{LAB}} < -2.5$ , are shown in the left panel of Fig. 4.36. The ratio between them is presented in the right panel. Note that the boxes indicate the combined statistical and systematic uncertainties. One can see that the ratio is consistent with unity within uncertainty, indicating that the fast simulation can reproduce the absorber effect as in the full simulation. Further studies within sub-rapidity ranges, for example,  $-3.1 < y_{\text{LAB}} < -2.5$  and  $-4 < y_{\text{LAB}} < -3.1$ , lead to the same conclusion.

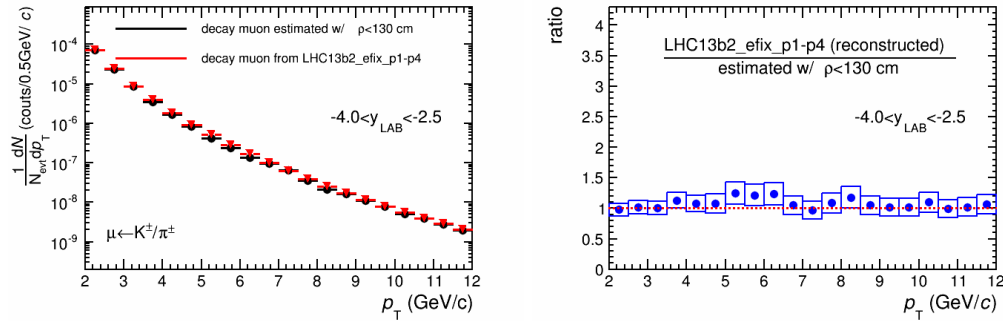


Figure 4.36: Left:  $p_T$  distributions from the fast and the full simulations in the rapidity range  $-4 < y_{\text{LAB}} < -2.5$ . Right: ratio of the distribution from the full distribution to that from the fast simulation. The boxes correspond to the combined statistical and systematic uncertainties.

#### 4.2.5.3 Absorber Effect

The absorber effect is expected to be the same within symmetric rapidity intervals in the laboratory frame. It can be checked via the backward-to-forward ratio, which is defined as

$$\frac{\text{backward}}{\text{forward}} = \frac{Y(-4.46 < y_{\text{CMS}} < -2.96)}{Y(2.03 < y_{\text{CMS}} < 3.53)} = \frac{Y(-4 < y_{\text{LAB}} < -2.5)}{Y(-4 < y_{\text{LAB}} < -2.5)} \quad (4.17)$$

The backward-to-forward ratio of charged pions is shown in the upper two panels of Fig. 4.37, and the results without (i.e. no cut on  $\rho$ ) and with absorber effect (i.e.  $\rho < 130$  cm) are presented in the left and right panels, respectively. One can see that they are very close to each other since the absorber effect cancels out in the defined ratio. A same conclusion is also found at muon level, as shown in the bottom two plots of Fig. 4.37. It is interesting to see that the defined ratio is similar at hadron and muon level.

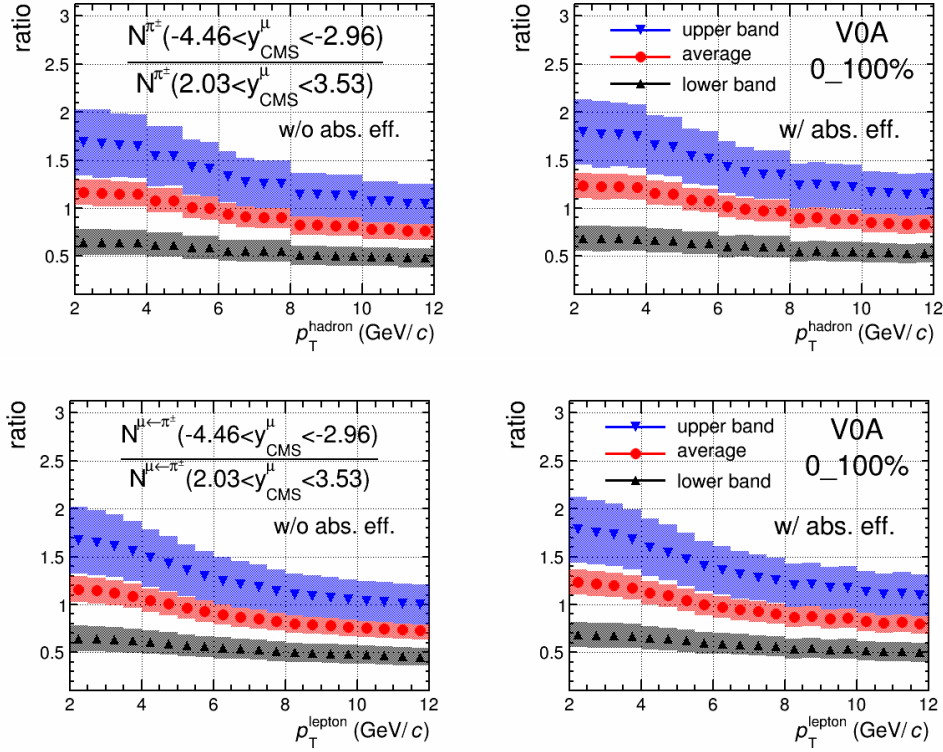


Figure 4.37: Upper left: backward-to-forward ratio of charged pions which decay into muons in  $2.5 < |y_{\text{LAB}}| < 4$  (i.e. corresponding to  $2.03 < |y_{\text{CMS}}| < 3.53$  at forward and  $-4.46 < |y_{\text{CMS}}| < -2.96$  at backward rapidity in the CMS frame) without taking into account the absorber effect (i.e. no cut on decay length  $\rho$ ). The lower, upper and mean value are obtained via Eq. 4.9, 4.10 and 4.13, respectively. The shadowed region denotes the corresponding systematic uncertainty. Upper right: similar to the upper left one, but including the absorber effect ( $\rho < 130$  cm). Bottom: similar to the upper two plots, but for the muons from pion decays.

Alternatively, the absorber effect can be checked by means of the backward-to-forward ratio defined within symmetric rapidity intervals in the center-of-mass frame, which are the ones used in the  $R_{\text{FB}}$  analysis (Eq. 6.7)

$$\frac{\text{backward}}{\text{forward}} = \frac{Y(-3.53 < y_{\text{CMS}} < -2.96)}{Y(2.96 < y_{\text{CMS}} < 3.53)} = \frac{Y(-3.07 < y_{\text{LAB}} < -2.5)}{Y(-4 < y_{\text{LAB}} < -3.43)} \quad (4.18)$$

The absolute value of mean rapidity is larger in the denominator than that in the

numerator in the laboratory frame, indicating that  $p_z$  is higher and that the related decay probability of charged hadrons is lower. That means that the backward-to-forward ratio can be enhanced when including the absorber effect. The results of charged pions are shown in the upper two plots of Fig. 4.38, and the ones without and with absorber effect are presented in the left and right panel, respectively. One can see that the backward-to-forward is enhanced by a factor of about 2 in the given  $p_T$  region. A same conclusion is found at muon level, as shown in the bottom two plots of Fig. 4.38. Remark that the enhancement factor ( $\sim 2$ ) is consistent with the one obtained with other analysis methods [316].

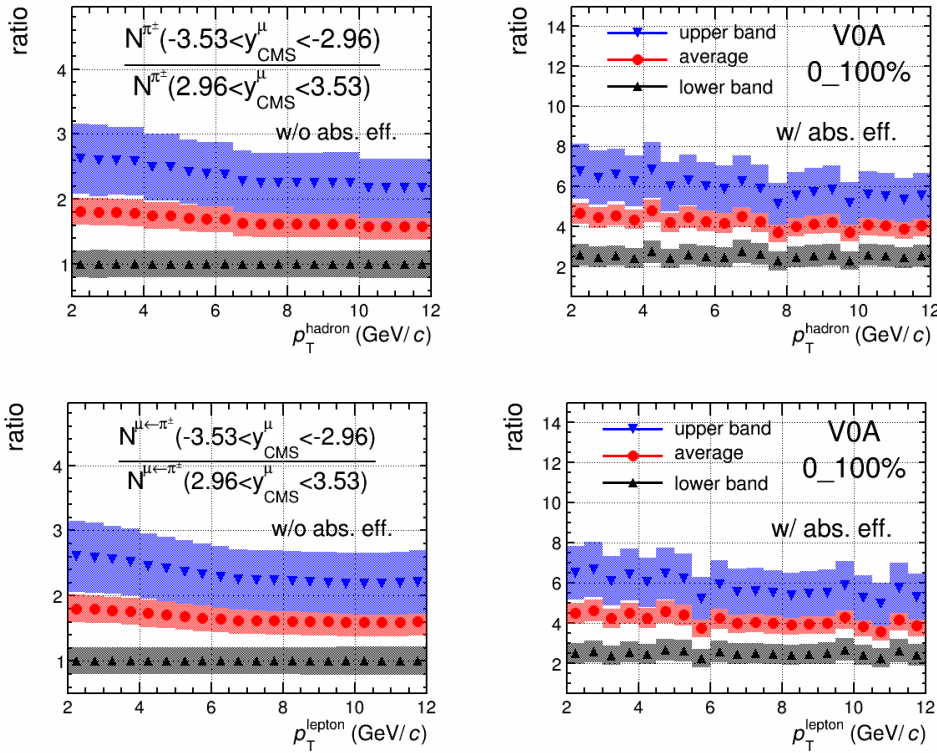


Figure 4.38: Similar to Fig. 4.37, but in the rapidity range  $2.96 < |y_{\text{CMS}}| < 3.53$ .

#### 4.2.5.4 Trigger induced Bias with the Used Analysis Strategy

It is argued [259] that, due to the large mass of heavy quarks, one expects the events with charm/beauty to yield more particles than the other events. The probability to have these events can be increased for the low (MSL) and high (MSH)  $p_T$  triggered muon data with thresholds set at 0.5 and 4.2 GeV/c, respectively. Hence, the mean multiplicity of the signal and of the background is expected to be larger than that in Minimum-Bias (MB) event. In our analysis, the background both at forward and backward rapidity is obtained for MB, and then, in order to extract the signal, it is subtracted from the inclusive muons obtained with MSL/MSH data.



First, we calculated the mean multiplicity of SPD tracklets in MC simulations. It is about 51 without requesting the matching between tracker tracks and trigger tracks, while it is about 52 with matching and when passing the all/low  $p_T$  cut. The deviation is very small.

Then, we estimated the mean multiplicity of SPD tracklets in data. The later is about 50 and 54 in MB and MSL triggered events, respectively. The deviation is  $\sim 6\%$  between them, and it could be due the mean  $p_T$  of muons which can be shifted by the trigger threshold [317]. Further checks by varying the obtained background within 6% were performed, giving about 2% (at maximum) deviation on final measurements at  $p_T = 2$  GeV/ $c$ . Finally, this contribution is neglected since the total systematic uncertainty is  $> \sim 16\%$  nearby 2 GeV/ $c$ .

### 4.3 Background within Individual Event Activity Classes in p–Pb Collisions

In this section, I discuss the background subtraction within different event activity classes. The general idea is to follow the strategy used in multiplicity integrated collisions both at forward and backward rapidity. The resulting challenges are discussed in detail. Finally, the obtained background together with the uncertainty is shown within selected rapidity intervals and event activity bins for different estimators.

#### 4.3.1 Challenges and Solutions

We can follow a similar strategy for background estimation as employed in multiplicity integrated analysis, to get the results within different event activity bins. However, there are some issues to be considered:

- charged  $K^\pm/\pi^\pm$  inputs measured in the central barrel with different event activity estimators (V0A, CL1 and ZNA): indeed,  $p_T$  distributions of charged  $K^\pm$  are missing below 3 GeV/ $c$  for the results based on CL1 and ZNA, as well as the related systematic uncertainty. Also, one needs to implement the  $p_T$  extrapolation for pions and kaons up to 24 and 40 GeV/ $c$ , respectively, as well as the possible extrapolation for kaons down to 2 GeV/ $c$ , in order to obtain the decay muons in the range  $2 < p_T^\mu < 16$  GeV/ $c$ . This problem can be fixed by means of fitting procedure with different functions. See Sec. 4.3.2 for details.
- event activity determination at pure kinematic level: note that the rapidity extrapolation factor (see Eq. 4.5) is defined from the Monte-Carlo event generators at kinematic level, whereas, the event activity determination should be implemented with the reconstructed multiplicities if one follows the normal procedure such as in Pb–Pb analysis (see Sec. 3.3 and Ref. [258]). We can use the Optical Glauber Model [35] that takes into account the pure geometry of the colliding system, to determine the event activity binning at kinematics level. More detailed information is shown in Sec. 4.3.3.

- deviation between data and MC: within individual event activity classes, the  $\eta$ -dependence of the charged particles in MC can be checked with the corresponding measurements at the LHC. The available data allows one to tune the MC in order to decrease the deviation between them as more as we can. Concerning the  $p_T$ -dependence, we can follow the strategy employed in the multiplicity integrated analysis by using different model predictions to cover the deviation. See Sec. 4.3.4.
- asymmetry factor ( $Y_{\text{asym}}$ ) of charged hadrons measured within desired event activity bins: as mentioned in previous section, the charged hadron distributions at backward rapidity are obtained by scaling the ones at forward rapidity. The related scaling factor is  $Y_{\text{asym}}$ , which is defined as the ratio of the distributions in symmetric rapidity intervals between backward and forward rapidity. It is measured by the CMS Collaboration in the multiplicity integrated analysis. One needs to get/estimate the event activity dependence of the  $Y_{\text{asym}}$  which can be accessed by means of a measurement within a given  $E_T$  range, where  $E_T$  indicates the transverse energy. This is discussed in Sec. 4.3.5.

### 4.3.2 Charged Hadron Spectra with Different Estimators

The charged  $K^\pm/\pi^\pm$  distributions measured at central rapidity with ALICE have been updated recently. The modifications are:

- the rapidity acceptance changes from  $|y_{\text{CMS}}^{K^\pm/\pi^\pm}| < 0.3$  to  $0 < y_{\text{CMS}}^{K^\pm/\pi^\pm} < 0.5$ ; further checks are done and the deviation of the measured multiplicity density with respect to that in MC is small;
- only the total systematic uncertainty is available;
- some information is missing concerning the results based on CL1 and ZNA
  - systematic uncertainty for both pions and kaons;
  - distribution of kaons are not available in the range  $p_T < 3 \text{ GeV}/c$ .

#### 4.3.2.1 Charged Hadron Inputs

Figure 4.39 shows the relative statistical and systematic uncertainty of charged pions with different event activity estimators. The results based on V0A, CL1 and ZNA are presented in the upper, middle and bottom panels, respectively. The systematic uncertainty of the results with V0A seems to be dominated by the correlated components within different event activity intervals, which are summed linearly when combining V0A intervals. The maximum value is about 7.4% in the  $p_T$  range  $2 < p_T^{K^\pm/\pi^\pm} < 15 \text{ GeV}/c$ . It is argued [318] that  $\sim 7\%$  can be the conservative systematic uncertainty with CL1 and ZNA.

The results for charged kaons are shown in Fig. 4.40. The relative uncertainties with taking V0A, CL1 and ZNA as the event activity estimators, are also presented in the upper, middle and bottom panels, respectively. The systematic uncertainty is

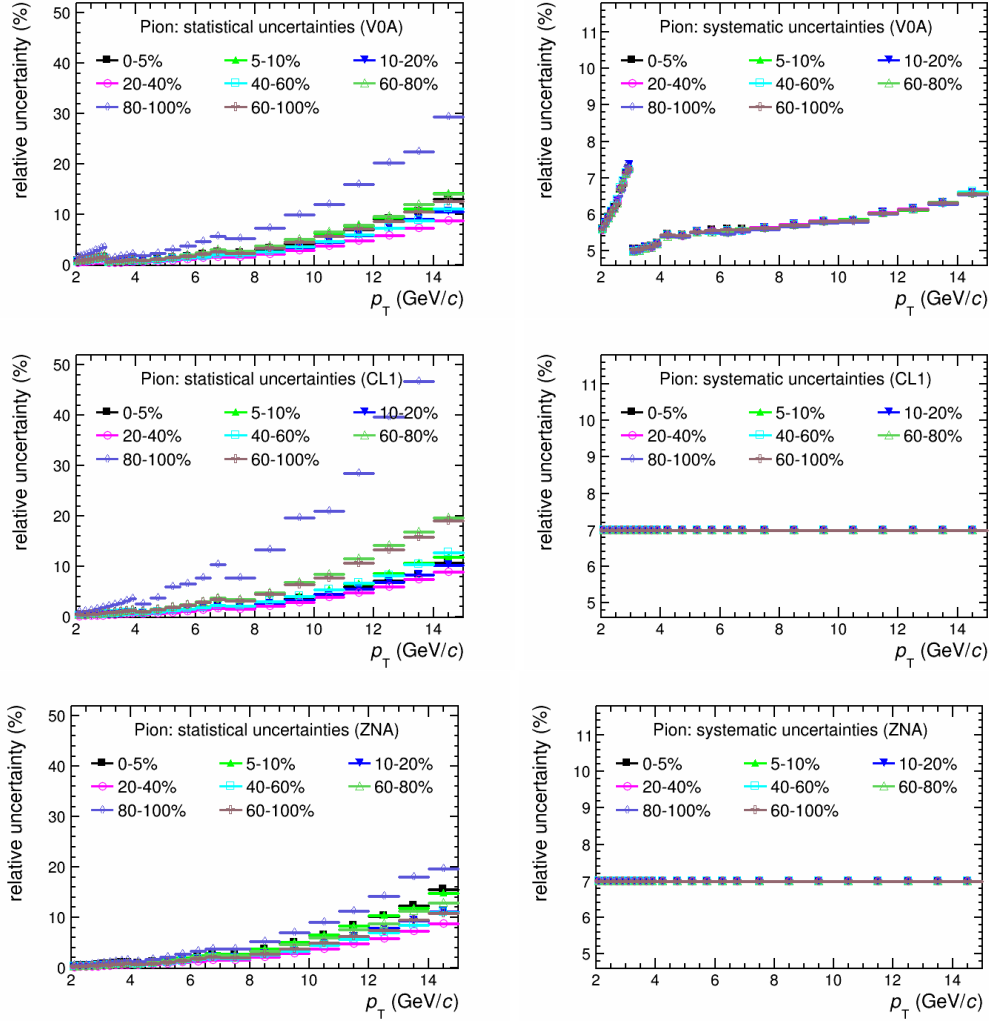


Figure 4.39: Relative statistical and (total) systematic uncertainty of charged pions measured at central rapidity  $0 < y_{\text{CMS}} < 0.5$  with V0A (upper), CL1 (middle) and ZNA (bottom).

$\sim 10\%$  maximum with V0A in the given  $p_T$  region. Since the systematic uncertainty with CL1 and ZNA is missing, it is suggested [318] to use a conservative estimation:  $\sim 17\%$  at  $p_T = 3 \text{ GeV}/c$ , while it is  $\sim 9\%$  at  $p_T = 9 \text{ GeV}/c$ .

#### 4.3.2.2 Transverse Momentum Extrapolation

Concerning the high  $p_T$  extrapolation, one can implement the same procedure both for pions and kaons, as discussed in Sec. 4.2.2. For the  $p_T$  extrapolation at low  $p_T$  of charged kaon distributions, we can employ a similar method in order to achieve it:

- combine the statistical and systematic uncertainty via  $\sqrt{(\text{stat.})^2 + (\text{syst.})^2}$ ;

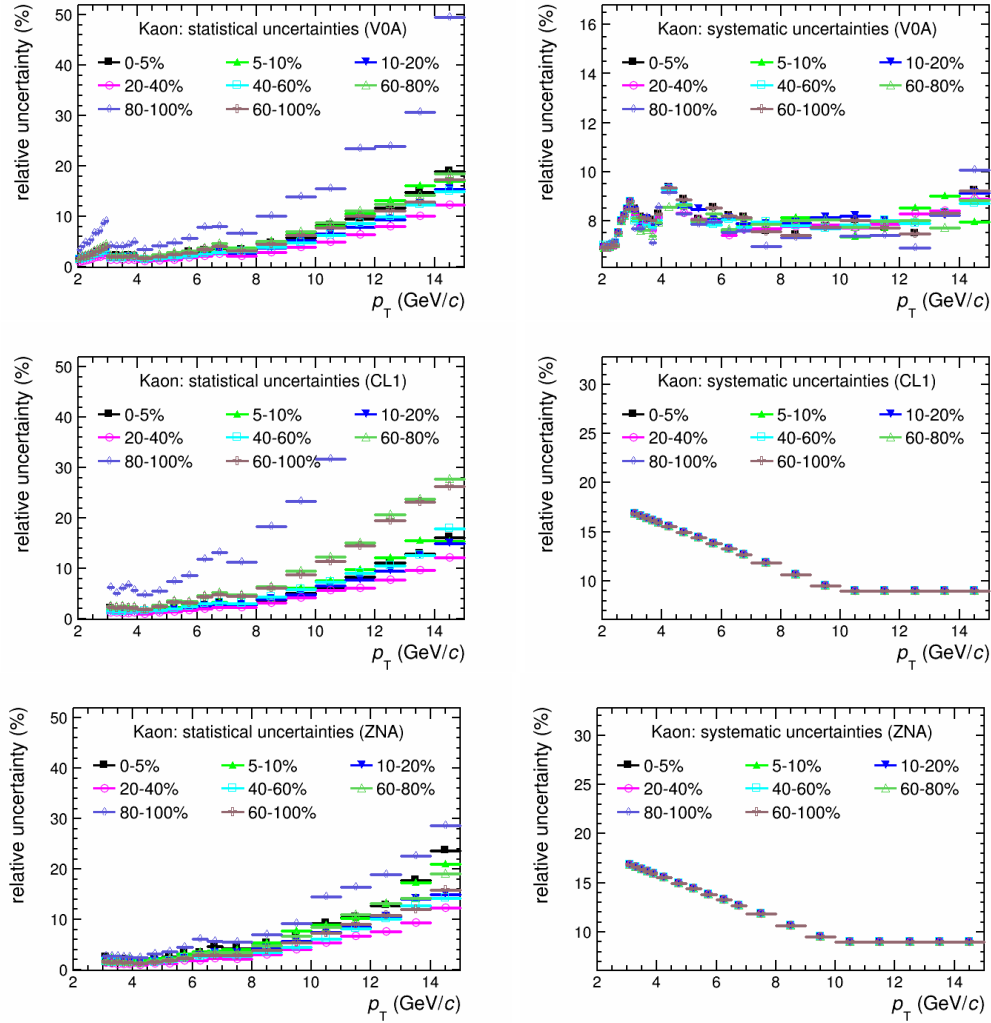


Figure 4.40: Same as Fig. 4.39, but for charged kaons.

- fit the distribution in the intermediate  $p_T$  region with 3 kinds of functions: Blast Wave, Levy-Tails and Gaussian; then extrapolated down to 2 GeV/c;
- take the average between them as the central value in the range  $p_T < 3$  GeV/c, and the dispersion can be obtained as well;
- the systematic uncertainty on the interpolation procedure can be estimated as  $\sqrt{(\text{dispersion})^2 + (17\%)^2}$ , where 17% is the uncertainty from the inputs spectra at  $p_T = 3$  GeV/c (see Fig. 4.40).

As an example, the results for charged kaons in 10 – 20% with ZNA, are shown in Fig. 4.41 in the interval  $2 < p_T^{K^\pm} < 40$  GeV/c. The  $p_T$  distribution interpolated down to  $p_T = 2$  GeV/c by using different fitting functions (red, green and blue curves), as well as the results extrapolated up to  $p_T = 40$  GeV/c as displayed.

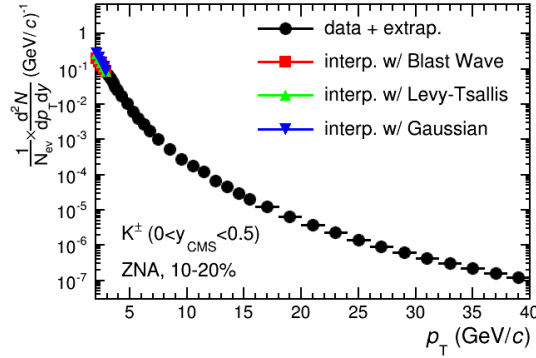


Figure 4.41:  $p_T$  distributions of charged kaons in 10 – 20% with taking ZNA as the event activity estimator, after the  $p_T$  interpolation down to  $p_T = 2$  GeV/ $c$  and the  $p_T$  extrapolation up to  $p_T = 40$  GeV/ $c$ . See text for details.

Finally, as mentioned in Sec. 4.2.2, the statistical and systematic uncertainties can be added in quadrature. The  $p_T$  extrapolated distributions of charged pions with different estimators together with the related (total) uncertainty, are shown in Fig. 4.42. The results based on V0A, CL1 and ZNA are presented in the upper, middle and bottom panels, respectively. Note that the relative error in 80 – 100%, based on CL1, is about 60% nearby 15 GeV/ $c$ . It is induced by the statistical fluctuations in data.

Figure 4.43 shows the  $p_T$  interpolated/extrapolated distributions of kaons within different event activity classes, based on various estimators, as well as the related (combined) systematic uncertainty in the  $p_T$  range  $2 < p_T^{K^\pm} < 40$  GeV/ $c$ . Note that large value of relative uncertainty observed in peripheral collisions are due to the statistical fluctuations.

### 4.3.3 Event Activity Determination

#### 4.3.3.1 Event activity determination via the measured multiplicity

As shown in Eq. 3.28 of Sec. 3.3, the event activity classification can be accessed by using the signal amplitude measured with V0 which is proportional to the measured particle multiplicity. One can slice the sample events according to the charged-particle multiplicity to obtain the desired fraction of the total integral, the so-called event activity. Figure 4.44 shows the distribution of the sum of signal amplitudes measured with V0A, which is reproduced by the NBDGlauber fit with the optimized parameters ( $\mu = 11.0$  and  $k = 0.44$ ). The Negative Binomial Distribution (NBD) is defined as

$$P(n; \mu, k) = \frac{\Gamma(n+k)}{\Gamma(n+1)\Gamma(k)} \cdot \frac{(\mu/k)^n}{(\mu/k+1)^{n+k}} \quad (4.19)$$

where,  $P(n)$  denotes the probability of the contributions  $n$  to the amplitude from each nucleon-nucleon collision [283];  $\Gamma$  indicates the gamma function;  $m$  is the mean

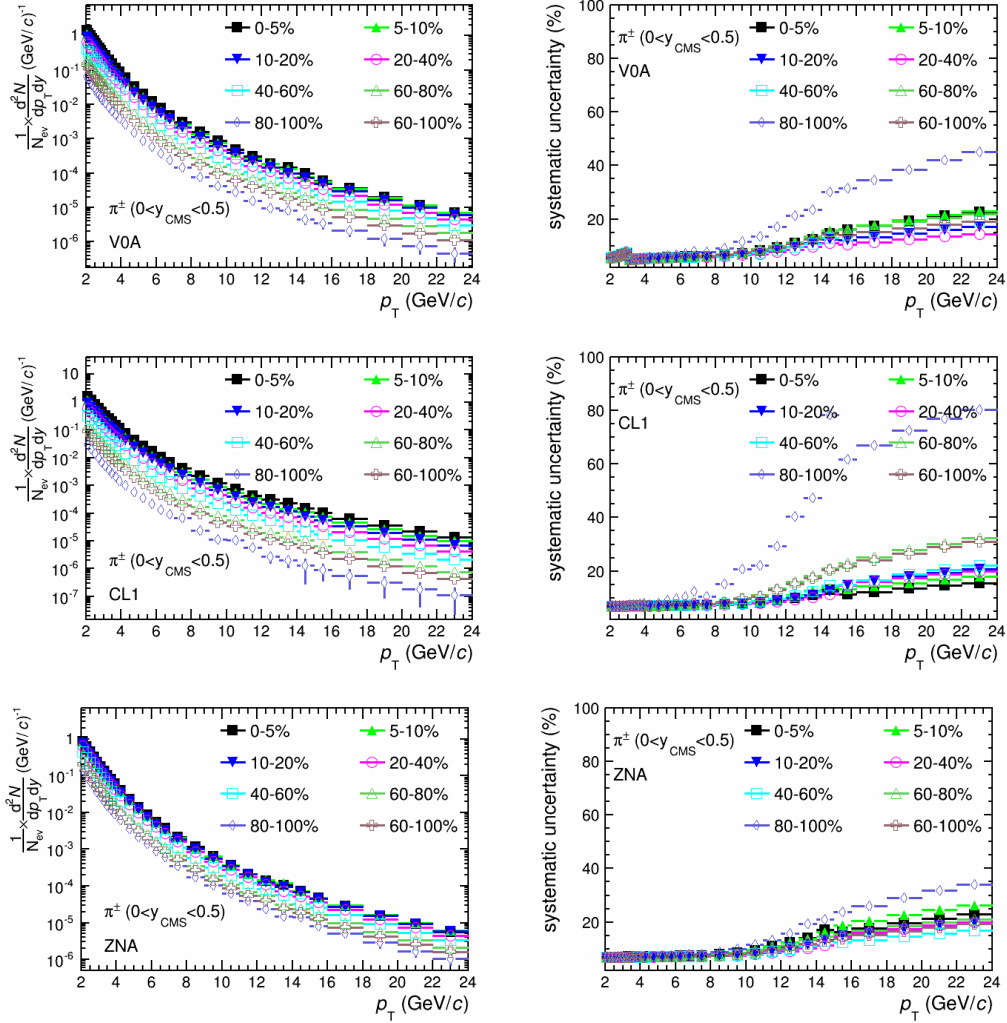


Figure 4.42:  $p_T$  distributions of charged pions within different event activity bins with taking V0A (upper), CL1 (middle) and ZNA (bottom) as the event activity estimators. The distribution and the related total systematic uncertainty are shown in the left and right panel, respectively.

amplitude per participant and the dispersion parameter  $k$  is related to the relative width given by  $\sigma/\mu = \sqrt{1/\mu + 1/k}$ . The event activity classes are indicated by the vertical bands with various colours. The related multiplicity ranges are summarized in Tab. 4.1. The obtained total cross section from the Glauber fit is  $\sim 2.11$  b, and it is very close to the measurement performed in ALICE [277].

With the sliced ranges of charged-particle multiplicity, one can estimate the geometrical properties (impact parameter  $b$ , number of participants  $N_{\text{part}}$  and number of binary collisions  $N_{\text{coll}}$ ) of the p-Pb collisions for the associated event activity classes. The results are summarized in Tab. 4.2, together with the ones reported in Ref. [283] that are shown for comparison. One can see that they are consistent,

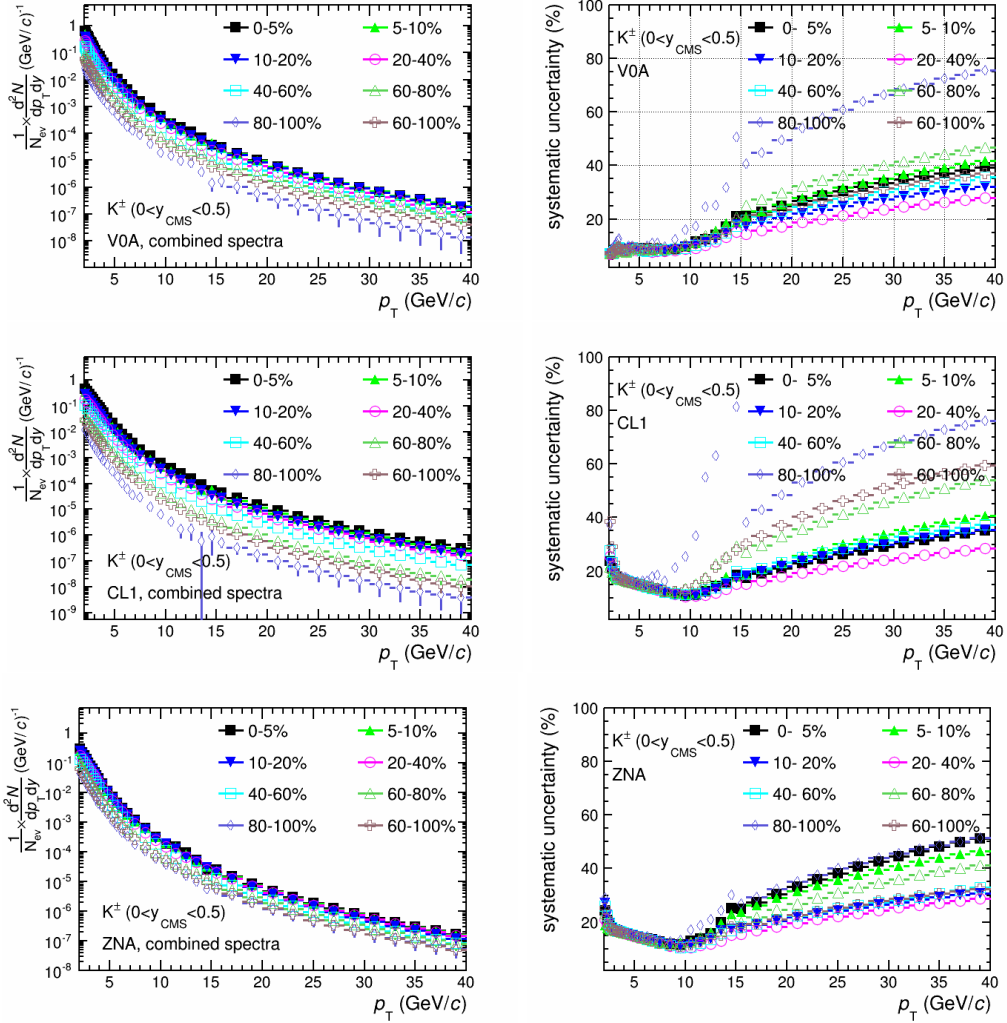


Figure 4.43: Same as Fig. 4.42, but for kaons with both the  $p_T$  interpolation/extrapolation, shown in the range  $2 < p_T^{K^\pm} < 40$  GeV/c.

event activity class	multiplicity range
0 – 5%	(227, 600)
5 – 10%	(186, 227)
10 – 20%	(141, 186)
20 – 40%	(87, 141)
40 – 60%	(50, 87)
60 – 80%	(21, 50)
80 – 100%	(1, 21)

Table 4.1: Multiplicity range for different event activity class. See text for details.

indicating that the above simulation procedure is reasonable.

Figure 4.45 shows the number of events as a function of the impact parameter for

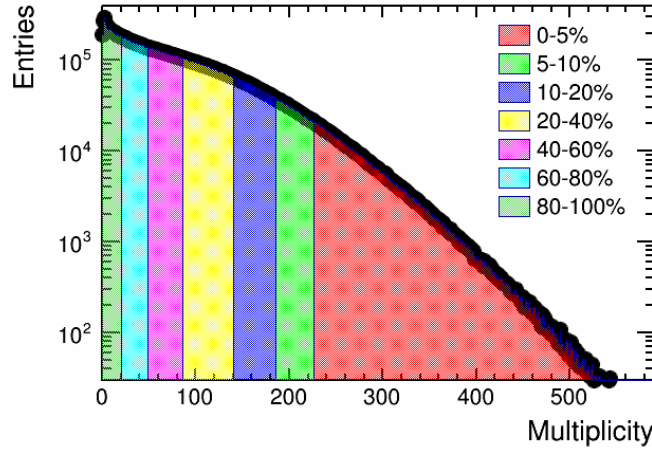


Figure 4.44: Distribution of the sum of amplitudes in the V0A hodoscopes (Pb-going), reproduced by the NBD-Glauber fit ( $N_{\text{part}} \times NBD$ ,  $\mu = 11.0$  and  $k = 0.44$ ). Event activity classes are indicated by vertical bands. See Ref. [283] for details.

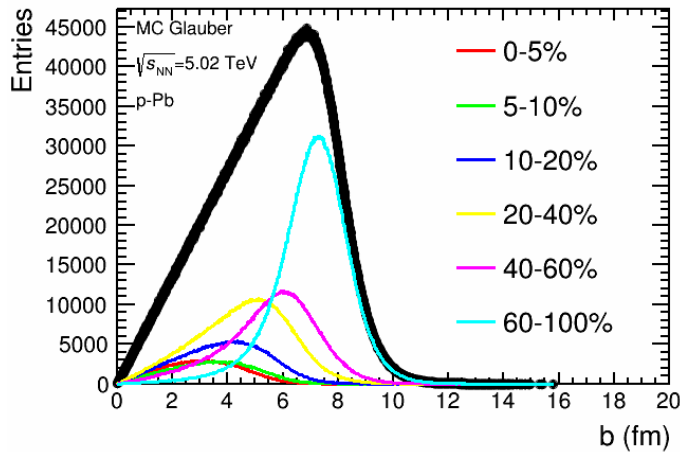


Figure 4.45: Event entries versus impact parameter with the event activity class defined by the MC Glauber model. See text for details.

different event activity classes as obtained from a Glauber Monte-Carlo simulation. The results within individual event activity classes are presented by the curves with various colours, which are defined by the corresponding multiplicity ranges (see Tab. 4.1). A overlap region among neighboring bins is found in p-Pb collisions at  $\sqrt{s_{\text{NN}}} = 5.02$  TeV, whereas, it is not case for the related results in Pb-Pb collisions at  $\sqrt{s_{\text{NN}}} = 2.76$  TeV [258]. As mentioned in Sec. 3.3, this is induced by the multiplicity fluctuations which are more significant in p-Pb collisions.



event activity class	Ref. [283]			this analysis		
	$\langle b \rangle$ (fm)	$\langle N_{\text{part}} \rangle$	$\langle N_{\text{coll}} \rangle$	$\langle b \rangle$ (fm)	$\langle N_{\text{part}} \rangle$	$\langle N_{\text{coll}} \rangle$
0 – 100%	5.56	7.88	6.88	5.56	7.89	6.89
0 – 5%	3.12	15.8	14.8	3.11	15.8	14.9
5 – 10%	3.50	14.0	13.0	3.48	14.1	13.1
10 – 20%	3.85	12.7	11.7	3.85	12.7	11.7
20 – 40%	4.54	10.4	9.36	4.53	10.4	9.43
40 – 60%	5.57	7.42	6.42	5.53	7.49	6.54
60 – 80%	6.63	4.81	3.81	6.61	4.86	3.86
80 – 100%	7.51	2.94	1.94	7.51	2.94	1.94

Table 4.2: Mean values of geometrical variables ( $\langle b \rangle$ ,  $\langle N_{\text{part}} \rangle$  and  $\langle N_{\text{coll}} \rangle$ ) calculated within the event activity classes. They are obtained with a Glauber Monte Carlo calculation, coupled to a NBD to fit the V0A distribution (see Tab. 4.1).

#### 4.3.3.2 Event Activity Determination via Pure Geometry of Colliding System

As introduced in Sec. 3.3, the event activity classification can also be achieved by means of the Optical Glauber Model [35], which takes into account the pure geometry of the colliding system. The centrality intervals defined by slicing events according to the impact parameter via Eq. 3.27, and the inelastic cross section  $d^2\sigma_{\text{inel}}^{\text{AB}}/db^2$  based on the Optical-limit approximation [35], can be calculated as

$$\frac{d^2\sigma_{\text{inel}}^{\text{AB}}}{db^2} = 1 - [1 - \hat{T}_{\text{AB}}(b) \cdot \sigma_{\text{inel}}^{\text{NN}}]^{\text{AB}} \quad (4.20)$$

where,  $A$  (target) and  $B$  (projectile) are the two colliding nuclei, as well as the related mass numbers;  $\sigma_{\text{inel}}^{\text{NN}}$  is the inelastic cross section for the binary collisions;  $\hat{T}_{\text{AB}}(b)$  is the nuclear overlap function, representing the effective overlap area of specific nucleons in  $A$  and  $B$ . It is calculated as,

$$\hat{T}_{\text{AB}}(b) = \int d^2s \hat{T}_{\text{A}}(s) \hat{T}_{\text{B}}(s - b) \quad (4.21)$$

$$\hat{T}_{\text{A}}(s) = \int dz_{\text{A}} \hat{\rho}_{\text{A}}(s, z_{\text{A}}) \quad (4.22)$$

where,  $\hat{T}_{\text{A}}(s)$  (thickness function) denotes the probability per unit transverse area of a given nucleon being located in the target flux tube (Fig. 4.46);  $\hat{\rho}_{\text{A}}(s, z_{\text{A}})$  is the normalized probability per unit volume to find a nucleon at location  $(s, z_{\text{A}})$ , and it can be quantified by the parameterized distributions such as Wood-Saxon (or Fermi [35]). The probability to have  $n$  nucleon-nucleon interactions is given by the binomial distribution.

Figure 4.47 presents the results based on the Optical Glauber Model with  $\sigma_{\text{inel}}^{\text{NN}} = 70$  mb in p-Pb collisions at  $\sqrt{s_{\text{NN}}} = 5.02$  TeV. The nuclear charge density in projectile and target versus the radius, is shown in the upper left panel, as

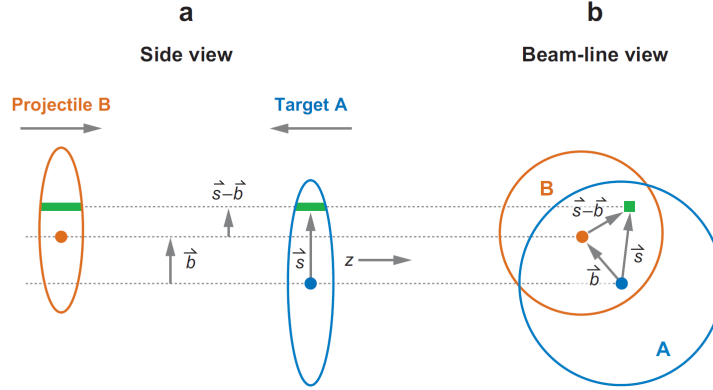


Figure 4.46: Schematic representation of the colliding geometry via Optical Glauber Model, with transverse (a) and longitudinal (b) views. Figure taken from Ref. [35].

well as the related thickness function displayed in the upper right panel. The total number of participants and binary collisions are plotted as a function of the impact parameter, in the bottom left and bottom right panels, respectively,.

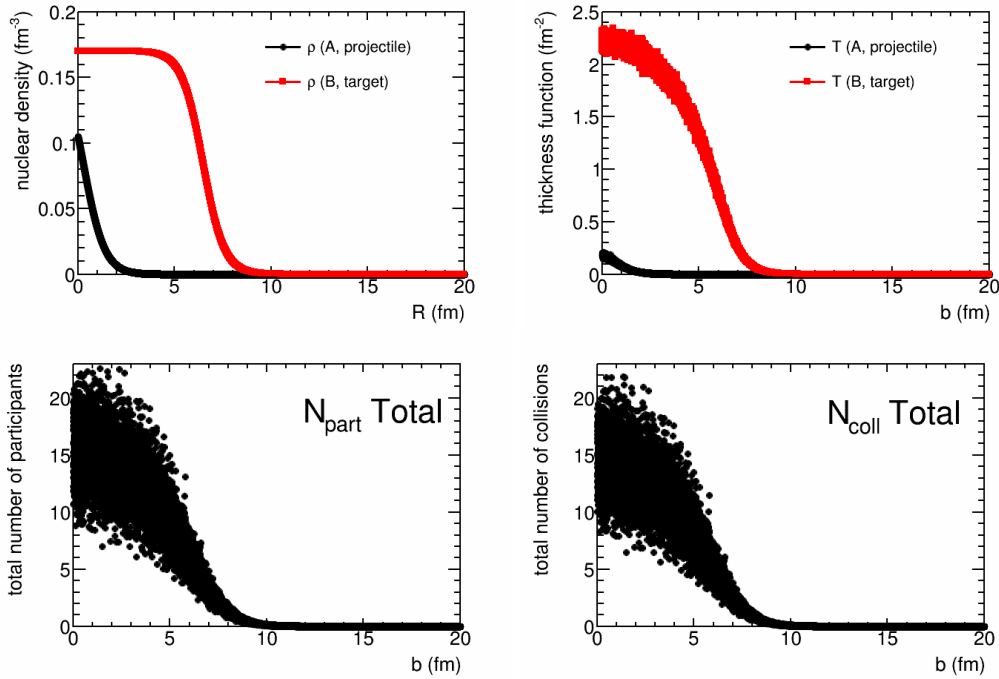


Figure 4.47: Geometrical variables in p-Pb collisions at  $\sqrt{s_{NN}} = 5.02$  TeV, based on the Optical Glauber Model: nuclear charge density (upper left), thickness function (upper right), total number of participants (bottom left) and total number of binary collisions (bottom right).

The  $b$ -differential cross section in p-Pb collisions, calculated according to Eq. 4.20, is shown in the left panel of Fig. 4.48. The trends are similar with the

one obtained in d–Au collisions at  $\sqrt{s_{NN}} = 0.2$  TeV [35]. Based on this result, one can calculate the event activity by slicing the cross section to have the desired fraction with respect to the total integral, as shown in the right panel. It is found that the event activity increases monotonously with increasing  $b$ , which is different compared with the one observed with the MC Glauber (see Fig. 4.45). The corresponding ranges of the impact parameter within a given event activity interval are summarized in Tab. 4.3.

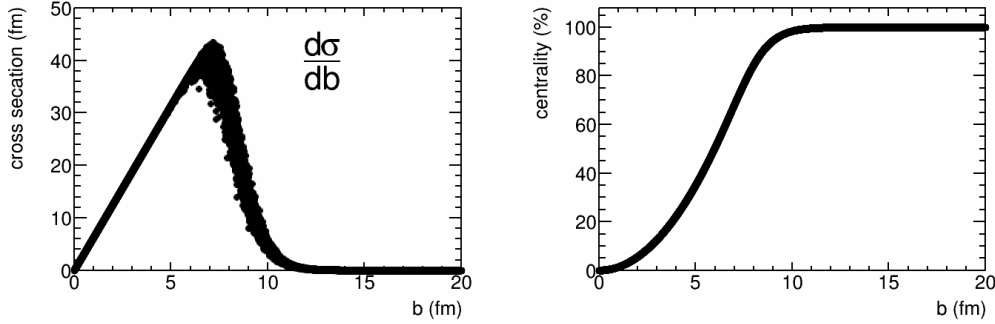


Figure 4.48: Left: total inelastic cross section estimated via Optical Glauber Model in p–Pb collisions at  $\sqrt{s_{NN}} = 5.02$  TeV. Right: event activity versus the impact parameter, which is obtained by slicing the  $b$ -differential cross section to obtain the desired fraction of the total integral.

event activity class	impact parameter range (fm)
0 – 5%	(0.0, 1.9)
5 – 10%	(1.9, 2.7)
10 – 20%	(2.7, 3.8)
20 – 40%	(3.8, 5.3)
40 – 60%	(5.3, 6.6)
60 – 100%	(6.6, 20.0)

Table 4.3: Impact parameter ranges within a given event activity classes. See text for details.

With the results shown in Tab. 4.3, one can define the event activity classes at pure particle level by slicing the impact parameter distribution. Hence, we can get the event entries versus the impact parameter based on the MC Glauber. The results are presented in Fig. 4.49.

#### 4.3.3.3 Deviation of the Results Based on Different Models

Based on the results shown in Fig. 4.45 and 4.49, one can make a comparison between the results based on MC Glauber and Optical Glauber models.

Fig. 4.50 shows the impact parameter range defined via different models within a given event activity bin. The mean value of  $b$  (see Tab. 4.2) based on MC Glauber

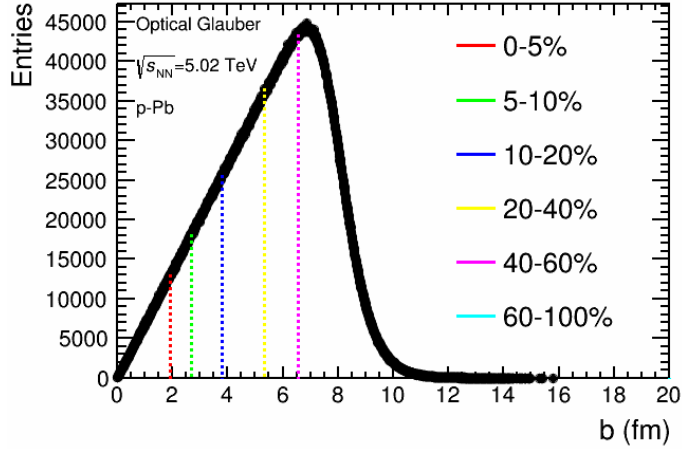


Figure 4.49: Event entries versus impact parameter with the event activity class defined by the Optical Glauber. See text for details.

Model with NBD are shown on the  $x$ -axis together with the dispersion shown as vertical bars. The impact parameter range for the different event activity intervals (see Tab. 4.3) as obtained from the geometrical slicing are shown in the  $y$ -axis as the two dashed lines. One can see that they are consistent within uncertainties for all the event activity classes. However, there is a clear trend with increasing event activity which defines the bias as discussed in Ref. [283]. Note that  $b_{\max} = 10$  fm and it is shown out of  $y$ -axis in the bottom right panel (60 – 100%).

Hence, for each event activity bin, firstly, we can calculate the total number of events within the related impact parameter windows defined via the two approaches, as shown in the left panel of Fig. 4.51. Then, the difference allows to give the systematic uncertainty on the determination procedure, as presented in the right panel of Fig. 4.51. One can see that the number of events based on different models are similar, representing a  $\sim 7 - 12\%$  deviation. Consequently, the event activity determination at pure kinematics can be implemented by means of the Optical Glauber Model (i.e. geometry slicing) in the following analysis, slicing the impact parameters according to Tab. 4.3.

#### 4.3.4 Deviation between Data and Monte-Carlo

With the event activity determination at particle level, one can extract the  $\eta$  or  $y$  distributions of charged hadrons within a given event activity class in MC simulation at particle level for p-Pb collisions, and then, compared with the available measurements at the LHC.

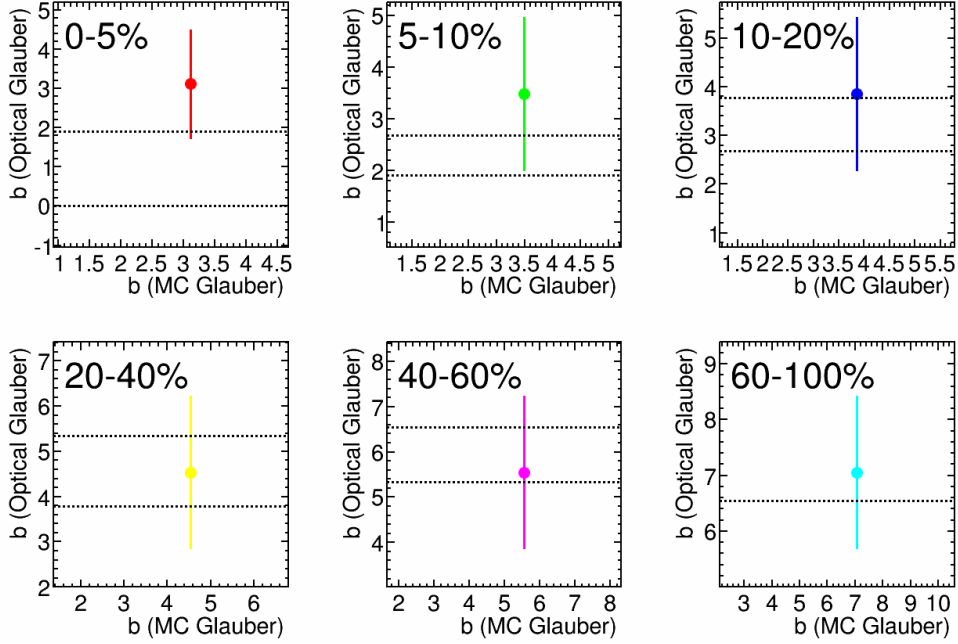


Figure 4.50: Comparison of impact parameter ranges obtained by means of MC Glauber ( $x$ -axis, geometrical slicing) and Optical Glauber ( $y$ -axis, multiplicity slicing) within a given event activity interval. The results are derived from Fig. 4.45 and 4.49, respectively. See text for details.

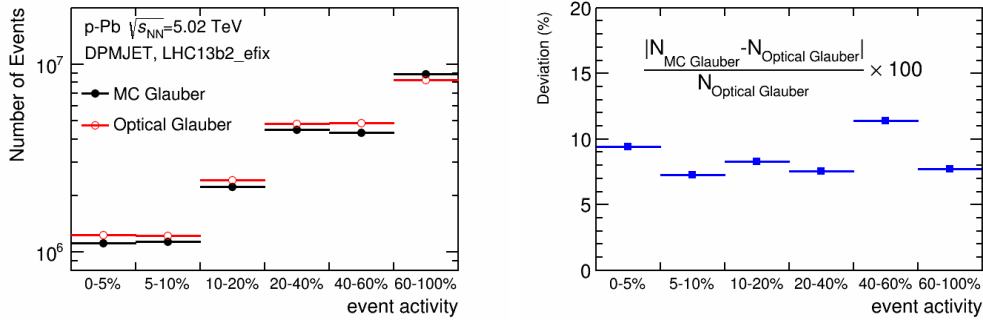


Figure 4.51: Left: total number of events within a given event activity bin; the results based on the related impact parameter range defined by MC (multiplicity slicing) and Optical (geometry slicing) Glauber model as shown as black and red points, respectively. Right: deviation with respect to the one based on Optical Glauber.

#### 4.3.4.1 $\eta$ spectra of charged particles versus event activity measured by ATLAS

The left panel of Fig. 4.52 shows the event activity dependence of the  $\eta_{\text{LAB}}$  distributions (up to  $\eta_{\text{LAB}} = \pm 2.7$ ) of charged particles measured with ATLAS in

p–Pb collisions at  $\sqrt{s_{NN}} = 5.02$  TeV. The distributions measured in central and semi-central collisions to that in peripheral collisions, the so-called central-to-peripheral ratio, is presented in the right panel, as well as the fitted curves (Toy Model) that are extracted from Ref. [319]. We can see that a linear behavior of the central-to-peripheral ratio is observed in each event activity interval. The  $\eta$  distributions are reported for  $p_T > 0$ , and the related shapes are consistent within uncertainties with the ones measured in  $p_T > 0.1$  GeV/c [319].

One can implement the  $\eta$  extrapolation based on the method discussed in Sec. 4.2.2. As an example, Fig. 4.53 shows the results in the 5 – 10% interval. The sampling procedure is implemented independently in the backward (positive, blue points) and forward (negative, red points) regions. The obtained trials are fitted with the Gaussian function and extrapolated to  $\eta_{LAB} = 6$  (blue lines) and  $\eta_{LAB} = -7$  (red lines), and the related envelopes formed by the extrapolated trials enable to give the mean value together with the systematic uncertainty. They are shown as pink and green boxes at backward and forward rapidity, respectively. The extrapolated results are summarized in the left panel of Fig. 4.54, as well as the corresponding systematic uncertainties which are shown in the right panel. It is  $\sim 60\%$  (40%) maximum at  $\eta_{LAB} = -7$  ( $\eta_{LAB} = 6$ );

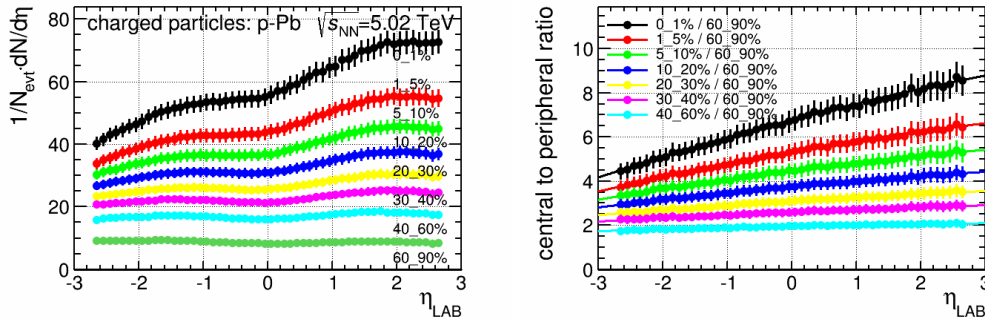


Figure 4.52: Left:  $\eta$  spectra of charged particles within different event activity bins measured by the ATLAS Collaboration. Right: distributions measured in central and semi-central collisions to that in peripheral collisions together with the fitted results which are obtained from [319]. Extracted from Ref. [319]

With the combined results in 0 – 90%, one can make a comparison with the ones based on model predictions. The upper panel of Fig. 4.55 shows the  $\eta$  distributions measured by ATLAS (0 – 90%, red, [319]) and ALICE (0 – 100%, blue, [308]), as well as the ones predicted by DPMJET (black) and HIJING (green). Within uncertainties, ALICE measurements can be described by DPMJET and HIJING, as shown in the bottom panel and, as already discussed in Sec. 4.2.2. There is a visible deviation between ALICE and ATLAS measurements, induced by different acceptance where the multiplicity is measured [319]. In addition, the shape of the  $\eta_{CMS}$  distribution is similar within uncertainties between ATLAS and model predictions, validating the  $\eta$  extrapolation procedure (Fig. 4.54). Note that same conclusion can be found for AMPT generator.

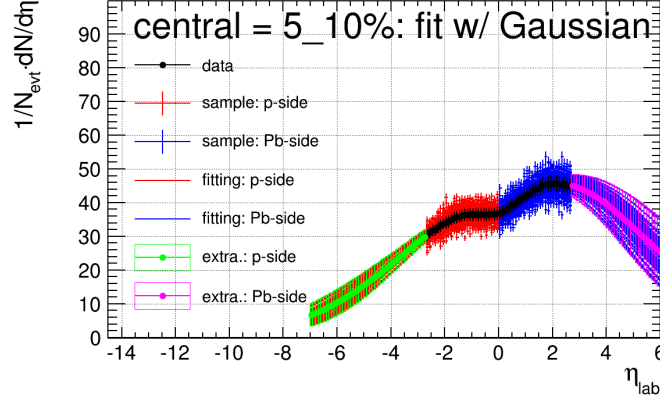


Figure 4.53:  $\eta$  extrapolation with Gaussian function in the range 5 – 10%. Similar to the procedure for  $p_T$  extrapolation, as shown in Sec. 4.2.2.

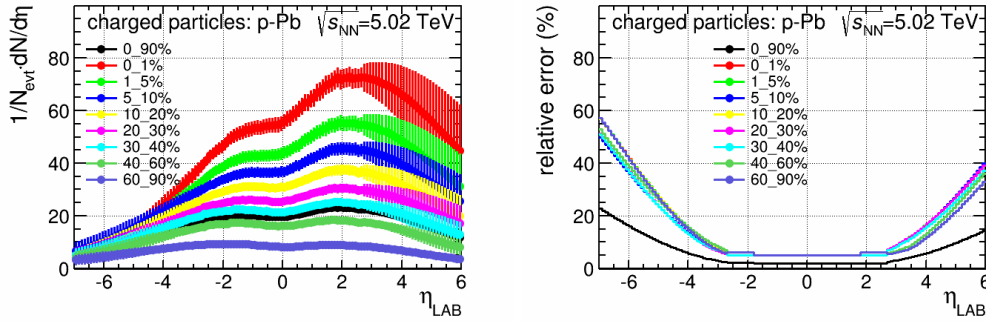


Figure 4.54: Left: same as the left panel of Fig. 4.52 but with  $\eta$  extrapolation to have the results in the range  $-7 < \eta_{LAB} < 6$ . Right: the related systematic uncertainty.

Alternatively, one can compare the distributions in event activity intervals between data and MC, The obtained results are shown in Fig. 4.56. It is found that:

- measurements performed by ALICE and ATLAS (with  $\eta$  extrapolation) are consistent within uncertainties, in the overlap region;
- DPMJET predictions enable to reproduce well the shape of the measurement;
- HIJNG predictions can describe the data at backward (positive  $\eta_{LAB}$ , Pb-going direction), however, they show large deviations at forward rapidity (negative  $\eta_{LAB}$ , p-going direction).

The comparison between data and MC allows to validate the  $\eta$  extrapolation procedure. In addition, one can scale the DPMJET and HIJNG productions based on the ATLAS measurements to decrease the deviation as much as possible. The subsequent analysis concerning the models can depend on the tuned predictions.

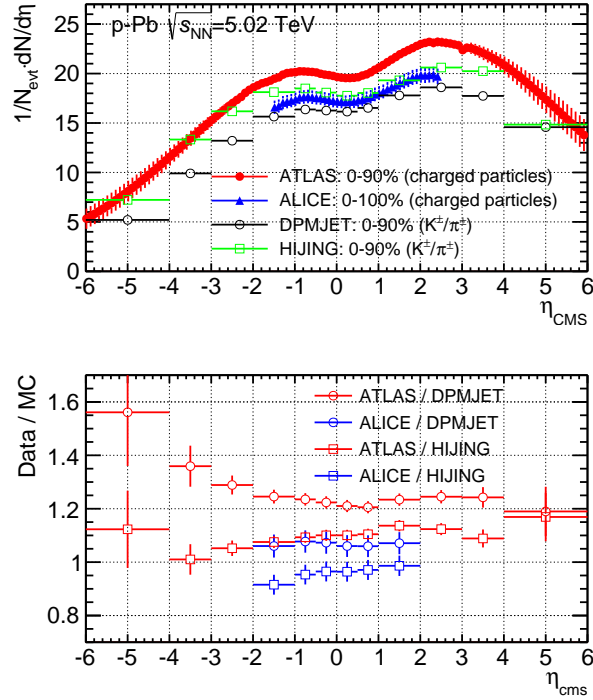


Figure 4.55: Up:  $\eta$  distributions of charged particles measured by ALICE (0–100%) and ATLAS (0–90%), as well as  $K^\pm/\pi^\pm$   $\eta$  distributions from DPMJET (0–90%) and HIJING (0–90%). Bottom: ratio of the distributions in data and MC. See text for details.

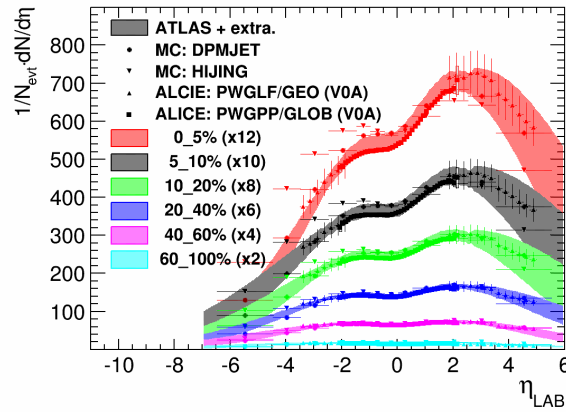


Figure 4.56:  $\eta$  distribution of charged particles measured by ALICE at mid-rapidity (squares) and forward rapidity (triangles), and ATLAS with the extrapolation (dashed area).  $K^\pm/\pi^\pm$   $\eta$  distributions from DPMJET (circles) and HIJING (inverse triangles) shown for comparison (see the text).

#### 4.3.4.2 Data-based Scaling for MC Predictions

Further comparisons between ATLAS (with the extrapolation) and MC (DPMJET and HIJING) for different event activity classes are shown in Fig. 4.57. The two vertical dashed lines denote the acceptance of ATLAS in the center-of-mass frame. One can see that data and MC results are consistent within uncertainties. The ratios among them are presented in Fig. 4.58.

We take these ratios (Fig. 4.58) as the weight to scale the  $\eta$  distributions of charged particle to reproduce the available data. The weight can be expressed as,

$$W_\eta \equiv W_\eta(\eta, cent.) = \frac{(dN/d\eta)_{Data}}{(dN/d\eta)_{MC}} \quad (4.23)$$

with which we can modify the  $p_T$  distributions of charged particles in MC via,

$$W_{p_T} \equiv W_{p_T}(p_T, cent.) = \frac{\Sigma_\eta [W_\eta(\eta, cent.) * (dN/dp_T)_{MC}]}{\Sigma_\eta (dN/dp_T)_{MC}} \quad (4.24)$$

where, "cent." denotes the considered event activity interval.

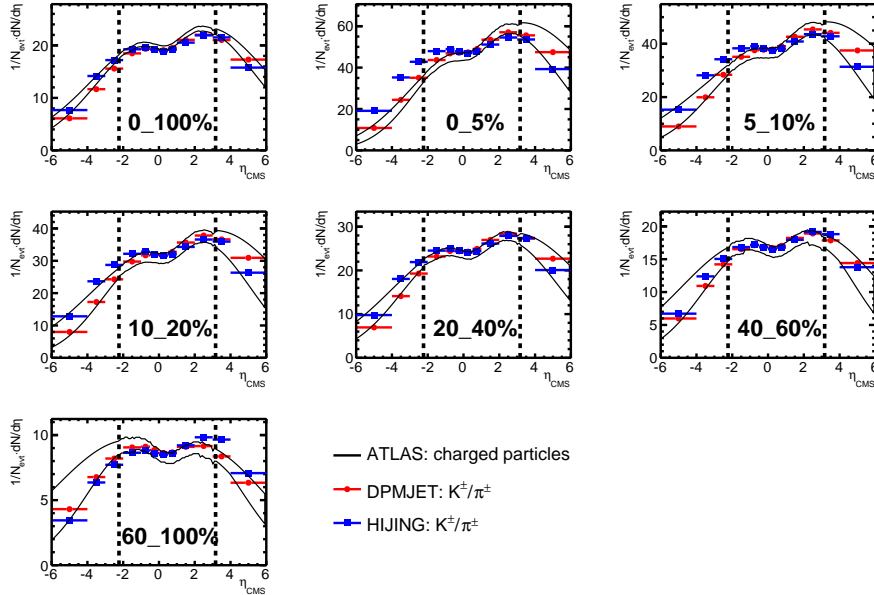


Figure 4.57:  $\eta$  distributions of charged particles measured by ATLAS with the extrapolation (band) up to  $\eta_{CMS} = \pm 6$  within different event activity bins. The two vertical dashed lines indicate the acceptance of ATLAS. The results of  $K^\pm/\pi^\pm$  predicted by DPMJET (red) and HIJING (blue) are shown for comparison.

#### 4.3.5 Rapidity Extrapolation

The rapidity extrapolation procedure is required in order to extrapolate the charged  $K^\pm/\pi^\pm$  distributions from mid-rapidity to forward and backward rapidities.

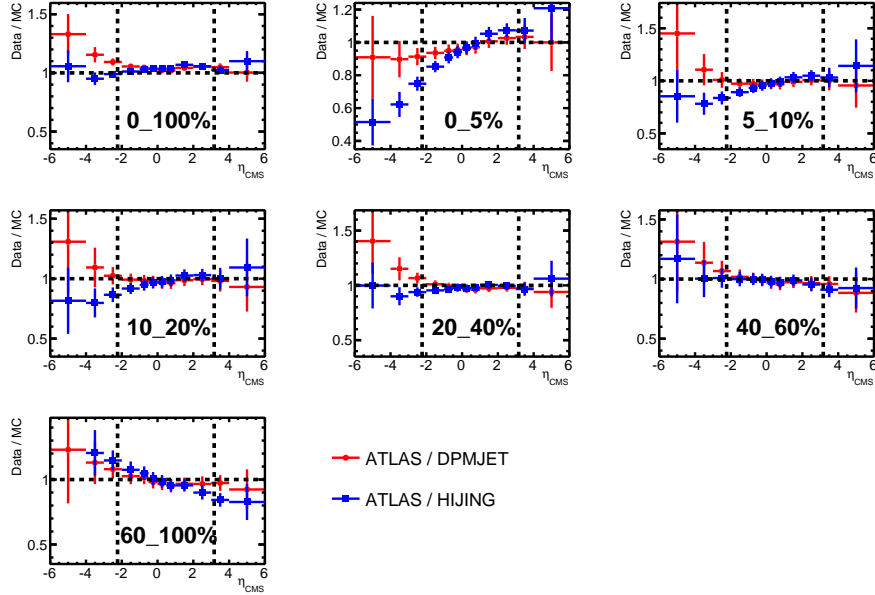


Figure 4.58: Comparison of the  $\eta$  distributions of charged particles measured by ATLAS with respect to the ones of  $K^\pm/\pi^\pm$  predicted by DPMJET and HIJING. The two vertical dashed lines indicate the acceptance of ATLAS.

The extrapolation factor is obtained from MC at forward rapidity in multiplicity integrated collisions, while the results at backward rapidity are obtained by scaling the distribution from forward to backward rapidity, by means of the CMS measurements. The related scaling factor  $Y_{\text{asym}}$  is defined by the distributions measured in symmetric rapidity intervals between backward and forward rapidities. The event activity dependence of  $Y_{\text{asym}}$  is needed in order to follow the similar strategy as in multiplicity integrated collisions.

In the left panel of Fig. 4.59, the asymmetry factor  $Y_{\text{asym}}(1.3 < |\eta_{\text{CMS}}| < 1.8)$  measured in the CMS Collaboration is shown for different ranges of the total transverse energy  $E_T$  produced in the collision, which is the event activity [309], as well as the ratio of the  $Y_{\text{asym}}$  obtained in multiplicity integrated collisions shown in the right panel. The black points are the results used in multiplicity integrated analysis, as presented in the right panel of Fig. 4.16. The red ones indicate the results in the range  $E_T > 40$  GeV, while the blue ones concern  $E_T < 20$  GeV. Note that:

- $E_T > 40$  GeV: high multiplicity events (central collisions), the asymmetry factor is enhanced when comparing with the results in multiplicity integrated collisions in the range  $p_T < 10$  GeV/ $c$ ; also a pronounced rise above unity is visible in  $p_T > 10$  GeV/ $c$ ;
- deviation with respect to  $Y_{\text{asym}}$  in multiplicity integrated collisions, is  $\sim 20\%$  in the range  $p_T < 10$  GeV/ $c$ ;
- $E_T < 20$  GeV: the asymmetry factor is similar to the multiplicity integrated

one within the whole  $p_T$  range;

- it is argued [320] that  $E_T > 40$  GeV and  $E_T < 20$  GeV correspond to the event activity classes  $\sim < 3\%$  and  $\gtrsim 73\%$ , respectively.

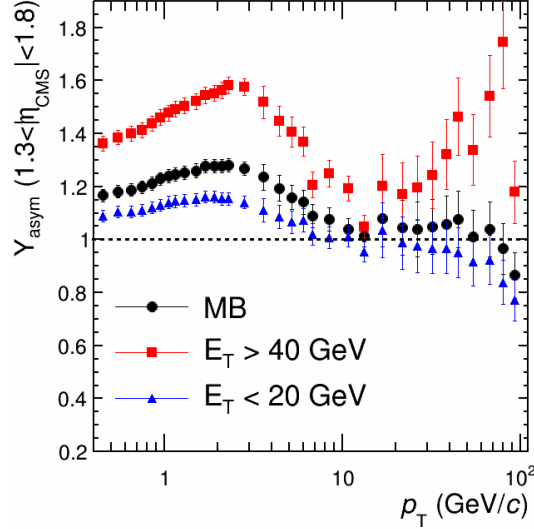


Figure 4.59:  $Y_{\text{asym}}(1.3 < |\eta_{\text{CMS}}| < 1.8)$  of charged particles measured by CMS for multiplicity integrated collisions (black),  $E_T > 40$  GeV (red) and  $E_T < 20$  GeV (blue). The vertical bars indicate the systematic uncertainty. Adapted from Ref. [309].

One may notice that these event activity classes are not the ones that we need. A parameterization procedure is proposed to estimate the  $Y_{\text{asym}}(1.3 < |\eta_{\text{CMS}}| < 1.8)$  within desired event activity classes. Three scenarios are proposed.

First, we take as input the measurements in multiplicity integrated collisions  $Y_{\text{asym}}^{0-100\%}$  and the one in the most central collisions  $Y_{\text{asym}}^{0-3\%}$ , and the results in a given event activity bin  $x\%$  ( $Y_{\text{asym}}^{x\%}$ ) can be obtained by assuming a  $N_{\text{part}}$  scaling behavior, which is quantified as

$$Y_{\text{asym}}^{x\%} = \frac{N_{\text{part}}^{x\%} - N_{\text{part}}^{0-100\%}}{N_{\text{part}}^{0-3\%} - N_{\text{part}}^{0-100\%}} \cdot Y_{\text{asym}}^{0-3\%} + \frac{N_{\text{part}}^{0-3\%} - N_{\text{part}}^{x\%}}{N_{\text{part}}^{0-3\%} - N_{\text{part}}^{0-100\%}} \cdot Y_{\text{asym}}^{0-100\%} \quad (4.25)$$

The left panel of Fig. 4.60 presents  $Y_{\text{asym}}(1.3 < |\eta_{\text{CMS}}| < 1.8)$  estimated within different event activity classes. Note that the results in 0–100% and 0–3% are the same as the measurements (i.e. black and red points in Fig. 4.59). The vertical bars denote the systematic uncertainty based on Eq. 4.25.  $Y_{\text{asym}}$  estimated in 73–100% can be compared with the available data in 73–100% (i.e. blue points in Fig. 4.59), as shown in the middle panel. It is found that they are consistent well with each other, in most of the  $p_T$  bins. Further comparison is shown in the right panel.

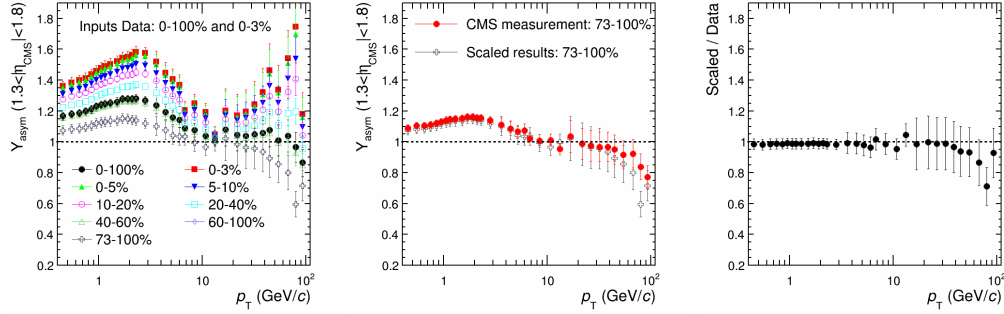


Figure 4.60: Left:  $Y_{\text{asym}}(1.3 < |\eta_{\text{CMS}}| < 1.8)$  of charged particles within different event activity classes. They are obtained by using a parameterization procedure, which takes as input the CMS measurements in multiplicity integrated collisions (0 – 100%) and the one with  $E_T > 40$  GeV (0 – 3%). Middle: ratio of  $Y_{\text{asym}}(1.3 < |\eta_{\text{CMS}}| < 1.8)$  estimated in 73 – 100% to the available data. Right: further comparison between the estimated results and data. The vertical bars indicate the systematic uncertainty. See text for details.

Second, we take as input the measurements in multiplicity integrated collisions  $Y_{\text{asym}}^{0-100\%}$  and the one in the most peripheral collisions  $Y_{\text{asym}}^{73-100\%}$ , and the results in a given event activity bin  $x\%$  ( $Y_{\text{asym}}^{x\%}$ ) can be obtained by assuming a  $N_{\text{part}}$  scaling behavior, which is quantified as

$$Y_{\text{asym}}^{x\%} = \frac{N_{\text{part}}^{x\%} - N_{\text{part}}^{0-100\%}}{N_{\text{part}}^{73-100\%} - N_{\text{part}}^{0-100\%}} \cdot Y_{\text{asym}}^{73-100\%} + \frac{N_{\text{part}}^{70-100\%} - N_{\text{part}}^{x\%}}{N_{\text{part}}^{73-100\%} - N_{\text{part}}^{0-100\%}} \cdot Y_{\text{asym}}^{0-100\%} \quad (4.26)$$

Same as Fig. 4.60, Fig. 4.61 shows  $Y_{\text{asym}}(1.3 < |\eta_{\text{CMS}}| < 1.8)$  estimated within

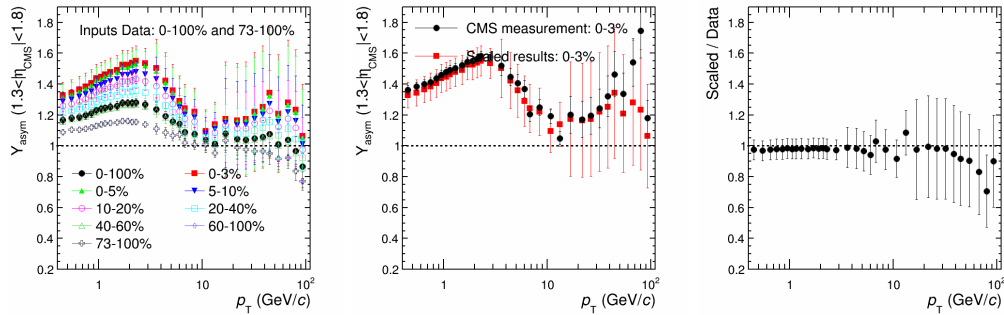


Figure 4.61: Same as Fig. 4.60, but taking as input the CMS measurements in 0 – 100% and in 73 – 100%.

different event activity classes, as well as the comparison between the obtained results and available data in 0 – 3%. Same conclusion can be found.

Third, we take as input  $Y_{\text{asym}}$  measured in the most central ( $Y_{\text{asym}}^{0-3\%}$ ) and peripheral collisions ( $Y_{\text{asym}}^{73-100\%}$ ), and the results in a given event activity bin  $x\%$  ( $Y_{\text{asym}}^{x\%}$ ) can be obtained by assuming a  $N_{\text{part}}$  scaling behavior, which is quantified as

$$Y_{\text{asym}}^{x\%} = \frac{N_{\text{part}}^{x\%} - N_{\text{part}}^{0-3\%}}{N_{\text{part}}^{73-100\%} - N_{\text{part}}^{0-3\%}} \cdot Y_{\text{asym}}^{73-100\%} + \frac{N_{\text{part}}^{73-100\%} - N_{\text{part}}^{x\%}}{N_{\text{part}}^{73-100\%} - N_{\text{part}}^{0-3\%}} \cdot Y_{\text{asym}}^{0-3\%} \quad (4.27)$$

Same as Fig. 4.60, Fig. 4.62 shows  $Y_{\text{asym}}(1.3 < |\eta_{\text{CMS}}| < 1.8)$  estimated within

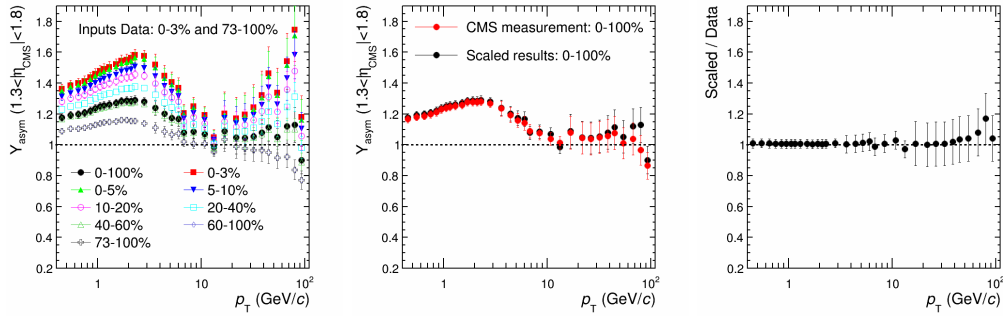


Figure 4.62: Same as Fig. 4.60, but taking as input the CMS measurements in 0–3% and in 73–100%.

different event activity classes, as well as the comparison between the obtained results and available data in 0–100%. Same conclusion can be found.

Note that, based on different scenarios,  $Y_{\text{asym}}(1.3 < |\eta_{\text{CMS}}| < 1.8)$  estimated within different event activity bins are close to each other. Hence, we take the averaged results among them as the final ones.

$$\text{mean} = \frac{\text{scenario1} + \text{scenario2} + \text{scenario3}}{3} \quad (4.28)$$

They are shown in the left panel of Fig. 4.63, as well as the systematic uncertainty presented in the right panel. Note that the systematic uncertainty from the experimental data together with the dispersion of the mean value are included already.

### 4.3.6 Estimated Background and Systematic Uncertainty

Based on the method discussed in previous sub-sections, one can implement a similar strategy as in multiplicity integrated collisions for background estimation within a given event activity interval.

As an example, the obtained background in 5–10% both at forward ( $2.03 < y_{\text{CMS}} < 3.53$ ) and backward rapidity ( $-4.49 < y_{\text{CMS}} < -2.96$ ), is shown in the upper and lower panels of Fig. 4.64, respectively. One can see that the  $\pi^\pm$  and  $K^\pm$  components are consistent within uncertainties, and the total systematic uncertainty is about 20–25% and 30–40% at forward and backward rapidities, respectively.

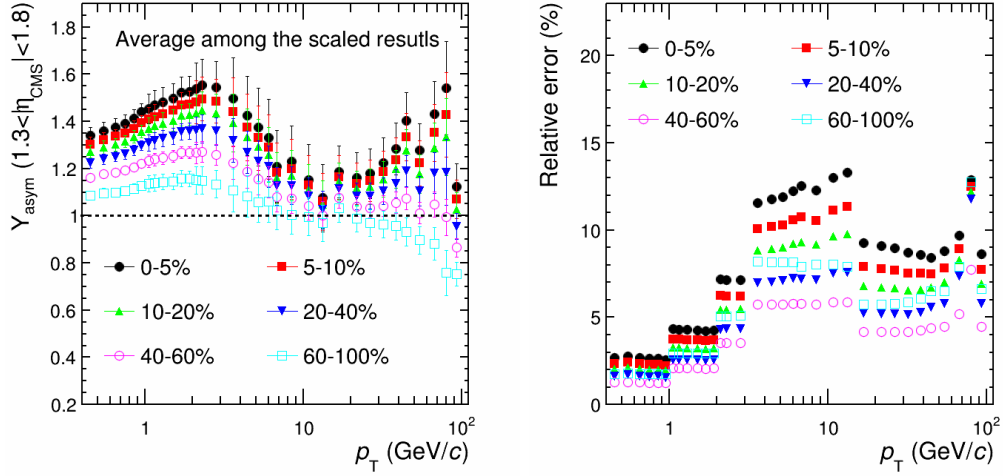


Figure 4.63: Left: average results of  $Y_{\text{asym}}(1.3 < |\eta_{\text{CMS}}| < 1.8)$  based on different scenarios for the parameterization procedure. Right: the corresponding systematic uncertainty within different event activity classes. See text for details.

The estimated background in the rapidity range  $2.03 < y_{\text{CMS}} < 3.53$  together with the related fraction relative to inclusive muons, for different event activity bins and different estimators, are shown in Fig. 4.65. It is found that the background fractions are similar in different event activity bins. Further comparisons show that the maximum deviation of the fraction with respect to the one in multiplicity integrated collisions is  $\sim 40\%$ . The obtained background at backward rapidity ( $-4.46 < y_{\text{CMS}} < -2.96$ ) is presented in Fig. 4.66. One can see that:

- results at backward rapidity have larger deviation compared with each other, while the results at forward rapidity have small deviation;
- ZNC results are missing since the charged hadron inputs are only measured for V0A, CL1 and ZNA. However, we are able to take "ZNA  $\approx$  ZNC" at backward rapidity (Pb-p, Pb-going direction) within the considered  $p_T$  region;
- there is a hint for the background fractions that are larger in peripheral with respect to the ones observed in central collisions. A similar behavior was found in the Pb-Pb analysis, indicating more suppression of background from peripheral to central collisions;
- note that V0A measures particles in the Pb fragmentation region in p-Pb collisions, while in Pb-p collisions it is in the proton fragmentation region.

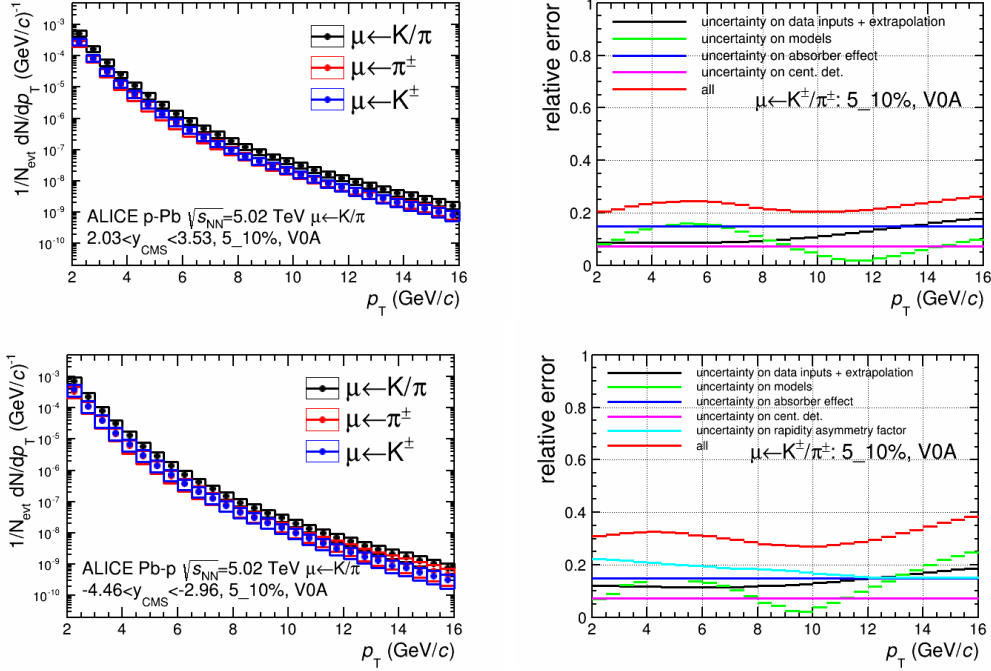


Figure 4.64: Upper left:  $p_T$  distributions of muons from  $\pi^\pm$  (red),  $K^\pm$  (blue) and  $K^\pm/\pi^\pm$  (black) decays at forward rapidity  $2.03 < y_{\text{CMS}} < 3.53$  in the event activity 5–10%. The used estimator is V0A. Upper right: the different sources of systematic uncertainty. Lower two: same as the upper plots but at backward rapidity  $-4.46 < y_{\text{CMS}} < -2.96$ .

### 4.3.7 Discussion

#### 4.3.7.1 Difference between $K^\pm$ and $\pi^\pm$ in the Scaling Procedure

We scale the  $\eta$  dependence of charged pions and kaons in MC to the primary charged particles measured with ATLAS (see Fig. 4.52). The corresponding scaling factor is defined as,

$$Y_{\text{Data-Tuned-MC}}^{\pi^\pm} = \frac{Y_{\text{Data}}^{\pi^\pm+K^\pm}}{Y_{\text{MC}}^{\pi^\pm+K^\pm}} \cdot Y_{\text{MC}}^{\pi^\pm} \quad (4.29)$$

where,  $Y_{\text{Data-Tuned-MC}}^{\pi^\pm}$  and  $Y_{\text{MC}}^{\pi^\pm}$  denote  $\pi^\pm$  distributions with and without scaling in MC;  $Y_{\text{Data}}^{\pi^\pm+K^\pm}$  and  $Y_{\text{MC}}^{\pi^\pm+K^\pm}$  indicate the charged-hadron distributions in data and MC, respectively. One should implement the above procedure based on the measurements of  $\pi^\pm$  and  $K^\pm$ .

$$Y_{\text{Data-Tuned-MC}}^{\pi^\pm} = \frac{Y_{\text{Data}}^{\pi^\pm}}{Y_{\text{MC}}^{\pi^\pm}} \cdot Y_{\text{MC}}^{\pi^\pm} \quad (4.30)$$

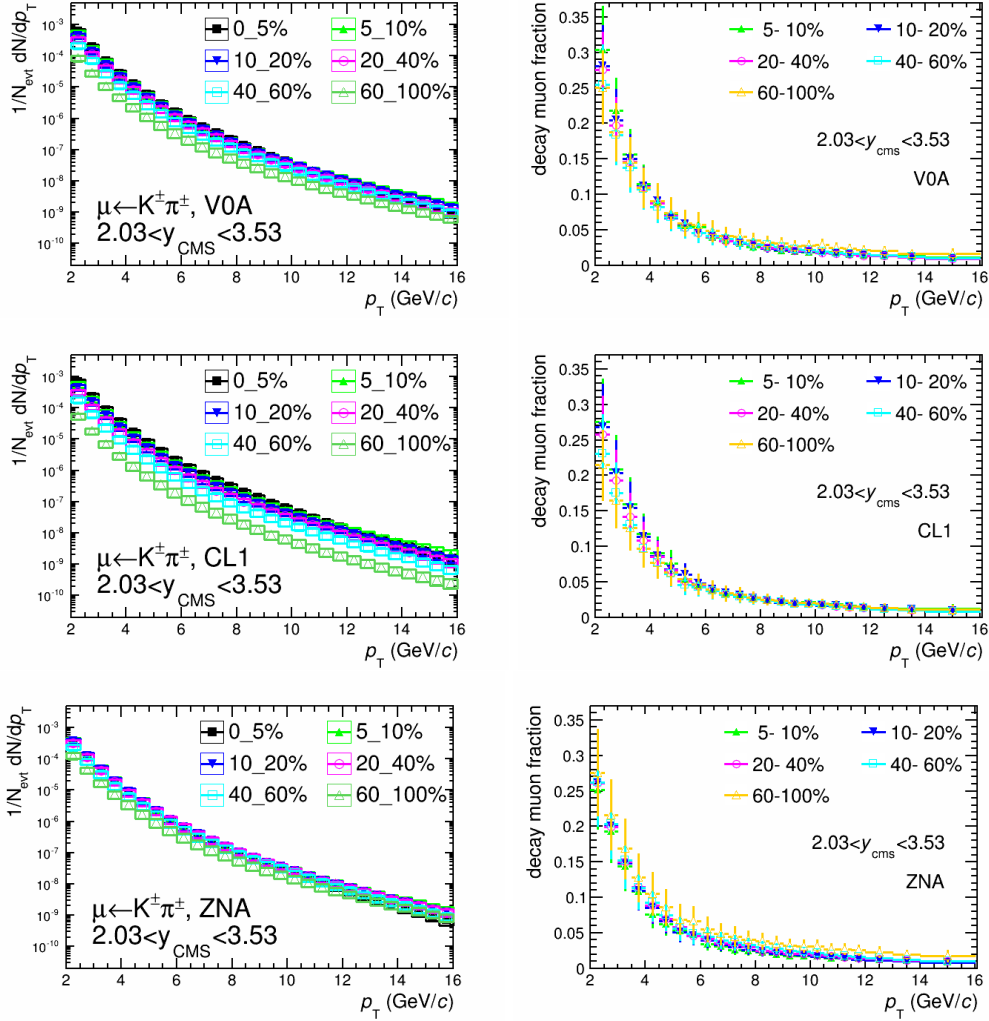


Figure 4.65: Upper left:  $p_T$  distributions of muons from  $K^\pm/\pi^\pm$  decays within different event activity bins at forward rapidity  $2.03 < y_{\text{CMS}} < 3.53$ . The results are based on V0A. Upper right: background to inclusive muon ratio. Middle: same as upper plots but for CL1 estimator. Bottom: same as upper plots but for ZNA estimator.

It is necessary to mention that Eq. 4.29 and 4.30 are approximately equal to each other if the following assumption is validated.

$$\frac{Y_{\text{Data}}^{K^\pm}}{Y_{\text{Data}}^{\pi^\pm}} \approx \frac{Y_{\text{MC}}^{K^\pm}}{Y_{\text{MC}}^{\pi^\pm}} \quad (4.31)$$

That means that the kaon to pion ratio is similar in data and in MC.

Figure 4.67 shows the particle ratios in pp, p-Pb and Pb-Pb collisions measured with ALICE and CMS at mid-rapidity. One can see that the observed kaon to pion ratio is  $\sim 0.12 - 0.15$  in p-Pb collisions at  $\sqrt{s_{\text{NN}}} = 5.02$  TeV, and it seems not to be

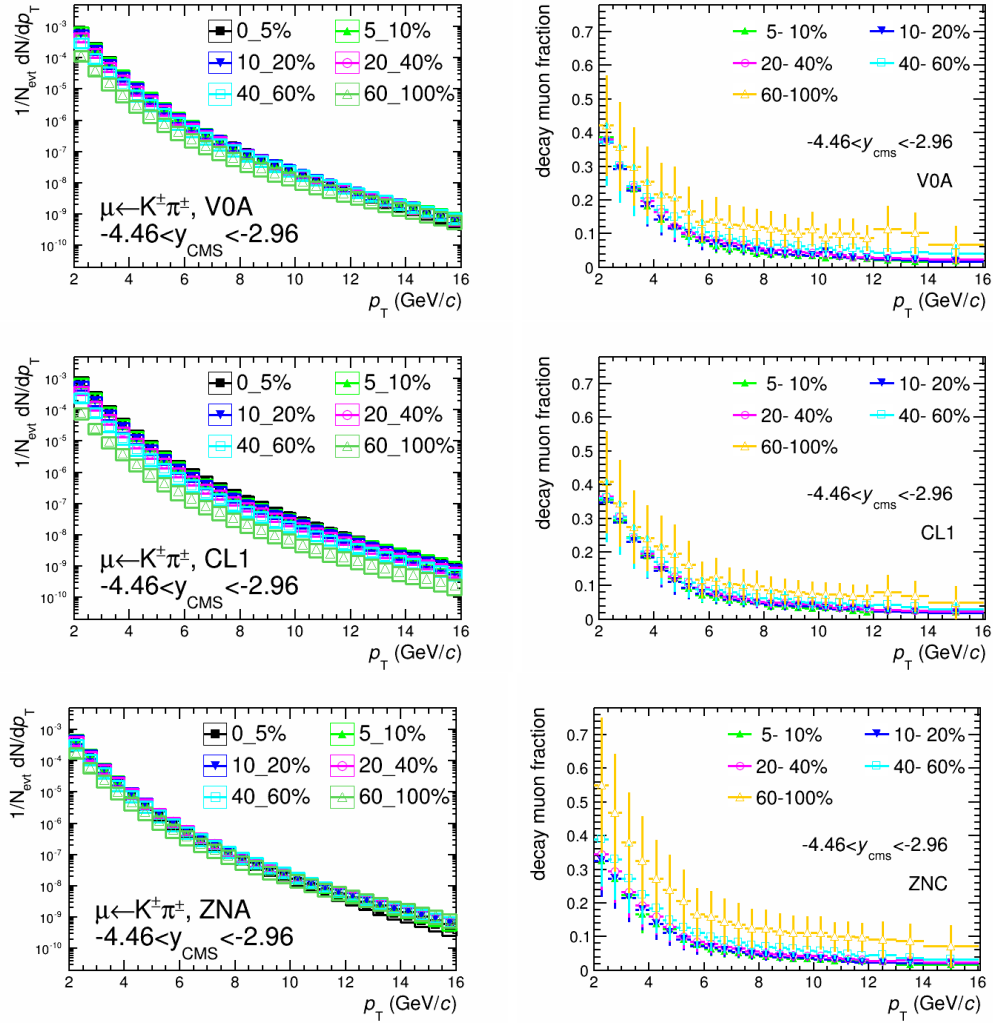


Figure 4.66: Same as Fig. 4.65 but for  $-4.46 < y_{\text{CMS}} < -2.96$

sensitive to the event activity. The kaon to pion ratio from DPMJET is shown in Fig. 4.68. The ratio at mid-rapidity is  $\sim 0.13 - 0.14$ . Ratios at mid-rapidity within different event classes are close to each other. The corresponding ratio from HIJING is  $\sim 0.12 - 0.13$ . Models calculation therefore well describe the ALICE and ATLAS measurements. Hence, the assumption proposed in Eq. 4.31 is validated. Note that the cross check is implemented by the comparison of the  $p_T$ -integrated  $K/\pi$  ratio in data and MC. The mismatch of the  $p_T$  distribution of pions and kaons between data and MC would give a possible systematic effect.

#### 4.3.7.2 Rapidity Extrapolation at Backward Rapidity

In the previous section, we validated with a conservative strategy the background estimation at backward rapidity in multiplicity integrated collisions: 2 times the asymmetry factor  $Y_{\text{asym}}^{\text{Data}}(1.3 < |\eta_{\text{CMS}}| < 1.8)$  of charged particles measured by

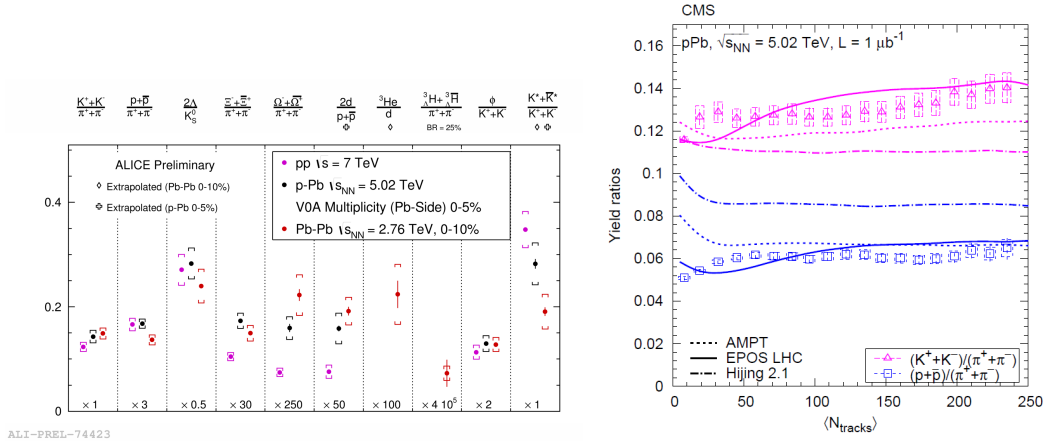


Figure 4.67: Left: ratios of particle yields measured in pp, p–Pb, and Pb–Pb collisions with ALICE at mid-rapidity; Right: ratios of particle yields in the range  $|y| < 1$  as a function of the track multiplicity for  $|\eta| < 2.4$ . Model predictions are shown for comparison. Figures taken from Ref. [321] (left) and [322] (right), respectively.

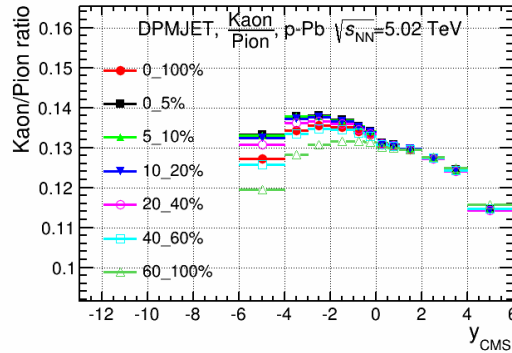


Figure 4.68: Kaon to pion ratio predicted by DPMJET within various event activity classes.

CMS to cover the difference of rapidity range with respect to  $0 < |\eta_{CMS}| < 6$  (see Sec. 4.2.3 for details). It is necessary to check that this approach is correct when performing the measurements within event activity bins. A double ratio defined as  $Y_{asym}^{MC}(2 < |\eta_{CMS}| < 6)$  with respect to  $Y_{asym}^{MC}(1 < |\eta_{CMS}| < 2)$ , which has an acceptance close to the one measured with CMS,  $Y_{asym}^{Data}(1.3 < |\eta_{CMS}| < 1.8)$ , allows to access the validation procedure. The results predicted by HIJING are shown in Fig. 4.69. It is found that the defined double ratio is smaller than 2 in most of the event activity bins, while the one in 0 – 5% is close to unity within uncertainties. Consequently, it is still conservative to follow the same strategy as in multiplicity integrated collisions to estimate the background at backward within a given event

activity bin.

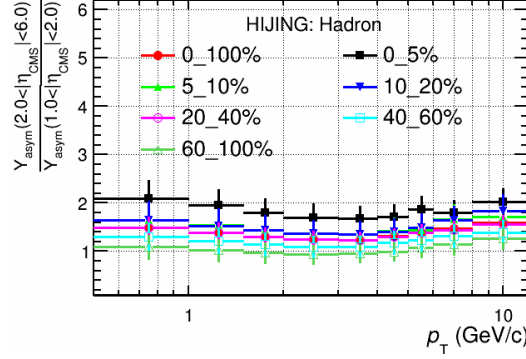


Figure 4.69: Ratio of the asymmetry factor in  $2 < |\eta_{\text{CMS}}| < 6$  in with respect to the one in  $1 < |\eta_{\text{CMS}}| < 2$ . Results are obtained with HIJING for different event activity classes. See the text for details.

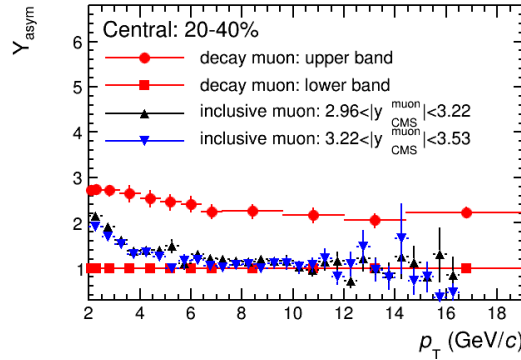


Figure 4.70: Asymmetry factor in data  $Y_{\text{asym}}^{(\text{inclusive muon})}$ : results are obtained within  $2.96 < y_{\text{CMS}} < 3.22$  (black) and  $3.22 < y_{\text{CMS}} < 3.53$  (blue). The results based on the estimated decay muons (red) are shown for comparison. The related upper and lower band are defined in the same way as in the multiplicity integrated collisions (Eq. 4.11 and 4.12).

Alternatively, we can extract the hints about this upper band according to the data. It is known that the  $p_T$  distribution of inclusive muons is dominated by the muons from heavy-flavour hadron decays at high  $p_T$ , while it is dominated by the muons from primary hadron decays (i.e. decay muons) at low  $p_T$ . Hence, one can compare  $Y_{\text{asym}}^{(\text{inclusive muon})}$  with  $Y_{\text{asym}}^{(\text{decay muon})}$  in the low  $p_T$  region. If the employed strategy for background estimation at backward rapidity is reasonable, the upper and lower band of  $Y_{\text{asym}}^{(\text{decay muon})}$  calculated by using the maximum and minimum value of decay muons (see Eq. 4.11 and 4.12), allow to cover  $Y_{\text{asym}}^{(\text{inclusive muon})}$  at low  $p_T$ . The results are shown in Fig. 4.70.  $Y_{\text{asym}}^{(\text{inclusive muon})}$  results are shown as black and blue points corresponding to the results obtained in  $2.96 < y_{\text{CMS}} < 3.22$  and



$3.22 < y_{\text{CMS}} < 3.53$ , respectively, in 20 – 40%.  $Y_{\text{asym}}^{(\text{decay muon})}$  results in 20 – 40% are displayed as the red points. It is found that  $Y_{\text{asym}}^{(\text{inclusive muon})}$  is close to unity in  $p_{\text{T}} > 5 - 6 \text{ GeV}/c$ , indicating no visible difference at forward and backward rapidity. Meanwhile, it is above unity in the low  $p_{\text{T}}$  region, which can be covered by  $Y_{\text{asym}}^{(\text{decay muon})}$  in this region, supporting the estimated background at backward rapidity. Note that a same conclusion can be given in the other event activity bins.

# The pp Reference

This chapter is dedicated to the so-called pp reference, i.e. the double differential production cross section of muons from heavy-flavour hadron decays, at forward ( $2.03 < y_{\text{CMS}} < 3.53$ ) and backward ( $-4.46 < y_{\text{CMS}} < -2.96$ ) rapidity, in pp collisions at  $\sqrt{s} = 5.02$  TeV.

As shown in Eq. 1.4, this pp reference is required in order to investigate any deviation from unity of the nuclear modification factor  $R_{\text{pPb}}$  which would reveal the presence of cold nuclear matter effects in p-Pb collisions.

$$\begin{aligned}
 R_{\text{pPb}}(p_{\text{T}}, y) &= \frac{1}{\langle N_{\text{coll}} \rangle} \times \frac{dN_{\text{pA}}^2/dp_{\text{T}}dy}{dN_{\text{pp}}^2/dp_{\text{T}}dy} \\
 &= \frac{1}{\langle T_{\text{pA}} \rangle} \times \frac{dN_{\text{pA}}^2/dp_{\text{T}}dy}{d\sigma_{\text{pp}}^2/dp_{\text{T}}dy} \\
 &= \frac{1}{A} \times \frac{d\sigma_{\text{pA}}^2/dp_{\text{T}}dy}{d\sigma_{\text{pp}}^2/dp_{\text{T}}dy}
 \end{aligned} \tag{5.1}$$

In Eq. 5.1,  $dN_{\text{pA}}^2/dp_{\text{T}}dy$  ( $d\sigma_{\text{pA}}^2/dp_{\text{T}}dy$ ) and  $dN_{\text{pp}}^2/dp_{\text{T}}dy$  ( $d\sigma_{\text{pp}}^2/dp_{\text{T}}dy$ ) are the differential yields (production cross section) of muons from heavy-flavour hadron decays in p-Pb and pp collisions, respectively;  $\langle T_{\text{pA}} \rangle = \langle N_{\text{coll}} \rangle / \sigma_{\text{NN}}^{\text{inel}}$  is the average nuclear overlap function,  $\langle N_{\text{coll}} \rangle$  is the mean number of binary collisions in p-Pb collisions, and  $\sigma_{\text{NN}}^{\text{inel}}$  is the inelastic nucleon-nucleon cross section;  $A$  is the mass number of Pb.

Due to the fact that a data sample of pp collisions at  $\sqrt{s} = 5.02$  TeV is not available<sup>§</sup>, the pp reference is built from pp data taken at 7 and 2.76 TeV and scaled to 5.02 TeV with a pQCD-driven approach. This approach is discussed in the following. Then, results obtained are shown. Finally, a couple of relevant points are further discussed.

## 5.1 pQCD-based Energy Scaling Procedure

It was shown, using MNR [286] NLO pQCD calculations for pp collisions at  $\sqrt{s} = 5.5$  and 14 TeV [192], that, despite the large uncertainty on the cross section at a given energy with different values of the heavy quark masses and factorization/renormalization scales, the ratio of the cross sections at the two energies is much less dependent on the choice of the calculation parameters [323]. On the other

<sup>§</sup>we have the pp data sample at  $\sqrt{s} = 5$  TeV at the end of 2015.



hand, it was found that the Fixed Order Next-to-Leading Log (FONLL, [140]) calculations can reproduce well the heavy-flavour production cross sections measured in hadronic and semi-leptonic decay channels within a board transverse momentum region, both at mid- and forward rapidity and at various center-of-mass energies. Consequently, we follow the strategy proposed in Ref. [323], using as input the available pp data at 7 and 2.76 TeV and using, for the energy scaling, FONLL calculations.

In this section, I introduce the mentioned strategy for the energy scaling with FONLL, as well as the determination of the corresponding systematic uncertainty. An additional rapidity shift specific to the asymmetric p-Pb system, which is missing in the original strategy proposed for symmetric colliding systems [323], is taken into account.

The pp reference for charged particles and J/Ψ analyse are obtained via a model-based approach (see Ref. [324] and [325] for details).

### 5.1.1 The Strategy

The basic parameter used in the energy interpolation/extrapolation procedure is the energy scaling factor,  $F_{\text{scal}}$ , defined as,

$$F_{\text{scal}}(\sqrt{s_x}|\sqrt{s_{\text{ref}}}; p_T, \Delta y) = \frac{\frac{d\sigma_{\text{pp}}}{dp_T}(\sqrt{s_x}, p_T, \Delta y)}{\frac{d\sigma_{\text{pp}}}{dp_T}(\sqrt{s_{\text{ref}}}, p_T, \Delta y)} \quad (5.2)$$

$F_{\text{scal}}(\sqrt{s_x}|\sqrt{s_{\text{ref}}}; p_T, \Delta y)$  allows one to scale the  $p_T$ -dependent distribution from (reference) energy  $\sqrt{s_{\text{ref}}}$  to the desired one  $\sqrt{s_x}$  within an integrated rapidity interval  $\Delta y$ .  $\frac{d\sigma_{\text{pp}}}{dp_T}(\sqrt{s}, p_T, \Delta y)$  is the corresponding  $p_T$ -differential production cross section of muons from heavy-flavour hadron decays, integrated in a rapidity interval, for pp collisions at a given CMS energy.

In order to validate the procedure, we can use the pp measurement at 7 TeV as the reference and the measurements at  $\sqrt{s} = 2.76$  TeV as the one to be estimated. In this case,  $F_{\text{scal}}$  can be obtained with both data and model (FONLL). Many measurements of heavy-flavour production, in particular the ones based on single muons at 2.76 and 7 TeV [159, 160] have shown that they are consistent within uncertainties with FONLL [42, 287]:

$$F_{\text{scal}}^{\text{Data}}(\sqrt{s_x}|\sqrt{s_{\text{ref}}}; p_T, \Delta y) \simeq F_{\text{scal}}^{\text{FONLL}}(\sqrt{s_x}|\sqrt{s_{\text{ref}}}; p_T, \Delta y) \quad (5.3)$$

Equation 5.3 allows one to re-write Eq. 5.2 as,

$$\begin{aligned} \frac{d\sigma_{\text{pp}}^{\text{Cal.}}}{dp_T}(\sqrt{s_{5.02}}, p_T, \Delta y) &\simeq F_{\text{scal}}^{\text{FONLL}}(\sqrt{s_{5.02}}|\sqrt{s_7}; p_T, \Delta y) \cdot \frac{d\sigma_{\text{pp}}^{\text{Data}}}{dp_T}(\sqrt{s_7}, p_T, \Delta y) \\ &= \frac{\frac{d\sigma_{\text{pp}}^{\text{FONLL}}}{dp_T}(\sqrt{s_{5.02}}, p_T, \Delta y)}{\frac{d\sigma_{\text{pp}}^{\text{FONLL}}}{dp_T}(\sqrt{s_7}, p_T, \Delta y)} \cdot \frac{d\sigma_{\text{pp}}^{\text{Data}}}{dp_T}(\sqrt{s_7}, p_T, \Delta y) \end{aligned} \quad (5.4)$$



Equation 5.4 shows that the data at 5.02 TeV can be calculated by scaling the one at 7 TeV. The corresponding scaling factor is based on FONLL predictions at the two energies.

## 5.1.2 Uncertainty Determination in Model

### 5.1.2.1 Predictions from FONLL: uncertainty determination at parton level

The hadronic production cross section in nucleon-nucleon collisions can be expressed via the "factorisation theorem" [15],

$$\sigma_{NN \rightarrow hQ}^{\text{hard}} = \sum_{i,j} f_i(x_1, \mu_F^2) \otimes f_j(x_2, \mu_F^2) \otimes \sigma_{ij \rightarrow Q}^{\text{hard}}(x_1, x_2, m_Q, \mu_F^2, \mu_R^2) \otimes D_{Q \rightarrow h}(z) \quad (5.5)$$

where,  $f(x, \mu_F^2)$ ,  $\sigma_{ij \rightarrow Q}^{\text{hard}}(x_1, x_2, m_Q, \mu_F^2, \mu_R^2)$  and  $D_{Q \rightarrow h}(z)$  are the parton distribution functions (PDFs), partonic cross section and fragmentation function (FF), respectively, and  $\mu_R$ ,  $\mu_F$  and  $m_Q$  the renormalization scale, factorization scale and the quark mass, respectively. The last three parameters are particularly important for the accuracy of pQCD predictions.

For calculations beyond LO, a conservative approach to estimate the uncertainty can be obtained from the change in the prediction when varying  $\mu_R$  and  $\mu_F$  around a central value  $\mu_0$  that is taken close to the physical scale of the process. The conventional range of variation is [2]

$$\frac{1}{2}\mu_0 < \mu_R, \mu_F < 2\mu_0 \quad (5.6)$$

However, there does not seem to be a broad consensus on whether  $\mu_R$  and  $\mu_F$  should be kept identical or varied independently. One common option is to vary them independently with the following restriction [2]

$$\frac{1}{2}\mu_R < \mu_F < 2\mu_R \quad (5.7)$$

The central values of FONLL predictions are obtained by means of [140]

$$\mu_R = \mu_F = \mu_0 = \sqrt{p_T^2 + m_Q^2} \quad (5.8)$$

where,  $p_T$  denotes the transverse momentum at parton level;  $m_Q$  indicates the quark mass, and its central value is  $m_c = 1.5 \text{ GeV}/c^2$  and  $m_b = 4.75 \text{ GeV}/c^2$  for charm and bottom, respectively [2]. Note that the quark mass are varied in the following calculations.

Using Eq. 5.6, 5.7 and 5.8, one gets the production cross section of heavy quark pairs (without considering the fragmentation function in Eq. 5.5) within given rapidity regions in pp collisions at  $\sqrt{s} = 5.02 \text{ TeV}$ . The corresponding results in the range  $2.03 < y_{\text{CMS}} < 3.53$  are presented in the upper left panel of Fig. 5.1. The rescaled results with respect to the central values for charm and bottom quarks are shown in the middle left and bottom left panel of Fig. 5.1, respectively. The uncertainty

on PDFs is given by different sets of inputs from CTEQ 6. One can see that the uncertainty on QCD scales dominates in the selected  $p_T$  region, while the one on PDFs is negligible. The latter is therefore not taken into account in the following. Similar results are obtained in the range  $-4.46 < y_{\text{CMS}} < -2.96$ , as displayed in the right three panels of Fig. 5.1.

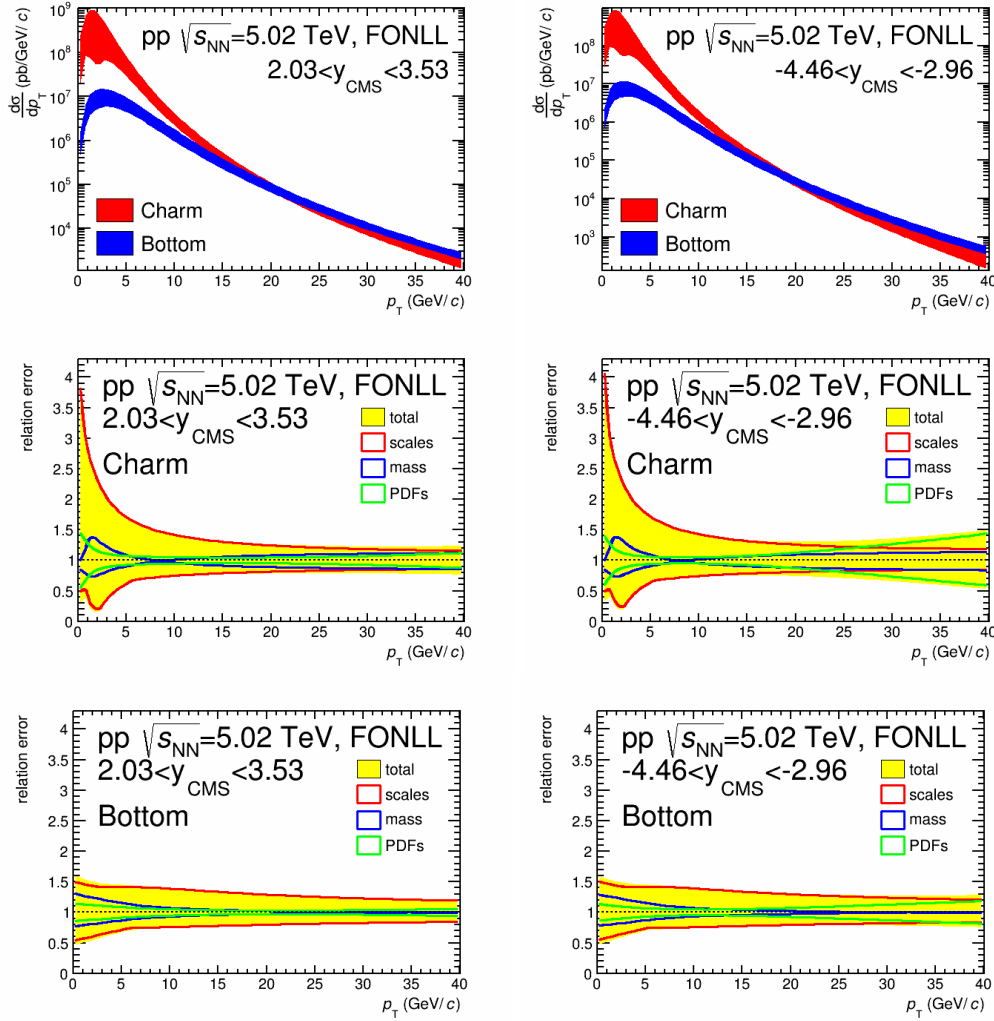


Figure 5.1: Left: production cross sections (up) of heavy quark pairs in  $2.03 < y_{\text{CMS}} < 3.53$  in pp collisions at  $\sqrt{s} = 5.02$  TeV, as well as the relative uncertainty for charm (middle) and bottom (bottom), respectively. Right: same as in the left panel but in the rapidity range  $-4.46 < y_{\text{CMS}} < -2.96$ .

The rapidity distributions of produced particles have a maximum at mid-rapidity ( $y_{\text{CMS}} \sim 0$ ) and they can be described by a Gaussian-like function. Hence, the production cross sections of heavy quarks pairs are expected to be larger in  $2.03 < y_{\text{CMS}} < 3.53$  than in  $-4.46 < y_{\text{CMS}} < -2.96$  since the mean value of the (absolute) rapidity is smaller within the former rapidity interval. The comparison of the results in the two rapidity intervals are shown in Fig. 5.2. The ratios forward/backward

both for charm and bottom are larger than unity for  $p_T > 2$  GeV/ $c$  which are consistent with the expectation.

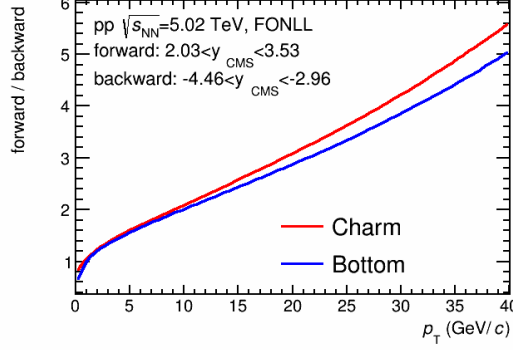


Figure 5.2: Ratio of the production cross sections of heavy-quark pairs generated within  $2.03 < y_{\text{CMS}} < 3.53$  and  $-4.46 < y_{\text{CMS}} < -2.96$  as a function of  $p_T$ . Results for charm and bottom are shown as the red and blue curves, respectively.

### 5.1.2.2 Predictions from FONLL: uncertainty determination at muon level

There are three different sources of heavy-flavour hadron decay muons.

- charm  $\mu$ : muons from charm hadron decays ( $\mu \leftarrow D \leftarrow \text{Charm}$ )
- bottom  $\mu$ : muons from beauty hadron decays ( $\mu \leftarrow B \leftarrow \text{Beauty}$ )
- feed down  $\mu$ : muons from beauty hadron decays via charm hadrons ( $\mu \leftarrow D \leftarrow B \leftarrow \text{Beauty}$ )

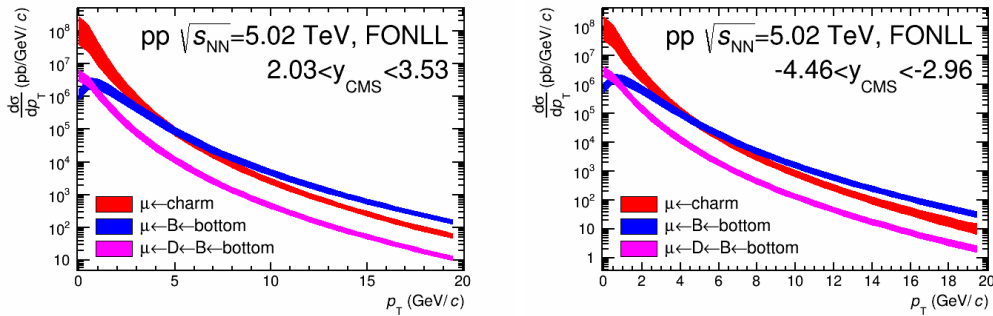


Figure 5.3: Production cross section of muons from heavy-flavour hadron decays within different channels and different rapidity regions:  $2.03 < y_{\text{CMS}} < 3.53$  (left) and  $-4.46 < y_{\text{CMS}} < -2.96$  (right), as a function of (muon)  $p_T$ .

The  $p_T$ -differential production cross section of muons from the three different sources in the range  $2.03 < y_{\text{CMS}} < 3.53$  and  $-4.46 < y_{\text{CMS}} < -2.96$ , are shown in

the left and right panels of Fig. 5.3. The uncertainties on QCD scales and quark mass obtained at parton level are propagated to the muon level and added to that from the fragmentation procedure. The latter results from the different scenarios of fragmentation functions, and it is found to be negligible [140]. Consequently, the relative uncertainty at muon and parton levels are identical.

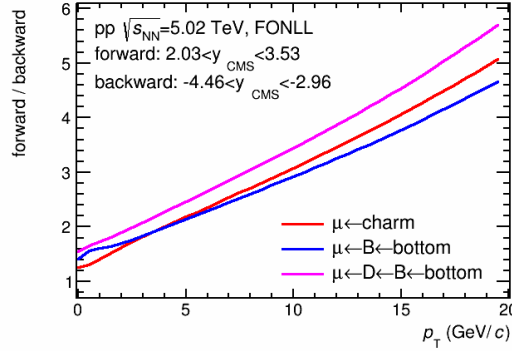


Figure 5.4: Ratio of the production cross sections of muons from different sources (shown in the text) within  $2.03 < y_{\text{CMS}} < 3.53$  and  $-4.46 < y_{\text{CMS}} < -2.96$ . Results for different sources are shown by the curves with different colors.

The production cross section for different muon sources at forward and backward rapidity are compared to each other in Fig. 5.4. As expected, the forward-to-backward ratio is larger than unity for the three sources, which is consistent with the observation made at parton level (Fig. 5.2).

When combining the different muon sources to build the total distribution, one needs to carefully propagate the errors since the uncertainty on the different sources are dependent with each other. Note that bottom  $\mu$  and feed down  $\mu$  originate both from bottom quarks, the parameters corresponding to these two sources cannot be changed independently. Finally, the following method is employed to propagate the uncertainties correctly [140, 42]:

1. add the central values of the production cross section of these three kind of muons together to get the central value of the production cross section for muons from open heavy-flavour hadron decays;
2. fix the other parameters in order to get the central cross section value of the combined results from the three kind of muons, one varies  $m_c$  and  $m_b$  independently. For both  $m_c$  and  $m_b$  one can choose three different values, this will give 9 kinds of combinations. The maximum and minimum differences between these 9 combinations and the central cross section value give the upper and lower uncertainties from the quark masses,  $\sigma_{\text{mass}}^{\text{max}}$  and  $\sigma_{\text{mass}}^{\text{min}}$ ;
3. similarly to the procedure just discussed, change the QCD scales independently for muons from charm and those from bottom (the bottom  $\mu$  and feed down  $\mu$ ) while keeping the other parameters unchanged, in order to estimate the upper and lower uncertainties from the QCD scales,  $\sigma_{\text{scales}}^{\text{max}}$  and  $\sigma_{\text{scales}}^{\text{min}}$ . For

each case, there are 7 combinations of  $\mu_R$  and  $\mu_F$  which satisfy the conditions of Eq. 5.7 and 5.8:

$$\begin{aligned}
 \mu_R &= \mu_0, & \mu_F &= \mu_0, \\
 \mu_R &= 0.5\mu_0, & \mu_F &= 0.5\mu_0, \\
 \mu_R &= 2\mu_0, & \mu_F &= 2\mu_0, \\
 \mu_R &= 2\mu_0, & \mu_F &= \mu_0, \\
 \mu_R &= \mu_0, & \mu_F &= 2\mu_0, \\
 \mu_R &= \mu_0, & \mu_F &= 0.5\mu_0, \\
 \mu_R &= 0.5\mu_0, & \mu_F &= \mu_0.
 \end{aligned} \tag{5.9}$$

When combining the charm and bottom together, one gets a total 49 combinations for the QCD scales.

Figure 5.5 shows the FONLL production cross sections of muons from charm and bottom, including both direct decay and the feed down component, in the range  $2.03 < y_{\text{CMS}} < 3.53$  (left) and  $-4.46 < y_{\text{CMS}} < -2.96$  (right), respectively, in pp collisions at  $\sqrt{s} = 5.02$  TeV. The related uncertainties on QCD scales and quark masses will be discussed in detail in the next section.

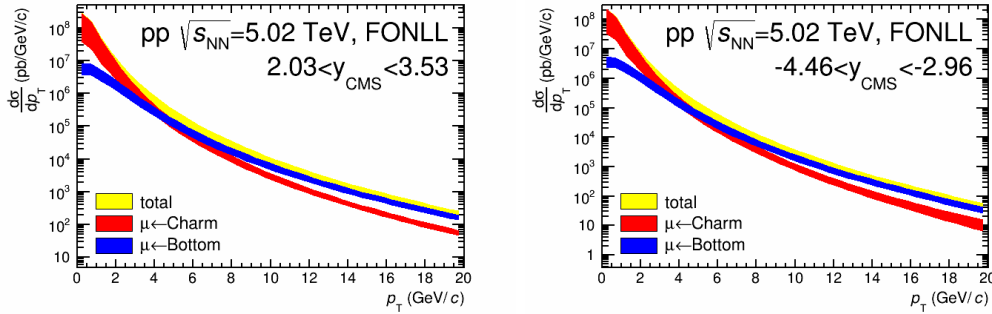


Figure 5.5: Production cross section of muons from charm and bottom, including direct decay and feed down component, in the rapidity regions:  $2.03 < y_{\text{CMS}} < 3.53$  (left) and  $-4.46 < y_{\text{CMS}} < -2.96$  (right), as a function of (muon)  $p_T$ .

Using the same procedure, one can obtain the corresponding results for pp collisions at  $\sqrt{s} = 7$  TeV. Then, the energy scaling factor is obtained via Eq. 5.2. One may note that, in Eq. 5.2, the same rapidity interval,  $\Delta y$ , is used for the two energies. The input data are also provided in this same rapidity interval (Eq. 5.4). This means that if we want to estimate the spectra within  $2.03 < y_{\text{CMS}} < 3.53$  and  $-4.46 < y_{\text{CMS}} < -2.96$  for pp collisions at  $\sqrt{s} = 5.02$  TeV, the data input should be provided within the same (or mirrored) region, which are out of the muon spectrometer acceptance ( $2.5 < y_{\text{CMS}} < 4$  or  $-4 < y_{\text{CMS}} < -2.5$  for pp collisions). The input data therefore needs to be extrapolated to a different rapidity interval. This is called the rapidity shift in the following. Next, I present the last step of the pp reference calculation by considering this additional effect, and the resulting scaling factors are presented later.

### 5.1.3 Strategy Validation for the Rapidity Shift

#### 5.1.3.1 Validation method

When considering the rapidity shift, the energy scaling factor defined in Eq. 5.2 becomes:

$$F_{\text{scal}}(\sqrt{s_x}|\sqrt{s_{\text{ref}}}, \Delta y_x|\Delta y_{\text{ref}}; p_T) = \frac{\frac{d\sigma_{\text{pp}}}{dp_T}(\sqrt{s_x}, p_T, \Delta y_x)}{\frac{d\sigma_{\text{pp}}}{dp_T}(\sqrt{s_{\text{ref}}}, p_T, \Delta y_{\text{ref}})} \quad (5.10)$$

It allows one to scale the  $p_T$ -dependent distribution within  $\Delta y_{\text{ref}}$  at (reference) energy  $\sqrt{s_{\text{ref}}}$  to the desired one within  $\Delta y_x$  at the desired energy  $\sqrt{s_x}$ .

In order to validate Eq. 5.10, one should consider the shift value obtained in p-Pb collisions at  $\sqrt{s_{\text{NN}}} = 5.02$  TeV, which is  $\sim 0.465$  in the proton direction. The first issue is that there is no available measurement (of muons from heavy-flavour hadron decays) performed with a rapidity shift exactly equal to this value. As shown in Fig. 5.6, the heavy-flavour hadron decay muons have been measured in pp collisions at  $\sqrt{s} = 7$  TeV in five individual rapidity bins as well as in the full acceptance ( $2.5 < y_{\text{CMS}} < 4$ ). The resulting sub-rapidity interval width is 0.3 which is close to the desired value 0.465. A test is made to study the rapidity shift: if Eq. 5.10 is validated with a rapidity shift of 0.3, then, we assume it is also the case for a rapidity shift of 0.465.

In order to validate Eq. 5.10, one needs the measurements reported at different colliding energies with respect to the ones at  $\sqrt{s} = 7$  TeV. The candidate is the heavy-flavour hadron decay muons measured in pp collisions at  $\sqrt{s} = 2.76$  TeV, shown in Fig. 5.7. Note that the corresponding measurements are performed in the range  $2 < p_T < 10$  GeV/ $c$ , and in the range  $2 < p_T < 12$  GeV/ $c$  at  $\sqrt{s} = 7$  TeV in  $2.5 < y_{\text{CMS}} < 4$ .

Taking as input measurements at 7 and 2.76 TeV, one can validate the energy scaling strategy by considering the rapidity shift as follows:

1. combine the measurements in 5 rapidity bins at 7 TeV ( $2.5 < y_{\text{CMS}} < 2.8$ ,  $2.8 < y_{\text{CMS}} < 3.1$ ,  $3.1 < y_{\text{CMS}} < 3.4$ ,  $3.4 < y_{\text{CMS}} < 3.7$  and  $3.7 < y_{\text{CMS}} < 4$ ) to get the results within broader regions
  - this allows one to get rid of statistical fluctuations, in particular at high  $p_T$ ;
  - the combined results are shown in 3 new intervals ( $2.8 < y_{\text{CMS}} < 4$ ,  $2.5 < y_{\text{CMS}} < 3.7$  and  $2.8 < y_{\text{CMS}} < 3.7$ ), illustrated in Fig. 5.8 by  $C_1$ ,  $C_2$  and  $C_3$ , respectively;
  - the results in the full acceptance ( $2.5 < y_{\text{CMS}} < 4$ ) are marked as  $C_0$ ;
  - when comparing the above 3 rapidity intervals with  $2.5 < y_{\text{CMS}} < 4$  ( $C_0$ ), one can see that  $2.8 < y_{\text{CMS}} < 4$  ( $C_1$ ) indicates the rapidity shift towards right direction,  $2.5 < y_{\text{CMS}} < 3.7$  ( $C_2$ ) denotes the rapidity shift towards left direction, and  $2.8 < y_{\text{CMS}} < 3.7$  ( $C_3$ ) a narrow range;

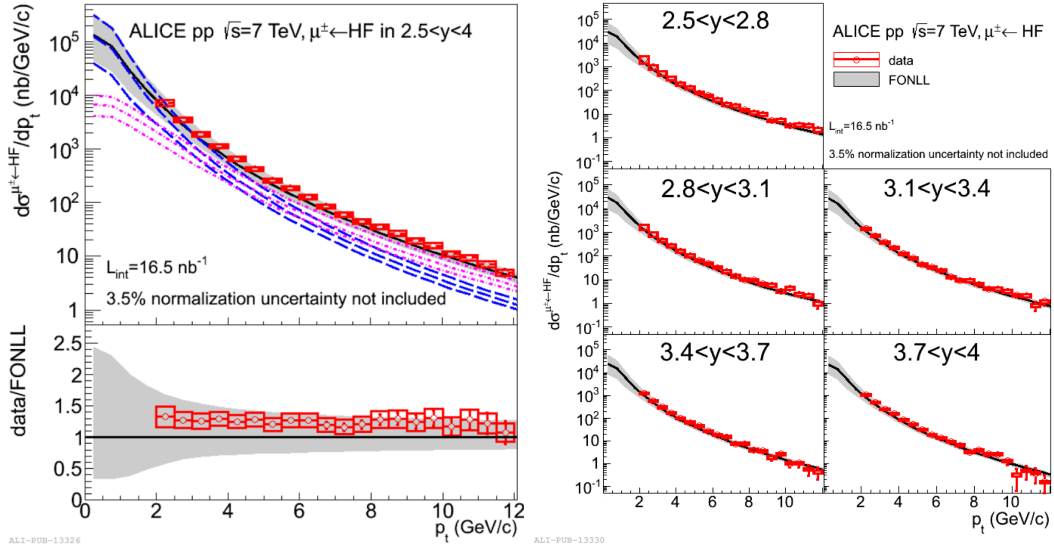


Figure 5.6: Left:  $p_T$ -differential cross section of muons from heavy-flavour hadron decays at forward rapidity ( $2.5 < y_{\text{CMS}} < 4$ ) in pp collisions at  $\sqrt{s} = 7$  TeV. Right: same as left in the five rapidity ranges reported in the figure. The grey bands represent FONLL predictions. Figures taken from Ref. [160]

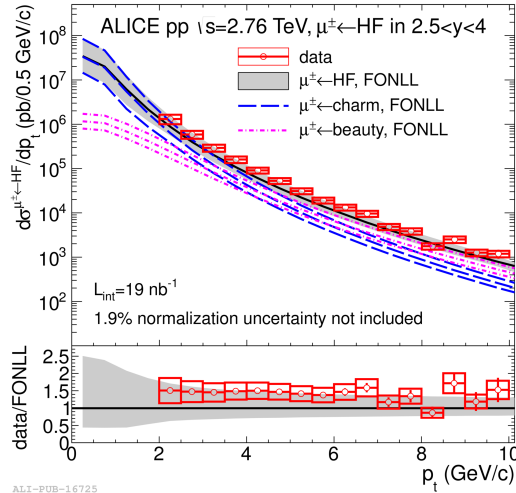


Figure 5.7:  $p_T$ -differential cross section of muons from heavy-flavour hadron decays at forward rapidity ( $2.5 < y_{\text{CMS}} < 4$ ) in pp collisions at  $\sqrt{s} = 2.76$  TeV. The grey bands represent the FONLL predictions. Figures taken from Ref. [159].

2. scale the obtained cross section within  $C_i$  ( $i = 0, 1, 2, 3$ ) at 7 TeV to the one within  $2.5 < y_{\text{CMS}} < 4$  at 2.76 TeV;
  - the difference among the scaled results are found to be small, indicating the applicability of Eq. 5.10;
  - the scaled results allow us to make a direct comparison with the related

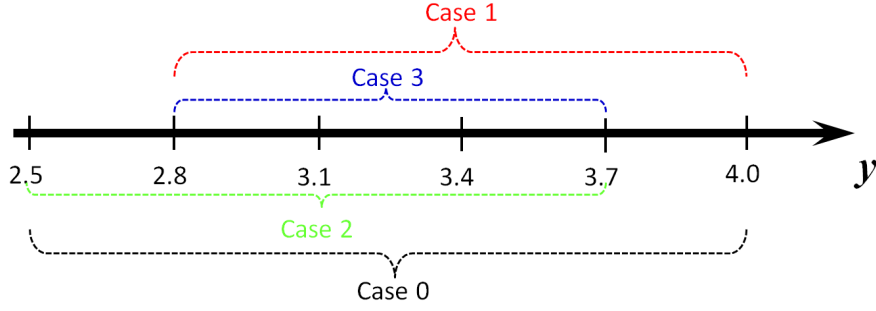


Figure 5.8: Scheme of the combination among rapidity bins;  $C_1$ ,  $C_2$  and  $C_3$  denote the combined rapidity regions of  $2.8 < y_{\text{CMS}} < 4$ ,  $2.5 < y_{\text{CMS}} < 3.7$  and  $2.8 < y_{\text{CMS}} < 3.7$ , respectively, together with  $C_0$  indicating the results in the full acceptance  $2.5 < y_{\text{CMS}} < 4$ .

measurement (see Fig. 5.7): the deviation between used model and data is included as well, resulting in a larger difference with respect to the data.

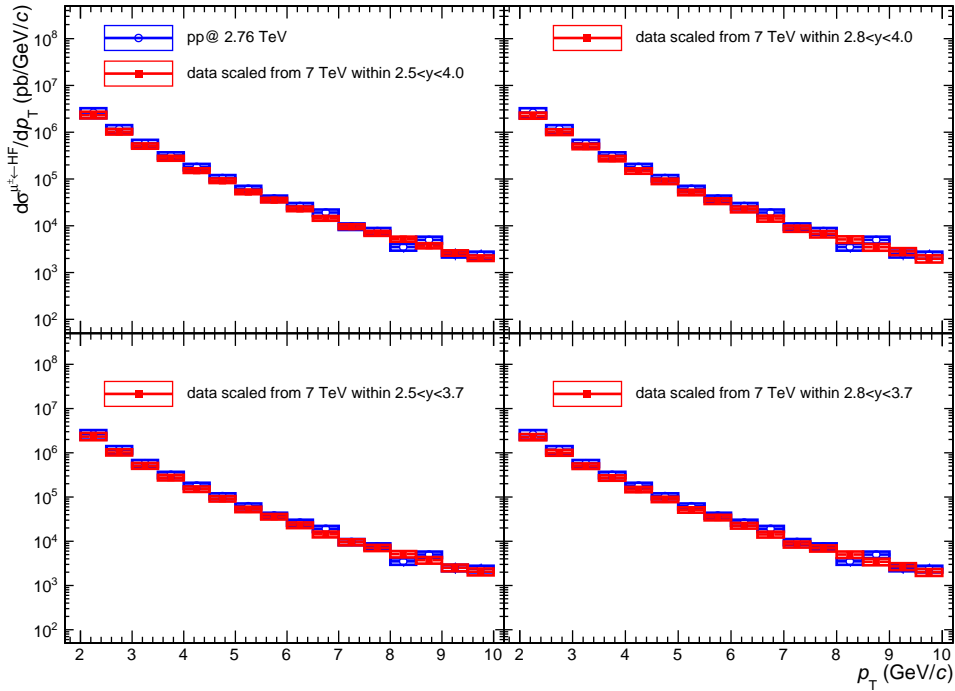


Figure 5.9:  $p_T$ -differential cross section of muons from heavy-flavour hadron decays, obtained after scaling the measurements within different rapidity intervals in pp collisions at 7 TeV (red) compared to the one obtained in the full acceptance in pp collisions at 2.76 TeV (blue).

Figure 5.9 shows the results in the full acceptance at 2.76 TeV scaled from the

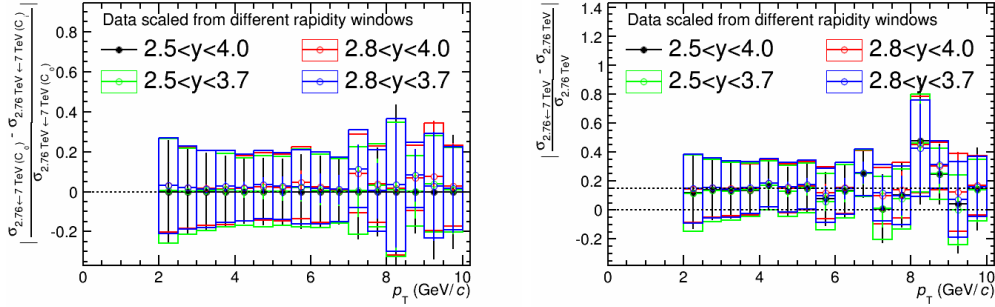


Figure 5.10: Relative deviation of the scaled results with respect to the one based on full acceptance (left) and the measurement at 2.76 TeV (right).

measurements within different rapidity intervals at 7 TeV. As it can be seen, the results are consistent within uncertainties. Note that the  $p_T$  range is limited by the measurement at 2.76 TeV. Further comparison among the scaled results are shown in the left panel of Fig. 5.10. The deviation with respect to the one in the full acceptance ( $C_0$ ) is negligible. The energy scaling strategy with a rapidity shift is therefore validated. When comparing the scaled results with the one from real measurement, as shown in the right panel of Fig. 5.10, one can see a 13 – 15% deviation in the  $p_T$  range  $2 < p_T < 10$  GeV/ $c$ , which can be induced by the difference between the model and data.

### 5.1.3.2 Systematic uncertainty on rapidity shift

The scaling procedure described above contains two parts: energy interpolation/extrapolation and rapidity extrapolation. This results in two independent systematic uncertainties. Concerning the latter one, it can be estimated by taking as input the available measurements performed within different rapidity ranges in pp collisions at  $\sqrt{s} = 7$  TeV. Based on the combined results ( $C_1$ ,  $C_2$  and  $C_3$ , see Fig. 5.8) of the production cross section of muons from heavy-flavour hadron decays, one can extrapolate the measurements in the three rapidity sub-windows, to get the corresponding results in the full acceptance without energy interpolation/extrapolation. The difference between the "real" measurement and the extrapolated ones corresponds to the systematic uncertainty.

The results, presented in Fig. 5.11, are consistent with each other. A more detailed comparison with respect to the measurement performed in the full acceptance is shown in Fig. 5.12: there is  $\sim < 3\%$  deviation for  $p_T < 8$  GeV/ $c$ . This deviation increases at higher  $p_T$ . Since these errors (i.e. systematic and statistical) are not considered in Fig. 5.12, the large deviations observed for  $p_T > 8$  GeV/ $c$  could arise from statistical fluctuations. This is indeed confirmed hereafter. When using a power-law function to fit the spectra in the high  $p_T$  region, as shown in the left panel of Fig. 5.13, the relative deviation remains smaller than  $\sim 3\%$  over the whole  $p_T$  range (right panel of Fig. 5.13).

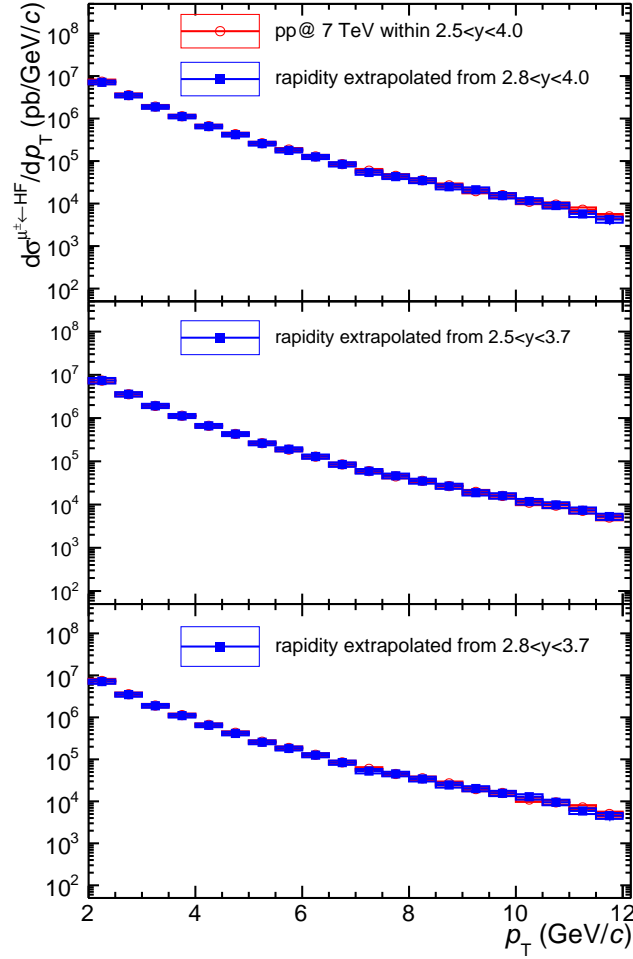


Figure 5.11:  $p_T$ -differential cross section of muons from heavy-flavour hadron decays, obtained by extrapolating the measurements within different rapidity intervals to the full acceptance in pp collisions at  $\sqrt{s} = 7$  TeV. Results obtained after scaling (blue) are compared to the measurements made in the full acceptance (red).

#### 5.1.4 Energy Scaling Factor

The energy scaling factor including the rapidity shift (Eq. 5.10) can be obtained by means of the  $p_T$ -differential cross section of muons from heavy-flavour hadron decays predicted by FONLL in the range  $2.03 < y_{\text{CMS}} < 3.53$  for pp collisions at  $\sqrt{s} = 5.02$  TeV, together with the one in the range  $2.5 < y_{\text{CMS}} < 4$  for pp collisions at  $\sqrt{s} = 7$  TeV.

The upper two plots in Fig. 5.14 show the scaling factor based on the different sets of charm and bottom masses ( $m_c=1.3, 1.5, 1.7$  and  $m_b=4.5, 4.75, 5.0$  GeV/ $c^2$ ) and assuming that quark masses are the same at 7 and 5.02 TeV [323] in the top left panel. One can see a clear  $p_T$ -dependence of the scaling factor, in particular in the range  $p_T < 4$  GeV/ $c$ . It decreases from  $\sim 0.9$  at  $p_T = 0$  to  $\sim 0.86$  at  $p_T = 2$  GeV/ $c$ ,

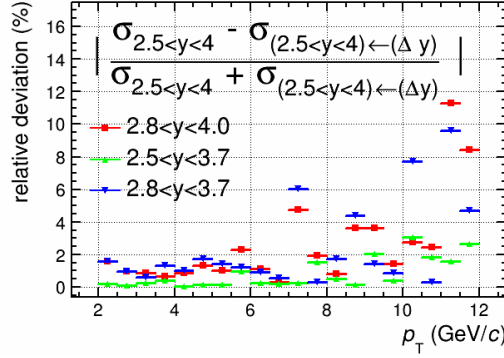


Figure 5.12: Relative deviation of the cross sections in the full acceptance extrapolated from the ones within different rapidity intervals with respect to the available measurement the same region.

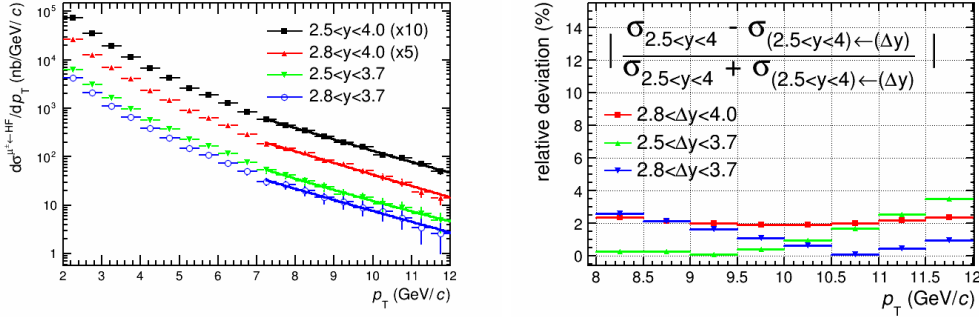


Figure 5.13: Left:  $p_T$ -differential cross section of muons from heavy-flavour hadron decays in pp collisions at  $\sqrt{s} = 7$  TeV. The distributions are presented in the four rapidity intervals reported in the figure. In the high  $p_T$  region, the distributions are fitted with power-law functions. Right: same as Fig. 5.12 but obtained with the results of the fits shown in the left panel.

and down to  $\sim 1\%$  at  $p_T = 20$  GeV/ $c$ . The corresponding relative uncertainty, changing within  $\sim < 1\%$ , is presented in the right panel. The quark mass related uncertainty can therefore be safely neglected at high transverse momentum ( $p_T > 2$  GeV/ $c$ ). A similar conclusion was made in Ref. [323] for the scaling procedure between 7 and 2.76 TeV.

The middle two plots in Fig. 5.14 present the obtained scaling factor based on various sets of QCD scales (see Eq. 5.6, 5.7) and assuming, like for the quark masses, that the QCD scales are the same at different collision energies. [323]. The QCD scales induced variation can be studied via two scenarios: same scales for charm and bottom (correlated scales, shown as colored lines, see Eq. 5.9) and different scales (un-correlated scales, shown as black lines), which give similar results for charm and bottom [323]. The corresponding uncertainty is  $\sim < 6\%$  in the range  $p_T < 2$  GeV/ $c$  and  $< 3\%$  at higher  $p_T$ .

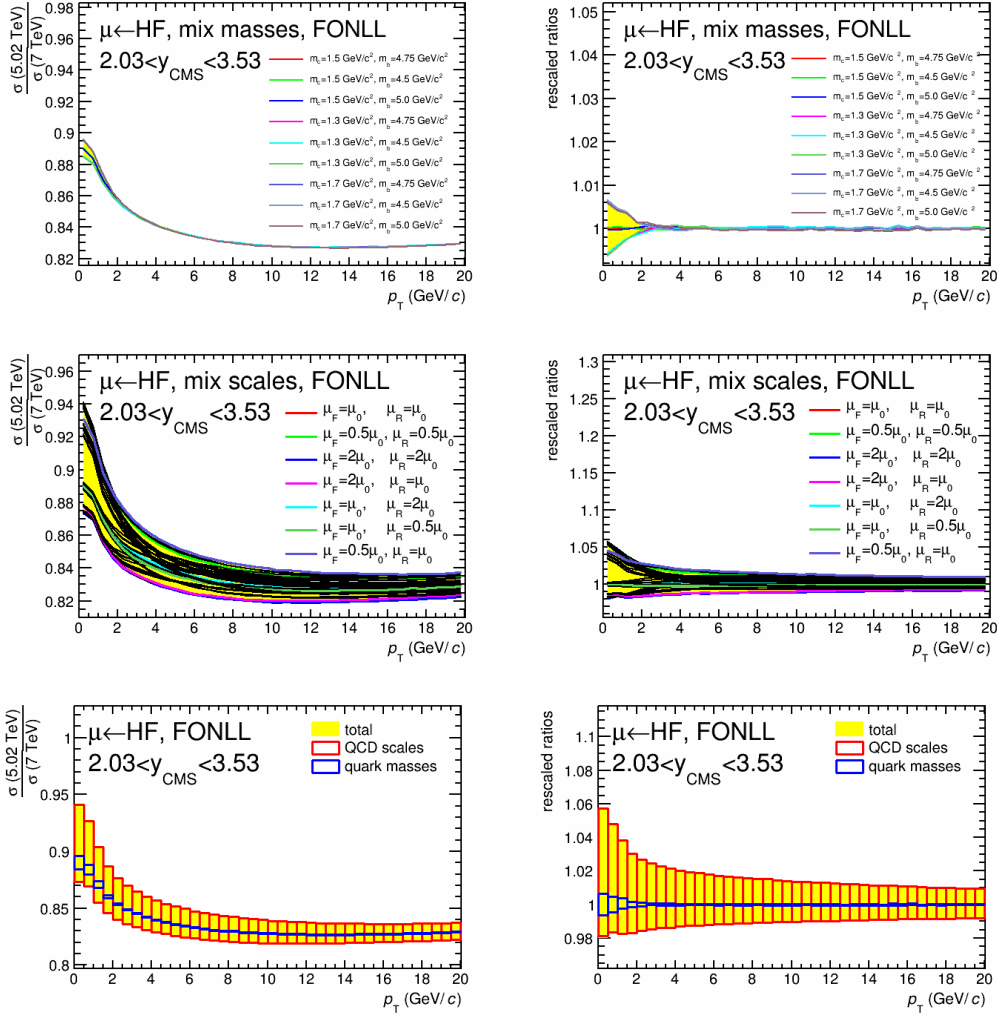


Figure 5.14: Upper: FONLL scaling factor from  $\sqrt{s} = 7$  TeV ( $2.5 < y_{\text{CMS}} < 4$ ) to 5.02 TeV ( $2.03 < y_{\text{CMS}} < 3.53$ ) for the measurement of the  $p_{\text{T}}$ -differential cross section of muons from heavy-flavour hadron decays with different combinations of **quark masses** as indicated on the figure (left), as well as the related relative systematic uncertainty (right). Middle: FONLL scaling factor with different combinations of **QCD scales** indicated on the figure (left); related relative systematic uncertainty (right). Bottom: FONLL scaling factor with different **QCD scales** (red boxes) and **quark masses** (blue boxes), as well as the total systematic uncertainty marked as yellow bands (left), and the corresponding relative systematic uncertainty (right).

Finally, the scaling factors versus (muon)  $p_{\text{T}}$  obtained with different combinations of quark masses (blue boxes) and QCD scales (red boxes) are shown in the bottom left panel of Fig. 5.14. Their related relative uncertainties are displayed on the right. One can see that the total uncertainty (yellow band) is  $\sim < 6\%$  in the

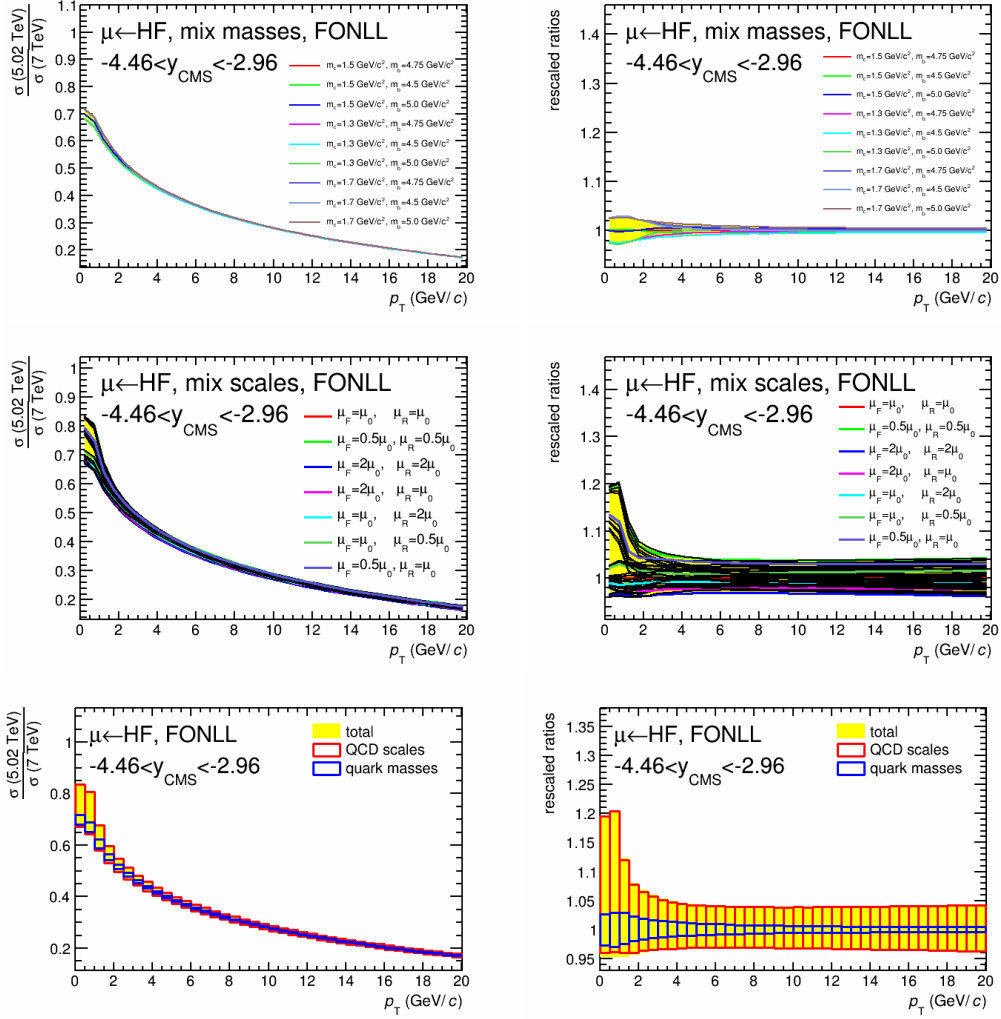


Figure 5.15: Same as Fig. 5.14 but for the rapidity interval  $-4.46 < y_{\text{CMS}} < -2.96$ .

range  $p_T < 2 \text{ GeV}/c$  and  $< 3\%$  at higher  $p_T$ .

Similar results, but in the rapidity range  $-4.46 < y_{\text{CMS}} < -2.96$ , are presented in Fig. 5.15. The total uncertainty on QCD scales and quark masses varies from  $\sim 20\%$  at  $p_T = 0$  to  $\sim 5\%$  at  $p_T = 4 \text{ GeV}/c$ . Note that the scaling factor obtained at backward rapidity is smaller than that obtained at forward rapidity: the forward interval is closer to mid-rapidity than the backward one.

## 5.2 The pp Reference Estimated at $\sqrt{s} = 5.02$ TeV

Equation 5.4 can be modified to account for the rapidity shift in Eq. 5.10 as,

$$\begin{aligned}
 & \frac{d\sigma_{pp}^{\text{Cal.}}}{dp_T}(\sqrt{s_{5.02}}, p_T, \Delta y_x) \\
 & \simeq F_{\text{scal}}^{\text{FONLL}}(\sqrt{s_{5.02}}|\sqrt{s_7}, \Delta y_x|\Delta y_{\text{ref}}; p_T) \cdot \frac{d\sigma_{pp}^{\text{Data}}}{dp_T}(\sqrt{s_7}, p_T, \Delta y_{\text{ref}}) \\
 & = \frac{\frac{d\sigma_{pp}^{\text{FONLL}}}{dp_T}(\sqrt{s_{5.02}}, p_T, \Delta y_x)}{\frac{d\sigma_{pp}^{\text{FONLL}}}{dp_T}(\sqrt{s_7}, p_T, \Delta y_{\text{ref}})} \cdot \frac{d\sigma_{pp}^{\text{Data}}}{dp_T}(\sqrt{s_7}, p_T, \Delta y_{\text{ref}})
 \end{aligned} \tag{5.11}$$

where  $\Delta y_x$  is the acceptance for pp collisions at  $\sqrt{s} = 5.02$  TeV, i.e.  $2.03 < y_{\text{CMS}} < 3.53$  ( $-4.46 < y_{\text{CMS}} < -2.96$ ) at forward (backward) rapidity. The corresponding reference region is  $2.5 < |y_{\text{CMS}}| < 4$  for pp collisions at  $\sqrt{s} = 7$  TeV (which is symmetric with respect to  $y_{\text{CMS}} = 0$ , see Fig. 5.6).

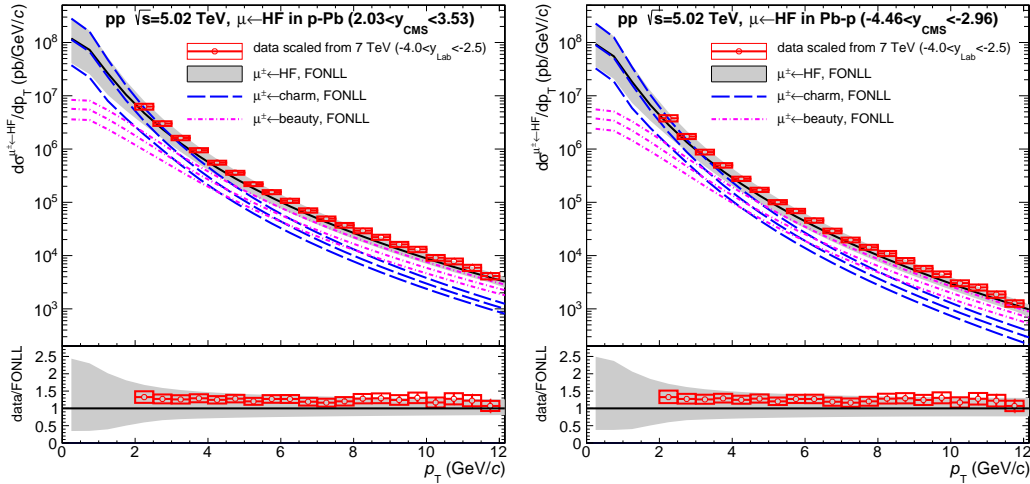


Figure 5.16: The reference for pp collisions at  $\sqrt{s} = 5.02$  TeV obtained by means of the energy scaling procedure, which takes as input the  $p_T$ -differential cross section of muons from heavy-flavour hadron decays measured within the full acceptance ( $2.5 < y_{\text{CMS}} < 4$ ) for pp collisions at 7 TeV, and the results are extrapolated to forward ( $2.03 < y_{\text{CMS}} < 3.53$ , left) and backward ( $-4.46 < y_{\text{CMS}} < -2.96$ , right) rapidity, respectively. In both panels, the solid curves are FONLL calculations and the bands display the theoretical systematic uncertainties. Also shown, are the FONLL calculations and systematic theoretical uncertainties for muons from charm (long dashed curves) and beauty (dashed curves) decays. Results obtained after scaling (red boxes) are compared to FONLL predictions (grey bands) in the bottom panels.

### 5.2.1 Results Based on the Measurement at $\sqrt{s} = 7$ TeV

The estimated pp reference at forward and backward rapidity is shown in the left and right panels of Fig. 5.16, respectively. One can see that they are consistent within uncertainties with FONLL predictions. Such an agreement was already observed for pp collisions at  $\sqrt{s} = 7$  and 2.76 TeV [160, 159]. Note that the absolute value of the cross-section is larger at forward than that at backward rapidity.

The corresponding statistical uncertainty is shown in Fig. 5.17. One may notice that this uncertainty is identical at forward and backward rapidity since both are induced exclusively by the measurement performed in pp collisions at  $\sqrt{s} = 7$  TeV. The relative uncertainty increases up to  $\sim 17\%$  for  $p_T = 12$  GeV/ $c$ .

The relative systematic uncertainty is presented in Fig. 5.18. It includes contributions from the data inputs, as well as the one from scaling factor both at forward and backward rapidity (see Fig. 5.14 and 5.15 for details). The two components are added in quadrature, resulting in a  $\sim 14\%$  maximum value ( $p_T$ -dependent) in the range  $p_T < 12$  GeV/ $c$  both at forward and backward rapidity.

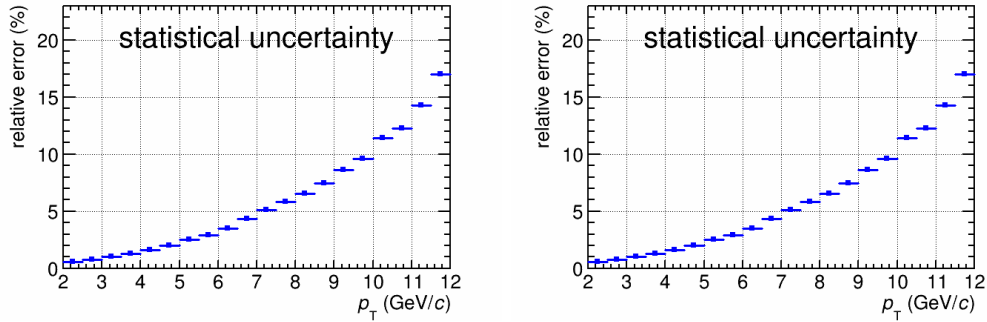


Figure 5.17: Relative **statistical uncertainty** of the estimated pp reference at forward ( $2.03 < y_{\text{CMS}} < 3.53$ , left) and backward ( $-4.46 < y_{\text{CMS}} < -2.96$ , right) rapidity.

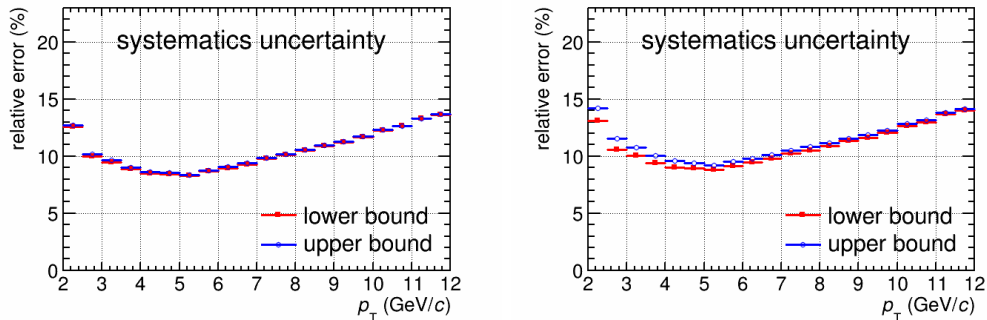


Figure 5.18: Relative **systematic uncertainty** of the estimated pp reference at forward ( $2.03 < y_{\text{CMS}} < 3.53$ , left) and backward ( $-4.46 < y_{\text{CMS}} < -2.96$ , right) rapidity.



## 5.2.2 Extrapolation to Higher Transverse Momentum

As discussed in the previous sub-section, the pp reference cross section of heavy-flavour hadron decay muons at  $\sqrt{s} = 5.02$  TeV is obtained via a pQCD-based (FONLL) energy scaling procedure and uses as input the  $p_T$ -differential cross sections measured at  $\sqrt{s} = 7$  TeV. The above procedure has been used to obtain the  $p_T$ -differential cross section up to  $p_T = 12$  GeV/ $c$  (Fig. 5.16). This limit in  $p_T$  comes from the upper  $p_T$  limit of the measurements at  $\sqrt{s} = 7$  TeV. One can use FONLL to extrapolate the data to higher  $p_T$ , but since the comparison between available data and FONLL presents some differences in the measured  $p_T$  range ( $p_T = 30$  GeV/ $c$  at maximum [156]), we therefore scale FONLL predictions to match the obtained pp reference in the range  $6 < p_T < 12$  GeV/ $c$ . This is done according to

$$\begin{aligned} & \frac{d\sigma_{pp}^{\text{Cal.}}}{dp_T}(\sqrt{s} = 5.02 \text{ TeV}) \\ &= \begin{cases} F_{\text{scal}}^{\text{FONLL}} \cdot \frac{d\sigma_{pp}^{\text{Data}}}{dp_T}(\sqrt{s} = 7 \text{ TeV}) & (2 < p_T < 12 \text{ GeV}/c) \\ K(\sqrt{s} = 5.02 \text{ TeV}) \cdot \frac{d\sigma_{pp}^{\text{FONLL}}}{dp_T}(\sqrt{s} = 5.02 \text{ TeV}) & (12 < p_T < 16 \text{ GeV}/c) \end{cases} \end{aligned} \quad (5.12)$$

where,  $K(\sqrt{s} = 5.02 \text{ TeV})$  denotes the deviation between data and FONLL within a certain  $p_T$  range, at a given energy, and it allows to tune the FONLL predictions to be consistent with data in this selected region.

$$K(\sqrt{s} = 5.02 \text{ TeV}) = \frac{\int_{\min}^{\max} dp_T' \frac{d\sigma_{pp}^{\text{Cal.}}}{dp_T'}(\sqrt{s} = 5.02 \text{ TeV})}{\int_{\min}^{\max} dp_T' \frac{d\sigma_{pp}^{\text{FONLL}}}{dp_T'}(\sqrt{s} = 5.02 \text{ TeV})} \quad (5.13)$$

The chosen  $p_T$  interval is  $6 < p_T < 12$  GeV/ $c$  where deviations between FONLL and data are the smallest. Note that the above  $p_T$  range was tested for the  $K$  factor calculation, and a small deviations with respect to  $6 < p_T < 12$  GeV/ $c$  was found.

Using Eq. 5.12 and 5.13, the pp references up to 16 GeV/ $c$  are shown in Fig. 5.19. The results in the range  $2 < p_T < 12$  GeV/ $c$  are the ones presented Fig. 5.16, and the results above 12 GeV/ $c$  are from the data-tuned FONLL predictions. The scaling factor  $K(\sqrt{s} = 5.02 \text{ TeV})$  is  $\sim 1.23$  both at forward and backward rapidity. Changing the lower limit of the  $p_T$  interval used to normalize FONLL predictions to the data from 6 to 4 GeV/ $c$  results in a deviation of about 2 – 3%. It can be neglected since the uncertainties from FONLL predictions are  $\sim 25\%$  and  $\sim 30\%$  in the range  $12 < p_T < 16$  GeV/ $c$ , at forward and backward rapidity, respectively.

Concerning the  $p_T$  extrapolation, alternatively, one can extrapolate the measurements at  $\sqrt{s} = 7$  TeV up to  $p_T = 16$  GeV/ $c$  via

$$\begin{aligned} & \frac{d\sigma_{pp}^{\text{Data+Ext.}}}{dp_T}(\sqrt{s} = 7 \text{ TeV}) \\ &= \begin{cases} \frac{d\sigma_{pp}^{\text{Data}}}{dp_T}(\sqrt{s} = 7 \text{ TeV}) & (2 < p_T < 12 \text{ GeV}/c) \\ K(\sqrt{s} = 7 \text{ TeV}) \cdot \frac{d\sigma_{pp}^{\text{FONLL}}}{dp_T}(\sqrt{s} = 7 \text{ TeV}) & (12 < p_T < 16 \text{ GeV}/c) \end{cases} \end{aligned} \quad (5.14)$$

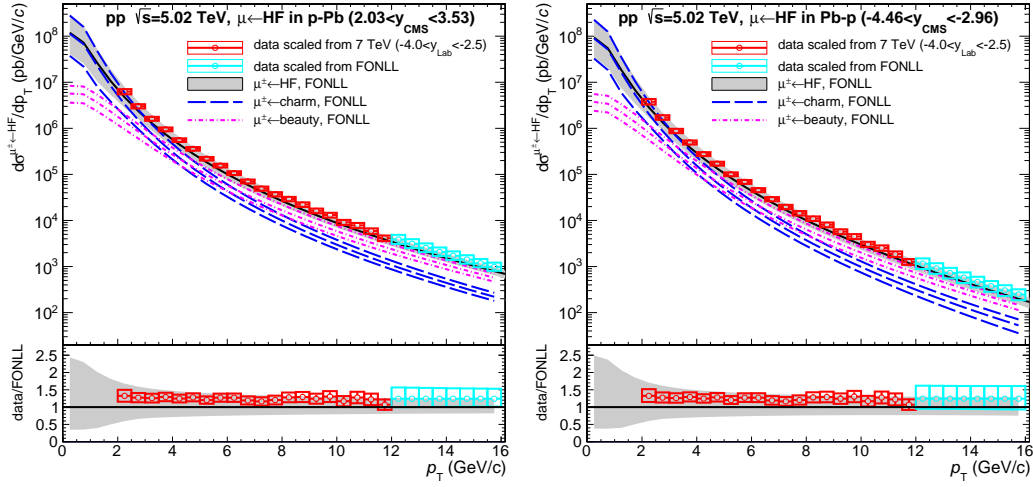


Figure 5.19: The reference for pp collisions at  $\sqrt{s} = 5.02$  TeV obtained by means of the energy scaling procedure in the range  $2 < p_T < 12$  GeV/c (i.e. red boxes), taking as input the  $p_T$ -differential cross section of muons from heavy-flavour hadron decays measured within the full acceptance ( $2.5 < y_{\text{CMS}} < 4$ ) for pp collisions at 7 TeV, and the results are extrapolated to forward ( $2.03 < y_{\text{CMS}} < 3.53$ , left) and backward ( $-4.46 < y_{\text{CMS}} < -2.96$ , right), respectively. Results above 12 GeV/c (i.e. light blue boxes) are obtained by tuning the  $p_T$ -differential cross section in pp collisions at  $\sqrt{s} = 5.02$  TeV, predicted by FONLL, to match the obtained pp reference in the range  $6 < p_T < 12$  GeV/c. FONLL predictions are similar with the ones presented in Fig. 5.16. Results obtained after scaling (red and light blue boxes) are compared to FONLL predictions (grey bands) in the bottom panels.

$$K(\sqrt{s} = 7 \text{ TeV}) = \frac{\int_{\min}^{\max} dp_T' \frac{d\sigma_{\text{pp}}^{\text{Data}}}{dp_T'}(\sqrt{s} = 7 \text{ TeV})}{\int_{\min}^{\max} dp_T' \frac{d\sigma_{\text{pp}}^{\text{FONLL}}}{dp_T'}(\sqrt{s} = 7 \text{ TeV})} \quad (5.15)$$

where,  $\frac{d\sigma_{\text{pp}}^{\text{Data+Ext.}}}{dp_T}(\sqrt{s} = 7 \text{ TeV})$  denotes the  $p_T$ -differential cross section in the range  $2 < p_T < 16$  GeV/c for pp collisions at  $\sqrt{s} = 7$  TeV. It consists of two parts: results below 12 GeV/c are from the available measurements, as well as the one based on FONLL predictions for  $p_T > 12$  GeV/c, tuned to match the above measurement in a certain  $p_T$  region. The scaling factor,  $K(\sqrt{s} = 7 \text{ TeV})$ , has similar definition with respect to the one shown in Eq. 5.13. Then, one can implement the energy scaling procedure to get the desired pp reference within a broader region.

$$\begin{aligned} & \frac{d\sigma_{\text{pp}}^{\text{Cal.}}}{dp_T}(\sqrt{s} = 5.02 \text{ TeV}) \\ &= F_{\text{scal}}^{\text{FONLL}} \cdot \frac{d\sigma_{\text{pp}}^{\text{Data+Ext.}}}{dp_T}(\sqrt{s} = 7 \text{ TeV}) \quad (2 < p_T < 16 \text{ GeV}/c) \end{aligned} \quad (5.16)$$

Equations 5.12 and 5.16 are expected to lead to same results at high  $p_T$  if there

is no energy-dependence of the defined factor,  $K$ . These are shown in Fig. 5.20 together with FONLL predictions. The left and right panel is for the results obtained at forward and backward rapidity, respectively. As expected, results extrapolated using Eq. 5.12 and 5.16 are very similar showing that the  $K$  factor has a weak energy dependence. Note that the results in the range  $2 < p_T < 12$  GeV/ $c$  are identical by definition.

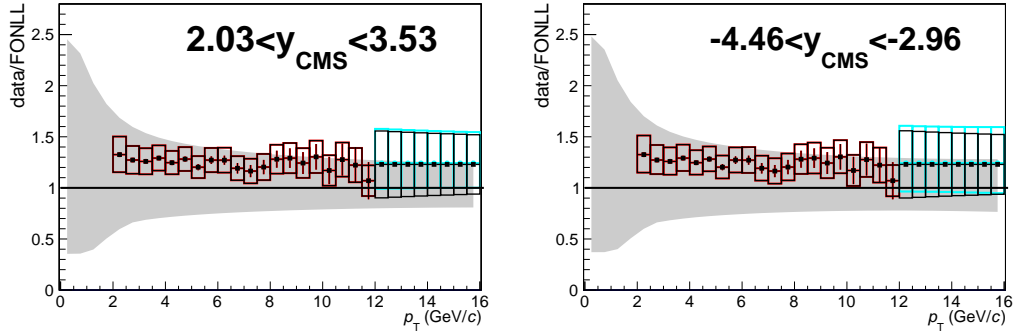


Figure 5.20: Left: ratio of the pp reference obtained with the mentioned two scenarios, Eq. 5.12 (red+light blue) and 5.16 (black), to the FONLL predictions at forward rapidity ( $2.03 < y_{\text{CMS}} < 3.53$ ). The shadowing region indicates the relative systematic uncertainty predicted by FONLL. Right: same as left panel but at backward rapidity ( $-4.46 < y_{\text{CMS}} < -2.96$ ). See text for details.

The different sources of systematic uncertainties are summarized in Tab. 5.1.

	forward rapidity ( $2.03 < y_{\text{CMS}} < 3.53$ )	backward rapidity ( $-4.46 < y_{\text{CMS}} < -2.96$ )
$F_{\text{scal}} \oplus$ Data inputs	$p_T < 12$ GeV/ $c$ : 8 – 14% $p_T > 12$ GeV/ $c$ : $\sim 25\%$ ( $p_T$ -dependent)	$p_T < 12$ GeV/ $c$ : 8 – 14% $p_T > 12$ GeV/ $c$ : $\sim 30\%$ ( $p_T$ -dependent)
rapidity extra.	$< 3\%$	
syst. on norm.	$3.5\%$ [160]	

Table 5.1: Different sources of systematic uncertainty on the estimated reference both at forward and backward rapidity for pp collisions at  $\sqrt{s} = 5.02$  TeV: combined systematic uncertainty on energy scaling and data input, the one on rapidity extrapolation/shift and normalization.

## 5.3 Discussion

### 5.3.1 Combination of the Results From Different Energies

In the previous section, the pp reference at  $\sqrt{s} = 5.02$  TeV was evaluated by taking as input the available measurement in  $2 < p_T < 12$  GeV/ $c$  for pp collisions at  $\sqrt{s} = 7$  TeV (Fig. 5.6). As input, one can also use the measured cross section in

pp collisions at  $\sqrt{s} = 2.76$  TeV (Fig. 5.7), and use the same procedure for energy scaling to estimate the reference at  $\sqrt{s} = 5.02$  TeV. Moreover, it opens the room to cross check the results based on 7 TeV data. Note that, due to the limited statistics, the 2.76 TeV data was reported in the range  $2 < p_T < 10$  GeV/c [159].

### 5.3.1.1 Results with taking as input the measurement at $\sqrt{s} = 2.76$ TeV

In analogy to the previous section, in the following, I show some control plots for the energy scaling procedure when taking as input the measurement in pp collisions at  $\sqrt{s} = 2.76$  TeV. The results are shortly described.

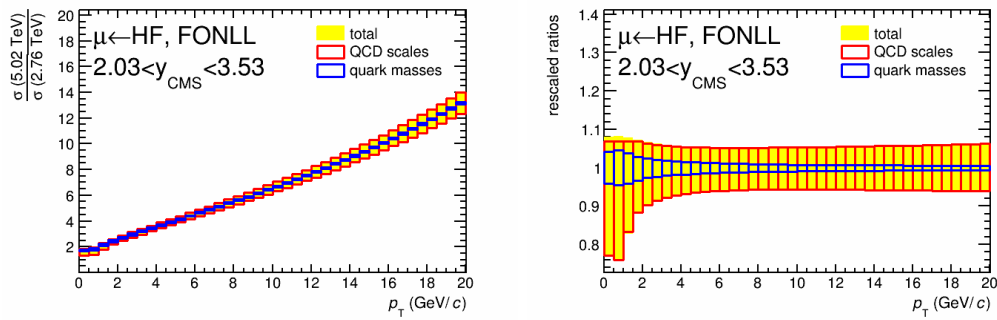


Figure 5.21: FONLL scaling factor from  $\sqrt{s} = 2.76$  TeV ( $2.5 < y_{\text{CMS}} < 4$ ) to 5.02 TeV ( $2.03 < y_{\text{CMS}} < 3.53$ ) for the measurement of the  $p_T$ -differential cross section of muons from heavy-flavour hadron decays with different QCD scales (red boxes) and quark masses (blue boxes), as well as the total systematic uncertainty marked as yellow bands (left), and the corresponding relative systematic uncertainty (right).

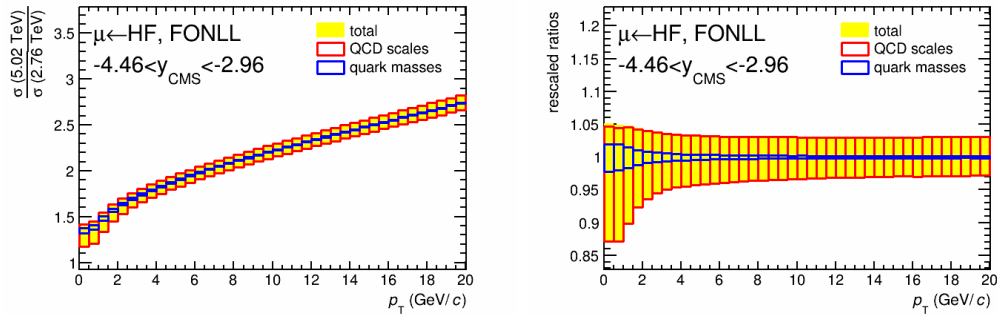


Figure 5.22: Same as Fig. 5.21 but scaling to 5.02 TeV in the range  $-4.46 < y_{\text{CMS}} < -2.96$ .

Figure 5.21 (Figure 5.22) presents the energy scaling factor based on FONLL calculations defined as the ratio of  $p_T$ -differential cross section for pp collisions at  $\sqrt{s} = 5.02$  TeV in  $2.03 < y_{\text{CMS}} < 3.53$  ( $-4.46 < y_{\text{CMS}} < -2.96$ ) over the one for pp collisions at  $\sqrt{s} = 2.76$  TeV in  $2.5 < y_{\text{CMS}} < 4$ . The obtained results including the

systematic uncertainty on QCD scalars and quark masses, are displayed in the left panel. The scaling factor is larger than unity (i.e. energy extrapolation), while it is smaller than unity (i.e. energy interpolation) for the results using the 7 TeV results as input (Fig. 5.14 and 5.15). The relative uncertainties are about 10% (7%) nearby 10 GeV/ $c$ , as shown in the right panel of Fig. 5.21 (Fig. 5.22).

The scaled results taking as input the measurements at 2.76 and 7 TeV, are shown in Fig. 5.23 both at forward (left panel) and backward rapidity (right panel), and in each panel, they are indicated as green and light blue boxes, respectively. The results after scaling are compared to FONLL predictions (gray), in the bottom panels. One can see that,

- within uncertainties, the estimated results based on different inputs are comparable both at forward and backward rapidity;
- the systematic uncertainty (including the ones on the experimental data and energy scaling factor) is significantly larger using 2.76 TeV results as input, because the experimental uncertainties at 2.76 TeV data are much larger than that at 7 TeV data, meanwhile, the uncertainties on the energy scaling factor at 2.76 TeV is larger (compatible) at forward (backward) rapidity.

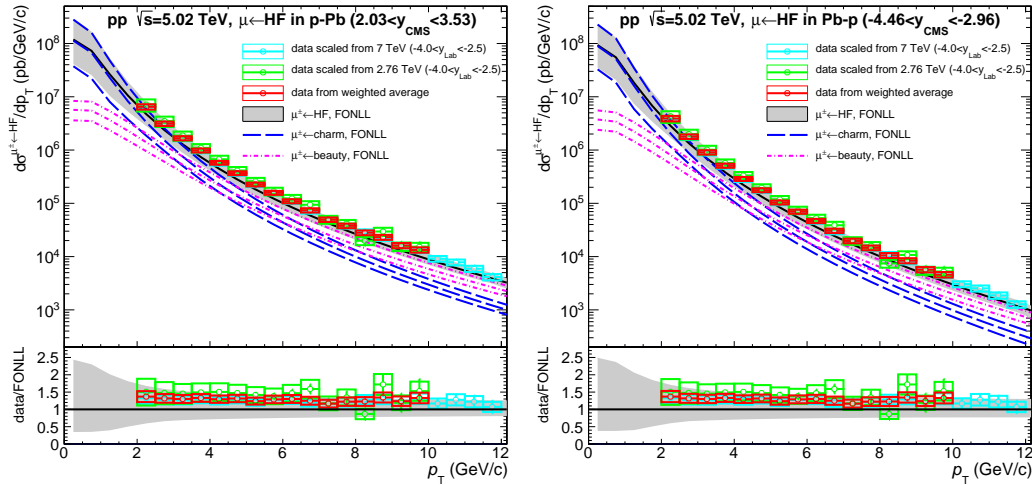


Figure 5.23:  $p_T$ -differential cross section of muons from heavy-flavour hadron decays for  $2.03 < y_{\text{CMS}} < 3.53$  (left) and  $-4.46 < y_{\text{CMS}} < -2.96$  (right) in pp collisions at  $\sqrt{s} = 5.02$  TeV. The results are obtained by taking the pp data from 2.76 TeV (green) and 7 TeV (light blue). Red markers correspond to the weighted averaged between them (see the text for details). FONLL predictions are represented by the grey band (muons from heavy-flavour hadron decays) and, by the blue (muons from charm decays) and magenta (muons from bottom decays) curves. The bottom panels show the comparison with FONLL predictions.

### 5.3.1.2 Combination and Deviation

One can combine the pp reference obtained by taking as input the measurements in pp collisions at  $\sqrt{s} = 7$  and 2.76 TeV. The weighted average between them can be calculated via [326]

$$\sigma_{5.02}^{\text{Data}} = \frac{W_7 \cdot \sigma_{5.02 \leftarrow 7} + W_{2.76} \cdot \sigma_{5.02 \leftarrow 2.76}}{W_7 + W_{2.76}} \quad (5.17)$$

$$W_i = \frac{1}{C_i} \quad (5.18)$$

$${}^{\S}C_i = \frac{1}{4}(\sigma_+ + \sigma_-)^2 - \frac{1}{2}(\sigma_+ - \sigma_-)^2 \quad (5.19)$$

where,  $\sigma_{5.02 \leftarrow 2.76}$  ( $7$ ) denotes the pp reference based on 2.76 (7) TeV data;  $\sigma_{5.02}^{\text{Data}}$  indicates the weighted average between them.  $W$  is the defined weight;  $\sigma_+$  and  $\sigma_-$  are the upper and lower systematic uncertainty in each  $p_T$  bin  $i$ .

The related results of the weighted average are presented as the red boxes in each panel of Fig. 5.23, and they are closer to the results based on 7 TeV data which have a smaller experimental systematic uncertainty than those for 2.76 TeV data. At forward rapidity, further comparisons between the average and the one based on 7 TeV data, are shown in Fig. 5.24. The deviation is about 3% in the whole  $p_T$  region. Similar results are found at backward rapidity.

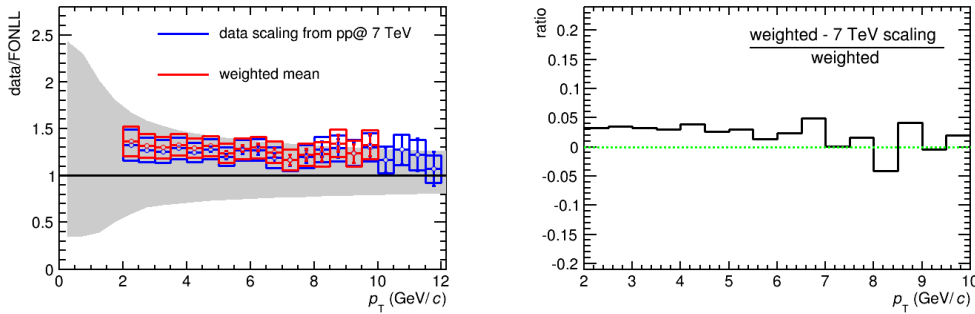


Figure 5.24: Left:  $p_T$ -differential cross section of muons from heavy-flavour hadron decays in  $2.03 < y_{\text{CMS}} < 3.53$  (forward) with the weighted mean (red) and results based on 7 TeV (blue). Right: the relative deviation between the results shown in the left panel.

### 5.3.2 Alternative Strategy for the Reference at High $p_T$

The  $p_T$  extrapolation of the pp reference has been discussed in Sec. 5.2.2. Alternatively, one can proceed by means of the method shown below:

<sup>\S</sup>arXiv: hep-ex/0006004

1. build the pp reference using the weighted average of the cross sections extrapolated from 7 TeV and 2.76 TeV data, as described in the previous sub-section,
2. implement the  $p_T$  extrapolation via a fitting procedure (similar to the one used in Sec. 4.2.2)
  - add in quadrature the systematic and statistical uncertainties in order to get the total one on the obtained pp reference;
  - sample each point by means of Gaussian distribution, while the related mean is the central value and the standard deviation is the total uncertainty obtained above; the sampled points can form new distributions;
  - fit the new distributions with a power-law function in order to extrapolate them up to higher  $p_T$ ; the central values of the extrapolated results are estimated as the mean of the fitted distributions, as well as the related systematic uncertainty given by the maximum deviation among them.
3. correct the extrapolated results with FONLL predictions at high  $p_T$  [327]
  - calculate the relative difference between the pp reference and FONLL predictions in current  $p_T$  region via

$$r_i = \frac{x_i}{a_i + \sigma_{a_i}} \quad (5.20)$$

where,  $i$  denotes the  $i$ -th  $p_T$  bin,  $x_i$  and  $a_i$  are the points in the current pp reference and FONLL predictions at 5.02 TeV, respectively;  $\sigma_{a_i}$  is the uncertainty on  $a_i$  given by FONLL directly;

- calculate the weighted mean of  $\{r_i\}$ , indicating as  $\bar{r}$ , with the weight defined as,

$$W_i = \left( \frac{a_i + \sigma_{a_i}}{\sigma_{x_i}} \right)^2 \quad (5.21)$$

where,  $\sigma_{x_i}$  is the uncertainty of  $x_i$ ;

- get the related dispersion of  $\bar{r}$ , denoting as  $\chi^2$ , in the current  $p_T$  region;
- build a modified dispersion between  $\bar{r}$  and the pp reference in the **extrapolated  $p_T$  region**,

$$\chi'^2 = \frac{1}{n-1} \times \frac{\sum_i W'_i \cdot (\alpha \cdot r'_i - \bar{r})^2}{\sum_i W'_i} \quad (5.22)$$

where,  $r'_i$  and  $W'_i$  are obtained in the extrapolated  $p_T$  region. Note that  $\bar{r}$  is calculated in the current  $p_T$  region;

- tune the parameter  $\alpha$  to have the minimum  $\chi^2$

$$\Delta\chi^2 = |\chi'^2 - \chi^2| \quad (5.23)$$

Remark that,  $\chi^2$  and  $\chi'^2$  are defined within the current and extrapolated  $p_T$  region, respectively;



- modify the pp reference and its uncertainty in the extrapolated region by the obtained value of parameter  $\alpha$ .

The basic assumption of the proposed method is that [327], the mean value and the related dispersion of  $\{r_i\}$  in the current  $p_T$  region and the extrapolated  $p_T$  region are the same. Then, using the observable obtained in the current  $p_T$  region to correct the one in the extrapolated  $p_T$  region, the final results contain both the information in the pp reference in the current  $p_T$  region and that of FONLL predictions in the extrapolated  $p_T$  region.

The procedure discussed above has not yet been tested but could be used in the future.



# Muons from Heavy-Flavour Hadron Decays in p–Pb Collisions at $\sqrt{s_{\text{NN}}} = 5.02$ TeV

---

In this chapter, I discuss the results of the measurements of muons from heavy-flavour hadron decays in p–Pb collisions at  $\sqrt{s_{\text{NN}}} = 5.02$  TeV. Section 6.1 is a summary of the analysis strategy discussed in the previous chapters, and the related systematic uncertainties are shown in Sec. 6.2. The measurements concerning the production cross section, nuclear modification factor and the forward-to-backward ratio are presented in Sec. 6.3, 6.4 and 6.5, respectively.

## 6.1 Summary of the Analysis Strategy

The data samples used for this analysis mainly consist of muon triggered events (MB events are used for normalization), requiring in addition to the MB trigger condition the presence of one track candidate above a  $p_{\text{T}}$  threshold in the muon trigger system (see Sec. 3.1 in Chap. 3). Two event samples were collected, one with a trigger  $p_{\text{T}}$  threshold of about 0.5 GeV/ $c$ , the other one with a trigger  $p_{\text{T}}$  threshold of 4.2 GeV/ $c$ . They are referred as muon single low (MSL) and muon single high (MSH) triggered events, respectively. Pile-up events (events with more than a single interaction per bunch crossing, see Sec. 3.3 in Chap. 3) amount to about 2% in the MB data sample<sup>§</sup>. The muon selection criteria consist of following procedures described in Sec. 3.2 in Chap. 3. The candidate tracks are required to be reconstructed in the rapidity range  $-4 < \eta_{\text{LAB}} < -2.5$  and polar angle (at the end of the absorber) range  $170^\circ < \theta_{\text{abs}} < 178^\circ$ . Then, muon tracks in the tracking system are requested to match track segments in the trigger system. In addition, a cut on the product of the track momentum and its distance of closet approach to the primary vertex ( $p \times \text{DCA}$ ), is applied in order to further reduce the contribution from fake tracks and beam-induced background. Tracks with  $p \times \text{DCA} > 6\sigma_{p \times \text{DCA}}$  are rejected. Finally, the measurement of muons from heavy-flavour hadron decays is performed in  $2 < p_{\text{T}} < 16$  GeV/ $c$  by combining MSL and MSH triggered events i.e. MSL up to  $p_{\text{T}} = 7$  GeV/ $c$  and MSH for  $7 < p_{\text{T}} < 16$  GeV/ $c$ .

Concerning the normalization procedure, the number of MB events is evaluated by means of the scaling factor which can be determined with two different approaches

---

<sup>§</sup>whereas, it is more significant in the most central collisions such as 0 – 5% (e.g.  $\sim 10\%$  for MSL with V0A centrality selection) which are however not considered in this analysis.



(see Sec. 3.1 in Chap. 3). With the approach based on the offline selection of muon triggered events in the MB data sample, the scaling factor is defined as the product between the inverse probability of having the MSH trigger condition verified in a MSL event and the one of having the MSL trigger condition verified in a MB event. The second method is based on the ratio of MB triggered events to that of muon triggered events (MSL or MSH) at level-0 corrected for pile-up, and taking into account the difference in the fraction of events passing the quality cuts for MB and MSL (MSH) trigger samples. Finally, the average between the two approaches using the number of MSL (MSH) events as a weight is considered.

The acceptance  $\times$  efficiency correction is obtained by employing a similar strategy as in pp [160] and Pb–Pb analysis [159] (see Sec. 3.4 in Chap. 3). The realistic detector simulation with AliRoot (see Sec. 3.4.2), is implemented by taking as input the kinematic distribution of heavy-quarks according to PYTHIA, which are tuned to match NLO pQCD calculations [286]. The efficiency correction factor, computed with the AliRoot correction framework (CORRFW), is defined as the ratio between distribution of the reconstructed muons after the offline selection procedure and the one of the simulation input. It is realized that charm and beauty give almost the same efficiencies for  $p_T > 2$  GeV/ $c$ . Consequently, the latter is used in this analysis. This was also the case in pp and Pb–Pb collisions [160, 159]. The dependence on event activity is not significant in p–Pb collisions. Note that the efficiency is the same for heavy-flavour hadron decay muons and inclusive muons for  $p_T > 2$  GeV/ $c$ .

The subtraction of the background composed of muons from charged pion and kaon decays at forward and backward rapidity from the corresponding measured  $p_T$ -differential muon yields corrected for acceptance, and tracking and trigger efficiency is based on a data-tuned Monte-Carlo cocktail (see Sec. 4.2 and 4.3 in Chap. 4). At backward rapidity, the event activity dependence is obtained by taking into account the measurements performed by CMS in p–Pb collisions at  $\sqrt{s_{NN}} = 5.02$  TeV [309]. Note that the contribution from W-boson semi-muonic decays within the relevant  $p_T$  region ( $2 < p_T < 16$  GeV/ $c$ ) is about 2% at maximum, which is included in the final systematic uncertainty on the background.

The pp reference  $p_T$ -differential cross sections of muons from heavy-flavour hadron decays at  $\sqrt{s} = 5.02$  TeV, both at forward and backward rapidity, is obtained by applying a pQCD-driven energy and rapidity scaling based on Fixed Order Next-to-Leading Log (FONLL [140]) calculations, to the measured  $p_T$ -differential cross sections in pp collisions at  $\sqrt{s} = 7$  TeV in the kinematic region  $2.5 < y < 4$  and  $2 < p_T < 12$  GeV/ $c$  [160] (see Sec. 5.2 in Chap. 5). The scaling factor is evaluated by considering different sets of factorization and renormalization scales and quark masses. Since the current measurement of the pp  $p_T$ -differential cross section at  $\sqrt{s} = 7$  TeV is limited to  $p_T < 12$  GeV/ $c$ , the  $p_T$ -differential cross sections in the  $p_T$  range  $12 < p_T < 16$  GeV/ $c$  at  $\sqrt{s} = 5.02$  TeV are obtained by scaling the  $p_T$ -differential cross sections in  $6 < p_T < 12$  GeV/ $c$  at  $\sqrt{s} = 5.02$  TeV from FONLL calculations to the one determined at the same energy by using the measurement at  $\sqrt{s} = 7$  TeV. It is worth mentioning that in the interval  $2 < p_T < 10$  GeV/ $c$ , the  $p_T$ -differential cross section of muons from heavy-flavour hadron decays is also mea-

sured at  $\sqrt{s} = 2.76$  TeV [159]. Therefore, it has been checked that by scaling the pp references at both energies to  $\sqrt{s_{NN}} = 5.02$  TeV, the results are consistent within uncertainties with respect to those obtained by using only the measurement at  $\sqrt{s} = 7$  TeV (see Sec. 5.3 in Chap. 5). As mentioned, the pp reference at  $\sqrt{s} = 5.02$  TeV can be obtained by taking as input the available measurements at both 7 and 2.76 TeV, then calculating the weighted average<sup>§</sup> between them, which is also consistent within uncertainties with the one obtained by scaling the 7 TeV data.

## 6.2 Summary of the Systematic Uncertainty

In this section, I discuss the various sources of systematic uncertainties related to the analysis procedure, as well as the error propagation in order to obtain the final results as a function of  $p_T$  and event activity.

### 6.2.1 Sources of Systematic Uncertainty

#### 6.2.1.1 Normalization Procedure

The systematic uncertainty on the normalization factor is about 1% both for MSL and MSH triggered events within different periods. It is estimated from the difference in the normalization factor based on offline and scaler methods. It is fully un-correlated among  $p_T$  and event activity intervals.

Concerning the cross section, the normalization is implemented using the visible cross section measured by the ALICE Collaboration in p-Pb collisions at  $\sqrt{s_{NN}} = 5.02$  TeV [277]. It is  $2.09 \text{ b} \pm 1.6\%(\text{corr. syst.}) \pm 2.6\%(\text{un-corr. syst.})$  and  $2.12 \text{ b} \pm 1.6\%(\text{corr. syst.}) \pm 2.3\%(\text{un-corr. syst.})$  for the p-Pb (forward) and Pb-p (backward) configurations, respectively. The correlated systematic uncertainty among different collisions systems is 1.6%. Note that the uncertainty on the measured cross section is correlated among  $p_T$  intervals.

The overlap function  $\langle T_{pA} \rangle$  and the corresponding systematic uncertainties for a given event activity class, are summarized in Tab. 6.1. They are calculated with different estimators (V0A, CL1 and ZNA), as well from a hybrid model (indicated as "mult"). The results for the latter one are based on the ZNA event classification and on the assumption that the number of charged-particle multiplicity at mid-rapidity is proportional to the number of participants ( $\langle N_{\text{part}} \rangle$ ), see Ref. [283] for details. Note that the systematic uncertainty on  $\langle T_{pA} \rangle$  is correlated among  $p_T$  intervals and un-correlated among event activity classes.

#### 6.2.1.2 Detector response

The systematic uncertainty on the detector response consists of the following components (see Sec. 3.4.3):

- trigger efficiency. It is estimated by means of the trigger response function (defined as the ratio of the inclusive muon distribution matching with the low

<sup>§</sup>the used weight is derived from the statistical and systematic uncertainties after the scaling.

event activity class	estimators			hybrid model
	V0A	CL1	ZNA	mult.
0 – 5%	0.211 (4.8%)	0.223 (4.8%)	0.214 (7.0%)	0.175 (9.5%)
5 – 10%	0.186 (3.6%)	0.194 (3.6%)	0.196 (5.0%)	0.166 (6.6%)
10 – 20%	0.167 (3.8%)	0.180 (3.8%)	0.177 (2.0%)	0.157 (5.2%)
20 – 40%	0.134 (3.7%)	0.136 (3.7%)	0.143 (2.0%)	0.137 (3.9%)
40 – 60%	0.092 (5.2%)	0.088 (5.2%)	0.093 (4.0%)	0.101 (5.9%)
60 – 100%	0.037 (23.4%)	0.037 (23.4%)	0.031 (6.0%)	0.046 (6.1%)

Table 6.1:  $\langle T_{pPb} \rangle$  (in  $\text{mb}^{-1}$ ) values and its systematic uncertainties from various event activity estimators V0A, CL1 and ZNA, as well as from an hybrid model. The latter indicated as "mult." is obtained assuming the charged-particle multiplicity at mid-rapidity is proportional to the number of participants ( $\langle N_{\text{part}} \rangle$ ) [283].

$p_T$  trigger condition with respect to the one matching with all  $p_T$  trigger condition) and the comparison of the efficiency corrected  $p_T$  distributions asking the matching with MSL and MSH triggered events. Finally, it is about 1% (4%) for MSL (MSH), independently of the data taking periods;

- tracking efficiency. It is estimated by comparing the results obtained with MC and real data [268]. It amounts to 2% (3%) at forward (backward) rapidity, independently of the data taking periods;
- matching efficiency. It is estimated as the difference between the results from MC simulation and data when applying different cuts on  $\chi^2$  for the matching between the tracker tracks and the trigger tracks. It is 0.5% for single muons;
- mis-alignment. It is estimated by taking the deviation of efficiency based on different mis-alignment scenarios with respect to the (default) one based on realistic detector response. It is estimated to  $0.5\% \times p_T$  (in  $\text{GeV}/c$ ).

It is necessary to mention that:

- all the components are un-correlated among  $p_T$  intervals, except the uncertainty on mis-alignment which is correlated among  $p_T$  intervals;
- all the components are correlated among event activity classes;
- all the components are un-correlated among different colliding systems.

### 6.2.1.3 Background subtraction

The systematic uncertainty on the estimation of the yields of muons from charged pion and kaon decays contains the following components.

- multiplicity integrated collisions:
  - $p_T$ -extrapolated mid-rapidity distributions of charged pions and kaons, respectively: 5 – 10% ( $p_T$  dependent);

- rapidity extrapolation obtained by comparing the results from DPMJET and HIJING models: 5 – 27% (2 – 30%) at forward (backward) rapidity;
- absorber-related effect on the decay of primary pions and kaons: 15% (Sec. 4.2.3);
- at backward rapidity, an additional systematic uncertainty arises from the procedure using the forward-backward asymmetry factor measured by the CMS Collaboration. It is calculated by varying the factor between unity and two times the measured value up to  $p_T = 5$  GeV/ $c$  for charged particles. It amounts to 15 – 18%. At higher  $p_T$ , a 15% uncertainty is included to consider the deviation from an symmetric distribution. These uncertainties are added in quadrature;
- different event activity classes:
  - the systematic uncertainty on the charged-particle inputs, as well as the rapidity extrapolation procedure, shows a contribution of 5 – 20% at forward, while it is about 10 – 30% at backward rapidity (Sec. 4.3.5);
  - the one on models, defined as the deviation between DPMJET and HIJING extrapolated results, within a given event activity interval, is about 2 – 30% ( $p_T$  dependent);
  - 15% resulting from absorber effect (same as in multiplicity integrated collisions);
  - in multiplicity integrated collisions, the systematic uncertainty on forward-backward asymmetry based on the CMS measurements is of about 17 – 20%;
  - the deviation of event activity classification based on MC and Optical Glauber Model: varies within  $\sim 7$ –12% (see the right panel of Fig. 4.51).

Note that:

- all the components are un-correlated among  $p_T$  intervals except the one on event activity determination procedure;
- all the components are un-correlated among event activity intervals excluding the one on absorber effect;
- the uncertainty on the data input (i.e. charged  $K^\pm/\pi^\pm$  measured at mid-rapidity) is correlated between p–Pb (forward) and Pb–p (backward) configurations. However, they are not the dominated component in each configuration (see Fig. 4.64), hence they are taken as un-correlated between p–Pb and Pb–p configurations in the following analysis;

#### 6.2.1.4 The pp reference

The systematic uncertainty on the pp  $p_T$ -differential cross sections at  $\sqrt{s} = 5.02$  TeV accounts for the following components:



- $p_T$ -differential cross section of muons from heavy-flavour hadron decays at  $\sqrt{s} = 7$  TeV
  - total uncertainty varying within 8 – 14% excluding the one of 3.5% on the normalization; it includes  $\sim 5\%$  from detector response and  $1\% \times p_T$  (in GeV/ $c$ ) from detector mis-alignment;
- scaling factor obtained from FONLL-based MC calculations using different sets of factorization and renormalization scales and quark masses. It amounts to 3% (7%) for  $p_T = 2$  GeV/ $c$  and 2% (4%) for  $p_T = 12$  GeV/ $c$  at forward (backward) rapidity. In the  $p_T$  extrapolated interval  $12 < p_T < 16$  GeV/ $c$ , the systematic uncertainty is estimated with FONLL calculations and amounts to 26% (30%) at forward (backward) rapidity;
- rapidity extrapolation of the pp reference. An additional 3% systematic uncertainty is added to account for the different rapidity coverage of the Muon spectrometer in p–Pb collisions as compared to pp collisions, due to the fact that the center-of-mass frame moves with rapidity  $\Delta y \approx 0.465$  in the proton direction as a consequence of the different energy of the p and Pb beams. It is obtained after comparison of the results in the full rapidity range with the ones in different sub-rapidity intervals, scaled to the full rapidity range using FONLL, in pp collisions at  $\sqrt{s} = 7$  TeV.

Note that:

- the uncertainty on normalization and mis-alignment are correlated among  $p_T$  intervals, while the others are un-correlated;
- the uncertainty on the data input (i.e. measurements of muons from heavy-flavour hadron decays in pp collisions at  $\sqrt{s} = 7$  TeV) is correlated between p–Pb (forward) and Pb–p (backward) configurations;
- all the components are fully correlated among event activity intervals.

### 6.2.1.5 Summary

Table 6.2 summarizes the different sources of the systematic uncertainty for  $Q_{pPb}$  and  $Q_{FB}$  as a function of  $p_T$  and event activity. Type I indicates the uncertainties correlated between event activity bins. Type II denotes the uncertainties correlated between colliding systems (pp and p–Pb/Pb–p). Type III stands for the uncertainties correlated between  $p_T$  bins. Type IV denotes the uncertainties correlated between p–Pb and Pb–p configurations.

### 6.2.2 Error Propagation

The total systematic uncertainty is obtained using the error propagation formula with the various components discussed above. The procedure is summarized in the following.



		$Q_{pPb}$		$Q_{FB}$			
		vs. $p_T$	vs. cent.	vs. $p_T$	vs. cent.		
Signal	mis-alignment		III	I	III	I	
	efficiency (detector response)			I		I	
	pile-up		III		III		
	background						
Ref.	7 TeV input	mis-alignment efficiency remaining		III+IV IV IV IV	I+IV	-	-
	rapidity shift (3%) normalization (3.5%) energy scaling		III+IV	I			
	$F_{norm}$ (1%)		III	I	III	I	
Norm.	$T_{pA}$ (NBD)	Glauber MC-closure		II+III	II	-	-
	$T_{pA}$ (Hybrid)	Glauber (3.4%) assumptions		II+III	I		

Table 6.2: Summary of the sources of the systematic uncertainty for  $Q_{pPb}$  and  $Q_{FB}$ . Type I indicates the uncertainties correlated between event activity bins. Type II denotes the uncertainties correlated between colliding systems (pp and p-Pb/Pb-p). Type III stands for the uncertainties correlated between  $p_T$  bins. Type IV denotes the uncertainties correlated between p-Pb and Pb-p configurations.

### 6.2.2.1 Uncertainties on the Nuclear Modification Factor

#### Results versus transverse momentum

Figure 6.1 shows the relative statistical uncertainty on the nuclear modification factor of muons from heavy-flavour hadron decays, as a function of  $p_T$ , in multiplicity integrated p–Pb collisions at  $\sqrt{s_{NN}} = 5.02$  TeV. The results obtained at forward ( $2.03 < y_{CMS} < 3.53$ ) and backward rapidity ( $-4.46 < y_{CMS} < -2.96$ ) are presented in the left and right panel, respectively. The statistical uncertainty is obtained according to

$$\left(\frac{\sigma_{R_{pPb}}}{R_{pPb}}\right)^2 = \left(\frac{\sigma_{HF}}{HF}\right)^2 + \left(\frac{\sigma_{Ref}}{Ref}\right)^2 \quad (6.1)$$

$$\left(\frac{\sigma_{HF}}{HF}\right)^2 = \left(\frac{\sigma_{Incl}}{HF}\right)^2 = \left(\frac{\sigma_{Incl}}{Incl}\right)^2 \times \left(\frac{Incl}{HF}\right)^2 \quad (6.2)$$

where,  $\sigma_{R_{pPb}}/R_{pPb}$ ,  $\sigma_{HF}/HF$ ,  $\sigma_{Incl}/Incl$  and  $\sigma_{Ref}/Ref$  correspond to the relative statistical uncertainty on  $R_{pPb}$ , the signal (muons from heavy-flavour hadron decays), inclusive muons and the pp reference, respectively. One can see from Fig. 6.1 that,

- the statistical uncertainty on  $R_{pPb}$  is  $\sim 17\%$  at maximum both at forward and backward rapidity within the  $p_T$  region of interest;
- the measurements combine MSL and MSH triggered events i.e. MSL up to  $p_T = 7$  GeV/ $c$  and MSH for  $7 < p_T < 16$  GeV/ $c$ , resulting in the sharp structure at  $p_T = 7$  GeV/ $c$ ;
- the pp reference in the range  $12 < p_T < 16$  GeV/ $c$  is derived from the FONLL calculations at  $\sqrt{s_{NN}} = 5.02$  TeV. As a consequence, there is only a systematic uncertainty from FONLL and no statistical uncertainty in this region, resulting in the other sharp structure at  $p_T = 12$  GeV/ $c$ .

The (total) relative statistical uncertainty on  $Q_{pPb}$  in different event activity classes, is presented in Fig. 6.2. The results obtained at forward and backward rapidity are presented in the left and right panel, respectively. The values are smaller than  $\sim 18\%$  ( $22\%$ ) at forward (backward) rapidity in the range  $p_T < 12$  GeV/ $c$ , and reach  $\sim 20\%$  ( $30\%$ ) at higher  $p_T$ . The description of the event activity estimators is given in Fig. 3.30. Note that the statistical uncertainty is similar for all the estimators.

The systematic uncertainties on  $R_{pPb}$  are calculated via,

$$\left(\frac{\sigma_{R_{pPb}}}{R_{pPb}}\right)^2 = \left(\frac{\sigma_{Norm}}{Norm}\right)^2 + \left(\frac{\sigma_{HF}}{HF}\right)^2 + \left(\frac{\sigma_{Ref}}{Ref}\right)^2 + \left(\frac{\sigma_{Det}}{Det}\right)^2 + \left(\frac{\sigma_{Mis}}{Mis}\right)^2 \quad (6.3)$$

$$\left(\frac{\sigma_{HF}}{HF}\right)^2 = \left(\frac{\sigma_{Bkg}}{HF}\right)^2 = \left(\frac{\sigma_{Bkg}}{Bkg}\right)^2 \times \left(\frac{Bkg}{HF}\right)^2 \quad (6.4)$$

where,  $\sigma_{R_{pPb}}/R_{pPb}$ ,  $\sigma_{Norm}/Norm$ ,  $\sigma_{HF}/HF$ ,  $\sigma_{Bkg}/Bkg$ ,  $\sigma_{Ref}/Ref$ ,  $\sigma_{Det}/Det$  and  $\sigma_{Mis}/Mis$  denote the relative systematic uncertainty on  $R_{pPb}$ , the normalization

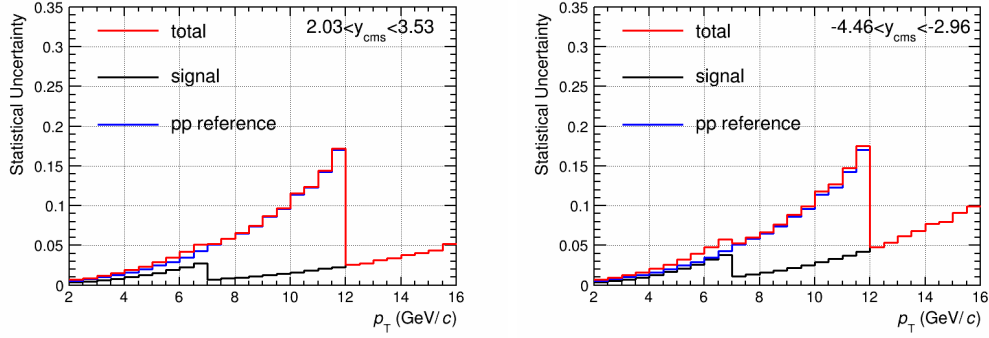


Figure 6.1: Left: relative statistical uncertainty on the nuclear modification factor of muons from heavy-flavour hadron decays, as a function of  $p_T$ , in multiplicity integrated p-Pb collisions at  $\sqrt{s_{NN}} = 5.02$  TeV at forward rapidity ( $2.03 < y_{CMS} < 3.53$ ). Right: same as the left panel but at backward rapidity ( $-4.46 < y_{CMS} < -2.96$ ).

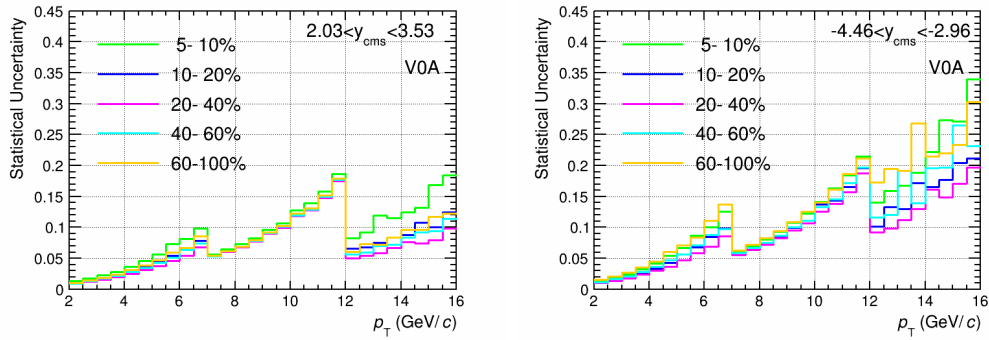


Figure 6.2: Same as Fig. 6.1 but within different event classes using V0A as the event estimator.

procedure (to be plotted separately), the signal, the background, the pp reference, the detector response and the mis-alignment, respectively. In multiplicity integrated collisions, the obtained results at forward and backward rapidity are shown in the left and right panels of Fig. 6.3, respectively. Different components correspond to the histograms with different colors in each panel. The total uncertainty, at forward rapidity, is dominated by the pp reference within the whole  $p_T$  region, while at backward rapidity it is dominated by the background subtraction in  $p_T \lesssim 3$  GeV/ $c$  and by the pp reference in  $p_T \gtrsim 3$  GeV/ $c$ . The maximum value is about 26% (30%) at forward (backward) rapidity.

Figure 6.4 shows the systematic uncertainty on  $Q_{pPb}$  at forward rapidity, for different event activity classes determined using V0A as the event activity estimator. The total systematic uncertainty is about  $\sim 30\%$  at maximum within the whole  $p_T$  region, and it is dominated by the uncertainty on background subtraction and pp reference. The corresponding results at backward rapidity are presented in Fig. 6.5.

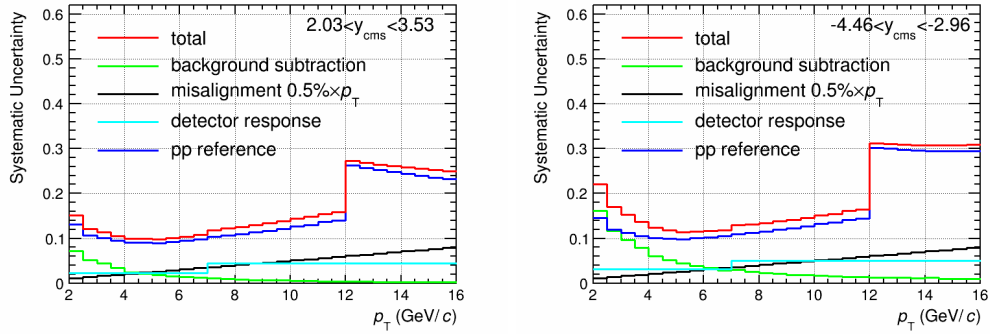


Figure 6.3: Left: relative systematic uncertainty on the nuclear modification factor of muons from heavy-flavour hadron decays, as a function of  $p_T$ , in multiplicity integrated p-Pb collisions at  $\sqrt{s_{NN}} = 5.02$  TeV at forward rapidity ( $2.03 < y_{CMS} < 3.53$ ); Right: same as the left panel but at backward rapidity ( $-4.46 < y_{CMS} < -2.96$ ).

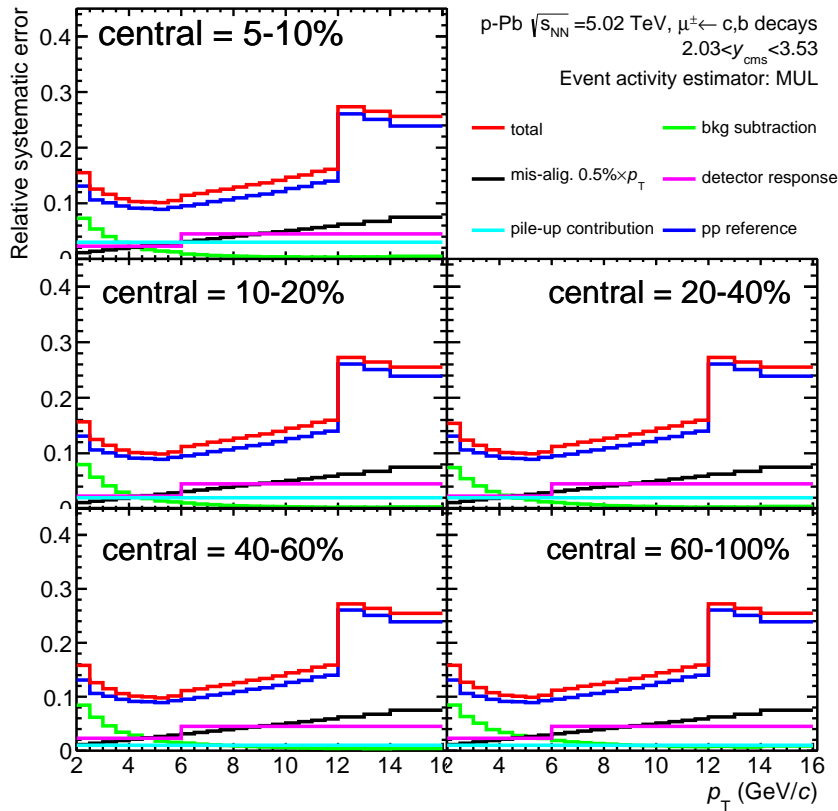


Figure 6.4: Same as the left panel of Fig. 6.3 but within different event activity classes using "mult." as the event activity estimator.

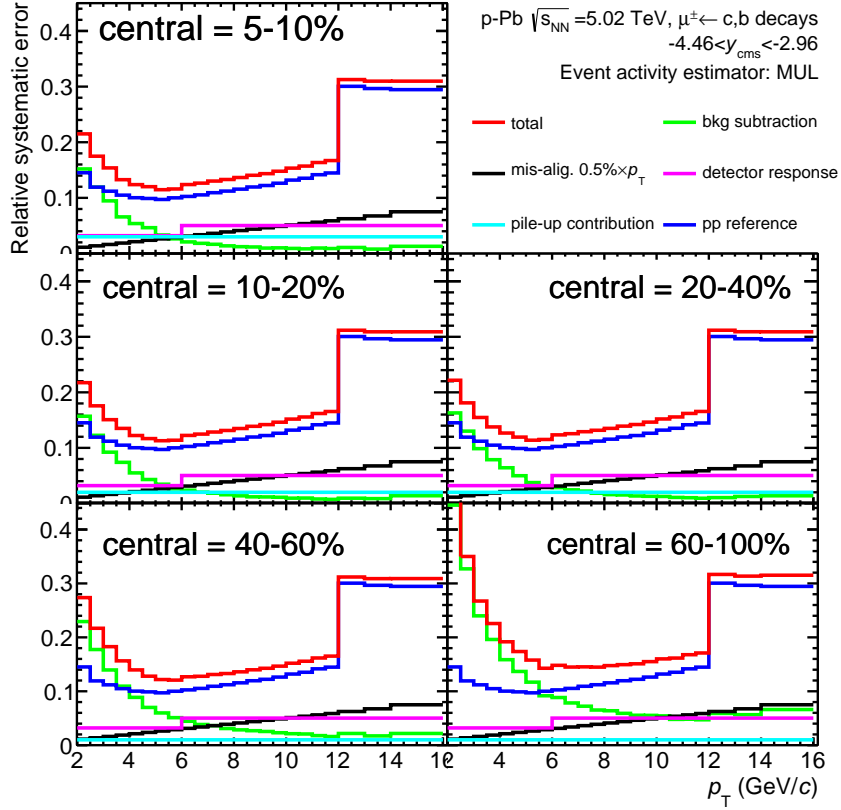


Figure 6.5: Same as the right panel of Fig. 6.3 but within different event activity classes using "mult." as the event activity estimator.

One can see that the total systematic uncertainty is about  $\sim 30\%$  at maximum within the whole  $p_T$  region, and it is dominated by the uncertainty on background subtraction and pp reference. The pp reference uncertainty dominates for  $p_T > 4$  GeV/ $c$ , while the uncertainty on background subtraction is more significant for  $p_T < 4$  GeV/ $c$ .

### Results versus event activity

Within a given  $p_T$  interval, the relative statistical uncertainty of  $Q_{pPb}$  can be obtained as,

$$\left(\frac{\sigma_{Q_{pPb}}}{Q_{pPb}}\right)^2 = \left(\frac{\sigma_{HF}}{HF}\right)^2 + \left(\frac{\sigma_{Ref}}{Ref}\right)^2 \quad (6.5)$$

$$\left(\frac{\sigma_{HF(Ref)}}{HF(Ref)}\right)^2 = \frac{1}{N_{Tot}} \quad N_{Tot} = \sum \left(\frac{N_i}{\sigma_i}\right)^2 \quad (6.6)$$

where,  $\sigma_{Q_{pPb}}/Q_{pPb}$ ,  $\sigma_{HF}/HF$ ,  $\sigma_{Ref}/Ref$  denote the relative statistical uncertainty on  $Q_{pPb}$ , the signal and the pp reference;  $N_i/\sigma_i$  indicates the inverse of the relative statistical uncertainty in each  $p_T$  bin  $i$ , and  $N_{Tot}$  is the total yield.

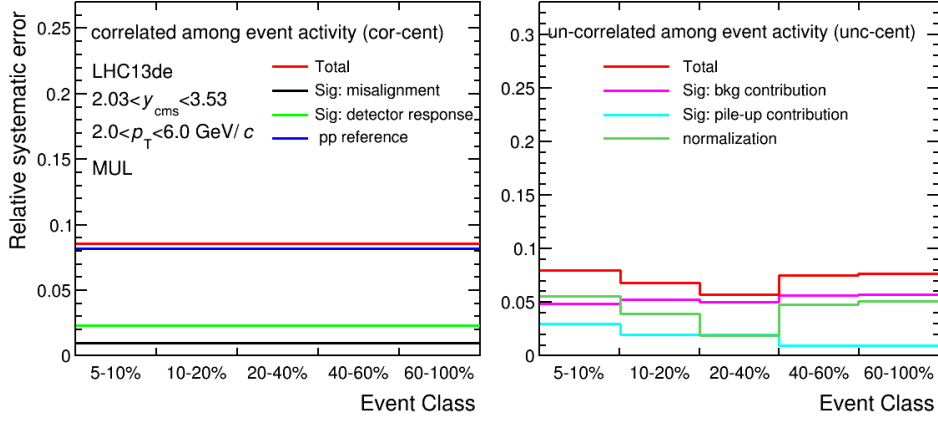


Figure 6.6: Relative systematic uncertainty on the nuclear modification factor of muons from heavy-flavour hadron decays at forward rapidity in  $2 < p_T < 6$  GeV/ $c$  as a function of event activity using "mult." as the event estimator, in p-Pb collisions at  $\sqrt{s_{NN}} = 5.02$  TeV. The left (right) panel shows the various components of the uncertainties that are correlated (un-correlated) among event activity classes.

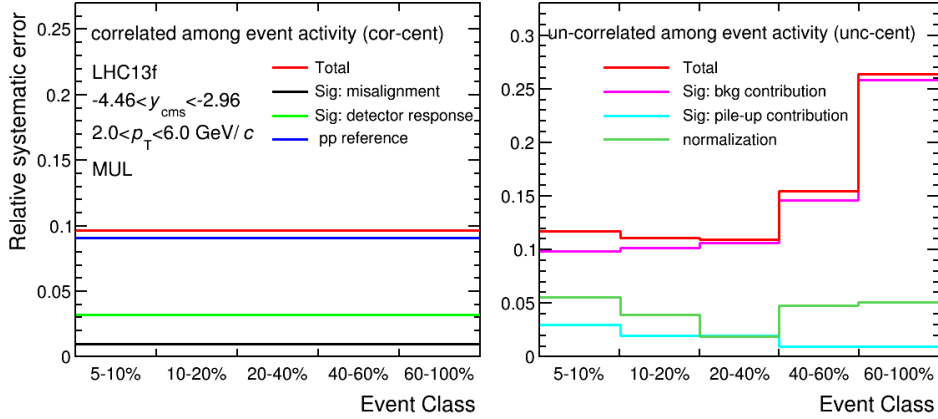


Figure 6.7: Same as Fig. 6.6 but at backward rapidity.

For the systematic uncertainty determination, one can find more detailed discussion in the appendix. Figure 6.6 shows the corresponding results at forward rapidity in  $2 < p_T < 6$  GeV/ $c$  as a function of event activity using "mult." as the event estimator. As discussed in Sec. 6.2.1, the uncertainties can be classified into two parts: the ones correlated (left) and un-correlated (right) among event activity intervals. One can see that the correlated components are dominated by the pp reference in all event activity bins. The total value is about 8% at maximum. The un-correlated part consists of the pile-up contribution, the background subtraction and the normalization procedure (mainly from  $\langle T_{pA} \rangle$ ), and the first two sources dominate. The total un-correlated uncertainty is about 8% at maximum within different event



activity bins.

The relative systematic uncertainty on  $Q_{pPb}$  at backward rapidity, is shown in Figure 6.7. The total value is about 10% at maximum. The total uncertainty of the un-correlated part is about 12% at maximum in central and semi-central collisions, while it is about 26% in the most peripheral collisions, and the dominant one is the one on background contribution.

### 6.2.2.2 Uncertainties on the Forward-to-Backward ratio

#### Results versus transverse momentum

The forward-to-backward ratio,  $R_{FB}$ , is defined as the ratio of the yield of muons from heavy-flavour hadron decays (i.e. signal) within a symmetric rapidity interval ( $2.96 < |y_{CMS}| < 3.53$ ) at forward and backward rapidity:

$$R_{FB}(2.96 < |y_{CMS}| < 3.53) = \frac{dN^{\text{forward}}/dp_T(2.96 < y_{CMS} < 3.53)}{dN^{\text{backward}}/dp_T(-3.53 < y_{CMS} < -2.96)}. \quad (6.7)$$

The statistical uncertainty on  $R_{FB}$  is calculated as

$$\left(\frac{\sigma_{R_{FB}}}{R_{FB}}\right)^2 = \left(\frac{\sigma_{HF}}{HF}\right)_{\text{forward}}^2 + \left(\frac{\sigma_{HF}}{HF}\right)_{\text{backward}}^2 \quad (6.8)$$

$$\left(\frac{\sigma_{HF}}{HF}\right)_{\text{forward(backward)}}^2 = \left(\frac{\sigma_{\text{Incl}}}{\text{Incl}} \times \frac{\text{Incl}}{HF}\right)_{\text{forward(backward)}}^2 \quad (6.9)$$

where,  $\sigma_{HF}/HF$  denotes the relative statistical uncertainty on the signal. The left panel of Fig. 6.8 shows the results in multiplicity integrated collisions. One can see that the statistical uncertainty on the signal component is similar within the two rapidity ranges, and the combined result is  $\sim 9\%$  at maximum in the measured  $p_T$  region. As for the nuclear modification factor, the forward-to-backward ratio is based on MSL and MSH triggered events for  $p_T < 7 \text{ GeV}/c$  and  $p_T > 7 \text{ GeV}/c$ , respectively. The right panel of Fig. 6.8 shows also the relative statistical uncertainty on  $Q_{FB}$  for different event activity classes. The activity estimator is V0A. The relative statistical uncertainty is about 24% (30%) at maximum in the range  $p_T < (>) 7 \text{ GeV}/c$ .

The systematic uncertainty on  $R_{FB}$  in multiplicity integrated collisions can be obtained by means of Eq. 6.3 but excluding: (1) the normalization component of 1.6% correlated among p-Pb and Pb-p configurations (see Sec. 6.2.1), that cancels; (2) the pp reference component, which does not enter in  $R_{FB}$ . The results are presented in Fig. 6.9. The systematic uncertainty on the background component dominates in the range  $p_T < 6 \text{ GeV}/c$ , as well as the one related to the mis-alignment and detector response at higher  $p_T$ . The total systematic uncertainty decreases with increasing  $p_T$  in the range  $2 < p_T < 7 \text{ GeV}/c$ , and it slightly increases with increasing  $p_T$  at higher  $p_T$ . It reaches a  $\sim 22\%$  at maximum at  $p_T = 2 \text{ GeV}/c$ .

The systematic uncertainty on  $Q_{FB}$  in different event activity intervals is presented in Fig. 6.10. As in multiplicity integrated collisions (Fig. 6.9), the total systematic uncertainty is dominated by the background component in the low  $p_T$

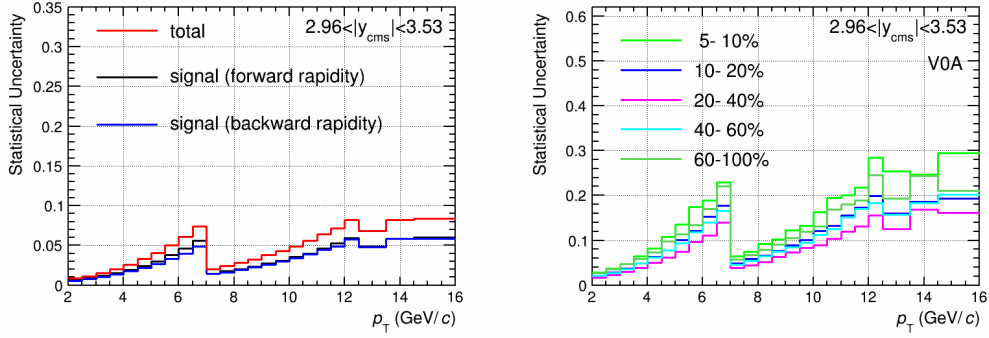


Figure 6.8: Left: relative statistical uncertainty on the forward-to-backward ratio of muons from heavy-flavour hadron decays, as a function of  $p_T$ , in multiplicity integrated p–Pb collisions at  $\sqrt{s_{NN}} = 5.02$  TeV. Right: same as left within different event activity classes using V0A as the event estimator.

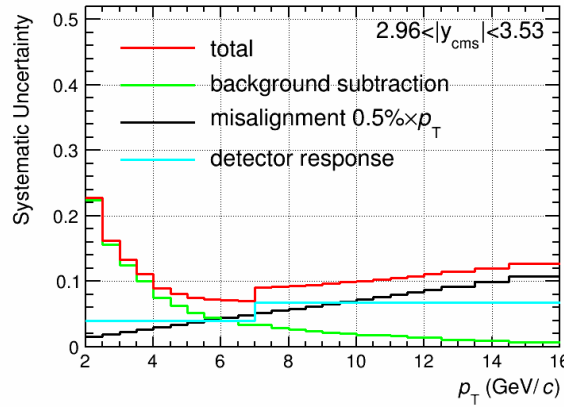


Figure 6.9: Relative systematic uncertainty on the forward-to-backward ratio of muons from heavy-flavour hadron decays, as a function of  $p_T$ , in multiplicity integrated p–Pb collisions at  $\sqrt{s_{NN}} = 5.02$  TeV.

region, and by the mis-alignment and detector response in the high  $p_T$  region. It is about 26% (46%) at maximum in the 5 – 10% (60 – 100%) event activity class. It is mainly induced by the background contribution which increases from central to peripheral collisions.

### Results versus event activity

By using Eq. 6.29 and 6.30 (shown in appendix) and after excluding the pp reference components, one can obtain the relative systematic uncertainty on  $Q_{FB}$  for  $2 < p_T < 6$  GeV/c, as shown in Fig. 6.11. The correlated and un-correlated components are presented in the left and right panel, respectively. The correlated part is dominated by the detector response ( $\sim 4\%$ ). The un-correlated part is

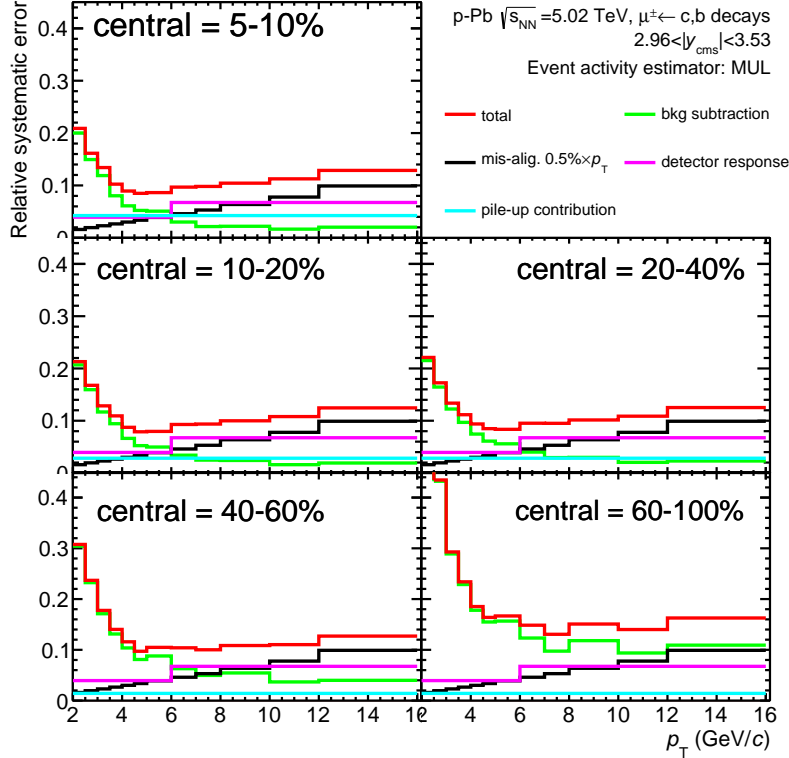


Figure 6.10: Same as Fig. 6.9 but within different event activity classes using "mult." as the event activity estimator.

dominated by the systematic uncertainty on background subtraction. It increases from central to peripheral collisions, resulting in a  $\sim 34\%$  systematic uncertainty at maximum in 60 – 100%.

### 6.3 Production Cross Section

Figure 6.12 shows the  $p_T$ -differential production cross section of muons from heavy-flavour hadron decays in multiplicity integrated p–Pb collisions at  $\sqrt{s_{NN}} = 5.02$  TeV. The measurements performed at forward and backward rapidity are presented with blue and green points, respectively. Vertical bars represent the statistical uncertainties and boxes the systematic uncertainties that include all components previously discussed, except the normalization uncertainty. The measurements are shown in the  $p_T$  interval  $2 < p_T < 16$  GeV/ $c$  using MSL-triggered events up to  $p_T = 7$  GeV/ $c$  and MSH-triggered events beyond. One can see that the cross section at forward rapidity is much larger (by about a factor 2) than that at backward rapidity, nearby  $p_T = 16$  GeV/ $c$ . It is difficult to go further in the interpretation due to the different rapidity coverage. However, a further cross check is implemented by means of FONLL predictions within these two rapidity intervals ( $2.03 < y_{CMS} < 3.53$  and  $-4.46 < y_{CMS} < -2.96$ ) at high  $p_T$ , where the cold nuclear matter effects are ex-

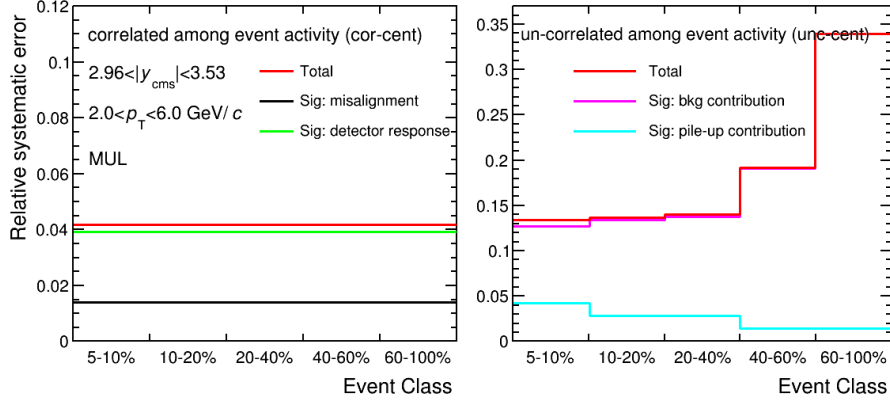


Figure 6.11: Relative systematic uncertainty on the forward-to-backward ratio of muons from heavy-flavour hadron decays, as a function of event activity using "mult." as the event estimator, in p-Pb collisions at  $\sqrt{s_{NN}} = 5.02$  TeV. The  $p_T$  range considered is  $2 < p_T < 6$  GeV/c. The left (right) panel shows the various components of the uncertainties that are correlated (un-correlated) among event activity classes.

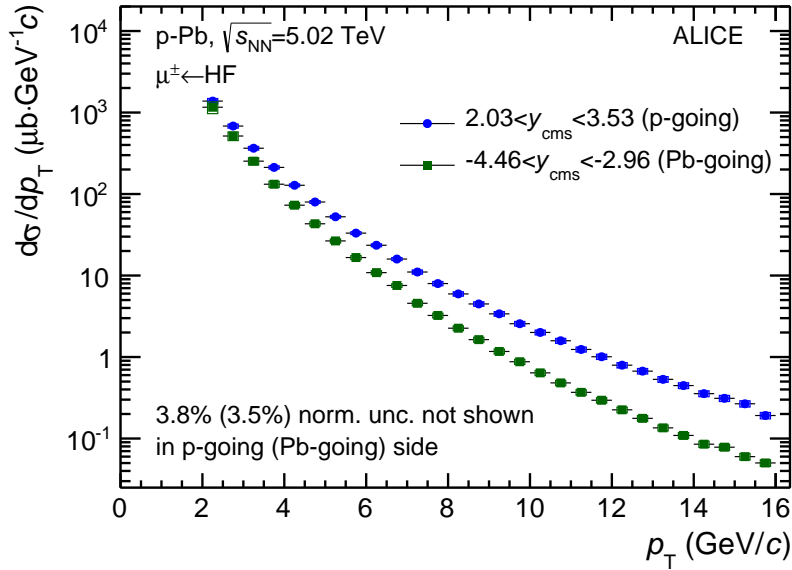


Figure 6.12:  $p_T$ -differential cross section of muons from heavy-flavour hadron decays in multiplicity integrated p-Pb collisions at  $\sqrt{s_{NN}} = 5.02$  TeV at forward ( $2.03 < y_{\text{CMS}} < 3.53$ , p-going, blue) and backward rapidity ( $-4.46 < y_{\text{CMS}} < -2.96$ , Pb-going, green). Statistical uncertainties (bars) and systematic uncertainties (boxes) are shown.



pected to be small. The deviation between them are similar to the ones shown in Fig. 6.12.

## 6.4 Nuclear Modification Factor

Cold nuclear matter effects have been studied by means of the nuclear modification factor. The  $p_T$  and event activity dependence are discussed in this section.

### 6.4.1 Measurements in Multiplicity Integrated Collisions

Figure 6.13 shows the  $p_T$ -differential  $R_{pPb}$  of muons from heavy-flavour hadron decays in p-Pb collisions at  $\sqrt{s_{NN}} = 5.02$  TeV at forward (upper panel) and backward rapidity (bottom panel) which probe the shadowing and anti-shadowing region, respectively (Fig. 3.1). Statistical uncertainties (bars), systematic uncertainties (open boxes) and normalization uncertainties (black box at  $R_{pPb} = 1$ ) are shown. One can see that  $R_{pPb}$  is compatible with unity within uncertainties over the whole  $p_T$  range. This evidences that CNM effects are small and that the strong suppression of the yields of muons from heavy-flavour hadrons decays observed in the 10% most central Pb-Pb collisions [159] results from final-state effects. At backward rapidity,  $R_{pPb}$  slightly larger than unity ( $\sim 2\sigma$ ) is observed at intermediate  $p_T$  ( $2 < p_T < 4$  GeV/c). It is however compatible with unity within systematic uncertainties.  $R_{pPb}$  is consistent with unity at higher  $p_T$ .

Figure 6.13 shows also comparisons to model predictions. Within uncertainties, the measurement performed at forward rapidity can be described by a pQCD calculation with the EPS09 [105] NLO parameterization of nuclear PDFs [286] (red curves). It is also well described by calculations including nuclear shadowing,  $k_T$  broadening and CNM energy loss [328] (green curve). This tends to demonstrate that the latter CNM effects are small, at least in the explored  $p_T$  range. At backward rapidity, the predictions based on EPS09 parameterization (red curves) can also reproduce the measurement within experimental and theoretical uncertainties. In addition, the data are compared to model predictions including incoherent multiple scattering effects of hard partons in the Pb nucleus both in initial-state and final-state interactions [329] (blue curves). The model reproduces within uncertainties the  $p_T$ -differential  $R_{pPb}$  over the whole  $p_T$  domain and, in particular, the Cronin-like enhancement in the intermediate  $p_T$  region.

The  $p_T$ -differential nuclear modification factor of muons from heavy-flavour hadron decays has been also studied in two sub-rapidity intervals. The results are shown in Fig. 6.14 at forward (upper panel) and backward rapidity (bottom panel). No significant variation of the nuclear modification factor is observed in the explored rapidity intervals within uncertainties.

### 6.4.2 Event Activity Dependence

The  $p_T$ -differential nuclear modification factor,  $Q_{pPb}$ , of muons from heavy-flavour hadron decays at forward rapidity, is shown in Fig. 6.15 in different event

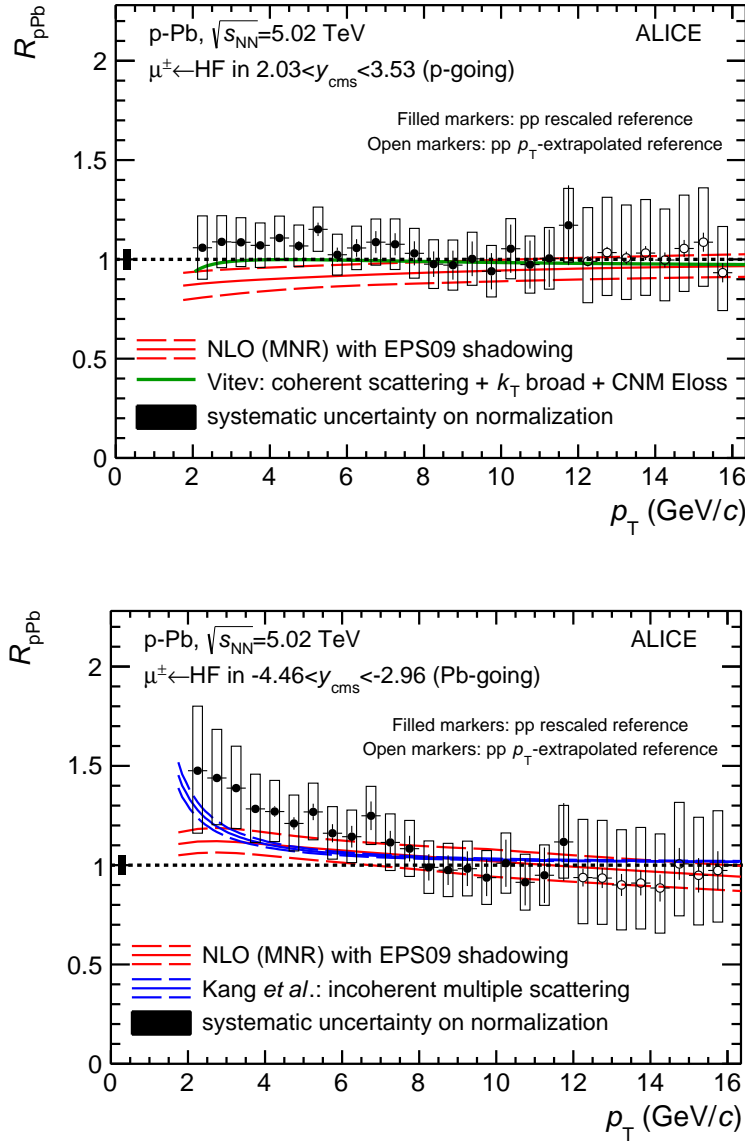


Figure 6.13:  $p_T$ -differential nuclear modification factor of muons from heavy-flavour hadron decays in p-Pb collisions at  $\sqrt{s_{NN}} = 5.02$  TeV at forward (upper) and backward rapidity (bottom). pQCD calculations with the EPS09 [105] NLO parameterization of nuclear PDFs [286], are shown as the red bands both at forward and backward rapidity. In addition, model calculations including nuclear shadowing,  $k_T$  broadening and CNM energy loss [328] are presented as green curves at forward rapidity. Another model calculation, considering the incoherent multiple scattering effects is displayed as blue bands at backward rapidity. Statistical uncertainties (bars), systematic uncertainties (open boxes) and normalization uncertainties (black box at  $R_{pPb} = 1$ ) are shown.

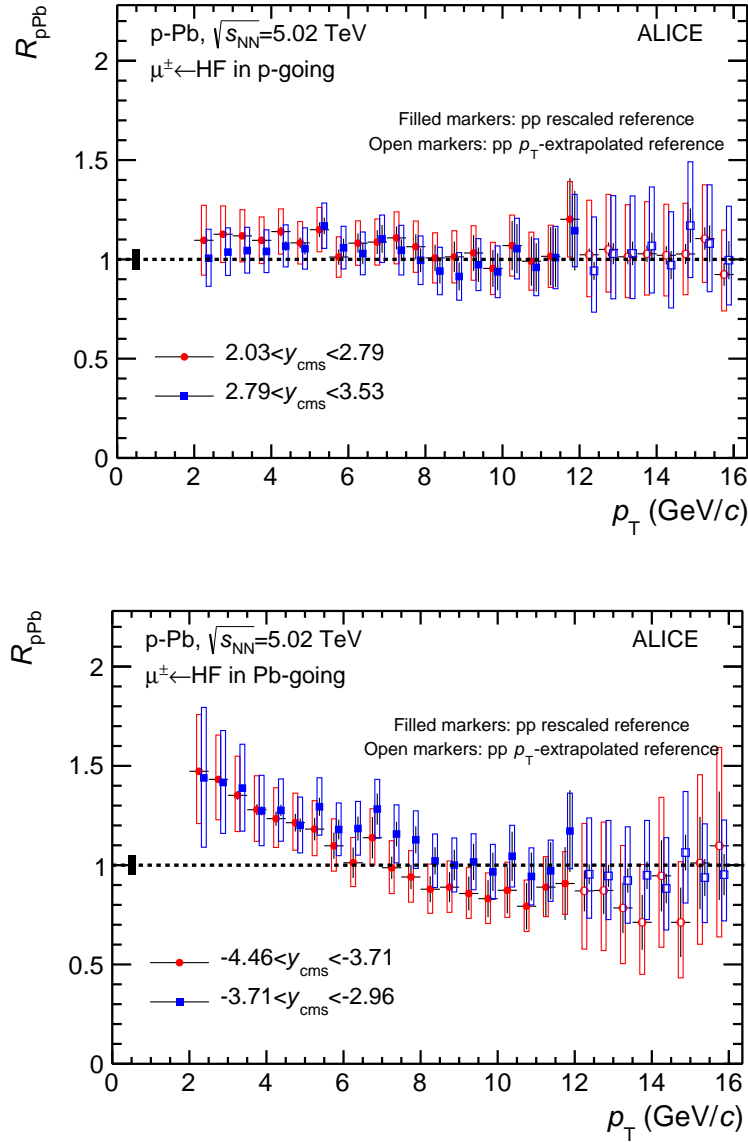


Figure 6.14:  $p_T$ -differential nuclear modification factor of muons from heavy-flavour hadron decays in p-Pb collisions at  $\sqrt{s_{NN}} = 5.02$  TeV in two sub-rapidity bins at forward (upper) and backward rapidity (bottom). Statistical uncertainties (bars), systematic uncertainties (open boxes) and normalization uncertainties same comment as in Fig. 6.13 are shown. For visibility, the points for the rapidity intervals  $2.79 < y_{CMS} < 3.53$  and  $-3.71 < y_{CMS} < -2.96$  are shifted horizontally.

activity classes. The employed estimator is "mult.". One can see that  $Q_{pPb}$  is consistent with unity within uncertainties in all event activity classes. Similar results have been obtained using V0A as event activity estimator (Fig. 6.25 in Appendix). Meanwhile, a similar behavior is also observed with CL1 (ZNA) except for the

activity class 60 – 100% where  $Q_{pPb}$  is below (above) unity over the whole  $p_T$  range (Fig. 6.26 and 6.27 in Appendix). Note that, (1) the different estimators are differently biased by fluctuations and jet-veto effect that affect the centrality estimation in p–Pb collisions [283]; (2) the  $p_T$  threshold between MSL- and MSH-triggered events is set at  $p_T = 6 \text{ GeV}/c$  due to the limited statistics within different event activity intervals.

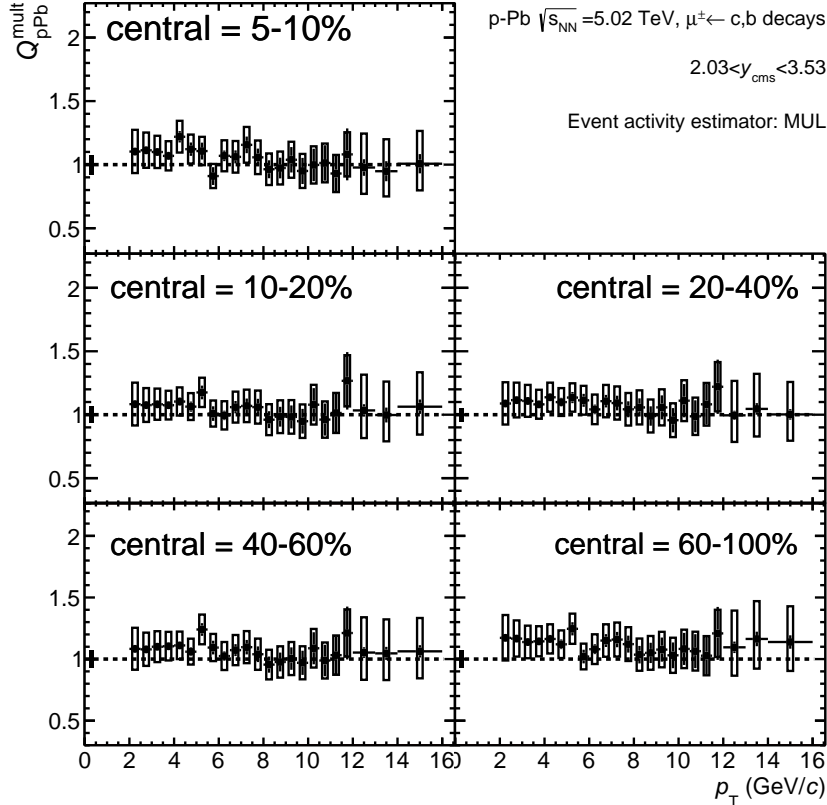


Figure 6.15:  $p_T$ -differential nuclear modification factor of muons from heavy-flavour hadron decays at forward rapidity within different event activity classes using "mult." as the event estimator, in p–Pb collisions at  $\sqrt{s_{NN}} = 5.02 \text{ TeV}$ . Statistical uncertainties (bars) and systematic uncertainties (open boxes) are shown.

Figure 6.16 presents the  $Q_{pPb}$  at backward rapidity with "mult." as the event activity estimator. One can see a visible enhancement ( $Q_{pPb} > 1$ ) in the range  $p_T \lesssim 8 \text{ GeV}/c$  in the most central event activity class (5 – 10%).  $Q_{pPb}$  becomes close to unity at higher  $p_T$ . The enhancement behavior tends to disappear toward peripheral collisions. A similar behavior is found when taking V0A and ZNC as event activity estimators (Fig. 6.28 and 6.30 in Appendix). Concerning the results based on CL1, they are also similar with the ones based on "mult." except for the most peripheral collisions, where  $Q_{pPb}$  is smaller than unity even considering the systematic uncertainties (Fig. 6.29 in Appendix).

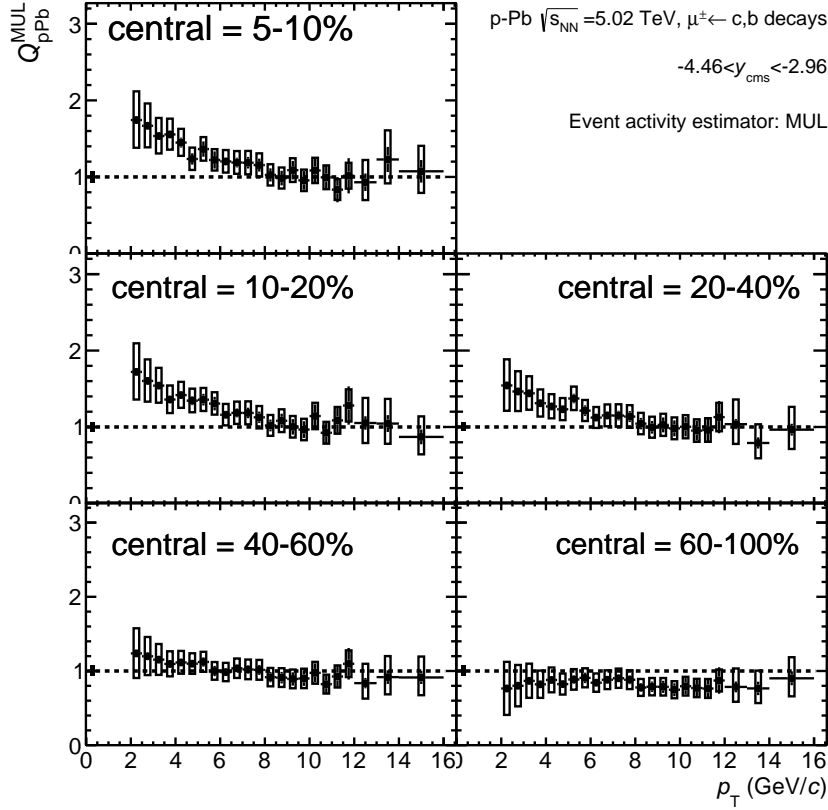


Figure 6.16: Same as Fig. 6.15 but at backward rapidity.

Figure 6.17 shows  $Q_{pPb}$  obtained at forward rapidity, within different  $p_T$  ranges,  $2 < p_T < 6$  GeV/ $c$  (left) and  $6 < p_T < 12$  GeV/ $c$  taking "mult." as the event activity estimator. In each panel, the open (filled) boxes indicate the systematic uncertainty un-correlated (correlated) among event activity bins. For  $2 < p_T < 6$  GeV/ $c$  (left),  $Q_{pPb}$  with "mult." is close to unity within uncertainties in all event activity intervals. For  $6 < p_T < 12$  GeV/ $c$  (right), similar results are found as in  $2 < p_T < 6$  GeV/ $c$ . Results based on different estimators can be found in Fig. 6.31 in appendix. See Ref. [330] for details.

Figure 6.18 shows  $Q_{pPb}$  obtained at backward rapidity, within different  $p_T$  ranges,  $2 < p_T < 6$  GeV/ $c$  (left) and  $6 < p_T < 12$  GeV/ $c$  taking "mult." as the event activity estimator. The open (filled) boxes indicate the systematic uncertainty un-correlated (correlated) among event activity bins. For  $2 < p_T < 6$  GeV/ $c$  (left),  $Q_{pPb}$  is larger than unity in central collisions at backward rapidity. Then, it is consistent with unity within uncertainties in semi-central and peripheral collisions. For  $6 < p_T < 12$  GeV/ $c$  (right),  $Q_{pPb}$  is close to unity within uncertainties excluding the results in 60 – 100%. Results based on different estimators can be found in Fig. 6.32 in appendix. See Ref. [330] for details.

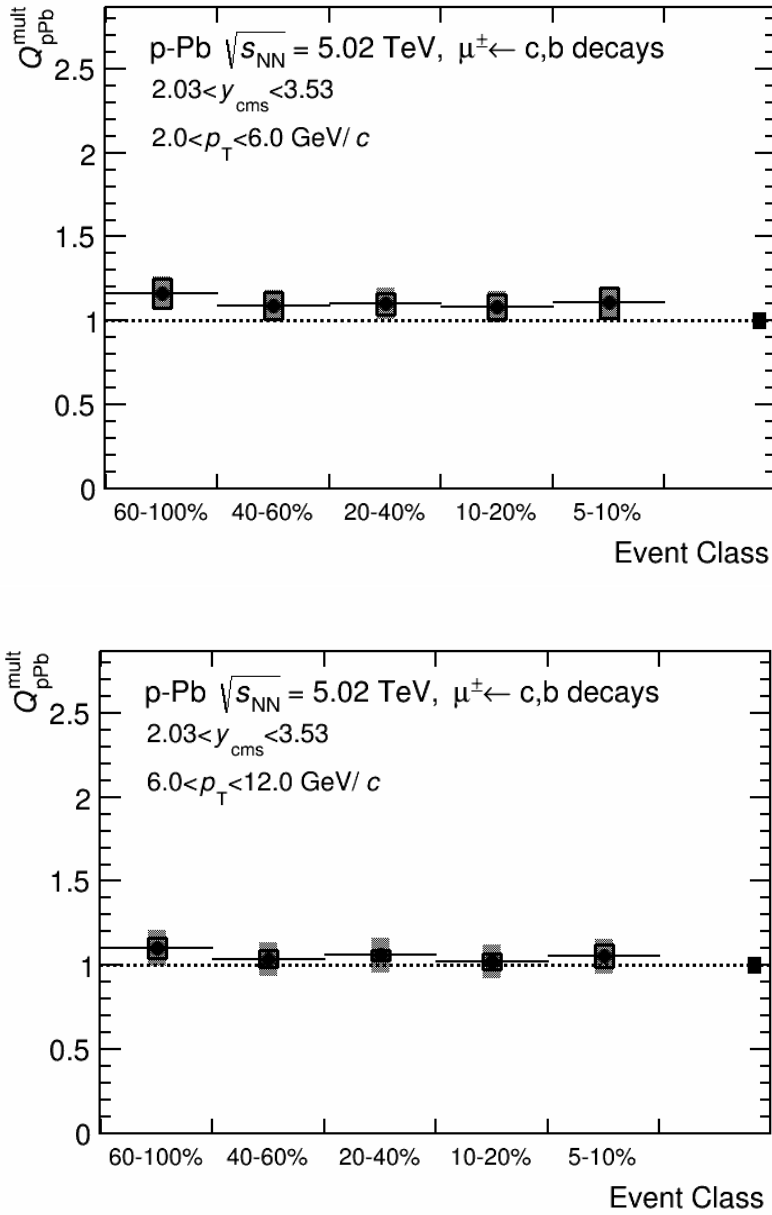


Figure 6.17: Nuclear modification factor of muons from heavy-flavour hadron decays at forward rapidity in  $2 < p_T < 6$  GeV/ $c$  (upper) and  $6 < p_T < 12$  GeV/ $c$  (bottom) as a function of event activity, in p-Pb collisions at  $\sqrt{s_{NN}} = 5.02$  TeV. The results are obtained with taking "mult." as the event activity estimator. In each panel, the open (full) boxes denote the uncertainties that are un-correlated (correlated) among event activity classes; the related statistical uncertainties shown as vertical bars are small and not visible.

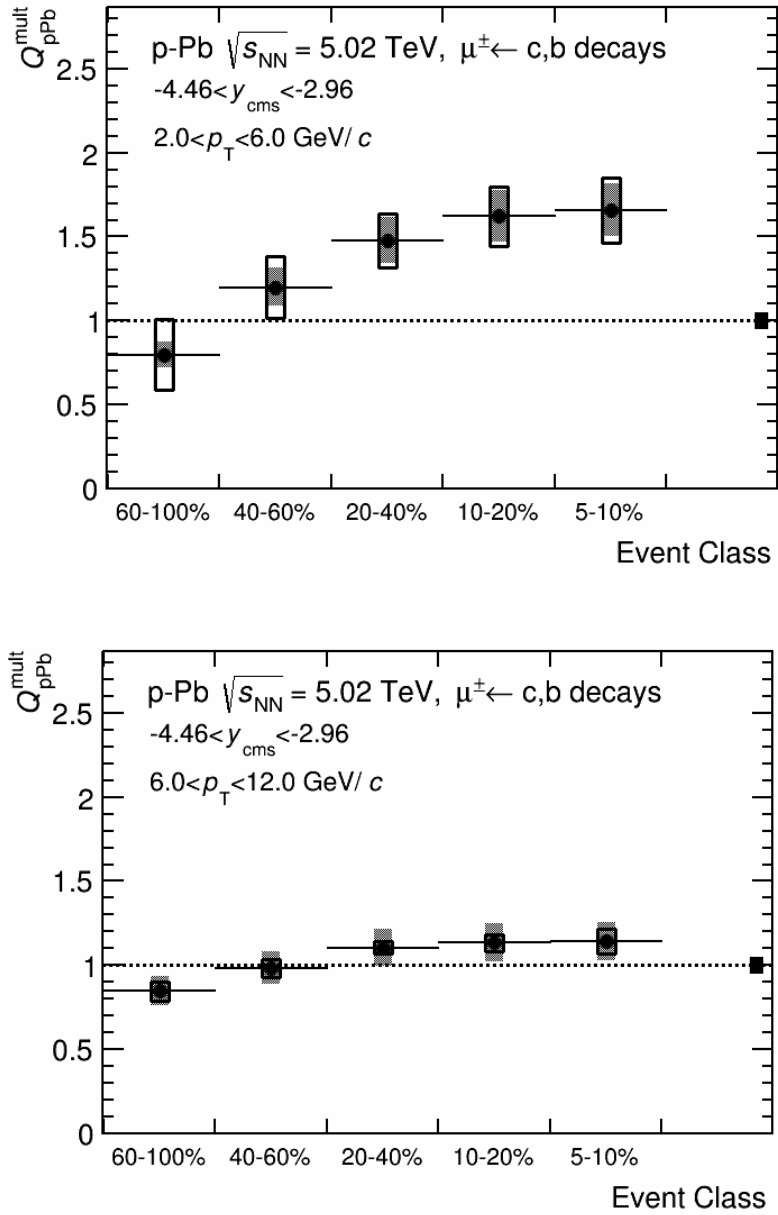


Figure 6.18: Same as Fig. 6.17 but at backward rapidity.

### 6.4.3 Discussion

#### 6.4.3.1 Measurements from PHENIX experiment at the RHIC

Figure 6.19 presents the  $p_T$  dependence of  $R_{dAu}$  of negative muons from heavy-flavour hadron decays at forward ( $1.4 < y_{CMS} < 2.0$ ) and backward rapidity ( $-2.0 < y_{CMS} < -1.4$ ), in different event activity classes (from upper to bottom: 60 – 88%, 0 – 20% and 0 – 100%, respectively) for d–Au collisions at  $\sqrt{s_{NN}} = 200$

GeV. One can see that the  $R_{dAu}$  shows no overall modification in the most peripheral collisions (upper) both at forward ( $1.4 < y_{CMS} < 2.0$ ) and backward rapidity ( $-2.0 < y_{CMS} < -1.4$ ), respectively, while a clear suppression at forward rapidity and an enhancement at backward rapidity are seen in the most central collisions (middle).

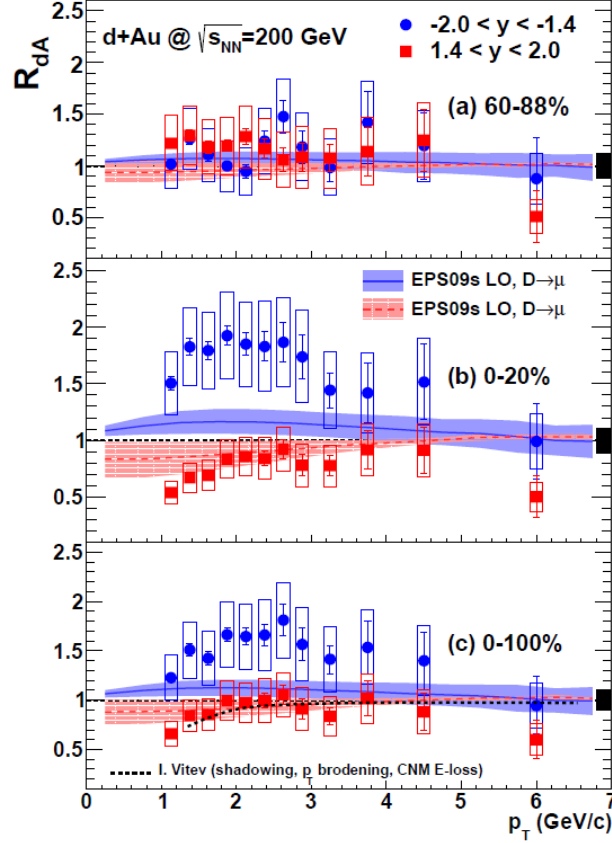


Figure 6.19: The nuclear modification factor  $R_{dAu}$ , for negatively charged heavy-flavor muons in d–Au collisions for the (a) 60 – 88%, (b) 0 – 20%, and (c) 0 – 100% most central collisions. The black boxes on the right side indicate the global scaling uncertainty. Vertical bars represent the statistical uncertainties, while the boxes denote the systematic uncertainties. The red dashed (blue solid) lines in each panel are calculations at forward (backward) rapidity based on the EPS09s nPDF set [331]. The theoretical calculation shown in (c) is for forward rapidity [328]. Figure taken from Ref. [182].

At forward rapidity, the suppression observed at low  $p_T$  could be due to the  $p_T$  broadening, combined with the gluon shadowing (or CGC) and/or partonic energy loss in cold nuclear matter [182]. At backward rapidity, the enhancement shows a  $p_T$  dependence consistent with  $p_T$  broadening and gluon anti-shadowing [182]. Note that,

- the shadowing bands shown in each plot are obtained from the EPS09 leading-order (LO) nuclear PDF (nPDF) set [331]; in peripheral collisions (upper), the

related predictions can describe well the measurements both at forward and backward rapidity. In central collisions (middle), the theoretical calculations describe, within uncertainty, the data at forward rapidity over the whole  $p_T$  range, while it does not reproduce the data at backward rapidity in the moderate  $p_T$  region [182]. The latter behavior suggests [182] the presence of other cold nuclear matter effects since the difference between forward and backward rapidity is significantly larger in the data than in the EPS09 nPDF calculation. Similar results are found in multiplicity integrated (0 – 100%) collisions (bottom);

- the dotted line in the bottom panel is the related prediction [328] for muons from D and B mesons decays at forward rapidity. This prediction, including cold nuclear matter effects such as shadowing, initial-state energy loss, and  $k_T$  broadening, is consistent with data at forward rapidity in the multiplicity integrated collisions [182].

In multiplicity integrated collisions (0 – 100%) at forward rapidity, the nuclear modification factor of heavy-flavour hadron decay muons measured by ALICE (Fig. 6.13) is similar to the one reported by the PHENIX Collaboration at RHIC (bottom panel of Fig. 6.19). When comparing the measurements of  $R_{pPb}$  from ALICE with the ones from PHENIX at forward/backward rapidity, one can realize that the corresponding rapidity coverages are different. As discussed in Ref. [329], the theoretical calculations include the incoherent multiple scattering effect at backward rapidity. The predictions can reproduce well the measurements both in ALICE and PHENIX. Meanwhile, a similar conclusion can be found with the model described in Ref. [332], suggesting a consistent behavior between the measurements in ALICE and PHENIX.

For the event activity dependence, the trends of the current measurements (Fig. 6.25 and 6.28) are also similar with the PHENIX data (upper and middle panels of Fig. 6.19) within the most central and peripheral collisions.

#### 6.4.3.2 Measurements in Pb–Pb collisions

Figure 6.20 shows the  $R_{AA}$  of muons from heavy-flavour hadron decays in the centrality classes 0 – 10% (red) measured at forward rapidity ( $2.5 < y < 4$ ) in Pb–Pb collisions at  $\sqrt{s_{NN}} = 2.76$  TeV, as well as  $R_{pPb}$  in multiplicity integrated p–Pb collisions at forward (black,  $2.03 < y_{CMS} < 3.53$ ) and backward rapidity (green,  $-4.46 < y_{CMS} < -2.96$ ), at  $\sqrt{s_{NN}} = 5.02$  TeV. A large suppression for  $R_{AA}$  is observed in the most central collisions, with a weak  $p_T$  dependence in the  $p_T$  range  $3 < p_T < 10$  GeV/ $c$ .  $R_{AA}$  measured at high  $p_T$  provide a hint for an increasing behavior toward larger  $p_T$ , which can be well described by the model including hot nuclear matter effects, the  $p_T$  shape of the parent parton and the fragmentation functions. When considering the same measurements in p–Pb collisions at  $\sqrt{s_{NN}} = 5.02$  TeV (black and green), which indicate the small cold nuclear effects are small, one can conclude that the suppression observed at high  $p_T$  in central Pb–Pb collisions is due to final state effects.

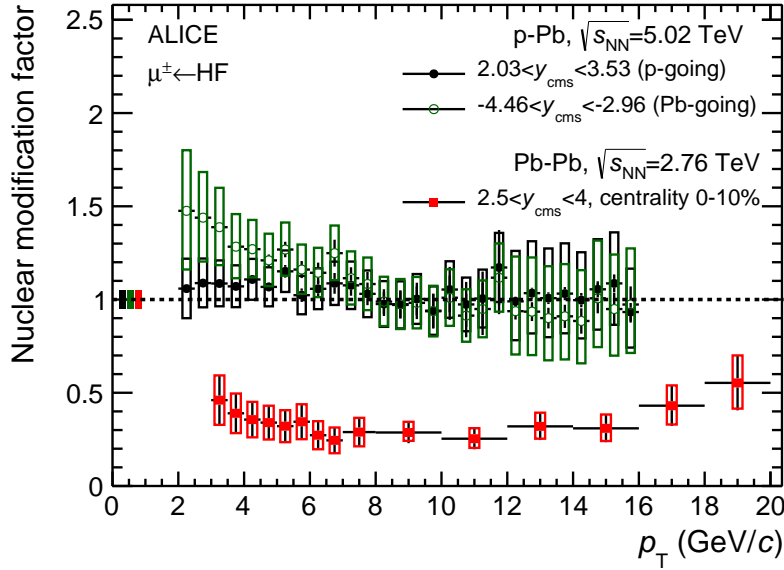


Figure 6.20: Nuclear modification factor of muons from heavy-flavour hadron decays in centrality classes 0–10% (red) measured at forward rapidity ( $2.5 < y < 4$ ) in Pb–Pb collisions at  $\sqrt{s_{NN}} = 2.76$  TeV, as well as the results in multiplicity integrated p–Pb collisions at forward (black,  $2.03 < y_{CMS} < 3.53$ ) and backward rapidity (green,  $-4.46 < y_{CMS} < -2.96$ ), at  $\sqrt{s_{NN}} = 5.02$  TeV.

A similar conclusion is found for D-mesons and electrons from heavy-flavour hadron decays at mid-rapidity [170, 173, 171].

## 6.5 Forward-To-Backward Ratio

### 6.5.1 Measurements in Multiplicity Integrated Collisions

Cold nuclear matter effects can also be studied by means of the forward-to-backward ratio,  $R_{FB}$  (Eq. 6.7). The main advantage of using such a ratio is that the pp reference and the nuclear overlap function cancel out. The drawback of this approach is the limited statistics, because the common  $y_{cms}$  interval covered at both forward and backward rapidity is small ( $\Delta y = 0.57$ ).

Figure 6.21 displays the  $p_T$ -differential cross section of muons from heavy-flavour hadron decays in multiplicity integrated p–Pb collisions at  $\sqrt{s_{NN}} = 5.02$  TeV. One can see that the yields at backward rapidity are larger than that at forward rapidity in the low  $p_T$  region, whereas they are compatible at high  $p_T$ .

Based on the results shown in Fig. 6.21,  $R_{FB}$  is presented in Fig. 6.22. It is smaller than unity in the range  $2 < p_T < 4$  GeV/ $c$  and close to unity at higher  $p_T$ . This is well reproduced by a pQCD calculation including the EPS09 [105] NLO parameterization of nuclear PDFs [286] in the full explored  $p_T$  range.

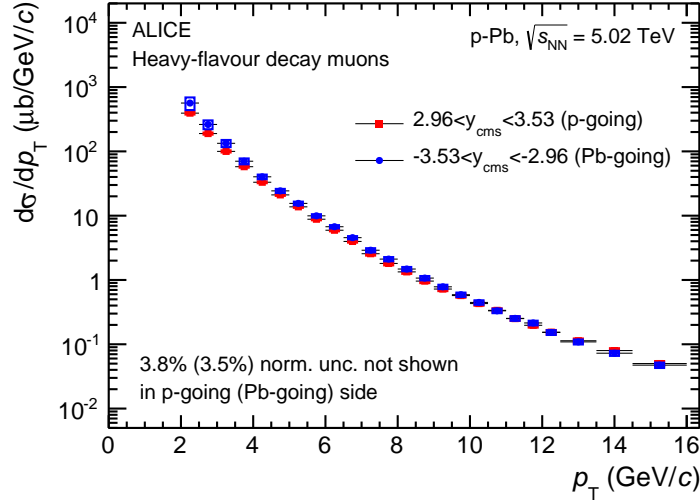


Figure 6.21:  $p_T$ -differential production cross sections of muons from heavy-flavour hadron decays measured at forward ( $2.96 < y_{\text{CMS}} < 3.53$ , red) and backward rapidity ( $-3.53 < y_{\text{CMS}} < -2.96$ , blue) as a function of  $p_T$ , in p-Pb collisions at  $\sqrt{s_{\text{NN}}} = 5.02$  TeV. The normalization procedure is the same as Fig. 6.12.

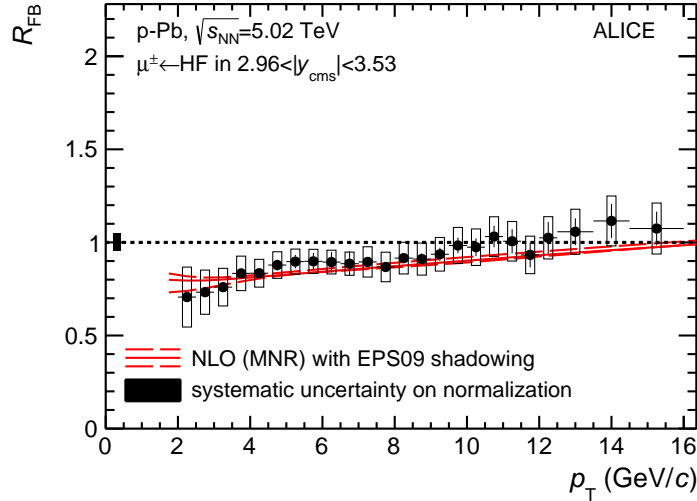


Figure 6.22: Forward-to-backward ratio of muons from heavy-flavour hadron decays. pQCD calculations with the EPS09 [105] NLO parameterization of nuclear PDFs [286], are shown as the red curves. Statistical uncertainties (bars), systematic uncertainties (open boxes) and normalization uncertainties (black box at  $R_{\text{FB}} = 1$ ) are shown.

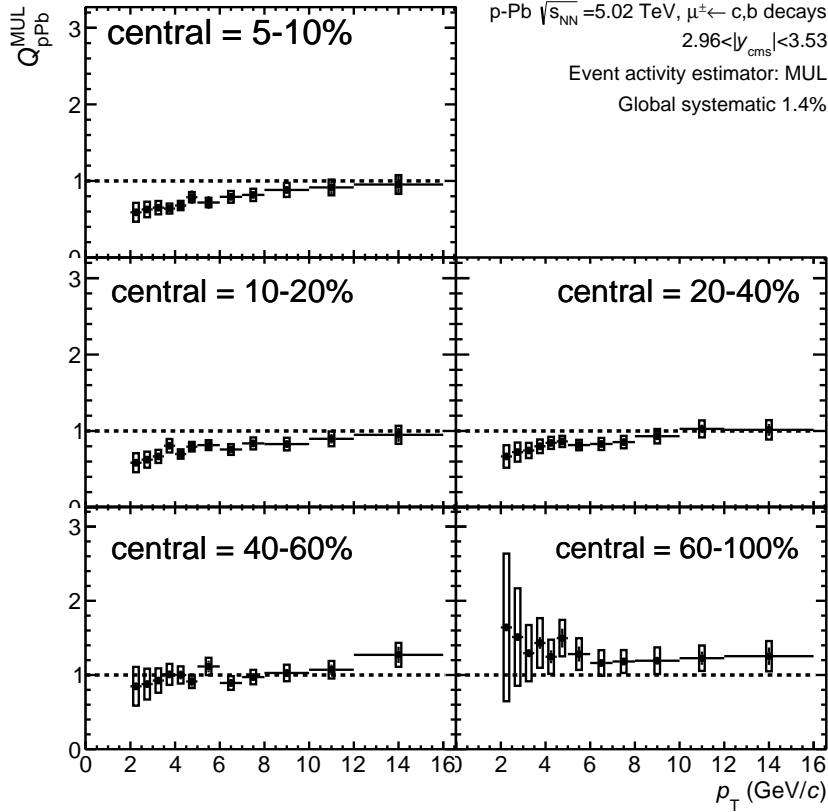


Figure 6.23: Same as Fig. 6.22 but within different event activity classes using "mult." as the event estimator.

## 6.5.2 Event Activity Dependence

The forward-to-backward ratio within event activity bins,  $Q_{FB}$ , is shown in Fig. 6.23 using "mult." as the event activity estimator.  $Q_{FB}$  is below unity in the low  $p_T$  region in central and semi-central collisions, and tends to increase towards peripheral collisions. Moreover,  $Q_{FB}$  is close to unity at higher  $p_T$  and it is larger than unity in the 60 – 100% event class for  $p_T \gtrsim 4.5$  GeV/c. Similar results are obtained using CL1 and ZN as the event estimators (Fig. 6.33 and 6.34 in Appendix).

Figure 6.24 presents the  $Q_{FB}$  of muons from heavy-flavour hadron decays in  $2 < p_T < 6$  GeV/c (left) and  $6 < p_T < 12$  GeV/c (upper) taking "mult." as the event activity estimator, as a function of the event activity class. For  $2 < p_T < 6$  GeV/c (bottom),  $Q_{FB}$  is smaller than unity within uncertainties in central and semi-central collisions. For  $6 < p_T < 12$  GeV/c (bottom panel), same trends in  $2 < p_T < 6$  GeV/c, but its deviation with respect to unity is less pronounced. Results based on different estimators are presented in Fig. 6.35 in appendix. See Ref. [330] for details.

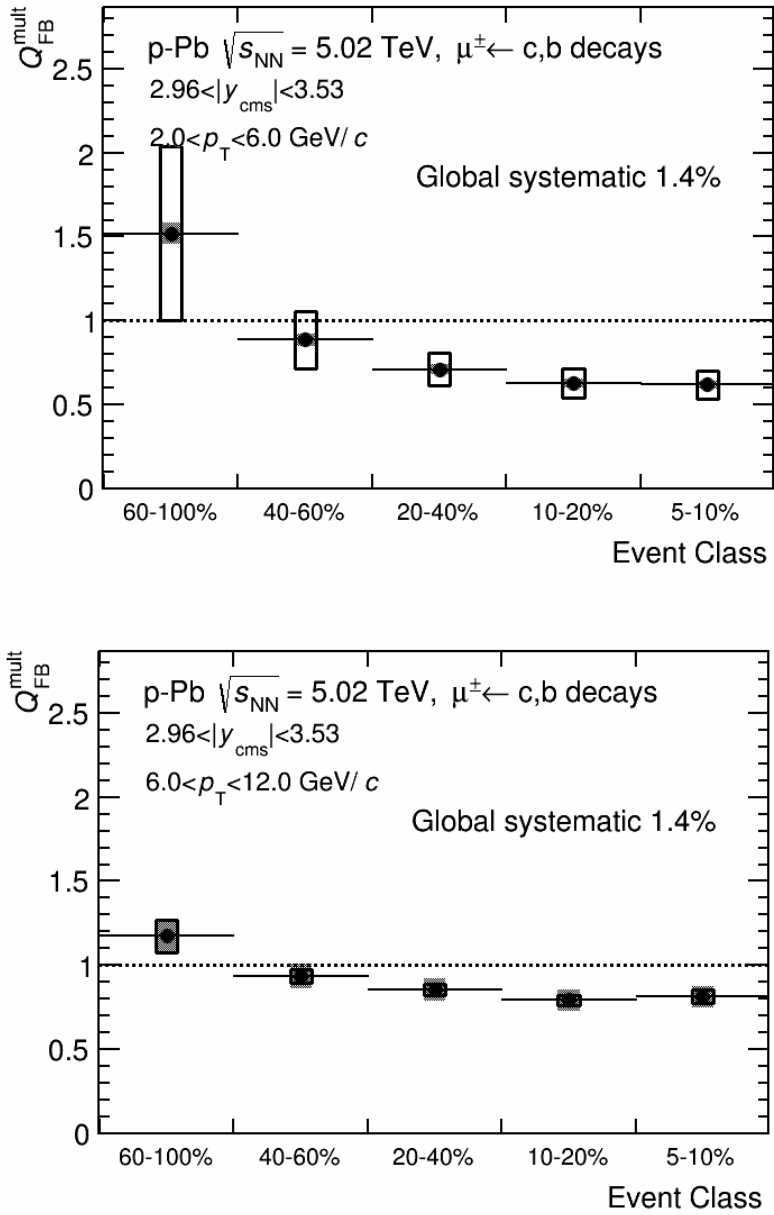


Figure 6.24: Forward-to-backward ratio of muons from heavy-flavour hadron decays in  $2 < p_T < 6$  GeV/ $c$  (upper) and  $6 < p_T < 12$  GeV/ $c$  (bottom) as a function of the collision event activity, in p-Pb collisions at  $\sqrt{s_{NN}} = 5.02$  TeV. The results are obtained with taking "mult." as the event activity estimator. The open (full) boxes denote the uncertainties that are un-correlated (correlated) among event activity classes; the related statistical uncertainties shown as vertical bars are small and not visible.



# Conclusions

---

In the first chapter of this thesis, a general discussion concerning the properties of Quark-Gluon Plasma and QCD phase transitions is presented. That concerns the measurements from SPS, RHIC and LHC energies together with model predictions. The motivation to study heavy-flavour production was mentioned as well. The chapter 2 was mainly devoted to the ALICE detector at CERN-LHC. Since the data used in this thesis were collected with the muon spectrometer, which is located at forward region ( $-4 < \eta_{\text{LAB}} < -2.5$ ), an emphasis was placed on it. Then, the offline framework (AliRoot) and the upgrade of the muon spectrometer in the upcoming run 2 (2015-2018) that should be operated after the second long shutdown, was introduced.

In order to quantify the cold nuclear matter effects on muons from heavy-flavour hadron decays, the nuclear modification factor and forward-to-backward ratio were measured with the data recorded during the 2013 p-Pb runs with the Muon spectrometer covering the forward rapidity region (p-going, p-Pb collisions), and backward rapidity (Pb-going, Pb-p collisions). The subsequent three chapters (chapter 3, 4, and 5) were dedicated to analyses details. Chapter 3 presented the information about the raw data and the acceptance  $\times$  efficiency correction. The former one included the muon selection criteria and the event activity classification. In chapter 4 the subtraction of background (muons from primary pion and kaon decays) both at forward ( $2.03 < y_{\text{CMS}} < 3.53$ ) and backward rapidity ( $-4.46 < y_{\text{CMS}} < -2.96$ ) was discussed. Within these two regions, the obtained results in multiplicity integrated collisions were detailed, as well as the ones as a function of event activity. Chapter 5 presented the pp reference, which was estimated by taking as input the pp cross section measured at  $\sqrt{s} = 7$  and 2.76 TeV and scaled to 5.02 TeV based on a pQCD-driven approach.

Chapter 6 summarized the measurements. The analyse procedures together with the related systematic uncertainties, were discussed. Concerning the measurements, the  $p_{\text{T}}$ -differential production cross sections of muons from heavy-flavour hadron decays were obtained in  $2 < p_{\text{T}} < 16$  GeV/ $c$  both at forward ( $2.03 < y_{\text{CMS}} < 3.53$ ) and backward rapidity ( $-4.46 < y_{\text{CMS}} < -2.96$ ) in multiplicity integrated collisions. The related nuclear modification factor  $R_{\text{pPb}}$  was found to be compatible with binary-scaled pp reference, i.e. close to unity, at forward, while a slight deviation from this scaling was observed in the intermediate  $p_{\text{T}}$  region  $2 < p_{\text{T}} < 4$  GeV/ $c$  at backward rapidity. Moreover, these trends were reflected in the forward-to-backward ratio  $R_{\text{FB}}$ . The measurements in multiplicity integrated collisions were in fair agreement with various theoretical calculations including cold nuclear matter effects based on a nuclear shadowing scenario or including other effects like  $k_{\text{T}}$  broadening and energy loss at forward rapidity. A model based on incoherent scattering effects reproduced the data at backward rapidity. The results confirmed that



the strong suppression of high  $p_T$  heavy-flavour hadron decay muons in central Pb–Pb collisions was due to the final-state effects induced by the hot and dense nuclear medium. Further measurements in different classes of event activity dependence were discussed. The measured  $Q_{pPb}$  showed small deviations with respect to unity within uncertainties from central to peripheral collisions at forward rapidity.  $Q_{pPb}$  measured at backward rapidity is clearly larger than unity at low  $p_T$  ( $p_T \lesssim 8 \text{ GeV}/c$ ) in the 5–10% event activity class, then it tends to unity toward peripheral collisions. These results were confirmed by the measurement of the forward-to-backward ratio  $Q_{FB}$ .

At final, I would like to share the following words that I like best.

**Don't be sorry, be better!**

— Sherlock Holmes

# Bibliography

- [1] A. Einstein. Zur Elektrodynamik bewegter Körper. *Annalen der Physik*, 17:891, 1905. (Cited on page 1.)
- [2] PDG. Review of Particles Physics. *Chinese Physics C*, 38(9), 2014. (Cited on pages xxxv, xxxviii, 1, 3, 10, 23, 29, 34, 36, 37, 114 and 177.)
- [3] The ATLAS and CMS Collaboration. Combined Measurement of the Higgs Boson Mass in pp Collisions at  $\sqrt{s} = 7$  and 8 TeV with the ATLAS and CMS Experiments. *arXiv:1503.07589*, 2015. (Cited on pages xxxiv and 2.)
- [4] Standard Model. [http://en.wikipedia.org/wiki/Standard\\_Model](http://en.wikipedia.org/wiki/Standard_Model), 2013. (Cited on pages xxxiv and 2.)
- [5] J. Goldstone, A. Salam and S. Weinberg. Broken Symmetries. *Phys. Rev.*, 127:965–970, 1962. (Cited on page 3.)
- [6] K. G. Wilson. Confinement of quarks. *Phys. Rev. D*, 10:2445–2459, 1974. (Cited on page 3.)
- [7] F. Karsch. Lattice Results on QCD Thermodynamics. *Nucl. Phys. A*, 698:199–208, 2002. (Cited on pages xxxv, 3, 4 and 5.)
- [8] F. Karsch. Lattice Simulations of the Thermodynamics of Strongly Interacting Elementary Particles and the Exploration of New Phases of Matter in Relativistic Heavy Ion Collisions. *J. Phys. Conf. Ser.*, 46:122–131, 2006. (Cited on pages xxxv, 3 and 4.)
- [9] Z. Fodor. Lattice QCD Results at Finite Temperature and Density. *Nucl. Phys. A*, 715:319–328, 2002. (Cited on pages xxxv, 3 and 4.)
- [10] Y. Aoki *et al.* The QCD transition temperature: results with physical masses in the continuum limit. *Phys. Lett. B*, 643:46–54, 2006. (Cited on page 3.)
- [11] S. Borsanyi *et al.* The QCD equation of state with dynamical quarks. *JHEP*, 1101:077, 2010. (Cited on page 3.)
- [12] S. Borsanyi *et al.* Continuum EoS for QCD with  $N_f = 2 + 1$  flavors. *PoS(LATTICE 2013)*, 155, 2013. (Cited on page 3.)
- [13] A. Bazavov *et al* [HotQCD Collaboration]. Chiral and deconfinement aspects of the QCD transition. *Phys. Rev. D*, 85:054503, 2012. (Cited on page 3.)
- [14] G. Dissertori and G. P. Salam. Quantum Chromodynamics. *J. Phys. G*, 37(7A):114, 07 2010. (Cited on page 3.)



- [15] J. C. Collins, D. E. Soper and G. F. Sterman. Heavy Particle Production in High-Energy Hadron Collisions. *Nucl. Phys. B*, 263:37, 1986. (Cited on pages 3, 15 and 177.)
- [16] A. Andronic, P. B. Munzinger and J. Stachel. Hadron production in central nucleus-nucleus collisions at chemical freeze-out. *Nucl. Phys. A*, 772:167–199, 2006. (Cited on pages 3 and 8.)
- [17] A. Andronic, P. B. Munzinger and J. Stachel. Thermal hadron production in relativistic nuclear collisions: the hadron mass spectrum, the horn, and the QCD phase transition. *Phys. Lett. B*, 673:142–145, 2009. (Cited on pages 3 and 8.)
- [18] A. Andronic, P. B. Munzinger and J. Stachel. The horn, the hadron mass spectrum and the QCD phase diagram—the statistical model of hadron production in central nucleus-nucleus collisions. *arXiv:nucl-th/0911.4931*, 2009. (Cited on pages 3 and 8.)
- [19] M. Gyulassy and L. McLerran. New Forms of QCD Matter Discovered at RHIC. *Nucl. Phys. A*, 750:30–63, 2005. (Cited on pages 4, 12 and 18.)
- [20] X. D. Ji. A Modern Introduction to Nuclear Physics: Quarks, Nuclei, and the Cosmos, <http://www.physics.umd.edu/courses/Phys741/xji>, 2012. (Cited on page 4.)
- [21] P. Jacobs and X. N. Wang. Matter in extremis: ultrarelativistic nuclear collisions at RHIC. *Nucl. Phys. A*, 54:443–534, 2005. (Cited on pages 4 and 12.)
- [22] B. J. Schaefer and M. Wagner. On the QCD phase structure from effective models. *Progress in Particle and Nuclear Physics*, 62:381, 2009. (Cited on pages xxxv, 4 and 6.)
- [23] S. Hands. The Phase Diagram of QCD. *Contemp. Phys.*, 42:209–225, 2001. (Cited on page 5.)
- [24] A. Bazavov *et al.* Strangeness at high temperatures: from hadrons to quarks. *Phys. Rev. Lett*, 111:082301, 2013. (Cited on page 5.)
- [25] O. Kaczmarek *et al.* The phase boundary for the chiral transition in (2+1)-flavor QCD at small values of the chemical potential. *Phys. Rev. D*, 83:014504, 2011. (Cited on page 5.)
- [26] A. Bazavov [HotQCD Collaboration]. The chiral and deconfinement aspects of the QCD transition. *Phys. Rev. D*, 85:054503, 2012. (Cited on page 5.)
- [27] S. Mujherjee. Overview of Lattice QCD Calculations on QCD Thermodynamics, LQCD workshop in ORNL, 2013, [https://www.olcf.ornl.gov/wp-content/uploads/2013/02/Swagato\\_LQCD.pdf](https://www.olcf.ornl.gov/wp-content/uploads/2013/02/Swagato_LQCD.pdf). (Cited on page 5.)



- [28] H. T. Ding. Recent lattice QCD results and phase diagram of strongly interacting matter,  
<https://indico.cern.ch/event/219436/session/3/contribution/717/material/slides/0.pdf>. (Cited on page 5.)
- [29] M. G. Alford, K. Rajagopal, T. Schaefer and A. Schmitt. Color superconductivity in dense quark matter. *Rev. Mod. Phys.*, 80:1455–1515, 2008. (Cited on page 5.)
- [30] A. Andronic *et al.* Hadron Production in Ultra-relativistic Nuclear Collisions: Quarkyonic Matter and a Triple Point in the Phase Diagram of QCD. *Nucl. Phys. A*, 837:65–86, 2010. (Cited on page 5.)
- [31] F. Karsch. <http://indico.vecc.gov.in/indico/conferenceOtherViews.py?view=nicecompact&confId=29>, 2015. (Cited on page 6.)
- [32] M. Płoskoó. Selected Topics from the Experiments with High–Energy Heavy–Ion collisions: Hot QCD in the laboratory,  
DOI 10.10007/978-3-319-12238-0\_3. (Cited on page 6.)
- [33] E. V. Shuryak. Quantum chromodynamics and the theory of superdense matter. *Physics Reports*, 61:71–158, 1980. (Cited on page 6.)
- [34] Y. J. Chen. PhD Thesis,  
<http://academiccommons.columbia.edu/catalog/ac%3A159130>. (Cited on pages xxxv, 7 and 113.)
- [35] M. L. Miller *et al.* Glauber Modeling in High Energy Nuclear Collisions. *Ann. Rev. Nucl. Part. Sci.*, 57:205–243, 2007. (Cited on pages xli, xlvi, lvii, 7, 41, 92, 93, 94, 147, 155, 156 and 157.)
- [36] J. Cleymans, H. Oeschler, K. Redlich and S. Wheaton. Comparison of chemical freeze-out criteria in heavy-ion collisions. *Phys. Rev. C*, 73:034905, 2006. (Cited on pages 7, 8 and 9.)
- [37] J. Cleymans and K. Redlich. Unified Description of Freeze-Out Parameters in Relativistic Heavy Ion Collisions. *Phys. Rev. Lett.*, 81:5284–5286, 1998. (Cited on page 7.)
- [38] U. Heinz. Concepts of heavy–ion physics. *arXiv:hep-ph/0407360*, 2004. (Cited on pages xxxv, xxxvi, 7, 8, 10, 20 and 21.)
- [39] C. B. Xu. Thermal Statistics, Hydrodynamics and Thermalization.  
<http://hepg.ustc.edu.cn/Seminar/xzb09>. (Cited on pages xxxv, 7, 9 and 10.)
- [40] W. Broniowski and W. Florkowski. Description of the RHIC  $p_{\perp}$  Spectra in a Thermal Model with Expansion. *Phys. Rev. Lett.*, 87:272302, 2001. (Cited on page 7.)



- [41] B. Müller, J. Schukraft and B. Wyslouch. First Results from Pb–Pb collisions at the LHC. *arXiv:nucl-ex/1204.1224*, 2012. (Cited on pages lvii, 8 and 17.)
- [42] X. M. Zhang. PhD Thesis,  
<https://tel.archives-ouvertes.fr/tel-00786269>  
<http://xzhang.web.cern.ch/xzhang/www/Welcome.html>. (Cited on pages xxxix, lvii, 8, 33, 43, 45, 53, 54, 55, 57, 63, 64, 85, 90, 91, 100, 101, 102, 103, 116, 176 and 180.)
- [43] P. B. Munzinger and J. Stachel. Hadron Production in Ultra-relativistic Nuclear Collisions and the QCD Phase Diagram: an Update. *arXiv:nucl-th/1101.3167*, 2011. (Cited on page 8.)
- [44] P. B. Munzinger. Ultrarelativistic nuclear collisions. *54 Cracow School on Theoretical Physics, Zakopane*, 2014. (Cited on pages xxxv and 9.)
- [45] M. Stephanov. QCD phase diagram: an overview. *PoS(LAT 2006)*, 024, 2006. (Cited on page 9.)
- [46] R. Preghenella. ALICE results on identified particle spectra in p–Pb collisions, <http://indico.cern.ch/event/216368/material/slides/0?contribId=21>. (Cited on page 9.)
- [47] J. Rafelski and B. Muller. Strangeness Production in the Quark–Gluon Plasma. *Phys. Rev. Lett.*, 48:1066, 1982. (Cited on page 10.)
- [48] J. Rafelski. Strangeness Production in the Quark–Gluon Plasma. *Ref. TH. 3745. CERN*, 1983. (Cited on page 10.)
- [49] J. Rafelski. Strange anti-baryons from quark–gluon plasma. *Phys. Lett. B*, 262:333–340, 1991. (Cited on page 10.)
- [50] G. Torrieri. Phenomenology of Strangeness enhancement in heavy ion collisions. *J. Phys. G*, 36:064007, 2019. (Cited on page 10.)
- [51] J. Rafelski. Strangeness and Quark–Gluon Plasma. *Acta Physica Polonica B*, 43:829, 2012. (Cited on page 10.)
- [52] J. Rafelski. Strangeness Production and Quark Gluon Plasma Properties. *SQM2011–Krakow, Poland*, 2011. (Cited on page 10.)
- [53] F. Becattini. Strangeness production in relativistic heavy ion collisions. *QGP school, Torino*, 2011. (Cited on page 10.)
- [54] X. L. Zhu.  $\Omega$  production in p+p, Au+Au and U+U collisions at STAR, <https://indico.cern.ch/event/219436/session/19/contribution/659/material/slides/0.pdf>. (Cited on page 10.)



- [55] D. Alexandre. Multi-strange baryon production in pp, p-Pb and Pb-Pb collisions measured with ALICE at the LHC, <https://indico.cern.ch/event/219436/session/19/contribution/207/material/slides/0.pdf>. (Cited on page 10.)
- [56] A. Tounsi and K. Redlich. Strangeness Enhancement and Canonical Suppression. *arXiv:hep-ph/0111159*, 2001. (Cited on page 10.)
- [57] I. Kraus *et al.* Particle production in p-p collisions and prediction for LHC energy. *Phys. Rev. C*, 79:014901, 2009. (Cited on page 10.)
- [58] D. Kikola for the STAR Collaboration. Quarkonia production and suppression in heavy ion collisions in STAR. *Conference Series*, 509:012093, 2014. (Cited on page 11.)
- [59] The ALICE Collaboration.  $J/\Psi$  Suppression at Forward Rapidity in Pb-Pb Collisions at  $\sqrt{s_{NN}} = 2.76$  TeV. *Phys. Rev. Lett.*, 109:072301, 2012. (Cited on pages xxxv and 11.)
- [60] R. Arnaldi.  $J/\Psi$  production in p-A and A-A collisions at fixed target experiments. *Nucl. Phys. A*, 830:345c-352c, 2009. (Cited on pages xxxv and 11.)
- [61] T. Matsui and H. Satz.  $J/\Psi$  Suppression by Quark-Gluon Plasma Formation. *Phys. Lett. B*, 178:416, 1986. (Cited on page 11.)
- [62] P. B. Munzinger and J. Stachel. The quest for the quark-gluon plasma. *Nature*, 448:302-309, 2007. (Cited on page 12.)
- [63] H. Satz. Quarkonium Binding and Dissociation: The Spectral Analysis of the QGP. *Nucl. Phys. A*, 783:249-260, 2007. (Cited on page 12.)
- [64] P. B. Munzinger and J. Stachel. The quest of quark-gluon plasma. *HASCO-Hadron Collider Summer School*, 2014. (Cited on page 12.)
- [65] E. G. Ferreira. Charmonium dissociation and recombination at LHC: Revisiting comovers. *Phys. Lett. B*, 731:57, 2014. (Cited on page 12.)
- [66] K. Zhou, N. Xu, P. F. Zhuang. Transverse Momentum Distribution as a Probe of  $J/\Psi$  Production Mechanism in Heavy Ion Collisions. *Nucl. Phys. A*, 834:249-252, 2010. (Cited on page 12.)
- [67] J. Y. Ollitrault. Flow systematics from SIS to SPS energies. *Nucl. Phys. A*, 638:195-206, 1998. (Cited on page 12.)
- [68] M. Luzum and J. Y. Ollitrault. Eliminating experimental bias in anisotropic-flow measurements of high-energy nuclear collisions. *Phys. Rev. C*, 87:044907, 2013. (Cited on page 12.)
- [69] R. Snellings. Elliptic Flow: A Brief Review. *New J. Phys.*, 13:05508, 2011. (Cited on page 12.)



- [70] P. Bozek, W. Broniowski and G. Torrieri. Hydrodynamic models of particle production. *J. Phys.: Conf. Ser.*, 509:012017, 2014. (Cited on page 12.)
- [71] K. Filimonov. Collective Flow in Heavy-Ion Collisions, [http://quark.phy.bnl.gov/%7Efbass/RBRC\\_plasma\\_filimonov.ppt](http://quark.phy.bnl.gov/%7Efbass/RBRC_plasma_filimonov.ppt). (Cited on page 12.)
- [72] Naomi van der Kolk. To flow or not to flow: A study of elliptic flow and nonflow in proton-proton collisions in ALICE, [http://www.nikhef.nl/pub/services/biblio/theses\\_pdf/thesis\\_N\\_v\\_d\\_Kolk.pdf](http://www.nikhef.nl/pub/services/biblio/theses_pdf/thesis_N_v_d_Kolk.pdf). (Cited on pages 12 and 13.)
- [73] Emanuele Lorenzo Simili. Elliptic Flow Measurement at ALICE, [http://www.nikhef.nl/pub/services/biblio/theses\\_pdf/thesis\\_EL\\_Simili.pdf](http://www.nikhef.nl/pub/services/biblio/theses_pdf/thesis_EL_Simili.pdf). (Cited on page 12.)
- [74] S. Jeon. Higher Harmonics in Heavy Ion Collisions. *Conference Series 422 (2013)*, 422:012004, 2013. (Cited on page 13.)
- [75] V. Greco, C. M. Ko and P. Lévai. Parton coalescence and antiproton/pion anomaly at RHIC. *Phys. Rev. Lett.*, 90:202302, 2003. (Cited on page 13.)
- [76] R. J. Fries, V. Greco and P. Sorensen. Coalescence Models For Hadron Formation From Quark Gluon Plasma. *Ann. Rev. Nucl. Part. Sci.*, 58:177–205, 2008. (Cited on page 13.)
- [77] R. J. Fries, S. A. Bass, B. Muller and C. Nonaka. Hadronization in heavy ion collisions: Recombination and fragmentation of partons. *Phys. Rev. Lett.*, 90:202303, 2003. (Cited on page 13.)
- [78] R. J. Fries, B. Muller, C. Nonaka and S. A. Bass. Hadronization in heavy ion collisions: recombination or fragmentation? *J. Phys. G*, 30:S223–S228, 2004. (Cited on page 13.)
- [79] A. Dobrin. Elliptic flow of identified particles in Pb-Pb collisions at the LHC, <https://indico.cern.ch/event/219436/session/9/contribution/244/material/slides/0.pdf>. (Cited on page 13.)
- [80] R. Haque. The centrality and energy dependence of the elliptic flow of light nuclei and hadrons in STAR, <https://indico.cern.ch/event/219436/session/9/contribution/579/material/slides/0.pdf>. (Cited on page 13.)
- [81] J. Stachel.  $v_2(\pi, K, p, \Xi, \Omega)$  20 – 40% model comparison, <https://aliceinfo.cern.ch/Figure/node/4837>. (Cited on pages xxxv and 13.)
- [82] The STAR Collaboration. Dielectron Mass Spectra from Au+Au Collisions at  $\sqrt{s_{NN}} = 200$  GeV. *Phys. Rev. Lett.*, 113:022301, 2014. (Cited on pages xxxvi, 14 and 15.)



- [83] J. Piśút. Background to the low mass dilepton production from QCD plasma in ion–ion collisions. *Acta Physica Polonica*, B17:911, 1986. (Cited on page 15.)
- [84] A. A. Grigorian. Physics of low mass dileptons produced in heavy ion collisions. *NA50-Up Note/97-1*, 1997. (Cited on page 15.)
- [85] A. Peshier and M. H. Thoma. Quark Dispersion Relation and Dilepton Production in the Quark–Gluon Plasma. *Phys. Rev. Lett.*, 84:841–844, 2000. (Cited on page 15.)
- [86] R. Rapp and J. Wambach. Chiral Symmetry Restoration and Dileptons in Relativistic Heavy–Ion Collisions. *Adv. Nucl. Phys.*, 5:1, 2000. (Cited on page 15.)
- [87] R. Rapp. Signatures of thermal dilepton radiation at ultrarelativistic energies. *Phys. Rev. C*, 63:054907, 2001. (Cited on page 15.)
- [88] G. E. Brown and M. Rho. Chiral restoration in hot and/or dense matter. *Physics Reports*, 369:333–380, 1996. (Cited on page 15.)
- [89] R. Rapp and J. Wambach. Low–Mass Dileptons at the CERN–SpS: Evidence for Chiral Restoration? *Eur. Phys. J*, A6:415–420, 1999. (Cited on page 15.)
- [90] B. R. Webber. Fragmentation and Hadronization. *Int. J. Mod. Phys. A*, 15s1:577–606, 2000. (Cited on page 15.)
- [91] David d’Enterria. Jet quenching. *arXiv:nucl-ex/0902.2011*, 2011. (Cited on pages xxxvi and 16.)
- [92] The ALICE Collaboration. Some results from the first two years of lead ion collisions, <http://aliceinfo.cern.ch/Public/en/Chapter1/results.html>. (Cited on page 15.)
- [93] C. Loizides. Jet physics in ALICE. *arXiv: nucl-ex/0501017*, 2005. (Cited on page 15.)
- [94] C. K. Bösing. Production of Neutral Pions and Direct Photons in Ultra–Relativistic Au+Au Collisions, [https://www.phenix.bnl.gov/phenix/WWW/talk/archive/theses/2005/Klein-Boeing\\_Christian-thesis.pdf](https://www.phenix.bnl.gov/phenix/WWW/talk/archive/theses/2005/Klein-Boeing_Christian-thesis.pdf). (Cited on page 16.)
- [95] D. Peressounko. Photon physics in ALICE, <https://indico.cern.ch/event/94968/session/3/contribution/38/material/slides/1.pdf>. (Cited on page 16.)
- [96] B. Bannier. Systematic studies of soft direct photon production in Au+Au collisions at  $\sqrt{s_{NN}} = 200$  GeV, [https://www.phenix.bnl.gov/phenix/WWW/talk/archive/theses/2014/Bannier\\_Benjamin-thesis.pdf](https://www.phenix.bnl.gov/phenix/WWW/talk/archive/theses/2014/Bannier_Benjamin-thesis.pdf). (Cited on page 16.)



- [97] The CMS Collaboration. Study of Z production in PbPb and pp collisions at  $\sqrt{s_{NN}} = 2.76$  TeV in the dimuon and dielectron decay channels. *JHEP*, 03:022, 2015. (Cited on pages xxxvi and 17.)
- [98] The CMS Collaboration. Study of W boson production in PbPb and pp collisions at  $\sqrt{s_{NN}} = 2.76$  TeV. *Phys. Lett. B*, 715:66, 2012. (Cited on pages xxxvi and 17.)
- [99] The CMS Collaboration. Measurement of isolated photon production in pp and PbPb collisions at  $\sqrt{s_{NN}} = 2.76$  TeV. *Phys. Lett. B*, 710:256, 2012. (Cited on pages xxxvi and 17.)
- [100] The CMS Collaboration. Study of high- $p_T$  charged particle suppression in PbPb compared to pp collisions at  $\sqrt{s_{NN}} = 2.76$  TeV. *Eur. Phys. J. C*, 72:1945, 2012. (Cited on pages xxxvi and 17.)
- [101] The CMS Collaboration. Suppression of non-prompt J/ $\Psi$ , prompt J/ $\Psi$ , and  $\Upsilon(1S)$  in PbPb collisions at  $\sqrt{s_{NN}} = 2.76$  TeV. *JHEP*, 05:063, 2012. (Cited on pages xxxvi and 17.)
- [102] The CMS Collaboration. Observation and studies of jet quenching in PbPb collisions at  $\sqrt{s_{NN}} = 2.76$  TeV. *Phys. Rev. C*, 84:024906, 2011. (Cited on pages xxxvi and 17.)
- [103] The CMS Collaboration. Measurement of the b-jet to inclusive jet ratio in PbPb and pp collisions at  $\sqrt{s_{NN}} = 2.76$  TeV with the CMS detector. *CMS-PAS-HIN-12-003*, 2012. (Cited on pages xxxvi and 17.)
- [104] A. Florent *et. al.* W production in pPb collision, [http://lir.in2p3.fr/sites/qgp2014/Talks/QGP-France2014\\_Florent.pdf](http://lir.in2p3.fr/sites/qgp2014/Talks/QGP-France2014_Florent.pdf). (Cited on pages xxxvi and 17.)
- [105] K. J. Eskola, H. Paukkunen and C. A. Salgado. EPS09—a New Generation of NLO and LO Nuclear Parton Distribution Functions. *JHEP*, 0904:065, 2009. (Cited on pages xxxvi, liii, liv, 18, 217, 218, 226 and 227.)
- [106] V. Emel'yanov, A. Khodinov, S. R. Klein and R. Vogt. The Effect of Shadowing on Initial Conditions, Transverse Energy and Hard Probes in Ultra-relativistic Heavy Ion Collisions. *Phys. Rev. C*, 61:044904, 2000. (Cited on page 18.)
- [107] P. R. Norton. The EMC effect. *Rep. Prog. Phys.*, 66:1253, 2003. (Cited on page 18.)
- [108] A. Bodek and J. L. Ritchie. Fermi Motion Effects in Deep Inelastic Lepton Scattering from Nuclear Targets. *Phys. Rev. D*, 23:1070, 1981. (Cited on page 18.)



- [109] F. Gelis. Initial state in relativistic nuclear collisions and Color Glass Condensate, <https://indico.cern.ch/event/219436/session/3/contribution/719/material/slides/0.pdf>. (Cited on pages xxxvi and 18.)
- [110] F. Gelis. Initial state in relativistic nuclear collisions and Color Glass Condensate. *Nucl. Phys. A*, 931:73–82, 2014. (Cited on pages xxxvi and 18.)
- [111] L. McLerran and R. Venugopalan. Computing Quark and Gluon Distribution Functions for Very Large Nuclei. *Phys. Rev. D*, 49:2233–2241, 1994. (Cited on page 18.)
- [112] L. McLerran and R. Venugopalan. Gluon Distribution Functions for Very Large Nuclei at Small Transverse Momentum. *Phys. Rev. D*, 49:3352–3355, 1994. (Cited on page 18.)
- [113] L. McLerran. The Color Glass Condensate and Small  $x$  Physics: 4 Lectures. *Lect. Notes Phys.*, 583:291–334, 2002. (Cited on page 18.)
- [114] E. Iancu and R. Venugopalan. The Color Glass Condensate and High Energy Scattering in QCD. *arXiv:hep-ph/0303204*, 2003. (Cited on page 18.)
- [115] R. Venugopalan. The Color Glass Condensate: A summary of key ideas and recent developments. *arXiv:hep-ph/0412396*, 2004. (Cited on page 18.)
- [116] J. P. Blaizot, T. Lappi, Y. M. Tani. On the gluon spectrum in the glasma. *Nucl.Phys.A*, 846:63–82, 2010. (Cited on page 19.)
- [117] T. Hirano and Y. Nara. Hydrodynamic afterburner for the Color Glass Condensate and the parton energy loss. *Nucl. Phys. A*, 743:305–328, 2004. (Cited on page 19.)
- [118] A. Bzdak and V. Skokov. Decisive test of color coherence in proton-nucleus collisions at the LHC. *Phys. Rev. Lett.*, 111:182301, 2013. (Cited on page 19.)
- [119] D. Antreasyan *et al.* Production of Hadrons at Large Transverse Momentum in 200–GeV, 300–GeV and 400–GeV p+p and p+n Collisions. *Phys. Rev. D*, 19:764–778, 1979. (Cited on pages xxxvi, 19 and 20.)
- [120] X. N. Wang. Systematic Study of High  $p_T$  Hadron Spectra in pp, pA and AA Collisions from SPS to RHIC Energies. *Phys.Rev.C61:064910,2000*, 61:064910, 2000. (Cited on page 19.)
- [121] G. G. Barnafoldi, G. Papp, P. Levai and G. Fai. Cronin Effect at Different Rapidities at RHIC. *J. Phys. G*, 30:S1125–S1128, 2004. (Cited on page 19.)
- [122] M. Krelina and J. Nemchik. Cronin effect at different energies: from RHIC to LHC. *EPJ Web of Conferences*, 66:04016, 2014. (Cited on page 19.)



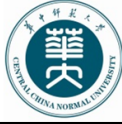
- [123] G. G. Barnaföldi. Cronin Effect at Different Rapidities at FERMILAB and at RHIC,  
[http://www.rmki.kfki.hu/~bgergely/rhic\\_04.pdf.gz](http://www.rmki.kfki.hu/~bgergely/rhic_04.pdf.gz). (Cited on page 19.)
- [124] J. D. BJORKEN. Energy Loss of Energetic Partons in Quark-Gluon Plasma: Possible Extinction of High  $p_T$  Jets in Hadron-Hadron Collisions. *FERMILAB-Pub-82/59-THY*, 1982. (Cited on page 20.)
- [125] R. Baier. Jet Quenching. *Nucl. Phys. A*, 715:209–218, 2003. (Cited on page 20.)
- [126] M. Gyulassy and X. N. Wang. Multiple Collisions and Induced Gluon Bremsstrahlung in QCD. *Nucl. Phys. B*, 420:583–614, 1994. (Cited on page 20.)
- [127] R. Baier, Yu. L. Dokshitzer, A. H. Mueller, S. Peigné and D. Schiff. Radiative energy loss of high energy quarks and gluons in a finite volume quark-gluon plasma. *Nucl. Phys. B*, 483:291–320, 1997. (Cited on pages xxxvi, 20 and 21.)
- [128] R. Abir *et al.* Soft gluon emission off a heavy quark revisited. *Phys. Rev. D*, 85:054012, 2012. (Cited on pages xxxvi and 21.)
- [129] J. Uphoff. Elastic and radiative heavy quark energy loss within a transport model,  
<https://indico.cern.ch/event/219436/session/17/contribution/354/material/slides/0.pdf>. (Cited on pages xxxvi and 21.)
- [130] Yu. L. Dokshitzer and D. E. Kharzeev. Heavy quark colorimetry of QCD matter. *Phys. Lett. B*, 519:199–206, 2001. (Cited on page 21.)
- [131] S. Wicks, W. Horowitz, M. Djordjevic and M. Gyulassy. Elastic, Inelastic, and Path Length Fluctuations in Jet Tomography. *Nucl. Phys. A*, 784:426–442, 2007. (Cited on pages xxxvi and 22.)
- [132] M. B. Gay Ducati, V. P. Goncalves and L. F. Mackedanz. QCD Collisional Energy Loss in an Increasingly Interacting Quark Gluon Plasma. *arXiv:hep-ph/0506241*, 2007. (Cited on page 22.)
- [133] H. van Hees and R. Rapp. Thermalization of Heavy Quarks in the Quark-Gluon Plasma. *Phys. Rev. C*, 71:034907, 2005. (Cited on page 22.)
- [134] S. Peigne and A. Peshier. Collisional energy loss of a fast heavy quark in a quark-gluon plasma. *Phys. Rev. D*, 77:114017, 2008. (Cited on page 22.)
- [135] A. Meistrenko, A. Peshier, J. Uphoff and C. Greiner. Collisional energy loss of heavy quarks. *Nucl. Phys. A*, 901:51–64, 2013. (Cited on page 22.)
- [136] S. Wicks. Influence of Elastic Energy Loss on Heavy Flavor Quenching,  
[https://www.phenix.bnl.gov/WWW/publish/xiewei/RBRC\\_Workshop\\_Dec/heavyworkshop/S-Wicks-HeavyFlavour.ppt](https://www.phenix.bnl.gov/WWW/publish/xiewei/RBRC_Workshop_Dec/heavyworkshop/S-Wicks-HeavyFlavour.ppt). (Cited on pages xxxvi and 22.)



- [137] X. Zhu *et al.*  $D\bar{D}$  Correlations as a sensitive probe for thermalization in high-energy nuclear collisions. *Phys. Lett. B*, 647:366–370, 2007. (Cited on pages xxxvi and 23.)
- [138] ALICE Collaboration. Measurement of charm production at central rapidity in proton–proton collisions at  $\sqrt{s} = 2.76$  TeV. *arXiv:hep-ex/1205.4007*, 2012. (Cited on pages xxxvii, 24 and 27.)
- [139] ALICE Collaboration. Beauty production in pp collisions at  $\sqrt{s} = 2.76$  TeV measured via semi–electronic decays. *arXiv:nucl-ex/1405.4144*, 2014. (Cited on pages xxxvii, 24 and 39.)
- [140] M. L. Mangano, P. Nason and G. Ridolfi. Heavy–quark correlations in hadron collisions at next–to–leading order. *Nucl. Phys. B*, 373:295–345, 1992. (Cited on pages xxxvii, 24, 28, 29, 176, 177, 180 and 202.)
- [141] J. Aichelin, P. B. Gossiaux and T. Gousset. Radiative and Collisional Energy Loss of Heavy Quarks in Deconfined Matter. *arXiv:nucl-th/1201.4192*, 2014. (Cited on pages xxxvii, 25 and 27.)
- [142] ALICE. Average D mesons  $R_{AA}$  vs  $N_{\text{part}}$  compared with CMS non prompt  $J/\Psi$  and theoretical models. *ALI-PREL-77105*, 2014. (Cited on page 25.)
- [143] M. Djordjevic. Heavy flavor puzzle at LHC: a serendipitous interplay of jet suppression and fragmentation. *Phys. Rev. Lett.*, 112:042302, 2014. (Cited on pages xxxvii, 25 and 26.)
- [144] ALICE. Average D meson in 0–7.5%, charged hadrons and pions  $R_{AA}$  in the 0–10%. *ALI-PREL-38713*, 2012. (Cited on page 25.)
- [145] M. Djordjevic. Theoretical predictions of jet suppression: A systematic comparison with RHIC and LHC data. *Nucl. Phys. A*, 931:505–509, 2014. (Cited on page 25.)
- [146] M. Djordjevic, M. Djordjevic and B. Blagojevic. RHIC and LHC jet suppression in non-central collisions. *arXiv:nucl-th/1405.4250*, 2014. (Cited on page 25.)
- [147] R. Rapp and H. van Hees. Heavy Quarks in the Quark-Gluon Plasma. *R. C. Hwa, X. N. Wang (Ed.), Quark Gluon Plasma 4, World Scientific*, page 111, 2010. (Cited on page 26.)
- [148] M. He, R. J. Fries and R. Rapp. Heavy–Quark Diffusion and Hadronization in Quark–Gluon Plasma. *Phys. Rev. C*, 86:014903, 2012. (Cited on pages 26 and 27.)
- [149] Mi. He, R. J. Fries and R. Rapp.  $D_s$  Meson as a Quantitative Probe of Diffusion and Hadronization in Nuclear Collisions. *Phys. Rev. Lett.*, 110:112301, 2013. (Cited on page 26.)



- [150] J. Uphoff, O. Fochler, Z. Xu and C. Greiner. Open heavy flavor in Pb+Pb collisions at  $\sqrt{s_{NN}}=2.76$  TeV within a transport model. *Phys. Lett. B*, 717:430–435, 2012. (Cited on page 27.)
- [151] T. Lang, H. van Hees, Ja. Steinheimer and M. Bleicher. Heavy quark transport in heavy ion collisions at RHIC and LHC within the UrQMD transport model. *arXiv:hep-ph/1211.6912*, 2012. (Cited on page 27.)
- [152] M. He. Toward a complete description of Heavy Flavor Transport in Medium, <https://indico.cern.ch/event/114962/session/17/contribution/164/material/slides/0.pdf>. (Cited on page 27.)
- [153] R. Fries. Quark Recombination, <http://indico.vicc.gov.in/indico/conferenceOtherViews.py?view=nicecompact&confId=29>. (Cited on pages xxxvii and 27.)
- [154] M. Cacciari, M. Greco and P. Nason. The  $p_T$  spectrum in heavy-flavour hadroproduction. *JHEP*, 9805:007, 1998. (Cited on pages xxxvii, 28, 29 and 37.)
- [155] M. Cacciari *et. al.* Theoretical predictions for charm and bottom production at the LHC. *JHEP*, 1210:137, 2012. (Cited on pages xxxvii, 28 and 29.)
- [156] The ALICE Collaboration. Measurement of electrons from semileptonic heavy-flavor hadron decays in pp collisions at  $\sqrt{s} = 7$  TeV. *Phys. Rev. D*, 86:112007, 2012. (Cited on pages xxxvii, 28, 29, 39 and 192.)
- [157] B. A. Kniehl *et. al.* Hadroproduction of D and B mesons in a massive VFNS. *arXiv:hep-ph/0507068*, 2005. (Cited on page 29.)
- [158] The ALICE Collaboration. Measurement of charm production at central rapidity in proton-proton collisions at  $\sqrt{s} = 7$  TeV. *JHEP*, 01:128, 2012. (Cited on page 29.)
- [159] ALICE Collaboration. Production of Muons from Heavy Flavor Decays at Forward Rapidity in pp and Pb-Pb Collisions at  $\sqrt{s_{NN}}=2.76$  TeV. *Phys. Rev. Lett.*, 109:112301, 2013. (Cited on pages xlix, 29, 39, 50, 114, 115, 136, 176, 183, 191, 195, 202, 203 and 217.)
- [160] ALICE Collaboration. Heavy flavour decay muon production at forward rapidity in proton-proton collisions at  $\sqrt{s} = 7$  TeV. *Phys. Lett. B*, 708:265–275, 2012. (Cited on pages xliii, xlix, 29, 39, 50, 71, 111, 114, 176, 183, 191, 194 and 202.)
- [161] The ALICE Collaboration. Average D mesons  $R_{AA}$  vs  $N_{part}$  compared with CMS non prompt J/Ψ and theoretical models (MC@sHQ+EPOS2), <https://aliceinfo.cern.ch/Figure/node/4674>. (Cited on pages xxxvii, 29 and 30.)



- [162] The ALICE Collaboration. Average D-meson  $R_{AA}$  in semi-central Pb–Pb collisions at  $\sqrt{s_{NN}} = 2.76$  TeV, <https://aliceinfo.cern.ch/Figure/node/8524>. (Cited on pages xxxvii and 31.)
- [163] The ALICE Collaboration. NHeavy flavor muon and electron  $R_{AA}$  in semi-central collisions, <https://aliceinfo.cern.ch/Figure/node/4735>. (Cited on page 30.)
- [164] The ALICE Collaboration. Heavy flavor muon and electron  $R_{AA}$  in the 0 – 10%, <https://aliceinfo.cern.ch/Figure/node/8669>. (Cited on pages xxxviii and 31.)
- [165] ALICE Collaboration. Azimuthal anisotropy of D meson production in Pb–Pb collisions at  $\sqrt{s} = 2.76$  TeV. *Phys. Rev. C* 90 (2014) 034904, 90:034904, 2014. (Cited on pages xxxviii and 32.)
- [166] The ALICE Collaboration. Heavy flavor decay electron and muon  $v_2$  in comparison: 20 – 40% centrality class In Pb–Pb collision, <https://aliceinfo.cern.ch/Figure/node/6805>. (Cited on pages xxxviii and 32.)
- [167] The ALICE Collaboration. Anisotropic flow of charged hadrons, pions and (anti-)protons measured at high transverse momentum in Pb–Pb collisions at  $\sqrt{s_{NN}} = 2.76$  TeV. *Phys. Lett. B*, 719:18–28, 2013. (Cited on page 33.)
- [168] S. Li (for the ALICE Collaboration). Nuclear modification factor and elliptic flow of muons from heavy-flavour hadron decays in Pb–Pb collisions  $\sqrt{s_{NN}} = 2.76$  TeV. *Nucl. Phys. A*, 932:32–37, 2014. (Cited on page 33.)
- [169] ALICE Collaboration. Elliptic flow of muons from heavy-flavour hadron decays at forward rapidity in Pb–Pb collisions at  $\sqrt{s_{NN}} = 2.76$  TeV. *arXiv:1507.03134; CERN-PH-EP-2015-173*, 2015. (Cited on page 33.)
- [170] The ALICE Collaboration. Measurement of prompt D–meson production in p–Pb collisions at  $\sqrt{s_{NN}} = 5.02$  TeV, <https://aliceinfo.cern.ch/Figure/node/6902>. (Cited on pages xxxviii, 33, 34 and 226.)
- [171] S. Li (for the ALICE Collaboration). Measurements of the heavy-flavour nuclear modification factor in p–Pb collisions at  $\sqrt{s_{NN}} = 5.02$  TeV with ALICE at the LHC. *Nucl. Phys. A*, 931:546–551, 2014. (Cited on pages 33, 34, 39 and 226.)
- [172] The CMS Collaboration. Measurements of the  $B^+$ ,  $B^0$  and  $B_s^0$  production cross sections in pPb collisions at  $\sqrt{s_{NN}} = 5.02$  TeV. *PAS-HIN-14-004*, 2014. (Cited on pages xxxviii and 34.)
- [173] The ALICE Collaboration. Nuclear modification factor of beauty hadron decay electrons and inclusive heavy flavour electrons,



- <https://aliceinfo.cern.ch/Figure/node/6730>. (Cited on pages xxxviii, 35 and 226.)
- [174] The ALICE Collaboration. Suppression of high transverse momentum D mesons in central Pb–Pb collisions at  $\sqrt{s_{NN}} = 2.76$  TeV. *JHEP*, 09:112, 2012. (Cited on page 35.)
- [175] E. Pereira de Oliveira Filho (for the ALICE Collaboration). Measurements of electrons from heavy–flavour hadron decays in pp, p–Pb and Pb–Pb collisions with ALICE at the LHC. *arXiv:hep-ex/1404.3983*, 2014. (Cited on page 35.)
- [176] The PHENIX Collaboration. Heavy–flavor electron–muon correlations in  $p+p$  and  $d+Au$  collisions at  $\sqrt{s_{NN}} = 200$  GeV. *Phys. Rev. C*, 89:034915, 2014. (Cited on pages xxxviii, 35 and 36.)
- [177] S.H. Neddermeyer and C. D. Anderson. Note on the Nature of Cosmic–Ray Particles. *Phys. Rev.*, 51:884, 1937. (Cited on page 36.)
- [178] D. Denisov. Detection of Muons,  
[http://www-ppd.fnal.gov/EPPOffice-w/Academic\\_Lectures](http://www-ppd.fnal.gov/EPPOffice-w/Academic_Lectures). (Cited on page 37.)
- [179] The PHENIX Collaboration). Nuclear–modification factor for open–heavy-flavor production at forward rapidity in Cu+Cu collisions at  $\sqrt{s_{NN}} = 200$  GeV. *Phys. Rev. C*, 86:024909, 2012. (Cited on page 38.)
- [180] S. Lim. PhD Thesis,  
[https://www.phenix.bnl.gov/phenix/WWW/talk/archive/theses/2014/Lim\\_Sanghoon-thesis\\_shlim.pdf](https://www.phenix.bnl.gov/phenix/WWW/talk/archive/theses/2014/Lim_Sanghoon-thesis_shlim.pdf). (Cited on page 38.)
- [181] PHENIX Collaboration. Nuclear–modification factor for open–heavy-flavor production at forward rapidity in Cu+Cu collisions at  $\sqrt{s_{NN}} = 200$  GeV. *Phys. Rev. C*, 86:024909, 2012. (Cited on page 39.)
- [182] PHENIX Collaboration. Cold–Nuclear–Matter Effects on Heavy–Quark Production at Forward and Backward Rapidity in d+Au Collisions at  $\sqrt{s_{NN}} = 200$  GeV. *Phys. Rev. Lett.*, 112:252301, 2014. (Cited on pages liv, 39, 224 and 225.)
- [183] PHENIX Collaboration. Measurement of Single Electrons and Implications for Charm Production in  $Au+Au$  Collisions at  $\sqrt{s_{NN}} = 130$  GeV. *Phys. Rev. Lett.*, 88:192303, 2014. (Cited on page 39.)
- [184] STAR Collaboration. Transverse Momentum and Centrality Dependence of High– $p_T$  Nonphotonic Electron Suppression in Au + Au Collisions at  $\sqrt{s_{NN}} = 200$  GeV. *Phys. Rev. Lett.*, 98:192301, 2007. (Cited on page 39.)
- [185] STAR Collaboration. Transverse Momentum and Centrality Dependence of High– $p_T$  Nonphotonic Electron Suppression in Au + Au Collisions at  $\sqrt{s_{NN}} = 200$  GeV. *Phys. Rev. Lett.*, 106:159902, 2011. (Cited on page 39.)



- [186] The ALICE Collaboration. Measurement of electrons from semileptonic heavy-flavor hadron decays in pp collisions at  $\sqrt{s} = 2.76$  TeV. *Phys. Rev. D*, 91:012001, 2015. (Cited on page 39.)
- [187] The ALICE Collaboration. Measurement of electrons from beauty hadron decays in pp collisions at  $\sqrt{s} = 7$  TeV. *Phys. Lett. B*, 723:13–23, 2012. (Cited on page 39.)
- [188] ALICE Collaboration. Measurement of electrons from heavy-flavour hadron decays in p–Pb collisions at  $\sqrt{s_{NN}} = 5.02$  TeV. *arXiv:1509.07491*; *CERN-PH-EP-2015-262*, 2015. (Cited on page 39.)
- [189] Wikipedia. Large Hadron Collider, [http://en.wikipedia.org/wiki/Large\\_Hadron\\_Collider](http://en.wikipedia.org/wiki/Large_Hadron_Collider). (Cited on page 41.)
- [190] K. Schweda. ALICE at the Dawn of LHC, <http://www.ep1.rub.de/EUNPC/programme/schweda.pdf>. (Cited on pages lvii and 41.)
- [191] Z. C. del Valle. PhD Thesis, <https://tel.archives-ouvertes.fr/tel-00198703/fr>. (Cited on pages lvii, 41, 46 and 101.)
- [192] ALICE Collaboration. ALICE: Physics Performance Report, Volume I. *J. Phys. G: Nucl. Part. Phys.*, 30(11):1517, 2004. (Cited on pages 41, 43 and 175.)
- [193] ALICE Collaboration. ALICE: Physics Performance Report, Volume II. *J. Phys. G: Nucl. Part. Phys.*, 32:1295, 2006. (Cited on page 41.)
- [194] The ALICE Collaboration. Performance of the ALICE experiment at the CERN LHC. *International Journal of Modern Physics A*, 29:1430044, 2014. (Cited on pages xxxix, lvii, 41, 43, 45, 50 and 85.)
- [195] ALICE Collaboration. <https://aliceinfo.cern.ch>. (Cited on pages xxxviii, 41, 42, 61 and 62.)
- [196] The LEP experiments. <http://public.web.cern.ch/public/en/research/lepexp-en.html>. (Cited on page 42.)
- [197] The ALICE Collaboration. ALICE DCal: An Addendum to the EMCAL Technical Design Report. *CERN-LHCC-2010-011*, *ALICE-TDR-014-ADD-1*, 2010. (Cited on page 43.)
- [198] Wikipedia. ALICE: A Large Ion Collider Experiment, [http://en.wikipedia.org/wiki/ALICE:\\_A\\_Large\\_Ion\\_Collider\\_Experiment](http://en.wikipedia.org/wiki/ALICE:_A_Large_Ion_Collider_Experiment). (Cited on page 43.)
- [199] ALICE Collaboration. ALICE Zero-Degree Calorimeter (ZDC): Technical Design Report, CERN-LHCC-99-005. (Cited on page 43.)



- [200] ALICE Collaboration. ALICE Photon Multiplicity Detector (PMD): Technical Design Report, CERN-LHCC-99-032. (Cited on page 44.)
- [201] ALICE Collaboration. ALICE forward detectors: FMD, T0 and V0: Technical Design Report, CERN-LHCC-2004-025. (Cited on page 44.)
- [202] ALICE Collaboration. The ALICE experiment at the CERN LHC. *JINST*, 3:S08002, 2008. (Cited on pages lvii, 45, 46 and 49.)
- [203] ALICE Collaboration. ALICE Inner Tracking System (ITS): Technical Design Report, CERN-LHCC-99-012. (Cited on page 46.)
- [204] ALICE Collaboration. Alignment of the ALICE Inner Tracking System with cosmic-ray tracks, arXiv:1001.0502, 2010. (Cited on page 46.)
- [205] K. Oyama. ALICE detector status and upgrade plans. *EPJ Web of Conferences*, 49:02002, 2013. (Cited on pages lvii, 46 and 58.)
- [206] ALICE Collaboration. ALICE time projection chamber: Technical Design Report, CERN-LHCC-2000-001. (Cited on page 46.)
- [207] ALICE Collaboration. ALICE transition–radiation detector: Technical Design Report, CERN-LHCC-2001-021. (Cited on page 46.)
- [208] ALICE Collaboration. ALICE: a transition radiation detector for electron identification within the ALICE central detector—an addendum to the Technical Proposal, CERN-LHCC-99-013. (Cited on page 46.)
- [209] ALICE Collaboration. ALICE Time–Of–Flight system (TOF): Technical Design Report, CERN-LHCC-2000-012. (Cited on page 47.)
- [210] ALICE Collaboration. ALICE Time–Of Flight system (TOF): addendum to the technical design report, CERN-LHCC-2002-016. (Cited on page 47.)
- [211] ALICE Collaboration. ALICE high–momentum particle identification: Technical Design Report, CERN-LHCC-98-019. (Cited on page 47.)
- [212] ALICE Collaboration. Technical design report of the photon spectrometer, CERN-LHCC-99-004. (Cited on page 47.)
- [213] ALICE Collaboration. ALICE electromagnetic calorimeter: addendum to the ALICE technical proposal, CERN-LHCC-2006-014. (Cited on page 47.)
- [214] D. Stocco. PhD Thesis,  
<http://inspirehep.net/record/809740/files/CERN-THESIS-2008-144.pdf>.  
(Cited on pages xxxix, 48, 52, 53, 62, 112 and 114.)
- [215] TWiki. Dimuon Forward Spectrometer: Tracking chambers,  
<https://twiki.cern.ch/twiki/bin/view/ALICE/MuonTracking>. (Cited on pages xxxix and 48.)



- [216] CERN. The ALICE Dimuon Spectrometer, [http://aliceinfo.cern.ch/Public/en/Chapter2/Chap2\\_dim\\_spec.html](http://aliceinfo.cern.ch/Public/en/Chapter2/Chap2_dim_spec.html). (Cited on pages xxxix, 50 and 53.)
- [217] L. Manceau (for the ALICE Collaboration). B-hadron cross-section measurement in pp collisions at  $\sqrt{s} = 14$  TeV with the ALICE muon spectrometer. *Eur. Phys. J. C*, 62:9–13, 2009. (Cited on page 50.)
- [218] P. Crochet *et al.* Electron–Muon Coincidence as a Measure of Charm and Bottom with ALICE, ALICE-INT-2000-01. (Cited on page 50.)
- [219] D. Stocco *et al.* Production of muons from W boson decays at forward rapidity in p–Pb collisions at  $\sqrt{s_{NN}} = 5.02$  TeV, <https://aliceinfo.cern.ch/Notes/node/237>. (Cited on pages 50, 58, 113 and 114.)
- [220] A. Morsch. Muon Identification in ALICE, <http://www-alt.gsi.de/documents/DOC-2006-Oct-102-1.pdf>. (Cited on pages xxxix, 51 and 52.)
- [221] P. Dupieux. The ALICE Muon Spectrometer and related Physics, <http://hal.in2p3.fr/in2p3-00133061/document>. (Cited on pages 51, 52 and 56.)
- [222] A. Korytov. Particle Detectors, [http://www.phys.ufl.edu/%7Ekorytov/phz5354/note\\_11\\_detectors.pdf](http://www.phys.ufl.edu/%7Ekorytov/phz5354/note_11_detectors.pdf). (Cited on page 51.)
- [223] A. Zinchenko *et al.* A new approach to cluster finding and hit reconstruction in muon chambers of ALICE, ALICE-INT-2003-006. (Cited on page 53.)
- [224] Wikipedia. Kalman filter, [http://en.wikipedia.org/wiki/Kalman\\_filter](http://en.wikipedia.org/wiki/Kalman_filter). (Cited on page 53.)
- [225] J. G. Branson *et al.* Production of the  $\frac{J}{\psi}$  and  $\psi'(3.7)$  by 225-GeV/ $c\pi^\pm$  and Proton Beams on C and Sn Targets. *Phys. Rev. Lett.*, 38:1331, 1977. (Cited on page 55.)
- [226] F. Guerin *et al.* ALICE Muon Trigger Performance, ALICE-INT-2006-0002. (Cited on pages 56, 57 and 58.)
- [227] P. Dupieux *et al.* The ALICE dimuon trigger: Overview and electronics prototypes, [http://www.iaea.org/inis/collection/NCLCollectionStore/\\_Public/32/008/32008166.pdf](http://www.iaea.org/inis/collection/NCLCollectionStore/_Public/32/008/32008166.pdf). (Cited on pages xxxix and 57.)
- [228] Valérie Ramillien–Barret. Performance and upgrade program of the forward muon spectrometer of the ALICE experiment at the LHC, <http://indico.cern.ch/event/295567/session/2/contribution/10/material/slides/0.pdf>. (Cited on pages lvii and 58.)



- [229] A. Dainese. ALICE Upgrade Performance Studies, <https://twiki.cern.ch/twiki/bin/viewauth/ALICE/UpgradePhys>. (Cited on page 58.)
- [230] M. Luciano *et al.* Upgrade of the Inner Tracking System Conceptual Design Report, CERN-LHCC-2012-013, LHCC-P-005. (Cited on page 58.)
- [231] ALICE Collaboration. Addendum to the Technical Design Report for the Upgrade of the ALICE Time Projection Chamber, CERN-LHCC-2015-002, ALICE-TDR-016-ADD-1. (Cited on page 58.)
- [232] ALICE Collaboration. Upgrade of the ALICE Experiment: Letter of Intent. *J. Phys. G*, 41:087001, 2014. (Cited on pages 58, 59 and 60.)
- [233] G. M. Garcia *et al.* Addendum of the Letter Of Intent for the Upgrade of the ALICE Experiment: The Muon Forward Tracker, CERN-LHCC-2013-014, LHCC-I-022-ADD-1. (Cited on pages 58, 61 and 114.)
- [234] M. Garcia *et al.* Technical Design Report for the Muon Forward Tracker, CERN-LHCC-2015-001, ALICE-TDR-018. (Cited on pages xxxix, 58 and 60.)
- [235] A. Dainese. Upgrade performance, ALICE Week, 13 March 2015, <https://indico.cern.ch/event/331319/session/16/contribution/27/material/slides/0.pdf>. (Cited on page 58.)
- [236] P. Dupieux. ALICE Muon Trigger upgrade, QGP–France 2013, <http://llr.in2p3.fr/sites/qgp2013/programme.php>. (Cited on page 59.)
- [237] P. Dupieux *et. al* (for the ALICE Collaboration). Upgrade of the ALICE muon trigger electronics. *JINST 9 C09013*, 2014. (Cited on page 60.)
- [238] A. Uras. Physics with the Upgraded Muon Spectrometer, QGP–France 2014, <http://llr.in2p3.fr/sites/qgp2014/programme.php>. (Cited on page 60.)
- [239] A. Uras. Towards a New MFT Simulation Run, ITS–MFT Mini–Week, 10–12 March, 2014, <https://indico.cern.ch/event/307046/session/6/contribution/47/material/slides/0.pdf>. (Cited on pages 60 and 61.)
- [240] A. Uras. Performance Study for a Muon Forward Tracker in the ALICE Experiment, arXiv:1201.0048. (Cited on page 61.)
- [241] The ROOT Team. Root Data Analysis Framework, <https://root.cern.ch/drupal>. (Cited on page 61.)
- [242] ALICE Collaboration. Technical design reports, <https://aliceinfo.cern.ch/secure/node/19718>. (Cited on page 61.)



- [243] A. Morsch *et al.* Computing in ALICE. *Nuclear Instruments and Methods in Physics Research A*, 502:339–346, 2003. (Cited on page 62.)
- [244] F. Carminati. The ALICE computing project,  
<http://cerncourier.com/cws/article/cern/49059>. (Cited on page 62.)
- [245] ALICE Collaboration. The ALICE Offline Bible,  
<https://aliceinfo.cern.ch>. (Cited on pages xxxix, 62 and 64.)
- [246] CERN. CERN Program Library,  
<http://cernlib.web.cern.ch/cernlib>. (Cited on page 62.)
- [247] A. Morsch. Event Generators for AliRoot,  
<http://morsch.web.cern.ch/morsch/AliGenerator.html>. (Cited on page 62.)
- [248] CERN. WLCG, <http://wlcg.web.cern.ch>. (Cited on page 63.)
- [249] CERN. The Worldwide LHC Computing Grid,  
<http://home.cern/about/computing/worldwide-lhc-computing-grid>. (Cited on page 63.)
- [250] P. Hristov. Repository split: reminder, discussion and decision,  
<https://indico.cern.ch/event/351206/session/0/contribution/6/material/slides/1.pdf>. (Cited on page 64.)
- [251] P. Hristov. Possible evolution of the ALICE software packages (offline),  
<https://indico.cern.ch/event/379819/session/0/contribution/50/material/slides/1.pdf>. (Cited on page 64.)
- [252] P. Buncic. Offline Report,  
<https://indico.cern.ch/event/331319/session/4/contribution/3/material/slides/1.pdf>. (Cited on page 64.)
- [253] Ananya *et al.* O<sup>2</sup>: A novel combined online and offline computing system for the ALICE Experiment after 2018. *Journal of Physics: Conference Series*, 513:012037, 2012. (Cited on page 64.)
- [254] B. von Haller. ALICE O<sup>2</sup> TDR,  
<https://indico.cern.ch/event/331319/session/4/contribution/4/material/slides/1.pdf>. (Cited on page 64.)
- [255] A. Morsch. Particle Production and binary scaling in p-Pb collisions at the LHC, LHC Seminar, 12 November 2013,  
<https://indico.cern.ch/event/281876>. (Cited on pages xxxix and 65.)
- [256] F. Antinori. Naming scheme for ALICE trigger classes,  
<http://aliweb.cern.ch/secure/Offline/sites/aliceinfo.cern.ch.secure.Offline/files/uploads/trigger/class-naming-01.pdf>. (Cited on page 66.)



- [257] M. Floris and Jan Fiete Grosse-Oetringhaus. Physics Event Selection in the 2009 data at 900 GeV,  
<https://indico.cern.ch/event/79474/contribution/2/material/slides/1.pdf>.  
(Cited on page 67.)
- [258] ALICE Collaboration. Centrality determination of Pb-Pb collisions at  $\sqrt{s_{NN}} = 2.76$  TeV with ALICE. *Phys. Rev. C*, 88:044909, 2013. (Cited on pages 67, 92, 93, 147 and 154.)
- [259] A. Dainese. PhD Thesis,  
<http://arxiv.org/pdf/nucl-ex/0405008.pdf>. (Cited on pages 67 and 146.)
- [260] L. Milano. Vertex and track reconstruction with the ALICE Inner Tracking System,  
[http://personalpages.to.infn.it/%7Emilano/presentations/LeonardoMilano\\_LHCBeyond.pdf](http://personalpages.to.infn.it/%7Emilano/presentations/LeonardoMilano_LHCBeyond.pdf). (Cited on page 67.)
- [261] E. Bruna *et al.* Vertex reconstruction for proton-proton collisions in ALICE, ALICE-INT-2009-018. (Cited on page 67.)
- [262] M. Cacciari, G. P.Salam and G. Soyez. SoftKiller, a particle-level pileup removal method,  
<http://arxiv.org/abs/1407.0408>. (Cited on page 68.)
- [263] Zuman Zhang. Multiplicity dependence of single muon production in p-Pb and Pb-p collisions at  $\sqrt{s_{NN}} = 5.02$  TeV,  
<https://indico.cern.ch/event/328428/contribution/1/material/slides/0.pdf>.  
(Cited on pages xlii, 69, 70, 99 and 100.)
- [264] S. Li. Update the results of single muons in p-Pb and Pb-p collisions,  
<https://indico.cern.ch/event/283536/contribution/0/material/slides/0.pdf>.  
(Cited on page 70.)
- [265] M. Winn. Update on J/Ψ in pPb,  
<https://indico.cern.ch/event/242050/contribution/0/material/slides/0.pdf>.  
(Cited on page 70.)
- [266] CERN. LHC Trigger,  
<http://www.lhc-closer.es/1/3/13/0>. (Cited on page 71.)
- [267] M. Gagliardi. Normalisation via scalers for pA and Ap,  
<https://indico.cern.ch/event/240410/contribution/1/material/slides/0.pdf>.  
(Cited on page 71.)
- [268] The ALICE Collaboration. J/Ψ production and nuclear effects in p-Pb collisions at  $\sqrt{s_{NN}} = 5.02$  TeV. *JHEP*, 02:073, 2014. (Cited on pages 71, 72, 97, 107 and 204.)



- [269] C. Hadjidakis. J/ $\Psi$  analysis update: normalization, <https://indico.cern.ch/event/238093/contribution/3/material/slides/2.pdf>. (Cited on page 72.)
- [270] L. Aphecetche *et al.* Luminosity determination for the J/ $\Psi \rightarrow \mu^+\mu^-$  in p+p interaction at  $\sqrt{s} = 7$  TeV, ALICE SCIENTIFIC NOTE–2011–001. (Cited on page 72.)
- [271] L. Antoine. Normalization factor of CPB11MUL trigger for LHC11h data, <https://indico.cern.ch/event/175923/contribution/0/material/slides/0.pdf>. (Cited on page 72.)
- [272] The ALICE Collaboration. Production of inclusive  $\Upsilon(1S)$  and  $\Upsilon(2S)$  in p–Pb collisions at  $\sqrt{s_{NN}} = 5.02$  TeV. *Phys. Lett. B*, 740:105–117, 2015. (Cited on pages 72 and 97.)
- [273] R. Arnaldi . A first look to pA data, <https://indico.cern.ch/event/230506/contribution/3/material/slides/1.pdf>. (Cited on page 72.)
- [274] D. Stocco. Private communication. (Cited on page 72.)
- [275] S. Li. Update on single muons in p–Pb/Pb–p collisions, <https://indico.cern.ch/event/224527/contribution/0/material/slides/0.pdf>. (Cited on page 73.)
- [276] Wikipedia. Weighted arithmetic mean, [http://en.wikipedia.org/wiki/Weighted\\_arithmetic\\_mean](http://en.wikipedia.org/wiki/Weighted_arithmetic_mean). (Cited on page 78.)
- [277] ALICE Collaboration. Measurement of visible cross sections in proton-lead collisions at  $\sqrt{s_{NN}} = 5.02$  TeV in van der Meer scans with the ALICE detector. *JINST*, 9:1100, 2014. (Cited on pages 82, 152 and 203.)
- [278] CERN. Luminosity from 2013 pPb/Pbp run, <http://laphecet.web.cern.ch/laphecet/alice/luminosity/pPb2013>. (Cited on page 83.)
- [279] X. M. Zhang. Using Correlation between  $\eta$  and  $\theta_{abs}$  to Remove Bkg in Single muon Analysis, <https://indico.cern.ch/event/132213/contribution/0/material/slides/0.pdf>. (Cited on page 90.)
- [280] X. M. Zhang. Single Muon Analysis: Question and Answer Time, <https://indico.cern.ch/event/132882/contribution/7/material/slides/0.pdf>. (Cited on page 90.)
- [281] D. Stocco and P. Pillot.  $p \times$  DCA and co., <https://indico.cern.ch/event/132882/contribution/5/material/slides/0.pdf>. (Cited on pages xli and 90.)



- [282] D. Stocco. Code for standard muon cuts,  
<https://indico.cern.ch/event/163405/contribution/4/material/slides/0.pdf>.  
(Cited on page 90.)
- [283] The ALICE Collaboration. Centrality dependence of particle production in p–Pb collisions at  $\sqrt{s_{NN}} = 5.02$  TeV. *Phys. Rev. C*, 91:064905, 2015. (Cited on pages xli, xlvi, lviii, 93, 94, 95, 96, 151, 152, 154, 155, 158, 203, 204 and 220.)
- [284] S. Li. Update on the measurements versus event activity,  
<https://indico.cern.ch/event/371188/contribution/1/material/slides/0.pdf>.  
(Cited on page 97.)
- [285] ALICE Collaboration. Documentation for CORRFW,  
<https://aliceinfo.cern.ch/secure/Offline/Activities/Analysis/CORRFW.html>.  
(Cited on page 101.)
- [286] M. L. Mangano, P. Nason and G. Ridolfi. Heavy–quark correlations in hadron collisions at next–to–leading order. *Nuclear Physics B*, 373:295–345, 1992.  
(Cited on pages liii, liv, 101, 175, 202, 217, 218, 226 and 227.)
- [287] J. B. Luo. Master Thesis,  
<http://wenku.baidu.com/view/0f0657dec1c708a1284a446c.html>. (Cited on pages xlii, 102, 112, 113 and 176.)
- [288] D. Stocco. MUON detection efficiency dependence with centrality,  
<https://aliceinfo.cern.ch/Figure/node/2399>. (Cited on pages xlii and 103.)
- [289] J. Martin. Muon Tracking Efficiency Studies in p–Pb and Pb–p,  
<https://indico.cern.ch/event/223720/session/1/contribution/5/material/slides/0.pdf>. (Cited on pages xlii, 105 and 107.)
- [290] D. Stocco. How to evaluate the trigger systematics?,  
<https://indico.cern.ch/event/247499/contribution/1/material/slides/0.pdf>.  
(Cited on pages xlii, 105 and 106.)
- [291] M. Leoncino. Trigger efficiency study for pA2013,  
<https://indico.cern.ch/event/241630/contribution/9/material/slides/0.pdf>.  
(Cited on pages 105 and 106.)
- [292] Z. M. Zhang. Study of the normalization between different triggers,  
<https://indico.cern.ch/event/286110/contribution/1/material/slides/0.pdf>.  
(Cited on page 107.)
- [293] L. Aphecetche *et al.* J/Ψ production in p–Pb collisions at  $\sqrt{s_{NN}} = 5.02$  TeV,  
<https://aliceinfo.cern.ch/Notes/node/169>. (Cited on page 108.)
- [294] The ATLAS Collaboration. ATLAS–CONF–2010–075,  
<http://inspirehep.net/record/1204013>. (Cited on page 113.)



- [295] S. Li. Muons from heavy-flavor hadron decays versus event activity in p-Pb collisions at  $\sqrt{s_{NN}} = 5.02$  TeV, [https://indico.cern.ch/event/443487/contribution/1/attachments/1152358/1654840/20150910\\_v1.pdf](https://indico.cern.ch/event/443487/contribution/1/attachments/1152358/1654840/20150910_v1.pdf). (Cited on page 113.)
- [296] N. Le Bris. Distance Closest Approach method (DCA) for the muon spectrometer, <https://indico.cern.ch/event/56621/contribution/0/material/slides/1.pdf>. (Cited on page 114.)
- [297] N. Le Bris, D. Stocco and F. Yermia. Low- $p_T$  heavy-flavour measurement in the semi-muonic channel using the Distance of Closest Approach analysis, <https://indico.cern.ch/event/56621/contribution/0/material/slides/1.pdf>. (Cited on page 114.)
- [298] A. Morsch and D. Stocco. ALICE-INT-2006-27. (Cited on page 114.)
- [299] L. Manceau. B [D] hadron cross-section via single muons in pp collisions at 14 TeV, <https://indico.cern.ch/event/64455/contribution/4/material/slides/2.pdf>. (Cited on page 114.)
- [300] D. Stocco *et al.* Measurement of forward-rapidity heavy-flavour muons in proton-proton collisions at  $\sqrt{s} = 7$  TeV with ALICE, <https://indico.cern.ch/event/108026/contribution/2/material/slides/1.pdf>. (Cited on page 114.)
- [301] X. M. Zhang. Heavy Flavour Physics with the ALICE Muon Spectrometer at the LHC, <http://llr.in2p3.fr/sites/qgp2010/Talks/Mercredi/XiaomingZhang.pdf>. (Cited on page 114.)
- [302] L. V. Palomo. Background subtraction in p-Pb and Pb-p collisions with the vertex method, <https://indico.cern.ch/event/314061/contribution/2/material/slides/0.pdf>. (Cited on page 114.)
- [303] S. Li. Production of muons from heavy-flavour decays in p-Pb and Pb-p collisions at  $\sqrt{s_{NN}} = 5.02$  TeV, <https://indico.cern.ch/event/223720/session/4/contribution/31>. (Cited on page 115.)
- [304] H. Appelshäuser (for the ALICE Collaboration). Particle production at large transverse momentum with ALICE. *J. Phys. G: Nucl. Part. Phys*, 38:124014, 2011. (Cited on page 115.)
- [305] S. Schuchmann (for the ALICE Collaboration). High  $p_T$  suppression of  $\Lambda$  and  $K_s^0$  in Pb-Pb collisions at  $\sqrt{s_{NN}} = 2.76$  TeV with ALICE. *J. Phys. G: Nucl. Part. Phys*, 38:124080, 2011. (Cited on page 115.)



- [306] The PHENIX Collaboratino. Measurement of single muons at forward rapidity in  $p + p$  collisions at  $\sqrt{s} = 200$  GeV and implications for charm production. *Phys. Rev. D*, 76:092002, 2007. (Cited on pages 115 and 116.)
- [307] A. O. Velasquez (for the ALICE Collaboration). Production of  $\pi/K/p$  from intermediate to high  $p_T$  in pp, p–Pb and Pb–Pb collisions measured by ALICE. *Nuclear Physics A*, 32:146–151, 2014. (Cited on pages xliii, 117 and 123.)
- [308] The ALICE Collaboration. Pseudorapidity density of charged particles in p–Pb collisions at  $\sqrt{s_{NN}} = 5.02$  TeV. *Phys. Rev. Lett.*, 110:032301, 2013. (Cited on pages xliv, 118, 126, 127 and 160.)
- [309] The CMS Collaboration. Nuclear effects on the transverse momentum spectra of charged particles in pPb collisions at  $\sqrt{s_{NN}} = 5.02$  TeV, <https://twiki.cern.ch/twiki/bin/view/CMSPublic/PhysicsResultsHIN12017>. (Cited on pages xliv, xlviii, 118, 128, 130, 164, 165 and 202.)
- [310] The ALICE Collaboration. Charged particle  $p_T$  spectrum in p–Pb and pp compared to DPMJET, <https://aliceinfo.cern.ch/Figure/node/4232>. (Cited on pages 118 and 127.)
- [311] A. Ortiz and P. Christiansen. Identification of pions, kaons and protons at high  $p_T$  in p–Pb collisions, <https://indico.cern.ch/event/272865/session/0/contribution/19/material/slides/1.pdf>. (Cited on page 123.)
- [312] M. J. Kweon.  $R_{AA}$  of  $D \rightarrow e$  and (inclusive–cocktail)/ $c \rightarrow e$ , <https://indico.cern.ch/event/154411/contribution/2/material/slides/0.pdf>. (Cited on page 123.)
- [313] M. J. Kweon. Answering questions from Physics Forum on  $R_{AA}$  of  $D \rightarrow e$  and Updating Results, <https://indico.cern.ch/event/153633/contribution/7/material/slides/0.pdf>. (Cited on page 123.)
- [314] The ALICE Collaboration. Transverse Momentum Distribution of Charged Particle Production in p–Pb Collisions at  $\sqrt{s_{NN}} = 5.02$  TeV, <https://aliceinfo.cern.ch/Figure/node/3852>. (Cited on pages xliv, 127 and 128.)
- [315] ALICE Collaboration. Elliptic flow of muons from heavy-flavour hadron decays at forward rapidity in Pb–Pb collisions at  $\sqrt{s_{NN}}=2.76$  TeV. *arXiv:1507.03134*, 2015. (Cited on page 136.)
- [316] F. Prino. Private communication. (Cited on page 146.)
- [317] M. Lenhardt *et al.* Study of the single muon and  $J/\Psi$  production as a function of the charge particle density in proton–proton collisions at 7 TeV,



- <https://twiki.cern.ch/twiki/pub/ALICE/InternalAnalysisNotes/JpsiHighMultiplicityPPEvents.pdf>. (Cited on page 147.)
- [318] A. Ortiz. Private communication. (Cited on pages 148 and 149.)
- [319] The ATLAS Collaboration. Measurement of the centrality dependence of the charged particle pseudorapidity distribution in proton–lead collisions at  $\sqrt{s_{NN}} = 5.02$  TeV with the ATLAS detector, <http://atlas.web.cern.ch/Atlas/GROUPS/PHYSICS/CONFNOTES/ATLAS-CONF-2013-096/>. (Cited on pages xlvi and 160.)
- [320] The CMS Collaboration. Studies of dijet transverse momentum balance and pseudorapidity distributions in pPb collisions at  $\sqrt{s_{NN}} = 5.02$  TeV. *Eur. Phys. J. C*, 74:2951, 2014. (Cited on page 165.)
- [321] The ALICE Collaboration. Particle ratios in pp, pPb and PbPb collisions, <https://aliceinfo.cern.ch/Figure/node/6521>. (Cited on pages xlvi and 172.)
- [322] The CMS Collaboration. Study of the production of charged pions, kaons, and protons in pPb collisions at  $\sqrt{s_{NN}} = 5.02$  TeV. *Eur. Phys. J. C*, 74:2487, 2014. (Cited on pages xlvi and 172.)
- [323] R. Averbeck *et al.* Reference heavy flavour cross sections in pp collisions at  $\sqrt{s} = 2.76$  TeV, using a pQCD–driven  $\sqrt{s}$ –scaling of ALICE measurements at  $\sqrt{s} = 7$  TeV. *arXiv:1107.3243*, 2011. (Cited on pages 175, 176, 186 and 187.)
- [324] F. Arleo, D. d’Enterria and A. S. Yoon. Single–inclusive production of large– $p_T$  charged particles in hadronic collisions at TeV energies and perturbative QCD predictions. *JHEP*, 06:035, 2010. (Cited on page 176.)
- [325] ALICE and LHCb Collaboration. Reference pp cross–sections for  $J/\Psi$  studies in proton–lead collisions at  $\sqrt{s_{NN}} = 5.02$  TeV and comparisons between ALICE and LHCb results, [https://aliceinfo.cern.ch/Notes/sites/aliceinfo.cern.ch/Notes/files/notes/public/scompar/2014-Jan-29-public\\_note-ALICE-PUBLIC-2013-002.pdf](https://aliceinfo.cern.ch/Notes/sites/aliceinfo.cern.ch/Notes/files/notes/public/scompar/2014-Jan-29-public_note-ALICE-PUBLIC-2013-002.pdf). (Cited on page 176.)
- [326] S. Li. Reference and background in the high  $p_T$  region, <https://indico.cern.ch/event/285013/contribution/1/material/slides/0.pdf>. (Cited on page 197.)
- [327] X. M. Zhang. Private communication. (Cited on pages 198 and 199.)
- [328] I. Vitev). Non–Abelian energy loss in cold nuclear matter. *Phys. Rev. C*, 75:064906, 2007. (Cited on pages liii, liv, 217, 218, 224 and 225.)
- [329] Z. B. Kang *et al.* Multiple scattering effects on heavy meson production in p+A collisions at backward rapidity. *Phys. Lett. B*, 740:23, 2015. (Cited on pages 217 and 225.)



- [330] S. Li *et. al.* Event activity dependence of muons from heavy-flavour hadron decays in p–Pb collisions at  $\sqrt{s_{NN}} = 5.02$  TeV, <https://aliceinfo.cern.ch/Notes/node/417>. (Cited on pages 221 and 228.)
- [331] I. Helenius *et. al.* Modeling the Impact Parameter Dependence of the nPDFs With EKS98 and EPS09 Global Fits. *Nucl. Phys. A*, 910–911:510–513, 2013. (Cited on pages liv and 224.)
- [332] I. Vitev. Non–Abelian energy loss in cold nuclear matter. *Phys. Rev. C*, 75:064906, 2007. (Cited on page 225.)

# Appendix

---

## Error propagation for $Q_{\text{pPb}}$ measured as a function of event activity

For the systematic uncertainty, one can denote " $cor - p_T$ " (" $cor - cent$ ") and " $unc - p_T$ " (" $unc - cent$ ") the uncertainties that are correlated and un-correlated among  $p_T$  (event activity), respectively. The correlated uncertainties are added linearly, while the un-correlated ones are added in quadrature. All the components discussed in the thesis are summarized below.

- BG: systematic uncertainty on signal from background contribution
  - DL: decay length ( $unc - p_T, cor - cent$ );
  - CD: centrality determination via impact parameter ( $cor - p_T, unc - cent$ );
  - RM: the remaining parts ( $unc - p_T, unc - cent$ );
- MA: systematic uncertainty on mis-alignment ( $0.5\% \times p_T, cor - p_T, cor - cent$ );
- DR: systematic uncertainty on detector response ( $unc - p_T, cor - cent$ );
- NM: systematic uncertainty on normalization
  - normalization factor  $F_{\text{norm}}$  ( $unc - p_T, unc - cent$ );
  - $T_{\text{pA}}$  ( $cor - p_T, unc - cent$ );
- RF: systematic uncertainty on the pp reference
  - DR: detector response ( $unc - p_T, cor - cent$ )
  - MA: misalignment ( $1\% \times p_T, cor - p_T, cor - cent$ )
  - RS: rapidity shift effect ( $unc - p_T, cor - cent$ )
  - NM: normalization ( $cor - p_T, cor - cent$ )
  - RM: the remaining components such as background subtraction ( $unc - p_T, cor - cent$ )

$p_T$  integration procedure:

- **correlated uncertainties among  $p_T$  intervals from signal**

$$\begin{aligned} \left(\frac{\sigma_{\text{HF}}}{\text{HF}}\right)_{cor-p_T}^2 &= \left(\frac{\sigma_{\text{DL}}}{\text{HF}}\right)_{cor-p_T,cor-cent}^2 + \left(\frac{\sigma_{\text{CD}}}{\text{HF}}\right)_{cor-p_T,unc-cent}^2 \\ &+ \left(\frac{\sigma_{\text{MA}}}{\text{HF}}\right)_{cor-p_T,cor-cent}^2 + \left(\frac{\sigma_{\text{NM}}}{\text{HF}}\right)_{cor-p_T,unc-cent}^2 \end{aligned} \quad (6.10)$$

$$\begin{aligned} \left(\sigma_{\text{DL}}\right)_{\text{cor-}p_{\text{T}},\text{cor-cent}} &= \Sigma \left[ \left(\frac{\sigma_{\text{DL}}}{\text{DL}}\right)_i \times \left(\frac{\text{Bkg}}{\text{HF}}\right)_i \times \left(\text{HF}\right)_i \right] \\ &= 0.15 \times \Sigma \left[ \left(\frac{\text{Bkg}}{\text{Sig}}\right)_i \times \left(\text{Sig}\right)_i \right] \end{aligned} \quad (6.11)$$

$$\left(\sigma_{\text{CD}}\right)_{\text{cor-}p_{\text{T}},\text{unc-cent}} = \Sigma \left[ \left(\frac{\sigma_{\text{CD}}}{\text{CD}}\right)_i \times \left(\frac{\text{Bkg}}{\text{HF}}\right)_i \times \left(\text{HF}\right)_i \right] \quad (6.12)$$

$$\left(\frac{\sigma_{\text{MA}}}{\text{Sig}}\right)_{\text{cor-}p_{\text{T}},\text{cor-cent}} = 0.5\% \times p_{\text{T}}^{\text{mean}} \quad (6.13)$$

$$\left(\sigma_{\text{NM}}\right)_{\text{cor-}p_{\text{T}},\text{unc-cent}} = \Sigma \left[ \left(\frac{\sigma_{\text{NM}}}{\text{NM}}\right)_i \times \left(\text{HF}\right)_i \right] = \frac{\sigma_{\text{T}_{\text{pA}}}}{\text{T}_{\text{pA}}} \times \Sigma \left(\text{Sig}\right)_i \quad (6.14)$$

where,  $(\sigma_{\text{DL}}/\text{DL})_i$ ,  $(\sigma_{\text{CD}}/\text{CD})_i$  and  $(\sigma_{\text{NM}}/\text{NM})_i$  are the relative systematic uncertainties on decay length, centrality determination, detector response and normalization, respectively, in each  $p_{\text{T}}$  bin  $i$ , and  $(\text{Bkg}/\text{HF})_i$  is the related background to signal ratio;  $\sigma_{\text{MA}}$  denotes the systematic uncertainty on misalignment within the desired  $p_{\text{T}}$  range.

- **un-correlated uncertainties among  $p_{\text{T}}$  intervals from signal**

$$\begin{aligned} \left(\frac{\sigma_{\text{HF}}}{\text{HF}}\right)_{\text{unc-}p_{\text{T}}}^2 &= \left(\frac{\sigma_{\text{DR}}}{\text{HF}}\right)_{\text{unc-}p_{\text{T}},\text{cor-cent}}^2 + \left(\frac{\sigma_{\text{RM}}}{\text{HF}}\right)_{\text{unc-}p_{\text{T}},\text{unc-cent}}^2 \\ &+ \left(\frac{\sigma_{\text{NM}}}{\text{HF}}\right)_{\text{unc-}p_{\text{T}},\text{unc-cent}}^2 \end{aligned} \quad (6.15)$$

$$\left(\sigma_{\text{DR}}\right)_{\text{unc-}p_{\text{T}},\text{cor-cent}} = \Sigma \left[ \left(\frac{\sigma_{\text{DR}}}{\text{DR}}\right)_i \times \left(\text{HF}\right)_i \right] \quad (6.16)$$

$$\left(\sigma_{\text{RM}}\right)_{\text{unc-}p_{\text{T}},\text{unc-cent}} = \Sigma \left[ \left(\frac{\sigma_{\text{RM}}}{\text{RM}}\right)_i \times \left(\frac{\text{Bkg}}{\text{HF}}\right)_i \times \left(\text{HF}\right)_i \right] \quad (6.17)$$

$$\left(\sigma_{\text{NM}}\right)_{\text{unc-}p_{\text{T}},\text{unc-cent}} = \frac{\sigma_{\text{F}_{\text{norm}}}}{\text{F}_{\text{norm}}} \times \Sigma \left(\text{Sig}\right)_i \quad (6.18)$$

where,  $(\sigma_{\text{DR}}/\text{DR})_i$  and  $(\sigma_{\text{NM}}/\text{NM})_i$  denote the relative systematic uncertainty on detector response, normalization in each  $p_{\text{T}}$  bin  $i$ ;  $(\sigma_{\text{RM}}/\text{RM})_i$  indicates the one on signal which is obtained from the un-correlated (among  $p_{\text{T}}$ ) components affecting the background subtraction.

- **correlated uncertainties among  $p_{\text{T}}$  intervals from the pp reference**

$$\left(\frac{\sigma_{\text{Ref}}}{\text{Ref}}\right)_{\text{cor-}p_{\text{T}}}^2 = \left(\frac{\sigma_{\text{MA}}}{\text{Ref}}\right)_{\text{cor-}p_{\text{T}},\text{cor-cent}}^2 + \left(\frac{\sigma_{\text{NM}}}{\text{Ref}}\right)_{\text{cor-}p_{\text{T}},\text{cor-cent}}^2 \quad (6.19)$$

$$\left(\frac{\sigma_{\text{MA}}}{\text{Ref}}\right)_{\text{cor-}p_{\text{T}},\text{cor-cent}} = 1\% \times p_{\text{T}}^{\text{mean}} \quad (6.20)$$

$$\left(\sigma_{\text{NM}}\right)_{\text{cor-}p_{\text{T}},\text{cor-cent}} = \Sigma \left[ \left(\frac{\sigma_{\text{NM}}}{\text{NM}}\right)_i \times \left(\text{Ref}\right)_i \right] = 0.035 \times \Sigma \left(\text{Ref}\right)_i \quad (6.21)$$

where,  $\sigma_{\text{MA}}/\text{Ref}$  indicates the relative systematic uncertainty on misalignment within selected  $p_{\text{T}}$  range;  $(\sigma_{\text{NM}}/\text{NM})_i$  denotes the one on normalization in each  $p_{\text{T}}$  bin  $i$ .

- **un-correlated uncertainties among  $p_{\text{T}}$  intervals from the pp reference**

$$\begin{aligned} \left(\frac{\sigma_{\text{Ref}}}{\text{Ref}}\right)_{\text{unc-}p_{\text{T}}} &= \left(\frac{\sigma_{\text{DR}}}{\text{Ref}}\right)_{\text{unc-}p_{\text{T}},\text{cor-cent}}^2 + \left(\frac{\sigma_{\text{RS}}}{\text{Ref}}\right)_{\text{unc-}p_{\text{T}},\text{cor-cent}}^2 \\ &+ \left(\frac{\sigma_{\text{RM}}}{\text{Ref}}\right)_{\text{unc-}p_{\text{T}},\text{cor-cent}}^2 \end{aligned} \quad (6.22)$$

$$\left(\sigma_{\text{DR}}\right)_{\text{cor-}p_{\text{T}},\text{cor-cent}} = \Sigma \left[ \left(\frac{\sigma_{\text{DR}}}{\text{DR}}\right)_i \times \left(\text{Ref}\right)_i \right] = 0.05 \times \Sigma \left(\text{Ref}\right)_i \quad (6.23)$$

$$\left(\sigma_{\text{RS}}\right)_{\text{cor-}p_{\text{T}},\text{cor-cent}} = \Sigma \left[ \left(\frac{\sigma_{\text{RS}}}{\text{RS}}\right)_i \times \left(\text{Ref}\right)_i \right] = 0.03 \times \Sigma \left(\text{Ref}\right)_i \quad (6.24)$$

$$\left(\sigma_{\text{RM}}\right)_{\text{unc-}p_{\text{T}},\text{cor-cent}} = \Sigma \left[ \left(\frac{\sigma_{\text{RM}}}{\text{RM}}\right)_i \times \left(\text{Ref}\right)_i \right] \quad (6.25)$$

where,  $(\sigma_{\text{DR}}/\text{DR})_i$ ,  $(\sigma_{\text{RS}}/\text{RS})_i$  and  $(\sigma_{\text{RM}}/\text{RM})_i$  are the relative systematic uncertainties on detector response, rapidity shift effect and signal induced by the un-correlated (among  $p_{\text{T}}$ ) components in background.

When presenting the measurements as a function of event activity, one has to separate the systematic uncertainties into two parts:

- **correlated uncertainties among event activity classes from signal**

$$\begin{aligned} \left(\frac{\sigma_{\text{HF}}}{\text{HF}}\right)_{\text{cor-cent}}^2 &= \left(\frac{\sigma_{\text{DL}}}{\text{HF}}\right)_{\text{unc-}p_{\text{T}},\text{cor-cent}}^2 + \left(\frac{\sigma_{\text{MA}}}{\text{HF}}\right)_{\text{cor-}p_{\text{T}},\text{cor-cent}}^2 \\ &+ \left(\frac{\sigma_{\text{DR}}}{\text{HF}}\right)_{\text{unc-}p_{\text{T}},\text{cor-cent}}^2 \end{aligned} \quad (6.26)$$

Note that each items shown in the formula are defined already in previous parts.

- **un-correlated uncertainties among event activity classes from signal**

$$\begin{aligned} \left(\frac{\sigma_{\text{HF}}}{\text{HF}}\right)_{\text{unc-cent}}^2 &= \left(\frac{\sigma_{\text{CD}}}{\text{HF}}\right)_{\text{cor-}p_{\text{T}},\text{unc-cent}}^2 + \left(\frac{\sigma_{\text{RM}}}{\text{HF}}\right)_{\text{unc-}p_{\text{T}},\text{unc-cent}}^2 \\ &+ \left(\frac{\sigma_{\text{NM}}}{\text{HF}}\right)_{\text{cor-}p_{\text{T}},\text{unc-cent}}^2 + \left(\frac{\sigma_{\text{NM}}}{\text{HF}}\right)_{\text{unc-}p_{\text{T}},\text{unc-cent}}^2 \end{aligned} \quad (6.27)$$



- correlated uncertainties among event activity classes from the pp reference

$$\begin{aligned} \left(\frac{\sigma_{\text{Ref}}}{\text{Ref}}\right)_{\text{cor-cent}}^2 &= \left(\frac{\sigma_{\text{DR}}}{\text{Ref}}\right)_{\text{unc-pT,cor-cent}}^2 + \left(\frac{\sigma_{\text{MA}}}{\text{Ref}}\right)_{\text{cor-pT,cor-cent}}^2 \\ &+ \left(\frac{\sigma_{\text{RS}}}{\text{Ref}}\right)_{\text{unc-pT,cor-cent}}^2 + \left(\frac{\sigma_{\text{NM}}}{\text{Ref}}\right)_{\text{cor-pT,cor-cent}}^2 \\ &+ \left(\frac{\sigma_{\text{RM}}}{\text{Ref}}\right)_{\text{unc-pT,cor-cent}}^2 \end{aligned} \quad (6.28)$$

Hence, the systematic uncertainties on  $Q_{\text{pPb}}$  that are correlated and uncorrelated among event activity are calculated as,

$$\left(\frac{\sigma_{Q_{\text{pPb}}}}{Q_{\text{pPb}}}\right)_{\text{cor-cent}}^2 = \left(\frac{\sigma_{\text{HF}}}{\text{HF}}\right)_{\text{cor-cent}}^2 + \left(\frac{\sigma_{\text{Ref}}}{\text{Ref}}\right)_{\text{cor-cent}}^2 \quad (6.29)$$

$$\left(\frac{\sigma_{Q_{\text{pPb}}}}{Q_{\text{pPb}}}\right)_{\text{unc-cent}}^2 = \left(\frac{\sigma_{\text{HF}}}{\text{HF}}\right)_{\text{unc-cent}}^2 \quad (6.30)$$

$Q_{pPb}$  shown as a function of  $p_T$  using V0A/CL1/ZNA as the event activity estimator

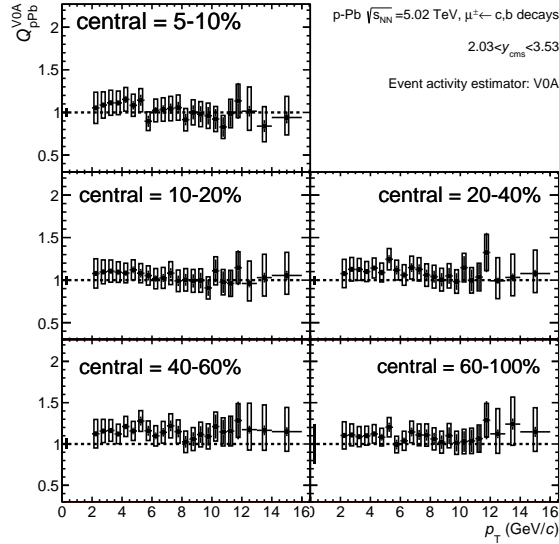


Figure 6.25:  $p_T$ -differential nuclear modification factor of muons from heavy-flavour hadron decays at forward rapidity within different event activity classes using V0A as the event estimator, in p-Pb collisions at  $\sqrt{s_{NN}} = 5.02$  TeV. Statistical uncertainties (bars) and systematic uncertainties (open boxes) are shown.

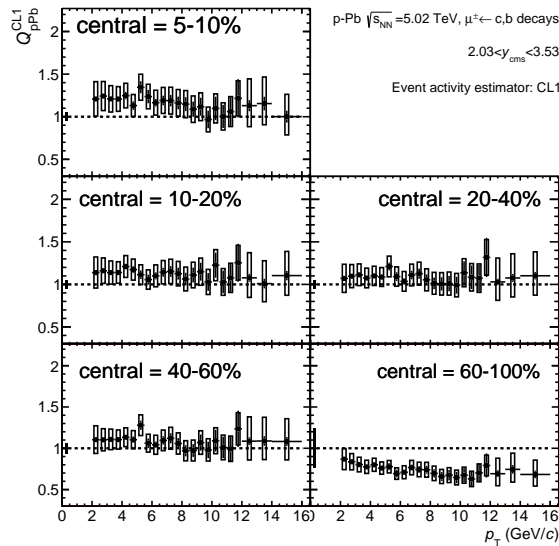


Figure 6.26: Same as Fig. 6.25 but using CL1 as the event estimator.

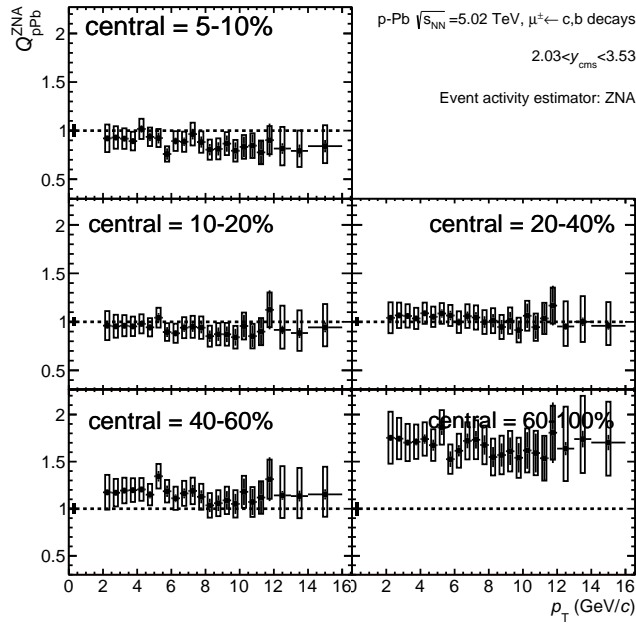


Figure 6.27: Same as Fig. 6.26 but using ZNA as the event estimator.

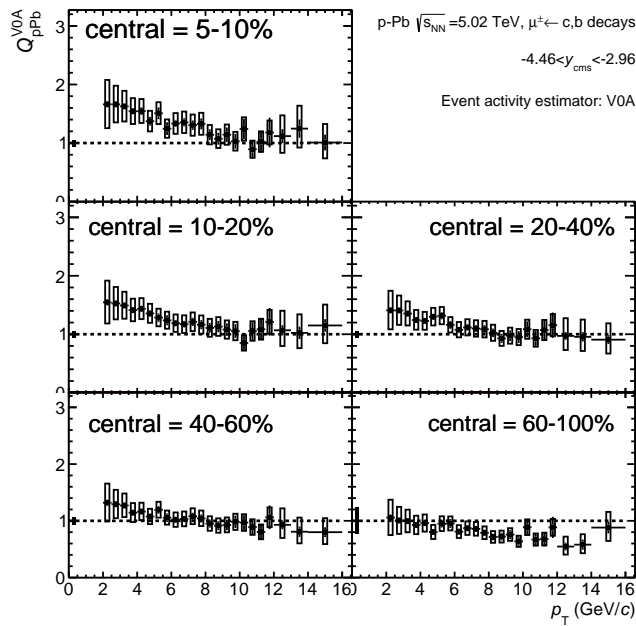


Figure 6.28: Same as Fig. 6.25 but at backward rapidity.

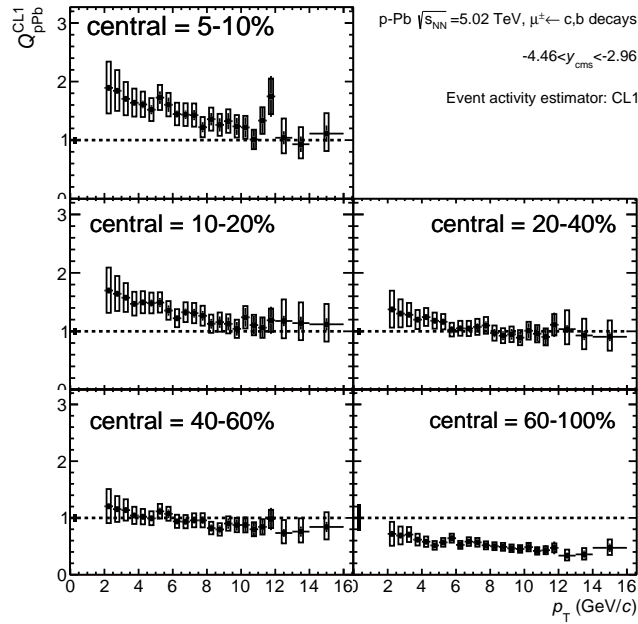


Figure 6.29: Same as Fig. 6.26 but at backward rapidity.

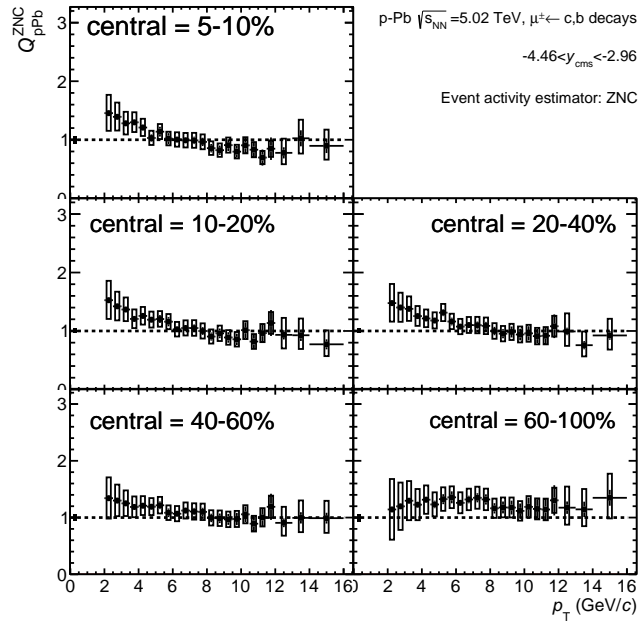


Figure 6.30: Same as Fig. 6.27 but at backward rapidity.

$Q_{pPb}$  shown as a function of event activity using V0A, CL1 and ZNA as the event activity estimators

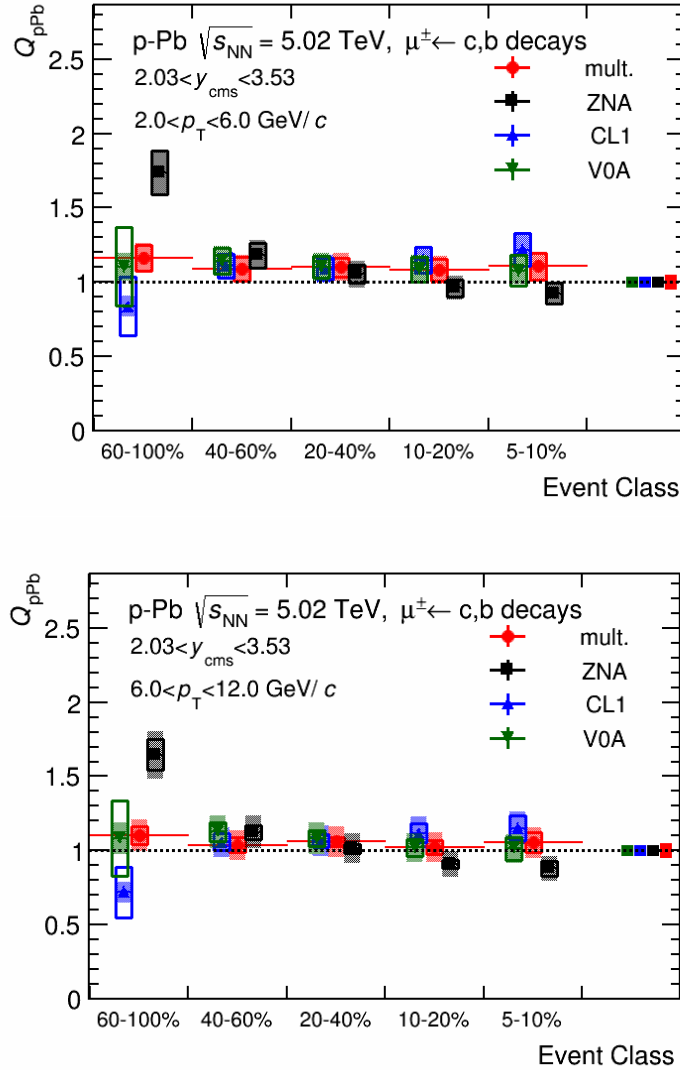


Figure 6.31: Nuclear modification factor of muons from heavy-flavour hadron decays at forward rapidity in  $2 < p_T < 6$  GeV/c (upper) and  $6 < p_T < 12$  GeV/c (bottom) as a function of event activity, in p-Pb collisions at  $\sqrt{s_{NN}} = 5.02$  TeV. The results obtained with different estimators are shown. In each panel, the open (full) boxes denote the uncertainties that are un-correlated (correlated) among event activity classes; the related statistical uncertainties shown as vertical bars are small and not visible.

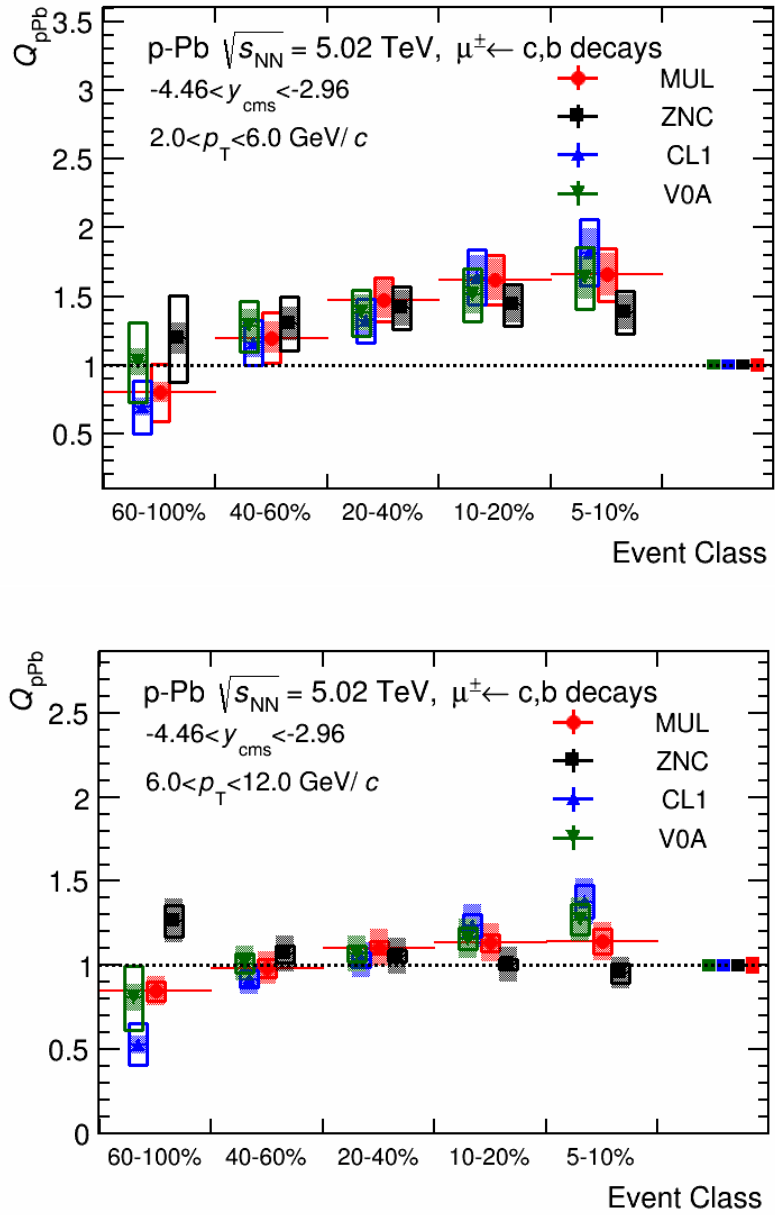


Figure 6.32: Same as Fig. 6.31 but at backward rapidity.

$Q_{FB}$  shown as a function of  $p_T$  using CL1 and ZNC as the event activity estimators

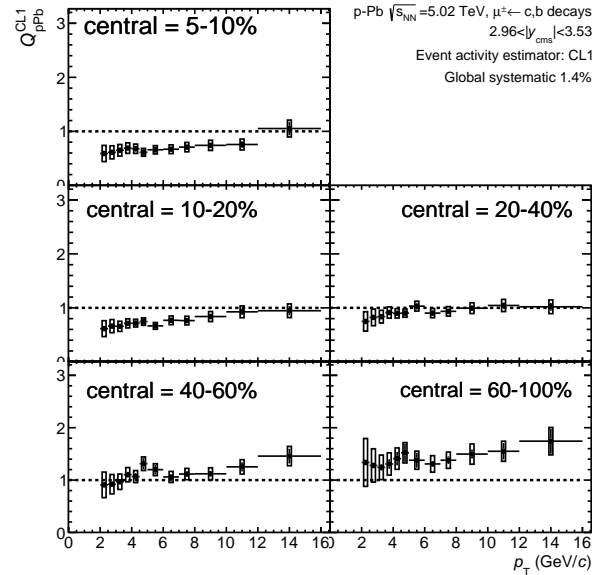


Figure 6.33: Forward-to-backward ratio of muons from heavy-flavour hadron decays in different event activity classes using CL1 as the event estimator. Statistical uncertainties (bars) and systematic uncertainties (open boxes) are shown.

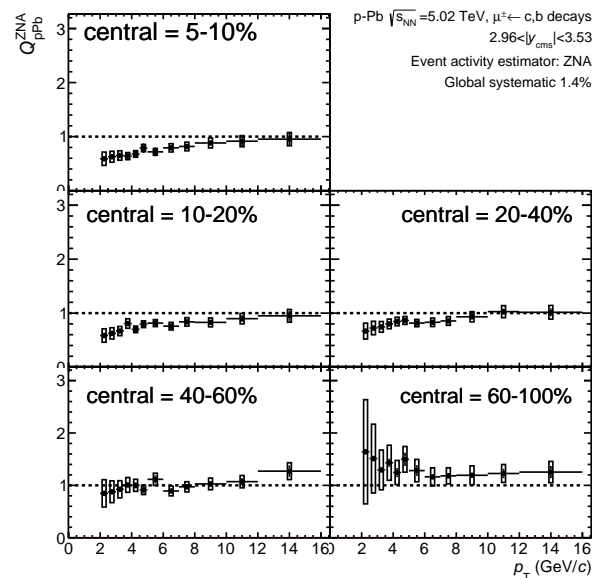


Figure 6.34: Same as Fig. 6.33 but with taking ZN as the event activity estimator.

$Q_{FB}$  shown as a event activity using CL1 and ZNC as the event activity estimators

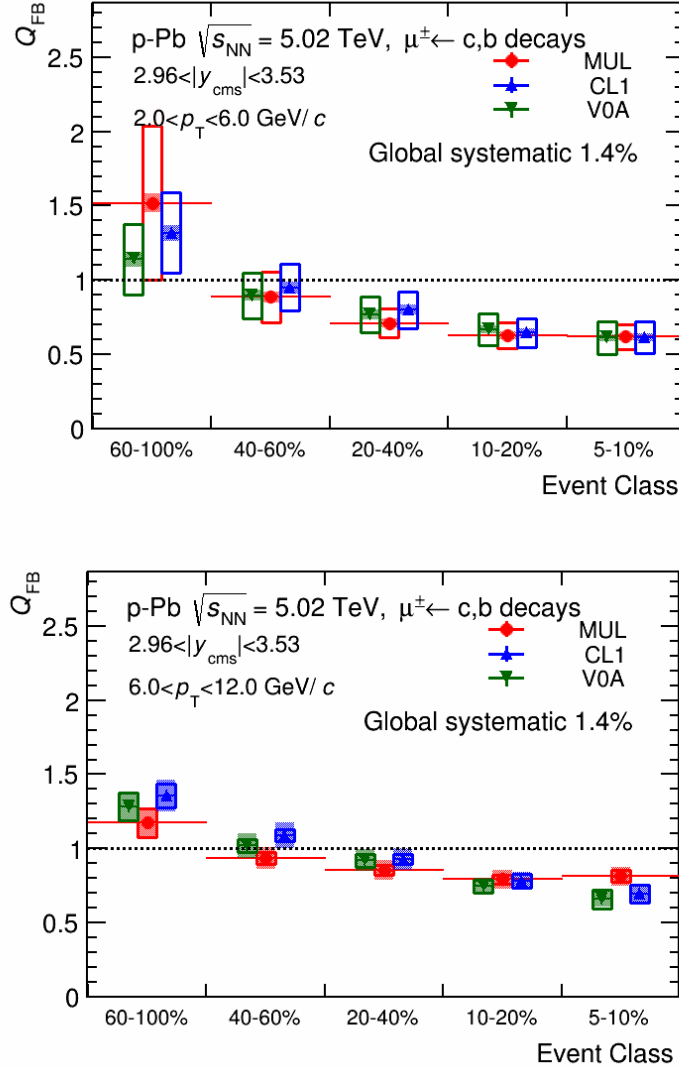


Figure 6.35: Forward-to-backward ratio of muons from heavy-flavour hadron decays in  $2 < p_T < 6$  GeV/ $c$  (upper) and  $6 < p_T < 12$  GeV/ $c$  (bottom) as a function of collision event activity, in p–Pb collisions at  $\sqrt{s_{NN}} = 5.02$  TeV. The results are obtained with various event activity estimators. The open (full) boxes denote the uncertainties that are un-correlated (correlated) among event activity classes; the related statistical uncertainties shown as vertical bars are small and not visible.



# Publication List

---

## Direct Contributions

1. S. Li as member of the ALICE Collaboration Paper Committee for the publication, **Production of muons from heavy-flavour hadron decays in p–Pb at  $\sqrt{s_{\text{NN}}} = 5.02$  TeV.**
2. S. Li for the ALICE Collaboration, **Nuclear modification factor and elliptic flow of muons from heavy-flavour hadron decays in Pb–Pb collisions at  $\sqrt{s_{\text{NN}}} = 2.76$  TeV,** *Nuclear Physics A*, **932** (2014) 32–37.
3. S. Li for the ALICE Collaboration, **Measurements of the heavy-flavour nuclear modification factor in p–Pb collisions at  $\sqrt{s_{\text{NN}}} = 5.02$  with ALICE at the LHC,** *Nuclear Physics A*, **931** (2014) 546–551.
4. S. Li, X. Zhang, Z. Zhang, N. Bastid and P. Crochet, **Production of muons from heavy-flavour hadron decays in p–Pb and Pb–p collisions at  $\sqrt{s_{\text{NN}}} = 5.02$  TeV,** *ALICE-ANA-2014-XXX* (2014).
5. F. Bossu, J. Senosi, J. Zhu, Z. Buthelezi, S. Li and D. Stocco, **Production of muons from W boson decays at forward rapidity in p–Pb collisions at  $\sqrt{s_{\text{NN}}} = 5.02$  TeV,** *ALICE-ANA-2014-XXX* (2014).
6. S. Li and S. Feng, **Gluon Saturation Model with Geometric Scaling for Net-Baryon Distributions in Relativistic Heavy Ion Collisions,** *Plasma Science and Technology*, **14** (2012) No.7.
7. S. Li and S. Feng, **Gluon saturation and baryon stopping in the SPS, RHIC, and LHC energy regions,** *Chinese Physics C*, **36** (2011) 136–141.

## As Member of the ALICE Collaboration

116 publications from January 2013 to June 2015.



# Presentation List

---

## Oral presentations at Conferences and Workshops

1. "Muons from heavy-flavour hadron decays in p–Pb collisions at  $\sqrt{s_{\text{NN}}} = 5.02$  TeV", ALICE MUON Meeting, 25–29 May, 2015, Chia, Italy
2. "Nuclear modification factor of muons from heavy-flavour hadron decays with new theoretical predictions", Physics Forum, 12 November, 2014, CERN, Switzerland
3. "Muons from open heavy-flavour decays in p–Pb collisions at  $\sqrt{s_{\text{NN}}} = 5.02$  TeV with ALICE", Rencontres QGP-France, 15-18 September, 2014, Etretat, France
4. "Measurements of the heavy-flavour nuclear modification factor in p–Pb collisions at  $\sqrt{s_{\text{NN}}} = 5.02$  TeV with ALICE at the LHC", Quark Matter 2014-XXIV International Conference on Ultrarelativistic Nucleus-Nucleus Collisions, 19-24 May, 2014, Darmstadt, Germany
5. "Production of muons from heavy-flavour hadron decays in p–Pb collisions at  $\sqrt{s_{\text{NN}}} = 5.02$  TeV", Physics Forum, 6 May, 2014, CERN, Switzerland
6. "Production of muons from heavy-flavour hadron decays in p–Pb collisions at  $\sqrt{s_{\text{NN}}} = 5.02$  TeV with ALICE", 7th France China Particle Physics Laboratory (FCPPL) WorkShop, 8-10 April, 2014, Clermont-Ferrand, France
7. "Nuclear modification factor and elliptic flow of muons from heavy-flavour decays in Pb-Pb collisions at  $\sqrt{s_{\text{NN}}} = 2.76$  TeV with ALICE", 6th International Conference on Hard and Electromagnetic Probes of High-Energy Nuclear Collisions (M. Gines on behalf of S. Li), 4-8 November, 2013, Cape Town, South Africa
8. "Production of muons from heavy-flavour decays in p–Pb and Pb–p collisions at  $\sqrt{s_{\text{NN}}} = 5.02$  TeV", ALICE Physics Week, 15 October, 2013, Wuhan, P. R. China
9. "Muons from open heavy-flavour decays in pp, Pb-Pb and p-Pb collisions with ALICE", Rencontres QGP-France, 9-12 September, 2013, Etretat, France
10. "Heavy-flavour decay muons in p-Pb Collisions at  $\sqrt{s_{\text{NN}}} = 5.02$  TeV", Physics Forum, 8 July, 2013, CERN, Switzerland
11. "Production of muons from heavy-flavour decays in p–Pb and Pb–p collisions at  $\sqrt{s_{\text{NN}}} = 5.02$  TeV", Physics Forum, 17-21 June, 2013, CERN, Switzerland



12. "Production of muons from heavy-flavour decays in p–Pb collisions at  $\sqrt{s_{NN}} = 5.02$  TeV", ALICE Physics Week, 19-24 May, 2013, Padova, Italy
13. "Single muons in p–Pb and Pb–p collisions at  $\sqrt{s_{NN}} = 5.02$  TeV", MUON Workshop, 9 May, 2013, Barolo, Italy
14. "W $\rightarrow\mu$  analysis at forward rapidity in Pb–Pb Collisions at  $\sqrt{s_{NN}} = 2.76$  TeV with ALICE", ALICE Physics Week, 27 November-1 December, 2012, Puebla, Mexico
15. "Production of W in pp collisions: simulation results", MUON Workshop, 30 April-5 May, 2012, Cape Town, South Africa

## ALICE Physics Working Group (PWG) and Physics Analysis Group (PAG)

~ 95 presentations from March 2012 to August 2015.

# Acknowledgments

---

To all the people I am indebted for the work shown in this thesis.

I would like to extend my gratitude to all my supervisors, Daicui Zhou at IOPP Wuhan in China, Nicole Bastid and Philippe Crochet at LPC Clermont-Ferrand, for the patient guiding and helpful discussions during the past four years. I gained a lot concerning their experience and personal ability for the data analysis. A big thanks goes to all of them for carefully reading the manuscript and valuable suggestions. Moreover, Nicole and Philippe provide endless help to my family when we are at Clermont-Ferrand.

Thanks to the whole ALICE Group at Wuhan for providing the chance for me to be involved in the program of France China Particle Physics Laboratory (FCPPL). I would like to thank X. Cai, Z.-B. Ying, Y.-X. Mao, H. Pei and D. Wang who gave a lot suggestions for the studies.

Thanks to the whole ALICE Group at LPC for the welcome and support, in particular to P. Dupieux, X. Lopez, F. Manso, S. Porteboeuf–Houssais, P. Rosnet, B. Vulpescu and L. Valencia–Palomo for useful suggestions and fruitful discussions.

I am grateful to X.-M. Zhang who raises me up with encouragement when I shift to the experimental study. Thank you very much for lot of discussions even through the nights. Also, thanks to him for providing the template of this manuscript.

I am also grateful to F. Antinori, R. Averbeck, Z. Conese del Valle, A. Dainese, S. Grigoryan, L. Manceau, G. Martinez, A. Morsch, P. Pillot, A. Rossi, J. Schukraft, D. Stocco, A. Uras for many suggestions of the analysis. Thanks to F. Prino for the carefully reading and valuable suggestions of this manuscript.

To my friends in the same office R.-N. Dang, J.-B. Luo, W.-Z. Luo, X.-Y. Peng, X.-W. Ren, M.-L. Wang, H.-T. Zhang, Y.-H. Zhang, Z.-M. Zhang, H.-S. Zhu, J.-H. Zhu, X.-R. Zhu for the help in my routine life.

A special thanks to my parents, my sister family and my girls. Without your support, I cannot stand here. You are all my best love.

My warmest thanks should be given to Juliette for taking care of Yang and Emma. "You are the angel in our lives". Thank you.

Shuang Li  
June 10, 2015  
Clermont-Ferrand



## Résumé

Les collisions d'ions lourds au LHC permettent l'étude des propriétés de la matière nucléaire soumise à des conditions extrêmes de température et densité d'énergie où on assisterait à la formation du Plasma de Quarks et Gluons (QGP). La mesure des saveurs lourdes ouvertes (charme et beauté) est particulièrement intéressante pour l'étude des propriétés du QGP. L'étude des collisions d'ions lourds au LHC nécessite aussi la mesure des collisions pp et p-Pb. Les collisions p-Pb permettent en particulier d'étudier les effets nucléaire froids et d'interpréter les effets nucléaires chauds observés dans les collisions Pb-Pb. Cette thèse est dédiée à l'étude de la production des saveurs lourdes ouvertes via les muons simples dans les collisions p-Pb à  $\sqrt{s_{NN}} = 5.02$  TeV aux rapidités avant et arrière avec le détecteur ALICE au LHC. La référence pp est estimée à partir des mesures pp à  $\sqrt{s} = 2.76$  TeV et 7 TeV et utilisant des calculs pQCD pour l'extrapolation à  $\sqrt{s} = 5.02$  TeV. Les mesures du facteur de modification nucléaire ( $R_{pPb}$ ) et du rapport des sections efficaces aux rapidités avant et arrière indiquent que les effets nucléaires froids sont faibles sur tout le domaine en impulsion transverse ( $p_T$ ) aux rapidités avant ( $R_{pPb} \simeq 1$ ). Aux rapidités arrière, le facteur de modification nucléaire est sensiblement plus grand que un dans la région  $2 < p_T < 4$  GeV/c. Les résultats confirment que la forte suppression des taux de production des muons issus du charme et de la beauté mesurée dans les collisions centrales Pb-Pb est due au milieu dense et chaud. Le facteur de modification nucléaire et le rapport des sections efficaces aux rapidités avant et arrière sont aussi mesurés en fonction de la centralité dans les collisions p-Pb. Le facteur de modification nucléaire reste compatible avec l'unité à grand  $p_T$  dans les collisions centrales.

Mots-clés: LHC, expérience ALICE, collisions p-Pb, matière nucléaire froide, facteur de modification nucléaire, rapport des sections efficaces aux rapidités avant et arrière, pQCD.

## Abstract

The LHC heavy-ion physics program aims at investigating the properties of strongly-interacting matter in extreme conditions of temperature and energy density where the Quark-Gluon Plasma (QGP) is formed. In high-energy heavy-ion collisions, heavy quarks (charm and beauty) are regarded as efficient probes of the properties of the QGP. The heavy-ion physics program requires also the study of proton-proton (pp) and proton-nucleus (p-Pb) collisions. The study of p-Pb collisions is used to investigate cold nuclear matter effects and to validate and quantify hot nuclear matter effects which are observed in nucleus-nucleus (Pb-Pb) collisions. This thesis work is devoted to the study of open heavy-flavour production at forward and backward rapidity via single muons in p-Pb collisions at  $\sqrt{s_{NN}} = 5.02$  TeV with the ALICE experiment at the LHC. The pp reference using available measurements at 2.76 and 7 TeV and a pQCD-driven method for the scaling to 5.02 TeV is estimated. The measurements of the nuclear modification factor ( $R_{pPb}$ ) at forward and backward rapidity and forward-to-backward ratio in p-Pb collisions, indicate that cold nuclear matter effects are small over the whole transverse momentum ( $p_T$ ) region at forward rapidity ( $R_{pPb}$  compatible with unity within uncertainties). In the backward rapidity, the nuclear modification factor deviates from unity in the intermediate  $p_T$  region ( $2 < p_T < 4$  GeV/c). These results confirm that the strong suppression measured at high  $p_T$  in central Pb-Pb collisions is due to final-state effects induced by the hot and dense nuclear medium. The results of the nuclear modification factor and forward-to-backward ratio as a function of centrality in p-Pb collisions are discussed. Even in central collisions, the nuclear modification factor is compatible with unity at high  $p_T$ .

Keywords: LHC; ALICE experiment; p-Pb collisions; single muons; cold nuclear matter; nuclear modification factor; forward-to-backward ratio; pQCD

